Finanziato dall'Unione europea NextGenerationEU

Ministero dell'Università e della Ricerca

Italiadomani PIANO NAZIONALE DI RIPRESA E RESILIENZA

UNIVERSITÀ DEGLI STUDI FIRENZE Da un secolo, oltre.

DOTTORATO DI RICERCA IN

SCIENZE CHIMICHE

CICLO XXXVIII - PNRR NextGenerationEU

Structural and kinetic characterization of dual-target Carbonic Anhydrase inhibitors for therapeutic use as anticancer agents

Settore Scientifico Disciplinare

CHEM-03 /A

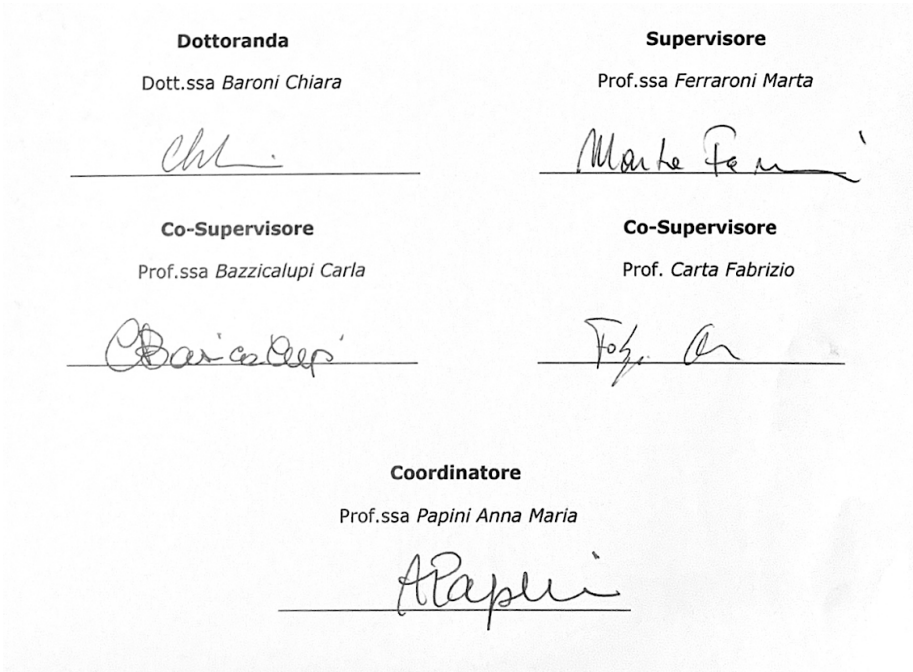

Dipartimento di Chimica 'Ugo Schiff'

Corso di Dottorato in Scienze Chimiche
Ciclo XXXVIII

Structural and kinetic characterization of dual-target Carbonic Anhydrase inhibitors for therapeutic use as anticancer agents

Candidate

Chiara Baroni (ID number DT31785)

Thesis Advisor

Prof. Marta Ferraroni

Co-Advisors

Prof. Carla Bazzicalupi
Prof. Fabrizio Carta

Academic Year 2024/2025

A Federico

Contents

Abstract **1**

1 Introduction **6**

1.1 Polypharmacology in Cancer Therapy 6

1.2 Carbonic Anhydrase 8

1.2.1 hCA structures 9

1.2.2 The catalytic reaction 10

1.2.3 pH regulation in tumor cells: coordinated role of hCAs and transporters 13

1.2.4 hCA IX 15

1.2.5 hCA XII 17

1.2.6 hCA inhibitors (hCAIs) 18

1.3 Histone Deacetylase 21

1.3.1 Class I HDAC structures and drug design 22

1.3.2 The catalytic reaction 24

1.3.3 HDAC complexes 25

2 Methods **29**

2.1 Protein x-ray Crystallography 29

2.1.1 Introduction 29

2.1.2 Crystallization process 29

2.1.3 Crystal symmetry and diffraction theory 32

2.1.4 Cryo-crystallography and data collection 34

2.1.5 The phase problem 36

2.1.6 From the electron density to model 38

2.2 Cryogenic electron microscopy (cryo-EM) 40

2.2.1 Cryo-EM as a structural biology method 40

2.2.2 Electron microscope 41

2.2.3 Sample preparation 43

2.2.4 Image formation . . . 45
2.2.5 Data collection . . . 47
2.2.6 Data processing . . . 48

3 Design and evaluation of compounds targeting carbonic anhydrase and histone deacetylase 52
3.1 Introduction . . . 52
3.2 Results . . . 55
3.2.1 *In vitro* hCA Inhibition assay . . . 55
3.2.2 Crystallographic studies . . . 58
3.2.3 Design of Novel Inhibitors . . . 63
3.2.4 *In vitro* hCA Inhibition assay on new dual-target compounds 65
3.2.5 *In vitro* HDAC inhibition assay . . . 66
3.3 Discussion and Conclusion . . . 73
3.4 Materials and Methods . . . 76

4 Cryo-EM studies of the PG Domain in the Anticancer Target Carbonic Anhydrase IX 86
4.1 Introduction . . . 86
4.2 Results . . . 88
4.2.1 Cryo-EM data of free hCA IX and hCA IX in complex with c11H9 and c2C7 antibodies . . . 88
4.2.2 Mass photometry results . . . 90
4.2.3 Cryo-EM data of hCA IX/c11H9 complex at a 1:2 molar ratio . . . 93
4.3 Discussion and Conclusion . . . 94
4.4 Materials and Methods . . . 95

5 Lasamide, a Potent Human Carbonic Anhydrase Inhibitor from the Market: Inhibition Profiling and Crystallographic Studies 97
5.1 Summary . . . 97

6 X-ray crystallographic and kinetic studies of biguanide containing aryl sulfonamides as carbonic anhydrase inhibitors 103
6.1 Summary . . . 103

7 O-derivatization of natural tropolone and β-thujaplicin leading to effective inhibitors of human carbonic anhydrases IX and XII 108
7.1 Summary . . . 108

Bibliography 116

Abstract

The onset and progression of tumor growth involve numerous aberrant proteins and signaling pathways, highlighting the complexity of developing effective therapies. While single-target approaches frequently face limitations, polypharmacology has emerged as a promising strategy to overcome drug resistance and improve therapeutic outcomes.
Human Carbonic Anhydrases (hCAs) are a family of metalloenzymes involved in multiple metabolic pathways. Consequently, alterations in their expression or activity are associated with several pathological conditions, including cancer. Notably, the membrane-bound isoforms IX and XII are recognized as solid tumor markers, being overexpressed in various cancer cell lines.
This Ph.D. project focused on the application of structural biology techniques, with particular emphasis on X-ray crystallography, to support structure-based drug design aimed at improving the efficacy and selectivity of hCA dual-target anticancer inhibitors. The designed compounds integrate the classical pharmacophore of hCA inhibitors, the sulfonamide zinc-binding group, with additional pharmacophores exhibiting antitumor activity.

A significant part of the work focused on the development and characterization of a series of dual-target compounds that integrate the classical zinc binding groups of hCA and histone deacetylase (HDAC) inhibitors (the sulfonamide and benzamide groups, respectively). This strategy has shown a pronounced synergistic effect in several previous studies, highlighting its potential relevance in cancer therapy.
The thesis presents the X-ray crystallographic characterization of the dual-target inhibitors in complex with representative hCA isoforms and their inhibition profiles. Inhibition potency was further evaluated against HDAC1 and HDAC3 corepressor complexes, multiprotein assemblies regulating the biological functions and activity of HDACs. The structural insights, the inhibition data, and the molecular docking analyses aimed at elucidating binding modes of the

compounds within the HDACs active site guided the structure-based design and synthesis of novel derivatives. The initial series of dual-target inhibitors exhibited limited selectivity for cancer-related hCA isoforms but good inhibition potency against the HDAC complexes. In contrast, newly synthesized derivatives showed enhanced efficacy against both cancer-associated hCA isoforms and the HDAC complexes.

Moreover, other enzymatic pathways were explored, including the study of dual inhibitors obtained through the combination of the zinc-binding sulfonamide moiety of hCA inhibitors with the biguanide group of metformin, an antidiabetic and emerging anticancer drug. The study showed strong inhibition and remarkable selectivity of these derivatives against the hCA cancer-related isoforms and clarified the molecular determinants of the inhibitor-protein interactions. Additionally, Lasamide, a synthetic precursor and contaminant in Furosemide synthesis, and O-functionalized derivatives of Tropolone and β-Thujaplicin were investigated to evaluate their inhibitory efficacy against hCA enzymes and binding mode for future structure-based optimization.

At the same time, cryo-electron microscopy (cryo-EM) was applied to investigate the structural organization of the full extracellular domain (ECD) of the tumor-associated hCA IX, including the catalytic and the proteoglycan-like (PG) domain. Among the hCA family, the PG domain is unique to hCA IX, and it has been postulated to play a crucial role in modulating the catalytic activity of the enzyme. However, only the catalytic hCA IX domain has been structurally characterized using X-ray diffraction analysis, as the crystallization of the hCA IX ECD has proven particularly challenging.
Preliminary data were obtained that likely will help future studies aimed at determining the structure of the whole ECD of hCA IX, contributing to the understanding of the various pathophysiological processes in which this unique enzyme is involved and improving structure-based strategies for the development of more selective and effective hCA IX anticancer inhibitors.

Overall, this work combined different structural biology techniques with functional analysis, mainly to evaluate and improve the inhibition profile of hCA dual-target inhibitors. The results will provide insights for the rational design of next-generation multitarget anticancer agents.

Italian version

L'insorgenza e la progressione della crescita tumorale coinvolgono numerose proteine aberranti e vie di segnalazione, evidenziando la complessità nello sviluppo di terapie efficaci. Mentre gli approcci a bersaglio singolo incontrano spesso limitazioni, la polifarmacologia è emersa come una strategia promettente per superare la resistenza ai farmaci e migliorare gli effetti terapeutici.
Le Anidrasi Carboniche umane (hCA) sono una famiglia di metalloenzimi coinvolti in molteplici vie metaboliche. Di conseguenza, alterazioni nella loro espressione o attività sono associate a diverse patologie, incluso il cancro. In particolare, le isoforme transmembrana IX e XII sono riconosciute come marcatori dei tumori solidi, essendo sovraespresse in varie linee cellulari tumorali.
Questo progetto di dottorato si è concentrato sull'applicazione di tecniche di biologia strutturale, con particolare attenzione alla cristallografia a raggi X, per supportare la progettazione razionale di farmaci volta a migliorare l'efficacia e la selettività di inibitori duali antitumorali delle hCA. I composti progettati integrano il farmacoforo classico degli inibitori di hCA, il gruppo sulfonamidico legante lo zinco, con ulteriori farmacofori caratterizzati da attività antitumorale.

Una parte significativa del lavoro si è concentrata sullo sviluppo e la caratterizzazione di una serie di composti dual-target che integrano i farmacofori classici degli inibitori di hCA e delle Istone Deacetilasi (HDAC) (rispettivamente il gruppo sulfonamidico e benzamidico). Questa strategia ha mostrato in studi precedenti un pronunciato effetto sinergico, sottolineandone la potenziale rilevanza nella terapia del cancro.
La tesi presenta la caratterizzazione cristallografica a raggi X degli inibitori duali in complesso con isoforme rappresentative delle hCA, insieme ai loro profili di inibizione. L'attività inibitoria è stata inoltre valutata nei confronti di complessi corepressori di HDAC1 e HDAC3, assemblaggi multiproteici che regolano le funzioni biologiche e l'attività di tali enzimi. Inoltre, i dati strutturali, i dati di inibizione e le analisi di docking molecolare finalizzate a chiarire i modi di legame dei composti nel sito attivo delle HDAC hanno guidato la progettazione e la sintesi di nuovi derivati. La prima serie di inibitori duali ha mostrato una selettività limitata verso le isoforme di hCA correlate al cancro, ma una buona potenza inibitoria nei confronti dei complessi di HDAC. Al contrario, i nuovi derivati hanno mostrato una migliore efficacia sia contro le isoforme associate al cancro delle hCA che contro i complessi delle HDAC.

Inoltre, sono state esplorate altre vie enzimatiche, incluso lo studio di in-

ibitori duali ottenuti combinando la porzione sulfonamidica legante lo zinco degli inibitori di hCA con il gruppo biguanide della metformina, un farmaco antidiabetico ed emergente come agente antitumorale. Lo studio ha evidenziato una forte inibizione e una notevole selettività di questi derivati verso le isoforme hCA correlate al cancro, chiarendo i determinanti molecolari delle interazioni inibitore-proteina.
Ulteriori studi hanno riguardato la Lasamide, un precursore sintetico e contaminante nel processo di sintesi della Furosemide, e i derivati O-funzionalizzati del Tropolone e del β-Thujaplicin per valutarne l'efficacia inibitoria sulle hCA e il loro modo di legame, in vista di future ottimizzazioni basate sulla struttura.

Parallelamente, la crio-microscopia elettronica (cryo-EM) è stata applicata per indagare l'organizzazione strutturale dell'intero dominio extracellulare (ECD) dell'isoforma IX delle hCA, comprendente il dominio catalitico e quello proteoglicano-simile (PG). Tra le isoforme delle hCA, il dominio PG è caratteristico della hCA IX e si ipotizza che svolga un ruolo cruciale nella modulazione dell'attività catalitica dell'enzima. Tuttavia, solo il dominio catalitico di hCA IX è stato caratterizzato strutturalmente tramite diffrazione a raggi X, poiché la cristallizzazione dell'ECD si è rivelata particolarmente complessa.
Dati preliminari ottenuti potrebbero supportare studi futuri volti a determinare la struttura dell'intero ECD di hCA IX, contribuendo alla comprensione dei processi patofisiologici in cui questo enzima è coinvolto e migliorando le strategie di design razionale per sviluppare inibitori antitumorali più selettivi ed efficaci.

Complessivamente, questo lavoro ha combinato diverse tecniche di biologia strutturale con analisi funzionali, principalmente per valutare e migliorare il profilo inibitorio degli inibitori duali delle hCA. I risultati forniranno informazioni per la progettazione razionale di agenti antitumorali multitarget di nuova generazione.

This thesis is based on the following publications:

- Melfi, F., D'Agostino, I., Carradori, S., Carta, F., Angeli, A., Costa, G., Renzi, G., Čikoš, A., Vullo, D., Rešetar, J., Ferraroni, M., Baroni, C., Mancuso, F., Gitto, R., Ambrosio, F. A., Marchese, E., Torcasio, R., Amodio, N., Capasso, C., Alcaro, S., Supuran, C. T. O-derivatization of natural tropolone and β-thujaplicin leading to effective inhibitors of human carbonic anhydrases IX and XII. Eur. J. Med. Chem. 2025, 290, 117552. DOI: 10.1016/j.ejmech.2025.117552

- Baroni, C., Bozdag, M.; Renzi, G.; De Luca, V.; Capasso, C.; Bazzicalupi, C.; Selleri, S.; Ferraroni, M.; Carta, F.; Supuran, C. T. X-ray crystallographic and kinetic studies of biguanide containing aryl sulfonamides as carbonic anhydrase inhibitors. RSC Med. Chem. 2025, 16 (4), 1633–1640. DOI: 10.1039/D4MD01018C.

- Baroni, C., D'Agostino, I.; Renzi, G.; Kilbile, J. T.; Tamboli, Y.; Ferraroni, M.; Carradori, S.; Capasso, C.; Carta, F.; Supuran, C. T. Lasamide, a Potent Human Carbonic Anhydrase Inhibitor from the Market: Inhibition Profiling and Crystallographic Studies. ACS Med. Chem. Lett. 2024, 15 (10), 1749–1755. DOI: 10.1021/acsmedchemlett.4c00341.

1 Introduction

1.1 Polypharmacology in Cancer Therapy

Cancer is a complex and multifactorial disorder that results from the simultaneous action of various gene alterations along with the influence of multiple environmental factors [1]. Those conditions lead cells to abnormal and uncontrolled proliferation, which can sometimes spread to other areas of the body through the systemic circulation and lymphatic system, causing metastasis. Initially, conventional cancer treatments, such as radiotherapy and chemotherapy, aimed to interfere with rapid cell growth without effectively distinguishing between tumors and healthy cells, causing a wide range of side effects and toxicity [2, 3]. To overcome these issues, targeted therapy has become a more attractive method for the treatment of cancer, since it allows achieving selective actions with specific cell molecules involved in carcinogenesis and tumor growth [3]. For years, pharmaceutical research has focused on the development of single-target drugs to selectively direct the pharmaceutical effect on a specific target, such as genes or proteins, to prevent problems related to "off-target" interactions [4, 5]. However, single-target therapy may not always achieve the desired effect due to the emergence of drug resistance, such as the expression of drug pumps, the alteration of targets, the inactivation of drugs, or the adaptation of new growth pathways by cancer cells [6, 7, 8]. Moreover, since the onset and progression of tumor growth simultaneously involve different types of aberrant proteins and signaling pathways, directing therapy against a single target may not be sufficient to treat the problem [2]. From this point of view, multi-target drugs provide many advantages over the single-target approach. A multi-target drug is a single therapeutic agent in which different pharmacophores are combined within the same molecular structure, allowing the compound to interact with two or more biological targets [9]. This structural integration enables a more effective therapeutic action, resulting from a synergistic strategy that is suitable for complex and multifactorial disorders such as cancer. Moreover, altering

different pathways at the same time reduces the possibility of drug resistance outcome, as targeted cells cannot restore all affected pathways simultaneously [9, 10, 11]. Multi-target treatment should not be confused with combination therapy, which is based on the parallel administration of two or more active agents. This approach has some significant limitations, such as the interaction between drugs, leading to variability in drug exposure and, as a result, to drug overdose or undertreatment effects, with serious clinical consequences. Therefore, toxic side effects and poor patient compliance are common problems with combination therapy [12]. Instead, multi-target treatment improves patient compliance by simplifying dosing regimens, reducing drug-drug interactions, and providing more predictable pharmacokinetics [13]. Consequently, it is recognized as a promising strategy for the treatment of cancer, as it provides multiple benefits in treatment, leading to improved overall survival with reduced side effects for patients [2].

1.2 Carbonic Anhydrase

CAs are a family of zinc metalloenzymes that catalyze the reversible hydration of carbon dioxide to bicarbonate ions and protons through a metal/hydroxide mechanism [14].

$$CO_2 + H_2O \leftrightarrows HCO_3^- + H^+$$

Eight genetically unique classes have been identified, the α-, β-, γ-, δ-, ζ-, η-, θ-, and ι-classes [15, 16, 17, 18, 19, 20, 21]. CA classes display a heterogeneous distribution across organisms. Mammals uniquely encode α-CAs [22, 14, 23, 24, 25], whereas plants possess both α- and β-CAs [26]. Bacteria, Archaea, and cyanobacteria contain α-, β-, γ-, and ι-CAs [26, 22, 27, 28, 29, 30, 31], while marine diatoms encode α-, δ-, ζ-, θ-, and ι-CAs [32, 33, 34]. In protozoa, α-, β-, and η-CAs have been detected, with the recently discovered η-class likely playing a key role in *de novo* purine and pyrimidine biosynthesis [35]. Within fungi, the β-CA class is predominant. However, many filamentous ascomycetes harbor multiple β-CA genes and may additionally encode α-CAs [36, 37, 38].
All CAs are metalloenzymes whose catalytic activity depends on a metal ion within the active site [27, 28, 29, 31]. Three amino-acid residues coordinate the catalytic metal ion: typically three histidines in the α-, γ-, δ-, and likely θ-classes; one histidine and two cysteines in β- and ζ-CAs; and two histidines and one glutamine in η-CAs [39]. Simultaneously, a water molecule or hydroxide ion serves as the fourth ligand and acts as the nucleophile during catalysis [27, 28, 31, 14, 40, 41].
Although Zn^{2+} is the predominant cofactor for α-, β-, δ-, η-, and possibly θ-CAs, some classes can bind alternative metal ions such as Co^{2+}, Cd^{2+}, or Fe^{2+}. Notably, γ-CAs are typically Fe^{2+}-dependent but can also coordinate Zn^{2+} or Co^{2+}, while ζ-CAs function with either Cd^{2+} or Zn^{2+} and are therefore classified as cambialistic enzymes [25, 42, 43, 44, 45, 46, 47, 48, 49, 50, 51].
Structurally, the α-CAs are usually active as monomers or dimers, β-CAs as dimers, tetramers or octamers, while γ-CAs must form trimers to achieve catalytic activity [43, 44, 47, 52]. γ-CA monomers contain a tandemly repeated hexapeptide essential for the left-handed fold of the trimeric β-helix structures [53]. Structural studies show that θ-CAs closely resemble some β-CAs, while the crystal structure of ζ-CAs reveals three practically identical repeats in a single polypeptide chain [51]. By contrast, no structural information is yet available for the δ- and η-CA classes [15].

As mentioned above, the human CAs (hCAs) belong to the α-class. In particular, humans express 15 α-CAs that differ in catalytic efficiency, subcellular/tissue localization, quaternary structure, and physiological role [54]. Human α-CA isoforms can be subdivided into cytosolic CAs (CA-I, CA-II, CA-III, CA-VII and CA XIII), mitochondrial CAs (CA-VA and CA-VB), secreted CAs (CA-VI), membrane-associated (CA-IV, CA-IX, CA-XII and CA-XIV) and those without CA activity: the CA-related proteins (CARP VIII, X and XI) [22, 54]. The catalytic inactivity of CARPs is related to the lack of essential histidine residues, which coordinate the catalytic zinc ion within the active site [55].
Notably, hCA II is a highly abundant cytosolic isoform and the most extensively investigated member of the hCA family.

1.2.1 hCA structures

To date, the three-dimensional crystal structures of the catalytic domains of all catalytically active hCAs have been determined [56, 57, 58, 59, 60], except for the mitochondrial hCA VA and VB isoforms, for which the corresponding murine enzyme, mCAV, has been characterized [61].
Due to their high sequence identity, all hCAs share a highly conserved structure, characterized by a central ten-stranded β-sheet core, surrounded by α- and 3_{10}-helices, and additional β-strands [62] (figure 1.1, panel A).

The active site is displaced within a conical cavity, in which the catalytic zinc ion is tetra-coordinated with three conserved histidines together with a solvent molecule or hydroxide ion (figure 1.1, panel A). Notably, the catalytic site is divided into two parts, the hydrophobic and hydrophilic regions (figure 1.1, panel B). The hydrophobic site contains the residues involved in CO_2 binding, while the hydrophilic part presents a set of residues useful for proton transfer during the catalytic reaction [63, 64, 65].

Although structural elements are very well conserved, quaternary structure differences can be identified. Indeed, while hCAs I-IV, VA, VB, VII, XIII, and XIV occur as monomers, hCAs VI, IX, and XII are dimers [62]. Moreover, the main sequence variations within the active sites are located in the region 125-136 [66, 67], which is considered an important site for achieving selectivity in drug design.

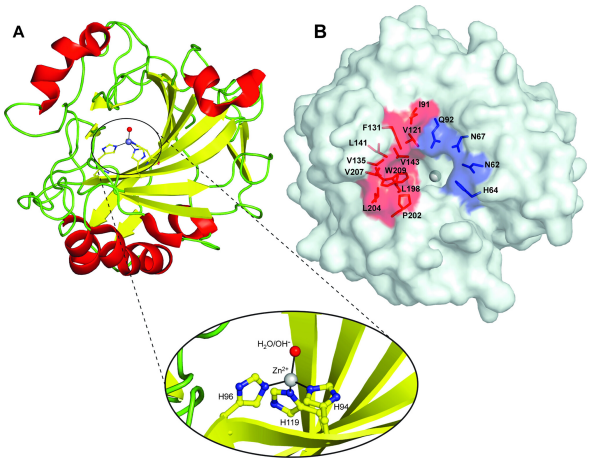

Figure 1.1. A) Ribbon diagram of hCA II (PDB code 1CA2), selected as a representative hCA isoform structure. α-helices and β-strands are shown in red and yellow, respectively. The inset provides an enlarged view of the active site, highlighting the coordination of the catalytic Zn^{2+} ion with the three histidine residues. B) Solvent-accessible surface of hCA II is shown, with residues defining the hydrophobic half of the active site cleft shown in red and those defining the hydrophilic half in blue (figure from [60]).

1.2.2 The catalytic reaction

CAs are recognized as some of the most catalytically efficient enzymes known. Notably, hCA II displays a turnover rate of 1.1 μs^{-1} while the fastest isoform, the Sulfurihydrogenibium azorense Carbonic Anhydrase (SazCA), reaches 4.4 μs^{-1} [68, 69].

The catalytic reaction is characterized by a two-step mechanism, in which the first step consists of the nucleophilic attack of zinc-bound hydroxide ion to CO_2 with the production of a bicarbonate ion, while the second step involves the regeneration of the initial condition [70, 71] (figure 1.2).

The reaction begins with an empty hydrophobic pocket and a hydroxyl group coordinated with the zinc ion (figure 1.2, **A**). Then, as CO_2 enters the active site and binds to the hydrophobic pocket [73], the nucleophilic attack on the partially positive carbon is activated, forming HCO_3^- anchored to zinc (figure 1.2, **B** and **C**) [74]. Then, the binding of a water molecule displaces HCO_3^- from its position (figure 1.2, **D**).

The second reaction step is based on the regeneration of the zinc-bound hydroxyl ion through the deprotonation of the new water molecule bound to zinc and the transfer of the proton to the bulk solvent via an ordered water network (ZnH_2O/OH^-, DW, W1, W2, W3a, and W3b) in the active site that acts as

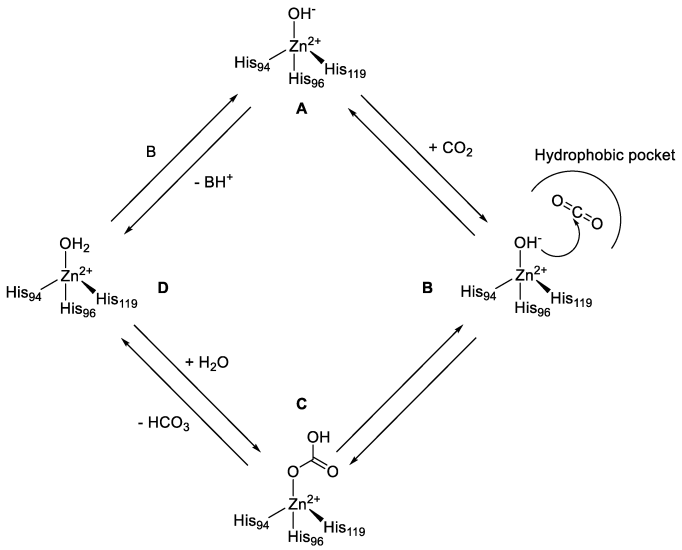

Figure 1.2. Mechanism of the catalytic reaction of CAs (figure from [72]).

a proton wire [75, 76]. The proton wire is composed of six water molecules stabilized through a hydrogen-bonding network placed in the hydrophilic region of the active site. Residues in hCA II involved in stabilizing these water molecules include Tyr7, Asn62, Asn67, Thr199, and Thr200 [76, 77]. First, the proton is shuttled from the six water molecules to a specific residue, His64, and then transferred to the bulk solvent [77, 78]. It is important to note that when CO_2 binds to the protein, His64 starts a conformational change (which will be complete when the HCO_3^- is released) from the "out" to the "in" position, moving the imidazole ring toward the cavity of the active site. His64 plays an important role in the catalysis of CO_2 hydration, as it allows the regeneration of zinc-bound hydroxyl [79, 75].

The CO_2 binding sites were hypothesized through free-energy perturbation simulations by Liang and Lipscomb [80], who identified three potential substrate binding pockets, of which one was recognized as the potential catalytic site and the other two as binding locations for CO_2 replenishment. The binding pocket was located approximately 4 Å from the catalytic zinc, interacting with residues His119, Val121, Val143, Leu198, Thr199, Val207, and Trp209. The predicted orientation of CO_2 within this pocket was consistent with the nucleophilic attack mechanism by the catalytic zinc-bound hydroxide. Subsequently, these predictions were validated by the cryocooled crystallographic structures of both holo and apo (without the zinc ion) hCA II obtained under CO_2 pressure [64, 63]. This analysis also confirmed the role of Thr199 as a gatekeeper residue.

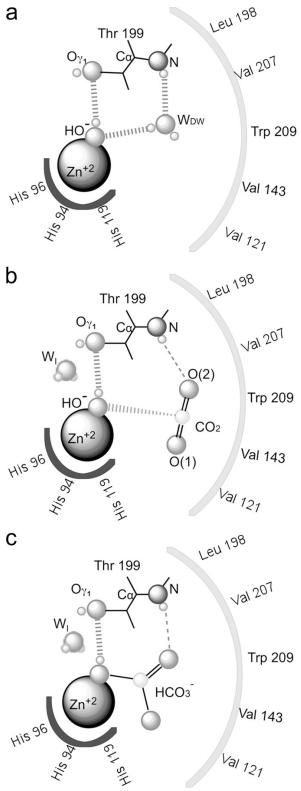

Figure 1.3. Proposed catalytic mechanism of hCA II. A schematic representation of three discrete stages of the reaction cycle: a) the unbound state, characterized by the presence of the deep water molecule (DW); b) CO_2 binding, during which DW is displaced and a hydrogen bond forms between the substrate and the backbone amide of Thr199; c) formation of bicarbonate (figure from [64]).

As seen in previous studies, this residue is proposed to be important for the orientation of the hydroxide group, the specificity of anion, inhibitor binding, and proton transfer [81, 82, 83]. The hCA II structure in combination with CO_2 also revealed that one oxygen of the CO_2 molecule interacts (3.5 Å) with the amide of Thr199, while the other is positioned between the zinc ion and Val121 (figure 1.3, panel b). CO_2 binds to the active site by displacing the so-called "deep water" DW (figure 1.3, panels a). This configuration places both CO_2 oxygens at nearly equivalent distances from the oxygen of the zinc-bound hydroxide, positioning the carbon atom at an optimal distance for nucleophilic attack.

A similar interaction is observed for the bicarbonate ion [84]: one oxygen coordinates directly to the zinc, occupying the position of the hydroxide, while the remaining two oxygens adopt an orientation analogous to that of CO_2, with

one forming a hydrogen bond to the NH of Thr199 (figure 1.3, panel c).
Another key residue recognized as a gatekeeper element, together with Thr199, is Glu106. This residue is most likely ionized [85] and thus serves as a hydrogen-bond acceptor for the hydroxyl group of Thr199. Consequently, the hydroxyl group of Thr199 accepts a hydrogen bond from the zinc-bound solvent molecule [82] (figure 1.4). This association preserves an active catalytic configuration that triggers the entire mechanism through a nucleophilic attack by the zinc-bound hydroxide ion on CO_2, thereby increasing $k_{(cat)}$ and facilitating the conversion of CO_2 into bicarbonate [86].

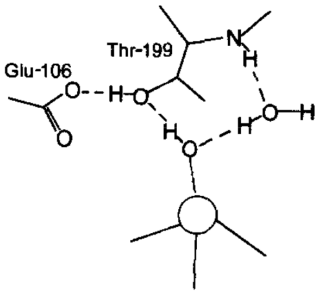

Figure 1.4. Schematic representation of the structures of the hydrogen-bonded system involving Glu106, Thr199, DW and the zinc-bound H_2O or OH^- of hCAII (figure adapted from [82]).

1.2.3 pH regulation in tumor cells: coordinated role of hCAs and transporters

Since reversible hydration of carbon dioxide is linked to several metabolic pathways, hCAs play important physiological roles in pH and CO_2 homeostasis, respiration and transport of CO_2/bicarbonate, as well as in various biosynthetic reactions [22]. Hence, alterations in their expression or activity have been associated with many human diseases, including glaucoma, epilepsy, sterility, obesity, and cancer [87, 14].
In many solid tumors, the rapid proliferation of cancer cells overtakes the capacity of the vascular system, leading to areas with inadequate oxygen supply. Hypoxia conditions cause a metabolic shift from glucose metabolism to glycolysis, called Warburg Effect [88, 89], which, together with mitochondrial respiration, produces a high amount of acid metabolic end-products such as lactate, protons, and carbon dioxide.
To prevent the accumulation of these metabolites and maintain a slightly

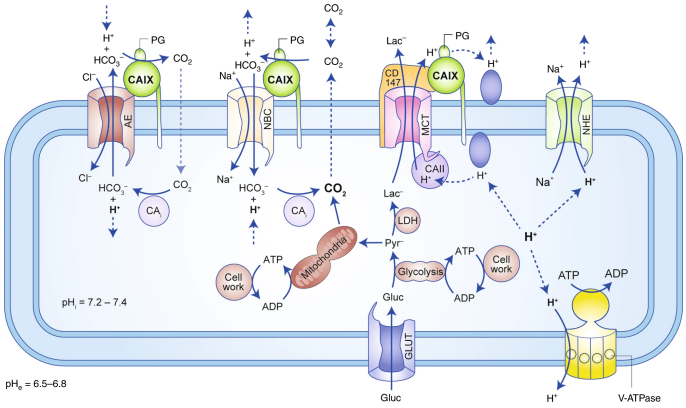

Figure 1.5. Tumor pH regulation mechanism (figure from [90]).

alkaline intracellular pH essential for cell proliferation, a coordinated interplay between hCAs and various transporter proteins regulates acid/base homeostasis in cancer cells (figure 1.5). Lactate and H^+ produced by anaerobic glycolysis are excreted by the monocarboxylate transporter (MCTs) in a 1:1 stoichiometry [91, 92, 93, 94]. In addition, H^+ leaves the cell through the Na^+/H^+ exchanger 1 (NHE1) [95] and by vacuolar H^+-ATPase (V-ATPase) [96, 97], while lactate can be eliminated by passive diffusion between the gap junctions of tumor cells [98]. On the other hand, CO_2 produced by mitochondrial respiration can leave the cell through passive diffusion over the plasma membrane, gas channels [99, 100], or can be hydrated in the cell by intracellular hCAs action, forming HCO_3^- and H^+. The release of CO_2 is also supported by the catalytic function of extracellular hCAs. In fact, cancer cells mainly express membrane-bound hCA isoforms IX and XII, and intracellular hCA isoforms I and II [101, 102, 103, 104, 105, 106]. Finally, the intracellular concentration of HCO_3^- is controlled by its uptake and extrusion via the Na^+/HCO_3^- cotransporter (NBC) and Cl^-/HCO_3^- exchangers (AEs), thereby maintaining intracellular pH and buffering capacity [107, 108]. It is believed that hCA IX works in close spatial and functional cooperation with the bicarbonate transporters. In fact, the bicarbonate ions generated by hCA IX catalysis are directly transferred to the bicarbonate transporter for cytosol uptake [108, 109]. There, they interact with protons, leading to the production of CO_2 that can leave the cell through diffusion, with acidification of the pericellular milieu which is also enhanced by the previous CO_2 hydration operated by hCA IX [110, 111]. On the other hand, hCA IX also seems to cooperate with proton exporters, providing bicarbonate ions to facilitate extracellular proton mobility [112].

All of these metabolic regulations result in acidification of the extracellular

pH to as low as ∼pH 6.5, which is related to tumor progression and immune suppression [90]. Indeed, acidic pH_e promotes extracellular matrix remodeling, restricts HCO_3^- dependent buffering, and induces proteases activation and expression, thereby facilitating tumor cell dissemination and invasion [113].

1.2.4 hCA IX

hCA IX is a transmembrane α-CA that plays a key role in the acidification of the microenvironment of many solid tumors. Its enzymatic activity is maintained under acidic conditions, as demonstrated by *in vitro* studies, showing an optimal pKa of approximately 6.5. Furthermore, although its activity is inhibited by increasing bicarbonate concentrations, it remains largely unaffected by lactic acid [114, 115], likely reflecting an evolutionary adaptation that enables the enzyme to function in the harsh tumor cell environment, which is characterized by high extracellular lactate levels and increased acidity.
In healthy tissues, hCA IX expression is largely restricted to the gastrointestinal epithelium, whereas it is frequently overexpressed on the surface of several tumor types [116], including malignancies of the brain, breast, kidney, and colon [117, 116], particularly in their more aggressive variants. Due to its involvement in key oncogenic processes, such as tumor progression, cell proliferation, adhesion, and malignant invasion [110], hCA IX has emerged as a clinically relevant tumor-associated target [118, 119].
The main regulator of hCA IX expression is HIF-1 [120]. HIF-1 is a heterodimer transcription factor composed of an oxygen sensitive subunit α (HIF-1α) and a constitutively expressed subunit β (HIF-1β) [121, 74]. Under normal oxygen conditions (normoxia), HIF-1α is hydroxylated at the Pro402 and Pro564 residues by prolyl hydroxylase domain proteins (PHDs), allowing recognition by the von Hippel-Lindau tumor suppressor protein (pVHL), which mediates ubiquitylation and proteasomal degradation [122]. Moreover, the factor inhibiting HIF-1 enzyme (FIH-1) hydroxylates Asn803 in the C-terminal activation domain of HIF-1α, preventing its binding to coactivators [123]. However, in hypoxia condition, PHDs and FIH-1 are inactive, leading HIF-1α to nuclear translocation, where it dimerizes with HIF-1β and activates the expression of genes containing the hypoxia-responsive element (HRE) in their promoter sequence. HRE is also present on the CA9 promoter, thus regulating the expression of the hCA IX isoform under hypoxic conditions [74, 124].

Structurally, hCA IX is a homodimeric glycoprotein, which is characterized

by an overall fold and active site homologous to other α-CAs, with a mixed α/β-topology and a conserved zinc active site. The dimerization is stabilized by the formation of an intramolecular (between Cys156 and Cys336) and a symmetric intermolecular (Cys174) disulfide bond [119]. hCA IX is composed of an N-terminal signal peptide (SP, residues 1-37), followed by a large extracellular domain (ECD, residues 38-414), one transmembrane helix (TM, residues 415-433), and a short intracellular tail (IC, residues 434-459) (figure 1.6).

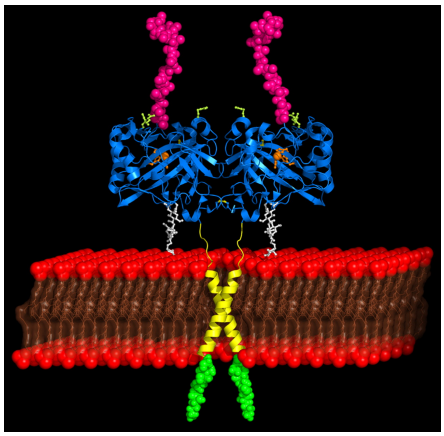

Figure 1.6. Proposed model of structural arrangement of the full-length hCA IX homodimer on cell membrane (figure from [66]). The ECD, PG domains, TM and IC are depicted in the figure in blue, magenta, yellow and green, respectively.

Interestingly, the ECD includes a proteoglycan-like domain (PG, residues 53-111) and a catalytic domain (residues 137-391), connected by a short linker. The PG domain, named for its homology to the keratan sulfate attachment domain of a large human aggregate proteoglycan (namely aggrecan) [125], is unique to hCA IX among hCAs and has been postulated to play a crucial role in modulating the catalytic activity of the enzyme. Indeed, the catalytic activity of the ECD has been shown to be greater than that of the catalytic CA domain alone [119]. Despite its functional relevance, detailed X-ray structural and functional data are still unavailable (for a detailed review of the topic, see paragraph 4.1).

Several post-translational modifications have also been identified in hCA IX. O-linked glycosylation by heparan or chondroitin sulfate glycosaminoglycan chains occurs at Thr115 in the N-terminal region of the PG domain. Additionally, N-linked glycosylation of a high mannose sugar chain at Asn346 localized on the catalytic domain [119], and three phosphorylation sites on IC region, namely Thr443, Ser448, and Tyr449 [126, 109].

1.2.5 hCA XII

hCA XII, as hCA IX, is a membrane-associated α-CA isoform representing a tumor marker in human cancers [127].
Structurally, hCA XII is a dimeric glycoprotein shorter in length than hCA IX and composed of an N-terminal extracellular domain (containing the active site, residues 1–269), a transmembrane helix (residues 270–296), and an intracellular domain (residues 297–325) that shows two potential sites for phosphorylation, which may regulate metabolic signaling by recruiting kinases [128, 129] (figure 1.7).
The hCA XII adopts a β-fold architecture observed in other hCA isoforms [128], with the catalytic zinc ion tetracoordinated to three conserved histidines and one water molecule within the active site [129]. However, hCA XII differs from other soluble and membrane-associated CA isozymes by existing as a stable isologous dimer both in solution and in crystal.
The dimer interface features a series of conserved and hCA XII specific residues and is stabilized by 19 hydrogen bonds. Notably, two of these interactions are performed by the highly conserved residue Gln249 [128]. In this dimer configuration, the active site and C-termini are positioned on opposite regions of the enzyme. As a result, when the C-termini anchor the protein to the membrane, the active sites face the extracellular space and are correctly oriented for catalysis. The transmembrane region contains two specific motifs, GXXXG and GXXXS, that serve for the dimerization of transmembrane α-helices [129, 128]. The structure of the transmembrane helices is not known. Figure 1.7 shows a model of this region based on the glycophorin A dimer structure described by MacKenzie et al. [130], which contains the same GXXXG motif [131, 132, 133]. Moreover, hCA XII contains two glycosylation sites, the Asn52 and Asp136 residues, and a single disulfide bond between Cys23 and Cys203, essential for structural stabilization and proper function of the enzyme [129].

hCA XII is expressed in various human tissues, such as the gut [134], kidneys [135], reproductive organs [136], sweat glands [137, 138, 139, 140], and eyes [141] (its overexpression in the eye has been associated with glaucoma [141]).
In all these tissues, hCA XII contributes to regulate pH homeostasis, fluid acidification and concentration, reproductive tissue homeostasis [104, 136], and the regulation of salt balance in sweat [139, 140]. However, hCA XII expression is higher in tumor tissues, including renal, colorectal, brain, breast, and

cervical cancers [135, 142, 143]. In breast cancer, elevated expression of hCA XII correlates with a favorable prognosis, positive estrogen receptor α (ER α) status, and better overall survival [144, 145].
The expression of hCA XII is regulated in different cell lines by HIF-1 [129, 146, 147] and, in breast tumors, is positively correlated with the expression of the ER α [148, 149]. In fact, when estrogen binds to the ER α, the receptor interacts with a distal enhancer located upstream of the transcription start site of the CA12 gene. This enhancer binds the ER α through an imperfect estrogen response element (ERE) and recruits p160 coactivators that facilitate transcriptional activation. In addition, this enhancer communicates with the CA12 gene promoter by chromosomal looping, increasing the transcription of the CA12 gene [150].

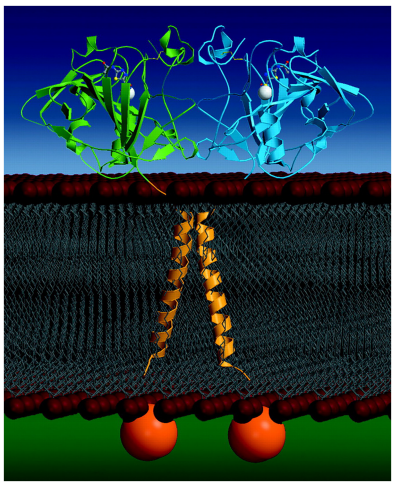

Figure 1.7. Schematic representation of the hCA XII dimer in the membrane. The extracellular CA domains are colored blue and green, respectively. Zinc ions appear as white spheres, disulfide linkages are yellow, and acetazolamide molecules appear as balls-and-sticks. The transmembrane helices are depicted in yellow, while the intracellular C-terminal regions, shown as orange spheres, contain putative phosphorylation sites which remain structurally uncharacterized. Notably, the membrane association orients the enzyme active sites toward the extracellular milieu, ready for catalysis (figure from [128]).

1.2.6 hCA inhibitors (hCAIs)

Different hCA inhibitors (hCAIs) and activators (hCAAs) have been designed and synthesized [151]. In particular, distinct CA inhibition mechanisms have been identified: the coordination of the catalytic zinc (II) ion in a tetrahedral or trigonal bipiramidal geometry (e.g. sulfonamides); the anchoring of inhibitors

to the zinc-bound water molecule or hydroxide ion (e.g. phenols and sulfocoumarins); the occlusion of the entrance of the active site (e.g. coumarins and bioisosters); and the binding out of the cavity of the active site (e.g. carboxylic acid derivative) [152, 151, 54, 153].

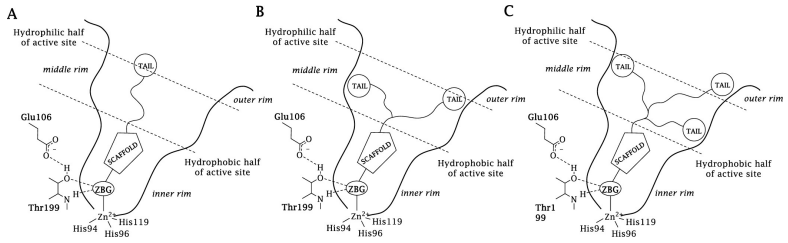

Figure 1.8. The tail (A), two tails (B) and three tails (C) approaches for the CAIs design (figure from [153]).

Due to the high structural homology among the active sites of different isoforms, achieving selective inhibition remains challenging. However, over the last two decades, alternative approaches have been developed, including the so-called "ring" and "tail" strategies [154]. The ring strategy attempts to screen for different ring systems, such as aromatic or heterocyclic scaffolds, on which a sulfonamide zinc-binding group or other chelating groups are added, to find inhibitors with promising interactions with the hCA binding site. In contrast, the tail approach involves inhibitors built on a general scaffold containing a zinc-binding group (e.g. aromatic or heteroaromatic sulfonamides) to which one or more "tails" are attached. These tails can interact with the middle and outer rims of the hCA active sites, which contain the highly variable region among isoforms, thereby enhancing selectivity.[155]. Three different mechanisms are validated for the "tail" approach: the tail, two-tails, and three-tails approaches (figure 1.8) [153].

Classical hCAIs, which are in clinical use, include compounds such as acetazolamide, sulthiame, and ethoxzolamide, whereas more recent drugs or investigational agents comprise dorzolamide, celecoxib, and saccharin. Many of these compounds were originally developed as diuretics. Several hCAIs are also employed in the treatment of glaucoma, and in recent years, new derivatives have been identified with potential applications as anti-obesity, anti-infective, and anti-tumor agents [156, 157, 158, 159].
Among the newly developed hCAIs anti-tumor agents, SLC-0111, an ureido-substituted benzenesulfonamide, stands out as a potent hCA IX inhibitor that disrupts pH homeostasis in tumor cells, altering their survival and invasiveness

[160, 161]. Preclinical studies show that SLC-0111 enhances the efficacy of chemotherapeutic agents such as cisplatin in head and neck squamous carcinoma models, leading to reduced tumor growth and invasion [162]. The compound has also progressed to Phase Ib/II clinical trials, where its safety and tolerability were evaluated in patients with advanced solid tumors [163, 161, 164, 165, 166].

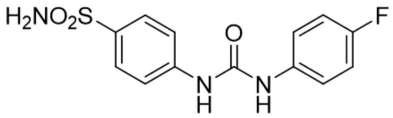

Figure 1.9. Chemical structure of SLC-0111.

In recent years, numerous studies have focused on the development of dual-target inhibitors of hCA enzymes as potential treatment of complex diseases, including cancer, inflammatory disorders, glaucoma, and neurological conditions [167, 168]. Notable examples include the molecules designed by Nocentini et al. for the treatment of glaucoma, which combine the classical hCAI pharmacophore (benzenesulfonamide) with β-adrenergic receptor (AR) blocker (aryloxy-2-hydroxypropylamine) [169]. The (AR) blocker acts on the sympathetic nerve endings in the ciliary epithelium, while the hCA I reduces the rate of bicarbonate production and thereby the transport of water, retaining sodium within the fluid [170, 171]. For neurological disorders such as oxaliplatin-induced neuropathy (OINP), Angeli et al. synthesized and characterized a series of compounds capable of modulating both hCA isoforms and the transient receptor potential vanilloid 1 (TRPV1) [172]. These molecules were obtained by modifying the structure of the TRPV1 antagonist, the SB-705498, through the introduction of a sulfonamide moiety, bioisosteric replacement of ureido with thioureido linkers, strategic aromatic substitutions, and introduction of stereocenters. The resulting inhibitors exhibited significant activity against hCA isoforms, while selected compounds also displayed moderate TRPV1 agonism. In the oncology field, dual-target inhibitors have also been developed to modulate tumor-associated hCAs and human telomerase (hTL), the latter being a key driver of the uncontrolled proliferative capacity of cancer cells [173, 174]. The compounds were designed by coupling the azidothymidine moiety, which targets hTL, with various hCAI scaffolds, including benzenesulfonamide, coumarin, and sulfocoumarin, via a 1,2,3-triazole-containing linker [175, 176]. The most effective inhibitors of hCA IX and XII were subsequently evaluated for their antitelomerase activity in PC3 and HT-29 cell lines, demonstrating a marked ability to suppress hTL function [177, 178].

1.3 Histone Deacetylase

Eukaryotic DNA wraps around histone proteins to form compact nucleosomes (figure 1.10), stabilized by ionic interactions between the positively charged histones and the negatively charged DNA backbone. These tight interactions restrict access to the enzymes involved in transcription. Then, gene expression is regulated epigenetically through coordinated actions between histone acetylase (HAT) and histone deacetylase (HDAC) proteins. HATs allow the loss of histone protein-DNA interactions by acetylation of the conserved lysine residues on histone proteins, neutralizing positive charges and increasing the access of RNA polymerase II for gene expression.

On the other hand, chromatin compaction is catalyzed by HDACs, which remove acetyl groups from lysine residues on histone surfaces, producing acetate and suppressing gene transcription [179, 180, 181]. HDACs also act on the regulation of the deacetylation of non-histone proteins, controlling various biological pathways [182]. The human genome encodes at least 18 deacetylase isoforms, classified into the HDAC and sirtuin (SIRT) families based on their cofactor dependence [180, 181]. HDACs are zinc-metalloenzymes divided into class I (comprises HDAC1, 2, 3, and 8), class II (comprises HDAC4, 5, 6, 7, 9, and 10), and class IV (comprises HDAC11). Class II HDACs are further divided into classes IIa (HDAC4, HDAC5, HDAC7, and HDAC9) and IIb (HDAC6 and HDAC10), and differ in the presence of one or two catalytic domains, respectively. However, SIRT proteins belong to class III (comprising seven members SIRT 1-7), which require nicotinamide adenine dinucleotide (NAD^+) as a cofactor for enzyme activity [183, 181].

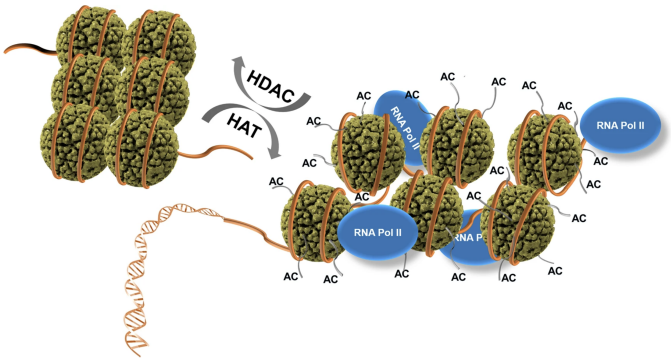

Figure 1.10. Schematic representation of the coordinated interplay between HAT and HDAC in the regulation of gene expression (figure from [181]).

Given the crucial role of HDACs in transcription regulation, altered expression

and mutation of HDAC-encoding genes, as well as the imbalance between HDACs and HATs action, have been linked with the development of several diseases, including neurodegenerative and metabolic disorders, diabetes, and cancer [184, 185]. In particular, in cancer development, this dysregulation leads to abnormal transcription of genes that govern critical cellular processes, including proliferation, cell cycle control, and apoptosis. Therefore, HDAC inhibitors (HDACIs) have been studied for the development of anticancer therapies [186].

1.3.1 Class I HDAC structures and drug design

The overall structure of the HDAC family consists of two highly conserved regions, the N-terminal and central structural domains [185], while the C-terminal domain is characterized by more variability, with differences in length and amino acid sequences between HDAC types [187].

Among the HDAC classes, class I enzymes are overexpressed in many different types of cancer, including gastric [188, 189, 190], breast [191], and prostate tumors [192, 193, 194], thus representing key tumor targets [195]. However, because of the high structural homology of the active site, the development of an effective selective inhibitor is challenging.
Structurally, class I HDACs show a globular catalytic domain and an unstructured C-terminal tail [196]. The catalytic core features a central β-sheet surrounded by α-helices and loops, with the zinc-containing active site based at the end of a tube-like channel. Perpendicular to this tunnel lies an additional cavity, known as the "foot pocket", which has been proposed to serve as an exit pathway for the acetate product [197, 198]. The structure of this pocket represents one of the key distinguishing features among the HDAC isoforms and has therefore been exploited for the design of isoform selective inhibitors. Specifically, HDAC1–3 can accommodate bulky groups, while in HDAC8 the presence of a tryptophan residue (Trp141) reduces the accessibility to this region [198, 199, 200]. Additional selectivity can arise from surface variations that surround the rim of the active site. In fact, HDAC3, unlike HDAC1 and 2, contains in this region a tyrosine residue (Tyr198) and further away from the active site an extended loop with structural and sequence variations with respect to HDAC1 and 2 [201, 202].
Functionally, Class I HDACs are catalytically inactive in their solitary state and must be incorporated into specific corepressor complexes that differ in

biological function [203]. An exception among class I isoforms is HDAC8, which is fully active in isolation [204, 205]. This dependence on multiprotein assemblies offers valuable opportunities for designing complex-specific inhibitors. While HDAC1 and 2 are interchangeably recruited (due to their high structural homology [206, 207]) to the NuRD (nucleosome remodeling and deacetylase) [208, 209, 210], SIN3 (switch-independent 3) [211, 212], MiDAC (mitotic deacetylase) [213, 214], CoREST (co-repressor of REST) [215], MIER (mesoderm induction early response) [216] and RERE (arginine-glutamic acid dipeptide reapets) [217] complexes, HDAC3 is exclusively recruited into the SMRT/NCoR (silencing mediator of retinoic acid and thyroid hormone receptor and nuclear receptor corepressor, respectively) [218] complex.
Interestingly, the deacetylase activity of SMRT/NCoR, NuRD and MiDAC complexes is activated in the presence of inositol phosphates, which bind to a basic pocket [202, 219, 220, 214].

To date, classical HDACIs exert their action by chelating the catalytic zinc ion within the active site. Based on their pharmacophore, these inhibitors can be classified into distinct pharmaceutical classes, such as hydroxamic acid, benzamides, cyclic peptides, and aliphatic acids [179]. Among these, most clinically approved HDACIs belong to the hydroxamic acid class, which act as pan-inhibitors of all 11 HDAC isoforms. This lack of selectivity is likely to contribute to their adverse side effects. In contrast, benzamide-based inhibitors exhibit a certain degree of selectivity toward class I HDAC enzymes, showing nanomolar potency against HDAC1 and HDAC2 and only micromolar activity against HDAC3 [221]. Beyond this traditional mechanism, several alternative strategies could be explored to achieve isoform selectivity or complex specificity among class I HDACs. These include inhibition of the allosteric site, i.e. the inositol phosphate binding site, the combination of the allosteric and active site inhibitors, the alteration of protein-protein interface interactions to prevent complex formation, the design of dual inhibitors that act on multiple subunits of the corepressor complexes, and the reduction of HDAC activity by reducing inositol phosphate levels [222]. Together, these approaches represent promising strategies to achieve better selectivity in the therapeutic targeting of class I HDACs.

Several selective class-I HDACIs are currently being evaluated in clinical trials for a variety of malignancies, including solid tumors and hematologic cancers. Among these compounds, the benzamide 2-amino anilide Mocetinostat has

been explored for the treatment of lymphoma and lung cancer [223, 224], the hydroxamic-acid derivative Pracinostat is being assessed for its efficacy in acute myeloid leukemia [225], while the thiol-based HDAC inhibitor OKI-179 is under investigation for the treatment of solid tumors [226].
In 2006, the pan-HDAC inhibitor SAHA (vorinostat) was approved by the U.S. Food and Drug Administration (FDA) for the treatment of cutaneous T-cell lymphoma, while the China National Medical Products Administration (NMPA) accepted the CS055 (chidamide) and MS-275 (entinostat) for the treatment of peripheral T-cell lymphoma and Hormone receptor-positive HER2-negative breast cancer, respectively [227, 228]. Other HDACIs include CI-994, a class I HDACI that selectively targets HDACs 1–3. CI-994 has been shown to promote functional recovery following stroke and demonstrates promising effects against cognitive dysfunctions in preclinical animal models [229, 230, 231, 232, 233, 234]. However, HDAC inhibitors used as monotherapy exhibit limited efficacy and are often associated with a broad range of adverse effects. In this context, dual-targeting HDACIs offer the potential to overcome these limitations and reduce side effects. Several dual-target agents have been reported in the literature, including the HDAC/DNA-targeting inhibitor EDO-S101, the HDAC/phosphoinositide 3-kinase (PI3K) inhibitor CUDC-907, the HDAC/lysine-specific histone demethylase 1 (LSD1) inhibitor 4SC-202, and CUDC-101, a dual HDAC/receptor kinases epidermal growth factor receptor (EGFR) inhibitor [227].

1.3.2 The catalytic reaction

At the beginning of the catalytic reaction, the zinc ion is pentacoordinated by two aspartates, one histidine, and two water molecules, one of which is then replaced by the acetylated lysine of the histone protein [235, 236].
The coordination of the lysine acetyl group with the zinc ion, together with the formation of a hydrogen bond with the hydroxyl group of a tyrosine residue, Tyr306, induces polarization of the substrate carbonyl group [237, 200, 238, 239, 240, 179, 235]. This polarization facilitates the nucleophilic attack by a water molecule, which is previously deprotonated by a nearby histidine, His143, which activates water as a nucleophile. His143 has been proposed to work as a general acid/base catalyst [239], first accepting the proton of the activated water molecule and then donating it to the amine group of the reaction intermediate, leading to the formation of acetate and free lysine. On the other hand, His142 exerts an electrostatic effect, and together with Tyr306 and the

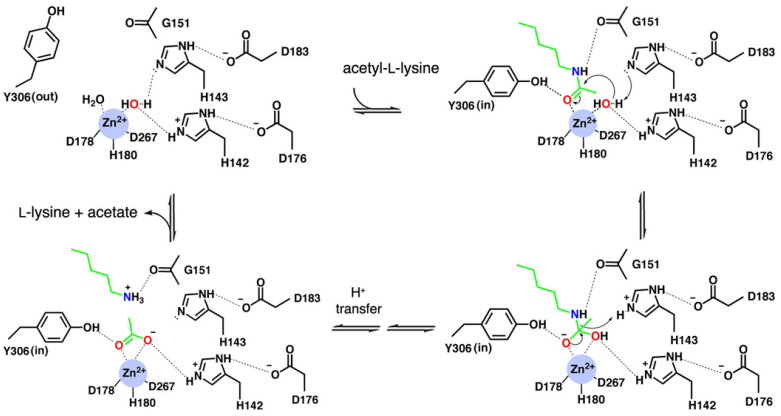

Figure 1.11. Mechanism of the catalytic reaction of HDACs (figure from [179]). In the figure the active site of HDAC8 isoform is shown.

Zn^{2+}, stabilizes the tetrahedral intermediate within the active site [240]. The catalytic activities of these two histidine residues are modulated by hydrogen bonds with Asp176 and Asp183. Moreover, the substrate orientation is further stabilized by a hydrogen bond between the NH moiety of the acetylated lysine and the backbone carbonyl of Gly151 [239, 235]. After the catalysis reaction, the acetate remains bound to the zinc ion before leaving through an internal channel [241, 242], restoring the enzyme to its initial state.

1.3.3 HDAC complexes

Class I HDAC1-3 exist in the nucleus as components of large multiprotein complexes, through which they acquire distinct biological functions [243, 222]. Their integration into complexes enhances their enzymatic activity, which is limited in their isolated form and characterized by a reduced substrate specificity [220, 202, 203].

The complexes differ in size (from $\sim$ 200 kDa to $\sim$ 2 MDa) and number of distinct subunits (from 3 to >14). Moreover, the recruitment and activation of HDACs is mediated by the ELM2–SANT domain, except for SIN3, which uses the HDAC interaction (HID) domain [220, 219].

NuRD

NuRD complex plays an important role in the commitment of cell lineage and DNA damage repair [244, 245]. It is located at the level of gene promoters, enhancers, and the intragenic region, where it regulates gene expression through two coordinated mechanisms: chromatin deacetylation mediated by HDAC

activity and nucleosome remodeling through the chromodomain helicase DNA binding protein 3/4/5 (CHD3/4/5) [246, 247, 210].
Structurally, the complex comprises seven subunits, each with multiple paralogues. The structural components are HDAC1/2, CHD3/4/5, cyclin dependent kinase associated protein (CDK2AP1), metastasis associated scaffold proteins (MTA1/2/3), retinoblastoma-binding proteins 4 and 7 (RBBP4/7), methyl-DNA binding domain proteins (MBD2/3), and the GATA-type zinc finger proteins (GATAD2a/b) [248, 249].
NuRD is a dimeric complex, in which two MTA1 subunits each recruit one HDAC1/2 molecule through the dimeric ELM2-SANT domain and two RBBP4/7 copies by the C-terminus sequence. Dimerisation occurs through the ELM2-SANT domain present in MTA1. MBD2/3 has been shown to interact at the dimerization interface of MTA1 in substoichiometric quantities that exhibit a 1:2:2 ratio of MBD2/3:HDAC1:MTA1 [210].

SIN3

SIN3 complex consists of five subunits: the SIN3A/B, HDAC1/2, suppressor of defective silencing 3 (SDS3), sin3-associated protein p30 (SAP30), and RBBP4/7 [250, 251]. Unlike the other HDAC complexes, SIN3 lacks the ELM2-SANT domain and uses the HID to recruit the HDAC1/2 protein [252]. In the SIN3A corepressor, RBBP4/7 interacts with the HID domain and C-terminal sequence, while in the SIN3B complex, the same protein is linked through chemical crosslinking [253]. The complex shows a dimer structure mediated by an extended coiled-coil region of SDS3 [254]. Functionally, both SIN3A and SIN3B play an important role in embryogenesis and T-cell development [255].

SMRT/NCoR

SMRT (NCoR2) and NCoR1 are large homologous corepressor proteins that exert their role in transcriptional repression [256]. The homology between the two corepressors is evidenced by the high level of overall amino acid sequence identity ($\sim 40\%$). Therefore, NCoR1 and SMRT share a similar overall structure containing conserved functional domains [257]. Alteration of their expression is linked to several disorders, such as leukemias, and can affect the regulation of metabolism, lifespan, and circadian physiology [258, 259, 260, 261, 262, 263].
SMRT and NCoR form stoichiometric complexes with HDAC3, G protein pathway suppressor 2 (GPS2), and transducin beta-like protein 1 (TBL1), and its homologue TBLR1 [218, 264, 265]. TBL1 protein forms a tetrameric domain

that interacts with both SMRT and GPS2 enzymes, showing an important role in the assembly of this multiprotein complex [266]. In turn, SMRT interacts with HDAC3 through its deacetylase activation domain (DAD), located in the SANT1 domain [265, 267].

MiDAC

MiDAC plays an important role in cell cycle regulation, as its components are associated with the Cyclin A2/CDK2 complex [268]. It is also involved in cancer development and proper alignment of chromosomes during mitosis in cancer cell lines [269, 270, 271, 272]. The complex is composed of three proteins: HDAC1/2, mitotic deacetylase-associated SANT domain protein (MIDEAS), and deoxynucleotidyl transferase terminal interacting protein 1 (DNTTIP1) [273]. MiDAC is a tetramer with a distinctive X-shaped architecture in which four HDAC proteins are positioned at the extremities. This arrangement suggests that the complex may simultaneously target multiple nucleosomes. The ELM2-SANT domain of MIDEAS interacts with the DNTTIP1 dimerisation domain, while the SANT domains of MIDEAS drive tetramerization [274].

CoREST

Among the HDAC corepressor complexes, CoREST stands out for combining both histone demethylase and deacetylase functions, mediated by lysine-specific demethylase 1 (LSD1) and HDAC1/2, held together through the RCOR 1/2/3 scaffold protein [215, 275]. RCOR contains the ELM2–SANT domain that binds to HDAC1/2 [220], and the LINKER-SANT2 domain that recruits the TOWER domain of LSD1 [276]. It has been proposed that the RCOR-SANT2 domain also interacts with nucleosomal DNA [277, 278]. Functionally, CoREST acts as a chromatin-modifying complex that interacts with the repressor element-1 silencing transcription factor (REST) to regulate neuronal gene expression and stem cell fate [279]. Histone H3 tail is the classic enzymatic target of CoREST complex, where K4 is methylated while K9 is acetylated. Transcriptional repression arise from the remotion of these marks [279, 280, 215, 281].

MIER

The MIER complex is still poorly characterized, although the MIER1 homologue has recently been studied in the deacetylase context. MIER1 is a monomeric complex composed of MIER1, HDAC1/2 (recruited by the ELM2-SANT domain of MIER1 sequence), and bromo-adjacent-homology-domain containing protein

1 (BAHD1) [282]. The component 1 Q subcomponent-binding protein (C1QBP) was also identified and shown to co-purify with intact nucleosomes carrying H3K27 di- or tri-methylated, suggesting that the MIER1 complex may act on the polycomb repressive complex 2 (PRC2) to expand repressed chromatin regions and promote the deposition of histone octamer in DNA nucleosome-depleted regions [282, 283, 284].

RERE

As the MIER complex, RERE remains poorly characterized. It adopts a monomeric structure composed of HDAC1/2 and RERE proteins [285]. The RERE protein contains a BAH domain, which recognizes modified histone tails within the nucleosome [283, 286]. Functionally, it promotes neural progenitor proliferation and neuronal differentiation [287, 284].

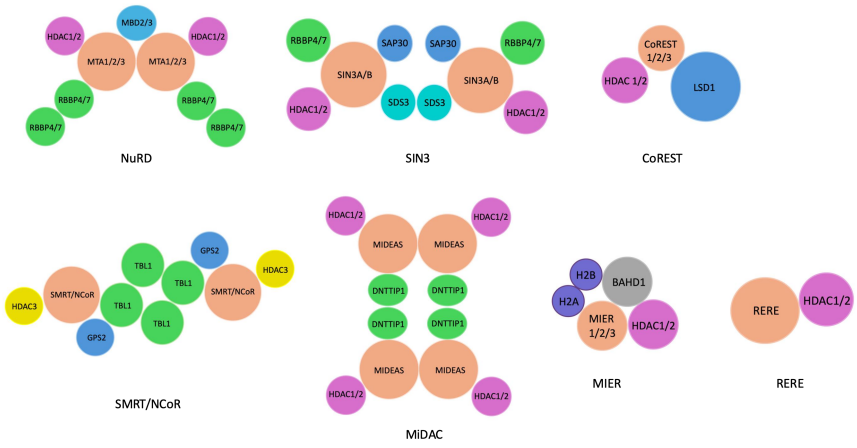

Figure 1.12. Schematic representation of HDAC corepressor complexes (figure adapted from [222, 284]).

2 Methods

2.1 Protein x-ray Crystallography

2.1.1 Introduction

Protein crystallography is a powerful technique developed in the late 19th century to determine the atomic structure of proteins, nucleic acids, and larger macromolecular assemblies, such as viruses and ribosomes. Together with NMR spectroscopy and cryo-electron microscopy (cryo-EM), it forms the basis of structural biology, providing detailed insights into the structural and functional properties of large molecules. Nowadays, this technique is often combined with other analytical methods, such as UV–Vis spectroscopy, enzymatic and biophysical assays, producing information that can be used to improve selectivity and potency of pharmaceutical compounds [288].

Single-crystal X-ray crystallography is the most common experimental method to obtain a detailed model of a macromolecular structure. This technique is based on the analysis and interpretation of X-ray diffraction patterns produced by identical molecules arranged in an ordered crystal lattice. The workflow begins with the growth of high-quality crystals from purified proteins, followed by data collection of their X-ray diffraction patterns, to produce an electron density map. The molecular structure is then determined by interpreting this map through computer-assisted model building consistent with the electron density obtained.

2.1.2 Crystallization process

Macromolecular crystallization involves systematically exploring the parameters that influence crystal formation to identify and optimize conditions that produce high-quality crystals. This process requires extensive and iterative trials, with results guiding the following optimization.

Purified protein is usually dissolved in an aqueous buffer that contains a chemical agent called precipitant. The role of precipitants is to alter protein-solvent and protein-protein interactions, promoting the protein-controlled precipitation of ordered crystals from solution, rather than disordered aggregates. Based on their different nature, the precipitants are usually divided into four categories: salts, organic solvents, polymers, and surfactants. Notably, precipitants of different categories can be combined, and in some cases, they may not even be required to induce precipitation, as is often observed in the crystallization of antibodies [289].
Macromolecular crystals are composed of approximately 50% of solvent, even if this percentage can range from 25 to 90, depending on the macromolecule that occupies the remaining volume. Then, we can consider the resulting crystal as an ordered gel permeated by extensive interstitial spaces through which solvent and other small molecules, such as drugs, can freely diffuse [288]. Although similar in morphology and appearance, the low-molecular-mass compound crystals differ in their practical and physical properties from the protein ones. Usually, protein crystals are smaller, softer, more fragile, more prone to dehydration, and diffract X-rays less effectively than small-molecule crystals. They are also sensitive to radiation, so that often multiple crystals are required to obtain a full data set for structure determination. The use of cryogenic temperature, intense synchrotron X-ray sources, and high-efficiency CCD detectors limited some of these issues [290, 291].
Crystal formation occurs in two distinct stages: nucleation and growth.
Nucleation is a first-order phase transition by which molecules move from a disordered state to an ordered one. During this phase, partially ordered aggregates of molecules develop in small ordered assemblies, which we refer to as nuclei. Crystallization proceeds from the nuclei through dislocation growth and two-dimensional nucleation, by which successive layer addition of molecules occurs to the formed cluster of nuclei. Both nucleation and growth depend on supersaturation, a non-equilibrium state where the protein concentration exceeds its solubility limit, in conditions induced by high protein and/or precipitant concentration. Equilibrium is then restored through the formation and growth of a solid phase, such as crystals, as the system returns to the saturation limit [292].

In figure 2.1, the phase diagram of macromolecular crystallization is shown. The diagram is divided into an undersaturated and a supersaturated regions by the line that represents the maximum solubility of protein in solution at specific

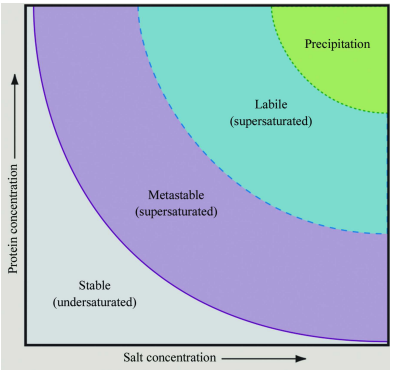

Figure 2.1. Phase diagram of macromolecules crystallization (figure from [292]).

concentrations of a precipitant. The supersaturation region is divided into two subregions: metastable and labile. In the metastable region, nucleation does not occur, although crystallization can proceed from existing nuclei. On the other hand, in the labile region, spontaneous nucleation and crystallization can occur. Finally, at very high supersaturation, the precipitation region is reached, where proteins aggregate in a disordered way to form amorphous precipitates. Moreover, slow precipitation leads to the formation of larger crystals, while rapid precipitation may produce many small crystals or an amorphous solid. Small crystal formation can also occur from a persistent condition of nucleation [292].

The vapor diffusion technique is the most commonly used method for crystallization, including the sitting and hanging drop techniques (figure 2.2). In this method, a small drop (2–10 μl) of protein solution is mixed with an equal or similar volume of crystallization solution, containing a precipitating agent and a buffer to control the pH, and placed on a siliconized glass coverslip. Then, the glass is inverted and sealed over a reservoir containing 500–1000 μl of the crystallization solution. Under these conditions, the difference in precipitant concentration between the drop and the reservoir (with a higher precipitant concentration in the reservoir) drives the system toward equilibrium through vapor diffusion. In this way, the protein solution can become supersaturated in the drops, leading to the formation of crystals [289].

If the crystals initially obtained are not suitable for diffraction analysis, several techniques can be used to improve crystallization growth. The easiest way involves the use of additives, like salt, alcohols, or other small organic molecules at low concentration, which are directly added to the crystallization drops and

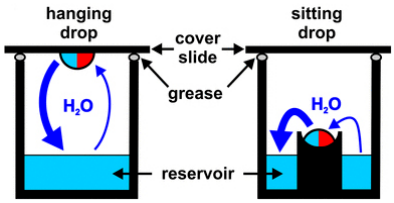

Figure 2.2. Schematic representation of the vapor diffusion techniques: the hanging and sitting drop (figure from [293]).

can influence the crystallization process. Another effective approach is seeding. In this technique, fragments of crashed small crystals, obtained from previous crystallization trials, are added to the crystallization drop. This is typically done by ensuring that the system is in a region of the phase diagram that favors crystal growth but not nucleation. The added seeds serve as preformed nuclei, allowing the crystals to grow under controlled conditions [294].

2.1.3 Crystal symmetry and diffraction theory

Crystals are a three-dimensional, ordered, and periodic array of atoms or molecules on a lattice.

The crystal structure is fully characterized by a unit cell (defined by three lengths, a, b, and c, and their mutual angles α, β, and γ) and a set of three basis vectors, along which the entire crystal can be constructed by translating the original cell. The system of translations forms the so-called crystal lattice. The lattice is a three-dimensional assembly of mathematical points that reflects the translational symmetry of the entire crystal [295].

Relations between the unit cell lengths and the angles between them define seven possible crystal systems: cubic, tetragonal, orthorhombic, monoclinic, triclinic, trigonal/rhombohedral, and hexagonal (figure 2.3). The Bravais lattice classification further considers structural details, dividing these seven crystal systems into 14 distinct Bravais lattices. In addition to the simple primitive (P) unit cell, crystals can also present body-centered (I), face-centered (F), or base-centered (C) unit cells (figure 2.3). Finally, crystals can be classified into 230 space groups, which provide a mathematical description of their symmetry by combining translations, rotations, reflections, and inversions. For protein crystals, however, only 65 space groups are relevant. This restriction arises because the chirality of amino acid residues excludes the presence of inversion centers and reflection planes. A complete list of all space groups can be found in the International Tables for Crystallography.

Any set of regularly spaced planes that can be drawn through the lattice can be considered as a potential source of diffraction. A specific set of equivalent

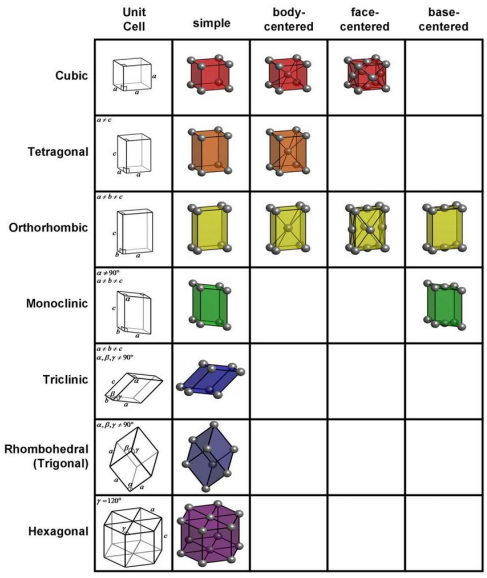

Figure 2.3. The seven crystal systems and fourteen Bravais lattices (figure from [296]).

parallel planes is identified by three indices *hkl* known as *Miller indices* or *lattice indices*. The h, k, and l indices indicate the number of sections produced by the intersection of the plane with the crystallographic x, y, and z axes, respectively. An increase in the Miller index values corresponds to a decrease in the interplanar spacing between crystal planes.

To describe the pattern of reflected X-rays produced by crystalline solids, in 1913, William Lawrence Bragg and his father, William Henry Bragg, proposed the Bragg diffraction equation. They observed that, for certain specific wavelengths and angles of incidence, these crystals produce intense peaks of reflected radiation. The results were explained by modeling the crystal as a series of discrete, parallel planes separated by an interplanar spacing d. The incident X-ray beam would produce a Bragg peak when the reflection from different planes interfered constructively. Constructive interference occurs when the phase differences between reflected waves from successive planes at interplanar spacing d are an integer multiple of 2π. This, in turn, happens if the difference in path length for rays reflected from successive planes ($2\mathrm{d}\sin\theta$) is equal to an integral number of wavelengths ($n\lambda$) of the incident X rays, namely

$$2\mathrm{d}_{hkl} \sin\theta = n\lambda \tag{2.1}$$

Thus, the rays reflected from successive planes emerge in phase, interfering constructively to produce an intense diffracted beam. On the contrary, for other angles of incidence θ, waves reflected from successive planes are out of phase, so they interfere destructively.
The angle of diffraction θ is inversely related to the interplanar spacing d. This implies that crystals with large unit cells and therefore larger interplanar spacings exhibit smaller diffraction angles, resulting in numerous reflections occurring within a convenient angle from the incident beam. In contrast, crystals with small unit cells and small interplanar spaces result in fewer measurable reflections [295].

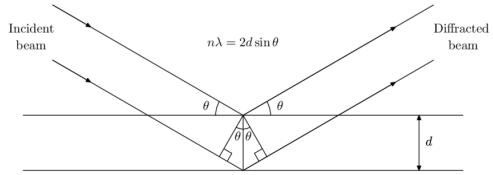

Figure 2.4. Schematic illustration of Bragg's law (figure from [297]).

2.1.4 Cryo-crystallography and data collection

Crystals are usually analyzed frozen at 100 K in a nitrogen flux. Cryo-cooling offers numerous advantages, such as reducing X-ray radiation damage, extending crystal lifetime, improving resolution by decreasing thermal disorder, and allowing longer exposure times.
For the measurements, crystals must be cooled rapidly to prevent ice formation and reach a stable glassy state, using a cryostat with a stream of liquid nitrogen vapor shielded by a flux of dry air to avoid moisture. Moreover, to prevent ice formation and promote vitrification, the mother liquor is supplemented with cryoprotectants such as glycerol, ethylene glycol, or low molecular weight PEGs [298].
However, small cryoprotectant molecules, such as glycerol, can sometimes penetrate the protein active site and establish interactions with surrounding residues, potentially altering the binding mode of inhibitors in structure-based analysis. For this reason, in these types of studies, the use of bulkier cryoprotectants is generally preferred, as they are less likely to access the active site [299].
X-rays are electromagnetic radiation with wavelengths ranging from 0.1 to

100 Å. For crystallographic applications, the most useful wavelength range lies between approximately 0.5 and 1.6 Å. X-rays in this range can be generated by bombarding a metal target, commonly copper, molybdenum, or chromium, with electrons emitted from a heated filament and accelerated by an electric field, as occurs in conventional X-ray tubes, either with fixed or rotating anodes.
Particle storage rings represent the most powerful sources of X-rays. In these facilities, electrons or positrons circulate at velocities close to the speed of light, driven by energy from radio-frequency transmitters and constrained to circular trajectories by strong magnetic fields. When a charged particle, such as an electron, is forced into curved motion, it emits energy tangentially to its path, known as synchrotron radiation.
Synchrotron radiation offers several advantages for macromolecular crystallography. The high intensities of the beam, several orders of magnitude greater than those produced by conventional X-ray tubes, enable rapid data collection, even from very small or weakly diffracting crystals. Additionally, synchrotron beams are highly focused, improving spot separation in diffraction images, which is particularly beneficial for crystals with large unit cells and packed reflections. Finally, synchrotron sources provide a continuous X-ray spectrum, making the whole range (1.6-0.5 Å) available to select an appropriate wavelength [300].
At a fixed wavelength, a Bragg reflection occurs only when the incident X-ray beam makes exactly the correct angle with the reflecting planes. Because real crystals exhibit a degree of structural disorder, a reflection must be fully recorded by rotating the crystal through its diffracting position. Typically, the crystal is rotated about an axis perpendicular to the incident X-ray beam. Diffraction images are recorded using area detectors, such as CCD cameras or image plates, which are capable of simultaneously collecting a large number of diffracted beams during small angular rotations of the crystal.

Several experimental parameters are optimized during data collection to ensure accurate measurements.

- Exposure time: it is calculated considering the efficiency of the crystal diffraction
- Rotation angle ($\Delta\phi$): depending on the unit cell parameters, the resolution limit, and the crystal mosaicity (a measure of the degree to which a crystal is composed of numerous small domains slightly misaligned with one another)
- Position (2θ) and distance from detector: it is calculated based on the

resolution limit

- Rotation range: depending on the crystal symmetry and according to Friedel's law ($I_{hkl} = I_{-h\,-k\,-l}$, where I represents the reflection intensities), which states that half of the reflections in the reciprocal lattice are redundant. Therefore, a data collection in which the crystal is rotating through 180° about any reciprocal-lattice axis should be sufficient to record all unique reflections regardless of the crystal symmetry

On the other hand, the quality of a data collection is reflected by other parameters.

- Completeness: at a given resolution, it represents the number of unique reflections measured relative to the total number of unique reflections (a good value is $> 90\%$)
- Redundancy: it is the number of independent observations per unique reflection, and it is calculated as the total number of intensity measurements out of the total number of unique reflections measured (usually 2-3 times)
- Pearson correlation coefficient CC½: the percentage correlation between intensities measured in two randomly chosen half-datasets
- Mean intensity (I/σ): signal to noise ratio (usually the value is between 10-20)

2.1.5 The phase problem

In crystallography, diffraction arises from the interaction of X-rays with the electron clouds of the atoms, producing a diffraction pattern.
The position of the spots in the diffraction pattern corresponds to the points of a lattice known as the reciprocal lattice, which is related to the real one by mathematical equations. In the reciprocal lattice, the interplanar spacings are inversely proportional to those of the real lattice.
The intensity of each diffraction spot reflects the sum of the X-rays diffracted along one particular direction by the electrons in the protein, which is related to the spatial density of the electrons in the crystal.
The radiation scattered in a particular direction by the crystal unit cell can be described through a periodic function called structure factor F_{hkl}, which represents the combined contribution of all atoms to the reflection from the *hkl* plane

$$F_{hkl} = \sum_{j}^{n} f_j e^{i2\pi \mathbf{r}_j \cdot \mathbf{S}} \tag{2.2}$$

in which f_j is the scattering factor of atom j in a unit cell containing n atoms, r_j is the position vector of atom j and S is the scattering vector, calculated as the difference between the wave vectors of elastic diffuse radiation and incident radiation. The amplitude of F_{hkl} is proportional to the square root of the reflection intensities recorded at the detector and can therefore be calculated from measured reflection intensities.
Structure factors are related to the electron density ρ of the unit cell through a Fourier transform operation (Eq. 1.3). The electron density is expressed as a Fourier sum of structure factors corresponding to specific reflections observed in the diffraction pattern.

$$\rho(x,y,z) = \frac{1}{V} \sum_{h,k,l} |F_{hkl}| \, \mathrm{e}^{-\mathrm{i}[2\pi\,(hx+ky+lz)-\alpha_{hkl}]} \tag{2.3}$$

V is the volume of the unit cell, the Miller indices hkl associate the scattered radiation in a specific direction to the corresponding lattice planes, and α_{hkl} is the phase of the structure factor. The number of reflections determines the level of detail observable in the calculated electron density map and depends on the resolution of the data. In protein crystallography, the resolution is defined either as the maximum diffraction angle at which reflection intensities can still be measured, or, more commonly, as the minimum interplanar spacing corresponding to that angle. A higher resolution thus corresponds to smaller interplanar distances.

F_{hkl} is a periodic function characterized by amplitude and phase. While the amplitude can be determined from the measured reflections, the phase cannot be directly obtained. To compute ρ(x,y,z) from the structure factors, it is important to calculate the phase of the diffracted rays. This is called "the phase problem".
Methods for solving the phase problem are classified as direct or indirect, both providing an initial estimation of the phase to generate interpretable electron density maps that can later be refined. Direct methods use probabilistic approaches to derive phases from observed amplitudes via mathematical relationships, but their application to complex biological macromolecules is limited. On the other hand, indirect methods are widely used in protein crystallography, and include experimental approaches such as Single and Multiple Isomorphous

Replacement (SIR and MIR), which exploits intensity variations in isomorphous heavy-atom derivatives; Single- and Multi-wavelength Anomalous Diffraction (SAD and MAD), and Single- and Multiple-Isomorphous Replacement with Anomalous Scattering (SIRAS and MIRAS), which rely on anomalous scattering of selected atoms and often require synchrotron radiation. Another commonly used approach, Molecular Replacement (MR), estimates initial phases from the atomic coordinates of a structurally similar molecule, properly oriented and positioned within the unit cell of the protein crystal [301]. With this method, an available structural model that is assumed to approximate the unknown structure and a set of measured diffraction intensities are chosen. All possible orientations and positions of the model within the unknown crystal lattice are systematically explored, and the solution that gives the best agreement between the calculated and observed diffraction patterns is identified. The phases of the reflections for the unknown crystal are then derived from those calculated for the model, as if the model itself had crystallized in the target lattice. An initial electron density map is subsequently computed using these model-derived phases in combination with the experimentally observed structure factor amplitudes [302].

2.1.6 From the electron density to model

The initial electron density map, calculated via Fourier transform using experimental phases obtained from ab initio methods or MR, must be improved through an iterative refinement process, as the initial phases are only approximate and the resulting map may be poorly defined or unclear. Anyway, the initial phases must be good enough for a first interpretation. The process involves incorporating all features that can be reliably identified or inferred from the map into the phasing model for subsequent iterations. Without introducing new information to modify the original model, the map cannot improve. Such modifications may include solvent flattening, non-crystallographic symmetry averaging, or the inclusion of a partial atomic model. Then, the initial atomic model is optimized through a combined process of map interpretation and refinement of the atomic coordinates. The refinement process aims at minimizing the differences between calculated and observed structure factors through least-squares or maximum likelihood methods. The minimization methods work on the refinement of several atom parameters, such as the positions and the B factors, which indicate the vibrational motion and disorder of the atoms in the model. For example, atoms located at the end of the side chains usually

exhibit more flexibility than those in the main chain and have higher B values. Another important parameter is the occupancy, which reflects the fraction of molecules in which each atom occupies a specific position in the model. Hence, an occupancy of 1.00 means that a specific atom is present in all the molecules forming the crystal. This parameter is important since, in some cases, distinct conformations can be observed for a short sequence of the protein structure, such as a side-chain or for a ligand bound to the protein, that can be modelled using partial occupancies.
To check the quality of the refinement process, two parameters can be calculated: R_{free} and R_{factor}.

$$R_{\text{factor}} = \frac{\sum | \, |F_{\text{obs}}| - |F_{\text{calc}}| \, |}{\sum |F_{\text{obs}}|} \tag{2.4}$$

The R_{factor} quantifies the agreement between the observed and calculated structure factors, where a value of zero denotes perfect correspondence between them. In the refinement procedure, it is possible to make spurious adjustments that reduce the value of R, without improving the quality of the model. To address this issue, a new reliability index, known as R_{free}, was introduced. R_{free} is calculated using a small, randomly selected subset of reflections, around 5%, that are excluded from the refinement process. Together with these two parameters, the deviation from ideal bond lengths, angles, torsion angles, chiral centres, and Ramachandran plot values give information related to the chemical, stereochemical, and conformational reasonability of the model [294].

2.2 Cryogenic electron microscopy (cryo-EM)

2.2.1 Cryo-EM as a structural biology method

Cryo-EM has recently emerged as a powerful structural biology technique for obtaining high-resolution density maps of macromolecular structures.
The first electron microscope was developed in 1933 by Max Knoll and Ernst Ruska [303]. While it is now extensively used in structural biology, the technique was originally not optimized for imaging biological samples. Indeed, two main problems were related to the use of electron microscopy (EM): first, maintaining the samples under the high-vacuum conditions required inside the microscope column (vacuum is essential to prevent the scattering of the electron beam with the air molecules, which would reduce image quality and resolution), and second, preventing structural damage caused by the highly energetic electron beam [304]. In 1981, Jacques Dubochet and Alasdair McDowall revolutionized EM by introducing the rapid vitrification of biological samples in a thin layer of ice, marking the birth of cryo-EM [305, 306, 307]. This innovation preserved the samples in a hydrated state close to their native one and minimized beam-induced damage. Despite early limitations related to low image contrast and high noise levels, advances in computational image processing, together with the development of new algorithms and software, have improved the reconstruction of 3D structures from noisy 2D projections [304]. Further improvements in image quality and acquisition speed were achieved with the introduction of direct electron detectors, which allow precise tracking of particle motion during data collection [304]. Consequently, the number of structures deposited in the Electron Microscopy Data Bank (EMDB) has grown exponentially in the last years, allowing the study of complex biological assemblies and membrane proteins previously inaccessible to X-ray crystallography [308]. Membrane complexes can also be studied in lipid vesicles that mimic the membrane cell structure and function. Moreover, because cryo-EM does not require crystallization, it is also suitable for analyzing flexible samples.
Notably, single-particle cryo-EM technique allows visualization of single conformational states, providing valuable insights into molecular dynamics [304]. However, for decades, high-resolution structural determination of macromolecules smaller than 200 kDa by cryo-EM single-particle analysis was considered infeasible. The introduction of direct electron detectors enabled the previously underestimated potential of cryo-EM for studying small complexes. Then, advances in sample preparation, imaging strategies, and data-processing algo-

rithms further improved the ability to visualize small biological targets. As a result, structures of macromolecules with molecular weights of $\sim$ 39 kDa have now been determined [309, 310]. Specific strategies can be used to study smaller proteins, including increasing the apparent size of the target protein by forming complexes with chaperone molecules, such as antigen-binding fragments (Fabs) or nanobodies [311].

2.2.2 Electron microscope

Electron microscopes consist of an electron source, a series of electromagnetic lenses, which are copper coils under tension, and an image-detecting system [312]. Electron detectors have evolved from photographic film to modern direct electron detectors capable of accurately recording the position of almost every incident electron [313].

The standard electron source is usually a tungsten filament heated to 2000-3000 °C. In this condition, the electron energy is higher than the work function of tungsten, resulting in the thermal emission of electrons, which are then accelerated toward the anode by an electric field. To date, the most advanced electron source is the field emission gun (FEG) [314]. The beam then passes through an aperture that blocks electrons scattered at high angles, preventing them from reaching the image plane and thus improving image contrast and beam coherence. Next, condenser lenses convert the diverging electron beam into a parallel one, regulating the beam size that then interacts with the sample. Subsequently, the objective lens provides the primary magnification (20-50x) of the image obtained. Like the condenser lens, the objective lens is coupled with the objective lens aperture, which stops electrons from being widely scattered, increasing the contrast of the image.

Before electrons reach the detector, the image is further magnified by the intermediate and projector lenses (figure 2.5).

Similar to optical lenses, the electromagnetic ones exhibit a series of defects, including spherical and chromatic aberrations and astigmatism [315] (figure 2.6). Spherical aberration is an image distortion that occurs because the focal point of rays varies with their distance from the optical axis. Rays passing through the periphery of the lens are stronger than those near the axis (paraxial rays). Chromatic aberration results from differences in electron energy caused by voltage variation in the electron source, electron energy spread in the primary beam, and energy loss due to inelastic events when the beam passes through the sample. These effects result in image blurring and a loss of fine detail. Notably,

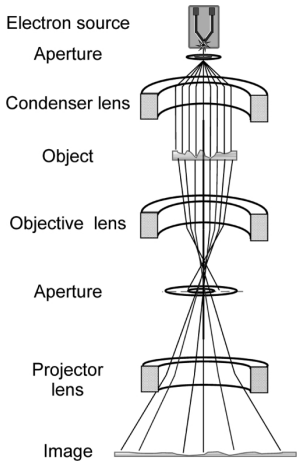

Figure 2.5. Structural representation of the different components of an electron microscope (figure from [312]).

lenses focus rays with longer wavelengths more strongly, causing the formation of that part of the image in a plane close to the object and producing "colored" halos around edges in the image. On the other hand, astigmatism is caused by an asymmetric magnetic field in the lenses: a deviation from axial symmetry produces a slightly stronger field in one direction than in the perpendicular one. Consequently, two image planes result from these directions, so that the image of a point becomes an ellipse. This effect can be corrected by using stigmator coils [312].

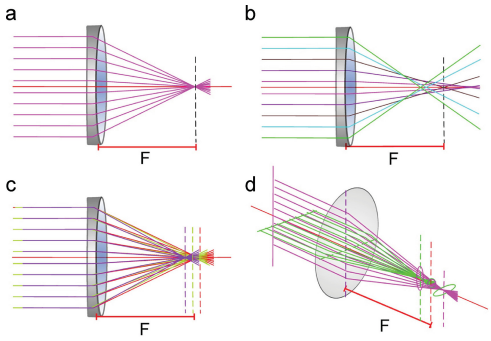

Figure 2.6. Different types of defect of electromagnetic lenses: a) perfect lens, b) spherical, c) chromatic, and d) astigmatic aberration. F represents the focal length of the lens (figure from [312]).

2.2.3 Sample preparation

Structural biology experiments, including cryo-EM, begin with the preparation of a highly purified protein solution under conditions similar to its native cellular environment [316]. To this aim, parameters such as pH, salt concentration, and the presence of specific additives are carefully optimized. The resulting protein solution is then applied to a specific EM grid and blotted with filter paper to remove the excess. Subsequently, the blotted grids are rapidly plunged into liquid ethane (-180 °C), kept cold by liquid nitrogen [307] (figure 2.7, panels A and B). The blotting method is the first and most used technique to obtain a thin layer of ice on grids. However, alternative approaches, such as liquid droplet deposition and pin-printing techniques, are also employed to achieve faster freezing time and thinner ice layers [317, 318].
The vitrification procedure preserves the sample in its native and hydrated state and partially protects it from radiation damage, keeping the protein within an ice layer [319].

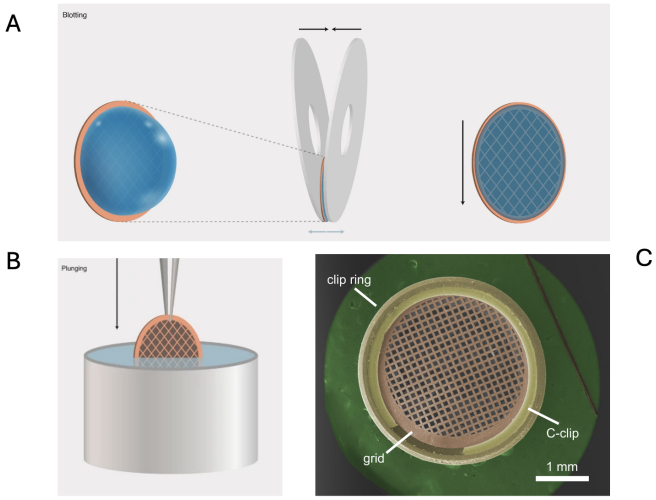

Figure 2.7. Schematic representation of the blotting (A) and plunging (B) steps used for grid preparation. After sample application onto the grid, excess liquid is removed by filter paper pads. The grid is then rapidly immersed into a cryogen bath, with the grid edge making initial contact, followed by the rest of the grid. Panel (C) shows a scanning electron microscopy image of an autogrid cartridge, highlighting its individual components (figure adapted from [320, 321]).

Moreover, the rapid freezing procedure allows the sample to reach a solid state without ice crystal formation, preserving it at low temperatures during transfer and observation in the electron microscope. Data collection is influenced by

the sample vitrification procedure. The perfect condition is obtained when the vitrification forms an amorphous thin ice layer in which the protein is incorporated, while a thick ice layer reduces the contrast of the particle, making the subsequent process of particle picking more difficult [322]. On the other hand, if the ice layer is too thin, the number of particles per hole decreases and/or a larger fraction of them may be directly exposed to the vacuum of the column, thus increasing the probability of sample damage [323, 324]. To prevent these issues, parameters such as blotting time, blotting force, chamber temperature, and humidity can be controlled to regulate ice thickness. In addition, the type of sample support, the grid batch, and the hydrophilicity of the support can also influence the final ice layer [304].
Moreover, during the preparation of the grids and before the vitrification, the samples may be exposed to the surface of the thin aqueous film where potentially damaging air–water interface interactions can occur. To reduce this problem, grids can be covered with a thin supporting layer that provides an adherent surface for the specimens [325]. Usually, this film is made of carbon or graphene oxide and needs to be as thin as possible to avoid background noise during grid imaging. Those types of covered grids can be directly purchased or prepared by using a carbon evaporator.
Obtaining a homogeneous, contamination-free sample with particles uniformly distributed within a thin layer of vitreous ice is a critical step in grids preparation. There is no universally optimal condition applicable to all samples, as different proteins exhibit distinct properties and behaviors. For instance, soluble proteins typically present hydrophilic residues on their surface, allowing them to adopt multiple orientations when embedded in thin ice. In contrast, membrane proteins contain hydrophobic residues within their transmembrane regions that can interact with the air–water interface, often resulting in partial unfolding, structural damage, and pronounced preferential orientation [326]. Consequently, only a limited set of particle views may be observed during imaging, which complicates the reconstruction of a complete 3D structure during image processing. The use of detergents, amphipols, or nanodiscs that mimic the lipid bilayer during purification can solve these issues [327]. Additionally, detergents may be included during grid preparation to reduce interactions between the sample and the air–water interface, thereby minimizing preferential orientation and improving particle distribution.

The grids are composed of a mesh base and a foil, which vary depending on the samples used. Meshes are made of different metals, such as copper, gold, or nickel. Among these, copper is the most used, whereas gold grids are preferred

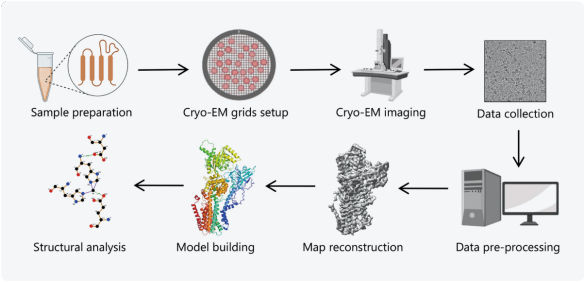

Figure 2.8. Typical structural analysis workflow using single-particle cryo-EM technique (figure from [328]).

when higher resolution is required, as gold provides better electrical conduction and heat dissipation, resulting in a more stable imaging environment. Meshes are covered on the top by perforated foil, containing regularly spaced holes of defined size. Since proteins are purified in aqueous-based solutions, the grids need to be made hydrophilic to allow the sample to spread across their surface. This is achieved by glow-discharging the grids using a plasma cleaner under controlled gas conditions, typically using a mix of argon and oxygen. If plasma cleaning were performed in air, the surface of the grid would mainly interact with oxygen and water, which are reactive, resulting in a negatively charged surface, which is the opposite of the desired effect. By using an argon–oxygen mixture, organic contaminants are removed, and the grid's hydrophobicity is temporarily reduced, enabling the deposition of a liquid sample [329].
Before loading the grids inside the autoloader of the microscope, they need to be prepared by clipping them with a c-shaped ring. The rings secure the grids and allow them to be fitted into the autogrid cartridge, preventing them from falling into the column during the analysis (figure 2.7, panel C).

2.2.4 Image formation

Image contrast results from the interaction of the incident electron beam with the nucleus or electron clouds of the atom of the sample. There are three distinct ways to achieve image contrast, depending on the type of interaction: electrons may pass through the specimen unaffected, undergo elastic scattering without loss of energy, or lose part of their energy via inelastic processes (figure 2.9). Inelastic interactions can ionize atoms in the specimen, induce X-ray emission, chemical bond rearrangement, and free radicals, altering the sample structure and leading to a less contrasted image. Thus, although electron microscopes provide advantages in high-resolution imaging (due to their short

wavelength), the interaction with the electron beam causes radiation damage to the sample. To minimize radiation damage, a low-dose system is employed during measurement setup, including area selection, alignment, and focusing [312]. Moreover, it is possible to equip microscopes with an energy filter, which discards inelastically scattered electrons, providing a more contrasted image.
Differences in beam–sample interaction generate two types of image contrast: amplitude and phase contrast [312]. Amplitude contrast results from the absorption of part of the incident beam in the specimen, while phase contrast arises from the phase shift between the unscattered and elastically scattered electrons. In this case, the shift depends on the electron path length, which can vary through the objective lens defocusing (when the focal point is just after the sample). So it is possible to obtain images with different contrasts during data collection by modulating the defocus. Moreover, since biological samples are mainly composed of light atoms (such as H, O, N, and C), only a small fraction of the electrons is absorbed, resulting in a low amplitude contrast. The use of the objective diaphragm aperture increases the amplitude contrast since it stops electrons scattered at high angles.
Image formation results from the scattering of electrons by the sample and the ability of the lenses to refocus them. First, after the beam-sample interaction, the electrons are collected in the focal plane of the objective lens, forming a diffraction spectrum that can be mathematically described as the Fourier transform of the object. Then the electrons are recombined to produce a magnified image. The image formation from the diffracted spectrum is mathematically described through the inverse Fourier transform of the object [330].

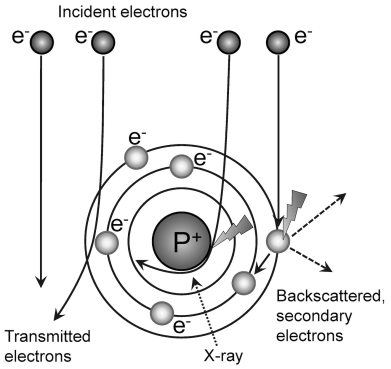

Figure 2.9. Schematic representation of the different types of electron beam–sample interactions. From left to right: electrons that pass through the specimen unaffected, elastic scattered electrons, and inelastic scattered electrons resulting from the interaction with the nucleus or the atomic electrons (figure from [312]).

2.2.5 Data collection

An automated data collection system is designed to perform repetitive and time-consuming tasks, such as identifying suitable specimen areas and acquiring large datasets. After the alignment of the microscope and the insertion of the grids, an atlas is collected. The atlas is a collection of images acquired at low magnification and low electron dose that, when combined, reconstruct the image of the entire analyzed grid. This essentially represents a map that enables a quick evaluation of the grid quality and the identification of promising areas for data collection. Then, a region with good ice thickness is selected, and at higher magnification, a square containing many good holes is chosen. Next, data collection is automated, and each selected hole is analyzed, producing multiple movies per hole that are ready for processing (figure 2.10).

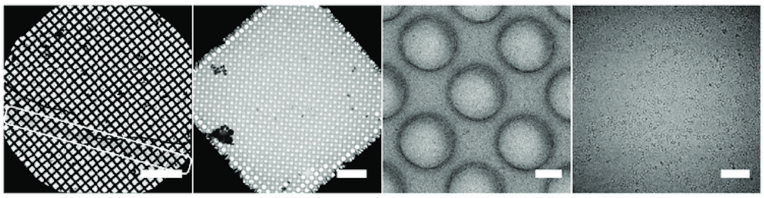

Figure 2.10. From left to right: low-magnification overview of the entire grid (atlas); a selected square showing the regular pattern of holes; higher-magnification image showing the holes in the selected square and high-magnification view displaying the distribution of particles within the ice (figure from [318]).

Despite the automation of data collection, some parameters must be manually set before acquisition, including the magnification, defocus range, total electron dose, and exposure time.

Magnification determines the pixel size of the images and the resolution limit of the dataset. Indeed, theoretical maximum resolution is defined by the Nyquist frequency, which corresponds to two times the pixel size. In practice, this limit is not often reached at small pixel sizes, because there is a loss of high-resolution signal due to factors such as microscope optics and electron source.

As mentioned above, phase contrast is achieved by introducing a controlled defocus during data collection. Usually, images are acquired with defocus values ranging from –0.5 to –3 μm, providing a balance between images with high resolution information and enough contrast to identify particles.

Moreover, it is also important to set an appropriate electron dose for the incident beam. A high amount of high-energy electrons can cause radiation damage, whereas a low dose may result in insufficient image signal. A procedure

known as dose weighting is used to optimize the electron dose for the sample by regulating the beam size, intensity, and exposure time during data acquisition. Usually, electron doses range from 30 to 60 electron/Å^2, with 30 to 40 frames per movie, although higher doses can also be used. Indeed, the total dose can be increased to reach a better contrast for difficult samples[331].

2.2.6 Data processing

After data collection, the data processing procedure consists of four major steps: pre-processing, processing, refinement and model building.
The first step involves motion correction, which is essential because interactions with the electron beam cause molecular vibrations that adversely affect image quality [332, 333, 334]. During data collection, several thousand movies are collected, each containing different frames. The frames allow tracking the movements of the particles during the data acquisition. The correction is performed using software that aligns individual frames of the movie to one another, producing a clear and highly contrasted micrograph that can be used for the rest of the data processing. Moreover, during movie acquisition, the sample is exposed to an increasing electron dose that is proportional to the total exposure time. Therefore, the earliest frames of the movie exhibit less radiation damage, lower contrast, and higher-resolution detail compared to the later frames, which exhibit increased radiation damage, higher contrast, and lower-resolution information. The motion correction software also applies a dose-weighting procedure that allows the preservation of high-resolution data from the earliest frames while reducing the degraded high-resolution signal from the later frames, resulting in aligned micrographs of optimal quality [331].
In electron microscopy, recorded images are only projections of the sample, which are affected by aberrations that distort the "true" representation of the object. The Contrast Transfer Function (CTF) models the effect of defocus and microscope aberrations, such as spherical aberration and astigmatism, on single particle images [335]. The CTF is a sinusoidal wave that starts at zero at low spatial frequencies (low resolution information) and oscillates between +1 and -1, corresponding to positive and negative contrast, respectively. Therefore, the CTF defines how contrast is transmitted and lost. When the CTF crosses zero, no contrast is transferred, resulting in a loss of information. Computer programs such as Gctf [336] and CtfFind4 [335] perform CTF estimation and correction, representing a crucial step in image processing. During data collection, all the parameters are maintained consistent, except for astigmatism

and defocus. A range of defocus values is essential to obtain the maximum amount of information from the dataset, since it reduces the effects of missing information introduced by the zero crossings of the CTF. Information lost at the zero crossings of a CTF with a defocus of –0.5 μm can be recovered using another CTF at –1 μm defocus, which exhibits zero crossings at different spatial frequencies (figure 2.11).
Following motion and CTF correction, the obtained micrograph is used for particle picking, which represents the final step of the pre-processing procedure. In this case, particles of interest are identified for extraction in the subsequent image processing steps. While particles were initially selected manually, modern

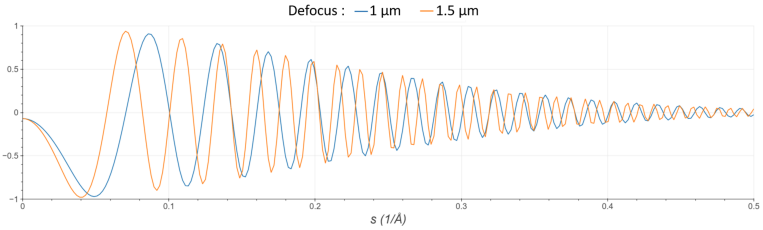

Figure 2.11. Examples of CTF curves at different defocus values (figure from [331]).

cryo-EM now relies on automated or semi-automated algorithms that accelerate this step and can outperform manual picking, especially for large datasets. Semi-automatic methods use manually selected particles to generate 2D class averages as templates for automatic picking. Recent advances in machine learning have led to particle pickers software, including DeepPicker [337], crYOLO [338], Topaz [339], Warp [340], and DeepCryoPicker [341], which train neural networks to distinguish good particles in a dataset. Generic models or user-provided data, usually a set of good particles with different views extracted from micrographs acquired at various defoci, can be used to train the algorithm, enabling it to learn how to distinguish the object of interest from noise or contamination. These tools are often combined with algorithms that enhance particle contrast without compromising resolution, improving performance on noisy datasets.
The particle-picking procedure provides the coordinates of each identified particle on the corresponding micrographs. Particles are then extracted inside a centered box, which is usually 50% bigger than the longest view of the particle. After all particles are extracted into a particle stack, they undergo 2D classification to provide an initial assessment of the heterogeneity of the sample. In this process, particles are compared with each other and grouped into classes

based on their orientation. Factors such as x and y translations, rotations, and CTF are considered to align similar particles, which are then averaged to enhance the signal. The 2D classifications allow a first analysis of the sample. It provides a clear visualization of the different particle orientations present in the dataset, allowing the identification of potential preferential orientation. In addition, 2D classification reveals the first detailed structural features of the particles. The absence of expected features may indicate insufficient data quality, arising from either data collection or sample preparation. Finally, this step facilitates the removal of poorly aligned particles, as well as contributions from noise and contamination.

After 2D classification, the remaining good particles are used for 3D structure determination. The projection-slice theorem provides the theoretical foundation for reconstructing a 3D object from 2D projections.

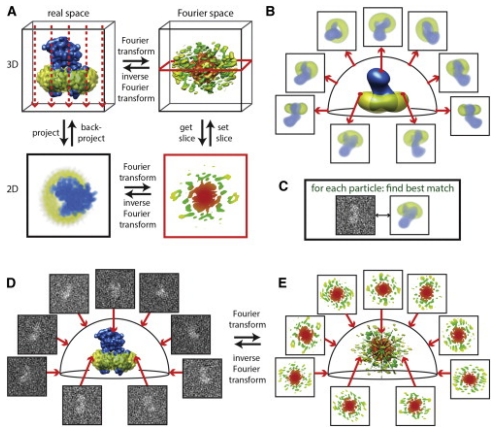

Figure 2.12. Cryo-EM 3D structure determination. (A) The Projection-slice theorem. In the real space (left column), the 2D projection of a 3D object corresponds to the central 2D slice of the 3D Fourier transform of that object (right column). (B) From an initial reference, different orientations of the particles are generated from computational projections. (C) Each experimental particle is then compared to the reference projection to (D) identify the best-matching orientation relative to the 3D structure. (E) The projection-slice theorem and back projections of the 2D images are then applied using an inverse Fourier transform to generate the 3D structure. These steps are then iteratively repeated to progressively improve the quality of the 3D reconstruction (figure from [342].

According to this theorem, the Fourier transform of a 2D projection corresponds to a central slice of the 3D Fourier transform of the object (figure 2.12). Therefore, by correctly combining all the 2D Fourier slices with respect to the 3D Fourier transform, the original 3D structure of the object can be obtained using the inverse Fourier transform. Thus, an ab initio 3D model is generated

from selected particles of 2D classes [343]. Starting from the initial 3D model, further refinement is carried out using software that implements a Bayesian approach [343, 344]. Then, the 3D model is iteratively refined by first comparing projections of the ab initio model with the experimental images, providing information about the relative orientations of the particles. Subsequently, images are recombined by back-projection, incorporating prior information to generate an updated model for the next iteration. In the final iteration, two sets of data are separated, which are independently refined and compared using the Fourier Shell Correlation (FSC) to assess the resolution of the final map [345]. Finally, the resulting 3D map serves as the basis for model building and refinement.

3 Design and evaluation of compounds targeting carbonic anhydrase and histone deacetylase

3.1 Introduction

Numerous multi-target inhibitors directed against the HDAC and hCA enzyme families have been described in the literature as promising therapeutic candidates for several pathological conditions (see paragraphs 1.2.6 and 1.3.1).
In particular, the combination of HDAC and hCA inhibitors has demonstrated a pronounced synergistic effect in several studies, underscoring its potential relevance in cancer therapy.
Indeed, a highly synergistic anti-proliferative action has been observed across various cancer cell lines following the combined administration of the hCA IX inhibitor SLC-0111 and the second-generation HDAC inhibitor suberoylanilide hydroxamic acid (SAHA) [346]. Similarly, co-treatment with SLC-0111 and the HDAC inhibitor Pyroxamide effectively suppressed the proliferation, migration, and invasion of diffuse intrinsic pontine glioma cells, while promoting histone acetylation and reducing the proportion of cells in the S phase [347]. In addition, the co-administration of the hCA inhibitor Acetazolamide (AAZ) and the HDAC inhibitor Entinostat resulted in a pronounced decrease in cell viability and migration in neuroblastoma cell lines compared to single-agent treatments [348, 349].
Recently, Bozdag et al. [350] designed and synthesized a series of HDAC/CA dual-target inhibitors, demonstrating *in vitro* inhibitory activities comparable to those of the respective reference compounds, along with well-defined selectivity profiles toward both enzyme families. Notably, the best *in vitro* performing compounds toward the tumor-related isoforms hCA IX and HDAC3 were highly effective in reducing the proliferation *in vitro* of multiple tumor cell lines, while

displaying significantly lower toxicity toward normal endothelial colony-forming cells (ECFCs), even relative to the clinically approved HDAC inhibitor SAHA. Based on all these promising results, a new generation of dual-target agents incorporating the classical HDAC and CA pharmacophores was designed and synthesized by the group of Prof. Fabrizio Carta in the Neurofarba Department at the University of Florence. A schematic representation of the structures of the dual-target compounds is provided in the figure 3.1. A benzamide and a benzenesulfonamide group are linked together with a variable range of spacers.

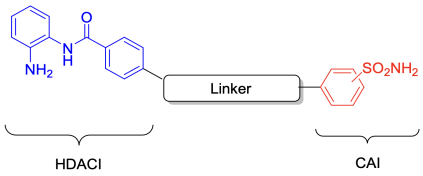

Figure 3.1. The schematic structure of the dual-target compound designed and synthesized for this study (figure from [350]).

In this study, both structural and inhibition analyses were performed on the new series of compounds using the physiologically relevant hCA isoforms I, II, IX, and XII. For the crystallographic analysis, the hCA XII-mimic construct was used. The hCA XII-mimic, as well as the hCA IX-mimic, consists of engineered variants of hCA II in which specific residues have been substituted to reproduce the active sites of the corresponding transmembrane isoforms [351, 352]. The use of these engineered constructs is preferred over the native proteins, as membrane-associated CAs are challenging to express in quantities that are soluble, properly folded, and suitable for crystallographic studies [353]. Moreover, in collaboration with Prof. John W. R. Schwabe at the Department of Molecular and Cell Biology of the University of Leicester (UK), selected HDAC complexes were expressed and purified. The inhibition efficacy of the dual-target agents was then evaluated on four HDAC corepressor complexes: two with HDAC1, the CoREST and MiDAC complexes, and two with HDAC3, the NCoR1 and NCoR2 complexes.
In addition, structural investigations were carried out on the Bozdag et al. compounds [350] to elucidate differences in their binding modes and to correlate these findings with the reported inhibition data.
The work aims to gain useful insights that will provide a structural and functional basis for the rational design of more potent and selective dual-target inhibitors. To this aim, docking analyses were also performed in collaboration with Prof. Paola Gratteri and Dr. Alessandro Bonardi at the Neurofarba

Department of the University of Florence, to provide a preliminary assessment of the binding modes of the compounds within the HDAC complexes.

3.2 Results

3.2.1 *In vitro* hCA Inhibition assay

The series of new synthesized compounds is shown in figure 3.2.

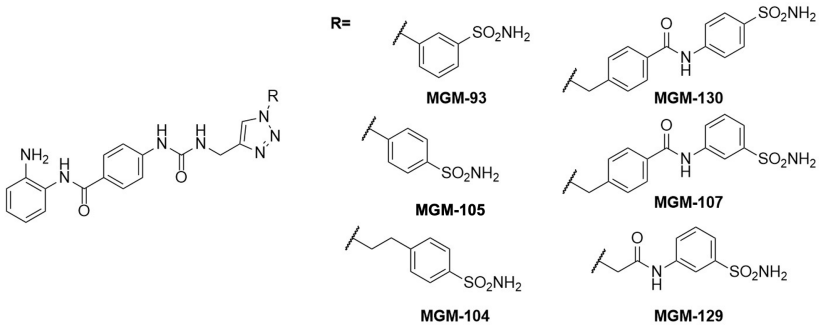

Figure 3.2. Chemical structures of HDAC-CA dual-target inhibitors series.

The inhibition profiles of the dual-target agents, along with the reference hCAI drug AAZ, were analyzed by a stopped-flow CO_2 hydrase assay on the physiologically relevant hCA isoforms I, II, IX, and XII, as shown in table 3.1. Compared to the reference inhibitor AAZ, the tested dual-target compounds generally do not exhibit greater efficacy, except for isoform I. Moreover, compared to the previous series of inhibitors reported in Bozdag et al. work [350] (figure 3.3 and table 3.1, data marked with an *), the new dual-target agents don't show pronounced selectivity against cancer-related isoforms. The following structure-activity relationships (SARs) may be determined from the inhibition data.

MGM-93, the shortest within the series of compounds together with MGM-105, is the most potent inhibitor of hCA I in the series, displaying a K_I of 4.0 nM. However, in MGM-105, shifting the sulfonamide group from meta- to para-position on the benzene ring drastically decreases the efficacy against the isoform I (K_I=154.9 nM).

The regioisomeric effect is not observed for the isoform II, where both compounds display comparable inhibitory potency (K_I= 44.4 and 44.2 nM). Interestingly, the behavior is reversed in isoforms IX (MGM-93, K_I=242.0 nM and MGM-105, K_I=69.3 nM) and XII (MGM-93, K_I= 73.7 nM and MGM-105, K_I= 17.5 nM), with MGM-105 emerging as the most potent inhibitor of hCA IX and XII among all compounds in the series.

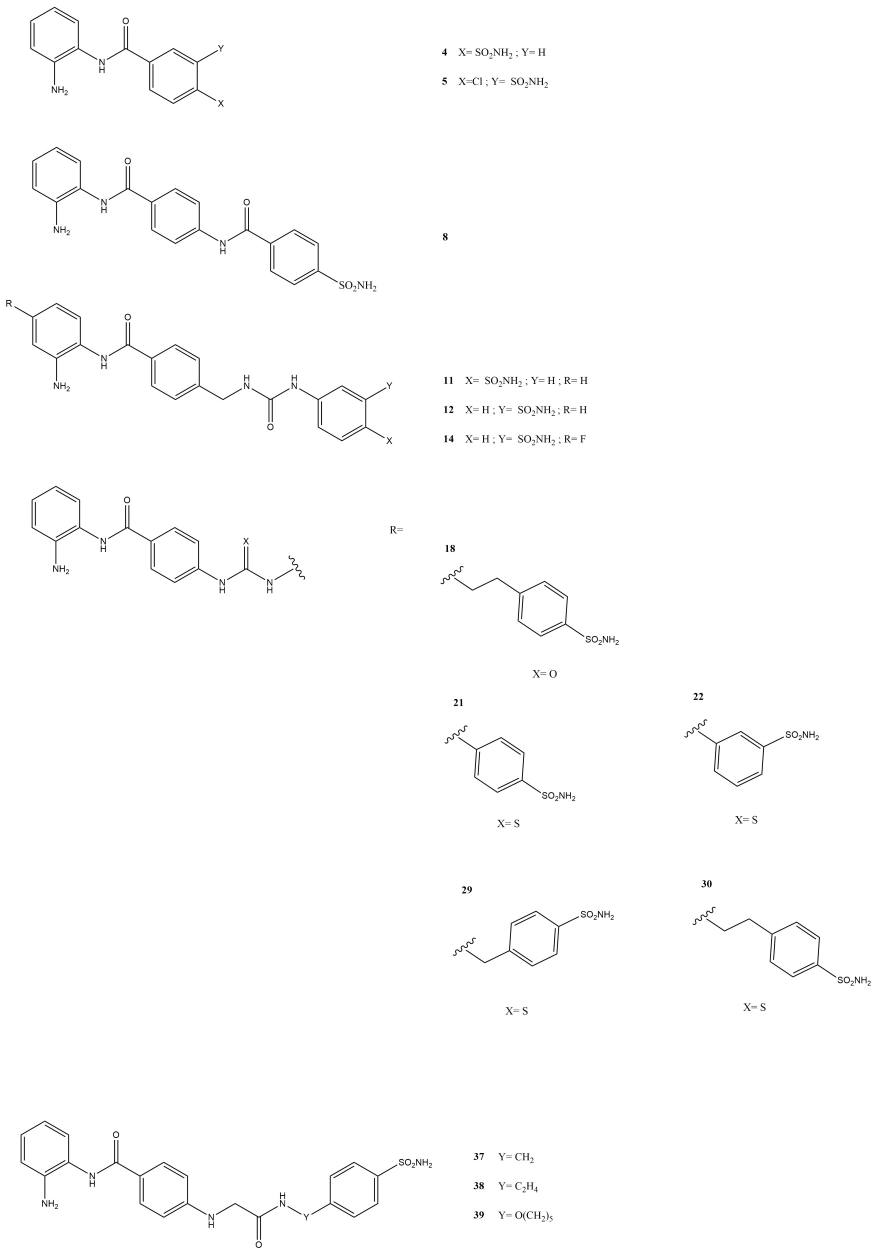

Figure 3.3. Chemical structure of Bozdag et al. compounds [350].

The introduction of a bulky spacer, such as the benzyl amide moiety, leads to a marked reduction in the efficacy against all the hCA isoforms, with a stronger effect observed when the sulfonamide group is in meta-position, MGM-107, than in para-position, MGM-130.

Conversely, compounds bearing less bulky spacers, such as MGM-129 and

MGM-104, maintain a high efficacy toward the hCA I and II isoforms, with MGM-104 showing a higher inhibition potency on isoform II compared to the other compounds of the series (K_I=27.9 nM). On the other hand, the introduction of a spacer in the inhibitor structure reduces its potency against isoform IX.

Notably, for the hCA XII isoform, incorporation of an amide group in MGM-129 resulted in a marked decrease in inhibitory efficacy (K_I = 660.5 nM) compared to all other structural modifications examined. On the other hand, the presence of an alkyl spacer in MGM-104 did not significantly affect the compound's inhibitory activity (K_I = 32.4 nM). Overall, the placement of the sulfonamide group in the meta position appears to reduce inhibitory efficacy against the hCA XII isoform.

Table 3.1. Inhibition constants (K_I, nM) of the synthesized compounds against selected hCA isoforms. All measurements were conducted in technical triplicates (errors were in the range of ±5–10 % of the reported values; data not shown). Data marked with an * were taken from [350].

Compound	hCA I	hCA II	hCA IX	hCA XII
MGM-93	4.0	44.4	242.0	73.7
MGM-104	7.4	27.9	286.8	32.4
MGM-105	154.9	44.2	69.3	17.5
MGM-107	745.9	2874	2402	78.0
MGM-129	9.3	37.1	133.4	660.5
MGM-130	88.2	74.6	174.1	60.9
4 *	17.7	3.7	29.3	8.4
5 *	2447	248.0	31.4	8.6
8 *	131.4	12.9	27.5	20.2
11 *	144.6	7.4	31.0	7.3
12 *	533.8	7.7	28.2	8.1
14 *	553.6	7.2	30.8	7.5
18 *	79.4	19.9	29.2	6.9
21 *	97.7	9.4	29.0	9.3
22 *	426.0	88.4	28.6	9.2
29 *	59.7	6.7	28.4	61.4
30 *	63.7	9.1	105.9	67.9
37 *	8537	82.3	18.4	12.5
38 *	7235	59.9	15.7	9.0
39 *	53.9	6.2	31.7	74.7
AAZ	**250.0**	**12.1**	**25.9**	**5.7**

3.2.2 Crystallographic studies

We determined the crystallographic structures of several compounds from the previously reported series [350] as well as some of the newly synthesized derivatives, in complex with hCA I, hCA II, and the hCA XII-mimic. In particular, we solved the structures of compounds 5, 12, 29, and 30 in complex with hCA II, and compound 5 also in complex with the hCA XII-mimic. In addition, the structures of MGM-104, MGM-105, and MGM-129 were determined in complex with hCA II, while MGM-105 also with hCA I.

Analysis of the electron density maps revealed a clear density for the benzenesulfonamide group of the inhibitors, confirming their binding to the enzymes. The inhibitors exhibit the classical binding mode of the sulfonamide moiety in the active site of all isoforms, interacting directly with the zinc ion, forming hydrogen bonds with Thr199/198 (numbering of hCAI/II and hCAXII-mimic, respectively) (figures 3.4, 3.5, 3.6 and 3.7) and establishing hydrophobic interactions through the benzene ring with residues Val121 and Leu198/197 (numbering of hCAI/II and hCAXII-mimic, respectively).

By analyzing the structures obtained for the series of compounds reported by Bozdag et al. [350] and correlating them with the corresponding K_I, we noticed that the presence of the thiourea group seems to direct the selectivity towards the cytosolic hCA II isoform, as suggested by the K_I values of inhibitors 30 and 18, in which the only structural difference is the substitution of the thiourea by the urea group. As observed in the structures of the complexes of 29 and 30 with hCA II, this selectivity effect could be related to a sulfur-aromatic interaction engaged by the sulfur of the thiourea group with Phe131 (figures 3.4 panels A and B, PDB: 28NC, 28ND). In the hCA XII isoform, Phe131 is replaced by an alanine residue, preventing the formation of this particular sulfur-aromatic interaction. Unlike the other two compounds, inhibitor 12 lacks the thiourea group and adopts a different orientation within the enzyme cavity, forming hydrophobic interactions with Phe131 residue (figure 3.4, panel C, PDB: 28NE).
On the other hand, in figure 3.5, we compare the binding mode of 5 within the active site of the hCA XII and II isoforms to understand the better selective action of the compound on the cancer-related isoform hCA XII. From the structural analysis, the inhibitor establishes a higher network of interactions within the active site of hCA XII than the hCA II isoform (figure 3.5 panels

A and B, PDB: 28NG, 28NF). Analyzing the mutations in the active site of hCA XII-mimic with respect to the hCAII isoform, we realized that the Asn67Lys variation in the hCAXII-mimic is the only one that could influence the binding mode of the inhibitor. Indeed, lysine is more flexible and bulkier than asparagine, which may induce a different organization of the inhibitor within the enzyme cavity due to steric hindrance. The inhibitor in hCA II forms a hydrogen bond with Asn67, whereas in hCA XII-mimic, it is oriented in the opposite direction to Lys67.

We also determined the crystal structures of the new series inhibitors, MGM-104 (PDB: 28LR), MGM-105 (PDB: 28LS), and MGM-129 (PDB: 28LT), in complex with hCA II (figures 3.6 and 3.8), revealing a similar binding mode within the enzyme active site. Although MGM-105 assumes a more bent conformation, overall, the positions of the three inhibitors in the hCA II active sites are similar, and they interact mainly with the hydrophobic region of the catalytic cavity. In particular, all compounds establish hydrophobic interactions with Val121, Leu198, and Pro202 and participate in a conserved water-mediated hydrogen bond with Thr200.
Moreover, MGM-105 and MGM-129 exhibit similar water-mediated interactions, involving Asn67, Asn62, and Gln92 via the triazole ring, as well as Gln136 and Gly132 through the benzamide moiety. In contrast, MGM-104 retains only the water-mediated interaction with Gln92 while uniquely establishing a π-stacking interaction between its triazole ring and the aromatic side chain of Phe131. The slightly higher inhibitory efficacy of MGM104 (K_I= 27.9 nM) against hCA II is likely related to this additional interaction.
The compound MGM105 has a very different orientation within the active site of hCA I (PDB: 28NH) compared to that assumed in the active site of hCA II (figures 3.7 and 3.9), with the tail displaced in the opposite direction and making interactions with different regions of the outer rim of the catalytic cavity. However, the positions of the two inhibitor molecules bound to the active sites of chain A and B in the asymmetric unit of the hCA I crystal are very similar. Hydrophobic contacts are established with residues Leu198, Val62, and Lys170, while water bridges are formed with residues His67, Asn69, and Gln92. Moreover, the compound adopts an orientation that allows the formation of a π-stacking interaction with Phe91.
Unfortunately, further insights cannot be derived, as it was not possible to solve the structures of other compounds of this series in complex with hCA I due to scarce electron density corresponding to the region of the inhibitors.

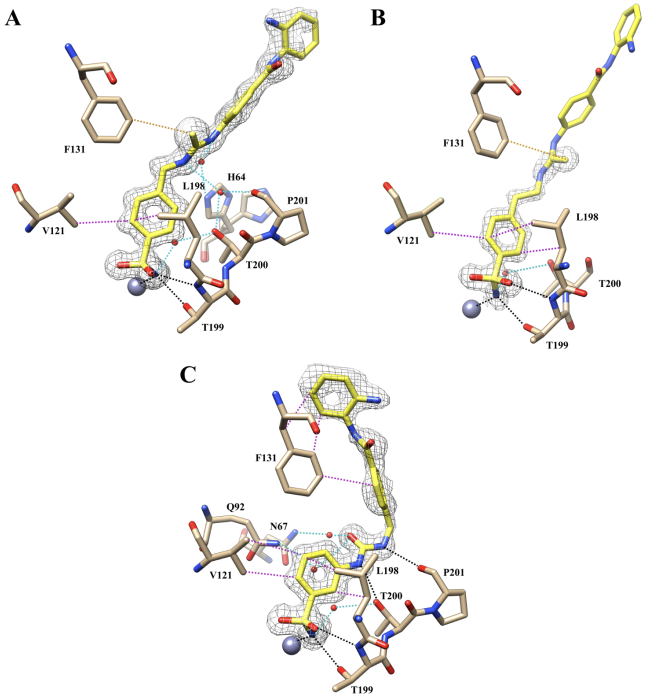

Figure 3.4. Binding mode of the inhibitors 29 (panel A, PDB: 28NC), 30 (panel B, PDB: 28ND), and 12 (panel C, PDB: 28NE) in complex with hCA II isoform. Residues involved in the binding of the inhibitor are shown. Hydrogen bonds, water bridges, and hydrophobic interactions are depicted as black, cyan, and violet dotted lines. The gray sphere represents the zinc ion in the protein active site. In panels A and B, the sulfur-aromatic interaction with the Phe131 is depicted as orange dotted lines.

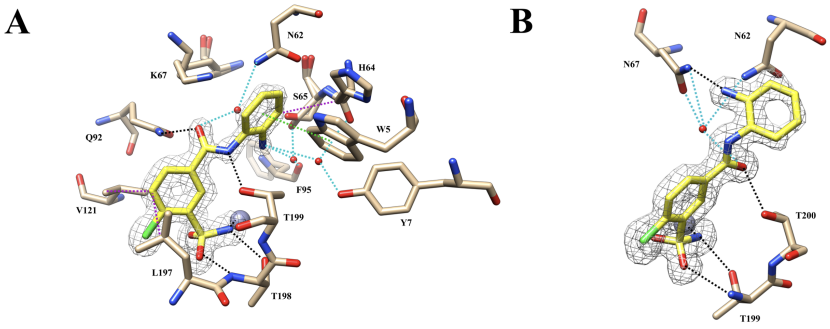

Figure 3.5. Comparison of the inhibitor 5 within hCA XII-mimic (panel A, PDB: 28NG) and II (panel B, PDB: 28NF) active sites. Hydrogen bonds, water bridges, hydrophobic interactions, and π-stacking interactions are depicted as black, cyan, violet, and green dotted lines, respectively.

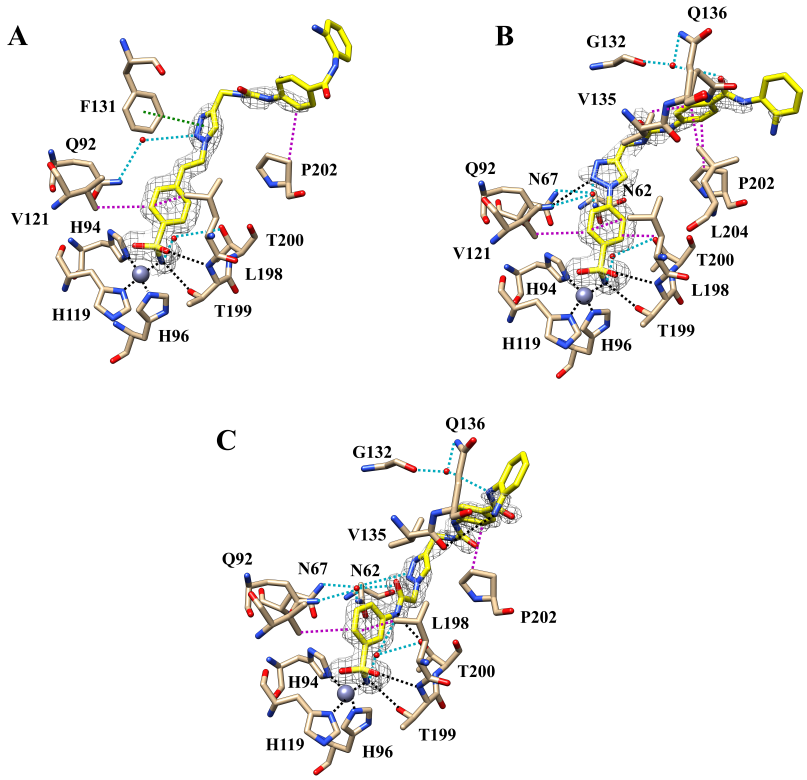

Figure 3.6. Binding mode of the inhibitors MGM-104 (panel A, PDB: 28LR), MGM-105 (panel B, PDB: 28LS), and MGM-129 (panel C, PDB: 28LT) in complex with the hCA II isoforms. Residues involved in the binding of the inhibitor are shown. Hydrogen bonds, water bridges, hydrophobic interactions, and π-stacking interactions are depicted as black, cyan, violet, and green dotted lines, respectively.

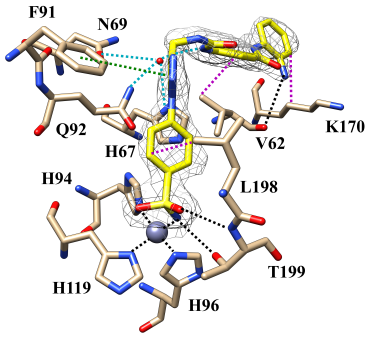

Figure 3.7. The binding mode of MGM-105 in complex with hCA I isoform (PDB: 28NH). Hydrogen bonds, water bridges, hydrophobic interactions, and π-stacking interactions are depicted as black, cyan, violet, and green dotted lines, respectively.

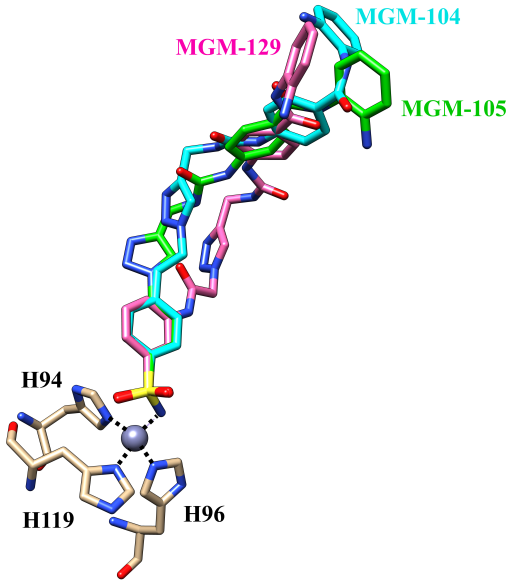

Figure 3.8. Comparison of the three inhibitors MGM-104, MGM-105, and MGM-129 (cyano, green, and pink, respectively) within the active site of hCA II.

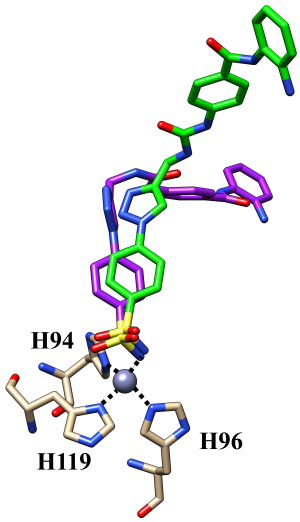

Figure 3.9. Comparison of the different orientations of MGM-105 within the active site of hCA I (violet) and hCA II (green).

3.2.3 Design of Novel Inhibitors

Based on crystallographic data and hCA inhibition assay results, a list of new inhibitor structures was designed to improve selectivity towards the cancer-related hCA isoforms IX and XII (figure 3.10). The structures of these novel dual-target agents reflect those of the compounds described in Bozdag et al. work [350], which demonstrated better efficacy against the hCA IX and XII isoforms. In addition, the new inhibitors incorporate a phenyl or a p–(*N*, *N*-dimethylamino) phenyl ring adjacent to the benzene sulfonamide moiety to enhance the steric hindrance and direct the selectivity toward the cancer-related isoforms, following the "tail approach" strategy (see paragraph 1.2.6). Indeed, the presence of Phe131 within the hCA II active-site cavity increases steric hindrance, thereby limiting the accommodation of compounds bearing bulky substituents, in contrast to hCA IX and hCA XII, which feature a valine and an alanine at this position, respectively. Furthermore, based on crystallographic results showing that the thiourea moiety increases selectivity toward the cytosolic hCA II isoform, the urea group was selected for the new compounds.
The introduction of an *N*-(2-aminobiphenyl) benzamide moiety was also considered for some compounds, as a steric bulk group in the benzamide region may favor interactions with HDAC isoforms 1–3 over HDAC8, due to the distinct structural features of the "foot pockets" area located near the active site (see paragraph 1.3.1).

To obtain a preliminary evaluation of the binding mode of these proposed compounds with the HDAC complexes, molecular docking analyses were performed using the available protein structures reported in the literature of the MiDAC and NuRD complexes with HDAC1 (PDBs: 6Z2K, 7AO8) [274, 210]. The compounds showed a good interaction with the complexes, coordinating the zinc ion with the benzamide moiety. Notably, the presence of a protonatable group at physiological pH (e.g. a tertiary amine group), introduced for synthetic feasibility, enables the formation of salt-bridge interactions with aspartate and glutamate residues located at the entrance of the HDAC1 active site within the MiDAC complex (figure 3.11). These interactions are not observed with the NuRD complex (data not shown) as access to the active site entrance is sterically prevented by the multiprotein assembly. Consequently, the compounds exhibit better selectivity toward the MiDAC complex.
Among the proposed new inhibitor structures, the T_5 was first selected as a prototype for developing new dual-target derivatives (figure 3.12). This structure integrates all the key features expected to enhance selectivity toward

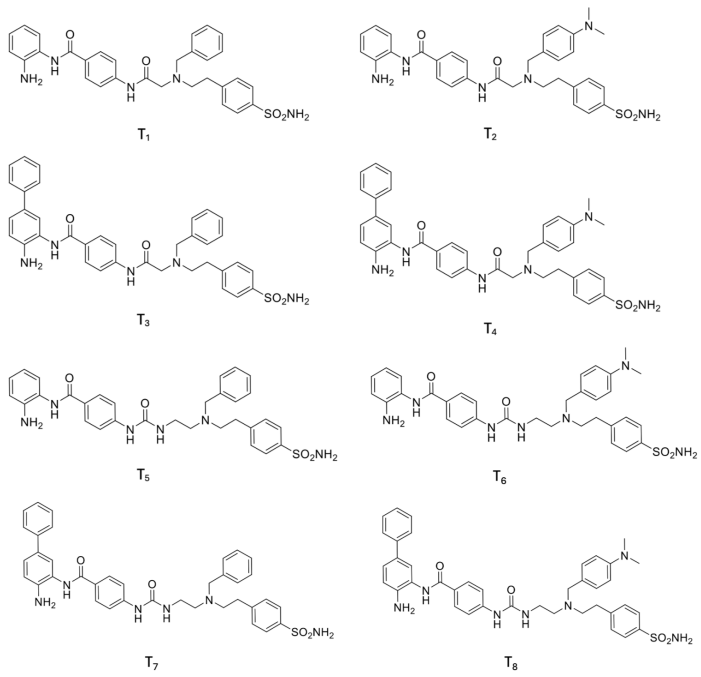

Figure 3.10. Chemical structure of the proposed compounds.

the cancer-related hCA isoforms, while retaining the same core scaffold as compound 18, which exhibits the best inhibitory efficacy against the hCA IX and XII isoforms.

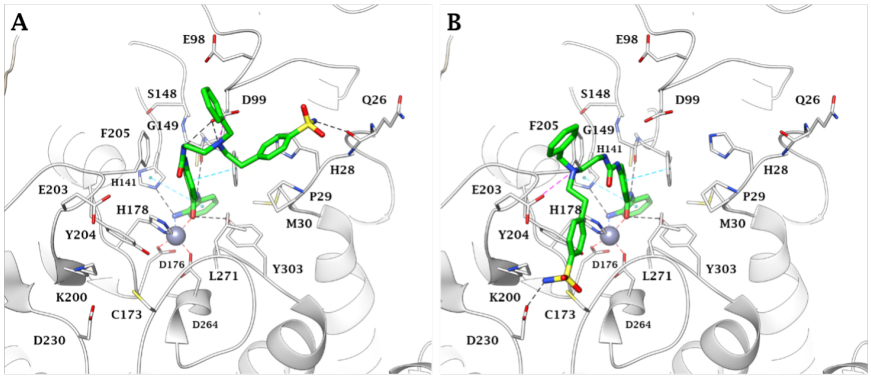

Figure 3.11. Predicted binding mode A) 1, and B) 2 of compound T_5 within HDAC1/MiDAC complex (PDB: 6Z2K [274]). H-bond, π-stacking, and salt-bridged interactions are depicted as black, cyan, and magenta dashed lines. The Zinc ion is represented as a gray sphere.

Moreover, the prototype exhibits better docking score values compared to the

other structures analyzed in complex with the HDAC1/MiDAC complex.
To increase steric hindrance and assess its impact on the selectivity of the compounds, a fluorine, chlorine, or bromine substituent was further introduced into the molecular structures.

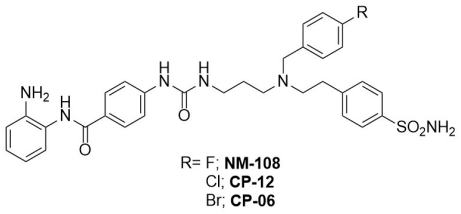

Figure 3.12. Chemical structure of the newly synthesized dual-target inhibitors.

3.2.4 *In vitro* hCA Inhibition assay on new dual-target compounds

The inhibition profiles of the new compounds were analyzed against selected hCA isoforms I, II, IX, and XII using a stopped-flow CO_2 assay (table 3.2).
The introduction of the structural modifications significantly improves selectivity against the cancer-associated isoforms IX and XII over the cytosolic ones. This effect is marked in NM-108 and CP-12, in which the incorporation of fluorine and chlorine substituents results in increased inhibitory potency against isoforms IX and XII, with a strong reduction in activity toward hCA I and II. Specifically, NM-108 exhibits the highest inhibition efficacy against hCA XII (K_I = 5.1 nM), whereas CP-12 is the most potent inhibitor of hCA IX (K_I = 4.6 nM). In contrast, the introduction of a bromine atom strongly reduces the inhibition efficacy on hCA I and II without effectively increasing the inhibition potency against the cancer-related isoform.
A structural characterization of these new derivatives in complex with selected hCA isoforms could not be obtained due to the scarce density in the region of

Table 3.2. Inhibition constants (K_I, nM) of the modified compounds against selected hCA isoforms. All measurements were conducted in technical triplicates (errors were in the range of ±5–10 % of the reported values; data not shown).

Compound	hCA I	hCA II	hCA IX	hCA XII
NM-108	760.3	70.3	6.1	5.1
CP-12	972.6	179.3	4.6	18.1
CP-06	5339.5	337.6	20.1	42.8
AAZ	**250.0**	**12.1**	**25.9**	**5.7**

the inhibitors in the electron density maps.

3.2.5 *In vitro* HDAC inhibition assay

The inhibition profiles of the compounds were evaluated by analyzing the interaction with four HDAC complexes, the CoREST, MiDAC, SMRT (NCoR2), and NCoR1, in the absence of the allosteric regulator inositol hexaphosphate ($InsP_6$) (table, 3.3). In this study, the experimental conditions used for the HDAC inhibition assay differ from those reported by Bozdag et al. work [350]. Overall, the compounds act as effective inhibitors across the enzymatic panel and exhibit better inhibition potency against the HDAC complexes compared to the reference inhibitor CI-994; however, they display limited selectivity toward the individual complexes. CI-994 inhibition values marked with an * were reported in Pytel et al. work [221] and were obtained under comparable experimental conditions. The compounds exhibit good inhibition potency against the HDAC1/CoREST, HDAC3/NCoR2, and HDAC3/NCoR1 complexes, with better efficacy against the HDAC1/CoREST. Lower inhibition efficacy is observed against the HDAC1/ MiDAC complex.

Table 3.3. IC_{50} values (μM) for the dual-target inhibitors against Class I HDAC complexes. All measurements were conducted in technical triplicates, and IC_{50} values with their standard errors were obtained using GraphPad Prism. Data marked with an * were taken from [221]. UR= Unreliable; N.D.= not determined.

Compound	HDAC3/NCoR2	HDAC3/NCoR1	HDAC1/CoREST	HDAC1/MiDAC
MGM-93	0.26 ± 0.05	0.31 ± 0.03	0.058 ± 0.011	2.08 ± 0.87
MGM-104	0.092 ± 0.005	0.043 ± 0.002	0.035 ± 0.007	N.D.
MGM-105	0.036 ± 0.001	0.49 ± 0.01	0.028 ± 0.003	2.22 ± 0.82
MGM-107	0.146 ± 0.006	0.32 ± 0.02	UR	0.42 ± 0.12
MGM-129	0.185 ± 0.008	0.39 ± 0.02	0.074 ± 0.017	N.D.
MGM-130	0.21 ± 0.04	0.29 ± 0.01	0.067 ± 0.012	N.D.
NM-108	0.034 ± 0.013	0.32 ± 0.01	0.29 ± 0.03	1.90 ± 0.37
CP-12	0.080 ± 0.005	0.150 ± 0.008	UR	1.16 ± 0.24
CP-06	0.13 ± 0.02	0.20 ± 0.02	UR	1.10 ± 0.28
CI-994	**0.157 ± 0.005**	**0.80 ± 0.09**	**0.53 ± 0.09***	**4.58 ± 1.1***

NCoR1 and NCoR2 are large homologous corepressor proteins that share conserved amino acid regions (see paragraph 1.3.3), so the results obtained for the two complexes should be comparable. Nevertheless, in this work, two constructs of different lengths were used for NCoR1 and NCoR2; notably, the additional amino acid sequence present in the NCoR1 construct lies in front of the entrance of the active site cavity, partially obstructing access. Interestingly, the compounds show comparable inhibition profiles against the two complexes, except for MGM-105 and NM-108, whose IC_{50} values are approximately 14-fold

and 9-fold higher, respectively, in NCoR1. These two compounds represent the most potent inhibitors of NCoR2 (MGM-105: $IC_{50} = 0.036 \pm 0.001\ \mu M$; NM-108: $IC_{50} = 0.034 \pm 0.013\ \mu M$), whereas in NCoR1 the most effective compound is MGM-104 ($IC_{50} = 0.043 \pm 0.002\ \mu M$).
The strongest inhibitory effect is observed against the HDAC1/CoREST complex, for which MGM-105 emerges as the most potent inhibitor of the series ($IC_{50} = 0.028 \pm 0.003\ \mu M$). The IC_{50} values marked as UR correspond to fits in which the calculated error exceeds the IC_{50} itself. This occurs because the calculated IC_{50} falls below both the protein concentration used in the assay (10 nM) and the sensitivity limits of the instrument, making an accurate determination difficult. To obtain reliable measurements in this potency range, an alternative experimental method, such as testing lower inhibitor concentrations in combination with reduced enzyme levels, or a more sensitive instrument would be required.
A weaker inhibitory effect is observed against HDAC1/MiDAC, except for MGM-107, which displays appreciable potency ($IC_{50} = 0.42 \pm 0.12\ \mu M$). Interestingly, the new synthesized compounds show a slightly better efficacy compared to the MGM-series inhibitors. This may be related to the predicted salt bridges observed in the docking analysis between the tertiary amine group of the compound T5, the parent compound of the new series, and the aspartate and glutamate residues located at the entrance of the HDAC1 active site. However, it should be noted that the docking studies and inhibition assays were performed using constructs of different lengths. In particular, the MIDEAS domain of the MiDAC complex used for docking studies includes residues 717–887 (PDB: 6Z2K, [274]), while the construct for the inhibition assays spans residues 628–887 (PDB: 9R4I, [354]). In the latter case, the additional segment partially occludes the entrance of the active site of the protein, which may affect ligand binding and could account for the reduced efficacy of the compounds against this complex. A dedicated structural analysis would be valuable to elucidate this aspect further. The values indicated as N.D. refer to calculated IC_{50} that could not be determined accurately, as they fall at concentrations higher than the range of concentrations tested. To accurately determine the IC_{50} values for these compounds, experiments would need to be conducted using a higher inhibitor concentration range.

The inhibition curves are summarized in figure 3.13, 3.14, 3.15, 3.16, and 3.17.

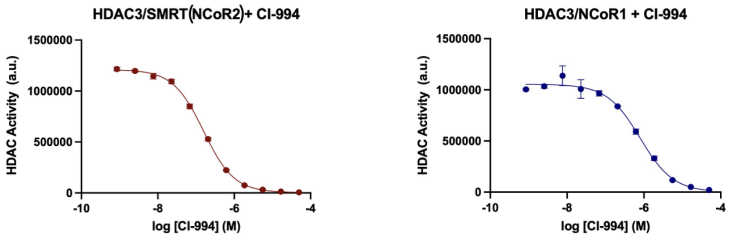

Figure 3.13. Inhibition curves of the reference inhibitor CI-994 against the HDAC3/NCoR2 and NCoR1 corepressor complexes. Experiments were performed in technical triplicate. Error bars represent ± S.E.M. (n=3).

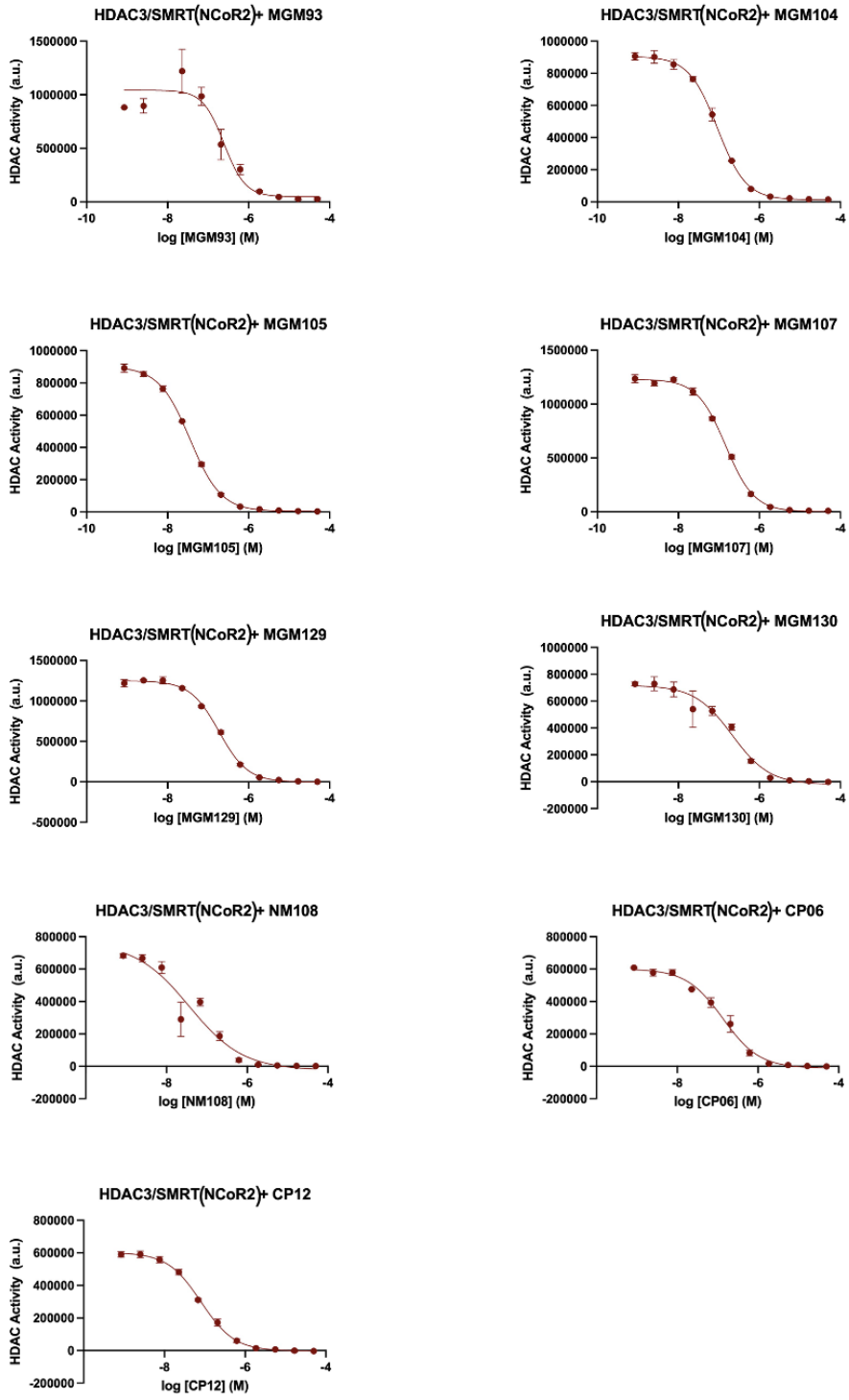

Figure 3.14. Inhibition curves of dual-target compounds against the HDAC3/SMRT NCoR 2 corepressor complex. Experiments were performed in technical triplicate. Error bars represent ± S.E.M. (n = 3).

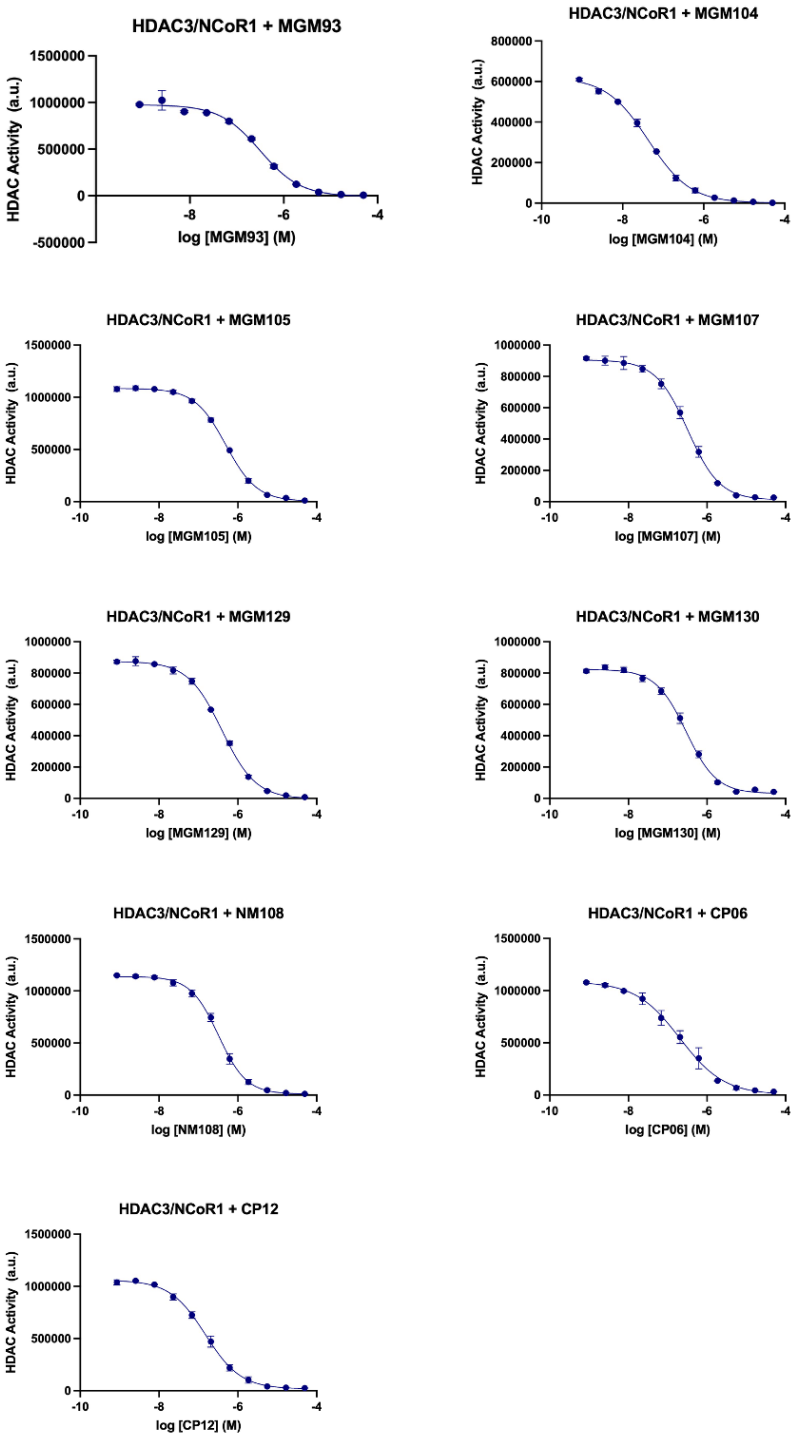

Figure 3.15. Inhibition curves of dual-target compounds against the HDAC3/NCoR 1 corepressor complex. Experiments were performed in technical triplicate. Error bars represent ± S.E.M. (n = 3).

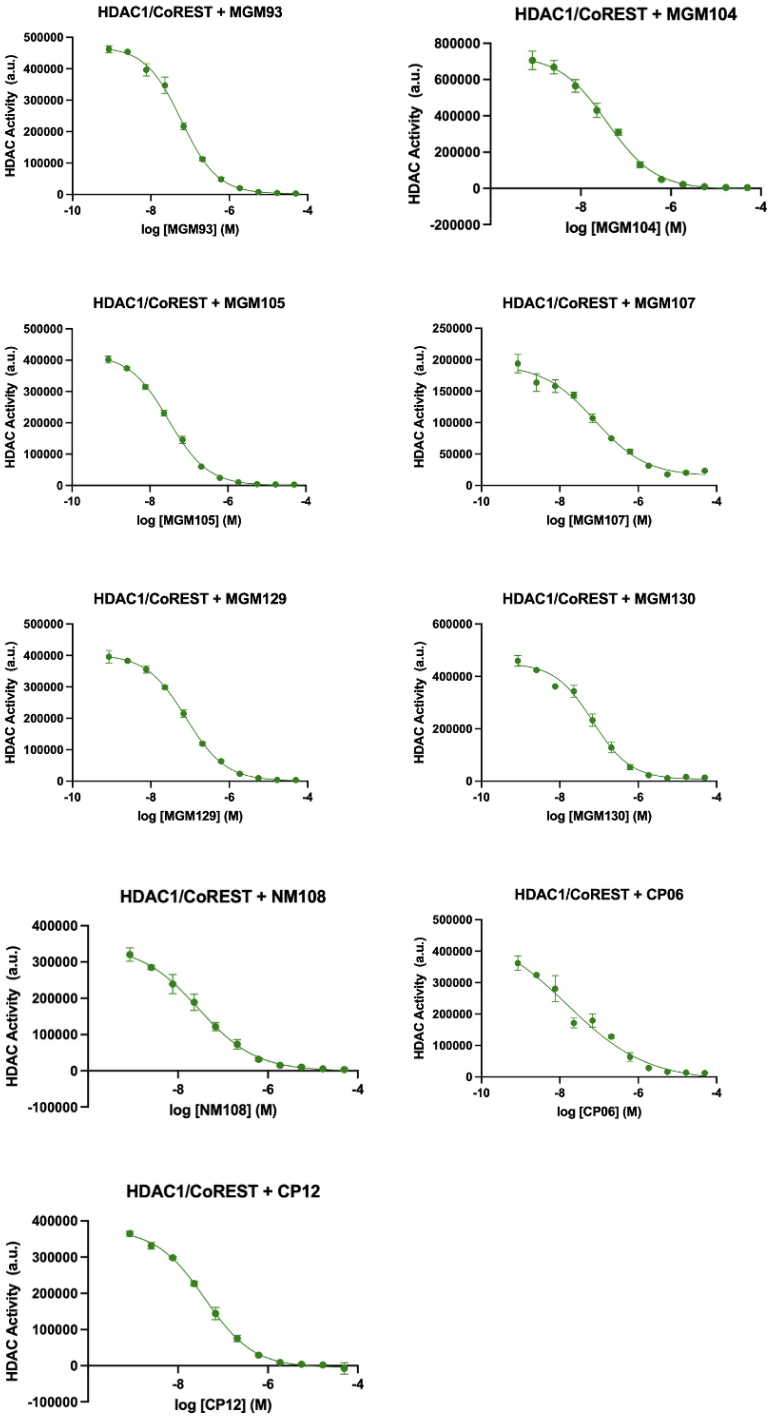

Figure 3.16. Inhibition curves of dual-target compounds against the HDAC1/CoREST corepressor complex. Experiments were performed in technical triplicate. Error bars represent ± S.E.M. (n = 3).

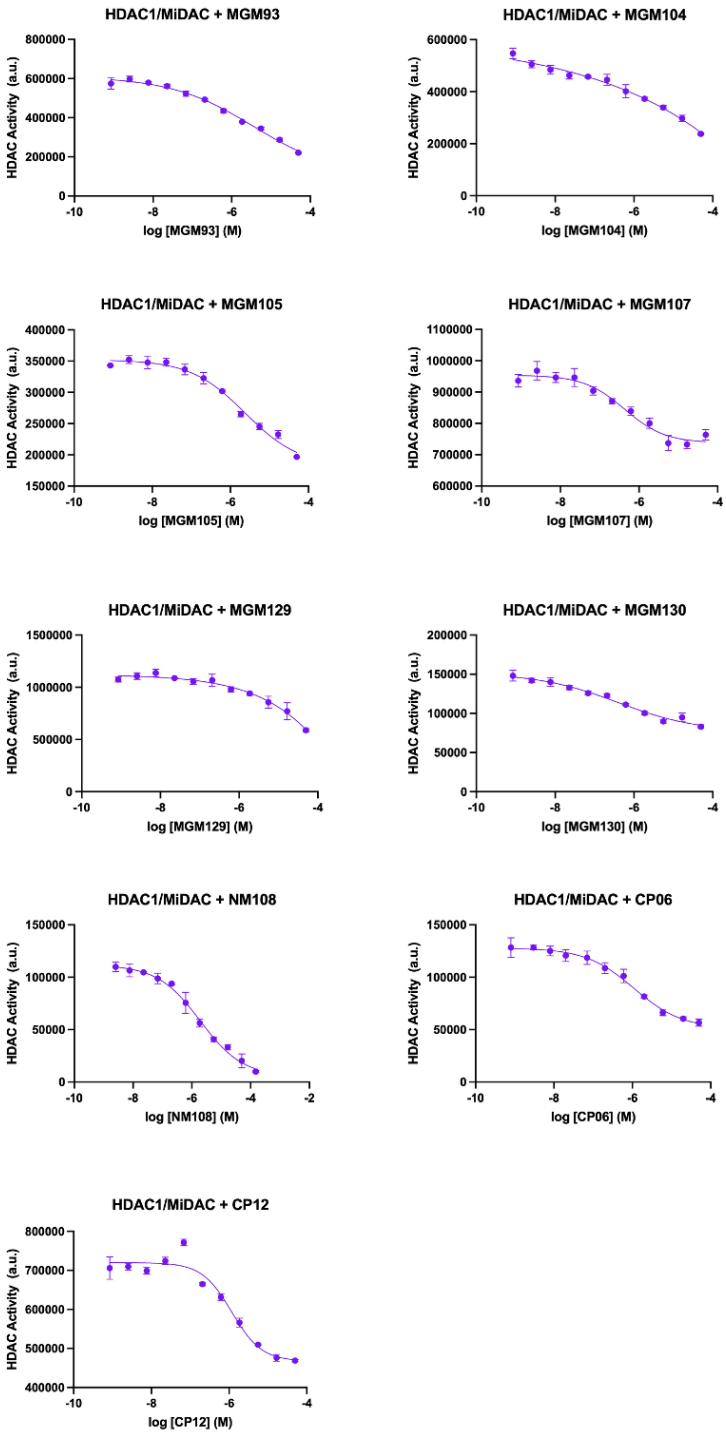

Figure 3.17. Inhibition curves of dual-target compounds against the HDAC1/MiDAC corepressor complex. Experiments were performed in technical triplicate. Error bars represent ± S.E.M. (n = 3).

3.3 Discussion and Conclusion

A comprehensive structural and functional evaluation of dual-target anticancer inhibitors, designed to simultaneously modulate hCAs and class I HDACs, was conducted. The combination of biochemical, crystallographic, and computational analyses elucidated the structure–activity relationships governing efficacy and selectivity across the different enzyme isoforms.

Based on previous studies of effective dual-target HDAC/CA inhibitors reported by Bozdag et al. [350], a new series of dual-target agents was designed and synthesized, incorporating the classical pharmacophores of both HDACs and hCAs: the benzamide and sulfonamide moieties, respectively.
The inhibitory activity of the novel compounds was assessed *in vitro* using the stopped-flow technique against hCA I, II, IX, and XII isoforms. Overall, the new series didn't outperform the reference inhibitor AAZ in potency and exhibited limited selectivity toward the cancer-associated isoforms (hCA IX and XII) compared to the previous series [350], while maintaining significant inhibitory activity against the cytosolic hCA I isoform. Both the spacer length and the regiochemistry of the sulfonamide moiety were found to influence isoform-specific inhibition. Notably, the shortest compound, MGM-93, displayed high potency against hCA I, whereas shifting the sulfonamide from the meta to para position in MGM-105 markedly reduced activity toward this isoform. In contrast, MGM-105 emerged as the most effective inhibitor against the cancer-associated hCA IX and XII isoforms. Interestingly, for hCA XII, the presence of an amide-containing spacer led to a decrease in activity, and meta-substitution of the sulfonamide further reduced efficacy.

Crystallographic analyses were performed on both the new and previous series [350] in complex with hCA I, II, and a hCA XII-mimic. The structures revealed a conserved zinc-binding mode mediated by the sulfonamide group.
The thiourea group present in Bozdag et al. compounds [350] appears to direct selectivity toward the cytosolic hCA II isoform, due to the formation of sulfur–aromatic interaction with Phe131. This residue is replaced by Ala in hCA XII and Val in hCA IX, preventing the formation of this interaction and probably explaining the lower efficacy of the thiourea-containing inhibitors for these isoforms.
Structures of MGM-104, -105, and -129 in complex with hCA II further highlight the importance of Phe131 for stabilizing inhibitors in the active site. Notably,

MGM-104 displayed the highest potency against the hCA II, despite adopting a binding mode largely similar to that of MGM-105 and -129. The difference is an additional π–π stacking interaction with Phe131, which likely accounts for its slightly enhanced inhibitory activity.
Based on crystallographic data and hCA inhibition assay results, a list of new inhibitor structures was designed to improve selectivity towards the cancer-related hCA isoforms IX and XII. Moreover, to preliminarily evaluate the binding of the proposed compounds to HDAC complexes, molecular docking was performed using the reported structures of the MiDAC and NuRD in complexes with HDAC1 (PDBs: 6Z2K, 7AO8 [274, 210]). Notably, protonatable groups at physiological pH (e.g., tertiary amines) facilitated salt-bridge formation with aspartate and glutamate residues in the HDAC1 active site in MiDAC complex. These interactions are not observed in the NuRD complex as access to the active site entrance is sterically prevented by the multiprotein assembly. Consequently, the compounds exhibit better selectivity toward the MiDAC complex.
Among the newly designed inhibitors, T_5 was selected as a prototype for developing dual-target derivatives, as it incorporates key features expected to enhance selectivity toward cancer-associated hCA isoforms and a good docking score in the docking analyses with the HDAC1 complex. To further explore steric effects on selectivity, fluorine, chlorine, and bromine substituents were introduced into the molecular structures.
The introduction of these structural modifications significantly enhances selectivity toward the cancer-associated isoforms IX and XII over the cytosolic isoforms; however, a further sequential increase in steric bulk ultimately leads to a loss of efficacy.

The inhibitory profiles against the HDAC complexes were also assessed by evaluating their efficacy against four corepressor complexes, the HDAC1/CoREST, HDAC1/MiDAC, HDAC3/SMRT (NCoR2), and HDAC3/NCoR1 in the absence of the allosteric regulator $InsP_6$. Overall, the compounds act as effective inhibitors across the entire enzymatic panel and displayed higher inhibitory potency than the reference compound CI-994; however, no marked selectivity toward individual HDAC complexes was observed. The compounds showed better inhibitory potency against the HDAC1/CoREST, HDAC3/NCoR2, and HDAC3/NCoR1 complexes, with the highest efficacy observed for HDAC1/CoREST, whereas reduced inhibitory potency was detected against the HDAC1/MiDAC complex. These findings are consistent with those reported by Pytel et al. [221], in which the inhibition profiles of different HDACIs have been analyzed in the

presence and absence of allosteric regulator $InsP_6$ and on six HDAC corepressor complexes. The results highlighted, in the absence of $InsP_6$, a potent inhibition efficacy of benzamide-based HDACIs against HDAC1/ 2-CoREST, HDAC3-SMRT, and HDAC1-MIER1 complexes and lower inhibition on HDAC1-MiDAC, HDAC1-NuRD, and HDAC1-RERE.

In conclusion, the MGM series does not represent an effective class of selective inhibitors for anticancer hCA isoforms, although they display good efficacy against HDAC corepressor complexes. In contrast, the newly synthesized compounds exhibit good inhibitory potency against both cancer-associated hCA isoforms and the HDAC complexes. In future studies, structural investigations of HDAC corepressor complexes in combination with the tested compounds could provide detailed insights into the molecular determinants of inhibitor binding, allowing a direct correlation between inhibitory potency and specific interaction patterns within the active site. Overall, these studies would contribute to a more comprehensive understanding of the structure–function relationships governing HDAC and hCA inhibition and would further support the rational design of optimized dual-target inhibitors.

3.4 Materials and Methods

Expression and purification of HDAC corepressor complexes

The HDAC complexes were expressed and purified following established procedures described in earlier work [221].
Human embryonic kidney suspension cells HEK293F were used for the expression of HDAC corepressor complexes. The cell stock was maintained at a density of between 0.35 x 10^6 - 2.0 x 10^6 cells per mL in a 250 mL Erlenmeyer flask (Corning, Fisher Scientific) containing 60 mL of culture. For large-scale cultures, cells were grown in 1 L (490 cm^3) roller bottles (Corning, Fisher Scientific) with a maximum working volume of 300 mL. Cultures were grown in FreeStyle^{TM} 293 expression media (+ GlutaMA^{TM}) (Gibco) and incubated at 37 °C in a 5% CO_2 shaking incubator (N-BIOTEK) at 120 RPM.
300 μg of total DNA (1:1 construct ratios) was diluted in 30 mL of sterile PBS (Sigma) (1710 of the transfection volume) and 600 μL of polyethylenimine (PEI) transfection reagent (1 mg/mL, filtered) (ratio of DNA to PEI - 1 μg:2 μg). The mixture was shaken and incubated at room temperature for 20 minutes, and then added to 300 mL of the cell culture, at a density of 1 x 10^6 cells per mL. The volumes and quantities of reagents were calculated proportionally to the working cell volumes. Then, the cells were incubated at 37 °C and 120 RPM in a 5% CO_2 incubator (N-BIOTEK). After 48 hour of incubation, the cells were harvested by spinning at 4000 RPM (3501 × g, Sorvall SLC-6000) for 15 minutes at 4 °C. The cell pellets were used for purification (it can be stored at -80 °C).
Usually, for a 1.2 L of cell transfection, the cell pellet is dissolved in 30 mL of lysis buffer composed of 50 mM Tris/Cl (pH 7.5), 100 mM of potassium acetate, 5% v/v glycerol, 0.4 % v/v triton X-100, and Roche complete EDTA-free protease inhibitor (1 tablet per 50 mL) and lysed by sonication (QSONICA, 5 cycles of 15 seconds on, 30 seconds off, 40 % amplitude). Insoluble material was pelleted by centrifugation at 30000 RPM for 30 min at 4 °C (108,000 × g, Avant^{TM} J-30I, Beckman Coulter, JA-30.50 rotor). 1 mL of pre-washed anti-FLAG M2 resin (Sigma) was then added to the obtained lysate and incubated for 30 minutes at 4 °C. Then, the mixture was centrifuged at 4000 RPM for 2 minutes at 4 °C and the resulting supernatant was discarded. The protein-resin mixture was then washed once with 10 mL of lysis buffer and then four times with 10 mL of wash buffer composed of 50 mM Tris/Cl (pH 7.5), 100 mM potassium acetate, and 5 % v/v glycerol. Then, the resin-protein mixture

was further washed four times with 10 mL of cleavage buffer (50 mM Tris/Cl (pH 7.5), 100 mM potassium acetate, 5 % glycerol, and 0.5 mM TCEP). Then, the protein-resin mixture was resuspended in 6 mL of cleavage buffer. To this, 50-60 μL of 2.1 mg/mL of Tobacco etch virus (TEV) protease was added and incubated overnight at 4 °C to allow the cleavage of the protein from the resin. The protein solution was then concentrated to 500 μL using a 4 mL Amicon®Ultra centrifugal filter (Merck Millipore) with a membrane nominal molecular weight cut-off of 10 kDa. The concentrated protein was then filtered through a 0.22 μm centrifugal filter (Merck Millipore).
The HDAC corepressor complexes were purified on the AKTA purifier system (GE Healthcare) using Superose 6 (10/300 GL) or Superdex 200 (10/300 GL) column (GE Healthcare). Before sample loading, the columns were equilibrated using the gel filtration buffer composed of 25 mM Tris/Cl (pH 7.5), 50 mM KCl, 0.5 mM TCEP. The fractions were collected in a 96-well plate (500 μL per fraction). A 10 μL aliquot from fractions showing absorbance at 280 nm was mixed with 3 μL of 6x SDS sample buffer (60% glycerol, 375 mM Tris/Cl, (pH 6.8), 12% SDS, 300 mM DTT, and 0.3 mg/mL bromophenol blue) for SDS-PAGE analysis. Samples were loaded onto a NuPAGE®4 - 12% Bis-Tris gel (Novex) and electrophoresed using NuPAGE®MES SDS running buffer at 200 V, 125 mA, and 100 W until the bromophenol blue dye front reached the bottom of the gel. SeeBlue Plus2 pre-stained marker (Invitrogen) was used as a molecular weight marker, and the gel was stained with Instant Blue Coomassie Stain (Expedeon). The collecting fractions containing purified proteins were concentrated using a 0.5 mL Amicon Ultra centrifugal filter (Merck Millipore) with a membrane nominal molecular weight cut-off of 10 kDa. Protein assay dye reagent (Bio-Rad) was used to determine the concentration of the protein. 200 μL of the reagent was diluted in 800 μL of double-diluted water and used as reagent blank. Then, 2 μL of the protein solution was added to the mixture, and the absorbance was measured at 595 nm. The protein concentration (mg/mL) was determined by multiplying the absorbance value by a factor of 17, derived from a BSA standard curve. Protein complexes were flash-frozen in liquid nitrogen in the presence of 25% glycerol and subsequently stored at -80 °C.

Table 3.4. HDAC assays were performed using the indicated HDAC complexes. Full-length proteins were used unless otherwise stated (table adapted from [221]).

HDAC Complex	Complex components	Molecular weight
HDAC3/NCoR2	Due to data embargo, the underlying dataset cannot be disclosed at this time	
HDAC3/NCoR1	Due to data embargo, the underlying dataset cannot be disclosed at this time	
HDAC1/CoREST	HDAC1, CoREST (86-485), LSD1	193,824 Da
HDAC1/MiDAC	HDAC1, MIDEAS (628-887), DNTTIP1	121,340 Da

Expression and purification of hCA IX and XII-mimic isoform

A clone encoding the hCA mimic isoforms H-tag protein, based on the hCA II sequence modified by ten and nine (for hCA IX and XII isoform, respectively) active-site substitutions, was obtained from GenScript and subcloned into the pET43 vector using the BamH I and Xho I restriction sites. Competent BL21 (DE3) cells were transformed with plasmids containing the engineered gene. A fresh 1 L culture was grown in LB broth supplemented with ampicillin (100 μg/mL). Cells were incubated at 37 °C until they reached mid-log phase (OD600 = 0.6–0.7), at which point protein expression was induced by the addition of 0.5 mM isopropyl β-D-1-thiogalactopyranoside (IPTG). After 30 min, 0.5 mM $ZnSO_4$ was added, and the cells were allowed to grow for an additional 4.5 h. Cells were harvested by centrifugation at 5000 RPM for 20 min, and the resulting pellet was resuspended in 20 mM Tris/HCl buffer (pH 8.3). Cell disruption was performed by sonication using 10 cycles of 10 seconds on and 120 seconds off at 50% amplitude (Bandelin Sonoplus). The lysate was then centrifuged at 12000 g for 45 min. Next, the supernatant was incubated with pre-equilibrated (in lysis buffer) nickel affinity gel resin (His-Select HF, Sigma) for 30 min. After centrifugation at 1500 g, the resin was washed with buffer containing 50 mM Tris/HCl (pH 8.3), 500 mM NaCl, and 20 mM imidazole. Bound protein was eluted using the same buffer supplemented with 250 mM imidazole. The collected fractions were dialyzed against 20 mM Tris/HCl (pH 8.3). At this stage, the recombinant protein was approximately 95% pure, with a yield of about 3.2 mg/L of bacterial culture.

HDAC inhibition assay

The HDAC assays were performed as previously described in [221]. A fluorescent inhibition assay was performed on Class I HDAC corepressor complexes. The assay was carried out in black 96-well plates (Corning #3991). Each well contained a final reaction volume of 50 μL. All measurements were performed in triplicate. First, the inhibitors were dissolved in DMSO to reach a concentration of 50 mM, then they were diluted to 250 μM with 20% DMSO HDAC assay buffer, containing 20% DMSO, 50 mM Tris pH 7.5, 50 mM NaCl, and 0.1 mg/mL of BSA. The resulting solution is further diluted serially to obtain a wider range of concentrations (from 250 μM to 0.0042 μM with 1:3 dilution). 10 μL of each of these solutions was added to the well, followed by the addition of 30 μL of the HDAC complex (final concentration of 10 nM) in HDAC assay buffer (50 mM Tris pH 7.5, 50 mM NaCl, 0.1 mg/mL BSA). The plates were

then incubated at 20 °C, 100 RPM for 1 hour. After, 10 μL of the Boc-(Ac)Lys-AMC substrate (100 μM) dissolved in HDAC assay buffer was added to each well. Then, the mixtures were incubated at 30 °C, 100 RPM for another hour. 50 μL of the developer buffer (50 mM Tris pH 7.5, 100 mM NaCl, 10 mg/mL trypsin) is then added to stop the reaction. After 10 minutes of incubation at 30 °C and 100 RPM, the plate is disposed in a Victor X5 plate reader (Perkin Elmer, λex = 335 nm, λem = 460 nm) to measure the fluorescence intensities produced. The IC_{50} values were calculated by GraphPad Prism 7 software by non-linear regression, log (inhibitor) vs. response – variable slope (four parameters).

hCA inhibition assay

To evaluate the ability of the dual-target agents to inhibit the CA-catalyzed function of CO_2 hydration, an applied photophysics stopped-flow instrument was used. Phenol red at a concentration of 0.2 mM was used as an indicator, working at a maximum absorbance of 557 nm, with 20 mM HEPES (pH 7.4) as a buffer, and 20 mM Na_2SO_4 (to maintain constant ionic strength), following the initial rates of the CA-catalyzed reaction for a period of 10–100 s. The CO2 concentrations ranged from 1.7 to 17 mM for the assessment of the kinetic parameters and inhibition constants. Enzyme concentrations varied between 5 and 12 nM. For each inhibitor, at least six traces of the initial 5–10% of the reaction were used to determine the initial velocity. The uncatalyzed rates were calculated in the same manner and subtracted from the total observed rates. Stock solutions of each inhibitor (0.1 mM) were prepared in distilled–deionized H2O, and dilutions up to 0.01 nM were done thereafter with the assay buffer. Inhibitor and enzyme solutions were preincubated together for 15 min at room temperature before the assay, to allow the formation of the complex. The inhibition constants were obtained by nonlinear least-squares methods using PRISM 3 and the Cheng–Prusoff equation as reported earlier and represent the mean from at least three different determinations [177]. hCAs I and II were purchased from Merck, while other isoenzymes were expressed and purified in-house [355].

In silico studies

Hardware Workstation SO Linux (32 processors)

Distribution: Linux version 4.15.0-122-generic gcc version 7.5.0 (Ubuntu 7.5.0-3)

Intel ® Xeon® Silver 4110 CPU @ 2.10 GHz (1200 MHz)
System memory (16 DIMM slots):

- Memory Capacity: Up to 4TB 3DS ECC DDR4-2933MHz RDIMM/L-RDIMM
- Memory Type: 2933/2666/2400/2133MHz ECC DDR4 RDIMM/LRDIMM
- Memory Voltage: 1.2V
- DIMM Sizes: RDIMM: 64GB; LRDIMM: 64GB; 3DS LRDIMM: 128GB

Graphic card: Nvidia Quadro P5000; 16GB GPU dedicated

Software Schrödinger Suite Release 2024-3, Schrödinger, LLC, New York, NY, 2024 www.schroedinger.com [356]

- Maestro v.14.1
- Epik, v.6.9
- Impact, v.10.4
- Prime, v.5.5
- Macromodel v. 14.5
- Glide, v.10.4
- Jaguar, v.12.5
- Desmond, v.7.9
- QikProp, v.4.6

Protein preparation All crystal structures used for computational studies (PDBs: 6Z2K, 7AO8 [274, 210]) were prepared using the Protein Preparation Wizard tool implemented in the Schrödinger suite, assigning bond orders, adding hydrogens, deleting water molecules, and optimizing H-bonding networks. The energy minimization protocol with a Root Mean Square Deviation (RMSD) value of 0.30 Å was applied using an Optimized Potentials for Liquid Simulation (OPLS4) force field [356, 357].
Ligand preparation The 3D ligand structures were prepared by Maestro (v.14.1) and evaluated for their ionization states at pH 7.4 ± 0.5 with Epik. The conjugate gradient method in Macromodel was used for energy minimization

(maximum iteration number: 2500; convergence criterion: 0.05 Kcal/mol/Å^2) [356].

Grid generation Grids for docking were centered on the centroid of complex ligands.

Docking studies For molecular docking studies, the software Glide SP (default settings) was used. The standard precision (SP) mode of the Glide Score function was applied to evaluate the predicted binding poses of all series [356]. Figures were generated with Chimera [358].

General synthetic scheme of the dual-target compounds

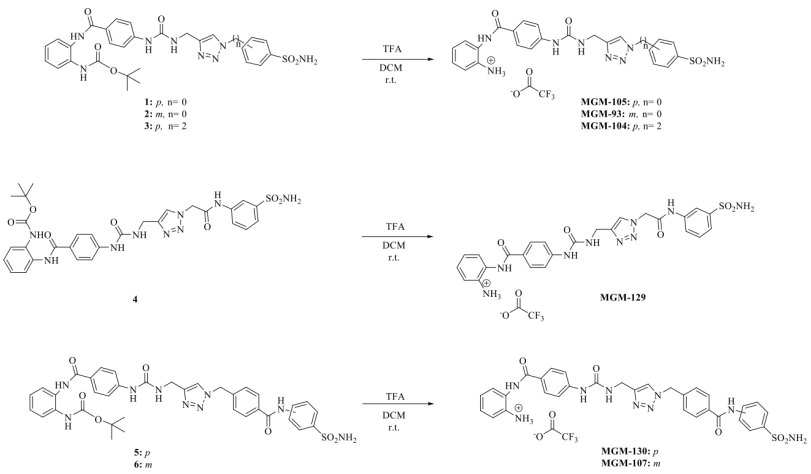

Scheme 1. Synthesis of compounds MGM 93, 104, 105, 107, 129 and 130. The synthesis of precursors 1-6 is not disclosed here.

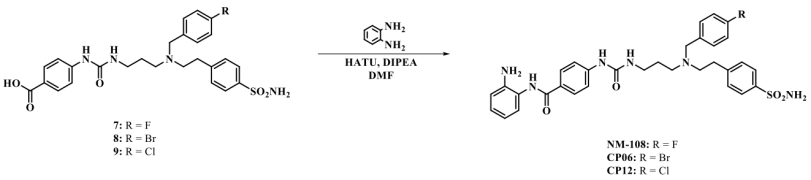

Scheme 2. Synthesis of compounds NM 108, CP 06 and CP 12. The synthesis of precursors 7-9 is not disclosed here.

Crystallization and X-ray data collection

Crystals of the hCA XII-mimic isoform (protein solution 8 mg mL^{-1} in Tris-HCl 20 mM, pH 8.3) were grown via the hanging drop vapor diffusion method in a

24-well Linbro plate. Drops were prepared using 1 μL protein solution mixed with 1 μL reservoir solution containing 1 M sodium citrate and 50 mM Tris-HCl (pH 7.5) and were equilibrated against 500 μL of the same solution at 296 K. After 24 hours of incubation, 0.3 μL of seeding solution were added to the prepared drops, to obtain higher quality crystals. Crystal growth was observed after fifteen days.
hCA II purchased from Sigma was dissolved in 50 mM Tris-HCl (pH 8.0) to obtain a final concentration of 10 mg mL^{-1}. Crystals of the hCA II isoform were obtained using the hanging drop vapor diffusion method in a 24-well Linbro plate. One microliter of hCA II was mixed with 1 μL of a solution of 1.5 M sodium citrate and 50 mM Tris-HCl (pH 8.0) and equilibrated against 500 μL of the same solution at 296 K. Crystal growth was observed after five days.
hCA I was purchased from Sigma. 2 μl of hCA I solution (10 mg/ml in Tris-HCl 20 mM pH 9.0) were mixed with 2 μl of a solution of 28-31% PEG4000, 0.2 M Sodium acetate, 0.1 M Tris pH 9.0, and were equilibrated against the same solution at 296 K.
The complexes of the isoforms with the inhibitors were prepared by soaking the crystals in the mother liquor solution containing the inhibitor at a concentration of 10 mM for 3 hours. Then, crystals were flash-frozen at 100 K using a solution obtained by adding 25% (v/v) PEG 400 to the mother liquor solution as a cryoprotectant [299].

X-ray diffraction data of hCAs isoforms in complex with the dual-target inhibitors were collected using synchrotron radiation at the XRD2 beamline at Elettra Synchrotron (Trieste, Italy) with a DECTRIS Pilatus 6 M detector and synchrotron radiation at the ID30B beamline at ESRF (Grenoble, France) with a DECTRIS Eiger2 X 9 M detector.

Structure determination

The crystal structures of hCA XII-mimic (PDB accession code: 4Q08), hCA II (PDB accession code: 3HS4) and hCA I (PDB accession code: 8CDX) without solvent molecules and other heteroatoms were used to obtain the initial phases of the structures using Refmac5 [359] from the CCP4 package [360]. Coordinates of the inhibitors were obtained using the program JLigand [361] and introduced into the model. Five percent of the unique reflections were selected randomly and excluded from the refinement data set for Rfree calculations. The initial |Fo–Fc| difference electron density maps unambiguously showed the inhibitor molecules. The inhibitors were introduced in the model with 1.0

occupancy. Refinements proceeded using standard protocols of positional and isotropic atomic displacement parameters or anisotropic for data at atomic resolution, alternating with the manual building of the models using COOT [362]. Inhibitor–enzyme interactions were analyzed using the PLIP web tool [363]. Atomic coordinates were deposited in the PDB (hCA II-29 accession code: 28NC; hCA II-30 accession code: 28ND; hCA II-12 accession code: 28NE; hCA XII-mimic-5 accession code: 28NG; hCA II-5 accession code: 28NF; hCA II-MGM-104 accession code: 28LR; hCA II-MGM-105 accession code: 28LS; hCA II-MGM-129 accession code: 28LT; hCA I-MGM-105 accession code: 28NH). Graphical representations were generated with Chimera [358].

Table 3.5. Statistics of the data collections and model refinements. Values in parentheses are for the highest resolution shell.

	hCA II/5	**hCA II/12**	**hCA II/29**	**hCA II/30**	**hCA XII-mimic/5**
PDB ID	28NF	28NE	28NC	28ND	28NG
Wavelength (Å)	1.0000	1.0000	1.0000	0.9999	1.0000
Space Group	P 21	P 21	P 21	P 21	P 21
Unit cell parameters					
a, b, c (Å)	42.06, 41.01, 72.25	42.35, 41.20, 72.39	42.29, 41.26, 72.36	42.32, 41.19, 72.35	41.99, 41.25, 71.86
α, β, γ (°)	90.00, 104.04, 90.00	90.00, 104.30, 90.00	90.00, 104.26, 90.00	90.00, 104.35, 90.00	90.00, 103.64, 90.00
Limiting resolution (Å)	40.80-1.40 (1.42-1.40)	41.04-1.24 (1.26-1.24)	70.13-1.13 (1.15-1.13)	39.97-1.30 (1.32-1.30)	40.81-1.30 (1.32-1.30)
Unique reflections	41742 (2182)	62630 (3038)	79697 (4451)	54853 (3021)	52794 (2887)
Rsym (%)	5.3 (45.3)	9.7 (166.9)	10.6 (152.4)	11.1 (181.3)	5.3 (99.2)
Rmeas (%)	5.8 (49.3)	10.5 (183.1)	11.6 (170.1)	12.1 (197.3)	5.8 (110.1)
Redundancy	6.2 (6.3)	6.1 (5.7)	5.8 (4.9)	6.2 (6.4)	5.5 (5.3)
Completeness overall (%)	88.6 (95.4)	90.4 (88.0)	87.2 (97.2)	92.1 (98.3)	89.7 (99.6)
$\langle I/\sigma(I) \rangle$	17.7 (4.4)	8.7 (1.0)	7.7 (1.1)	9.5 (1.0)	14.3 (1.8)
CC (1/2) (%)	99.9 (91.1)	99.7 (36.2)	99.6 (35.9)	99.8 (38.3)	99.9 (64.1)
Refinement statistics					
Resolution range (Å)	40.80-1.40	41.04-1.24	70.13-1.13	39.97-1.30	40.81-1.30
R factor (%)	11.60	12.73	12.30	13.85	12.09
R free (%)	15.14	16.48	15.57	17.75	15.68
r.m.s.d bonds (Å)	0.0103	0.0097	0.0102	0.0091	0.0102
r.m.s.d angles (°)	1.807	1.812	1.835	1.749	1.870
Ramachandran statistics (%)					
Most favored	97.3	96.5	96.9	96.9	96.5
Additionally allowed	2.7	3.5	3.1	3.1	3.5
Outlier regions	0.0	0.0	0.0	0.0	0.0
Average B factor (Å^2)					
All atoms	18.024	21.651	17.727	15.184	21.399
Inhibitor	20.100	31.300	27.8	45.400	21.000
Solvent	29.740	35.494	30.540	25.101	34.498

Table 3.6. Statistics of data collection and model refinement. Values in parentheses refer to the highest resolution shell.

	hCA II/MGM-104	**hCA II/MGM-105**	**hCA II/MGM-129**	**hCA I/MGM-105**
PDB ID	28LR	28LS	28LT	28NH
Wavelength (Å)	0.9677	0.9677	0.9677	0.9677
Space group	$P2_1$	$P2_1$	$P2_1$	P 21 21 21
Unit cell parameters				
a, b, c (Å)	42.20, 41.20, 72.20	42.38, 41.23, 72.36	42.31, 41.21, 72.38	62.70 70.95 121.39
α, β, γ (°)	90.00, 104.20, 90.00	90.00, 104.34, 90.00	89.86, 104.28, 90.02	90.00 90.00 90.00
Resolution range (Å)	41.20–1.52 (1.57–1.52)	41.23–1.52 (1.57–1.52)	41.08–1.48 (1.50–1.48)	61.25-1.89 (1.93-1.89)
Unique reflections	36 035 (3 597)	35 973 (3 531)	39 637 (1 972)	43 580 (2 776)
R_{sym} (%)	6.2 (72.0)	6.5 (71.0)	8.8 (114.8)	8.5 (58.3)
R_{meas} (%)	7.6 (88.6)	8.4 (91.8)	10.8 (140.9)	9.7 (66.2)
Redundancy	2.6 (2.6)	2.2 (2.3)	2.6 (2.5)	4.2 (4.4)
Completeness (%)	97.0 (98.9)	96.3 (97.0)	96.6 (98.4)	98.5 (97.8)
$\langle I/\sigma(I)\rangle$	8.7 (1.2)	8.6 (1.4)	6.3 (1.1)	11.8 (2.6)
$CC_{1/2}$ (%)	92.0 (81.0)	99.6 (48.8)	99.2 (34.9)	97.4 (74.4)
Refinement statistics				
Resolution range (Å)	41.20–1.52	41.23–1.52	41.08–1.48	61.25-1.89
R_{work} (%)	16.26	16.34	16.97	18.54
R_{free} (%)	19.53	20.15	19.79	21.94
r.m.s.d. bonds (Å)	0.0083	0.0084	0.0088	0.0070
r.m.s.d. angles (°)	1.73	1.72	1.76	1.5975
Ramachandran statistics (%)				
Most favored	96.5	97.3	97.3	97.3
Additionally allowed	3.5	2.7	2.7	2.5
Outliers	0.0	0.0	0.0	0.2
Average B factor (Å^2)				
All atoms	23.17	20.52	20.19	28.583
Inhibitor	65.60	55.00	38.70	47.300 - 39.00
Solvent	29.98	28.33	28.68	31.231

4 Cryo-EM studies of the PG Domain in the Anticancer Target Carbonic Anhydrase IX

4.1 Introduction

hCA IX, in contrast to the other hCAs, features a PG region extending from its N-terminal catalytic domain, which has been postulated to play a crucial role in modulating the catalytic activity of the enzyme [119, 364] (see paragraph 1.2.4).
The net negatively charged PG domain is a region of 58 amino acids long that contains 18 glutamate and 8 aspartate residues. The work from Innocenti et al. suggests that these acid residues in the PG domain could act as an intrinsic proton buffer, facilitating the high catalytic activity of hCA IX at acidic pH values (around 6.5) typical of hypoxic solid tumors [115]. Moreover, the PG domain appears to be involved in cell adhesion and intracellular communication [365, 364, 366]. In fact, both deletion of the PG region and treatment with the PG-binding antibody M75 lead to reduced cancer-cell adhesion and impaired spreading. Recent studies have highlighted the ability of the PG domain to act as a proton antenna to facilitate the movement of lactate and protons by monocarboxylate transporters in human breast adenocarcinoma cells [367].
Langella et al. also demonstrated that the PG domain is part of the intrinsically disordered protein (IDP) family, exhibiting high inherent flexibility and a largely unfolded structure. However, in the PG domain there are local segments that adopt polyproline II-like (PPII) conformations, which may play a role in recognizing binding partners [364, 366].

Nevertheless, only the catalytic CA domain has been structurally characterized using X-ray diffraction analysis, since the crystals of ECD are particularly challenging to obtain. Early attempts at crystallizing the complete ECD, as

reported by Hilvo et al., Alterio et al., and Koruza et al., resulted in the degradation of the protein [119, 66, 368]. Further structural insights into the ECD of the hCA IX isoform have been gained by Koruza et al., using the small angle X-ray scattering (SAXS) technique. Results highlight the inherent disorder and high flexibility of the PG domain and show that it can probably populate several different "average" positions. This intrinsic disorder may explain the challenge of obtaining a crystal structure of the full hCA IX ECD [368].

In this study, we applied cryo-EM to analyze and investigate the structure of the ECD of the hCA IX isoform, including both catalytic and PG domains, to overcome the crystallographic limitations.
To increase the molecular weight of the enzyme and try to stabilize the target domain for cryo-EM studies, we prepared complexes of the protein with three different hCA IX monoclonal antibodies (mAbs): two targeting the catalytic site, c2C7 and m4A2, and one recognizing the PG domain, c11H9. The mAbs were designed and synthesized by Anne Lenferink's group at the National Research Council of Canada [369, 370, 371].
Several experimental parameters, including detergent use and protein concentration, were systematically screened to identify the optimal conditions for grid preparation and data collection.

4.2 Results

4.2.1 Cryo-EM data of free hCA IX and hCA IX in complex with c11H9 and c2C7 antibodies

Initially, to determine the optimal experimental conditions for hCA IX analysis, several samples containing the protein at different concentrations (2, 0.5, 0.1, and 0.05 mg/mL) were prepared in the presence and absence of 4 mM of β-octylglucoside detergent and screened using the Glacios cryo-electron microscope.

Based on the screening data, the 2 mg/mL protein concentration in the presence of detergent exhibited the best protein distribution and signal, and was therefore selected for subsequent data acquisition and analysis (figure 4.1, panel A). Consequently, measurements on protein–antibody complexes with c11H9, c2C7, and m4A2 were performed using the same protein concentration, while exploring different detergents, including DDM and 3-[(3-cholamidopropyl)dimethylammonio]-1-propanesulfonate (CHAPS), to assess their effects on complex stability and distribution. Among the screened samples, the highest-quality data were obtained for the c11H9 and c2C7 antibodies in the presence of DDM and β-octylglucoside, respectively (figure 4.1, panels B and C).

The figure 4.1 shows the 2D and 3D classification results obtained from three cryo-EM datasets collected under different experimental conditions. On the left of each panel (A–C), the 2D class averages reveal particle projections with a range of orientations and structural features. On the right, the 3D classes illustrate different density map reconstructions obtained during refinement, reflecting the conformational heterogeneity present in the dataset.

Panel A presents the 2D and 3D classes of hCA IX in the absence of antibodies. The density maps display a globular volume connected to a ring, as revealed by the 3D classifications. This overall density conformation is preserved in the hCA IX complexes with c11H9 and c2C7 (panels B and C) antibodies, which interact with the proteoglycan-like and catalytic domains, respectively. In these complexes, more heterogeneous 3D classes are observed, indicating an increase in conformational flexibility upon antibody binding.

The limited resolution achieved (11-11.5 Å) is likely attributable to several factors, including a high degree of sample heterogeneity, the relatively small size of the protein (the construct used has a monomeric molecular weight of $\approx$ 67.4 kDa, corresponding to a dimeric molecular weight of $\approx$ 134.8 kDa),

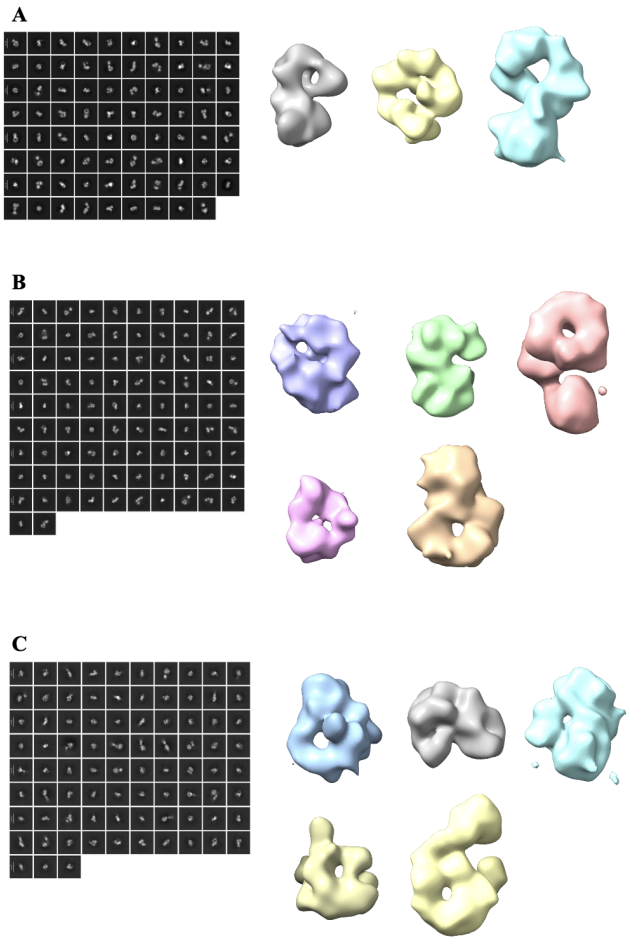

Figure 4.1. The image shows the 2D and 3D classes results from the cryo-EM dataset acquired under different experimental conditions. A) hCA IX with the addition of 4 mM of β-octylglucoside detergent; B) the hCA IX/c11H9 complex at a 1:1 ratio with the addition of DDM; C) hCAIX in complex with c2C7 antibody at a 1:1 ratio in the presence of β-octylglucoside. The reported resolutions by CryoSPARC are 11 Å for A) and 11.5 Å for B) and C).
Data collection parameters are summarized in table 4.1, where data in A), B), and C) correspond to hCA IX, hCA IX/c11H9 (1), and hCA IX/c2C7, respectively.

and potentially low antibody affinity. In addition, partial dissociation of the complex cannot be excluded and may have further contributed to the observed resolution limitations.

Due to the limited resolution, precise interpretation of the density maps at the molecular level is not feasible. However, the cryo-EM density map obtained for the free protein (figure 4.1, panel A) was used to guide a primary structural interpretation. The atomic model of the dimeric catalytic domain of hCA IX

(PDB=3IAI, [66]) and the homolog of the IgG1 fc tag, the fc-fragment of human IgG2 antibody (PDB=4HAG, [372]), was fitted into the density to generate an initial model of the protein. Due to the limited resolution, this represents a preliminary interpretation, and fine details such as side-chain orientations or flexible loops cannot be accurately resolved. Notably, the protein dimer fitted the globular region of the density map, whereas the Fc fragment is arranged in a ring-like conformation (figure 4.2). The density maps obtained for the analyzed complex structures (figure 4.1, panels B and C) closely resemble that of the free protein (figure 4.1, panel A), suggesting that the antibody moiety is not detectable under these conditions, which may be due to the high flexibility of the protein domain, or to a dissociation of the complex due to the presence of the detergent, or to less affinity of the antibodies to the protein.

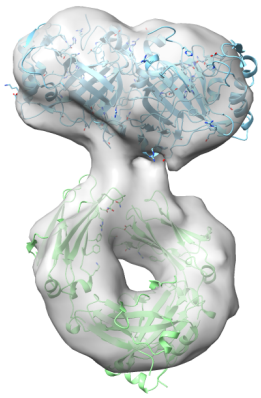

Figure 4.2. Cryo-EM density map of free hCA IX in the presence of β-octylglucoside detergent, with the catalytic domain of hCA IX ([66], PDB: 3IAI, shown in blue) and the Fc fragment of human IgG2 antibody ([372], PDB: 4HAG, shown in green) fitted, providing a preliminary interpretation of the observed density.

4.2.2 Mass photometry results

Mass photometry analysis was conducted to assess the stability of protein–antibody complexes in the presence of detergents used for the cryo-EM acquisition and to evaluate their binding affinity to the enzyme.
Figure 4.3 illustrates the different complexes observed under the experimental conditions employed. The peak detected between 142 and 163 kDa was interpreted as the signal corresponding to the protein dimer (monomeric molecular weight $\approx$ 67.4 kDa), overlapping with the antibody peak (150 kDa). Formation of the protein–antibody complex is indicated by the peak observed at

approximately 291–300 kDa. Peaks at higher molecular weights likely reflect the incremental association of additional protein or antibody molecules with the pre-formed complex, while the signal at 1123 kDa is most probably attributable to aggregates. The peak at a molecular mass below 142-163 kDa may correspond either to a minor fraction of monomeric species present in solution or to impurities within the sample. The data indicate that the protein/antibody complexes are formed, remain stable over time, and are not affected by the detergents under the experimental conditions. However, the antibodies display overall low affinity toward the enzyme, as evidenced by the persistent presence of free protein in solution. Notably, increasing the antibody concentration enhances complex formation in the case of c11H9, as reflected by the reduction of the 142–163 kDa peak, suggesting that a larger fraction of the protein is engaged in complex assembly. In contrast, for m4A2, a decrease in the protein–antibody complex peaks is observed, followed by an increase in the peaks corresponding to the free protein and free antibody. Conversely, the c2C7–protein complex exhibits a high degree of heterogeneity and only minimal complex formation, which does not increase significantly even upon raising the antibody concentration.

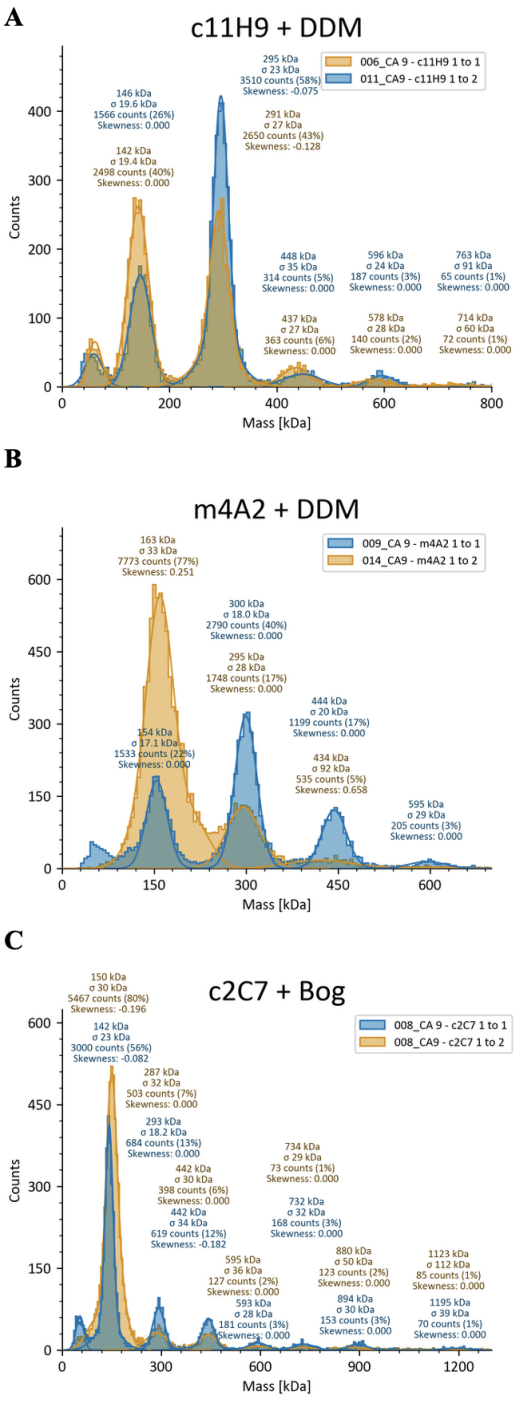

Figure 4.3. Molecular mass distribution histograms of: A) the hCA IX/c11H9 complex in the presence of DDM, with 1:1 and 1:2 molar ratios shown in yellow and blue, respectively; B) the hCA IX/m4A2 complex in DDM, and C) the hCA IX/c2C7 complex in the presence of β-octylglucoside, with 1:1 and 1:2 molar ratios shown in blue and yellow, respectively.

4.2.3 Cryo-EM data of hCA IX/c11H9 complex at a 1:2 molar ratio

Based on the mass photometry results, the hCA IX/c11H9 complex was analyzed at a 1:2 molar ratio, rather than the previously tested 1:1 ratio (Figure 4.1, panel B), while all other experimental parameters were kept identical to the previous conditions.

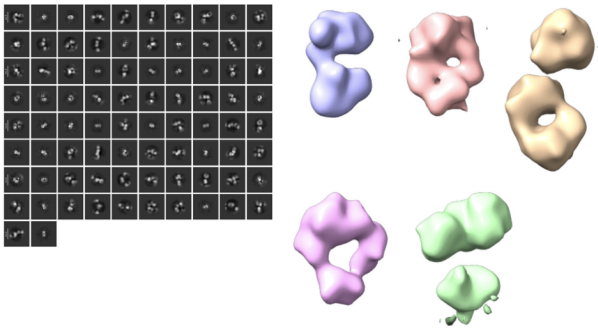

Figure 4.4. The image shows the 2D and 3D classes results from the cryo-EM dataset acquired for the hCA IX/c11H9 complex at a 1:2 ratio with the addition of DDM. The reported resolution by CryoSPARC is 10.5 Å.
Data collection parameters are summarized in Table 4.1 under the hCA IX/c11H9 (2) section.

Compared to the previous data, the new analysis exhibits an improved, but still low, resolution of 10.5 Å, while the heterogeneity of the molecular population in the sample remains unchanged, as indicated by the high number of 3D classes. Similarly, the resulting density map preserves the overall shape observed previously, and no binding events between the protein and the antibodies could be visualized. These observations confirm a high degree of flexibility in the analyzed protein region, which was not stabilized by interaction with another macromolecular component.

4.3 Discussion and Conclusion

The work results as a preliminary screening aimed at identifying the optimal experimental conditions for the structural analysis of the ECD domain of hCA IX, including the PG and catalytic domains. Although these analyses successfully established suitable parameters for sample preparation and data acquisition, the domain of interest, the PG domain, could not be resolved in the cryo-EM reconstructions, likely due to the inherent flexibility of the region. Nevertheless, the study provides valuable insight into the interaction profiles of the investigated antibodies c11H9 (selective for the PG domain), c2C7, and m4A2 (directed to the catalytic domain of the protein), revealing their relative affinities and binding behaviors toward the protein.

Cryo-EM screening identified 2 mg/mL protein in the presence of detergents as the most suitable condition for particle distribution and signal quality, enabling the acquisition of datasets for hCA IX alone and in complex with different antibodies. Despite these optimized conditions, the resulting density maps presented a low-resolution profile (10.5-11.5 Å). Moreover, the antibody components were not detected in the density maps, likely due to a combination of limited affinity and extensive conformational flexibility. Mass photometry analyses revealed the formation of protein–antibody complexes, while also demonstrating heterogeneous association and low-affinity behaviour, particularly for c2C7. Even when increasing the antibody concentration, as for the tested c11H9, the structural heterogeneity persisted and did not translate into detectable antibody or PG domain densities in the cryo-EM maps. In summary, these findings indicate that the antibodies analyzed do not provide sufficient stabilization of the PG domain of hCA IX to permit its structural characterization under the tested conditions, thereby confirming the intrinsic flexibility of the targeted region and highlighting the necessity for alternative stabilization strategies or binding partners in future studies. Approaches such as the use of higher-affinity Fab fragments may reduce sources of conformational heterogeneity and flexibility, helping to improve stability for high-resolution analyses. For instance, obtaining the Fab fragment of M75, a well-characterized monoclonal antibody that selectively targets the PG domain of the protein, may represent a promising candidate [373, 374, 125].

4.4 Materials and Methods

Protein preparation and complex formation

The recombinant hCA IX protein (amino acids 38–414) was purchased from ACROBiosystems (Cat. No. CA9-H5253). The protein carries a human IgG1 Fc tag at the C-terminus, and its calculated molecular weight is 67.4 kDa.
The protein was provided lyophilized from a filtered solution containing 20 mM MES (pH 6.5), 100 mM NaCl, with 10% trehalose as a protectant.
500 mg of the protein was dissolved in 200 μL of 20 mM MES (pH 6.5) and 100 mM NaCl. The solution was then concentrated using an ultracentrifugal filter with a nominal molecular weight cut-off of 30 kDa, followed by buffer exchange with Zeba^{TM} Spin Desalting Columns (Thermo Scientific^{TM}, 7K MWCO, ref: 89882). The final protein concentration was 2 mg/ml.

Protein–antibody complexes were prepared at defined stoichiometric ratios, using a 1:1 and 1:2 protein-to-antibody ratio of c2C7 (5.52 mg/ml in PBS buffer), m4A2 (3.46 mg/ml in PBS buffer), and c11H9 (6.88 mg/ml in PBS buffer).

Grids preparation

Cryo-EM grids (UltrAufoil R1.2/1.3 gold grids, 300 mesh) were plunge frozen using a Vitrobot Mark IV (Thermo Fisher Scientific (TFS)) operating at 100% humidity and 10°C.
Three microliters of protein or protein-antibody complexes solution were applied to the grids in the presence of detergents (4 mM) such as β-octylglucoside or n-dodecyl-β-D-maltoside (DDM), followed by 4–6 s of blotting before immediate vitrification in liquid ethane.

Mass photometry

Protein–antibody complexes were prepared at a concentration of 100 nM in a buffer containing 20 mM MES (pH 6.5) and 100 mM NaCl, and 4 mM of DDM or β-octylglucoside detergents. The complexes were assembled in duplicate at protein:antibody molar ratios of 1:1 and 1:2. Before measurement, the samples were allowed to thermally equilibrate on the lab bench for 5–10 minutes. Instrument calibration was performed using the BSA buffer. For each analysis, 2 μL of sample was deposited onto the coverslip and diluted to 10 nM, yielding a final volume of 20 μL. Data were acquired over 60–120 seconds.

The resulting mass photometry data were displayed as histograms, fitting the distribution peaks with Gaussian functions to determine the average molecular mass of each species. Relative populations were obtained directly from the areas under the fitted Gaussian peaks.

Cryo-EM data collection

All datasets were collected at the I.G.B.M.C. - Institut de génétique et de biologie moléculaire et cellulaire (Strasbourg, France) on a 200 KeV Glacios cryo-TEM microscope (ThermoFisher Scientific) equipped with a Gatan K2 Summit direct electron detector (Gatan, Inc.) in counting mode, with a magnification of 45000x. The results in a pixel size of 0.901 Å for all datasets. All data was collected using the SerialEM software [375] for automated data collection, using a 3x3 multi-hole setup, with 2 images per hole, on UltrAuFoil R1.2/1.3 grids from Quantifoil.

Table 4.1. Cryo-EM data collection parameters for hCA IX isolated and in complex with c11H9 and c2C7 mAbs.

	hCA IX	hCA IX/c11H9 (1)	hCA IX/c2C7	hCA IX/c11H9 (2)
Total dose (e-/Å^2)	41.97	48.68	36	40
Exposure time (s)	6	8	6	6.2
Total frames	30	40	35	40
Defocus range (μm)	-1.2 to -3.0	-1 to -2.5	-0.8 to -2.5	-1.6 to -2.6
Total images	2936	3524	2888	1613
Picked particles	281363	238436	289172	1033376
Selected particles (After sorting)	227801	219522	46966	372504

Cryo-EM data processing

All pre-processing steps (movie alignment, CTF estimation, and particle picking) were carried out using Warp [376]. All the next processing steps (2D classifications, ab-initio, homogeneous and heterogeneous refinements) were done using CryoSPARC [343]. The processing pipeline was similar for all datasets: movie alignment, CTF estimation, and automatic particle picking (using Warp's default trained model) were done as the data was being collected using Warp. Then, the particles were imported into CryoSPARC and used as input for a 2D classification to get rid of junk particles that were wrongly picked by Warp. Good 2D classes were then selected manually and used as input for an ab-initio refinement job in CryoSPARC. The resulting classes from the ab initio refinements were then refined further using the homogeneous and heterogeneous refinement jobs, resulting in reconstructions in the 10.5 to 11.5 Å resolution range.

5 Lasamide, a Potent Human Carbonic Anhydrase Inhibitor from the Market: Inhibition Profiling and Crystallographic Studies

Publication
Chiara Baroni et al., Lasamide, a Potent Human Carbonic Anhydrase Inhibitor from the Market: Inhibition Profiling and Crystallographic Studies. ACS Medicinal Chemistry Letters, 2024, Vol. 15, pp. 1749-1755.
DOI: 10.1021/acsmedchemlett.4c00341

5.1 Summary

Lasamide (LAS) is a synthetic precursor and contaminant in Furosemide (FUR) industrial production. Due to the presence of a primary sulfonamide, the prototypical CA inhibitor moiety, LAS represents a valuable scaffold for fragment-based drug discovery.

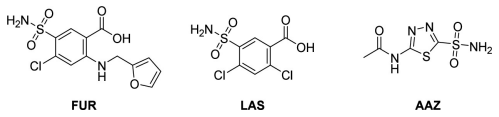

Figure 5.1. Chemical structures of Furosemide (FUR), Lasamide (LAS) and Acetazolamide (AAZ).

FUR is clinically used as a diuretic for the treatment of edema and hypertension in patients with congestive heart failure, liver, or kidney disorders. It primarily acts by inhibiting the luminal Na^+-K^+-$2Cl^-$ symporter, blocking the reabsorption of sodium, potassium, and chloride ions in the proximal and distal segments of the loop of Henle [377, 378, 379, 380]. Although FUR contains a primary

sulfonamide moiety typical of hCAIs, its inhibitory activity on human CA isoforms is weaker compared to Acetazolamide (AAZ), a reference CA-targeting diuretic [381].
LAS is an intermediate and highly toxic impurity generated during the industrial synthesis of FUR and is therefore strictly monitored, as exposure can cause allergic respiratory diseases, occupational asthma, and rhinitis, with symptoms sometimes persisting for years [382, 383, 384, 385, 386, 387].
In this project, LAS was evaluated through inhibition assays across all the hCA isoforms to characterize its inhibitory profile.

The inhibition activity of LAS against human (h) and murine (m) CAs was evaluated using the stopped-flow CO_2 hydration assay [388]. The inhibition efficacies were reported as inhibition constants (K_I) and compared to the reference compounds FUR and AAZ (table 5.1).
LAS proved to be a potent in vitro inhibitor for nearly all tested isoforms, except hCA III, for which it showed no inhibition. Notably, LAS inhibited the ubiquitous hCA I and II isoforms at subnanomolar levels and was especially effective against tumor-associated hCA IX, outperforming both FUR and AAZ. It also showed strong inhibition of hCA IV and mitochondrial hCAs VA, while showing lower, but still nanomolar, efficacy against mitochondrial hCA VB, isoforms IV–VII, and XII-XIV.

The binding modes of LAS in hCAs II, IX-, and XII-mimic active sites were characterized using X-ray crystallography (figure 5.2). The crystallographic structures revealed the canonical binding mode of the primary sulfonamide, coordinating the zinc ion and forming hydrogen bonds with Thr199, along with a network of hydrogen bonds and water-mediated interactions [54]. In the hCA II–LAS complex, the carboxyl group establishes hydrogen bonds with Thr200, Gln92, and His64, along with water bridges with Asn67 and Asn62. Notably, substitution of Asn67 with glutamine in hCA II to give the hCA IX-mimic does not prevent the formation of a stabilizing water bridge with the ligand, whereas replacement with lysine in the hCA XII-mimic eliminates these anchoring interactions. This loss likely accounts for the slightly reduced inhibitory potency of LAS toward this isoform. Overall, the potent inhibitory properties of LAS against hCA II, IX-mimic H-tag, and the hCA XII catalytic domain (KI of 0.33, 1.59, and 7.54 nM, respectively) can be attributed to the extensive network of interactions established by LAS within the enzyme

Table 5.1. Inhibition constants (K_I, nM) of LAS, FUR, and AAZ against various CA isoforms. K_I values are inhibition constants expressed as a mean ± SD of three independent experiments by the stopped-flow technique. Data for FUR (*) were previously reported. Errors were in the range of ±5–10% of the reported values (data not shown). All CAs are recombinant human proteins and full-length enzymes, except for the murine (m) XIII, and the isoforms IX and XII, which consist only of the catalytic domains.

CA isoform	LAS	FUR	AAZ
hCA I	0.52 ± 0.03	62*	250 ± 19
hCA II	0.33 ± 0.02	65*	12 ± 0.6
hCA III	$>5.0 \times 10^4$	3.2×10^{6}*	2.0×10^5
hCA IV	1.91 ± 0.17	564*	74 ± 4
hCA VA	3.49 ± 0.73	499*	63 ± 2
hCA VB	14.2 ± 1.1	322*	54 ± 5.8
hCA VI (from saliva)	11.7 ± 0.6	230 ± 15	16 ± 1
hCA VI (from milk)	8.51 ± 0.68	143 ± 8	23 ± 2
hCA VII	6.63 ± 0.34	513*	2.5 ± 0.1
hCA IX	2.61 ± 0.17	420*	25 ± 1.4
hCA XII	7.54 ± 0.72	261*	5.7 ± 0.4
mCA XIII	9.37 ± 0.78	550*	17 ± 1.6
hCA XIV	11.9 ± 1.2	52*	41 ± 2.1

active sites. Among the interactions that the inhibitor established within the active sites, the hydrogen bond with His64 is particularly interesting since this residue has an important role in the catalysis of CO_2 hydration by allowing the regeneration of the zinc-bound hydroxyl via proton transfer from the zinc-bound water to the bulk solvent [54].

Notably, the hCA IX-mimic H-tag crystallized in a cubic space group (I432), although the crystallization conditions adopted were the same as those usually used for hCA II and its mimic derivatives based on sodium citrate as the precipitant agent [389]. The new crystal form is probably due to the presence of the H-tag sequence positioned at the N-terminal end of the protein for purification purposes via nickel affinity chromatography. Histidines of the H-tag mediate contacts between molecules in the crystal lattice and coordinate a nickel ion likely originating from the metal affinity column (figure 5.3). The metal ion was observed bound to two histidine residues from the His-tag and to a third histidine contributed by a symmetry-related molecule. The coordination is completed by the carboxylate side chain of Asp132, resulting in a tetrahedral geometry. This interaction with Asp132 is interesting because it corresponds to one of the mutations (Gly132Asp) introduced into hCA II to generate the hCA

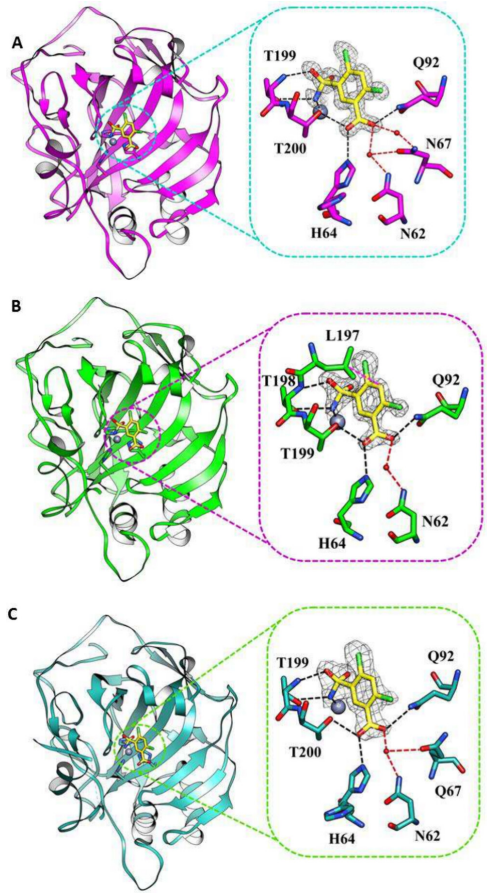

Figure 5.2. X-ray structures of LAS in complex with A) hCA II (pink, PDB: 8QH8), B) hCA XII-mimic (green, PDB: 8QHJ), and C) hCA IX-mimic H-tag (cyano, PDB: 8QHG). A zoomed-in view of the active site is also provided. Residues involved in the inhibitor–enzyme binding are shown in sticks and labeled. Hydrogen bonds and water bridges are depicted as black and red dotted lines, respectively. The gray sphere represents the zinc ion in the protein active site.

IX-mimic isoform.

Very similar metal coordination to the H-tag has already been observed in the structure of the thiocyanate complex of a β-CA from Mycobacterium tuberculosis [390]. A zinc ion was added at this position based on its B-factor value and the height of the corresponding electron-density peak. In our structure as well, considering the B-factors, the density peak, the coordination geometry, and the metal–ligand distances, we cannot exclude the possibility that a second zinc ion, rather than nickel, is coordinated by the His-tag. Nevertheless, this structural feature is not to be considered of biological significance, as it has already been recognized in the case of the above-cited β-CA.

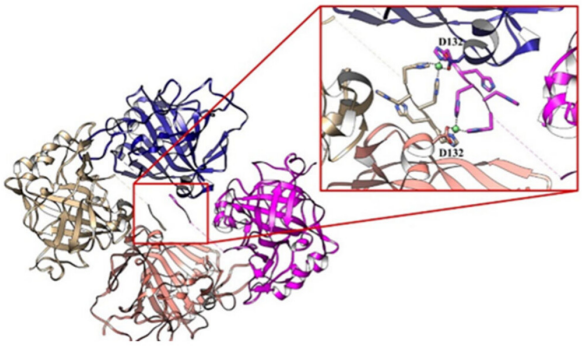

Figure 5.3. hCA IX-mimic H-tag arrangement in the cubic space group I432 crystal lattice. The figure also shows a focus on the N-terminal H-tag interacting with a Ni(II) ion. The green sphere represents the nickel ion, and the coordination bonds with the H-tag histidines and Asp132 are depicted as black lines. The dotted lines represent connections between the H-tag and the N-terminus of the enzyme, since the first N-terminal residues were not introduced in the model due to a lack of electron density.

Due to the availability of the X-ray structures, comparison of LAS binding mode with FUR bound to hCA II showed that while both compounds share sulfonamide-zinc interactions, LAS forms additional hydrogen bonds and water bridges that are limited in FUR due to its furanyl substituent, highlighting how structural differences influence binding networks and inhibitory potency (figure 5.4) [378, 379].

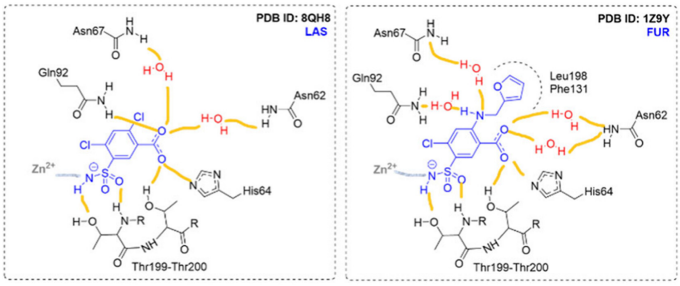

Figure 5.4. Bidimensional representation of the binding of LAS (PDB ID: 8QH8, left) and FUR (PDB ID: 1Z9Y, right) with hCA II. Compounds are in blue, amino acid residues involved in the interaction networks are in black and labeled, water molecules are in red, and the zinc ion is in gray. Polar interactions (hydrogen bond, water bridge, salt bridge) are represented with a solid yellow line.

LAS is a common synthetic intermediate and a known process-related impu-

rity in FUR formulations, characterized by a low-molecular-weight structure containing two competing metal-binding groups, a primary sulfonamide and a carboxylate. This structural simplicity makes LAS a valuable starting point for fragment-based drug discovery. Stopped-flow enzymatic assays revealed that LAS is a potent but non-selective hCAI, suppressing the physiologically relevant isoenzymes I and II at subnanomolar levels and inhibiting other isoforms (IV–VII, IX, XII–XIV) within the nanomolar range.

In summary, the detected strong inhibitory profile of LAS, together with the availability of high-resolution structural data, provides a solid insight for enhancing CA isoform selectivity through chemical derivatization, fragment-growing strategies, and rational tail design.

The corresponding publication is provided in the Appendix for comprehensive reference.

6 X-ray crystallographic and kinetic studies of biguanide containing aryl sulfonamides as carbonic anhydrase inhibitors

Publication
Chiara Baroni et al., X-ray crystallographic and kinetic studies of biguanide containing aryl sulfonamides as Carbonic anhydrase inhibitors. RSC Medicinal Chemistry, 2025, Vol. 16, pp. 1633-1640.
DOI: 10.1039/D4MD01018C

6.1 Summary

A small series of dual-target compounds was developed by combining the prototypical CA zinc-binding sulfonamide with the biguanide moiety of metformin, an emerging anticancer agent.

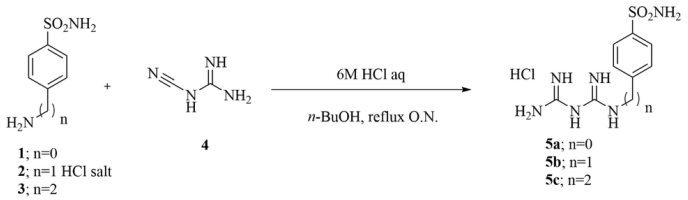

Figure 6.1. Synthetic procedure and chemical structure of the analyzed compounds.

Metformin is a widely used antidiabetic drug [391] that has recently been recognized for its cardiovascular protective, anti-inflammatory, and anticancer properties [392]. The anticancer effects of metformin are attributed to both direct and indirect actions, such as ATP depletion and the reduction of gluconeogenesis, respectively [393, 394, 395, 396, 397, 398].
Based on the antitumor properties of metformin and hCAIs, as well as the

advantages of a dual-targeting approach [2], a small series of compounds combining a biguanide and a benzenesulfonamide moiety was designed and synthesized. Their inhibitory activity was then characterized through enzymatic assays and structural analyses against key human CA isoforms.

The inhibition profile of compounds 5a–c was evaluated using the stopped-flow technique [388] with the physiologically relevant hCA isoforms I, II, VA, IX, and XII. The inhibitors exhibit low activity against cytosolic (hCA I and II) and mitochondrial (hCA VA) isoforms, with K_I values in the high- to low-micromolar range, with a structure–activity relationship indicating that longer alkyl spacers decrease inhibition potency. In contrast, all compounds exhibit strong inhibition of the tumor-associated hCAs IX and XII, with K_I values in the low nanomolar range, frequently showing greater potency than the reference inhibitor acetazolamide (AAZ). In this case, the elongation of the alkyl spacer slightly reduced potency for hCA IX but had no effect for hCA XII, against which the compounds show a remarkable selectivity.

Table 6.1. The inhibition constant K_I (nM) of the small series of compounds against the cytosolic hCAs I and II, mitochondrial VA, membrane-associated IX, and XII calculated by a CO_2 hydrase stopped-flow assay using acetazolamide (AAZ) as a reference drug. The data are means from 3 different assays, by the stopped-flow technique (errors were in the range of ±5–10% of the reported values).

Compound	hCA I	hCA II	hCA VA	hCA IX	hCA XII
5a	361.0	134.6	119.9	1.43	0.5
5b	375.1	369.5	678.8	2.44	2.6
5c	4435	501.0	995.9	20.2	1.7
AAZ	**250.0**	**12.1**	**63.0**	**25.6**	**5.7**

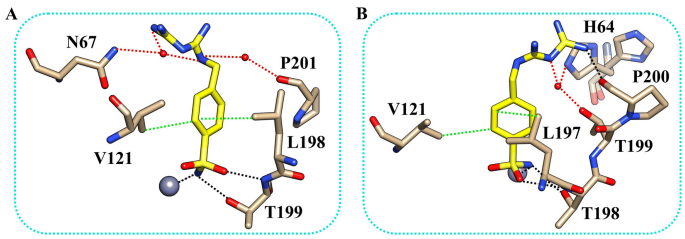

Figure 6.2. The binding mode of inhibitor 5b within the active site of hCA II (A) and hCA XII-mimic (B). Residues involved in the binding of the inhibitor are also shown. Hydrogen bonds, water bridges, and hydrophobic interactions are depicted as black, red, and green dotted lines. The gray sphere represents the zinc ion in the protein active site. The side chain of His64 was modeled in two conformations.

The X-ray crystallographic structures of hCA II and hCA XII-mimic in complex with inhibitor 5b were determined, revealing classical sulfonamide binding to the zinc ion and hydrogen bonding with Thr199/198 (numbering of hCA II and hCA XII, respectively) (figure 6.2). The biguanide tail adopts distinct orientations in the two isoforms. In the active site of hCA II, it forms water bridges with Asn67, while in the hCAXII mimic, the inhibitor interacts with the amino acid residues in the opposite region of the protein cavity, Thr199 and His64 (figures 6.2, 6.3).

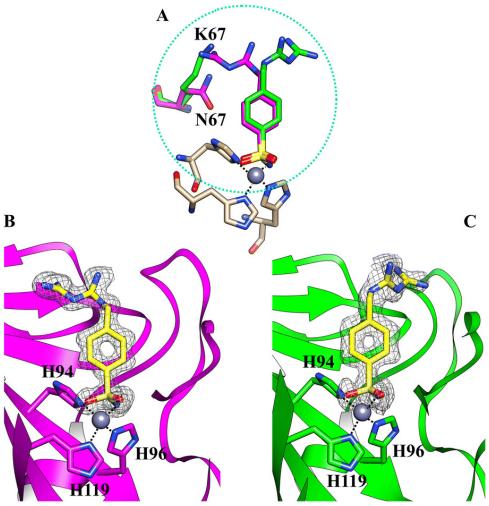

Figure 6.3. (A) Comparison of the two different orientations of the inhibitor 5b within the active site of hCA II (magenta) and hCAXII-mimic (green), respectively; (B) the active site of hCA II complexed with inhibitor 5b (PDB: 8ROU); (C) the active site of hCAXII-mimic complexed with inhibitor 5b (PDB: 8RNS). The 2Fo–Fc density map for the inhibitor is also shown.

This effect seems to be related to the Asn67Lys mutation in hCA XII-mimic, where lysine, due to its steric hindrance and higher flexibility than asparagine, may induce a different organization of the inhibitor within the enzyme cavity.

In the case of the inhibitor 5c, it was not possible to accurately determine its binding mode, since the acquired density maps do not show the biguanide portion of the molecule for both hCAII and hCAXII mimic complexes.
However, two distinct inhibitor molecules were detected within the active site of hCA II. In numerous complexes of hCA II with inhibitors, it has been observed that a second inhibitor molecule binds near the N-terminal end of the protein [399, 400]. Nevertheless, in this case, a second inhibitor molecule is bound within the active site, likely reducing the affinity of the inhibitor by introducing

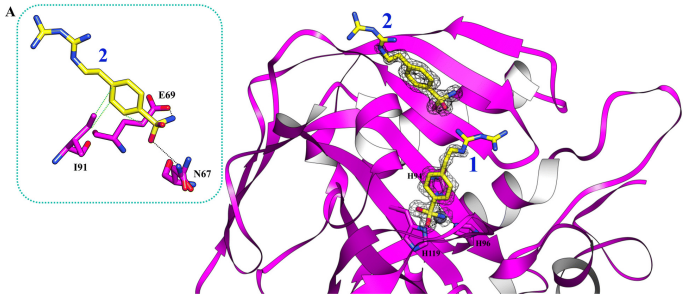

Figure 6.4. The active site of hCA II complexed with inhibitor 5c (PDB: 9H0V). Molecules of the inhibitor are labeled as 1 and 2. The binding mode of molecule 2 is shown in panel A. Hydrogen bonds and hydrophobic interactions are depicted as black and green dotted lines.

disorder into the binding cavity. The binding of a second inhibitor molecule was not observed in the hCA XII-mimic complex and can be explained by comparing the sequences of the two isoforms. In fact, residues interacting with the second molecule are mutated in the hCA XII-mimic sequence (Asn67Lys, Glu69Asn, and Ile91Thr) in a way that prevents the interaction.

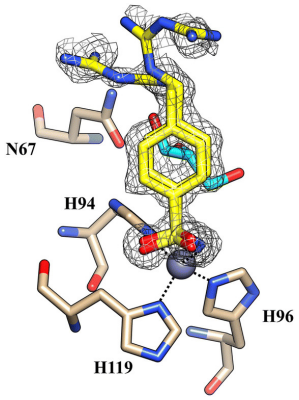

Figure 6.5. The active site of hCA II complexed with inhibitor 5b (PDB: 8ROW) from data collected using glycerol as a cryoprotectant. Glycerol is depicted in cyan.

Glycerol is the most commonly used cryoprotectant in X-ray protein crystallography [401] and is routinely employed to prevent ice formation when freezing CA crystals of various isoforms and their inhibitor complexes. However, glycerol can penetrate the protein active site and form hydrogen bonds with surrounding residues, potentially altering the binding mode of the inhibitor. In our study, glycerol was observed bound within the active site of hCA II in complex with 5b. The inhibitor is disordered, with its tail modeled in two conformations of

differing occupancies, as illustrated in figure 6.5. This disorder may result from steric hindrance caused by the cryoprotectant, affecting complex formation. To prevent cryoprotectant interference within the active site, the experiments were repeated using the larger molecule PEG 400. In this case, the inhibitor adopted a single, well-defined orientation within the protein cavity (figure 6.3 panel B), providing a more accurate representation of its binding mode.

In summary, aryl sulfonamides bearing a biguanide tail, compounds 5a–c, were reported as selective inhibitors of the tumor-associated hCA IX and XII isoforms, and the binding modes of 5b and 5c with hCA II and XII-mimic were determined using X-ray crystallography. The aryl sulfonamide portion of 5b inserted deeply into the catalytic cavities of hCA II and XII, while the flexible biguanide tail formed multiple interactions with residues at the top of the clefts, determining ligand orientation and stabilization in an isoform-dependent manner. Notably, the Asn67Lys mutation in the XII-mimic drove selectivity toward the tumor-associated isoform over hCA II. Additionally, a secondary 5c molecule was identified in the catalytic site, suggesting a potential long-range allosteric mechanism that could be exploited to fine-tune CA activity. This second molecule of inhibitor 5c binds in a region characterized by residues that are mutated in the hCA XII isoform (Asn67Lys, Glu69Asn, and Ile91Thr). The aforementioned region appears critical in discriminating between these two isoforms. Consequently, it should be specifically targeted to achieve selectivity, also by introducing conformational instability and/or steric hindrance within the cavity in light of the long-range mechanism observed for the inhibitor 5c.

The corresponding publication is provided in the Appendix for comprehensive reference.

7 O-derivatization of natural tropolone and β-thujaplicin leading to effective inhibitors of human carbonic anhydrases IX and XII

Publication
Francesco Melfi et al., O-Derivatization of Natural Tropolone and β-Thujaplicin Leading to effective Inhibitors of Human Carbonic Anhydrases IX and XII. European Journal of Medicinal Chemistry, 2025, Vol. 290.
DOI: 10.1016/j.ejmech.2025.117552

7.1 Summary

Tropolone (TRP) is a seven-membered aromatic compound featuring a ketone and an enolic hydroxyl group, which together confer acidic, metal-chelating, and strong hydrogen-bonding properties [402, 403, 404]. Naturally produced by bacteria, fungi, and yeast, TRP is often found as part of more complex natural compounds [405, 406] and has been studied extensively for its antioxidant, antimicrobial, and antiparasitic activities [407, 408], which are likely associated with its ability to disrupt microbial membranes and metabolism through metal chelation activity [409, 410, 411].
Among tropolonoids, the thujaplicins (TJP) are particularly interesting, and they are naturally occurring in certain coniferous trees. This class of compounds bears an isopropyl group in different positions of the TRP core, such as C2, C3, and C4, resulting in α-, β-, and γ-TJP, respectively. The Greek alphabet refers to the functionalization position with respect to the OH moiety on the ring. β-TJP is a widely used product and exhibits diverse bioactivities, including antimicrobial, anticancer, and antidiabetic effects [412, 413, 414, 415].
Tropolonoids act as a bidentate metal-chelating ligand [416]. The metal-binding

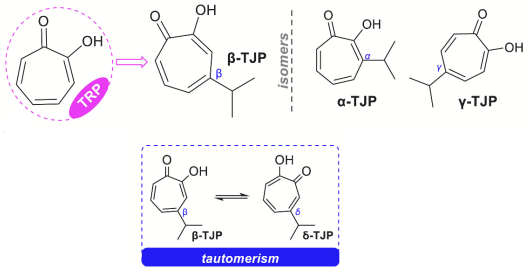

Figure 7.1. Chemical structure of natural tropolone (TRP) and β-thujaplicin (β-TJP) with the latter isomers α-thujaplicin (α-TJP) and γ-thujaplicin (γ-TJP) along with a representative example of tautomerism (β-δ TJP).

ability of TRP is supported by several X-ray structures of TRP-metalloenzyme complexes, for example, with human tyrosinase-related protein 1 and hCA II [404, 417]. Early studies showed inhibition analysis of TRP and β-TJP against relevant hCA isoforms, revealing position-dependent differences in potency and binding interactions. These findings, combined with the biological importance of CAs, motivated the exploration of TRP and TJP scaffolds through the synthesis of O-functionalized derivatives as potential inhibitors of human and microbial α-CAs.

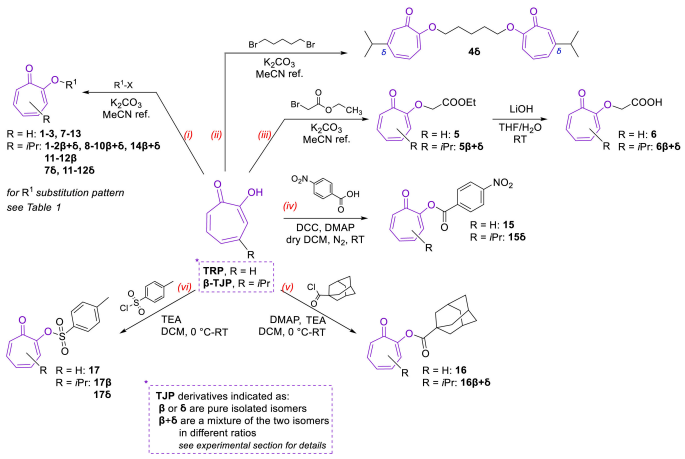

Figure 7.2. Synthetic procedure for the preparation of TRP and TJP derivatives 1–17. The Greek letters β or δ indicate the position of the isopropyl moiety on the TJP scaffold with respect to the hydroxyl group, as conventional. Compounds indicated as β+δ are a mixture of the two isomers in different ratios. The R^1 substitution pattern is reported in Table 7.1.

To investigate the chelating properties of TRP and β-TJP, a series of O-functionalized derivatives was synthesized (figure 7.2). In particular, ethers

and esters were obtained by reacting the tropolonoid cores with appropriate reagents, mainly halides, under basic conditions. In some cases, regioisomers could not be separated, so biological testing was performed on the mixtures after determining the molar ratio of each component. For a detailed description of the synthesis procedure, see the published article.
TRP and β-TJP compound derivatives were evaluated against a broad panel of α-CA, from humans (hCAs I, II, VA, VII, IX, XII) to assess potency and isoform selectivity (table 7.1). The inhibition profiles were analyzed using a stopped-flow CO_2 hydration assay. From the analysis, all synthesized compounds were detected to be less potent than the reference inhibitor, acetazolamide (AAZ). The significance of these inhibitory results is assessed when compared to other known hCAI classes. While benzenesulfonamides are highly potent, their isoform selectivity is often poor [418, 419]. Conversely, coumarins exhibit lower potency but better selectivity, whereas inorganic ions and phenolic and polyphenolic compounds generally show micromolar to millimolar inhibition with limited discrimination among isoforms [420, 421, 422, 423]. Within this context, the tropolonoid derivatives, though not highly potent, display good isoform selectivity. However, their potency and selectivity do not follow a clear trend and depend on individual structural features, as reflected in the SAR analysis.

The binding mode of the compounds was first investigated through crystallographic studies of β-TJP (figure 7.3). Analysis of the electron density maps showed a clear density for the studied ligand, confirming its binding to the enzyme. The ligand forms a bidentate coordination with the catalytic Zn(II), with Zn–O distances of 2.17 and 2.20 Å. The aromatic ring establishes hydrophobic interactions with residues Leu198 and Val121, while one oxygen atom forms water-mediated hydrogen bonds with the backbone NH and side-chain OH of Thr199, similar to the classical sulfonamide interactions [424]. Comparison with the previously reported hCA II–TRP structure [404] shows that β-TJP adopts a nearly identical orientation and interaction pattern within the active site.

Despite extensive attempts, the X-ray structures of hCAII complexes with TRP and TJP derivatives could not be obtained. Hence, computational modeling was conducted to clarify the binding modes and interaction energies of TRP and TJP derivatives with various hCA isoforms. All compounds fit well

Table 7.1. Inhibitory K_I values (μM) of TRP and TJP derivatives and reference compound AAZ against selected hCA isoforms through the stopped-flow CO_2 hydration assay. K_I values are reported as means of three independent experiments. Errors are in the range of ± 5–10 % of the reported values.

CPD	Core	R^1	hCA I	hCA II	hCA VA	hCA VII	hCA IX	hCA XII
TRP	TRP	-H	>100	>100	>100	>100	>100	>100
TJP	TJP	-H	4.98	90.6	7.50	>100	23.9	>100
1	TRP		0.05	>100	>100	>100	19.0	7.76
$1\beta + \delta$	TJP		0.66	76.0	>100	>100	2.29	>100
2	TRP		>100	44.5	8.75	5.20	8.94	6.74
$2\beta + \delta$	TJP		>100	2.95	9.56	2.78	3.77	7.50
3	TRP		>100	>100	84.2	1.52	0.54	6.21
4δ	TJP		>100	6.36	31.6	7.10	1.33	73.7
6	TRP		>100	3.96	8.11	4.87	25.6	4.24
$6\beta + \delta$	TJP		>100	>100	>100	71.3	2.53	6.36
7	TRP		>100	>100	>100	>100	37.7	6.07
7δ	TJP		>100	7.44	7.95	0.96	0.26	4.57
8	TRP		8.31	>100	>100	>100	>100	1.35
$8\beta + \delta$	TJP		>100	70.2	14.2	9.62	0.44	8.09
9	TRP		6.22	3.43	>100	>100	13.3	0.99
$9\beta + \delta$	TJP		>100	>100	>100	33.9	39.5	5.84
10	TRP		>100	>100	>100	>100	34.5	2.64
$10\beta + \delta$	TJP		>100	>100	>100	2.78	2.73	4.71
11	TRP		8.01	27.6	>100	>100	>100	1.60
11β	TJP		>100	41.4	8.96	5.41	1.41	4.52
11δ	TJP		>100	>100	21.7	6.18	0.94	3.57
12	TRP		>100	>100	6.63	6.19	4.30	3.11
12β	TJP		>100	>100	83.5	>100	47.4	54.6
12δ	TJP		>100	>100	>100	>100	>100	2.08
13	TRP		>100	3.70	61.1	2.82	2.28	7.28
13δ	TJP		>100	3.02	89.4	3.95	0.53	5.31
$14\beta + \delta$	TJP		>100	2.80	>100	5.73	0.49	5.03
15	TRP		84.4	43.9	>100	>100	>100	1.20
15δ	TJP		>100	8.72	>100	9.60	0.37	5.23
16	TRP		>100	>100	85.6	>100	43.5	2.11
$16\beta + \delta$	TJP		>100	>100	>100	>100	38.1	3.52
17	TRP		94.2	80.9	>100	>100	>100	>100
17β	TJP		>100	>100	39.0	9.33	0.42	4.37
17δ	TJP		>100	6.97	4.45	5.27	0.40	8.09
AAZ	**Reference**		**0.25**	**0.01**	**0.06**	**0.002**	**0.03**	**0.01**

within the enzyme active sites and showed favorable interaction energies.

For hCA I, the most active compounds (1, 1δ, 11, 9, and 8) occupy the cat-

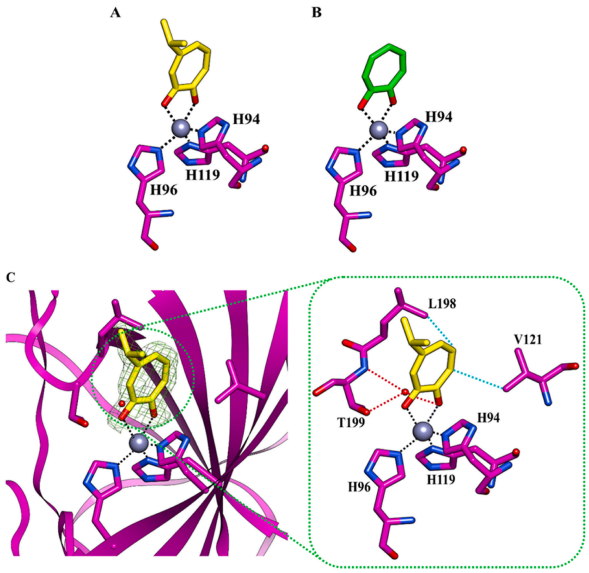

Figure 7.3. The structures show the active site of hCA II complexed with (A) β-TJP (PDB ID: 9H0W) and (B) TRP (PDB ID: 5THJ) [404]. The gray sphere represents the catalytic zinc ion while the coordination bonds are depicted as black dotted lines. (C) The active site of hCA II complexed with β-TJP (PDB ID: 9H0W). The ligands β-TJP and TRP are represented in yellow and green sticks, respectively. Residues involved in the binding of the inhibitor are also shown in magenta sticks. Water bridges and hydrophobic interactions are depicted as red and cyan dotted lines, whereas coordination interactions are in gray dotted lines. The gray sphere represents the catalytic zinc ion. A |2Fo-Fc| map is shown for the ligand contoured at 1 sigma.

alytic pocket and form an H-bond with Gln92. Notably, the 2-nitrobenzyloxy group of compound 11 creates a π-stacking interaction with Phe91, while the 4-cyanobenzyloxy moiety of compound 8 participates in π-stacking with His94 and coordinates the catalytic zinc ion.

Against hCA II, zinc coordination is observed for compounds 2β+δ, 6, 4δ, 9, and 14β+δ. Compound 2β+δ forms a halogen bond with Asn62 via its 3-chloropropyl tail, whereas 7δ establishes three halogen bonds through its 4-bromobenzoxy group. Importantly, several TJP derivatives (2β+δ, 4δ, 7δ, 14β+δ) reproduce the hydrophobic interactions identified in the β-TJP–hCA II crystal structure.

For hCA VA, the p-tosyl group of 17δ forms π-stacking with Tyr100 and coordinates the zinc ion via the β-TJP carbonyl. Other active molecules including β-TJP itself, 2, 2β+δ, 6, 7δ, 12, and 11β also coordinate the catalytic Zn(II). Additionally, compound 6 forms a salt bridge with Arg282, while 11β forms one with Glu142.

Regarding hCA VII, the highly potent inhibitor 7δ engages in a halogen bond with Thr199, π-stacking with His94, and an H-bond with Gln92. The nitro derivative 10β+δ coordinates the metal and forms two H-bonds with Gln67 and Thr199.

For hCA IX (figure 7.4), most active compounds anchor through zinc coordination and form an extensive network of interactions. Compound 6δ forms a halogen bond with Glu106, while 2β+δ interacts similarly through the chlorine atom with Tyr11. The naphthyl group of 13δ establishes two π-stacking interactions with His94. Compounds 8β+δ and 14β+δ form an H-bond with Gln92 and π-stacking with His94. Interestingly, 17β reproduces these interactions and additionally forms an H-bond with Thr201. The nitro derivative 11δ establishes an H-bond with Gln92 and a salt bridge with Glu106.

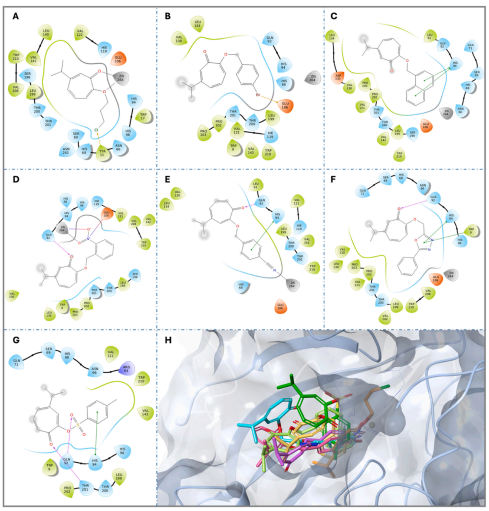

Figure 7.4. 2D interaction diagram for compounds A) 2δ; B) 7δ; C) 13δ; D) 11δ; E) 8β; F) 14δ; G) 17δ in complex with hCA IX; H) shows the superposition of the seven most active compounds 2δ (orange sticks), 7δ (violet sticks), 13δ (light green sticks), 11δ (light yellow sticks), 8β (magenta sticks), 14δ (cyan sticks), and 17β (green sticks). hCA IX is represented as a slate surface, the zinc ion and the coordinating histidine residues within the active site are shown as a yellow ball and slate sticks, respectively. For derivatives in mixture, the best-scored isomer is shown.

Finally, for hCA XII (figure 7.5), the binding modes of the most active inhibitors are characterized by zinc coordination and polar interactions. The adamantane derivatives 16 and 16β+δ form H-bonds with Gln92. The 4-nitrobenzyloxy TRP derivative 9 and the cyano-substituted TRP derivative 8 are involved in π-stacking with His94 and H-bond with Thr200. In contrast, compound 15 forms a salt bridge with Lys170 through its nitro group.

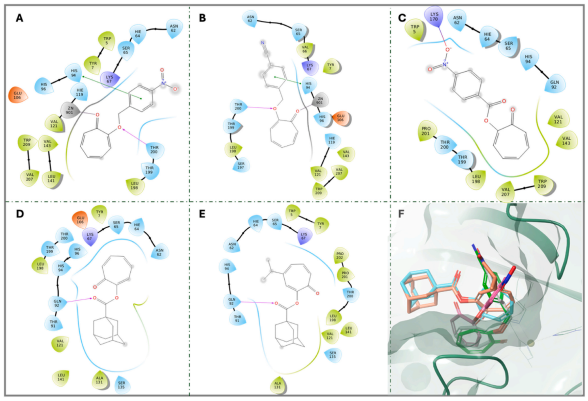

Figure 7.5. 2D interaction diagram for A) 9; B) 8; C) 15; D) 15; E) 17β compounds in complex with hCA XII; F) shows the superposition of the five most active compounds (9 in white carbon sticks, 8 (green sticks), 15 (salmon sticks), 15 (cyan sticks), and 17β (magenta sticks). hCA XII is represented as a forest surface, the zinc ion and the coordinating histidine residues within the active site are shown as a yellow ball and forest sticks, respectively. For derivatives in mixture, the best scored isomer is shown.

The antiproliferative activity was evaluated using multiple myeloma (MM) as a model [425]. Western blot analysis of ten MM cell lines showed that MM cells markedly overexpress hCA IX and hCA XII compared to healthy cells, with hCA IX being the predominant isoform, suggesting their potential as MM biomarkers and therapeutic targets. One of the derivative compounds, the 17β, was examined for chemical stability and tested for antiproliferative effects in a multiple myeloma model, where it showed strong pro-apoptotic activity and low toxicity toward healthy cells.

In conclusion, to identify natural-product-based scaffolds for biomedical applications, we conducted a multidisciplinary study on O-substituted troponoloids. The natural products TRP and β-TJP were derivatized through O-alkyl/acyl or sulfonyl substitutions under basic conditions to generate a broad library of compounds, yielding both TRP derivatives and mixtures of β- and δ-TJP regioisomers formed through keto–enol rearrangement. The compounds were screened in vitro against a panel of physiologically and pathologically relevant hCA isoforms. The resulting K_I values represent the first structure–activity relationship dataset for synthetic TRP and TJP O-derivatives. X-ray crystallography of the hCA II/β-TJP complex revealed a bidentate coordination to

Zn(II) supported by water-mediated hydrogen bonds to Thr199, resembling the canonical binding mode of sulfonamide inhibitors. The binding modes of TRP and selected TJP-O-derivatives were further explored in silico for hCA VA, VII, IX, and XII. Among the tested compounds, the 17β isomer showed promising chemical stability and potent anti-proliferative activity against MM cell lines while sparing healthy cells. Overall, these findings support troponoloids as a promising new class of natural scaffolds with potential for therapeutic exploration.

The corresponding publication is provided in the Appendix for comprehensive reference.

Appendix

ACS Medicinal Chemistry Letters

pubs.acs.org/acsmedchemlett Letter

Lasamide, a Potent Human Carbonic Anhydrase Inhibitor from the Market: Inhibition Profiling and Crystallographic Studies

Chiara Baroni,[&] Ilaria D'Agostino,[&] Gioele Renzi, Jaydeo T. Kilbile, Yasinalli Tamboli, Marta Ferraroni,* Simone Carradori, Clemente Capasso, Fabrizio Carta,* and Claudiu T. Supuran

Cite This: *ACS Med. Chem. Lett.* 2024, 15, 1749−1755 Read Online

ACCESS | Metrics & More | Article Recommendations | Supporting Information

ABSTRACT: Lasamide is a synthetic precursor and a contaminant of the diuretic Furosemide manufacturing process and represents a highly valuable building block for fragment-based drug discovery approaches. We assessed the ability of Lasamide to inhibit in vitro the human-expressed Carbonic Anhydrases by means of the stopped-flow technique, and we assessed its binding modes within hCAs II and XII-mimic catalytic clefts by X-ray crystallography. Interestingly, an unprecedented crystal form for the hCA IX mimic H-tag is reported and discussed herein.

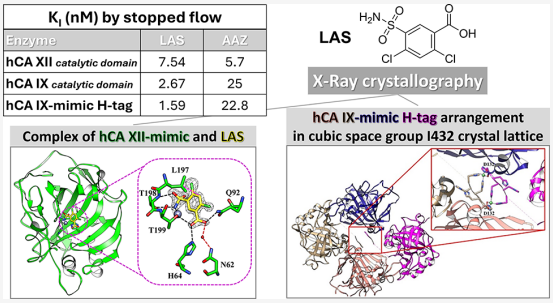

KEYWORDS: *Carbonic Anhydrase Inhibitors, Lasamide, Fragment based drug discovery, X-ray crystallography*

Downloaded via UNIV DEGLI STUDI DI FIRENZE on October 20, 2025 at 12:20:19 (UTC).
See https://pubs.acs.org/sharingguidelines for options on how to legitimately share published articles.

Furosemide (**FUR**, Figure 1) is a diuretic currently used in clinics for the management of edema and hypertension in patients affected by congestive heart failure and liver and kidney disorders. **FUR** mainly acts by inhibition of the luminal Na-K-2Cl symporter, thus preventing the reabsorption of sodium, potassium, and chloride ions at the proximal and distal tubules of the loop of Henle.[1]

Since **FUR** contains the prototypic Carbonic Anhydrase (CA; EC 4.2.1.1) inhibitor moiety (i.e., the primary sulfonamide), its effects on the human (h) expressed enzymes have been assessed,[2−4] revealing a weaker inhibition profile when compared to the reference Acetazolamide (**AAZ**, Figure 1, Table 1), a diuretic drug that acts when administered systemically by inhibition of the hCAs located at the proximal tubules of nephrons.[5]

The industrial synthesis of **FUR** accounts for the condensation of furfurylamine with the key intermediate 2,4-dichloro-5-sulfamoylbenzoic acid, Lasamide (**LAS**, Figure 1) under basic conditions.[6−8] The reliable and efficient manufacturing process of **FUR** has been analyzed for contaminants and impurities, and **LAS** has been found and identified as "impurity B". Its presence is monitored and controlled to ensure that **FUR** formulations meet regulatory standards for purity and safety.[9,10] Notably, **LAS** was classified as a highly hazardous substance since personnel working in **LAS**-based **FUR** production were found to suffer from allergic respiratory diseases, occupational asthma, and rhinitis, with related symptoms persisting for years after the contact.[11] Hypotheses of CA VIII involvement in the protection of the airway epithelium were formulated due its downregulation in patients with severe asthma.[12,13] Evidence for CA XII and other isoforms expressions in the nasal mucosa of patients affected with allergic rhinitis were reported and associated with significant genetic variabilities between isoforms and individuals.[14] The functional significance of such variability is highly speculative at the moment since the mechanisms associated with **LAS** toxicity have not been established yet.

LAS is quite attractive from the medicinal chemistry viewpoint since it bears two functional groups (i.e., primary sulfonamide and carboxylic acid) packed within a small scaffold and thus is highly valuable for fragment-based drug discovery processes such as fragment merging, growing, and/or linking.[15] The fact that **LAS** is a fundamental building block for the development of potentially druggable compounds is supported by scientific contributions with **LAS**-based compounds as CA inhibitors (CAIs).[16−18] To the best of our knowledge, previous reports in the literature include IC_{50} values of **LAS** on the bovine (b) CA isoform,[19] specific human (h) CAs I and II,[20−22] and determination of dissociation constants (K_d) on the whole hCAs panel.[23]

Herein, we experimentally assessed **LAS** inhibition constants (K_Is) for all human (h) and murine (m) CAs through the

Received: July 15, 2024
Revised: September 15, 2024
Accepted: September 20, 2024
Published: September 30, 2024

© 2024 American Chemical Society

https://doi.org/10.1021/acsmedchemlett.4c00341
ACS Med. Chem. Lett. 2024, 15, 1749−1755

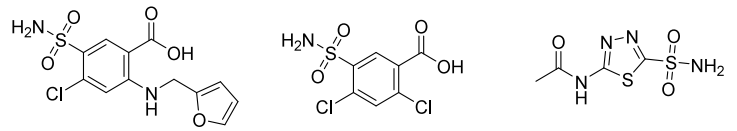

Figure 1. Chemical structure of Furosemide (**FUR**), Lasamide (**LAS**), and Acetazolamide (**AAZ**).

Table 1. Inhibition Data of LAS, FUR, and AAZ on Human (h) and Murine (m) CAs through the Stopped-Flow CO_2 Hydration Assay[24]

	K_I (nM)[a]		
CA isoform	LAS	FUR	AAZ
hCA I	0.52 ± 0.03	62*	250 ± 19
hCA II	0.33 ± 0.02	65*	12 ± 0.6
hCA III	>5.0 × 10^4	3.2 × 10^6*	2.0 × 10^5
hCA IV	1.91 ± 0.17	564*	74 ± 4
hCA VA	3.49 ± 0.73	499*	63 ± 2
hCA VB	14.2 ± 1.1	322*	54 ± 5.8
hCA VI from saliva	11.7 ± 0.6	230 ± 15	16 ± 1
hCA VI from milk	8.51 ± 0.68	143 ± 8	23 ± 2
hCA VII	6.63 ± 0.34	513*	2.5 ± 0.1
hCA IX	2.61 ± 0.17	420*	25 ± 1.4
hCA XII	7.54 ± 0.72	261*	5.7 ± 0.4
mCA XIII	9.37 ± 0.78	550*	17 ± 1.6
hCA XIV	11.9 ± 1.2	52*	41 ± 2.1

[a]K_I values are inhibition constants expressed as a mean ± SD of three independent experiments by the stopped-flow technique.[24] Data for **FUR** (*) were previously reported. Errors were in the range of ±5−10% of the reported values (data not shown). All CAs are recombinant human proteins and full-length enzymes, except for the murine (m) XIII, and the isoforms IX and XII which are the only catalytic domains.

stopped-flow technique and deciphered its binding mode on the relevant isoforms by means of X-ray crystallography.

RESULTS AND DISCUSSION

Inhibitory Activity on Human Carbonic Anhydrases. The inhibition profile of **LAS** on the whole panel of human expressed CAs was determined through the stopped-flow CO_2 hydration assay.[24] The inhibition potencies were reported as K_I values in Table 1 and compared to the reference compounds **AAZ** and **FUR** (IC_{50} curves are available in the Supporting Information file).

K_I values in Table 1 clearly define **LAS** as potent in vitro CAI toward the whole panel of isoenzymes tested, except for the poorly investigated isoform hCA III. In-depth data analysis accounts for the ubiquitous hCA I and II isoforms being inhibited at subnanomolar concentrations (i.e., K_Is of 0.52 and 0.33 nM, respectively) with the latter being 1.6-fold more affected. Although the selectivity of **LAS** for such enzymes is low, it is worth considering that the most inhibited isoform (i.e., hCA II) is known to be ubiquitously expressed and the most kinetically efficient among all the panel in reversibly hydrating the substrate CO_2 (K_{cat}/K_M 1.5 × 10^8).[25] Such a consideration, although limited to in vitro kinetics, is somehow relevant in predicting any possible CA-dependent impact at the physiological level of **LAS**.

As anticipated, no inhibitory activity was detected toward the hCA III when tested up to the highest concentration (50 μM), whereas its activity on the hCA IV isoform was 1.91 nM, thus 38.7-fold more potent when compared to **AAZ** (K_I of 74.0 nM).

Stronger discrimination was noticed between the mitochondrial-expressed hCAs VA and VB, with the former being inhibited 4.1 times more effectively, showing KIs of 3.49 and 14.2 nM, respectively. As for these isoforms, the kinetic trend observed for **LAS** was opposite when compared to **FUR** and **AAZ** (Table 1). Slight K_I differences were reported for all compounds tested on the hCA VI isoforms isolated from saliva and milk specimens. Both **LAS** and **FUR** were slightly more effective inhibitors for the milk-retrieved hCA VI (i.e., 1.4- and 1.6-fold, respectively) over the salivary one. On the contrary, **AAZ** was 1.4-fold more potent for the salivary hCA VI. Such data gave evidence of the poor effects of protein glycosylation[26] on kinetics at least for the compounds considered in this study. **LAS** and **FUR** were weaker inhibitors of the central nervous system-abundantly expressed hCA VII when compared to the reference **AAZ** with K_I values of 6.63, 513, and 2.5 nM, respectively (Table 1). Among the tumor associated hCA IX and XII, **LAS** was a particularly effective inhibitor of the former with a K_I value of 2.61 nM, whereas its congener **FUR** and the reference **AAZ** were 160.9- and 9.6-fold weaker, respectively. As for the hCA XII isoform, **LAS** was slightly less potent inhibitor when compared to **AAZ** (K_Is of 7.54 and 5.7 nM, respectively). Data for the hCA XIII and for the hCA XIV accounted for **LAS** being a low nanomolar inhibitor (K_Is of 9.37 and 11.9 nM, respectively) and more potent than both **FUR** and **AAZ** (Table 1). As a side note, it is relevant to consider that the K_I value of **FUR** for the hCA XIV (i.e., 52 nM) is comparable to that of the hCA I and II isoforms (K_Is of 62 and 65 nM, respectively).

As part of our investigations, we evaluated for the first time whether the presence of the H-tag on the produced hCA IX-mimic isoform could affect the kinetics. The kinetic constants K_{cat} and K_m are reported in Table 2 and are comparable to those of the hCA IX catalytic domain.

Table 2. Kinetic Parameters for the CO_2 Hydration Reaction Catalyzed by the Recombinant hCA IX Proteins at 20 °C and pH 7.5

hCA IX	K_{cat} (s^{-1})	K_m (mM)	K_{cat}/K_m (M^{-1} s^{-1})
Catalytic domain[a]	3.8 × 10^5	6.9	5.5 × 10^7
Mimic H-tag	4.8 × 10^5	7.8	6.4 × 10^7

[a]Data were previously reported.[25]

Data in Table 3 clearly showed that the H-tag attached to the enzyme did not significantly affect the inhibition potency of **LAS** and **AAZ** when compared with the standard hCA IX (catalytic domain). For instance, **LAS** was up to 1.6-fold more effective on the H-tag-bearing enzyme (K_Is of 2.61 and 1.59 nM for hCA IX catalytic domain and hCA IX-mimic H-tag, respectively), whereas the K_I values for **AAZ** were almost

https://doi.org/10.1021/acsmedchemlett.4c00341
ACS Med. Chem. Lett. 2024, 15, 1749−1755

Table 3. Inhibition Data of LAS, FUR, and AAZ on the hCA IX-mimic H-tag through the Stopped-Flow CO_2 Hydration Assay[24]

	K_I (nM)[a]		
Enzyme	LAS	FUR	AAZ
hCA IX-mimic H-tag	1.59 ± 0.2	120 ±3	22.8 ± 2

[a] K_I values are inhibition constants expressed as a mean ± SD of three independent experiments by a stopped-flow technique.[24]

superimposable (Tables 1 and 3). As for **FUR**, the H-tag enhanced the potency for such compound by 3.5-fold (i.e., K_Is of 120 and 420 nM for H-tag mimic and catalytic domain hCA IX, respectively).

Overall, **LAS** showed higher affinity for the panel of enzymes considered when compared to its congener **FUR** and in a large majority to the reference **AAZ**. Although the selectivity indexes of **LAS** for the various isoforms are not robust, the K_I results are of high interest as they report the high effectiveness of such compound for the investigated targets and therefore indicate **LAS** as a promising chemical platform to develop adequate isoform-selective CA modulators.

Crystallographic Studies. The crystallographic structures of hCA II, hCA XII-mimic, and hCA IX-mimic H-tag in complex with **LAS** were determined (Figures 2A–C).[27] Inspection of the electron density maps revealed clear density for the aryl-sulfonamide group, thus confirming for **LAS** the canonical binding mode of primary sulfonamides within all three hCA isoforms by direct interaction with the zinc ion and hydrogen bonding with T199 (Figure 2A–C).[27] The inhibitor is also stabilized by a rich network of hydrogen bonds and water-mediated bridged interactions.

In the hCA II-**LAS** complex (Figure 2A), the carboxyl group of the compound established hydrogen bonds with T200, Q92, and H64 and additional water bridges with N67 and N62. Interestingly, the N67Q mutation in hCA II to give the hCA IX-mimic does not prevent the formation of a water bridge with the ligand (Figure 2C). Conversely, the N67K mutation (i.e., hCA XII-mimic) devoids the complex in Figure 2B of the anchoring water bridges, and that is likely to explain the slightly lower K_I value observed for **LAS** for this isoform (Table 1). Overall, the potent inhibitory properties of **LAS** against hCA II, IX-mimic H-tag, and XII catalytic domain (K_Is of 0.33, 1.59, and 7.54 nM, respectively, Tables 1 and 2), are mainly due to the rich network of interactions that the inhibitor established within the active sites. Among these, the hydrogen bond with H64 is particularly interesting since this residue has an important role in proton transfer in the catalysis of CO_2 hydration by allowing the regeneration of the zinc-bound hydroxyl via proton transfer from the zinc-bound water to bulk solvent.[27]

Unexpectedly, in this research, the crystals of hCA IX-mimic H-tag in this research grew according to a new crystal form in the cubic space group *I*432 although the crystallization conditions adopted were the same as those usually used for hCA II and its mimic derivatives based on sodium citrate as the precipitant agent.[28] The new crystal form was very likely formed due to the presence of the H-tag sequence, positioned at the *N*-terminal end of the protein for purification purposes via nickel affinity chromatography and not subsequently cleaved. The H-tag mediates contacts between molecules in the crystal lattice, and thus, it probably induced the reorganization of the proteins to a cubic crystal form. Only

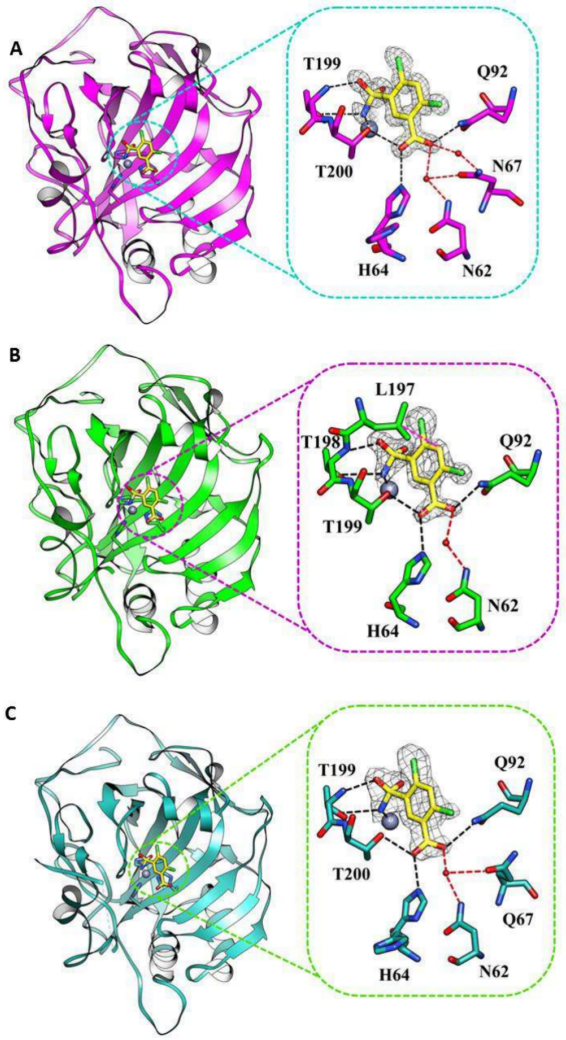

Figure 2. X-ray structures of **LAS** in complex with A) hCA II (pink, PDB: 8QH8), B) hCA XII-mimic (green, PDB: 8QHJ), and C) hCA IX-mimic H-tag (cyano, PDB: 8QHG). A zoomed-in view of the active site is also provided. Residues involved in the inhibitor–enzyme binding are shown in sticks and labeled. Hydrogen bonds and water bridges are depicted as black and red dotted lines, respectively. The gray sphere represents the zinc ion in the protein active site.

five of the six H-tag residues were visible in the electron density maps. In fact, the sixth H-tag and the first two *N*-terminal residues of hCA IX-mimic were not introduced in the model due to the absence of any justifiable density.

A metal ion was discovered bound to two H residues of an H-tag and to a third H residue from a symmetric molecule, leading to its identification as a nickel ion likely originating from the metal affinity column. The nickel coordination is completed by the carboxylate side chain of residue D132, thus completing the tetrahedral coordination geometry. The coordination with D132 is interesting, since it corresponds to one of the mutations (G132D) inserted in hCA II to obtain the hCA IX-mimic isoform. In Figure 3, the Ni(II) ion is

https://doi.org/10.1021/acsmedchemlett.4c00341
ACS Med. Chem. Lett. 2024, 15, 1749–1755

shown bound to the *N*-terminal H-tag and to D132 (symmetric counterparts are also shown).

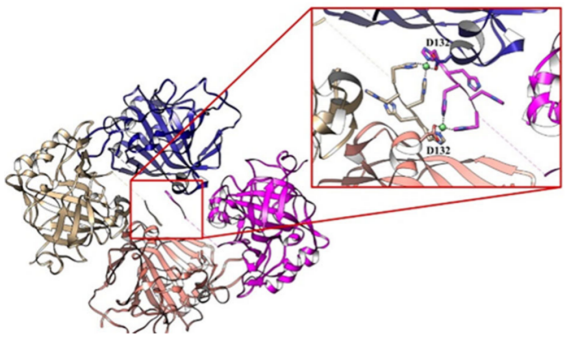

Figure 3. hCA IX-mimic H-tag arrangement in the cubic space group *I*432 crystal lattice. The figure also shows a focus on the *N*-terminal H-tag interacting with a Ni(II) ion. The green sphere represents the nickel ion, and the coordination bonds with the H-tag histidines and D132 are depicted as black lines. The dotted lines represent connections between the H-tag and the *N*-terminus of the enzyme.

Very similar metal coordination to the H-tag has been already observed in the structure of the thiocyanate complex of a β-CA from *Mycobacterium tuberculosis*.[29] In this case, a zinc ion was added in this position based on the B-factor value and the height of the peak in the electron density maps. Also, in our structure, considering the B-factor, the density peak, the coordination geometry, and the metal−ligand distances, we cannot exclude the presence of a second zinc coordinated to the H-tag as an alternative to the nickel ion. However, this structural feature is probably not to be considered of biological significance, as it has already been recognized in the case of the above-cited β-CA.

Interestingly, due to the availability of the X-ray structures of **LAS** (PDB ID: 8QH8) and **FUR** (PDB ID: 1Z9Y)[2,3] in complex with hCA II, we could compare their binding pose and gain an understanding of how the structural difference (chlorine atom in C4 position of **LAS** and the furanylmethylamino substituent in **FUR**) affect the interaction network generated in the enzyme−inhibitor complex and the enzymatic assays results (Figure 4).

The structures analyzed seem not to show significant differences for the interactions established by the sulfonamide moiety with both T199 (hydrogen bond) and the metal ion. Also, the carboxylic acid generates a hydrogen bond with the alcohol group of T200, a hydrogen bond with H64, and a water bridge with the N62 nitrogen atom. Interestingly, in **FUR** the presence of the furanyl ring allows the establishment of hydrophobic contacts, thus hampering additional water bridges. In fact, in **LAS**-hCA II complex, the carboxylic group forms a hydrogen bond and a water bridge with Q92 and N67, respectively. The same residues are instead involved in water bridges with the amino group in the C2 position of **FUR**.

CONCLUSIONS

LAS is a common intermediate in organic synthesis and a known production-related impurity in the formulation of **FUR**. The compound has relevant chemical peculiarities, such as the presence of two potentially competitive metal binding groups (i.e., a primary sulfonamide moiety and a carboxylate function) packed in a low-molecular-weight structure that can be exploited for the development of a vast series of derivatives by means of fragment-based drug discovery approaches. *In vitro* enzymatic assays, performed through the well-validated stopped-flow technique, highlighted a potent but unselective inhibitory activity of **LAS** on the whole panel of the analyzed CAs. **LAS** effectively inhibited the physiologically relevant isoenzymes I and II at subnanomolar concentrations, whereas other CAs (IV−VII, IX, XII−XIV) showed inhibition at higher values still contained within the nanomolar range. The **LAS** inhibitory profile was compared to its related and medium-high nanomolar CAI drug **FUR**, which differs for the furanylmethylamino moiety in place of a chlorine atom. Complexes of **LAS** with hCAs II, IX-mimic H-tag, and XII-mimic investigated by X-ray crystallography showed comparable interactions networks and a similar binding pose into the hCA II catalytic pocket to that of **FUR**. The absence of the furanyl ring in **LAS** determined the loss of hydrophobic contacts in favor of hydrogen bonds and water bridge mediated with the carboxylic function.

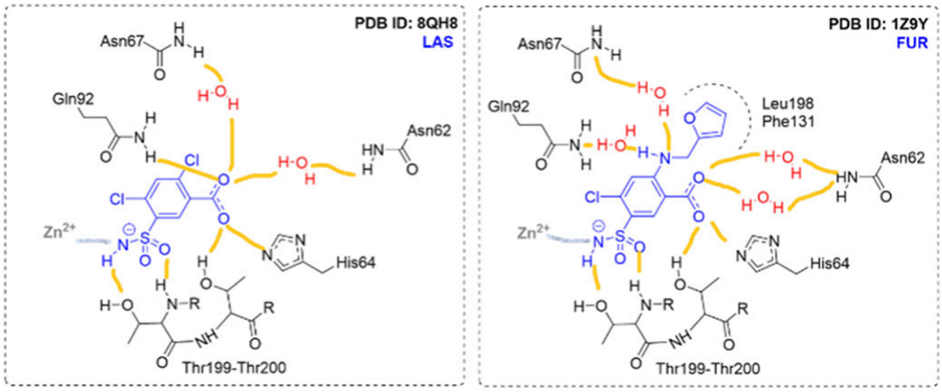

Figure 4. Bidimensional representation of the binding pose of **LAS** (PDB ID: 8QH8, left) and **FUR** (PDB ID: 1Z9Y, right) in cocrystal with hCA II. Compounds are in blue, amino acid residues involved in the interaction networks are in black and labeled, water molecules are in red, and the zinc ion is in gray. Polar interactions (hydrogen bond, water bridge, salt bridge) are represented with a solid yellow line.

https://doi.org/10.1021/acsmedchemlett.4c00341
ACS Med. Chem. Lett. 2024, 15, 1749−1755

In summary, the remarkably potent inhibitory profile and the availability of crystallographic data for **LAS** will be fundamental to addressing the isoform selectivity of the compound through chemical derivatization or the fragment-growing strategy combined with a rational tail approach.

EXPERIMENTAL SECTION

Chemistry. **LAS**, **FUR**, and **AAZ** were purchased from Merck s.r.l. (Italy) and used as they were received.

Production of hCA IX-mimic H-tag. Clones of the hCA IX-mimic H-tag protein, containing the hCA II sequence modified by 10 changes in the active site, were ordered from Genescript and subsequently subcloned into the pET43 vector by using the BamH I and Xho I restriction sites. Competent BL21 cells were transformed with plasmids containing the hCA IX-mimic gene. Subsequently, a fresh culture was grown at a 1 L scale in LB broth supplemented with ampicillin at a concentration of 100 μg/mL. The cells were incubated at 37 °C until they reached mid log phase (OD600 of 0.6−0.7), at which point protein expression was induced by the addition of 0.5 mM isopropyl β-D-1-thiogalactopyranoside (IPTG). After 30 min, 0.5 mM $ZnSO_4$ was added, and the cells were allowed to grow for an additional 4.5 h. Cells were harvested by centrifugation at 5,000 rpm for 20 min. The resulting pellet was resuspended in 20 mM Tris/HCl buffer (pH 8.3) and subjected to sonication, with 10 cycles of 10 s "on" and 120 s "off" at 50% amplitude (Bandelin Sonoplus). Following sonication, the lysate was centrifuged at 12,000*g* for 45 min. The supernatant was then incubated with nickel affinity gel resin (His Select HF, Sigma), which had been pre-equilibrated in the lysis buffer, for 30 min. After centrifugation at 1500*g*, the resin was washed with a buffer containing 50 mM Tris/HCl (pH 8.3), 500 mM NaCl, and 20 mM imidazole. The protein was eluted using the same buffer supplemented with 250 mM imidazole. The collected fractions were dialyzed against 20 mM Tris/HCl (pH 8.3). At this stage, the recombinant protein was 95% pure, resulting in a yield of about 3.2 mg/L of bacterial culture.

Carbonic Anhydrase Inhibition Assay. An Applied Photophysics stopped-flow instrument was used to evaluate the ability of the test compounds to inhibit the CA-catalyzed CO_2 hydration. Phenol red (at a concentration of 0.2 mM) was used as an indicator, working at the maximum absorbance of 557 nm, with 20 mM HEPES (pH 7.4) as a buffer, and 20 mM Na_2SO_4 (to maintain constant ionic strength), following the initial rates of the CA-catalyzed CO_2 hydration reaction for a period of 10−100 s. The CO_2 concentrations ranged from 1.7 to 17 mM for the assessment of the kinetic parameters and inhibition constants. Enzyme concentrations varied between 5 and 12 nM.[30,31] For each inhibitor, at least six traces of the initial 5−10% of the reaction were used to determine the initial velocity. The uncatalyzed rates were calculated in the same manner and subtracted from the total observed rates. Stock solutions of each inhibitor (0.1 mM) were prepared in distilled−deionized H_2O and dilutions up to 0.01 nM were done thereafter with the assay buffer. Inhibitor and enzyme solutions were preincubated together for 15 min at rt prior to the assay, to allow for the formation of the E−I complex. The inhibition constants were obtained by nonlinear least-squares methods using PRISM 3 and the Cheng−Prusoff equation as reported earlier[32] and represent the mean from at least three different determinations. hCAs I and II were purchased from Merck, while other isoenzymes were obtained *in-house*.[2,30]

Crystallography. *Crystallization and X-ray Data Collection.* Crystals of hCA XII-mimic (protein concentration 5 mg/mL in 20 mM Tris-HCl, pH 8.3) were grown via the sitting drop vapor diffusion method in 96-well plates (CrystalQuick, Greiner Bio-One, Germany). Drops were prepared using 1 μL of protein solution mixed with 1 μL of reservoir solution of 2.6 M ammonium sulfate, 100 mM Tris-HCl (pH 8.3), and were equilibrated against 100 μL of the same solution at 296 K. Crystal growth was observed after 1 week.

Crystals of hCA II were obtained using the hanging drop vapor diffusion method in a 24-well Linbro plate. One μL of 10 mg/mL solution of hCA II in Tris−HCl 50 mM (pH 8.0) was mixed with 1 μL of a solution of 1.5 M sodium citrate, 20 mM Tris-HCl (pH 8.0) and equilibrated against 500 μL of the same solution at 296 K. Crystal growth was observed after 5 days.

Crystals of hCA IX-mimic H-tag were obtained using the hanging drop vapor diffusion method in a 24-well Linbro plate. One μL of 5 mg/mL solution of hCA IX-mimic H-tag in Tris−HCl 20 mM (pH 8.3) was mixed with 1 μL of a solution of 1.5 M sodium citrate and 50 mM Tris-HCl (pH 7.5) and equilibrated against 500 μL of the same solution at 296 K. Crystal growth was observed after 2 weeks.

Although the crystallization conditions were highly similar to those already used for the crystallization of the hCA IX-mimic H-tag and for hCA II (see above). Crystals of hCA IX-mimic H-tag were obtained in a new crystal form belonging to the cubic space group *I*432 with unit cell dimension a = 157 Å, probably induced by the presence of the H-tag at the enzyme *N*-terminal.

The complexes of the three hCA isoforms with **LAS** were prepared by soaking the crystals in the mother liquor solution containing the inhibitor at a concentration of 5 mM for 1 h. To facilitate the dissolution of the inhibitor, 10% DMSO was added to the mother liquor solution. All crystals were flash-frozen at 100 K using a solution obtained by adding 20% (v/v) glycerol to the mother liquor solution as a cryoprotectant.

X-ray diffraction data of hCAs II and IX-mimic H-tag soaked with the inhibitor were collected using synchrotron radiation at the XRD2 beamline at Elettra Synchrotron (Trieste, Italy) with a wavelength of 0.9718 Å and a DECTRIS Pilatus 6 M detector, whereas data for hCA XII-mimic crystals were collected using synchrotron radiation at the ID30B beamline at ESRF (Grenoble, France) with a wavelength of 0.8731 Å and a DECTRIS Eiger2 X 9 M detector. Data were integrated and scaled using the program XDS.[33]

Structure Determination. The crystal structures of hCA IX-mimic (PDB: 4ZAO),[34] hCA XII-mimic (PDB: 4Q08),[35] and hCA II (PDB: 3HS4)[36] without solvent molecules and other heteroatoms were used to obtain initial phases of the structures using Refmac5[37] from the CCP4 package.[38] Coordinates of the inhibitor were obtained using the program JLigand[39] and introduced in the model. Five percent of the unique reflections were selected randomly and excluded from the refinement data set for Rfree calculations. The initial |Fo-Fc| difference electron density maps unambiguously showed the inhibitor molecule. The inhibitor was introduced into the model with 1.0 occupancy. Refinements proceeded using standard positional and isotropic atomic displacement parameters protocols, alternating with manual building of the models using COOT.[40] Anisotropic atomic displacement parameters were used to refine the structure of the hCA II/**LAS** complex. Atomic coordinates were deposited in the PDB (hCA II: 8QH8; hCA IX-mimic H-tag: 8QHG; hCA XII-mimic: 8QHJ). Graphical representations were generated by means of UCSF Chimera.[41]

ASSOCIATED CONTENT

Supporting Information

The Supporting Information is available free of charge at https://pubs.acs.org/doi/10.1021/acsmedchemlett.4c00341.

Statistics of the data collections and model refinements; IC_{50} curves for **LAS**; IC_{50} curves for **AAZ**; IC_{50} curves for **LAS**,**FUR**, and **AAZ** on hCA IX-mimic H-tag(PDF)

AUTHOR INFORMATION

Corresponding Authors

Marta Ferraroni − *Department of Chemistry "Ugo Schiff", University of Florence, 50019 Florence, Italy;* orcid.org/0000-0001-7258-738X; Email: marta.ferraroni@unifi.it

Fabrizio Carta − *NEUROFARBA Department, Sezione di Scienze Farmaceutiche e Nutraceutiche, University of Florence, 50019 Florence, Italy;* orcid.org/0000-0002-1141-6146; Email: fabrizio.carta@unifi.it

Authors

Chiara Baroni − *Department of Chemistry "Ugo Schiff", University of Florence, 50019 Florence, Italy*

Ilaria D'Agostino − *Department of Pharmacy, University of Pisa, 56126 Pisa, Italy; Department of Pharmacy, "G. d'Annunzio" University of Chieti-Pescara, 66100 Chieti, Italy; NEUROFARBA Department, Sezione di Scienze Farmaceutiche e Nutraceutiche, University of Florence, 50019 Florence, Italy*

Gioele Renzi − *NEUROFARBA Department, Sezione di Scienze Farmaceutiche e Nutraceutiche, University of Florence, 50019 Florence, Italy;* orcid.org/0009-0008-9109-030X

Jaydeo T. Kilbile − *University Department of Basic and Applied Sciences (Chemistry), MGM University, Aurangabad 431003 Maharashtra, India*

Yasinalli Tamboli − *King Abdullah International Medical Research Center (KAIMRC), King Saud Bin Abdulaziz University for Health Sciences, Ministry of National Guard-Health Affairs, Riyadh 14811, Saudi Arabia;* orcid.org/0000-0002-5161-0170

Simone Carradori − *Department of Pharmacy, "G. d'Annunzio" University of Chieti-Pescara, 66100 Chieti, Italy;* orcid.org/0000-0002-8698-9440

Clemente Capasso − *Department of Biology, Agriculture and Food Sciences, National Research Council (CNR), Institute of Biosciences and Bioresources, 80131 Naples, Italy*

Claudiu T. Supuran − *NEUROFARBA Department, Sezione di Scienze Farmaceutiche e Nutraceutiche, University of Florence, 50019 Florence, Italy;* orcid.org/0000-0003-4262-0323

Complete contact information is available at: https://pubs.acs.org/10.1021/acsmedchemlett.4c00341

Author Contributions

[&]These authors contributed equally. The manuscript was written through contributions of all authors. All authors have given approval to the final version of the manuscript.

Notes

The authors declare no competing financial interest.

■ ACKNOWLEDGMENTS

We acknowledge Elettra and XRD2 for providing beamtime and support under proposal 20220596. We also acknowledge the European Synchrotron Radiation Facility (ESRF) and the ID30B beamline for the provision of synchrotron radiation facilities.

■ ABBREVIATIONS

LAS, Lasamide; CAse, Carbonic Anhydrase; **FUR**, Furosemide; **AAZ**, Acetazolamide

■ REFERENCES

(1) IARC Working Group on the Evaluation of Carcinogenic Risks to Humans. *Pharmaceutical Drugs*; International Agency for Research on Cancer: Lyon (FR), 1990.

(2) Temperini, C.; Cecchi, A.; Scozzafava, A.; Supuran, C. T. Carbonic anhydrase inhibitors. Sulfonamide diuretics revisited–old leads for new applications? *Org. Biomol. Chem.* **2008**, *6* (14), 2499−2506.

(3) Temperini, C.; Cecchi, A.; Scozzafava, A.; Supuran, C. T. Carbonic anhydrase inhibitors. Comparison of chlorthalidone, indapamide, trichloromethiazide, and furosemide X-ray crystal structures in adducts with isozyme II, when several water molecules make the difference. *Bioorg. Med. Chem.* **2009**, *17* (3), 1214−1221.

(4) Liu, F.; Martin-Mingot, A.; Lecornué, F.; Jouannetaud, M. P.; Maresca, A.; Thibaudeau, S.; Supuran, C. T. Carbonic anhydrases inhibitory effects of new benzenesulfonamides synthesized by using superacid chemistry. *J. Enzyme Inhib. Med. Chem.* **2012**, *27* (6), 886−891.

(5) Farzam, K.; Abdullah, M. Acetazolamide. *StatPearls*. StatPearls Publishing: Treasure Island (FL), 2024.

(6) Humans IWG on the E of CR to Furosemide (Frusemide). In *Pharmaceutical Drugs*; International Agency for Research on Cancer, 1990.

(7) Zhu, W.; Liu, Y. Preparation method of furosemide. CN105906589A, 2016.

(8) Wang, Z.; Yang, Y.; Liu, J.; Shen, S.; Zhang, X. Preparation method of furosemide. CN106117168A, 2016.

(9) Miller, J. H.; Robert, J. L.; Sørensen, A. M. Reversed-phase ion-pair liquid chromatographic method for determining the impurities of furosemide. *J. Pharm. Biomed. Anal.* **1993**, *11* (3), 257−261.

(10) Xu, A.; Xue, Y.; Zeng, Y.; Li, J.; Zhou, H.; Wang, Z.; Chen, Y.; Chen, H.; Jin, J.; Zhuang, T. Isolation and characterization of an unknown process-related impurity in furosemide and validation of a new HPLC method. *Mol. Basel Switz.* **2023**, *28* (5), 2415.

(11) Klusácková, P.; Lebedová, J.; Pelclová, D.; Salandová, J.; Senholdová, Z.; Navrátil, T. Occupational asthma and rhinitis in workers from a lasamide production line. *Scand. J. Work Environ. Health* **2007**, *33* (1), 74−78.

(12) Modena, B. D.; Bleecker, E. R.; Busse, W. W.; Erzurum, S. C.; Gaston, B. M.; Jarjour, N. N.; Meyers, D. A.; Milosevic, J.; Tedrow, J. R.; Wu, W.; Kaminski, N.; Wenzel, S. E. Gene expression correlated with severe asthma characteristics reveals heterogeneous mechanisms of severe disease. *Am. J. Respir. Crit. Care Med.* **2017**, *195* (11), 1449−1463.

(13) Chen, J.; Smith, L.; Gaston, B. Characterization of the function of carbonic anhydrase 8. *Proc. IMPRS* **2024**, *6* (1), 1.

(14) Tarun, A. S.; Bryant, B.; Zhai, W.; Solomon, C.; Shusterman, D. Gene expression for carbonic anhydrase isoenzymes in human nasal mucosa. *Chem. Senses* **2003**, *28* (7), 621−629.

(15) Li, Q. Application of fragment-based drug discovery to versatile targets. *Front. Mol. Biosci.* **2020**, *7*, 180.

(16) Lebedev, A. A.; Mironova, L. I.; Pleshakov, M. G.; Matveeva, A. K.; Timokhina, I. A. Synthesis and pharmacological activity of derivatives of 2,4-dichloro-5-sulfamoylbenzoic acid. *Pharm. Chem. J.* **1985**, *19* (10), 697−700.

(17) Sławiński, J.; Brzozowski, Z.; Żołnowska, B.; Szafrański, K.; Pogorzelska, A.; Vullo, D.; Supuran, C. T. Synthesis of a new series of N4-substituted 4-(2-aminoethyl)benzenesulfonamides and their inhibitory effect on human carbonic anhydrase cytosolic isozymes I and II and transmembrane tumor-associated isozymes IX and XII. *Eur. J. Med. Chem.* **2014**, *84*, 59−67.

(18) Ferraroni, M.; Angeli, A.; Pinteala, M.; Supuran, C. T. Sulfonamide diuretic azosemide as an efficient carbonic anhydrase inhibitor. *J. Mol. Struct.* **2022**, *1268*, No. 133672.

(19) Navon, G.; Shani, J.; Panigel, R.; Schoenberg, S. Application of the carbonic anhydrase inhibitory effect of furosemide to the study of furosemide release from two of its diuretic derivatives. *J. Med. Chem.* **1975**, *18* (11), 1152−1154.

(20) Grüneberg, S.; Wendt, B.; Klebe, G. Subnanomolar Inhibitors from Computer Screening: A Model Study Using Human Carbonic Anhydrase II. *Angew. Chem., Int. Ed.* **2001**, *40* (2), 389−393.

(21) Yenikaya, C.; Sari, M.; Bülbül, M.; Ilkimen, H.; Celik, H.; Büyükgüngör, O. Synthesis, characterization and antiglaucoma activity of a novel proton transfer compound and a mixed-ligand Zn(II) complex. *Bioorg. Med. Chem.* **2010**, *18*, 930−938.

(22) Yenikaya, C.; Sari, M.; Bülbül, M.; Ilkimen, H.; Cinar, B.; Büyükgüngör, O. Synthesis and characterisation of two novel proton transfer compounds and their inhibition studies on carbonic anhydrase isoenzymes. *J. Enzyme Inhib. Med. Chem.* **2011**, *26* (1), 104−114.

(23) Zaksauskas, A.; Čapkauskaitė, E.; Jezepčikas, L.; Linkuvienė, V.; Kišonaitė, M.; Smirnov, A.; Manakova, E.; Gražulis, S.; Matulis, D. Design of two-tail compounds with rotationally fixed benzenesulfonamide ring as inhibitors of carbonic anhydrases. *Eur. J. Med. Chem.* **2018**, *156*, 61−78.
(24) Khalifah, R. G. The carbon dioxide hydration activity of carbonic anhydrase. I. Stop-flow kinetic studies on the native human isoenzymes B and C. *J. Biol. Chem.* **1971**, *246* (8), 2561−2573.
(25) Supuran, C. T. Carbonic anhydrases: novel therapeutic applications for inhibitors and activators. *Nat. Rev. Drug. Discovery* **2008**, *7* (2), 168−181.
(26) Yrjänäinen, A.; Patrikainen, M. S.; Azizi, L.; Tolvanen, M. E. E.; Laitaoja, M.; Jänis, J.; Hytönen, V. P.; Nocentini, A.; Supuran, C. T.; Parkkila, S. Biochemical and biophysical characterization of carbonic anhydrase VI from human milk and saliva. *Protein J.* **2022**, *41* (4-5), 489−503.
(27) Alterio, V.; Di Fiore, A.; D'Ambrosio, K.; Supuran, C. T.; De Simone, G. Multiple binding modes of inhibitors to carbonic anhydrases: how to design specific drugs targeting 15 different isoforms? *Chem. Rev.* **2012**, *112* (8), 4421−4468.
(28) Angeli, A.; Ferraroni, M.; Granchi, C.; Minutolo, F.; Chen, X.; Shriwas, P.; Russo, E.; Leo, A.; Selleri, S.; Carta, F.; Supuran, C. T. First-in-glass dual targeting compounds for the management of seizures in glucose transporter type 1 deficiency syndrome. *J. Med. Chem.* **2023**, *66* (14), 10010−10026.
(29) Covarrubias, A. S.; Bergfors, T.; Jones, T. A.; Högbom, M. Structural mechanics of the pH-dependent activity of beta-carbonic anhydrase from Mycobacterium tuberculosis. *J. Biol. Chem.* **2006**, *281* (8), 4993−4999.
(30) D'Agostino, I.; Mathew, G. E.; Angelini, P.; Venanzoni, R.; Angeles Flores, G.; Angeli, A.; Carradori, S.; Marinacci, B.; Menghini, L.; Abdelgawad, M. A.; Ghoneim, M. M.; Mathew, B.; Supuran, C. T. Biological investigation of N-methyl thiosemicarbazones as antimicrobial agents and bacterial carbonic anhydrases inhibitors. *J. Enzyme Inhib. Med. Chem.* **2022**, *37* (1), 986−993.
(31) D'Agostino, I.; Zara, S.; Carradori, S.; De Luca, V.; Capasso, C.; Kocken, C. H. M.; Zeeman, A.-M.; Angeli, A.; Carta, F.; Supuran, C. T. Antimalarial agents targeting Plasmodium Falciparum carbonic anhydrase: towards dual acting artesunate hybrid compounds. *Chem. Med. Chem.* **2023**, *18* (21), No. e202300267.
(32) Yung-Chi, C.; Prusoff, W. H. Relationship between the inhibition constant (K1) and the concentration of inhibitor which causes 50% inhibition (I50) of an enzymatic reaction. *Biochem. Pharmacol.* **1973**, *22* (23), 3099−3108.
(33) Kabsch, W. Integration, scaling, space-group assignment and post-refinement. *Acta Crystallogr. D Biol. Crystallogr.* **2010**, *66* (2), 133−144.
(34) Pinard, M. A.; Aggarwal, M.; Mahon, B. P.; Tu, C.; McKenna, R. A sucrose-binding site provides a lead towards an isoform-specific inhibitor of the cancer-associated enzyme carbonic anhydrase IX. *Acta Crystallogr. Sect. F Struct. Biol. Commun.* **2015**, *71* (10), 1352−1358.
(35) Kazokaitė, J.; Aspatwar, A.; Parkkila, S.; Matulis, D. An update on anticancer drug development and delivery targeting carbonic anhydrase IX. *Peer J.* **2017**, *5*, No. e4068.
(36) Sippel, K. H.; Robbins, A. H.; Domsic, J.; Genis, C.; Agbandje-McKenna, M.; McKenna, R. High-resolution structure of human carbonic anhydrase II complexed with acetazolamide reveals insights into inhibitor drug design. *Acta Crystallograph. Sect. F Struct. Biol. Cryst. Commun.* **2009**, *65* (10), 992−995.
(37) Murshudov, G. N.; Vagin, A. A.; Dodson, E. J. Refinement of macromolecular structures by the maximum-likelihood method. *Acta Crystallogr. D Biol. Crystallogr.* **1997**, *53* (3), 240−255.
(38) Winn, M. D.; Ballard, C. C.; Cowtan, K. D.; Dodson, E. J.; Emsley, P.; Evans, P. R.; Keegan, R. M.; Krissinel, E. B.; Leslie, A. G. W.; McCoy, A.; McNicholas, S. J.; Murshudov, G. N.; Pannu, N. S.; Potterton, E. A.; Powell, H. R.; Read, R. J.; Vagin, A.; Wilson, K. S. Overview of the CCP4 suite and current developments. *Acta Crystallogr. D Biol. Crystallogr.* **2011**, *67* (4), 235−242.
(39) Lebedev, A. A.; Young, P.; Isupov, M. N.; Moroz, O. V.; Vagin, A. A.; Murshudov, G. N. JLigand: a graphical tool for the CCP4 template-restraint library. *Acta Crystallogr. D Biol. Crystallogr.* **2012**, *68* (4), 431−440.
(40) Emsley, P.; Lohkamp, B.; Scott, W. G.; Cowtan, K. Features and development of Coot. *Acta Crystallogr. D Biol. Crystallogr.* **2010**, *66* (4), 486−501.
(41) Pettersen, E. F.; Goddard, T. D.; Huang, C. C.; Couch, G. S.; Greenblatt, D. M.; Meng, E. C.; Ferrin, T. E. UCSF Chimera–a visualization system for exploratory research and analysis. *J. Comput. Chem.* **2004**, *25* (13), 1605−1612.

https://doi.org/10.1021/acsmedchemlett.4c00341
ACS Med. Chem. Lett. 2024, 15, 1749−1755

SUPPORTING INFORMATION

Lasamide, a Potent Human Carbonic Anhydrase Inhibitor from the Market: Inhibition Profiling and Crystallographic Studies

Chiara Baroni[a†], Ilaria D'Agostino[b,c,d†], Gioele Renzi[d], Jaydeo T. Kilbile[e], Yasinalli Tamboli[f], Marta Ferraroni*[a], Simone Carradori[c], Clemente Capasso[g], Fabrizio Carta*[d] and Claudiu T. Supuran[d]

[a.] Department of Chemistry "Ugo Schiff", University of Florence, 50019, Sesto Fiorentino, Florence, Italy
[b.] Department of Pharmacy, University of Pisa, 56126, Pisa, Italy
[c.] Department of Pharmacy, "G. d'Annunzio" University of Chieti-Pescara, Chieti, Italy
[d.] NEUROFARBA Department, Sezione di Scienze Farmaceutiche e Nutraceutiche, University of Florence, 50019, Sesto Fiorentino, Florence, Italy
[e.] University Department of Basic and Applied Sciences (Chemistry), MGM University, Aurangabad-431003, Maharashtra, India
[f] King Abdullah International Medical Research Center (KAIMRC), King Saud Bin Abdulaziz University for Health Sciences, Ministry of National Guard-Health Affairs, Riyadh 14811, Saudi Arabia
[g.] Department of Biology, Agriculture and Food Sciences, National Research Council (CNR), Institute of Biosciences and Bioresources, 80131 Naples, Italy

Corresponding Authors: Prof. Marta Ferraroni (MF): e-mail: marta.ferraroni@unifi.it; Prof.Fabrizio Carta (FC): e-mail: fabrizio.carta@unifi.it

Table of Contents

Table S1. Statistics of the data collections and model refinements. S2

IC_{50} curves for **LAS** on hCAs I, II, IV, VA, VB, VI saliva, VI milk, VII, IX, XII, and XIV and mCA XIII S3

IC_{50} curves for **AAZ** on hCAs I, II, IV, VA, VB, VI saliva, VI milk, VII, IX, XII, and XIV and mCA XIII..... S4

IC_{50} curves for **LAS**, **FUR**, and **AAZ** on hCA IX-mimic H-tag S5

Table S1. Statistics of the data collections and model refinements.
Values in parentheses are for the highest resolution shell.

	hCA II/LAS	**hCA IX-mimic H tag /LAS**	**hCA XII-mimic/LAS**
PDB ID	8QH8	8QHG	8QHJ
Wavelength (Å)	0.9718	0.9718	0.8731
Space Group	P 21	I 432	P 21
Unit cell (a, b, c, α, β, γ) (Å,˚)	42.28, 41.30, 72.22, 90, 104.36, 90	157.33, 157.33, 157.33, 90, 90, 90	42.16, 41.57, 71.97, 90, 104.01, 90
Limiting resolution (Å)	1.04-69.96 (1.04-1.06)	1.91-78.67 (1.91-1.94)	1.62-39.74 (1.62-1.65)
Unique reflections	115908 (5826)	26027 (1279)	30766 (1497)
Rsym (%)	5.7 (73.5)	12.7 (264.4)	9.9 (89.4)
Rmeas (%)	6.2 (83.1)	12.8 (266.7)	12.2 (109.2)
Redundancy	5.9 (4.6)	58.3 (56.6)	2.8 (2.9)
Completeness overall (%)	99.8 (100)	100 (100)	99.2 (98)
<I/σ(I)>	14.6 (2.2)	44.4 (2.3)	8.1 (1.3)
CC (1/2) (%)	99.9 (67)	100 (78.8)	100 (95)
Refinement statistics			
Resolution range (Å)	69.96-1.04	78.67-1.91	39.74-1.62
Rfactor (%)	11.85	19.24	18.31
Rfree (%)	13.66	21.98	21.76
r.m.s.d. bonds (Å)	0.0122	0.0079	0.0085
r.m.s.d. angles (°)	1.7837	1.5584	1.5661
Ramachandran statistics (%)			
Most favored	96.9	97.3	96.9
additionally allowed	3.1	2.7	3.1
Outlier regions	0	0	0
Average B factor (Å^2)			
All atoms	14.886	36.259	19.636
inhibitor	10.80	34.5	18.1
solvent	28.677	35.747	27.617

IC_{50} curves for LAS on hCAs I, II, IV, VA, VB, VI saliva, VI milk, VII, IX, XII, and XIV and mCA XIII

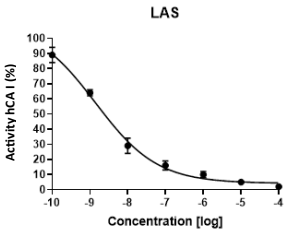

IC_{50} = 2.78 nM; K^2 = 0.9829

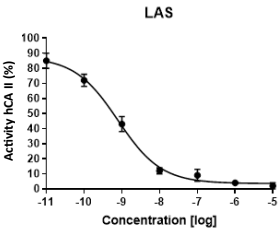

IC_{50} = 0.91 nM; K^2 = 0.9943

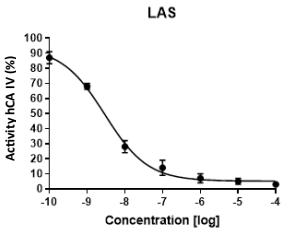

IC_{50} = 3.42 nM; K^2 = 0.9938

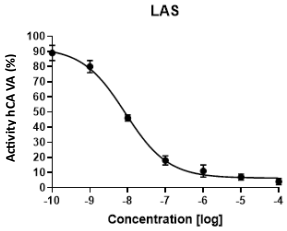

IC_{50} = 9.24 nM; K^2 = 0.9954

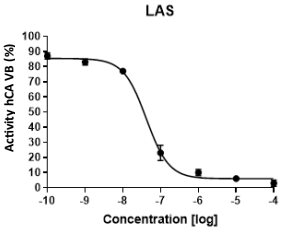

IC_{50} = 39.32 nM; K^2 = 0.9913

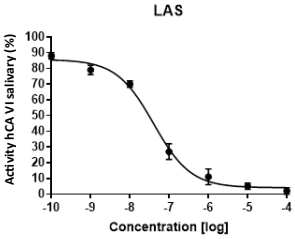

IC_{50} = 40.78 nM; K^2 = 0.9946

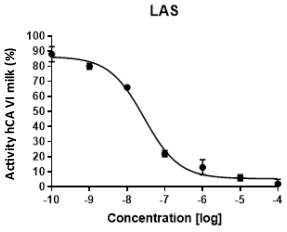

IC_{50} = 28.19 nM; K^2 = 0.9929

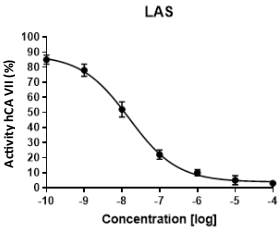

IC_{50} = 16.27 nM; K^2 = 0.9929

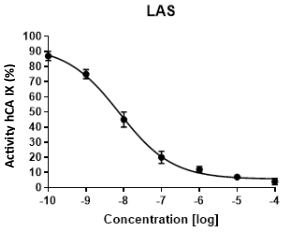

IC_{50} = 9.35 nM; K^2 = 0.9899

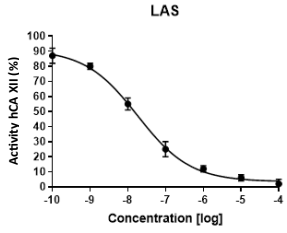

IC_{50} = 19.02 nM; K^2 = 0.9887

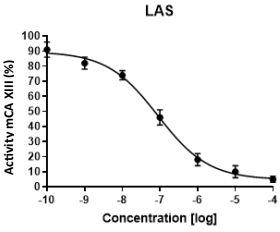

IC_{50} = 92.78 nM; K^2 = 0.9902

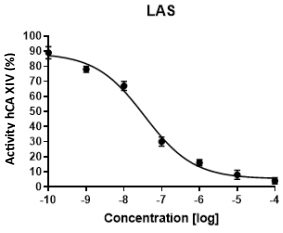

IC_{50} = 37.94 nM; K^2 = 0.9882

IC_{50} curves for AAZ on hCAs I, II, IV, VA, VB, VI saliva, VI milk, VII, IX, XII, and XIV and mCA XIII

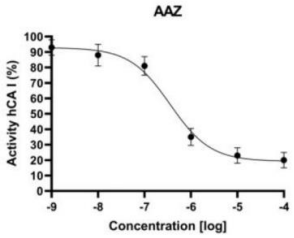

IC_{50} = 357.6 nM; K^2 = 0.9930

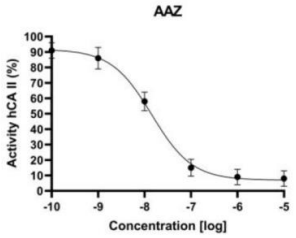

IC_{50} = 14.29 nM; K^2 = 0.9987

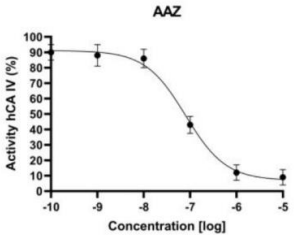

IC_{50} = 79.76 nM; K^2 = 0.9961

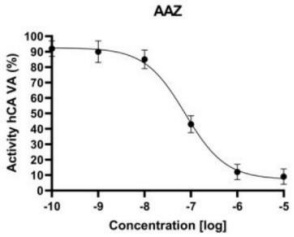

IC_{50} = 74.88 nM; K^2 = 0.9985

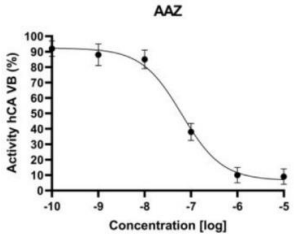

IC_{50} = 63.12 nM; K^2 = 0.9951

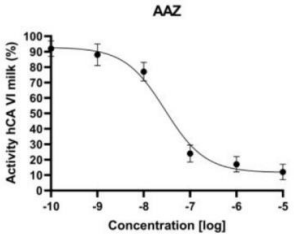

IC_{50} = 28.75 nM; K^2 = 0.9896

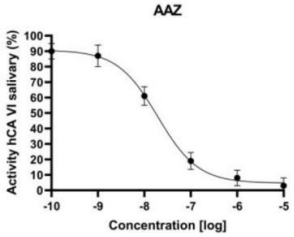

IC_{50} = 19.39 nM; K^2 = 0.9991

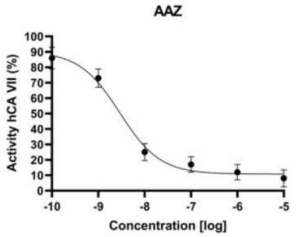

IC_{50} = 2.91 nM; K^2 = 0.9912

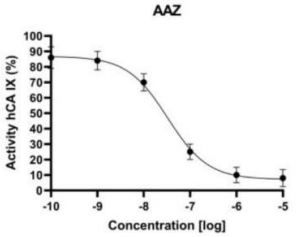

IC_{50} = 32.7 nM; K^2 = 0.9989

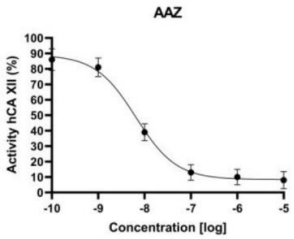

IC_{50} = 6.48 nM; K^2 = 0.9977

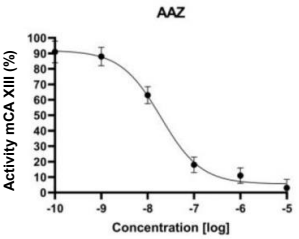

IC_{50} = 19.29 nM; K^2 = 0.9968

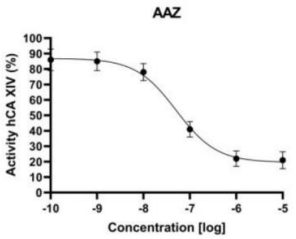

IC_{50} = 50.61 nM; K^2 = 0.9981

IC_{50} curves for LAS, FUR, and AAZ on hCA IX-mimic H-tag

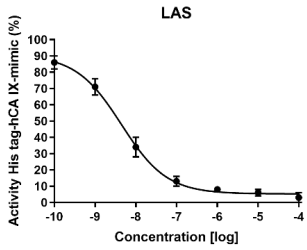

IC_{50} = 5.14 nM; K^2 = 0.9960

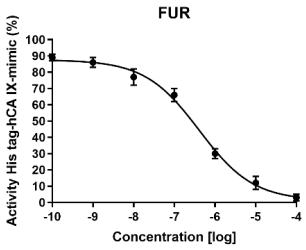

IC_{50} = 383 nM; K^2 = 0.9893

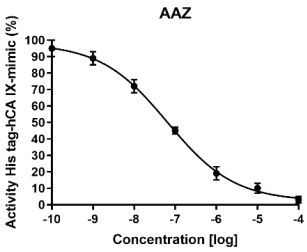

IC_{50} = 73.2 nM; K^2 = 0.9825

RSC
Medicinal Chemistry

ROYAL SOCIETY OF CHEMISTRY

RESEARCH ARTICLE

View Article Online
View Journal | View Issue

Check for updates

Cite this: *RSC Med. Chem.*, 2025, **16**, 1633

X-ray crystallographic and kinetic studies of biguanide containing aryl sulfonamides as carbonic anhydrase inhibitors†

Chiara Baroni, [a] Murat Bozdag, [b] Gioele Renzi,[b] Viviana De Luca,[c] Clemente Capasso,[c] Carla Bazzicalupi, [a] Silvia Selleri, [b] Marta Ferraroni, *[a] Fabrizio Carta *[b] and Claudiu T. Supuran [b]

Received 20th December 2024,
Accepted 23rd January 2025

DOI: 10.1039/d4md01018c

rsc.li/medchem

Here, we report a small series of dual-targeting compounds that combine the prototypical carbonic anhydrase (CA) zinc-binding sulfonamide moiety with the biguanide group of metformin, an emerging anticancer drug. The compounds reported similar *in vitro* inhibition profiles on a panel of physiologically relevant human (h)CAs, with marked selectivity for the cancer related IX and XII isoforms. The binding modes of representative inhibitors **5b** and **5c** within the active site of the hCA isoforms II and XII-mimic were assessed by X-ray crystallography, thus allowing us to clarify molecular features that may be useful for the design of more specific and potent inhibitors. For instance, we identified a mutation in the hCA XII-mimic which was found responsible for the selectivity of the ligands toward the tumor associated isoform. Interestingly, in the hCA II/**5c** complex, a second inhibitor molecule was bound to the catalytic cleft, probably affecting the inhibition properties of the canonical zinc-bound inhibitor.

Open Access Article. Published on 24 January 2025. Downloaded on 10/20/2025 1:21:01 PM.
This article is licensed under a Creative Commons Attribution 3.0 Unported Licence.

Introduction

Carbonic anhydrases (CAs) are a family of zinc metalloenzymes that catalyze the reversible hydration of carbon dioxide to bicarbonate ions and protons.[1] Twelve catalytically active CA isoforms are expressed in humans, showing different localization patterns.[2] Among the human (h)CAs, the membrane-bound isoforms IX and XII are recognized as significant solid tumor markers being overexpressed in various cancer cell lines mainly induced by hypoxia regulating factors (*i.e.* HIFs), and in the case of XII also by additional effectors.[3,4] The crucial role of CA IX/XII in cancer cells is maintaining the intracellular pH at ~6.5 to grant cells survival after the Warburg effect is established.[5,6] Since such isoforms are constitutively expressed only in gut tissues, they assume considerable importance as anticancer targets.[7]

The onset and progression of tumor growth involve numerous aberrant proteins and signaling pathways, highlighting the complexity of developing effective therapies. In contrast to single-targeting drugs traditionally used in association with each other, the development of chemical entities endowed with multi-pharmacological features provides clear advantages, such as improved patient compliance and more predictable pharmacokinetics.[8]

Hence, in the last decade, multitarget-based approaches have also been exploited based on high-affinity CA IX and XII inhibitors of the sulfonamide, coumarin, and sulfocoumarin types.[9–13] Original approaches included the epidermal growth factor receptor (EGFR),[14] telomerase enzyme,[15] and the P-glycoprotein transporter as additional targets.[16]

Metformin is a widely used antidiabetic drug.[17] In addition to its role in glycemic control in type 2 diabetes, it has been recently identified with cardiovascular protection, anti-inflammatory and anticancer properties.[18] The anticancer effects of metformin are attributed to both direct and indirect actions. Indirectly, metformin reduces gluconeogenesis, decreases hyperinsulinemia, and mediates the adenosine monophosphate protein kinase (AMPK) activation. All these pathways are believed to contribute to reducing cancer cell growth and progression.[19–21] In addition, metformin directly suppresses mitochondrial activity and reduces the availability of adenosine triphosphate (ATP) and, more in general, those biosynthetic precursors required for cell growth.[22–24] Valuable studies indicated that metformin acted as an inhibitor of the mammalian target of rapamycin (mTOR) signaling[25–28] and modulates the PD-L1/PD-1 axis *via* AMPK-dependent and independent mechanisms.[18,29,30]

[a] *Department of Chemistry "Ugo Schiff", University of Florence, Via della Lastruccia 3, 50019 Sesto Fiorentino, FI, Italy. E-mail: marta.ferraroni@unifi.it*
[b] *NEUROFARBA Department, University of Florence, Via Ugo Schiff 6, 50019 Sesto Fiorentino, FI, Italy. E-mail: fabrizio.carta@unifi.it*
[c] *Department of Biology, Institute of Bioscience and Bioresources (IBBR)-CNR, Via P. Castellino 111, 80131 Napoli, NA, Italy*

† Electronic supplementary information (ESI) available. See DOI: https://doi.org/10.1039/d4md01018c

Open Access Article. Published on 24 January 2025. Downloaded on 10/20/2025 1:21:01 PM.
This article is licensed under a Creative Commons Attribution 3.0 Unported Licence.

Here, we report a small series of compounds designed to merge within a single chemical scaffold, the prototypic CA inhibitor (CAI) moiety (*i.e.* the primary sulfonamide), and the biguanide group of metformin. The compounds obtained were investigated *in vitro* for their ability to inhibit the most relevant hCAs and their binding mode in the complex with hCAs II and XII-mimic was assessed using X-ray crystallographic studies.

Results and discussion

Synthesis of inhibitors of the carbonic anhydrases

The final compounds **5a–c** were synthesized by adding commercially available amines, bearing the primary sulfonamide moiety, to cyanoguanidine in *n*-butanol using a stoichiometric amount of hydrochloric acid solution in water (Scheme 1).[19]

Synthesized compounds were designed to carry a positive charge, ensuring their impermeability to membranes. The inclusion of a bis-guanidine moiety induces highly polar features in these compounds, allowing potential double protonation at a physiological pH (at the two guanidine moieties). The obtained compounds were purified through crystallization from isopropyl alcohol (IPA) and were fully characterized using ^{1}H-NMR, ^{13}C-NMR, and mass spectrometry (ESI-MS).

Enzyme inhibition studies

Compounds **5a–c** were evaluated *in vitro* for their ability to inhibit the physiologically relevant CA isoforms I, II, VA, IX, and XII through the stopped-flow technique.[31] Kinetic effectiveness was expressed as the means of the K_I values in Table 1 and it was compared to the standard CAI acetazolamide (AAZ).

The above reported compounds showed low inhibitory activity towards the cytosolic isoforms hCA I and II and mitochondrial VA with K_I values spanning between high and low-micromolar values (K_I values of 134.6 and 4435 nM). Overall, the structure–activity relationship (SAR) determined for these compounds indicates a progressive reduction of the inhibition potencies with the increase in the alkyl spacer length connecting the biguanide with the aryl sulfonamide groups (Table 1).

As for the tumor associated CAs IX and XII, all compounds showed high inhibition potencies. For instance, the hCA IX associated K_I values ranging between 1.43 and 20.2 nM was lower than that of the reference AAZ (*i.e.* K_I = 25.6 nM).

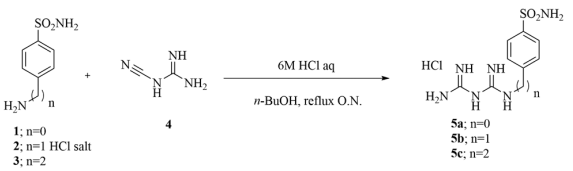

Scheme 1 Synthetic procedure for compounds **5a–c**.

Table 1 Inhibition of cytosolic hCAs I and II, mitochondrial VA, membrane-associated IX, and XII by a CO_2 hydrase stopped-flow assay using acetazolamide (AAZ) as a reference drug[31]

Compound	K_I[a] (nM)				
	hCA I	hCA II	hCA VA	hCA IX	hCA XII
5a	361.0	134.6	119.9	1.43	0.5
5b	375.1	369.5	678.8	2.44	2.6
5c	4435	501.0	995.9	20.2	1.7
AAZ	250.0	12.1	63.0	25.6	5.7

[a] Mean from 3 different assays, by the stopped-flow technique (errors were in the range of ±5–10% of the reported values).

Elongation of the tether in **5a** to afford **5b** reduced the inhibition potency up to 1.7-fold (K_I values of 1.43 and 2.44 nM for **5a** and **5b**, respectively). Further elongation, as in **5c**, significantly enhanced the K_I value up to 8.3-fold and thus was comparable to the reference AAZ (*i.e.* K_I of 20.2 nM).

All compounds showed remarkable selectivity for hCA XII as they exhibited K_I values between 0.5 and 2.6 nM, and thus up to 11.4-fold lower than that of AAZ (*i.e.* K_I = 5.7 nM). In this case, the progressive elongation of the alkyl tether did not induce a dependent reduction of the ligand affinity as demonstrated for the derivative **5c**, which was 1.5-fold more effective than its shorter derivative **5b** (*i.e.* K_I values of 2.6 and 1.7 nM for **5b** and **5c** respectively).

Overall, the *in vitro* data in Table 1 referring to **5a**, **5b** and **5c** showed marked potency and high selectivity for the tumor associated hCAs IX and XII over the cytosolic and mitochondrial isoforms. Such a kinetic fingerprint makes these compounds the ideal candidates for the development of CAI-based multitargeting new generation anticancer drugs.

Crystallographic studies

We determined the X-ray crystallographic structures of hCA II and hCA XII-mimic in the complex with inhibitor **5b** (Fig. 1). CA XII-mimic is an engineered CA II with a modified sequence constructed to mimic the CAXII active site.[32,33] The structures were solved using the data collected on flash-frozen crystals with PEG 400 as a cryoprotectant (see the Experimental part and discussion below).

Analysis of the electron density maps revealed a clear density for the benzenesulfonamide group of the inhibitor, confirming its binding to the enzymes.

The inhibitor presents the classical binding mode of the sulfonamide moiety in the active site of the two isoforms by directly interacting with the zinc ion and forming hydrogen bonds with Thr199/198 (numbering of hCA II and hCA XII, respectively) (Fig. 2). On the other hand, different hydrogen bonds and water bridge interactions are established within the active site of the two enzymes, resulting in two different orientations of the inhibitor tail. In fact, in the hCA II–**5b** complex, the nitrogen atoms of the biguanide group form water bridges with Asn67. In contrast, in the hCAXII–**5b** complex, the inhibitor interacts with the amino acid residues

 This journal is © The Royal Society of Chemistry 2025

Open Access Article. Published on 24 January 2025. Downloaded on 10/20/2025 1:21:01 PM.
This article is licensed under a Creative Commons Attribution 3.0 Unported Licence.

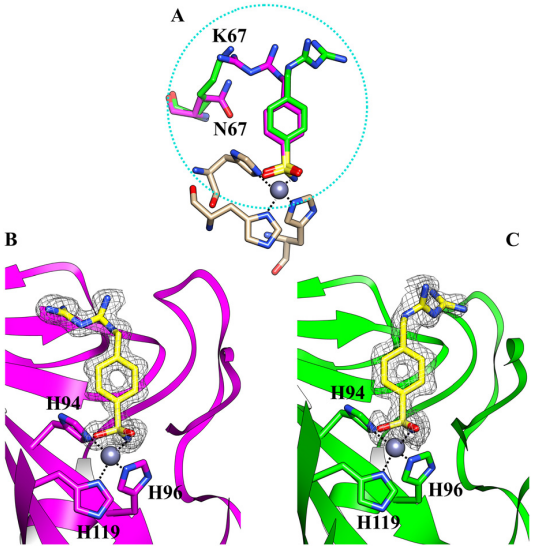

Fig. 1 (A) Comparison of the two different orientations of the inhibitor **5b** within the active site of hCA II (magenta) and hCAXII-mimic (green), respectively; (B) the active site of hCA II complexed with inhibitor **5b** (PDB: 8ROU); (C) the active site of hCAXII-mimic complexed with inhibitor **5b** (PDB: 8RNS). The 2Fo–Fc density map for the inhibitor is also shown.

in the opposite region of the protein cavity. Indeed, the nitrogen atoms of the biguanide group establish water bridges with Thr199 and His64. The phenyl ring of the inhibitor also has hydrophobic interactions with Val121 and Leu197/198.

By analyzing the mutations in the active site of hCAXII-mimic with respect to the hCA II isoform, we realized that the Asn67Lys variation in the hCA XII-mimic amino acid sequence is the only one that could influence the binding mode of the inhibitor. Lysine is more flexible and bulkier than asparagine, which may induce a different organization of the inhibitor within the enzyme cavity due to steric hindrance (Fig. 1A). The inhibitor tail in hCA II forms a water bridge with Asn67, whereas in hCA XII-mimic it is oriented in the opposite direction of Lys67.

Furthermore, no cryoprotectant molecules were detected within the active site of the isoforms, in contrast to what was observed in previous crystallographic analysis performed using glycerol as a cryoprotectant (Fig. 3).

Glycerol is the most widely used cryoprotecting agent in X-ray protein crystallography.[34] Hence, it is routinely used to prevent ice formation in freezing CA crystals of different isoforms and their complexes with inhibitors. Often, glycerol penetrates the protein active site, establishing hydrogen bonds with surrounding amino acid residues, which may alter the inhibitor binding mode. Indeed, our study found that glycerol is bound in the active site of hCA II in the complex with **5b**. Moreover, the inhibitor is disordered and its tail was modeled in two conformations, with different occupational values, as shown in Fig. 3. The disorder may be due to the steric hindrance of the cryoprotectant molecule which influences the complex formation. To avoid the presence of the cryoprotectant molecule within the active site, the analyses were repeated using a higher molecular dimension cryoprotectant agent, PEG 400. In this case, as already shown, we found that differently, the inhibitor assumes a unique orientation in the protein cavity (Fig. 1B), representing a more accurate determination of its binding mode.

Using PEG 400 as a cryoprotectant, we also determined the structure of hCA II and hCA XII-mimic in the complex with the inhibitor **5c**. The density maps of the hCA XII-mimic complex with inhibitor **5c** do not show the biguanide portion of the molecule, preventing an accurate determination of its binding mode (data not shown). A similar situation is observed for the hCA II complex, where the biguanide group position is also unclear (Fig. 4). However, it is noteworthy that two distinct inhibitor molecules are present within the active site of hCA II.

In numerous complexes of hCA II with inhibitors, it has been found that a second inhibitor molecule binds near the

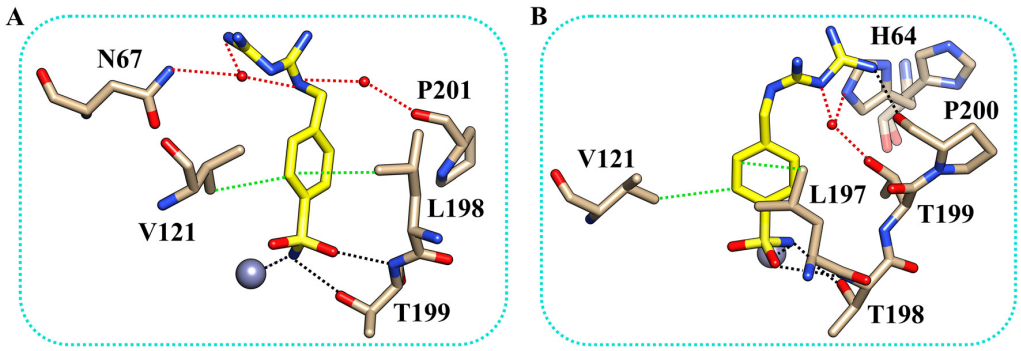

Fig. 2 The binding mode of inhibitor **5b** within the active site of hCA II (A) and hCA XII-mimic (B). Residues involved in the binding of the inhibitor are also shown. Hydrogen bonds, water bridges, and hydrophobic interactions are depicted as black, red, and green dotted lines. The gray sphere represents the zinc ion in the protein active site. The side chain of His64 was modeled in two conformations.

Open Access Article. Published on 24 January 2025. Downloaded on 10/20/2025 1:21:01 PM.
This article is licensed under a Creative Commons Attribution 3.0 Unported Licence.

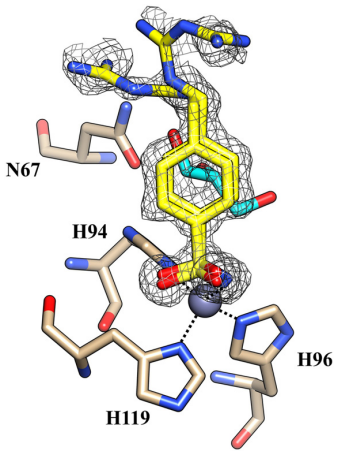

Fig. 3 The active site of hCA II complexed with inhibitor **5b** (PDB: 8ROW) from data collected using glycerol as a cryoprotectant. Glycerol is depicted in cyan.

N-terminal end of the protein (for example see ref. 35 and 36).

Nevertheless, in this case, a second inhibitor molecule is bound within the active site probably reducing the inhibitor affinity by introducing disorder within the binding cavity. This effect may explain the lower inhibition constant, K_I = 501.0 nM, in contrast to the significantly stronger affinity observed in the hCA XII–**5c** complex, where K_I = 1.7 nM. In panel A of Fig. 4, the binding mode of the second inhibitor molecule is shown. One oxygen and the nitrogen of the sulfonamide group establish hydrogen bonds with Asn67 and Glu69, respectively. Moreover, the phenyl ring forms hydrophobic interactions with Ile91 and Glu69. The binding of a second inhibitor molecule was not observed in the hCA XII-mimic complex and can be explained by comparing the sequences of the two isoforms. In fact, residues interacting with the inhibitor molecule 2 are mutated in the hCA XII-mimic sequence (Asn67Lys, Glu69Asn, and Ile91Thr) in a way that prevents the interaction with this second molecule bound to the upper part of the catalytic cavity.

Experimental section

Chemistry

Solvents and all reagents were purchased from Sigma-Aldrich, VWR, and TCI. Nuclear magnetic resonance (^{1}H NMR and ^{13}C NMR) spectra were recorded using a Bruker Advance III 400 MHz spectrometer in DMSO-d_6. Chemical shifts are reported in parts per million (ppm) and the coupling constants (J) are expressed in hertz (Hz). Splitting patterns are designated as follows: s, singlet; d, doublet; t, triplet; m, multiplet; brs, broad singlet; dd, doublet of doublets. The assignment of exchangeable protons (NH) was confirmed by the addition of D_2O. Analytical thin-layer chromatography (TLC) was carried out on Merck silica gel F-254 plates. Flash chromatography purifications were performed on Merck silica gel 60 (230–400 mesh ASTM) as the stationary phase, and ethyl acetate, *n*-hexane, acetonitrile, and methanol were used as eluents. The solvents used in MS measurements were acetone, acetonitrile (Chromasolv grade) purchased from Sigma-Aldrich (Milan, Italy) and mQ water 18 MΩ, obtained from Millipore's Simplicity system (Milan, Italy). The mass spectra were obtained using a Varian 1200 L triple quadrupole system (Palo Alto, CA, USA) equipped with an electrospray source (ESI) and negative ions. Stock solutions of analytes were prepared in acetone at 1.0 mg mL^{-1} and stored at 4 °C. Working solutions of each analyte were freshly prepared by diluting stock solutions in a mixture of mQ H_2O/ACN 1/1 (v/v) up to a concentration of 1.0 μg mL^{-1}. The mass

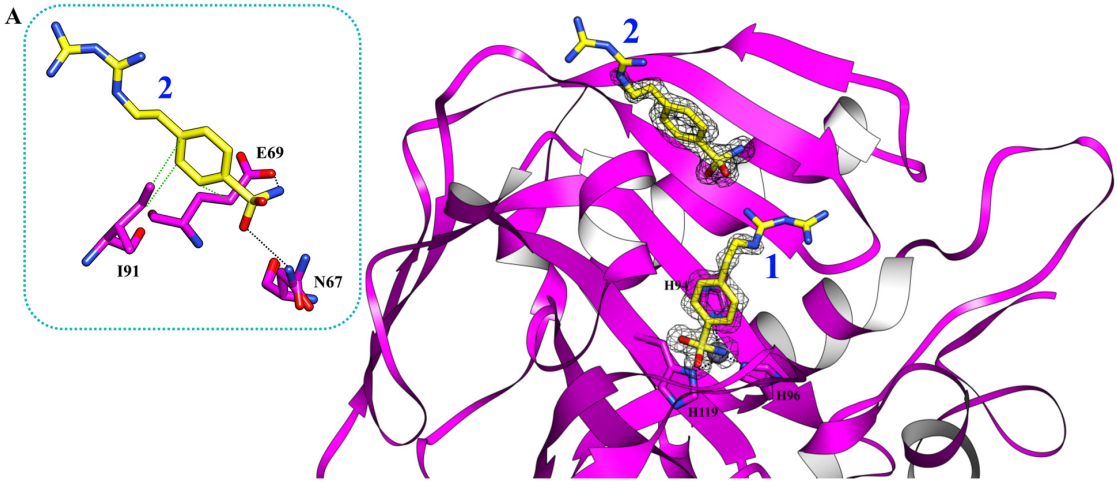

Fig. 4 The active site of hCA II complexed with inhibitor **5c** (PDB: 9H0V). Molecules of the inhibitor are labeled as 1 and 2. The binding mode of molecule 2 is shown in panel A. Hydrogen bonds and hydrophobic interactions are depicted as black and green dotted lines.

 This journal is © The Royal Society of Chemistry 2025

Open Access Article. Published on 24 January 2025. Downloaded on 10/20/2025 1:21:01 PM.
This article is licensed under a Creative Commons Attribution 3.0 Unported Licence.

spectra of each analyte were acquired by introducing, *via* a syringe pump at 10 L min^{-1}, the working solution. Raw data were collected and processed with Varian Workstation, version 6.8, software. All compounds reported here are >96% purity by NMR.

General synthetic procedure for compounds 5a, 5b and 5c

The synthesis of compounds **5a–c** was carried out by following the previously reported experimental procedure.[37] Specifically, the appropriate arylsulfonamide derivatives **1–3** (0.5 g, 1.0 equiv.) reacted with cyanoguanidine **4** (1.0 equiv.) in *n*-butanol (5 mL) followed by the addition of 6 M aqueous HCl (1.0 equiv.). The reaction mixture was heated to 100 °C under stirring for 6 h, and then the solvents were removed under vacuum to afford a residue that was crystallized from isopropyl alcohol (IPA) to obtain the desired products as white solids.

4-(3-Carbamimidoylguanidino)benzenesulfonamide hydrochloride salt 5a. Yield: 40%. ^{1}H-NMR (400 MHz, DMSO-d_6) δ 9.91 (brs, 1H, exchangeable with D_2O), 7.72 (d, J = 8.9 Hz, 2H), 7.59–7.41 (m, 6H, 4H exchangeable with D2O), 7.26 (s, 2H, exchangeable with D_2O), 7.09 (s, 2H, exchangeable with D_2O). 13C-NMR (100 MHz, DMSO-d_6) δ 162.5, 155.3, 143.1, 138.8, 127.4, 120.5. Experimental data are in agreement with the reported literature.[38]

4-((3-Carbamimidoylguanidino)methyl) benzenesulfonamide hydrochloride salt 5b. Yield: 58%. ^{1}H-NMR (400 MHz, DMSO-d_6) δ 7.72 (d, J = 8.3 Hz, 2H), 7.52 (d, J = 8.3 Hz, 2H), 7.41 (brs, 4H, exchangeable with D_2O), 7.25 (s, 2H, exchangeable with D_2O), 7.08 (brs, 2H, exchangeable with D_2O), 3.91 (m, 2H). ^{13}C NMR (100 MHz, DMSO-d_6) δ 163.9, 143.6, 142.5, 130.1, 126.9, 119.7, 46.8.

4-(2-(3-Carbamimidoylguanidino)ethyl) benzenesulfonamide hydrochloride salt 5c. Yield: 50%. ^{1}H-NMR (400 MHz, DMSO-d_6) δ 8.03 (brs, 3H, exchangeable with D_2O), 7.78 (d, J = 8.3 Hz, 2H), 7.46 (d, J = 8.3 Hz, 2H), 7.35 (s, 2H, exchangeable with D_2O), 3.06 (m, 2H), 2.97 (m, 2H). ^{13}C-NMR (100 MHz, DMSO-d_6) δ 163.9, 143.6, 142.5, 133.8, 130.1, 126.9, 36.5, 33.6. Experimental data are in agreement with the reported literature.[19]

Carbonic anhydrase inhibition

An Applied Photophysics stopped-flow instrument was used to evaluate the ability of the test compounds to inhibit the CA-catalyzed CO_2 hydration. Phenol red (at a concentration of 0.2 mM) was used as an indicator, working at a maximum absorbance of 557 nm, with 20 mM HEPES (pH 7.4) as a buffer, and 20 mM Na_2SO_4 (to maintain constant ionic strength), following the initial rates of the CA-catalyzed CO_2 hydration reaction for a period of 10–100 s. The CO_2 concentrations ranged from 1.7 to 17 mM for the assessment of the kinetic parameters and inhibition constants. Enzyme concentrations varied between 5 and 12 nM. For each inhibitor, at least six traces of the initial 5–10% of the reaction were used to determine the initial velocity. The uncatalyzed rates were calculated in the same manner and subtracted from the total observed rates. Stock solutions of each inhibitor (0.1 mM) were prepared in distilled–deionized H_2O and dilutions up to 0.01 nM were done thereafter with the assay buffer. Inhibitor and enzyme solutions were preincubated together for 15 min at r.t. before the assay, to allow the formation of the E–I complex. The inhibition constants were obtained by nonlinear least-squares methods using PRISM 3 and the Cheng–Prusoff equation as reported earlier[39] and represent the mean from at least three different determinations. hCAs I and II were purchased from Merck, while other isoenzymes were obtained in-house.[40]

Expression and purification of the hCA XII mimic

To generate the hCA XII mimic,[33] the CA II gene was used as the template, and nine specific mutations were introduced to reproduce key features of the hCA XII active site. These mutations were directly incorporated into the gene sequence during its design. The modified gene, containing these mutations, was synthesized by Genescript and subcloned into the pET43 vector using BamHI and XhoI restriction sites. Competent BL21 (DE3) cells were transformed with the plasmid containing the engineered gene. A fresh culture was grown at a 1 L scale in an LB broth supplemented with 100 μg mL^{-1} ampicillin. The cells were incubated at 37 °C until reaching the mid-log phase (OD_{600} = 0.6–0.7), at which point protein expression was induced by adding 0.5 mM isopropyl β-D-1-thiogalactopyranoside (IPTG). After 30 minutes, 0.5 mM $ZnSO_4$ was added to the culture, which was then incubated for an additional 4.5 hours. Cells were harvested by centrifugation at 5000 rpm for 20 minutes. The pellet was resuspended in 20 mM Tris-HCl buffer (pH 8.3) and subjected to sonication with 10 cycles of 10 seconds "on" and 120 seconds "off" at 50% amplitude (Bandelin Sonoplus). The lysate was clarified by centrifugation at 12 000 × g for 45 minutes. The supernatant was incubated with nickel affinity gel resin (His Select HF, Sigma), and pre-equilibrated in lysis buffer for 30 minutes. The resin was separated by centrifugation at 1500 × g and washed with a buffer containing 50 mM Tris-HCl (pH 8.3), 500 mM NaCl, and 20 mM imidazole. The protein was eluted using the same buffer supplemented with 250 mM imidazole. Eluted fractions were dialyzed against 20 mM Tris-HCl (pH 8.3). The purified recombinant protein was confirmed to be 95% pure, with a yield of approximately 3.2 mg per liter of bacterial culture. The engineered variant retained catalytic activity, demonstrating that the nine introduced mutations in the binding site did not disrupt the enzyme's intrinsic catalytic mechanism.

Crystallography

Crystallization and X-ray data collection. Crystals of the hCA XII-mimic isoform (protein solution 8 mg mL^{-1} in Tris-

Open Access Article. Published on 24 January 2025. Downloaded on 10/20/2025 1:21:01 PM.
This article is licensed under a Creative Commons Attribution 3.0 Unported Licence.

HCl 20 mM, pH 8.3) were grown *via* the hanging drop vapor diffusion method in a 24-well Linbro plate. Drops were prepared using 1 μL protein solution mixed with 1 μL reservoir solution containing 1 M sodium citrate and 50 mM Tris-HCl (pH 7.5) and were equilibrated against 500 μL of the same solution at 296 K. Crystal growth was observed after fifteen days.

hCA II purchased from Sigma was dissolved in 50 mM Tris-HCl (pH 8.0) to obtain a final concentration of 10 mg mL^{-1}.

Crystals of the hCA II isoform were obtained using the hanging drop vapor diffusion method in a 24-well Linbro plate. One microliter of hCA II was mixed with 1 μL of a solution of 1.5 M sodium citrate and 50 mM Tris-HCl (pH 8.0) and equilibrated against 500 μL of the same solution at 296 K. Crystal growth was observed after five days.

The complexes of the two isoforms with the inhibitors **5b** and **5c** were prepared by soaking the crystals in the mother liquor solution containing the inhibitor at a concentration of 10 mM for 2 hours.

Initially, all crystals were flash-frozen at 100 K using a solution obtained by adding 20% (v/v) glycerol to the mother liquor solution as a cryoprotectant. However, from the data obtained, we found that cryoprotectant molecules interact with the inhibitor within the protein active site. Hence, to avoid the cryoprotectant presence inside the enzyme active site with possible alteration of the inhibitor binding mode, we collected data using a different cryoprotectant solution obtained by adding 15% (v/v) of PEG 400 to the mother liquor solution. X-ray diffraction data were collected using synchrotron radiation at the XRD2 beamline at Elettra Synchrotron (Trieste, Italy) with a DECTRIS Pilatus 6 M detector.

Structure determination. The crystal structures of CA XII-mimic (PDB accession code: 4Q08) and CA II (PDB accession code: 3HS4) without solvent molecules and other heteroatoms were used to obtain the initial phases of the structures using Refmac5[41] from the CCP4 package.[42] Coordinates of the inhibitors were obtained using the program JLigand[43] and introduced in the model. Five percent of the unique reflections were selected randomly and excluded from the refinement data set for Rfree calculations. The initial $|F_o–F_c|$ difference electron density maps unambiguously showed the inhibitor molecules. The inhibitor **5b** was introduced in the model with 1.0 occupancy. Refinements proceeded using standard protocols of positional and anisotropic atomic displacement parameters alternating with the manual building of the models using COOT.[44] Inhibitor–enzyme interactions were analyzed using the PLIP web tool.[45] Atomic coordinates were deposited in the PDB (hCA II-**5b** accession code: 8ROU; hCA XII-**5b** accession code: 8RNS; hCA II-**5b** with glycerol as a cryoprotectant: 8ROW; hCA II-**5c**: 9H0V). Graphical representations were generated with Chimera.[46]

Conclusions

Herein, we reported aryl sulfonamides tailed with a biguanide moiety **5a–c** as selective inhibitors of the tumor associated hCA IX and XII isoforms, and we assessed the binding modes of **5b** and **5c** in the complex with hCA II and XII-mimic isoforms using X-ray crystallography. For instance, the aryl sulfonamide portion of **5b** was firmly placed deep into the catalytic cavities of hCAs II/XII, and the flexible biguanide tail was engaged in multiple interactions with the amino acids exposed at the top-end of the clefts, thus determining the specific orientation of the ligand as well its stabilization depending on the isoform. Noteworthily, the Asn67Lys mutation in the hCA XII-mimic was found to be mainly responsible for driving **5b** toward the tumor associated isoform over the cytosolic hCA II. Our investigations allowed us to identify a second **5c** ligand located at the N-terminal of the hCA II, proximal to the catalytic cleft, and thus reasonably able to influence the binding affinity of the main inhibitor. Such a mechanism may support a long-range allosteric hCA regulation mechanism not yet explored and may be potentially exploitable for the fine tuning of the metalloenzymes.

Data availability

The data supporting this article have been included as part of the ESI.† Crystallographic data for the structures of the complexes have been deposited at the PBD under accession codes 8ROU, 8RNS, 8ROW and 9H0V.

Conflicts of interest

There are no conflicts to declare.

Acknowledgements

FC, MF, and CB are grateful to the European Union – Next Generation EU, National Recovery and Resilience Plan (NRRP) – M4C2 Investment 1.5 – Research Programme ECS_00000017 – CUP B83C22003920001 for financial support. We acknowledge Elettra and XRD2 for providing beamtime and support under proposals 2022-0596 and 2024-0099.

References

1 C. T. Supuran, Structure and function of carbonic anhydrases, *Biochem. J.*, 2016, **473**(14), 2023–2032.
2 *Carbonic anhydrases in Metalloenzymes*, ed. C. T. Supuran, Academic Press, 2024, pp. 139–156.
3 C. T. Supuran, Carbonic anhydrase inhibition and the management of hypoxic tumors, *Metabolites*, 2017, **7**(3), 48.
4 S. Gruvberger, M. Ringnér, Y. Chen, S. Panavally, L. H. Saal, A. Borg, M. Fernö, C. Peterson and P. S. Meltzer, Estrogen Receptor Status in Breast Cancer Is Associated with Remarkably Distinct Gene Expression Patterns, *Cancer Res.*, 2001, **61**(16), 5979–5984.

 This journal is © The Royal Society of Chemistry 2025

Open Access Article. Published on 24 January 2025. Downloaded on 10/20/2025 1:21:01 PM.
This article is licensed under a Creative Commons Attribution 3.0 Unported Licence.

5 H. M. Becker, Carbonic anhydrase IX and acid transport in cancer, *Br. J. Cancer*, 2020, **122**(2), 157–167.
6 S. Daunys and V. Petrikaitė, The roles of carbonic anhydrases IX and XII in cancer cell adhesion, migration, invasion and metastasis, *Biol. Cell*, 2020, **112**(12), 383–397.
7 S. G. Nerella, P. S. Thacker, M. Arifuddin and C. T. Supuran, Tumor associated carbonic anhydrase inhibitors: Rational approaches, design strategies, structure activity relationship and mechanistic insights, *Eur. J. Med. Chem. Rep.*, 2024, **10**, 100131.
8 A. Doostmohammadi, H. Jooya, K. Ghorbanian, S. Gohari and M. Dadashpour, Potentials and future perspectives of multi-target drugs in cancer treatment: the next generation anti-cancer agents, *Cell Commun. Signaling*, 2024, **22**(1), 228.
9 C. T. Supuran, Multitargeting approaches involving carbonic anhydrase inhibitors: hybrid drugs against a variety of disorders, *J. Enzyme Inhib. Med. Chem.*, 2021, **36**(1), 1702–1714.
10 N. Krall, F. Pretto, W. Decurtins, G. J. L. Bernardes, C. T. Supuran and D. Neri, A Small-Molecule Drug Conjugate for the Treatment of Carbonic Anhydrase IX Expressing Tumors, *Angew. Chem., Int. Ed.*, 2014, **53**(16), 4231–4535.
11 S. S. Gardeen, S. J. Kurdziel, S. T. Nicolaou, J. E. Woods, S. A. Kularatne and P. S. Low, Development of a Small Molecule Tubulysin B Conjugate for Treatment of Carbonic Anhydrase IX Receptor Expressing Cancers, *Mol. Pharmaceutics*, 2018, **15**(6), 2289–2296.
12 S. Cazzamalli, B. Ziffels, F. Widmayer, P. Murer, G. Pellegrini, F. Pretto, S. Wulhfard and D. Neri, Enhanced Therapeutic Activity of Non-Internalizing Small-Molecule-Drug Conjugates Targeting Carbonic Anhydrase IX in Combination with Targeted Interleukin-2, *Clin. Cancer Res.*, 2018, **24**(15), 3656–3667.
13 S. Cazzamelli, A. Dal Corso, F. Widmayer and D. Neri, Chemically Defined Antibody– and Small Molecule–Drug Conjugates for in Vivo Tumor Targeting Applications: A Comparative Analysis, *J. Am. Chem. Soc.*, 2018, **140**(5), 1617–1621.
14 B. Zhang, Z. Liu, S. Xia, Q. Liu and S. Gou, Design, synthesis and biological evaluation of sulfamoylphenyl-quinazoline derivatives as potential EGFR/CAIX dual inhibitors, *Eur. J. Med. Chem.*, 2021, **216**, 113300.
15 E. Berrino, A. Angeli, D. D. Zhdanov, A. P. Kiryukhina, A. Milaneschi, A. De Luca, M. Bozdag, S. Carradori, S. Selleri, G. Bartolucci, T. S. Peat, M. Ferraroni, C. T. Supuran and F. Carta, Azidothymidine "Clicked" into 1,2,3-Triazoles: First Report on Carbonic Anhydrase–Telomerase Dual-Hybrid Inhibitors, *J. Med. Chem.*, 2020, **63**(13), 7392–7409.
16 E. Teodori, L. Braconi, S. Bua, A. Lapucci, G. Bartolucci, D. Manetti, M. N. Romanelli, S. Dei, C. T. Supuran and M. Coronnello, Dual P-Glycoprotein and CA XII Inhibitors: A New Strategy to Reverse the P-gp Mediated Multidrug Resistance(MDR) in Cancer Cells, *Molecules*, 2020, **25**(7), 1748.
17 C. J. Bailey, M. R. C. Path and R. C. Turner, Metformin, *N. Engl. J. Med.*, 1996, **334**(9), 574–579.
18 H. Zhu, Z. Jia, Y. R. Li and I. Danelisen, Molecular mechanisms of action of metformin: latest advances and therapeutic implications, *Clin. Exp. Med.*, 2023, **23**(7), 2941–2951.
19 E. Trefts and R. J. Shaw, AMPK: restoring metabolic homeostasis over space and time, *Mol. Cell*, 2021, **81**(18), 3677–3690.
20 Y. Yi, D. Chen, J. Ao, W. Zhang, J. Yi, X. Ren, J. Fei, F. Li, M. Niu, H. Chen, Y. Luo, Z. Luo and Z. J. Xiao, Transcriptional suppression of AMPKα1 promotes breast cancer metastasis upon oncogene activation, *Proc. Natl. Acad. Sci. U. S. A.*, 2020, **117**(14), 8013–8021.
21 E. J. Gallagher and D. LeRoith, Hyperinsulinaemia in cancer, *Nat. Rev. Cancer*, 2020, **20**(11), 629–644.
22 M. Foretz, B. Guigas, L. Bertrand, M. Pollak and B. Viollet, Metformin: from mechanisms of action to therapies, *Cell Metab.*, 2014, **20**(6), 953–966.
23 K. Vasan, M. Werner and N. S. Chandel, Mitochondrial metabolism as a target for cancer therapy, *Cell Metab.*, 2020, **32**(3), 341–352.
24 A. S. Krall, P. J. Mullen, F. Surjono, M. Momcilovic, E. W. Schmid, C. J. Halbrook, A. Thambundit, S. D. Mittelman, C. A. Lyssiotis, D. B. Shackelford, S. R. V. Knott and H. R. Christofk, Asparagine couples mitochondrial respiration to ATF4 activity and tumor growth, *Cell Metab.*, 2021, **33**(5), 1013–1026.
25 X. Liu, R. R. Chhipa, S. Pooya, M. Wortman, S. Yachyshin, L. M. L. Chow, A. Kumar, X. Zhou, Y. Sun, B. Quinn, C. McPherson, R. E. Warnick, A. Kendler, S. Giri, J. Poels, K. Norga, B. Viollet, G. A. Grabowski and B. Dasgupta, Discrete mechanisms of mTOR and cell cycle regulation by AMPK agonists independent of AMPK, *Proc. Natl. Acad. Sci. U. S. A.*, 2014, **111**(4), E435–E444.
26 X. Yu, Y. Zhang, S. Xiong, J. M. McDaniel, C. Sun, G. P. Chau, J. Gencel-Augusto, D. Chachad, R. L. Morrissey, X. Rao, J. Wang and G. Lozano, Omics analyses of a somatic Trp53R245W/+ breast cancer model identify cooperating driver events activating PI3K/AKT/mTOR signaling, *Proc. Natl. Acad. Sci. U. S. A.*, 2022, **111**(4), E435–E444.
27 J. S. Gutkind, A. A. Molinolo, X. Wu, Z. Wang, D. Nachmanson, O. Harismendy, L. B. Alexandrov, B. R. Wuertz, F. G. Ondrey, D. Laronde, L. D. Rock, M. Rosin, C. Coffey, V. D. Butler, L. Bengtson, C. Hsu, J. E. Bauman, S. M. Hewitt, E. E. W. Cohen, H.-H. S. Chow, S. M. Lippman and E. Szabo, Inhibition of mTOR signaling and clinical activity of metformin in oral premalignant lesions, *JCI Insight*, 2021, **6**(17), e147096.
28 D. Mossmann, S. Park and M. N. Hall, mTOR signalling and cellular metabolism are mutual determinants in cancer, *Nat. Rev. Cancer*, 2018, **18**(12), 744–757.
29 H. Yamaguchi, J. M. Hsu, W. H. Yang and M. C. Hung, Mechanisms regulating PD-L1 expression in cancers and associated opportunities for novel small-molecule therapeutics, *Nat. Rev. Clin. Oncol.*, 2022, **19**(5), 287–305.

Open Access Article. Published on 24 January 2025. Downloaded on 10/20/2025 1:21:01 PM.
This article is licensed under a Creative Commons Attribution 3.0 Unported Licence.

30 A. Ribas and J. D. Wolchok, Cancer immunotherapy using checkpoint blockade, *Science*, 2018, **359**(6382), 1350–1355.
31 R. G. Khalifah, The carbon dioxide hydration activity of carbonic anhydrase. I. Stop-flow kinetic studies on the native human isoenzymes B and C, *J. Biol. Chem.*, 1971, **246**(8), 2561–2573.
32 M. A. Pinard, M. Aggarwal, B. P. Mahon, C. Tu and R. McKenna, A sucrose-binding site provides a lead towards an isoform-specific inhibitor of the cancer-associated enzyme carbonic anhydrase IX, *Acta Crystallogr., Sect. F: Struct. Biol. Commun.*, 2015, **71**(10), 1352–1358.
33 P. Mujumdar, K. Teruya, K. F. Tonissen, D. Vullo, C. T. Supuran, T. S. Peat and S. Poulsen, An Unusual Natural Product Primary Sulfonamide: Synthesis, Carbonic Anhydrase Inhibition, and Protein X-ray Structures of Psammaplin C, *J. Med. Chem.*, 2016, **59**(11), 5462–5470.
34 E. Garman, Cool data: quantity and quality, *Acta Crystallogr., Sect. D: Biol. Crystallogr.*, 1999, **55**(10), 1641–1653.
35 D. K. Srivastava, K. M. Jude, A. L. Banerjee, M. Haldar, S. Manokaran, J. Kooren, S. Mallik and D. W. Christianson, Structural analysis of charge discrimination in the binding of inhibitors to human carbonic anhydrase I and II, *J. Am. Chem. Soc.*, 2007, **129**(17), 5528–5537.
36 K. M. Jude, A. L. Banerjee, M. K. Haldar, S. Manokaran, B. Roy, S. Mallik, D. K. Srivastava and D. W. Christianson, Ultrahigh resolution crystal structures of human carbonic anhydrases I and II complexed with "two-prong" inhibitors reveal the molecular basis of high affinity, *J. Am. Chem. Soc.*, 2006, **128**(9), 3011–3018.
37 T. Eysteinsson, A. García-Llorca, A. O. Hardarson, D. Vullo, F. Carta and C. T. Supuran, Membrane Permeability Is Required for the Vasodilatory Effect of Carbonic Anhydrase Inhibitors in Porcine Retinal Arteries, *Int. J. Mol. Sci.*, 2023, **24**(9), 8140.
38 O. Gungor and M. Kose, Design, synthesis, biological evaluation and molecular docking of cyclic biguanidine compounds as cholinesterase inhibitors, *J. Biomol. Struct. Dyn.*, 2023, **41**(20), 10885–10899.
39 E. Berrino, B. Michelet, K. Vitse, A. Nocentini, G. Bartolucci, A. Martin-Mingot, P. Gratteri, F. Carta, C. T. Supuran and S. Thibaudeau, Superacid-Synthesized Fluorinated Diamines Act as Selective hCA IV Inhibitors, *J. Med. Chem.*, 2024, **67**(21), 19460–19474.
40 C. Baroni, I. D'Agostino, G. Renzi, J. T. Kilbile, Y. Tamboli, M. Ferraroni, S. Carradori, C. Capasso, F. Carta and C. T. Supuran, Lasamide, a Potent Human Carbonic Anhydrase Inhibitor from the Market: Inhibition Profiling and Crystallographic Studies, *ACS Med. Chem. Lett.*, 2024, **15**(10), 1749–1755.
41 G. N. Murshudov, A. A. Vagin and E. J. Dodson, Refinement of macromolecular structures by the maximum-likelihood method, *Acta Crystallogr., Sect. D: Biol. Crystallogr.*, 1997, **53**(3), 240–255.
42 M. D. Winn, C. C. Ballard, K. D. Cowtan, E. J. Dodson, P. Emsley, P. R. Evans, R. M. Keegan, E. B. Krissinel, A. G. W. Leslie, A. McCoy, S. J. McNicholas, G. N. Murshudov, N. S. Pannu, E. A. Potterton, H. R. Powell, J. R. Randy, A. Vagin and K. S. Wilson, Overview of the CCP 4 Suite and Current Developments, *Acta Crystallogr., Sect. D: Biol. Crystallogr.*, 2011, **67**(4), 235–242.
43 A. A. Lebedev, P. Young, M. N. Isupov, O. V. Moroz, A. A. Vagin and G. N. Murshudov, JLigand: A Graphical Tool for the CCP 4 Template-Restraint Library, *Acta Crystallogr., Sect. D: Biol. Crystallogr.*, 2012, **68**(4), 431–440.
44 P. Emsley, B. Lohkamp, W. G. Scott and K. Cowtan, Features and development of Coot, *Acta Crystallogr., Sect. D: Biol. Crystallogr.*, 2010, **66**(4), 486–501.
45 M. F. Adasme, K. L. Linnemann, S. N. Bolz, F. Kaiser, S. Salentin, V. J. Haupt and M. Schroeder, PLIP 2021: expanding the scope of the protein–ligand interaction profiler to DNA and RNA, *Nucleic Acids Res.*, 2021, **49**(W1), W530–W534.
46 E. F. Pettersen, T. D. Goddard, C. C. Huang, G. S. Couch, D. M. Greenblatt, E. C. Meng and T. E. Ferrin, UCSF Chimera-A visualization system for exploratory research and analysis, *J. Comput. Chem.*, 2004, **25**(13), 1605–1612.

This journal is © The Royal Society of Chemistry 2025

Supplementary Information (SI) for RSC Medicinal Chemistry.
This journal is © The Royal Society of Chemistry 2025

Supplementary Material for

X-ray crystallographic and kinetic studies of biguanide containing aryl sulfonamides as Carbonic anhydrase inhibitors

Chiara Baroni[1], Murat Bozdag[2], Gioele Renzi[2], Viviana De Luca[3], Clemente Capasso[3], Carla Bazzicalupi[1], Silvia Selleri[2], Marta Ferraroni[1], Fabrizio Carta[2], and Claudiu T. Supuran[2]

[1] Department of Chemistry "Ugo Schiff", University of Florence, Via della Lastruccia 3, 50019 Sesto Fiorentino (FI), Italy;

[2] NEUROFARBA Department, University of Florence, Via Ugo Schiff 6, 50019 Sesto Fiorentino (FI), Italy

[3] Department of Biology, Institute of Bioscience and Bioresources (IBBR)-CNR, via P. Castellino 111, 80131 Napoli (NA), Italy

*Corresponding author: (fabrizio.carta@unifi.it and marta.ferraroni@unifi.it)

Index

^{1}H, ^{13}C, Spectra of compounds S2-S4

Table S1. Summary of Data Collection and Refinement Statistics of hCA II-**5b**, hCAII-**5b** with glycerol and mimic-hCA XII-**5b** S5

Table S2. Summary of Data Collection and Refinement Statistics of hCA II-**5c** S6

Figure S1. The amino acid sequence of the hCA XII-mimic protein S7

^{1}H NMR spectrum of compound **5a** (400 MHz, DMSO-*d6*)

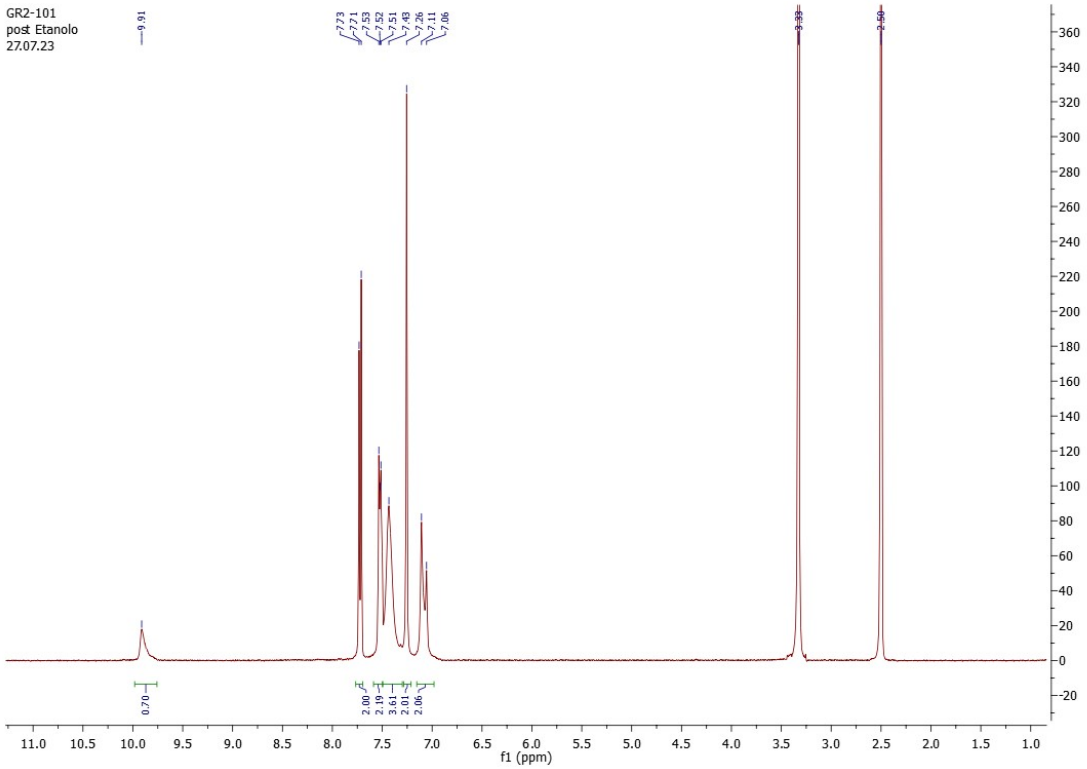

^{13}C NMR spectrum of compound **5a** (100 MHz, DMSO-*d6*)

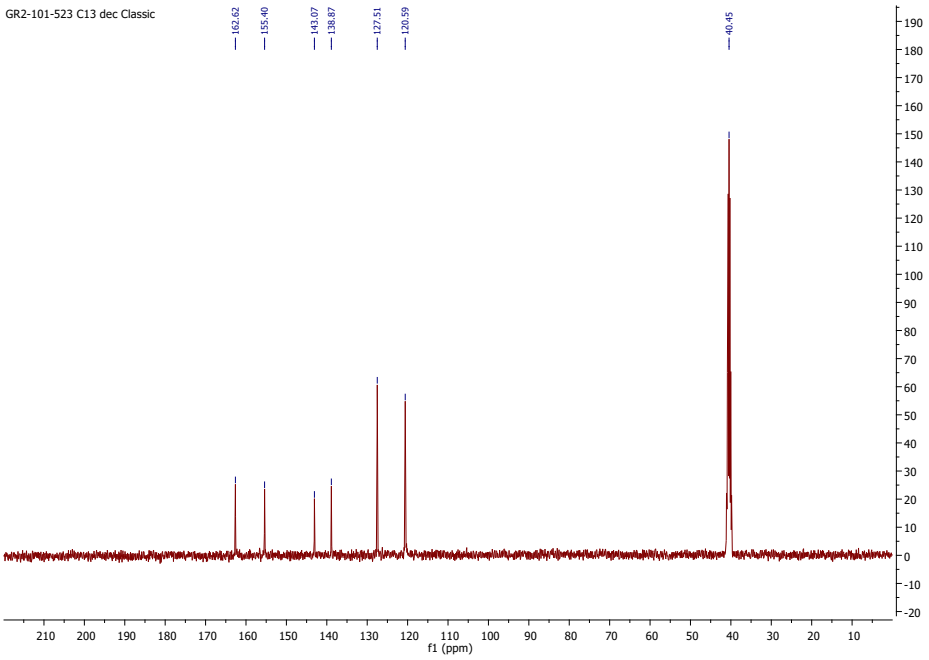

^{1}H NMR spectrum of compound **5b** (400 MHz, DMSO-*d6*)

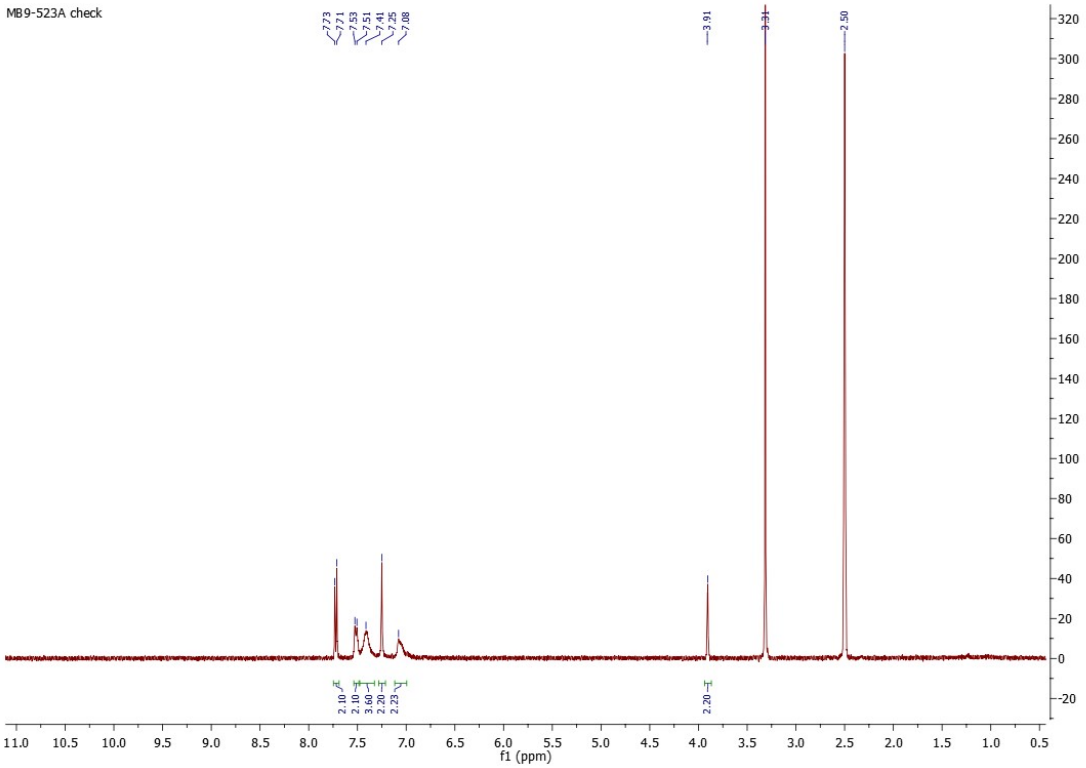

^{13}C NMR spectrum of compound **5b** (100 MHz, DMSO-*d6*)

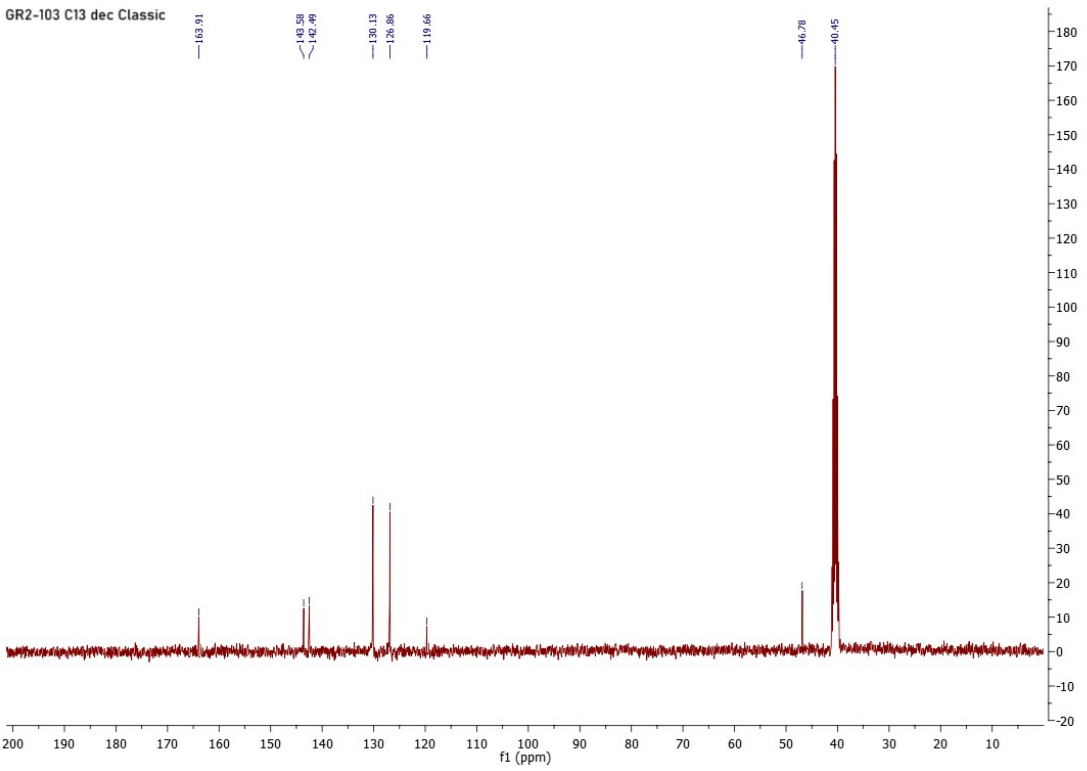

^{1}H NMR spectrum of compound **5c** (400 MHz, DMSO-*d6*)

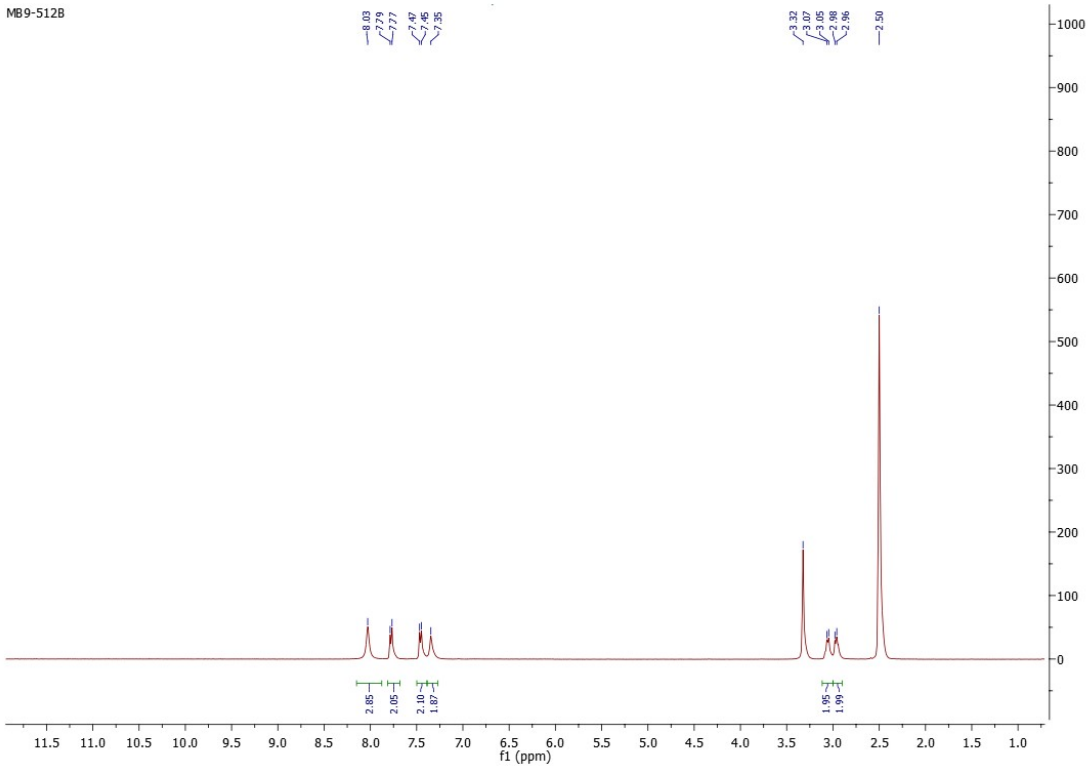

^{13}C NMR spectrum of compound **5c** (100 MHz, DMSO-*d6*)

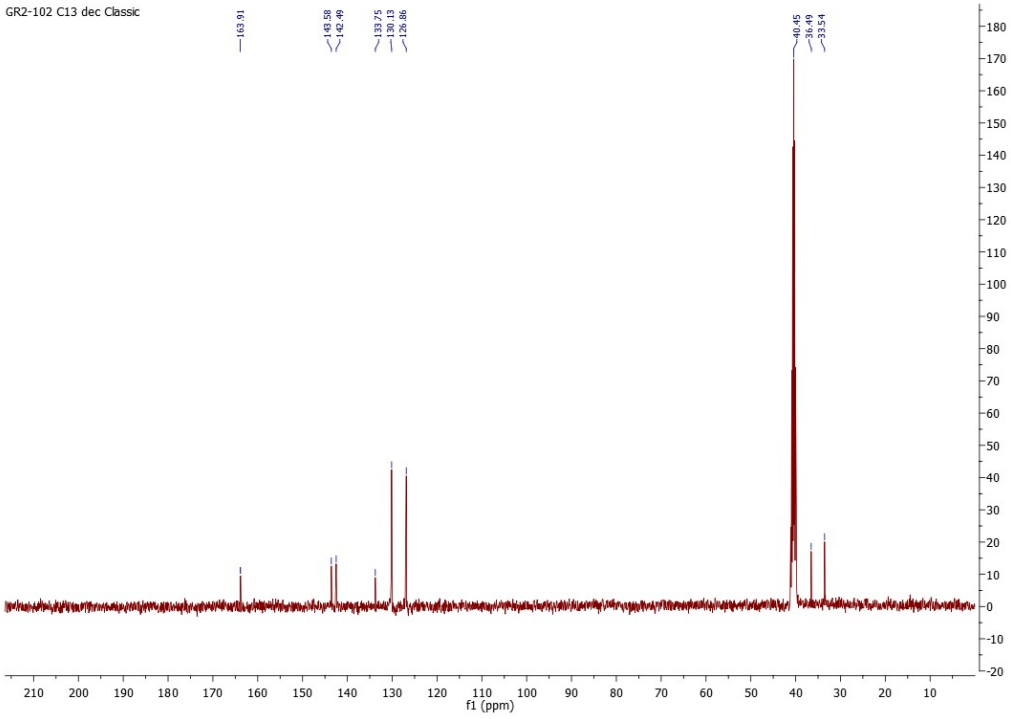

Table S1. Summary of Data Collection and Refinement Statistics Values in brackets refer to the highest resolution shell.

Data Collection statistics			
	CA II-5b	**CAII-5b with glycerol**	**CA XII-5b**
PDB ID	8ROU	8ROW	8RNS
Wavelength (Å)	1.0001	0.9718	1.0001
Space Group	P 2_1	P2_1	P 21
Unit cell (a, b, c, α, β, γ) (Å,)	42.28 41.09 72.29 90 104.20 90	42.44 41.30 72.03 90 104.29 90	41.98 41.33 71.81 90 103.87 90
Limiting resolution (Å)	70.08-1.08 (1.10-1.08)	40.02-1.05 (1.07-1.05)	40.76-1.14 (1.16-1.14)
Unique reflections	102568 (5042)	107024 (4661)	85727 (3897)
Rmerge	0.081 (1.403)	0.049 (0.706)	0.07 (1.351)
Rmeas	0.089 (1.591)	0.054 (0.801)	0.076 (1.547)
Redundancy	5.9 (4.5)	6.1 (4.5)	5.9 (4.3)
Completeness overall (%)	99.8 (99.7)	95.0 (83.7)	98.2 (90.0)
<I/σ(I)>	9.8 (1.1)	16.7 (2.2)	12.0 (1.1)
CC (1/2)	1.0 (0.3)	1.0 (0.7)	1.0 (0.4)
Refinement statistics			
Resolution range (Å)	70.08-1.08	40.02-1.05	40.76-1.14
Rfactor	0.1301	0.1160	0.1415
Rfree	0.1515	0.1386	0.1614
r.m.s.d. bonds (Å)	0.0118	0.0124	0.0113
r.m.s.d. angles ( )	1.8997	1.9011	1.7661
Ramachandran statistics (%)			
Most favored	97.3	97.3	96.9
additionally allowed	2.7	2.7	3.1
Outlier regions	0.0	0.0	0.0
Average B factor (Å^2)			
All atoms	15.1	13.9	17.9
Inhibitors	14.6	13.6 / 23.1	23.5
Solvent	17.1	15.8	20.0

Table S2. Summary of Data Collection and Refinement Statistics Values in brackets refer to the highest resolution shell.

Data Collection statistics	
	CA II-5c
PDB ID	9H0V
Wavelength (Å)	1.0002
Space Group	P 21
Unit cell (a, b, c, α, β, γ) (Å,)	42.43 41.26 72.47 90 104.72 90
Limiting resolution (Å)	35.56-1.40 (1.42-1.40)
Unique reflections	43258 (2316)
Rmerge	0.040 (0.200)
Rmeas	0.044 (0.216)
Redundancy	6.2 (6.7)
Completeness overall (%)	90.3 (97.4)
<I/σ(I)>	24.2 (8.6)
CC (1/2)	0.999 (0.981)
Refinement statistics	
Resolution range (Å)	35.56-1.40
Rfactor	0.0991
Rfree	0.1380
r.m.s.d. bonds (Å)	0.0105
r.m.s.d. angles ( )	1.9264
Ramachandran statistics (%)	
Most favored	96.1
additionally allowed	3.9
Outlier regions	0.0
Average B factor (Å²)	
All atoms	16.8
Inhibitors	22.4 / 30.9
solvent	31.6

>hCA II

MSHHWGYGKHNGPEHWHKDFPIAKGERQSPVDIDTHTAKYDPSLKPLSVSYDQATSLRILNNGHAFNVEFDDSQDKAVLKGGPLDGTYR
LIQFHFHWGSLDGQGSEHTVDKKKYAAELHLVHWNTKYGDFGKAVQQPDGLAVLGIFLKVGSAKPGLQKVVDVLDSIKTKGKSADFTNF
DPRGLLPESLDYWTYPGSLTTPPLLECVTWIVLKEPISVSSEQVLKFRKLNFNGEGEPEELMVDNWRPAQPLKNRQIKASFK

>hCA XII mimic

MSHHWGYGKHNGPEHWHKDFPIAKGERQSPVDIDTHTAKYDPSLKPLSVSYDQATSLRILNNGH**S**F**K**V**N**FDDSQDKAVLKGGPLDGTYR
L**T**QFHFHWGSLDGQGSEHTVDKKKYAAELHLVHWNTKYGD**AS**KA**S**QQPDGLAVLGIFLKVGSAKPGLQKVVDVLDSIKTKGKSADFTNF
DPRGLLPESLDYWTYPGSLTTPPL**N**E**T**VTWIVLKEPISVSSEQVLKFRKLNFNGEGEPEELMVDNWRPAQPLKNRQIKASFK

```
hCA II   MSHHWGYGKHNGPEHWHKDFPIAKGERQSPVDIDTHTAKYDPSLKPLSVSYDQATSLRIL  60
hCA XII  MSHHWGYGKHNGPEHWHKDFPIAKGERQSPVDIDTHTAKYDPSLKPLSVSYDQATSLRIL  60

         NNGHAFNVEFDDSQDKAVLKGGPLDGTYRLIQFHFHWGSLDGQGSEHTVDKKKYAAELHL  120
         NNGHSFKVNFDDSQDKAVLKGGPLDGTYRLTQFHFHWGSLDGQGSEHTVDKKKYAAELHL  120

         VHWNTKYGDFGKAVQQPDGLAVLGIFLKVGSAKPGLQKVVDVLDSIKTKGKSADFTNFDP  180
         VHWNTKYGDASKASQQPDGLAVLGIFLKVGSAKPGLQKVVDVLDSIKTKGKSADFTNFDP  180

         RGLLPESLDYWTYPGSLTTPPLLECVTWIVLKEPISVSSEQVLKFRKLNFNGEGEPEELM  240
         RGLLPESLDYWTYPGSLTTPPLNETVTWIVLKEPISVSSEQVLKFRKLNFNGEGEPEELM  240

         VDNWRPAQPLKNRQIKASFK  260
         VDNWRPAQPLKNRQIKASFK  260
```

Figure S1. Amino acid sequence alignment of hCA II and hCA XII. Residues of hCA II bolded in red were replaced with the corresponding residues from hCA XII to create the mimic proteins.

European Journal of Medicinal Chemistry 290 (2025) 117552

Contents lists available at ScienceDirect

European Journal of Medicinal Chemistry

journal homepage: www.elsevier.com/locate/ejmech

Research paper

O-derivatization of natural tropolone and β-thujaplicin leading to effective inhibitors of human carbonic anhydrases IX and XII

Francesco Melfi [a,1], Ilaria D'Agostino [b,1], Simone Carradori [a,*], Fabrizio Carta [c,**], Andrea Angeli [c], Giosuè Costa [d,e], Gioele Renzi [c], Ana Čikoš [f], Daniela Vullo [c], Josip Rešetar [a], Marta Ferraroni [g], Chiara Baroni [g], Francesca Mancuso [h], Rosaria Gitto [h], Francesca Alessandra Ambrosio [d], Emanuela Marchese [d], Roberta Torcasio [i,j], Nicola Amodio [i], Clemente Capasso [k], Stefano Alcaro [d,e], Claudiu T. Supuran [c]

[a] *Department of Pharmacy, "G. d'Annunzio" University of Chieti-Pescara, 66100, Chieti, Italy*
[b] *Department of Pharmacy, University of Pisa, 56126, Pisa, Italy*
[c] *Neurofarba Department, University of Florence, Sesto Fiorentino, 50019, Florence, Italy*
[d] *Dipartimento di Scienze della Salute, Università "Magna Græcia" di Catanzaro, Campus "S. Venuta", 88100, Catanzaro, Italy*
[e] *Net4Science Academic Spin-Off, Università "Magna Græcia" di Catanzaro, Campus "S. Venuta", 88100, Catanzaro, Italy*
[f] *NMR Centre, Ruđer Bošković Institute, Bijenička cesta 54, 10000, Zagreb, Croatia*
[g] *'Ugo Schiff' Chemistry Department, University of Florence, Via della Lastruccia 3, 50019 Sesto Fiorentino, Florence, Italy*
[h] *Department of Chemical, Biological, Pharmaceutical, and Environmental Sciences, University of Messina, Viale F. D'Alcontres 13, 98166, Messina, Italy*
[i] *Department of Experimental and Clinical Medicine, University "Magna Græcia" of Catanzaro, Campus "S. Venuta", 88100, Catanzaro, Italy*
[j] *Department of Biology, Ecology and Earth Sciences (Di.B.E.S.T.), University of Calabria, 87036, Rende, Italy*
[k] *Department of Biology, Agriculture and Food Sciences, Institute of Biosciences and Bioresources, CNR, Napoli, Italy*

ARTICLE INFO

Keywords:
Tropolone
Thujaplicin
Carbonic anhydrase
Cancer
Regioisomer
Multiple myeloma

ABSTRACT

Herein we report the chemical derivatization of the naturally occurring Tropolone (**TRP**) and its related compound β-Thujaplicin (β-**TJP**) as well as their *in vitro* assessment for inhibition of the physio/pathologically relevant hCAs isoforms I, II, VA; VII, IX and XII to obtain a first set of inhibition data useful for driving selected derivatives towards appropriate biomedical exploitation. The selected compound **17β** was characterized for its chemical stability and assessed for its antiproliferative activity on a multiple myeloma model and showed potent pro-apoptotic features jointly with a safe toxicity profile on healthy cells. The binding mode of β-**TJP** within the hCA II was assessed by means of X-ray crystallography of the hCA II/β-**TJP** complex and showed almost complete superposition with the hCA II/**TRP** adduct reported in the literature. The data produced were used to elaborate a binding prediction model of such compounds on the hCAs VA, IX, and XII which are directly connected to important diseases. Overall, the achievements reported in this work are in the sustainment of the exploitation of naturally occurring troponoloid-based structures for biomedical purposes and thus contribute to the field in extending the variety of available chemical features.

1. Introduction

Tropolone (**TRL**, Fig. 1), also known as hydroxytropone, is a seven-membered aromatic compound endowed with a cyclic ketone function and a vicinal enolic hydroxyl group. The latter seems to correspond to a combination of enol and phenol properties. Besides the peculiar acidity, the presence of the two moieties makes **TRP** be regarded as a vinylog of carboxylic acids, and in some cases, an effective bioisostere of benzoic acid [1]. In this context, it is recognized to establish a strong intramolecular and intermolecular association due to an H-bond and to be able to chelate metals through the two oxygen atoms of the molecule [2,3] (Fig. 1).

* Corresponding author.
** Corresponding author.
E-mail addresses: simone.carradori@unich.it (S. Carradori), fabrizio.carta@unifi.it (F. Carta).
[1] The authors contributed equally to this work.

https://doi.org/10.1016/j.ejmech.2025.117552
Received 18 February 2025; Received in revised form 20 March 2025; Accepted 21 March 2025
Available online 27 March 2025
0223-5234/© 2025 The Authors. Published by Elsevier Masson SAS. This is an open access article under the CC BY license (http://creativecommons.org/licenses/by/4.0/).

The exceptional structure of **TRP** came from natural sources and in particular it is produced by bacteria, fungi, and yeast, and was identified for the first time as a virulence factor of a plant pathogen [4]. In addition, different cyclization synthetic approaches have been reported to obtain the **TRP** nucleus in the laboratory [5–7]. However, it is often found as part of more complex natural compounds, such as colchicine [8], and about 200 molecules have been identified as natural **TRP**s [9]. **TRP** has been widely investigated for its antioxidant properties as well as its antibacterial, antiparasitic [10], and in general, antimicrobial [11] properties. On the basis of its polypharmacology, **TRP** is hypothesized to act by perturbing microbial membranes [12] and metabolism, especially due to its ionophoric, thereby metal chelating, action [13,14].

However, among tropolonoids, thujaplicins (**TJP**s, Fig. 1) attracted the interest of the scientific community. This class of compounds bears an isopropyl group in different positions of the **TRP** core, such as C2, C3, and C4, resulting in α-, β-, and γ-**TJP** (Fig. 1), respectively, with the Greek alphabet referring to the functionalization position with respect to the OH moiety (Scheme 1). Naturally occurring from certain coniferous trees, mainly the Cupressaceae family, *e.g.*, *Thuja* species, which has conferred the name to the derivatives. β-**TJP**, also known as Hinokitiol, found large applications in cosmetics, food, oral care, and beauty products due to its antioxidant [15], antimicrobial [16], anticancer [17], antidiabetic [18], and other activities. Multiple pharmacological potentialities of tropolonoids are associated with the chelating properties of the α-enolic ketone moiety, resulting in a bidentate ligand coordinating the metal ions [19], able to act as ionophores [20], or siderophores [21], thereby, affecting the homeostasis of metals in the cell cytoplasm or depleting the levels of metal cofactors and as modulators of enzymes function by impairing their folding or their catalytic activity.

Moreover, several X-ray structures of **TRP**-metalloenzyme complex have been deposited in the Protein Data Bank database (PDB, https://www.rcsb.org), *i.e.*, those of human tyrosinase-related protein 1 [22] and human Carbonic Anhydrase (hCA) II isoenzymes [3](discussed later), proving the zinc-binding properties of the nucleus. Also, several contrast agents with a tropolonoid-based structure have been reported [23].

Notably, a previous study by Cohen and coworkers reported the inhibitory activity of **TRP** and **TJP** towards hCA II, a human (h) isoenzyme of the superfamily of CAs (EC: 4.2.1.1), metalloenzymes catalyzing the hydration of carbon dioxide into bicarbonate ion and proton. Along with a large series of compounds, the two natural troponoloids were investigated on their ability to chelate the zinc ion, the cofactor of the enzyme. The study revealed low inhibition percentages (Inhib. % = 16–17 %) for both compounds when tested at 500 μM on the wild-type isoenzyme by means of the 4-nitrophenylacetate esterase assay. Remarkably, kinetic studies on two hCA II variants, *i.e.,* H94C and H94D, revealed a drop in the inhibitory activity (Inhib. % = 0%) and an increase in potency (Inhib. % = 47–49%), respectively, proving a specific interaction network in the active site of the enzyme [24]. Some years later, the same group reported **TRP** and its isostere thiotropolone (**TTRP**) (illustrated in Fig. 1 in one of the tautomeric forms) to inhibit the wild-type hCA II with inhibition constant (K_I) values of 1350 and 96 μM, respectively, proving the importance of the sulfur atom in the metal binding ability of such compounds. Again, in this study, the enzymatic assays on a different variant, hCA II L198G, containing a glycine residue in place of a leucine, led to an increase in the potency of both compounds (K_Is = 245 and 61 μM, respectively). X-ray crystallization studies confirmed the zinc-binding ability of **TRP** [3]. One year earlier, Costa et al. performed a structure-based virtual screening on a library of essential oils aimed at discovering new inhibiting chemotypes of the mitochondrial hCA VA, an isoform involved in lipogenesis and associated with obesity. During this study, β-**TJP** emerged and deeper *in silico* studies, *i.e.,* molecular dynamic simulations, confirmed the role of the tropolonoid zinc binding group in the interaction with the enzyme and enzymatic assays assessed a micromolar inhibition of hCAs I, II, and VA, with K_I values of 4.98, 90.60, and 7.50 μM, respectively [25]. Altogether, the potentialities of tropolonoids in inhibiting CAs and the multifaceted physiopathological role of these enzymes led us to investigate **TRP** and **TJP** core by generating a library of *O*-functionalized derivatives as putative inhibitors of representative α-CAs belonging to humans (main text) or other microorganisms (Table S1 in the Supplementary Material file).

2. Results and discussion

2.1. Synthesis of tropolonoid derivatives

Aimed at exploring the chelating properties of **TRP** and β-**TJP**, different *O*-functionalized derivatives were developed and, in particular, ethers and esters were prepared by reacting the tropolonoid nuclei with the suitable chemical, mainly halide, in a basic environment (Scheme 1).

For these reactions, the presence of a base, being inorganic as K_2CO_3 or organic as *N,N,N*-triethylamine (TEA) and *N,N*-dimethylaminopyridine (DMAP), all characterized by a pK_a of approximately 10, is necessary to allow the complete deprotonation of the enolic group of the tropolonoid making it to act as a nucleophile. However, instead of **TRP**, the treatment of β-**TJP** with such bases leads to the generation of two resonance forms, namely the β- and the δ-**TJP** enolates, and the following nucleophilic attack generates the corresponding β- and the

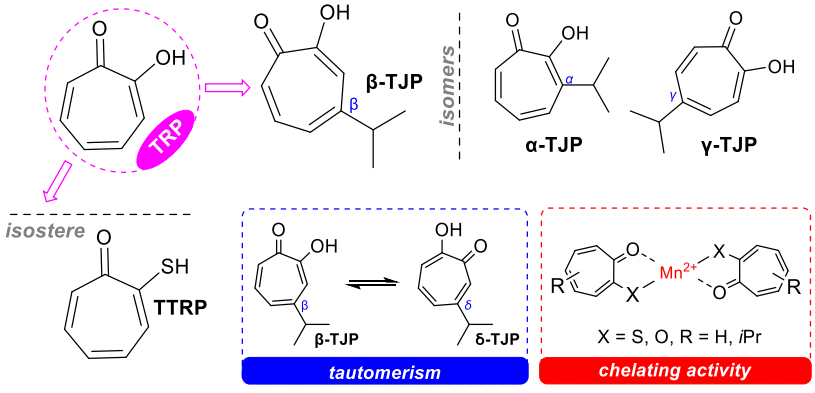

Fig. 1. Chemical structure of natural tropolone (**TRP**) and β-thujaplicin (β-**TJP**, or Hinokitiol) with the latter isomers α-thujaplicin (α-**TJP**) and γ-thujaplicin (γ-**TJP**) along with the synthetic derivative thiotropolone (**TTRP**). A representative example of tautomerism (β-δ **TJP**) and the mechanism of chelation are illustrated in the blue and red boxes, respectively. (For interpretation of the references to colour in this figure legend, the reader is referred to the Web version of this article.)

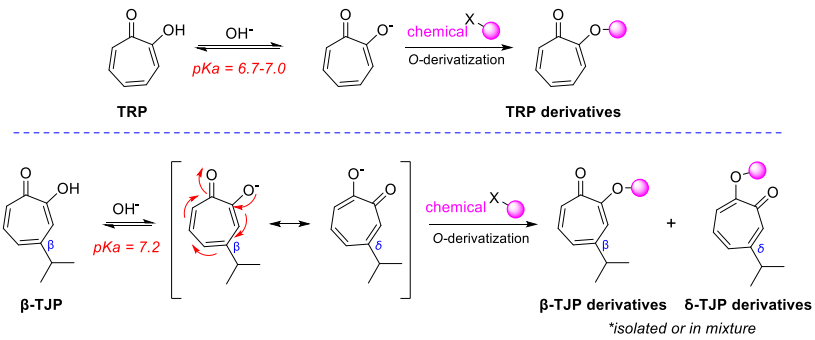

Scheme 1. General reaction scheme involving *O*-derivatization on **TRP** or β-**TJP** in basic environment, generating **TRP** derivatives and β- and δ-**TJP** derivatives. pK_a values for **TRP** and β-**TJP** are reported [5].

δ-**TJP** adducts (Scheme 1), as already reported [26–28]. However, the isolation and identification of the two **TJP** regioisomers are not a trivial job and require in-depth investigations, often based on a combination of NMR experiments. In detail, a large library of **TRP** and **TJP** derivatives was synthesized through different *O*-derivatization reactions, as depicted in Scheme 2.

First, *O*-alkylation *(i*, Scheme 2) was performed via nucleophilic substitution by using the suitable halogen derivative (R^1X) in a basic environment for potassium carbonate, furnishing **TRP** derivatives **1–3**, **7–13**. Interestingly, when we employed β-**TJP** as the starting material, in most cases the two β- and δ-regioisomers were generated. The isolation of both the pure regioisomers was successful only when the *O*-benzyl function was functionalized in the *ortho* position, *e.g.,* the 2-nitrobenzyloxy **TJP**s **11β** and **11δ** and the 2-trifluoromethylbenzyloxy derivatives **12β** and **12δ**. However, when the nitro group was moved to the *para* or *meta* position, the two **TJP** regioisomers were not isolated and a 50:50 mixture was obtained (**9β+δ** and **10β+δ**, respectively). Similar results were obtained for *O*-propargylated (**1β+δ**), *O*-chloropropyl (**2β+δ**), 4-cyano benzyloxy (**8β+δ**), and 2-(5-phenyl-1,3,4-oxadiazolyl)methoxy (**14β+δ**) **TJP**s with β:δ ratios close to 50:50 (with the exception of **1β+δ** with 55:45 ratio). Otherwise, in some cases, we isolated just one pure regioisomer and, in particular, 4-bromo benzyloxy **TJP 7δ** and the 1-naphthylmethoxy **TJP 13δ** in a reaction yield (= 52% in both cases) comparable to the others, thereby, we could assume they were the only regioisomer produced from the reaction.

The *O*-alkylation with ethyl bromoacetate led to derivatives **5** and **5β+δ**, which were then hydrolyzed by lithium hydroxide to free carboxylic acids **6** and **6β+δ** (*ii*, Scheme 2). Also, for these **TJP**s, the regioisomer mixture was not solved. Interestingly, we synthesized a **TJP** dimeric compound (**4δ**) by reacting 1,5-dibromopentane with an excess

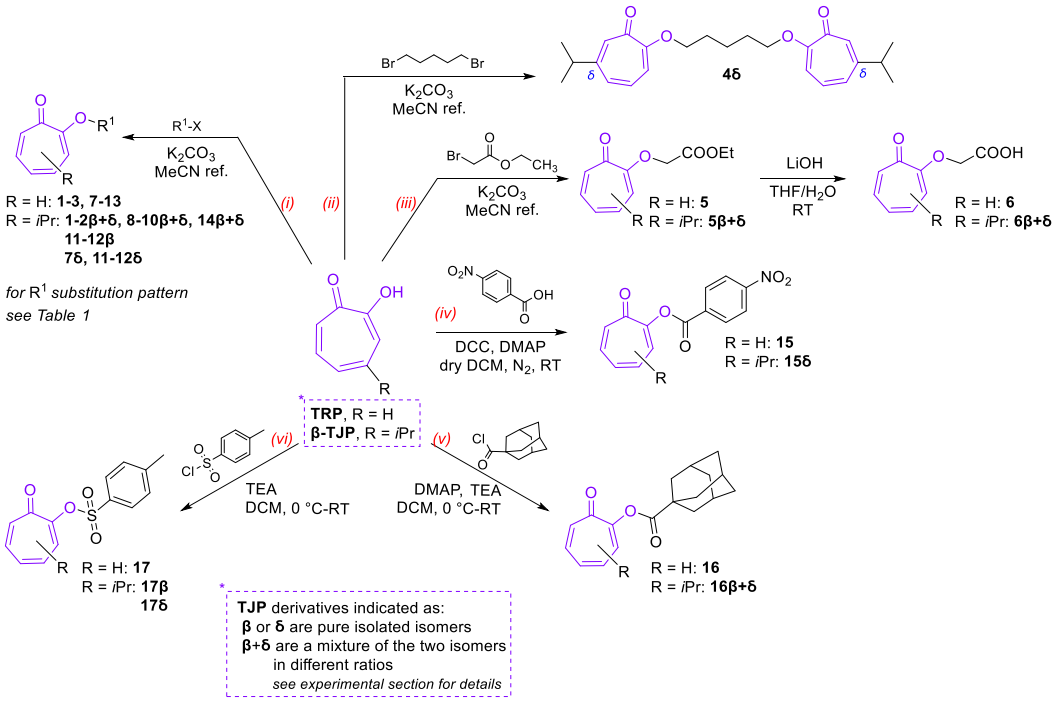

Scheme 2. Synthetic pathways for the preparation of **TRP** and **TJP** derivatives **1–17**. **TRP** (R=H) and **TJP** (R = *i*Pr) derivatives. The numbering code with Greek letters **β** or **δ** indicates the position of the isopropyl moiety on the **TJP** scaffold with respect to the hydroxyl group, as conventional (see Fig. 1). Compounds indicated as **β+δ** are a mixture of the two isomers in different ratios (see *Experimental Section* for details). The R^1 substitution pattern is reported in Table 1.

of β-**TJP** (*iii*, Scheme 2). The ^{1}H and ^{13}C NMR analysis for this compound highlighted the presence of δ-**TJP** scaffolds. Also, we prepared 4-nitrobenzoyl and adamantanoyl derivatives by reacting the tropolonoids with the suitable carboxylic acid or acyl chloride and, apart from the **TRP** derivatives **15** and **16**, the δ-**TJP** regioisomer **15δ** was isolated as the only product whereas the adamantanoyl **TJP** derivative was obtained as a regioisomeric mixture (**16β+δ**) (*iv*, Scheme 2). Peculiarly, the latter was the only case of a product with a β:δ ratio of 85:15 with a large preference for β-**TJP** regioisomer, resulting in being the major isomer.

In the end, tosylation of the OH moiety of **TRP** and β-**TJP** was performed by using tosyl chloride, and the corresponding tosylates **17**, **17β**, and **17δ** were afforded (Scheme 2). In this case, the products were already characterized and structures elucidated, although obtained through different reaction conditions, *e.g.,* by using pyridine as a base [28].

As already mentioned, we successfully isolated the two regioisomers obtained in the synthetic pathway. However, in some cases, although we did attempt to separate the regioisomers via direct phase, silica gel-based column chromatography, and employing various eluent conditions, the regioisomers often co-eluted, making the full separation not feasible. This could be due to their small structure and high structural similarity. As a result, we tested the mixture of regioisomers and relied on in-depth NMR techniques to determine their ratio for the reaction yield characterization and the following biological evaluation.

2.2. Insight into the chemical structure of TJP regioisomers mixtures 10β+δ and 8β+δ and pure products 11β and 11δ via NMR experiments

In order to elucidate the chemical structure of the **TJP** regioisomers, combined bidimensional NMR experiments were performed. In particular, Heteronuclear Single Quantum Correlation (HSQC), Heteronuclear Multiple Bond Correlation (HMBC) NMR and Nuclear Overhauser Effect Spectroscopy (NOESY) techniques were employed on the two β and δ regioisomers of two different **TJP**s (**10β+δ**) and **8β+δ**. The former experiments are generally used to determine the correlation of ^{1}H and ^{13}C nuclei single bonds (HSQC) and the nuclei separated by two, three, or more bonds. NOESY, instead, provides information on through-space nuclei interactions (see NMR spectra in the Supplementary Material file, Figs. S25–S28 and S37–S40). Interestingly, the analysis of HMBC NMR spectra for the investigated compounds **10β+δ** and **8β+δ** revealed two sets of resonance lines corresponding to two regioisomers in each sample (Fig. 2).

The main evidence for the unambiguous structural assignment of these compounds lies in the carbon chemical shift of atoms numbered 3. All four compounds analyzed show a ^{1}H–^{13}C HMBC interaction between the methyl doublets 9,10-CH_3 and 8-C, which in turn show interaction with 3-H. Based on the knowledge of the proton chemical shift of 3-H, its associated carbon can be easily identified from the ^{1}H–^{13}C HSQC spectrum. In the β isomers (marked in blue in Fig. 1), the 3-C chemical shifts are 118.0 ppm and 117.6 ppm for **10β+δ** and **8β+δ**, respectively. Both δ-**TJP** isomers (marked in red in Fig. 2) exhibit a carbon chemical shift of 3-C at 135.0 ppm. Additional confirmation for the elucidated structures was found in the NOESY spectra, in which both β-**TJP** isomers show a strong NOE interaction between 11-CH_2 and 3-H, while their δ-**TJP** counterparts exhibit the cross-peak between 11-CH_2 and 7-H. NMR analysis for pure isolated regioisomers **11β** and **11δ** was similar. In the β-**TJP** isomer (**11β**), the carbon chemical shift of 3-C is 117.0 ppm, while in the δ-**TJP** isomer (**11δ**) 3-C is found at 134.9 ppm. Analysis of NOE contacts (Fig. 3) confirmed the assignment.

Thanks to this analysis, the structure elucidation of the pure **TJP** regioisomers and the assessment of the β:δ ratio in the mixture was performed and helped the structure-activity relationships (SARs) and *in silico* further studies.

2.3. Inhibitory activity against α-carbonic anhydrases and SARs considerations

TRP compounds along with **TJP** derivatives as pure regioisomers or their mixture were tested against a panel of α-CAs endowed with specific physio-pathological roles, belonging to humans (hCAs I, II, VA, VII, IX, and XII) (Table 1), bacteria (VchCAα from *Vibrio cholerae* [29] and HpCAα from *Helicobacter pylori* [30]), protozoa (TcCAα from *Tripanosoma cruzi* [31]), and parasites (SmCAα *from Schistosoma mansoni* [32]) to further assess potency and isoform selectivity (Table S1).

All the synthesized compounds turned out to be less potent than the reference compound, acetazolamide (**AAZ**). The large dataset (Table 1) allowed the establishment of preliminary SARs which are herein reported based on the isoform.

- As regards the parent compounds, **TRP** did not show any activity on hCA I whereas β-**TJP** exhibited a low micromolar inhibitory activity (K_I = 4.98 μM). The majority of **TRP** and **TJP** derivatives were found almost all inactive towards this isoform. The most potent compound,

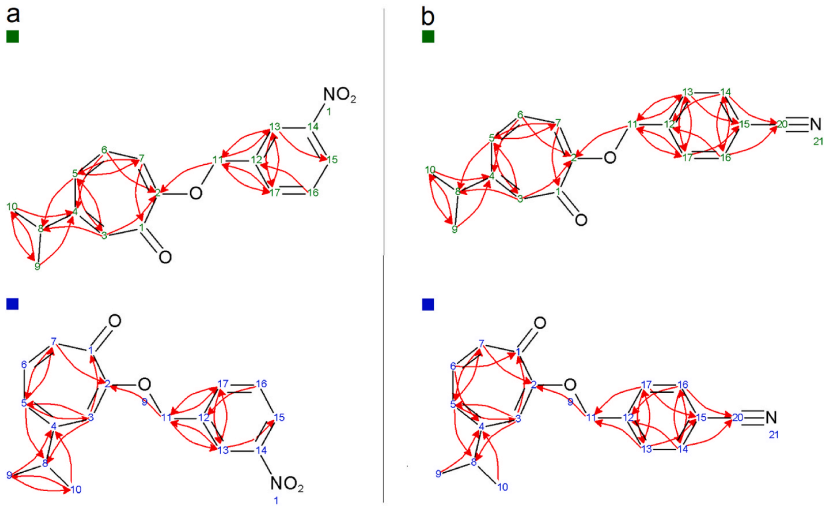

Fig. 2. Structure, numbering, and key ^{1}H–^{13}C HMBC interactions marked with red arrows for β-**TJP** (blue) and δ-**TJP** (green) for compounds (a) **10β+δ** and (b) **8β+δ**. (For interpretation of the references to colour in this figure legend, the reader is referred to the Web version of this article.)

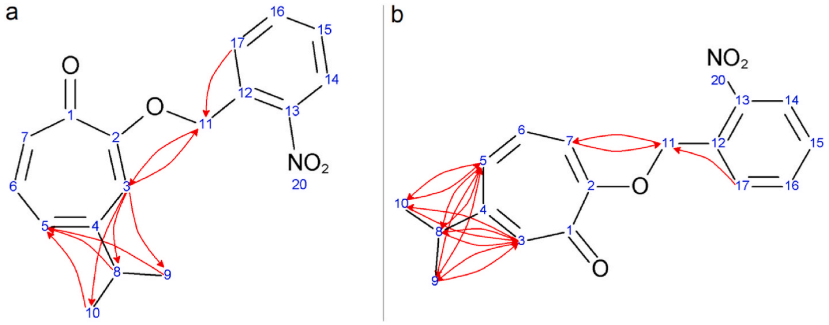

Fig. 3. Structure, numbering, and key $^{1}H–^{1}H$ NOESY interactions marked with red arrows for β-**TJP** and δ-**TJP** regioisomers of compounds (a) **11β** and (b) **11δ**. (For interpretation of the references to colour in this figure legend, the reader is referred to the Web version of this article.)

the *O*-propargylated **TRP** derivative **1** showed a K_I of 0.05 μM, while the corresponding mixture of β- and δ-**TJP**, namely **1β+δ**, resulted in being active as well, but less potent (K_I = 0.66 μM). Moreover, 4-cyanobenzyloxy (**8**), 4-nitrobenzyloxy (**9**), and 2-nitrobenzyloxy (**11**) **TRP** derivatives exhibited moderate results with K_I of 8.31, 6.22, and 8.01 μM, respectively, suggesting that nitro group led to inhibitory activity on hCA I only in *para* or *ortho* positions, whereas when in *meta*, as compound **10**, this electron-withdrawing function led to a decrease in potency (K_I > 100 μM).

- **TRP** and β-**TJP** were found inefficacious in inhibiting the physiologically relevant hCA II, whereas some derivatives showed a micromolar inhibition, thus confirming the *O*-derivatization to determine a gain in potency. In detail, the **TJP** isomers mixture of 3-chloropropyl (**2β+δ**) and 2-phenyl-oxadiazolyloxy (**14β+δ**) derivatives exhibited K_I values of 2.95 and 2.80 μM against hCA II, respectively, representing the most active derivatives of the series. Other promising compounds are the **TRP**-based compound with the acetyl moiety (**6**), 1-naphthylmethylene-oxy-**TRP** (**13**), and **13δ** with K_I values between 3.02 and 3.96 μM, and to a lesser extent, compound **4δ**, with alkyl linker between the two δ-**TJP**s, 4-bromobenzyloxy δ-**TJP** (**7δ**), 4-nitrobenzoate δ-**TJP** (**15δ**), and *p*-toluenesulfonate **δ-TJP** (**16δ**) with K_I values between 6.39 and 8.72 μM.
- Most of the synthesized compounds resulted in being inefficacious inhibiting hCA VA, with the best-in-class compound being the tosylate **17δ**, with a K_I value of 4.45 μM. It is interesting to note that the β-**TJP** analogue (**17β**, K_I = 39.0 μM) exhibited weaker inhibitory activity, whereas *p*-toluenesulfonate tropolone **17** was completely inactive on hCA VA (K_I > 100 μM), highlighting the importance of the presence of isopropyl group nearby ketone moiety instead of *O*-sulfonyl one, while compounds **2**, **2β+δ**, **6**, **7δ**, **11β**, and **12** exhibited K_i values between 6.63 and 9.56 μM. In detail, the **TRP** scaffold was favored than **TJP** core for compounds **2** (K_I = 8.75 μM) and **2β+δ** (K_I = 9.56 μM), while the elongation of the alkyloxy tail with two methylene moieties, and the substitution of chlorine with the bigger and more electron-withdrawing bromine, as in compound **3**, led to a dramatically decrease of activity of tropolone scaffold (K_I = 84.16 μM). Tropolone scaffold was recommended for acetyl derivatives (**6**, K_I = 8.11 μM), where the presence of isopropyl group led to an inefficacious compound (**6β+δ**, K_I > 100 μM). Among the benzyloxy derivatives, **TJP** was favored for 4-bromo- (**7δ**, K_I = 7.95 μM), and 2-nitrobenzyloxy (**11β**, K_I = 8.96 μM; **11δ**, K_I = 21.67 μM) compounds, whereas the substitution of the nitro group with the other electron-withdrawing trifluoromethyl one, in position 2, led to stronger results for tropolone derivative **12**, instead of TJP ones **12β** and **12δ**, with K_I values of 6.63, 83.51, and >100 μM, respectively. Further, independently from **TRP** and **TJP** scaffolds, the nitro group was not tolerated only in positions 4 (**9**, **9β+δ**, K_I > 100 μM) and 3 (**10**, **β+δ**, K_I > 100 μM). Moreover, β-**TJP** was moderately active in the inhibition of hCA VA, with a K_i of 7.50 μM.
- Both **TRP** and β-**TJP** did not display activity on hCA VII, while some of their derivatives showed a better profile. In particular, 4-bromobenzyloxy δ-**TJP** (**7δ**) exhibited a K_I of 0.96 μM, resulting in being the most potent derivative in this context, while its **TRP** analogue (**7**) resulted to be completely inactive, with K_I value > 100 μM. Among the alkyl derivatives, compounds **2**, **2β+δ**, and **3** exhibited moderate inhibitory activity on hCA VII, with K_I values of 5.20, 2.78, and 1.52 μM, respectively. The absence of isopropyl group of **6** increased more than 14-fold the inhibitory activity (**6**, K_I = 4.87 μM; **6β+δ**, K_I = 71.3 μM). Conversely, for benzyloxy compounds, **TRP** was not the first choice to reach potent hCA VII inhibitors, except for 2-trifluoromethyl derivative **12**, with K_I of 6.19 μM. Among the nitro derivatives, position 3 led to the most potent compound **10β+δ** (K_I = 2.78 μM) than position 4 (**9β+δ**, K_I = 33.91 μM) and position 2 (**11β**, K_I = 5.41 μM; **11δ**, K_I = 6.18 μM). It is interesting to note that the 4-nitrobenzoate, **15δ**, structurally similar to **9β+δ** resulted in being 3.5-fold more active. These data could be explained by the presence of carbonyl moiety, capable of accepting H-bonds, or for the presence of the single δ regioisomer. Nonetheless, δ-regioisomer led to slightly stronger inhibitory activity for *p*-tosylate derivatives (**17β**, K_I = 9.33 μM; **17δ**, K_I = 5.27 μM). Lastly, the bulkier naphthylmethylene-oxy moiety showed moderate inhibitory activity, where the **TRP** scaffold was more active than δ-**TJP** (**13**, K_I = 2.82 μM; **13δ**, K_I = 3.95 μM).
- As regards the two tumor-associated isoenzymes IX and XII, β-**TJP** emerged for moderate activity versus hCA IX (K_I = 23.88 μM). Several derivatives showed strong activity in the inhibition of hCA IX, with K_I values less than 1 μM. Indeed, the most active compounds against hCA IX are: **3** (K_i = 0.54 μM), **7δ** (K_i = 0.26 μM), **8β+δ** (K_i = 0.44 μM), **11δ** (K_i = 0.94 μM), **13δ** (K_i = 0.53 μM), **14β+δ** (K_i = 0.49 μM), **15δ** (K_i = 0.37 μM), **17β** (K_i = 0.42 μM), **17δ** (K_i = 0.40 μM). Other promising compounds are **1β+δ**, **2β+δ**, **4δ**, **6β+δ**, **10β+δ**, **11β**, **12**, **13** with K_I values between 1.41 and 4.30 μM. The bromo-alkyl **TRP 3** was the most selective compound toward hCA IX over hCA I and II, with a Selectivity Index (SI) > 185 for both hCA I and II (Selectivity Index was calculated as K_I of hCA I or II/K_I of hCA IX or XII). Whereas, the most potent compound, **7δ**, was not a selective hCA IX inhibitor, with a SI of 28.6 over hCA II. The replacement of bromine with another electron-withdrawing group as cyano in position 4 (**8β+δ**) led to a slight decrease of activity on hCA IX as well as an increase of selectivity over hCA II (SI = 159.6). If on the one hand nitro group did not show strong activity in positions 4 (**9** and **9β+δ**) and 3 (**10** and **10β+δ**), on the other hand, this moiety was suitable in position 2, especially for β- and δ-derivatives. Indeed, **11β** showed a K_I of 1.41 μM and the most active and selective **11δ** exhibited a K_I of 0.94 μM. The substitution of the nitro group in position 2 with trifluoromethyl one (**12β** and **12δ**) led to a dramatical decrease in activity, especially for δ-**TJP** scaffold. Further, the

Table 1
Inhibition data of **TRP**, **TJP**, and their derivatives, and reference compound **AAZ** on a panel of human (h) CA isoforms through the stopped-flow CO_2 hydration assay [33].

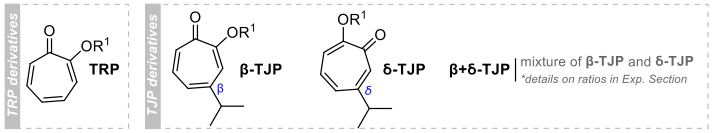

CPD	Core	R^1	K_I (μM)					
			hCA I	hCA II	hCA VA	hCA VII	hCA IX	hCA XII
TRP	TRP	-H	>100	>100	>100	>100	>100	>100
TJP	TJP	-H	4.98[a]	90.6	7.50	>100	23.9	>100
1	TRP		0.05	>100	>100	>100	19.0	7.76
1β+δ	TJP		0.66	76.0	>100	>100	2.29	>100
2	TRP		>100	44.5	8.75	5.20	8.94	6.74
2β+δ	TJP		>100	2.95	9.56	2.78	3.77	7.50
3	TRP	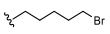	>100	>100	84.2	1.52	0.54	6.21
4δ	TJP	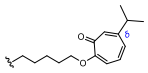	>100	6.36	31.6	7.10	1.33	73.7
6	TRP		>100	3.96	8.11	4.87	25.6	4.24
6β+δ	TJP		>100	>100	>100	71.3	2.53	6.36
7	TRP	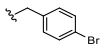	>100	>100	>100	>100	37.7	6.07
7δ	TJP		>100	7.44	7.95	0.96	0.26	4.57
8	TRP	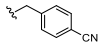	8.31	>100	>100	>100	>100	1.35
8β+δ	TJP		>100	70.2	14.2	9.62	0.44	8.09
9	TRP	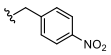	6.22	3.43	>100	>100	13.3	0.99
9β+δ	TJP		>100	>100	>100	33.9	39.5	5.84
10	TRP		>100	>100	>100	>100	34.5	2.64
10β+δ	TJP		>100	>100	>100	2.78	2.73	4.71
11	TRP		8.01	27.6	>100	>100	>100	1.60
11β	TJP		>100	41.4	8.96	5.41	1.41	4.52
11δ	TJP		>100	>100	21.7	6.18	0.94	3.57
12	TRP		>100	>100	6.63	6.19	4.30	3.11
12β	TJP		>100	>100	83.5	>100	47.4	54.6
12δ	TJP		>100	>100	>100	>100	>100	2.08
13	TRP	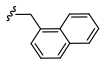	>100	3.70	61.1	2.82	2.28	7.28
13δ	TJP		>100	3.02	89.4	3.95	0.53	5.31
14β+δ	TJP	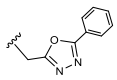	>100	2.80	>100	5.73	0.49	5.03
15	TRP	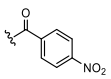	84.4	43.9	>100	>100	>100	1.20
15δ	TJP		>100	8.72	>100	9.60	0.37	5.23
16	TRP		>100	>100	85.6	>100	43.5	2.11
16β+δ	TJP		>100	>100	>100	>100	38.1	3.52
17	TRP		94.2	80.9	>100	>100	>100	>100
17β	TJP		>100	>100	39.0	9.33	0.42	4.37
17δ	TJP		>100	6.97	4.45	5.27	0.40	8.09
AAZ	Reference compound		0.25	0.01	0.06	0.002	0.03	0.01

K_I values are reported as means of three independent experiments. Errors are in the range of ± 5–10 % of the reported values.

presence of naphthylmethylene-oxy (**13**, K_I = 2.28 μM; **13β**, K_I = 0.49 μM) and 2-phenyloxadiazole (**14β+δ**, K_I = 0.49 μM) moieties led to selectivity only over hCA I. It is interesting to note that among the ester compounds, **TJP** scaffold always led to the strongest activity on hCA IX, indeed **15δ** was more than 270-fold stronger than **15**, while **17β** and **17δ** were 238- and 250-fold more active than **17**, respectively. Even though **17β** (SI > 238) was slightly weaker than **17δ**, the latter was less selective over hCA II (SI = 17.4).

- **TRP** and β-**TJP** resulted in being both inactive on hCA XII, nevertheless, their derivatives did not show strong inhibitory activity as for hCA IX, but, it is worth-noting that the strongest compounds are benzyloxy-**TRP** derivatives, like **8** (K_I = 1.35 μM), **9** (K_I = 0.99 μM), **10** (K_I = 2.64 μM), **11** (K_I = 1.60 μM), **15** (K_I = 1.20 μM), and **16** (K_I = 2.11 μM). All these compounds, except for the latter one, bear a nitro group. The adamantanoyl **16** was the most selective towards hCA XII over hCA I and II, with an SI of 47 for both isoforms. It is interesting to note that the introduction of acyl moiety in compound **15** led to a slight decrease (1.21-fold) of inhibitory activity with respect to **9.** **TRP** scaffold seems to be preferable, except for naphthylmethylene-oxy (**13**, K_I = 7.28 μM; **13β+δ**, K_I = 5.31 μM) and *p*-tosylate (**17**, K_I > 100 μM; **17β**, K_I = 4.37 μM; **17δ**, K_I = 8.09 μM) compounds.

In Fig. 4 the general SAR analysis about **TRP**- and **TJP**-derivatives as hCAs IX and XII inhibitors:

The significance of such inhibitory data could be assessed within the context of previously reported hCA inhibitors. In fact, the hCAs inhibitors landscape includes several chemical classes, with most potent chemotypes, such as benzenesulfonamides, are typically endowed with K_I values in the nanomolar or even sub-nanomolar range. However, they often suffer from a lack of isoform selectivity [34,35]. In contrast, coumarins, although being less potent (in the medium-to-high nanomolar range) show a better isoform selectivity, with a typical preference for isoforms other than the physiologically relevant hCAs I and II [36]. Conversely, inorganic ions are reported as high-micromolar or even millimolar inhibitors, with little discrimination among the isoforms [37], whereas phenols and polyphenols generally exhibit micromolar potency on several hCA isozymes [38,39].

In the light of such considerations, the herein-described tropolonoids, despite not exhibiting high inhibitory potency against the tested hCAs, seem to demonstrate a good isoform preference. Unfortunately, potency and selectivity of their inhibition do not follow a clear trend, as the compounds activity and selectivity vary on a case-by-case basis, depending on the structural features of each compound, as highlighted by the performed SAR analysis and summarized in Fig. 4.

2.4. Crystallographic structure of hCA II and β-TJP complex

The investigation of the binding poses of the compounds in the enzyme catalytic pocket started with crystallization studies on β-**TJP**. The crystallographic structure of hCA II complexed with β-**TJP** was obtained by soaking crystals of the enzyme in the inhibitor solution. Analysis of the electron density maps showed a clear density for the studied ligand, confirming its binding to the enzyme. The ligand forms bidentate coordination with the catalytic Zn(II) ion, with Zn–O bond distances of 2.17 and 2.20 Å (Fig. 5A). In the β-**TJP**-hCA II structure, the aromatic ring of the ligand establishes hydrophobic interactions with L198 and V121. Moreover, one of the oxygens on the β-**TJP** ring forms water-bridge hydrogen bonds with the peptide NH and the OH of T199, similar to the well-known interactions formed by the traditional

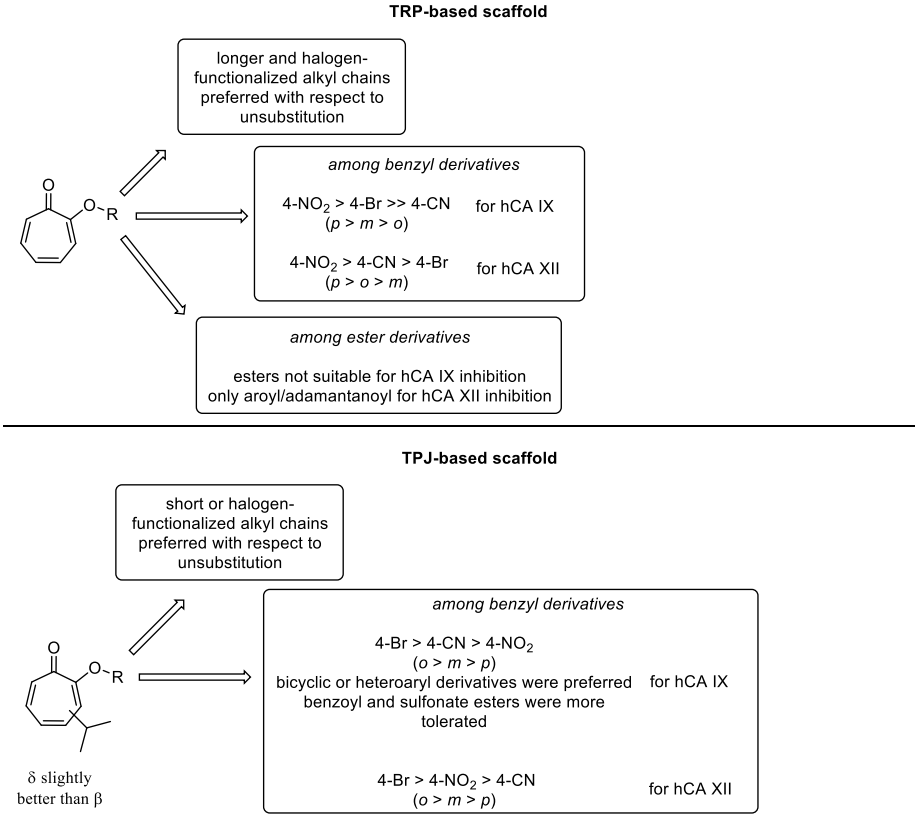

Fig. 4. Main SAR considerations against cancer-related isoforms visualized through substitution patterns.

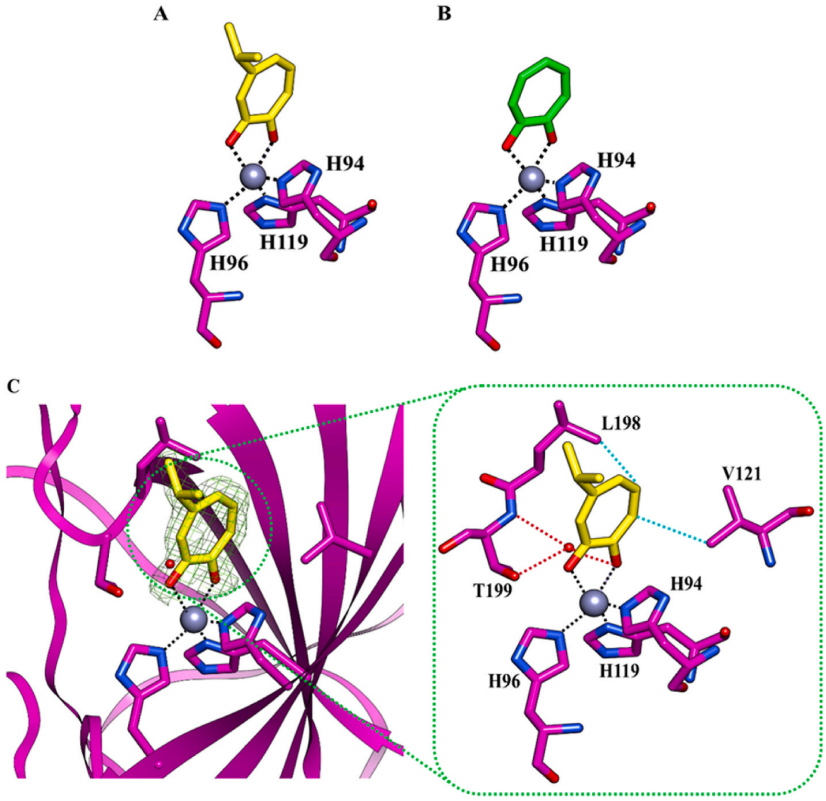

Fig. 5. The structures show the active site of CA II complexed with (**A**) β-**TJP** (PDB ID: 9H0W) and (**B**) **TRP** (PDB ID: 5THJ) [3]. The gray sphere represents the catalytic zinc ion while the coordination bonds are depicted as black dotted lines. (**C**) The active site of hCA II complexed with β-**TJP** (PDB ID: 9H0W). The ligands β-**TJP** and **TRP** are represented in yellow and green sticks, respectively. Residues involved in the binding of the inhibitor are also shown in magenta sticks. Water bridges and hydrophobic interactions are depicted as red and cyan dotted lines whereas coordination interactions are in gray dotted lines. The gray sphere represents the catalytic zinc ion. A |2Fo-Fc| map is shown for the ligand contoured at 1 sigma. (For interpretation of the references to colour in this figure legend, the reader is referred to the Web version of this article.)

sulfonamide inhibiting chemotype (Fig. 5C). Comparing our structure with that of hCA II with **TRP**, which was solved by Dick et al. [3] It is observed that both inhibitors adopt the same orientation and establish analogous interactions within the active site of hCA II (Fig. 5B).

2.5. *In silico investigation on hCAs and tropolonoid derivatives*

Modelling studies were carried out to investigate the binding mode and the energy interaction between the different hCA isoforms and **TRP** and **TJP** derivatives. Regarding the **TJP** derivatives in a mixture the recognition analysis was performed considering both the β-**TJP** and δ-**TJP** regioisomers.

Computational studies revealed that all the compounds are well accommodated in the targets' active site and are associated with a favorable energy interactions profile (data are reported in the Supplementary Material file, Tables S2-S4). In detail, the most active compounds (**1**, **1δ**, **11**, **9**, **8**) on hCA I are accommodated in the catalytic pocket engaging in an H-bond interaction with the Gln92. Interestingly, the 2-nitrobenzyloxy group of compound **11** forms a pi-stacking interaction with Phe91, while compound **8** through the 4-cyanobenzyloxy moiety establishes a pi-stacking interaction with His94 and metal coordination with the zinc ion (data are reported in the Supplementary Material file, Fig. S79).

Among the active compounds on the hCA II, zinc coordination is observed for compounds **2β+δ**, **6**, **4δ**, **9**, and **14β+δ**. The 3-chloropropyl tail of **2β+δ** establishes a halogen bond with Asn62, meanwhile the 4-bromobenzoxy function of **7δ** forms three halogen bond interactions: two with Thr199 and one with Thr200 (Fig. S80). Interestingly, we notice that among the analyzed **TJP** derivatives, compounds **2β+δ**, **4δ**, **7δ**, and **14β+δ** are involved in the same hydrophobic interactions observed in the **TJP**-hCA II crystallographic structure.

For hCA VA, the *p*-tosyl moiety of the most active compound **17δ** establishes a pi-stacking with the Tyr100, and through the carbonyl of β-**TJP** coordinates the metal in the binding site. Moreover, all other active compounds, β-**TJPs**, **2**, **2β+δ**, **6**, **7δ**, **12**, and **11β**, interact with the zinc ion of the binding site (Fig. S81). Furthermore, **6** is also involved in a salt-bridge interaction with Arg282, meanwhile, **11β** is engaged in a salt-bridge with Glu142.

Regarding the isoform VII, the 4-bromobenzyl tail of **7δ**, the most potent molecule in the inhibition of this isoform, establishes a halogen bond with Thr199, a pi-stacking interaction with His94 and an H-bond contact with Gln92. Moreover, the nitro derivative **10β+δ** is involved in the metal coordination and in two H-bond interactions with Gln67 and Thr199 residues (Fig. S82).

Analyzing the most active compounds on the hCA IX isoform we observed that most of them bind to the enzyme active site anchoring themselves to the catalytic zinc ion. Moreover, an interesting network of interactions takes place between ligands and the active site. In detail, the 4-bromobenzyloxy tail of **6δ** forms a halogen bond interaction with Glu106, while the chlorine atom of **2β+δ** forms the same interaction with Tyr11. The naphthyl portion of compound **13δ** is engaged in two

pi-stacking interactions with the imidazole ring of His94. Compounds **8β+δ** and **14β+δ** establish an H-bond interaction with Gln92 and a pi-stacking interaction with His94. Interestingly, **17β** isomer establishes the same interactions of the two last compounds and, in addition, is able to form another hydrogen bond with Thr201. Finally, the nitro derivative compound **11δ** establishes a hydrogen bond with Gln92 and a salt bridge interaction with Glu106 (Fig. 6).

The binding mode of most of the highly active compounds on the hCA XII isoform is characterized by the zinc atom coordination and polar interactions. Specifically, the adamantane derivatives **16** and **16β+δ** interact with the Gln92 via H-bond. The 4-nitrobenzyloxy **TRP9** and the cyano **TRP** derivative **8** are involved in a pi-stacking interaction with His94 and form an H-bond with Thr200. Conversely, **15**, through its nitro group, forms a salt bridge with Lys170 (Fig. 7).

2.6. Antiproliferative effect of representative tropolonoids on multiple myeloma cells

We investigated the antiproliferative activity of representative compounds of the series herein described using, as a model, multiple myeloma (MM), an incurable malignancy characterized by the accumulation of plasma cells in the bone marrow [40]. First, by Western blot we analyzed the protein expression levels of hCA IX and hCA XII in a panel of ten MM cell lines (namely AMO, AMO-BZB, NCI–H929, NCI–H929-BZB, NCI–H929-CFZ, KMS26, KMS26-BZB, MM1S, JJN3, U266) and peripheral blood mononuclear cells (PBMCs) from three different healthy donors. Results indicate that MM cell lines overexpress both hCAs IX and XII compared to healthy PBMCs, and hCA IX levels are overall higher than hCA XII in these cells (Fig. S83A in the Supplementary Material file). Thus, isoenzymes seem to play a crucial role in

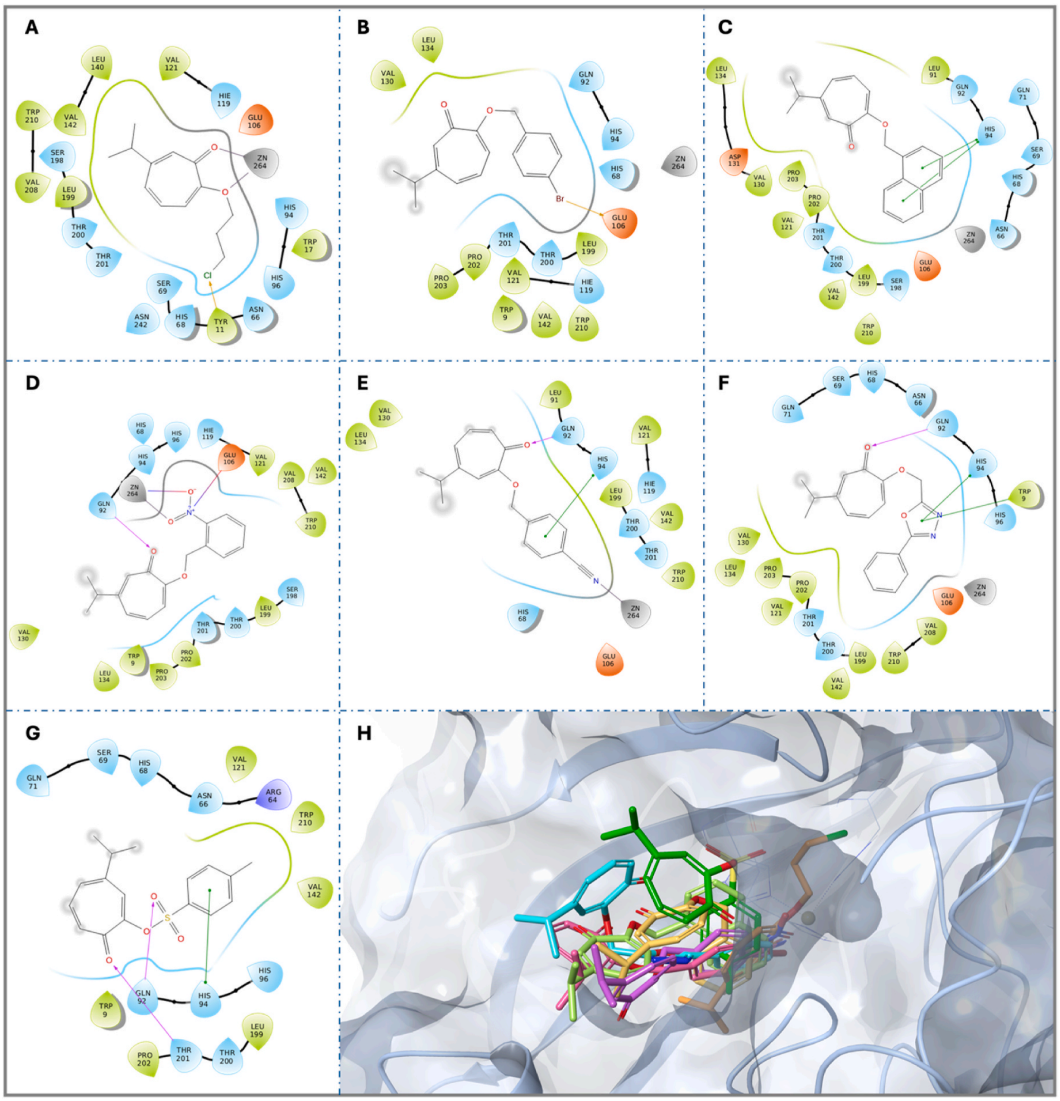

Fig. 6. 2D interaction diagram for compounds **A) 2δ**; **B) 7δ**; **C) 13δ**; **D) 11δ**; **E) 8β**; **F) 14δ**; **G) 17δ** in complex with hCA IX; **H)** shows the superposition of the seven most active compounds **2δ** (orange sticks), **7δ** (violet sticks), **13δ** (light green sticks), **11δ** (light yellow sticks), **8β** (magenta sticks), **14δ** (cyan sticks), and **17β** (green sticks). hCA IX is represented as a slate surface, the zinc ion and the coordinating histidine residues within the active site are shown as a yellow ball and slate sticks, respectively. For derivatives in mixture, the best-scored isomer is shown. (For interpretation of the references to colour in this figure legend, the reader is referred to the Web version of this article.)

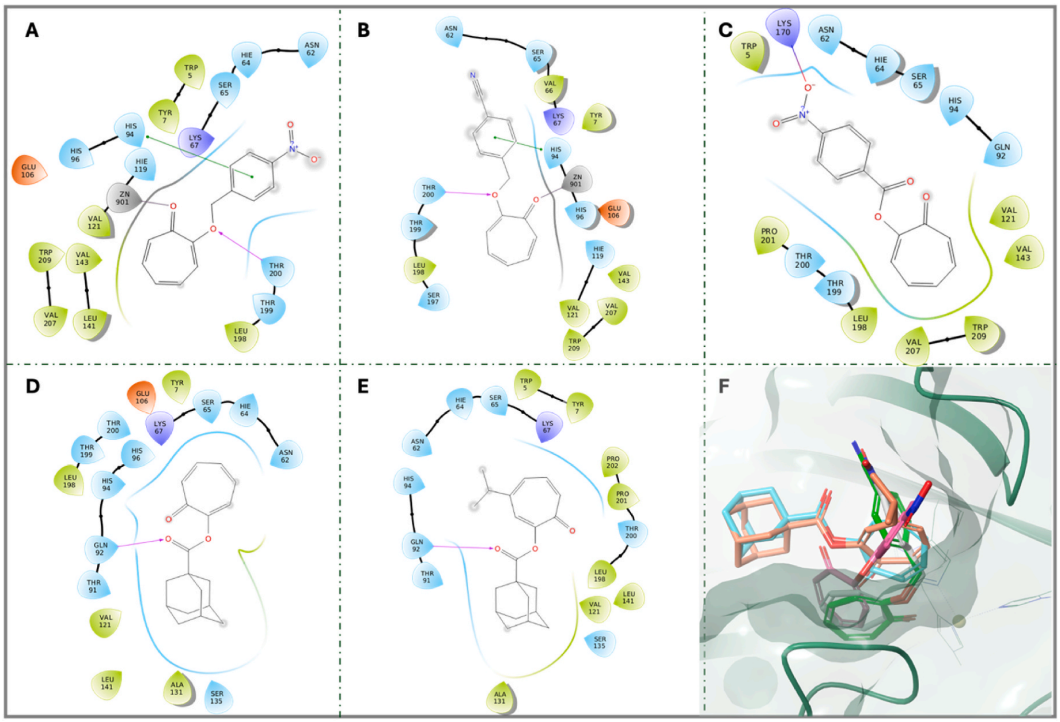

Fig. 7. 2D interaction diagram for **A**) **9**; **B**) **8**; **C**) **15**; **D**) **15**; **E**) **17β** compounds in complex with hCA XII; **F**) shows the superposition of the five most active compounds (**9** in white carbon sticks, **8** (green sticks), **15** (salmon sticks), **15** (cyan sticks), and **17β** (magenta sticks). hCA XII is represented as a forest surface, the zinc ion and the coordinating histidine residues withing the active site are shown as yellow a ball and forest sticks, respectively. For derivatives in mixture the best scored isomer is shown. (For interpretation of the references to colour in this figure legend, the reader is referred to the Web version of this article.)

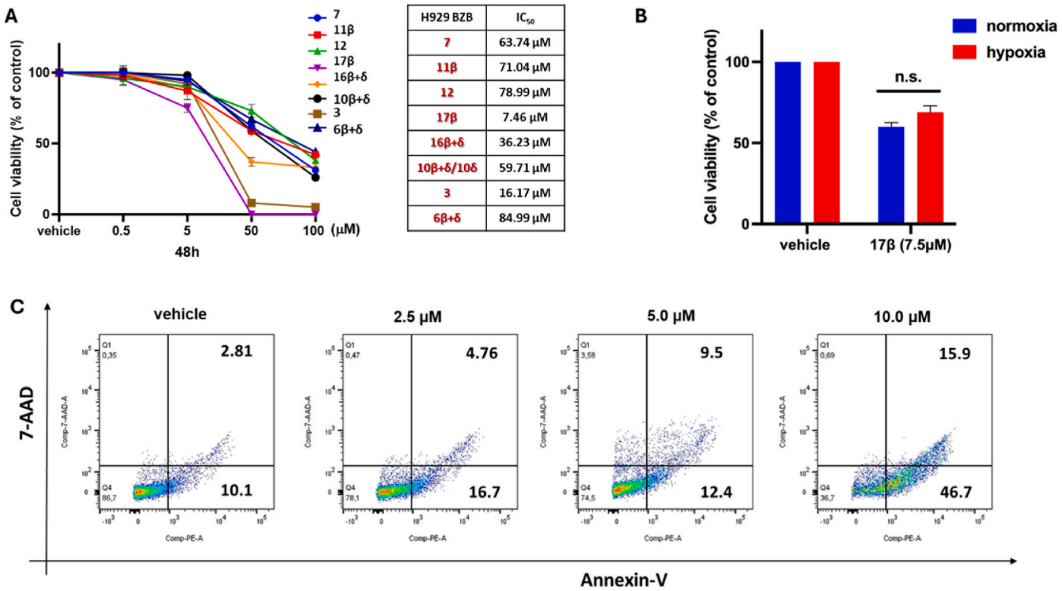

H929 BZB	IC_{50}
7	63.74 μM
11β	71.04 μM
12	78.99 μM
17β	7.46 μM
16β+δ	36.23 μM
10β+δ/10δ	59.71 μM
3	16.17 μM
6β+δ	84.99 μM

Fig. 8. **A**) Cell viability was evaluated using Cell Titer Glo assay (CTG) in H929-BZB cells treated with **TRP** derivatives; IC_{50} values are shown in the associated table. **B**) The viability of H929-BZB cells treated with 7.5 μM **17β** for 48 h, was evaluated under normoxic or hypoxic conditions, using the CTG assay; results are represented as the percentage of viable cells with respect to vehicle (DMSO); n.s.: not significant difference. **C**) Apoptosis was assessed via FACS analysis in H929-BZB treated for 48 h with **17β** at 2.5, 5, and 10 μM or vehicle (DMSO); dot plots show Annexin V-positive cells from independent biological replicates (n = 3). FACS quadrants: Q1, Q2, Q3, and Q4 represent dead cells (7-AAD+), late apoptosis cells (7-AAD + Annexin V+), early apoptosis cells (Annexin V+ 7-AAD−), living cells (7-AAD− Annexin V−), respectively.

the signature of these cells, being putative biomarkers for MM. According to these findings, the development of hCA IX and XII inhibitors could be a suitable and fully exploitable strategy to selectively target MM cells with no detrimental effect on healthy cells displaying low levels of such enzymes. Interesting pieces of information came from three of the investigated cell lines that showed a phenotype resistant to Bortezomib (BZB) (namely AMO-BZB, NCI–H929-BZB, KMS26-BZB) and one to Carfilzomib (CFZ) (namely NCI–H929-CFZ), two proteasome inhibitors. In fact, for most of these cell lines, the levels of hCA isoenzymes, especially hCA IX, seem to be slightly affected by the acquisition of drug resistance.

Thus, we selected NCI–H929-BZB cells to perform the *in vitro* evaluation of the antiproliferative effect for representative compounds (**6β**+**δ**, **3**, **7**, **12**, **11β**, **10δ**, **15β**, and **17β**). As a result, **17β** emerged as the compound with the lowest IC_{50} value (=7.46 μM, Fig. 8A), even capable of decreasing MM cell survival in hypoxic conditions (Fig. 8B), while sparing healthy PBMCs (Fig. S83B in the Supplementary Material file)

Since H929-BZB cells express high levels of hCA IX while neglectable levels of hCA XII, these data suggest that **17β** exerts anti-tumor activity against MM cell lines, even resistant to standard therapies, mainly via hCA IX inhibition, and can be thus considered *a bona fide* hCA IX inhibitor with low micromolar anti-MM activity. Moreover, FACS analysis indicates that treatment with **17β** can trigger potent pro-apoptotic activity, as demonstrated by the dose-dependent increase in Annexin V/7-AAD staining (Fig. 8C). Altogether, these findings indicate that compound **17β** exerts anti-MM activity with a safe toxicity profile on healthy cells.

2.7. Chemical stability of compound 17β

The presence of the tosyl ester moiety in **17β** prompted us to investigate its chemical stability at the pH values of the enzymatic assay. This was assessed by dissolving the compound in a mixture of DMSO-d_6/D_2O 1/1 *v/v* and monitoring it through ^{1}H NMR spectroscopy at different times (till 120 h). At t_0 (corresponding to the time of compound solubilization in the deuterated solvents and stirring), we could also slightly appreciate the presence of the signals of the two portions of the molecule **17β** after a limited hydrolysis, as evident by observing the aliphatic ppm range, till 120 h (^{1}H NMR overlapped spectra are provided in the Supplementary Material file, Fig. S84). However, further studies through HPLC-MS will be performed to confirm our hypothesis.

3. Conclusions

In agreement with our research interests to identify new scaffolds from natural sources worth investigating and developing for biomedical applications, we report a multidisciplinary study on *O*-substituted troponoloids. Specifically, the naturally occurring **TRP** and β-**TJP** were subjected to *O*-alkyl/acyl or sulfonyl substitutions under basic conditions to afford a large library of compounds that accounted for **TRP** *O*-derivatives and mixtures of β- and δ-**TJP** regioisomers depending on the keto-enolic rearrangement which takes place upon the deprotonation step. Although, in some cases, we were not able to separate the regioisomers resulting from the synthetic pathway, we decided to proceed with biological evaluation also for regioisomer mixtures after identifying the molar ratio they were present in the mixture. Compound regioisomeric structures were assigned by means of multidimensional- and NOESY-NMR experiments before being assessed *in vitro* for their ability to inhibit a panel of physio/pathologically relevant hCAs. Besides the effectiveness of the screened compounds in inhibiting such metalloenzymes along with variegate kinetic trends, it is worth highlighting that the reported K_I values constitute the first CA-directed structure-activity relationship (SAR) dataset on synthetic **TRP**-and **TJP**-*O*-derivatives. We are therefore confident that this work will contribute substantially to the field by giving first-hand structural information necessary to validate troponoloids as a new class of scaffolds endowed with biomedical features.

The binding mode of the natural product β-**TJP** within the hCA II catalytic cleft was assessed by means of X-ray crystallography of the hCA II/β-**TJP** complex. Electron density maps clearly showed bidentate coordination of the ligand with the catalytic Zn(II) ion further assisted by a network of water-bridged hydrogen bonds with the T199 residue, and thus similar to the canonical binding cluster reported for the prototypical CAIs of the sulfonamide type [41]. No relevant differences between hCA II/β-**TJP** and hCA II/**TRP** [3] were spotted also considering that the hydrophobic interactions with L198 and V121 place both ligands with identical orientations within the catalytic cleft.

Based on available experimental data, the binding modes of **TRP** and selected **TJP**-*O*-derivatives were predicted *in silico* on the mitochondrial hCA VA, hCA VII and the tumor-associated IX and XII isoforms. Finally, the selected **17β** isomer was studied for its chemical stability and screened along with other hCA IX/XII selective **TJP** derivatives for antiproliferative activity on multiple myeloma (MM) cell lines. The obtained data strongly indicated **17β** as a potent pro-apoptotic inducer with a safe toxicity profile on healthy cells used as a reference.

However, the bioactivity observed for the mixture of regioisomers is clearly the result of the combined effects of the two regioisomers individual effects, and, at the moment, we have limited knowledge regarding their combination, which could be synergistic, additive, or even antagonistic. However, observing the inhibitory data shown in Table 1, we could assume that no large differences in K_I values are generated by the isolated regioisomers. This seems to suggest that the regioisomerism does not significantly impact the affinity or bioactivity of the compound couples. Nevertheless, to confirm our hypothesis, we are still working on these compounds to gain and test the regioisomers individually, by exploring various separation techniques and regioselective syntheses. Overall, the data reported in our manuscript strongly support troponoloids as a new class of naturally occurring compounds potentially exploitable for biomedical applications by means of appropriate chemical manipulation. Further studies are currently ongoing in this direction.

4. Experimental section

4.1. Chemistry

4.1.1. General chemistry

All commercially available chemicals and solvents were used as purchased. Chromatographic separations were performed on columns packed with silica gel (230–400 mesh, for flash technique). Reactions were monitored through thin-layer chromatography (TLC) performed on 0.2-mm-thick silica gel-aluminum-backed plates (60 F254). TLC spot was visualized under short (254 nm) and long (365 nm) wavelengths ultra-violet irradiation and stained with basic permanganate stains. ^{1}H and ^{13}C NMR were recorded on a Bruker Avance spectrometer operating at 300/400/600 and 75/100/151 MHz, respectively. For compounds **8**, **9**, **11**, **15** and **17**, ^{1}H and ^{13}C NMR were recorded on a Varian Gemini 500 (Palo Alto, CA, USA) spectrometer operating at 500 and 125 MHz, respectively. Spectra are reported in parts per million (δ scale) and internally referenced to the $CDCl_3$, Acetone-d_6, CD_3OD, and DMSO-d_6 signal, respectively at δ 7.26, 2.05, 3.31, and 2.50 ppm. Data are shown as follows: chemical shift, multiplicity (s = singlet, d = doublet, t = triplet, q = quartet, qi = quintet, m = multiplet and/or multiplet resonances, br = broad signal), integration and coupling constants (*J*) in Hertz (Hz). Chemical shifts for carbon are reported in parts per million (*δ* scale) and referenced to the carbon resonances of the solvent ($CDCl_3$ at δ 77.0, CD_3OD at δ 49.0, and DMSO-d_6 at δ 39.0 ppm). Melting points were measured on a Stuart® melting point apparatus SMP3 (Merck s.r.l., Milan, Italy) and are uncorrected (temperatures are reported in °C). Elemental analyses for C, H, and N were recorded on a PerkinElmer 240 B microanalyzer and the analytical results were within ±0.4% of the

theoretical values for all compounds.

4.1.2. Synthetic procedures and characterization data for derivatives 1-16

4.1.2.1. General procedure for the synthesis of compounds 13, 7-14. Potassium carbonate (4.0 equivalents) was added in a solution of **TRP** or **TJP** (1.0 equivalent) and the proper halide (1.5 equivalents for the alkyl halides, whereas 3.0 equivalents for benzyl ones) in refluxing acetonitrile (0.4 M). Then, the reaction mixture was poured into an oversaturated aqueous solution of Na_2CO_3 and extracted with DCM three times. The combined organic layers were dried over sodium sulfate anhydrous, filtered, and evaporated *in vacuo* to obtain the crude product. The compounds were purified through flash column chromatography, employing silica gel and the suitable eluent (i.e., *n*-hexane/ethyl acetate, *n*-hexane/diethyl ether, DCM/MeOH).

2-(prop-2-yn-1-yloxy)cyclohepta-2,4,6-trienone (1). Orangish solid; m.p. 88–89 °C; 54 % yield. **^{1}H NMR** (600 MHz, $CDCl_3$): δ 2.54 (t, J = 2.4 Hz, 1H, C ≡ CH), 4.88 (s, 2H, OCH_2), 6.90 (dddd, J = 10.8, 5.3, 3.9, 0.8 Hz, 1H, Ar), 6.96 (d, J = 9.8 Hz, 1H, Ar), 7.03–7.10 (m, 1H, Ar), 7.21–7.24 (m, 2H, Ar). **^{13}C NMR** (151 MHz, $CDCl_3$) δ 56.7, 115.8, 129.2, 132.4, 138.0, 163.2. Anal. calcd for $C_{10}H_8O_2$: C, 74.99; H, 5.03. Found: C, 74.84; H, 5.09. Characterization data are in agreement with the previous literature [42,43].

4-isopropyl-2-(prop-2-yn-1-yloxy)cyclohepta-2,4,6-trienone (1β+δ). β:δ ratio assessed by ^{1}H NMR analysis: 55:45. The reported IUPAC name is referred to as the β isomer. Black-brown oil; 49 % yield. **^{1}H NMR** (600 MHz, $CDCl_3$): δ 1.28 (d, J = 12.0 Hz, 6H, CH_3 iPro), 1.33 (d, J = 12.0 Hz, 6H, CH_3 iPro), 2.61–2.62 (m, 2H, 2 x C ≡ CH), 2.89–2.93 (m, 2H, 2 x CH iPro), 4.92 (d, J = 6.0 Hz, 2H, OCH_2), 4.96 (d, J = 6.0 Hz, 2H, OCH_2), 6.86–6.88 (m, 1H, Ar), 6.90–6.91 (m, 1H, Ar), 6.94 (s, 1H, Ar), 7.03–7.08 (m, 2H, Ar), 7.15–7.32 (m, 3H, Ar). **^{13}C NMR** (75 MHz, $CDCl_3$): δ 22.0, 22.2, 38.3, 38.9, 56.4, 76.6, 76.8, 114.7, 117.8, 125.9, 130.6, 131.2, 135.1, 135.9, 136.9, 153.9, 157.6, 162.1, 162.4, 180.3. Anal. calcd for $C_{13}H_{14}O_2$: C, 77.20; H, 6.98. Found: C, 77.14; H, 7.01.

2-(3-chloropropoxy)cyclohepta-2,4,6-trienone (2). Orange oil; 86 % yield. **^{1}H NMR** (300 MHz, $CDCl_3$): δ 2.70 (qi, 2H, CH_2), 3.80 (q, 2H, $ClCH_2$), 4.20 (t, J = 6.15 Hz, 2H, OCH_2), 6.77–6.90 (m, 2H, Ar), 7.03–7.06 (m, 1H, Ar), 7.22–7.40 (m, 2H, Ar). **^{13}C NMR** (75 MHz, $CDCl_3$): δ 31.6, 41.4, 65.7, 114.1, 128.5, 133.0, 136.8, 137.2, 164.8, 180.3. Anal. calcd for $C_{10}H_{11}ClO_2$: C, 60.46; H, 5.58. Found: C, 60.53; H, 5.61.

2-(3-chloropropoxy)-4-isopropylcyclohepta-2,4,6-trienone (2β+δ). β:δ ratio assessed by ^{1}H NMR analysis: 50:50. The reported IUPAC name is referred to as the β isomer. Yellow oil; 57 % yield. **^{1}H NMR** (300 MHz, $CDCl_3$): δ 1.73 (d, J = 6.9 Hz, 6H, CH_3 iPro), 1.77 (d, J = 6.3 Hz, 6H, CH_3 iPro), 2.84–2.89 (m, 4H, 2 x CH_2), 3.26–3.37 (m, 2H, 2 x CH iPro), 4.30 (q, 4H, 2 x $ClCH_2$), 4.66–4.75 (m, 4H, 2 x OCH_2), 7.18–7.33 (m, 3H, Ar), 7.50 (q, 1H, Ar), 7.65–7.82 (m, 4H, Ar). **^{13}C NMR** (75 MHz, $CDCl_3$): δ 23.6, 24.0, 32.2, 32.3, 38.9, 39.5, 42.0, 66.0, 113.5, 116.3, 122.8, 125.7, 128.2, 130.2, 132.3, 135.1, 135.7, 137.6, 137.8, 154.9, 158.3, 164.6, 180.6. Anal. calcd for $C_{13}H_{17}ClO_2$: C, 64.86; H, 7.12. Found: C, 64.81; H, 7.09.

2-((5-bromopentyl)oxy)cyclohepta-2,4,6-trienone (3). Yellow oil; 21 % yield. **^{1}H NMR** (300 MHz, Acetone-d_6/$CDCl_3$ mixture to improve solubility): δ 1.48–1.63 (m, 2H, CH_2), 1.85–1.98 (qi, 4H, CH_2), 3.24 (t, J = 6.2 Hz, 2H, CH_2Cl), 4.03 (t, J = 6.2 Hz, 2H, OCH_2), 6.72 (d, J = 9.9 Hz, 1H, Ar), 6.78–6.84 (m, 1H, Ar), 7.03 (t, J = 10.2 Hz, 1H, Ar), 7.08–7.11 (m, 2H, Ar). **^{13}C NMR** (75 MHz, Acetone/$CDCl_3$ mixture to improve solubility): δ 24.7, 27.9, 32.3, 33.5, 69.0, 113.2, 127.8, 132.6, 136.3, 137.1, 180.6. Anal. calcd for $C_{12}H_{15}BrO_2$: C, 53.16; H, 5.58. Found: C, 53.11; H, 5.55.

2-((4-bromobenzyl)oxy)cyclohepta-2,4,6-trienone (7). Pale yellow solid; m.p. 99–101 °C; 55 % yield. **^{1}H NMR** (600 MHz, $CDCl_3$): δ 5.18 (s, 2H, OCH_2), 6.70–6.77 (m, 1H, Ar), 6.84 (dddd, J = 10.8, 7.0, 2.2, 0.6 Hz, 1H, Ar), 6.96 (ddt, J = 10.8, 9.7, 1.0 Hz, 1H, Ar), 7.25–7.18 (m, 2H, Ar), 7.30 (d, J = 8.7 Hz, 1H, Ar), 7.49 (d, J = 8.4 Hz, 1H, Ar). **^{13}C NMR** (151 MHz, $CDCl_3$) δ 70.2, 115.1, 122.3, 128.6, 128.9, 132.0, 132.5, 134.5, 136.5, 137.7, 164.3, 180.8. Anal. calcd for $C_{14}H_{11}BrO_2$: C, 57.76; H, 3.81. Found: C, 57.84; H, 3.86.

2-((4-bromobenzyl)oxy)-6-isopropylcyclohepta-2,4,6-trienone (7δ). Pale red solid; m.p. 76–77 °C; 52 % yield. **^{1}H NMR** (400 MHz, $CDCl_3$): δ 1.21 (d, J = 12.0 Hz, 6H, CH_3 iPro), 2.74–2.79 (qi, 1H, CH iPro), 5.17 (s, 2H, OCH_2), 6.62 (d, J = 12.0 Hz, 1H, Ar), 6.74–6.92 (m, 2H, Ar), 7.19 (s, 1H, Ar), 7.25–7.31 (m, 2H, Ar), 7.49 (d, J = 10.0 Hz, 2H, Ar). **^{13}C NMR** (75 MHz, $CDCl_3$): δ 22.0, 37.7, 71.8, 118.6, 122.0, 124.6, 129.3, 131.8, 135.1, 136.0, 136.4, 153.9, 164.9, 180.5. Anal. calcd for $C_{17}H_{17}BrO_2$: C, 61.28; H, 5.14. Found: C, 61.36; H, 5.11.

4-{[(7-Oxocyclohepta-1,3,5-trien-1-yl)oxy]methyl}benzonitrile (8). Off-white powder; m.p. 143–145 °C; 48 % yield. **^{1}H NMR** (500 MHz, DMSO-d_6): 5.27 (s, 2H, OCH_2), 6.94 (dd, J = 10.6 Hz and 8.4 Hz, 1H, Ar), 7.04–7.06 (m, 2H, Ar), 7.12–7.16 (m, 1H, Ar), 7.29–7.33 (m, 1H, Ar), 7.64 (d, J = 7.8 Hz, 2H, Ar), 7.87 (d, J = 7.8 Hz, 2H, Ar). **^{13}C NMR** (125 MHz, DMSO-d_6): δ 67.5, 115.3, 125.4, 128.9, 129.6, 129.7, 132.2, 133.6, 134.7, 137.1, 147.5, 163.8, 179.6. Characterization data are in agreement with the previous literature [44].

4-(((3-isopropyl-7-oxocyclohepta-1,3,5-trien-1-yl)oxy)methyl) benzonitrile (8β+δ). β:δ ratio assessed by ^{1}H NMR analysis: 50:50. The reported IUPAC name is referred to as the β isomer. Brownish oil; 70 % yield. **^{1}H NMR** (600 MHz, $CDCl_3$): δ 1.15 (d, J = 7.0 Hz, 6H, CH_3 iPro), 1.23 (d, J = 6.6 Hz, 6H, CH_3 iPro), 2.71–2.79 (m, 2H, 2 x CH iPro), 5.26 (s, 2H, OCH_2), 5.31 (s, 2H, OCH_2), 6.64 (d, J = 9.5 Hz, 2H, Ar), 6.70 (s, 2H, Ar), 6.79 (d, J = 8.8 Hz, 2H, Ar), 6.81 (dd, J = 11.4, 1.5 Hz, 2H, Ar), 6.92 (dd, J = 11.2, 9.7 Hz, 2H, Ar), 7.12 (d, J = 11.4 Hz, 2H, Ar), 7.19 (dd, J = 12.1, 8.8 Hz, 2H, Ar), 7.19 (d, J = 1.5 Hz, 2H, Ar), 7.57 (d, J = 8.1 Hz, 2H, Ar), 7.59 (d, J = 8.4 Hz, 2H, Ar), 7.67 (d, J = 6.6 Hz, 2H, Ar), 7.68 (d, J = 7.0 Hz, 2H, Ar). **^{13}C NMR** (151 MHz, $CDCl_3$): δ 23.0, 23.1, 38.3, 38.7, 69.5, 69.7, 112.0, 114.3, 117.6, 118.5, 118.5, 125.8, 127.4, 127.4, 130.4, 131.1, 132.5, 135.0, 135.8, 136.9, 141.0, 141.2, 153.6, 157.6, 162.9, 163.1, 180.1, 180.2. Anal. calcd for $C_{18}H_{17}NO_2$: C, 77.40; H, 6.13; N, 5.01. Found: C, 77.49; H, 6.16; N, 5.08.

2-((4-Nitrobenzyl)oxy)cyclohepta-2,4,6-trien-1-one (9). Off-white powder; m.p. 164–166 °C; 48 % yield. **^{1}H NMR** (500 MHz, DMSO-d_6): 5.33 (s, 2H, OCH_2), 6.92–6.94 (m, 1H, Ar), 7.05–7.07 (m, 2H, Ar), 7.13–7.17 (m, 1H, Ar), 7.30–7.32 (m, 1H, Ar), 7.71 (d, J = 8.2 Hz, 2H, Ar), 8.26 (d, J = 8.2 Hz, 2H, Ar). **^{13}C NMR** (125 MHz, DMSO-d_6): δ 69.2, 115.2, 124.1, 128.7, 128.9, 133.4, 137.1, 137.2, 144.3, 147.6, 163.9, 179.7. Characterization data are in agreement with the previous literature [45].

4-isopropyl-2-((4-nitrobenzyl)oxy)cyclohepta-2,4,6-trienone (9β+δ). β:δ ratio assessed by ^{1}H NMR analysis: 50:50. The reported IUPAC name is referred to as the β isomer. Orange solid; m.p. 92–94 °C; 75 % yield. **^{1}H NMR** (400 MHz, $CDCl_3$): 1.16 (d, J = 8.0 Hz, 6H, CH_3 iPro), 1.24 (d, J = 8.0 Hz, 6H, CH_3 iPro), 2.74–2.82 (m, 2H, 2 x CH iPro), 5.30 (s, 2H, OCH_2), 5.35 (s, 2H, OCH_2), 6.66 (d, J = 8.0 Hz, 1H, Ar), 6.73 (s, 1H, Ar), 6.81 (t, J = 8.0 Hz, 2H, Ar), 6.92 (t, J = 9.7 Hz, 1H, Ar), 7.13–7.25 (m, 3H, Ar), 7.64 (t, J = 8.9 Hz, 4H, Ar), 8.24 (dd, J = 7.1, 4.1 Hz, 4H, Ar). **^{13}C NMR** (75 MHz, $CDCl_3$): δ 23.0, 23.2, 38.4, 38.7, 69.4, 69.5, 114.5, 117.8, 124.0, 125.9, 127.5, 127.6, 130.6, 131.1, 135.1, 136.0, 137.0, 143.0, 143.2, 153.7, 157.7, 162.9, 180.1, 180.2. Anal. calcd for $C_{17}H_{17}NO_4$: C, 68.22; H, 5.72; N, 4.68. Found: C, 68.28; H, 5.74; N, 4.63.

2-((3-nitrobenzyl)oxy)cyclohepta-2,4,6-trienone (10). Pale pink solid; m.p. 130–132 °C; 77 % yield. **^{1}H NMR** (400 MHz, $CDCl_3$): δ 5.30 (s, 2H, OCH_2), 6.81 (d, J = 9.8 Hz, 1H, Ar), 6.85–6.97 (m, 1H, Ar), 7.02 (t, J = 8.1 Hz, 1H, Ar), 7.25 (m, 2H, Ar), 7.59 (t, J = 8.0 Hz, 1H, Ar), 7.86 (d, J = 7.7 Hz, 1H, Ar), 8.20 (d, J = 7.8 Hz, 1H, Ar), 8.29 (s, 1H, Ar). **^{13}C NMR** (100 MHz, $CDCl_3$): δ 64.1, 110.0, 115.0, 121.6, 122.8, 128.6, 129.4, 131.8, 132.8, 136.0, 137.2, 137.4, 163.4, 180.0. Anal. calcd for $C_{14}H_{11}NO_4$: C, 65.37; H, 4.31; N, 5.45. Found: C, 65.42; H, 4.35; N, 5.49.

4-isopropyl-2-((3-nitrobenzyl)oxy)cyclohepta-2,4,6-trienone

(10β+δ). β:δ ratio assessed by ^{1}H NMR analysis: 50:50. The reported IUPAC name is referred to as the β isomer. Yellow oil; 39 % yield. **^{1}H NMR** (600 MHz, $CDCl_3$): δ 1.18 (d, J = 7.0 Hz, 6H, CH_3 iPro), 1.24 (d, J = 6.6 Hz, 6H, CH_3 iPro), 2.75–2.82 (m, 2H, 2 x CH iPro), 5.29 (s, 2H, OCH_2), 5.34 (s, 2H, OCH_2), 6.73 (d, J = 9.9 Hz, 1H, Ar), 6.80 (s, 1H, Ar), 6.80 (d, J = 10.0 Hz, 1H, Ar), 6.82 (dd, J = 11.0, 1.5 Hz, 1H, Ar), 6.95 (dd, J = 11.0, 9.9 Hz, 1H, Ar), 7.12 (d, J = 12.5 Hz, 1H, Ar), 7.19 (d, J = 3.6 Hz, 1H, Ar) 7.19 (t, J = 10.3 Hz, 1H, Ar), 7.56–7.60 (m, 2H, Ar), 7.84 (d, J = 7.7 Hz, 1H, Ar), 7.87 (d, J = 7.7 Hz, 1H, Ar), 8.14–8.16 (m, 2H, Ar), 8.29 (t, J = 1.0, 1H, Ar), 8.33 (t, J = 1.0, 1H, Ar). **^{13}C NMR** (151 MHz, $CDCl_3$): δ 23.0, 23.2, 38.3, 38.7, 69.5, 69.6, 114.6, 118.0, 122.1, 122.2, 123.2, 125.9, 129.9, 130.5, 131.3, 133.3, 133.4, 135.0, 135.9, 137.0, 137.8, 138.1, 148.4, 153.8, 157.6, 163.0, 163.2, 180.1, 180.2. Anal. calcd for $C_{17}H_{17}NO_4$: C, 68.22; H, 5.72; N, 4.68. Found: C, 68.29; H, 5.68; N, 4.73.

2-((2-Nitrobenzyl)oxy)cyclohepta-2,4,6-trien-1-one (11). Off-white powder; m.p. 151–153 °C; 43 % yield. **^{1}H NMR** (500 MHz, DMSO-d_6): 5.52 (s, 2H, OCH_2), 6.96 (dd, J = 10.4 Hz and 8.2 Hz, 1H, Ar), 7.06–7.09 (m, 2H, Ar), 7.14–7.18 (m, 1H, Ar), 7.30–7.32 (m, 1H, Ar), 7.63–7.64 (m, 1H, Ar), 7.88–7.88 (m, 2H, Ar), 8.14–8.16 (dd, 1H, J = 8.2 Hz and 1.1 Hz, 1H, Ar). **^{13}C NMR** (125 MHz, DMSO-d_6): δ 67.5, 115.3, 125.4, 128.9, 129.6, 129.7, 132.2, 133.5, 134.7, 137.1, 137.2, 147.5, 163.8, 179.6. Characterization data are in agreement with the previous literature [44].

4-isopropyl-2-((2-nitrobenzyl)oxy)cyclohepta-2,4,6-trienone (11β). Yellow solid; m.p. 139–141 °C; 52 % yield. **^{1}H NMR** (600 MHz, $CDCl_3$): δ 1.19 (d, J = 6.6 Hz, 6H, CH_3 iPro), 2.78–2.80 (m, 1H, CH_3 iPro), 5.62 (s, 2H, OCH_2), 6.76 (s, 1H, Ar), 6.80 (d, J = 8.4 Hz, 1H, Ar), 7.15 (d, J = 12.1 Hz, 1H, Ar), 7.20 (dd, J = 12.5, 8.4 Hz, 1H, Ar), 7.51 (td, J = 7.8, 0.8 Hz, 1H, Ar), 7.73 (td, J = 7.6, 1.1 Hz, 1H, Ar), 8.10 (d, J = 7.7 Hz, 1H, Ar), 8.19 (dd, J = 8.1, 1.1 Hz, 1H, Ar). **^{13}C NMR** (151 MHz, $CDCl_3$): δ 23.2, 38.8, 67.4, 117.0, 125.0, 125.6, 128.6, 128.9, 132.6, 134.5, 135.7, 137.0, 146.6, 154.0, 163.0, 180.1. Anal. calcd for $C_{17}H_{17}NO_4$: C, 68.22; H, 5.72; N, 4.68. Found: C, 68.13; H, 5.67; N, 4.74. Characterization data are in agreement with the previous literature [26].

6-isopropyl-2-((2-nitrobenzyl)oxy)cyclohepta-2,4,6-trienone (11δ). Yellow solid; m.p. 139–140 °C; 31 % yield. **^{1}H NMR** (600 MHz, $CDCl_3$): δ 1.24 (d, J = 6.8 Hz, 6H, CH_3 iPro), 2.76–2.81 (m, 1H, CH_3 iPro), 5.58 (s, 2H, OCH_2), 6.71 (d, J = 9.5 Hz, 1H, Ar), 6.82 (dt, J = 11.0 Hz, 1H, Ar), 6.96 (ddd, J = 11.2, 10.2, 1.2 Hz, 1H, Ar), 7.21 (s, 1H, Ar), 7.50 (t, J = 7.9 Hz, 1H, Ar), 7.72 (t, J = 7.5 Hz, 1H, Ar), 8.08 (d, J = 8.1 Hz, 1H, Ar), 8.20 (d, J = 8.1 Hz, 1H, Ar). **^{13}C NMR** (151 MHz, $CDCl_3$): δ 23.0, 38.4, 67.4, 113.9, 125.0, 128.6, 128.7, 130.3, 131.4, 132.6, 134.6, 134.9, 146.4, 157.6, 163.2, 180.2. Anal. calcd for $C_{17}H_{17}NO_4$: C, 68.22; H, 5.72; N, 4.68. Found: C, 68.27; H, 5.76; N, 4.73.

2-((3-(trifluoromethyl)benzyl)oxy)cyclohepta-2,4,6-trienone (12). Pale pink solid; m.p. 99–100 °C; 58 % yield. **^{1}H NMR** (300 MHz, $CDCl_3$): δ 5.22 (s, 2H, OCH_2), 6.76–7.03 (m, 3H, Ar), 7.23–7.26 (m, 2H, Ar), 7.48–7.7.67 (m, 4H, Ar). **^{13}C NMR** (75 MHz, $CDCl_3$): δ 70.1, 115.2, 123.9, 125.1, 125.1, 128.7, 129.3, 130.6, 132.2, 136.4, 136.5, 137.7, 164.1, 180.6. Anal. calcd for $C_{15}H_{11}F_3O_2$: C, 64.29; H, 3.96. Found: C, 64.33; H, 3.91.

4-isopropyl-2-((3-(trifluoromethyl)benzyl)oxy)cyclohepta-2,4,6-trienone (12β). Orange oil; 31 % yield. **^{1}H NMR** (400 MHz, $CDCl_3$): δ 1.15–1.22 (m, 6H, CH_3 iPro), 2.75–2.87 (m, 1H, CH iPro), 5.38 (s, 2H, OCH_2), 6.77–6.90 (m, 2H, Ar), 7.22 (t, J = 3.7 Hz, 2H, Ar), 7.57 (t, J = 7.4 Hz, 1H, Ar), 7.65 (d, J = 7.4 Hz, 1H, Ar), 7.74 (d, J = 8.7 Hz, 2H, Ar). **^{13}C NMR** (100 MHz, $CDCl_3$): δ 23.1, 38.8, 70.2, 117.6, 123.9, 124.0, 125.1, 125.7, 129.4, 130.6, 135.8, 136.9, 138.7, 153.8, 163.1, 180.3. Anal. calcd for $C_{18}H_{17}F_3O_2$: C, 67.07; H, 5.32. Found: C, 67.00; H, 5.29.

6-isopropyl-2-((3-(trifluoromethyl)benzyl)oxy)cyclohepta-2,4,6-trienone (12δ). Orange oil; 36 % yield. **^{1}H NMR** (400 MHz, $CDCl_3$): δ 1.26 (tt, J = 6.7, 3.6 Hz, 6H, CH_3 iPro), 2.81 (quint, 1H, CH iPro), 5.28 (s, 2H, OCH_2), 6.72 (d, J = 9.7 Hz, 1H, Ar), 6.83 (d, J = 11.2, 1H, Ar), 6.96 (t, J = 10.5 Hz, 1H, Ar), 7.53 (t, J = 7.8 Hz, 1H, Ar), 7.61 (d, J = 8.0 Hz, 1H, Ar), 7.66–7.44 (m, 2H, Ar). **^{13}C NMR** (75 MHz, $CDCl_3$): δ 22.0, 38.4, 70.0, 114.3, 123.9, 123.9, 125.0, 125.1, 129.3, 130.3, 131.2, 135.0, 136.6, 157.6, 163.4, 180.3. Anal. calcd for $C_{18}H_{17}F_3O_2$: C, 67.07; H, 5.32. Found: C, 67.16; H, 5.36.

2-(naphthalen-1-ylmethoxy)cyclohepta-2,4,6-trienone (13). Orange solid; m.p. 116–117 °C; 75 % yield. **^{1}H NMR** (300 MHz, $CDCl_3$): δ 5.65 (s, 2H, OCH_2), 6.84–6.60 (m, 3H, Ar), 7.23 (t, J = 6.5 Hz, 2H, Ar), 7.42–7.62 (m, 4H, Ar), 7.82–7.91 (m, 2H, Ar), 8.04 (d, J = 7.8 Hz, 1H, Ar). **^{13}C NMR** (75 MHz, $CDCl_3$) δ 69.5, 115.4, 123.1, 125.3, 126.0, 126.0, 126.6, 128.4, 128.8, 129.0, 130.6, 131.0, 132.5, 133.7, 136.3, 137.6, 164.6, 180.7. Anal. calcd for $C_{18}H_{14}O_2$: C, 82.42; H, 5.38. Found: C, 82.46; H, 5.42.

6-isopropyl-2-(naphthalen-1-ylmethoxy)cyclohepta-2,4,6-trienone (13δ). Pale red solid; m.p. 93–94 °C; 52 % yield. **^{1}H NMR** (400 MHz, $CDCl_3$): δ 1.23 (d, J = 12.0 Hz, 6H, CH_3 iPro), 2.75–2.79 (m, 1H, CH iPro), 5.68 (s, 2H, OCH_2), 7.75 (d, J = 9.0 Hz, 1H, Ar), 6.84–6.88 (m, 1H, Ar), 7.21 (s, 1H, Ar), 7.41–7.60 (m, 4H, Ar), 7.81–7.90 (dd, J = 13.4, 12.0 Hz, 2H, Ar), 8.04 (d, J = 12.0 Hz, 1H, Ar). **^{13}C NMR** (75 MHz, $CDCl_3$): δ 23.0, 38.3, 69.3, 114.5, 123.2, 125.3, 126.0, 126.6, 128.8, 128.9, 129.9, 130.7, 131.0, 131.4, 133.7, 134.9, 157.3, 163.9, 180.5. Anal. calcd for $C_{21}H_{20}O_2$: C, 82.86; H, 6.62. Found: C, 82.92; H, 6.66.

4-isopropyl-2-((5-phenyl-1,3,4-oxadiazol-2-yl)methoxy)cyclohepta-2,4,6-trienone (14β+δ). β:δ ratio assessed by ^{1}H NMR analysis: 50:50. The reported IUPAC name is referred to as the β isomer. Brownish oil; yield 30 %. **^{1}H NMR** (300 MHz, DMSO-d_6): δ 1.14–1.18 (m, 12H, 2 x CH_3 iPro), 2.72–2.88 (m, 2H, 2 x CH iPro), 5.52 (s, 2H, OCH_2), 5.62 (s, 2H, OCH_2), 6.90–6.97 (m, 4H, Ar), 7.08–7.11 (m, 3H, Ar), 7.27 (dd, J = 12.3, 9.0 Hz, 1H, Ar), 7.57–7.65 (m, 6H, Ar), 7.98–8.01 (m, 4H, Ar). **^{13}C NMR** (75 MHz, DMSO-d_6): δ 25.9, 26.1, 42.3, 42.6, 64.3, 120.5, 123.5, 127.0, 130.6, 131.2, 131.3, 132.3, 133.0, 135.5, 136.1, 136.5, 138.1, 139.0, 142.6, 159.6, 164.1, 166.0, 166.1, 166.3, 166.4, 170, 184.2. Anal. calcd for $C_{19}H_{18}N_2O_3$: C, 70.79; H, 5.63, N, 8.69. Found: C, 70.72; H, 5.60, N, 8.75.

4.1.3. Synthesis of derivative 4δ

7,7'-(pentane-1,5-diylbis(oxy))bis(3-isopropylcyclohepta-2,4,6-trienone) (4δ). Potassium carbonate (4.0 equivalents) was added in a solution of β-**TJP** (2.0 equivalents) and 1,5-dibromopentane (1.0 equivalent for the alkyl halides, whereas 3.0 equivalents for benzyl ones) in refluxing acetonitrile (0.4 M). Then, the reaction mixture was poured into an oversaturated aqueous solution of Na_2CO_3 and extracted with DCM three times. The combined organic layers were dried over sodium sulfate anhydrous, filtered, and evaporated *in vacuo* to obtain the crude product. The compound was purified through flash column chromatography, employing silica gel and a mixture of 5% MeOH in 95% DCM as mobile phase.

Orangish oil; 19 % yield. **^{1}H NMR** (300 MHz, $CDCl_3$): δ 1.22 (d, J = 3.0 Hz, 6H, CH_3 iPro), 1.25 (d, J = 3.0 Hz, 6H, CH_3 iPro), 1.54–1.76 (m, 2H, CH iPro), 1.54–1.70 (m, 4H, 2 x CH_2), 1.96–2.01 (m, 3H, CH_2), 2.73–2.77 (m, 2H, CH iPro), 2.81–2.83 (m, 1H, CH iPro), 4.02–4.10 (m, 3H, OCH_2), 6.61–6.64 (m, 1H, Ar), 6.68 (m, 1H, Ar), 6.73–6.77 (m, 2H, Ar), 6.96 (m, 1H, Ar), 7.07–7.09 (m, 1H, Ar), 7.12–7.16 (m, 2H, Ar). **^{13}C NMR** (75 MHz, $CDCl_3$): δ 22.7, 23.2, 23.5, 28.2, 28.3, 28.4, 29.8, 32.3, 38.4, 39.1, 62.6, 69.0, 112.6, 115.2, 124.7, 129.3, 131.8, 134.5, 135.2, 136.9, 154.4, 157.6, 164.3, 164.4, 180.2, 180.4. Anal. calcd for $C_{25}H_{32}O_4$: C, 75.73; H, 8.13. Found: C, 75.80; H, 8.16.

4.1.4. Synthesis of derivatives 6 and 6β+δ

Ethyl bromoacetate (1.5 equivalents) was added to a mixture of **TRP** (1.0 equivalent) for **5** or **TJP** (1.0 equivalent) for **5β+δ** and K_2CO_3 (2.0 equivalents) in acetonitrile (0.4 M). The suspension was allowed to reflux overnight. Then, the reaction mixture was poured into an oversaturated aqueous solution of Na_2SO_4 and extracted with DCM three times. The combined organic layers were dried over anhydrous sodium sulfate, filtered and evaporated under reduced pressure. Both

intermediates were purified through column chromatography, with a mixture of *n*-hexane/ethyl acetate 97:3. To reach compounds **6** and **6β+δ**, **5** (1.0 equivalent) or **5β+δ** (1.0 equivalent) was dissolved in THF (0.12 M), whereas lithium hydroxide monohydrate (LiOH x H_2O) was dissolved in water (0.5 M). The aqueous solution was added to the organic solution dropwise, and the mixture was allowed to stir at room temperature for 2 h. Once reaction was completed, the mixture was diluted with water, and the pH was adjusted about 3.0. The reaction mixture was extracted with EtOAc for three times, dried over anhydrous sodium sulfate, filtered and evaporated under reduced pressure to obtain compound **6** and **6β+δ**.

2-((7-oxocyclohepta-1,3,5-trien-1-yl)oxy)acetic acid (6). Yellowish solid; m.p. 119–120 °C; 51 % yield. **^{1}H NMR** (600 MHz, DMSO-d_6): δ 4.83 (s, 2H, OCH_2), 6.90 (d, J = 9.9 Hz, 1H, Ar), 6.95 (dd, J = 10.8, 8.2, 1H, Ar), 7.05 (d, J = 12.1, 1H, Ar), 7.13 (m, 1H, Ar), 7.32 (m, 1H, Ar). **^{13}C NMR** (151 MHz, DMSO-d_6): δ 65.6, 115.4, 129.1, 133.5, 137.2, 137.4, 163.8, 169.6, 179.7. Anal. calcd for $C_9H_8O_4$: C, 60.00; H, 4.48. Found: C, 60.09; H, 4.52. Characterization data are in agreement with the previous literature [46].

2-((3-isopropyl-7-oxocyclohepta-1,3,5-trien-1-yl)oxy)acetic acid (6β+δ). β:δ ratio assessed by ^{1}H NMR analysis: 57:43. The reported IUPAC name is referred to as the β isomer. Yellow oil; 80 % yield. **^{1}H NMR** (300 MHz, $CDCl_3$): δ 1.25 (d, J = 7.2 MHz, 6H, CH_3 iPro), 1.30 (d, J = 7.2 MHz, 6H, CH_3 iPro), 2.82–2.90 (m, 1H, CH iPro), 2.91–3.02 (m, 1H, CH iPro), 3.93 (s, 2H, OCH_2), 3.98 (s, 2H, OCH_2), 7.02–7.14 (m, 4H, Ar), 7.19–7.32 (m, 2H, Ar), 7.39–7.46 (m, 1H, Ar). **^{13}C NMR** (75 MHz, $CDCl_3$): δ 22.0, 22.3, 38.4, 38.8, 55.4, 113.5, 115.6, 125.7, 125.7, 129.7, 129.7, 133.0, 133.2, 133.5, 133.5, 138.7, 138.7, 156.4, 160.1, 174.7, 174.7. Anal. calcd for $C_{12}H_{14}O_4$: C, 68.85; H, 6.35. Found: C, 68.80; H, 6.31.

4.1.5. General procedure for the synthesis of compounds 15 and 15δ

p-Nitrobenzoic acid (1.2 equivalents) was added to a stirring mixture of *N,N′*-dicyclohexylcarbodiimide (DCC) (1.5 equivalents) and dimethylaminopyridine (DMAP) (0.2 equivalents) in dry DCM (0.2 M) at room temperature under N_2. After the formation of the intermediate (ca. h), **TRP** or β-**TJP** (1.0 equivalent) was added, and the mixture was stirred for additional 24 h. Then, the reaction mixture was diluted with DCM and filtrated under vacuum to remove *N,N′*-dicyclohexylurea (DCU). The filtrate was then evaporated to give the crude product. The compound was purified through flash column chromatography, employing silica gel and the suitable eluent (mixtures of *n*-hexane/ethyl acetate)

7-Oxocyclohepta-1,3,5-trien-1-yl-4-nitrobenzoate (15). Off-white powder; 80 % yield, m.p. 175–177 °C **^{1}H NMR** (500 MHz, DMSO-d_6): 7.29–7.7.46 (m, 5H, Ar), 8.31 (d, J = 8.3 Hz, 2H, Ar), 8.40 (d, J = 8.8 Hz, 2H, Ar). Melting point data agree with the previous literature [47].

5-isopropyl-7-oxocyclohepta-1,3,5-trien-1-yl 4-nitrobenzoate (15δ). Orange oil; 60 % yield. **^{1}H NMR** (600 MHz, $CDCl_3$): 1.27 (d, J = 6.0 Hz, 6H, CH_3 iPro), 2.81–2.86 (m, 1H, CH iPro), 7.03 (d, J = 12 Hz, 1H, Ar), 7.13 (t, J = 9.0, 6.0 Hz, 1H, Ar), 7.22 (d, J = 12 Hz, 1H, Ar), 7.26 (d, J = 6.0 Hz, 1H, Ar), 8.32–8.36 (m, 4H, Ar). **^{13}C NMR** (151 MHz, $CDCl_3$): δ 23.0, 38.5, 123.7, 131.7, 134.6, 151.0, 162.4. Anal. calcd for $C_{17}H_{15}NO_5$: C, 65.17; H, 4.83; N, 4.47. Found: C, 65.22; H, 4.85; N, 4.50.

4.1.6. General procedure for the synthesis of compounds 16 and 16β+δ

TRP or β-**TJP** (1.0 equivalent) was added to a mixture of triethylamine (TEA) (2.0 equivalents) and DMAP (0.1 equivalents) in DCM (0.25 M) at 0 °C. Then, 1-adamantanecarbonyl chloride was added to the mixture and the yellowish reaction mixture was allowed to stir at room temperature for 48 h. Then, the reaction mixture was poured into water and extracted with DCM three times. The combined organic layers were dried over sodium sulfate anhydrous, filtered, and evaporated *in vacuo* to obtain the crude product. The compound was purified through flash column chromatography, employing silica gel and the suitable eluent (mixtures of DCM/MeOH).

7-oxocyclohepta-1,3,5-trien-1-yl adamantane-1-carboxylate (16). Yellow solid; m.p.: 118–120 °C; 65 % yield. **^{1}H NMR** (300 MHz, $CDCl_3$): δ 1.76 (t, J = 2.7 Hz, 6H, adamantane), 2.08 (d, J = 6.6 Hz, 9H, adamantane), 7.14–7.18 (m, 5H, Ar). **^{13}C NMR** (75 MHz, $CDCl_3$): δ 27.9, 36.4, 38.8, 41.2, 133.0, 133.9, 175.0. Anal. calcd for $C_{18}H_{20}O_3$: C, 76.03; H, 7.09. Found: C, 76.10; H, 7.03.

3-isopropyl-7-oxocyclohepta-1,3,5-trien-1-yl adamantane-1-carboxylate (16β+δ). β:δ ratio assessed by ^{1}H NMR analysis: 85:15. The reported IUPAC name is referred to as the β isomer. Yellow solid; m.p.: 46–48 °C; 41 % yield. **^{1}H NMR** (300 MHz, $CDCl_3$/Acetone mixture): δ 1.40 (d, J = 6.9 Hz, 6H, 2 x CH_3 iPro), 1.44 (d, J = 6.9 Hz, 6H, 2 x CH_3 iPro), 1.93 (s, 12H, adamantane), 2.25 (d, J = 8.4 Hz, 18H, adamantane), 2.91–3.08 (m, 2H, 2 x CH iPro), 7.10–7.11 (m, 2H, Ar), 7.20–7.27 (m, 4H, Ar), 7.43–7.52 (m, 1H, Ar). **^{13}C NMR** (75 MHz, $CDCl_3$): δ 22.9, 23.4 27.8, 28.0, 36.4, 36.5, 38.8, 41.1, 122.3, 132.0, 133.1, 133.5, 155.2, 175.1. Anal. calcd for $C_{21}H_{26}O_3$: C, 77.27; H, 8.03. Found: C, 77.20; H, 8.06.

4.1.7. General procedure for the synthesis of compounds 17, 17β and 17δ

Toluene 4-sulfonyl chloride (1.2 equivalents) in DCM (1.0 M) was added dropwise to a DCM (5.5 M solution of **TRP** or β-**TJP** (1.0 equivalent) and TEA (1.3 equivalents) at 0 °C. Then, the reaction mixture was allowed to stir at room temperature for 5 days. Then, the reaction mixture was poured into water and extracted with DCM three times. The combined organic layers were dried over sodium sulfate anhydrous, filtered, and evaporated *in vacuo* to obtain the crude product. The compound was purified through flash column chromatography, employing silica gel and the suitable eluent (mixtures of *n*-hexane/ethyl acetate).

(7-Oxocyclohepta-1,3,5-trien-1-yl)-4-methylbenzenesulfonate (17) Off-white powder, m.p. 157–159 °C, 88 % yield. **^{1}H NMR** (500 MHz, DMSO-d_6): 2.41 (s, 3H, $ArCH_3$), 7.08–7.11 (m, 2H, Ar), 7.24 (dd, J = 10.8, 8.3 Hz, 1H, Ar), 7.36–7.41 (m, 2H, Ar), 7.46 (d, 1H, J = 8.3 Hz, 2H, Ar), 7.81 (d, 1H, J = 8.3 Hz, 2H, Ar). Characterization data are in agreement with the previous literature [48].

3-isopropyl-7-oxocyclohepta-1,3,5-trien-1-yl 4-methylbenzenesulfonate (17β). White solid, 48 % yield. **^{1}H NMR** (600 MHz, $CDCl_3$): δ 1.23 (d, J = 6.0 Hz, 6H, CH_3 iPro), 2.43 (s, 3H, $ArCH_3$), 2.77–2.82 (m, 1H, CH iPro), 6.91–6.93 (m, 1H, Ar), 7.01–7.03 (m, 1H, Ar), 7.13 (dd, J = 15.0, 6.0 Hz, 1H, Ar), 7.34 (d, J = 6.0 Hz, 2H, Ar), 7.38 (d, J = 6.0 Hz, 1H, Ar), 7.91 (d, J = 12.0 Hz, 2H, Ar). **^{13}C NMR** (151 MHz, $CDCl_3$): δ 21.8, 22.8, 38.2, 128.7, 129.7, 130.4, 131.8, 133.6, 137.0, 139.0, 145.5, 152.5, 154.6, 179.0. Anal. calcd for $C_{17}H_{18}O_4S$: C, 64.13; H, 5.70. Found: C, 64.05; H, 5.75. Characterization data are in agreement with the previous literature [28].

5-isopropyl-7-oxocyclohepta-1,3,5-trien-1-yl 4-methylbenzenesulfonate (17δ). White solid, 58 % yield. **^{1}H NMR** (600 MHz, $CDCl_3$): δ 1.20 (d, J = 6.0 Hz, 6H, CH_3 iPro), 2.44 (s, 3H, $ArCH_3$), 2.72–2.76 (m, 1H, CH iPro), 6.87–6.90 (m, 1H, Ar), 6.87–6.99 (m, 1H, Ar), 7.06–7.07 (m, 1H, Ar), 7.35 (d, J = 6.0 Hz, 3H, Ar), 7.93 (d, J = 6.0 Hz, 2H, Ar). **^{13}C NMR** (151 MHz, $CDCl_3$): δ 21.8, 22.8, 34.5, 128.7, 129.3, 129.6, 129.7, 133.7, 136.6, 138.0, 145.5, 154.8, 157.4, 179.3. Anal. calcd for $C_{17}H_{18}O_4S$: C, 64.13; H, 5.70. Found: C, 64.18; H, 5.72. Characterization data are in agreement with the previous literature [28].

4.2. NMR analysis of regioisomers 10β+δ, 8β+δ, 11β, and 11δ

The solvents used for NMR analysis were purchased from EurIsotop (Saint-Aubin, France). Samples were dissolved in $CDCl_3$ and tetramethylsilane (TMS) was used as an internal reference. Full ^{1}H and ^{13}C assignments were made based on one- and two-dimensional NMR spectra (^{1}H, ^{13}C, COSY, NOESY, HSQC, and HMBC). All spectra were recorded at 25 °C on a Bruker Avance AV600 (Bruker Corporation, Billerica, Massachusetts, US) equipped with a 5 mm diameter BBO probe with a z-gradient accessory. NOESY spectra were obtained with a mixing time of

500 ms. The spectra were acquired using standard Bruker pulse sequences and the data was processed using ACD Spectrus software. Fully assigned NMR spectra with experimental parameters can be found in the Supplementary Material file.

4.3. X-ray crystallography

4.3.1. Crystallization and X-ray data collection

Crystals of the hCA II isoform were obtained using the hanging drop vapor diffusion method in a 24-well VDX plate. 1 μL of 10 mg/mL of hCA II in Tris–HCl 50 mM (pH 8.0) was mixed with 1 μL of a solution of 1.5 M sodium citrate, 20 mM Tris-HCl (pH 8.0) and equilibrated against 500 μL of the same solution at 296 K. Crystal growth was observed after five days. The protein complex with β-**TJP** was prepared by soaking the crystals in the mother liquor solution containing the inhibitor at a concentration of 10 mM for 3 h. Then, all crystals were flash-frozen at 100 K using a solution obtained by adding 15 % (*v/v*) PEG 400 to the mother liquor solution as a cryoprotectant. X-ray diffraction data were collected using synchrotron radiation at the ID30B beamline at ESRF (Grenoble, France) with a wavelength of 0.87313 Å and a DECTRIS Eiger2 X 9 M detector.

4.3.2. Structure determination

The crystal structures of hCA II (PDB ID: 3HS4) without solvent molecules and other heteroatoms were used to obtain the initial phases of the structures using Refmac5 [49] from the CCP4 package [50]. Coordinates of the inhibitor were obtained using the program JLigand [51] and introduced in the model. 5 % of the unique reflections were selected randomly and excluded from the refinement data set for R_{free} calculations. The initial |Fo–Fc| difference electron density maps unambiguously showed the inhibitor molecules. The inhibitor was introduced in the model with 1.0 occupancy. Refinements proceeded using standard protocols of positional, and isotropic atomic displacement parameters alternating with the manual building of the models using COOT [52]. Inhibitor-enzyme interactions were analyzed using the PLIP web tool [53]. Atomic coordinates were deposited in the PDB (PDB ID: 9H0W) and reported in Table 2. Graphical representations were generated with UCSF Chimera [54].

Table 2
Summary of data collection and atomic model refinement statistics for hCA II.

Data collection statistics	
	hCA II-β-TJP
PDB ID	9H0W
Wavelength (Å)	0.87313
Space Group	P 1 21 1
Unit cell (a, b, c, α, β, γ) (Å,°)	42.23, 41.05, 71.92, 90, 104.26, 90
Limiting resolution (Å)	41.05–1.44 (1.46–1.44)
Unique reflections	43458 (2148)
Rmerge	0.094 (1.250)
Rmeas	0.102 (1.355)
Redundancy	6.7 (6.8)
Completeness overall (%)	99.9 (100.0)
<I/σ(I)>	11.8 (1.5)
CC (1/2)	0.999 (0.522)
Refinement statistics	
Resolution range (Å)	41.05–1.44
Rfactor	0.1656
Rfree	0.1958
r.m.s.d. bonds (Å)	0.0105
r.m.s.d. angles (°)	1.9004
Ramachandran statistics (%)	
Most favored	97.3
additionally allowed	2.7
Outlier regions	0.0
Average B factor (Å²)	
All atoms	20.83
Inhibitor	23.00
Solvent	29.41

4.4. Carbonic anhydrases inhibition assays

An Applied Photophysics stopped-flow instrument was used to evaluate the ability of the test compounds to inhibit the CA-catalyzed CO_2 hydration [33]. 0.2 mM Phenol red was chosen as an indicator (absorbance maximum = 557 nm), with 20 mM HEPES (pH 7.4) as a buffer, and 20 mM Na_2SO_4 (to maintain constant the ionic strength), following the initial rates of the CA-catalyzed CO_2 hydration reaction for a period of 10–100 s. The CO_2 concentrations ranged from 1.7 to 17 mM for the determination of the kinetic parameters and inhibition constants. Enzyme concentrations spanned from 5 to 12 nM. Stock solutions of the inhibitor (0.1 mM) were prepared in distilled–deionized water and dilutions up to 0.01 nM were prepared with the assay buffer. Inhibitor and enzyme solutions were preincubated for 15 min at r.t. for the formation of the E–I complex. The inhibition constants were obtained by non-linear least-squares methods using PRISM 3 and the Cheng-Prusoff equation and represent the mean from at least three different determinations. Apart from hCAs I and II purchased from Merck, all the other CAs are recombinant and obtained *in-house.* [55–57].

4.5. Molecular modeling

4.5.1. Library preparation

The library of the compound was prepared by means of the LigPrep tool. Hydrogens were added, salts were removed, and ionization states were calculated using Epik at pH 7.4 ± 0.2 and then were submitted to MacroModel energy minimization, using OPLS_2005 as force field [58, 59].

4.5.2. Target preparation

The X-ray crystallographic structures of hCAs I, II, VII, IX, and XII isoforms were retrieved from the PDB IDs: 2NMX, 3K34, 3ML5, 5FL4, and 1JD0, respectively. For the hCA VA isoform, the model prepared according to our previously published work was used [60]. The receptor structures were optimized by means of the Protein Preparation Wizard tool [61], using OLPS_2005 as the force field. Residual crystallographic buffer components and water molecules were removed, hydrogen atoms were added, missing side chains were built using the Prime module, and side chains protonation states at pH 7.4 were assigned.

4.5.3. Molecular docking and eMBrAcE studies

In order to evaluate the reliability of our molecular recognition approach, redocking calculations by using the Glide Standard Protocol (SP) algorithm were performed. As reported in Table 3, Root Mean Square Deviation (RMSD) values, calculated between the best docking pose and the ligand co-crystallized into the catalytic binding site, demonstrate a reproduction of the experimentally determined binding modes for all examined models.

Molecular docking was carried out with Glide v. 8.9 software, by using the Standard Precision (SP) algorithm, and 25 poses per ligand were generated. [62,63]. Starting from the best docking pose of each compound post-docking energy minimization was performed by using the eMBrAcE tool [64] and the binding energies (E) of the receptor-ligand complexes were calculated [65].

Table 3
PDB IDs and RMSD values calculated between the best docking pose and the ligand co-crystallized.

hCA isoform	PDB IDs	RMSD values (Å)
I	2NMX	1.01
II	3K34	1.13
VII	3ML5	0.33
IX	5FL4	0.27
XII	1JD0	0.63

4.6. Chemical stability

5.0 mg of **17β** were dissolved in 0.5 mL of DMSO-d_6/D_2O 1/1 *v/v* and ^1H NMR spectra were recorded at t_0, 4, 6, 24, 48, 72, and 120 h to assess chemical stability of the sulfonate ester.

4.7. Antiproliferative assays

4.7.1. MM cell lines

MM cell lines NCI–H929, U266, MM1S, and JJN3 were purchased from DSMZ, with certified authentication performed by short tandem repeat DNA typing. NCI–H929 cells resistant to BZB (namely NCI–H929 BZB) and CFZ (namely NCI–H929 CFZ) were obtained following progressive exposure to increasing concentrations of proteasome inhibitors and kept at the final concentration of 20 nM of the two drugs. AMO and AMO BZB cells were kindly provided by Dr. C. Driessen (University of Tubingen, Germany). KMS26, KMS26 BZB were kindly provided by Prof. Antonino Neri (University of Milan).

All these cell lines were immediately frozen and used from the original stock within 6 months. Cells were cultured in RPMI-1640 medium enriched with 10 % heat-inactivated fetal bovine serum (FBS) (Gibco®, Life Technologies, Carlsbad, CA), 100 μg/mL streptomycin (P/S) (Gibco®, Life Technologies, Carlsbad, CA), and 100 U/mL of penicillin. MM cells were incubated at 37 °C in a 5 % CO_2 atmosphere; for hypoxic conditions, cells were incubated in a dedicated Eppendorf Galaxy 48R incubator in 1 % O_2.

PBMCs were isolated using Ficoll-Hypaque density gradient sedimentation (Lonza Group, Basel, Switzerland), following the approval of the Institutional Review Board n. 266/2021 (University of Catanzaro, Italy).

4.7.2. Western blotting

Cell lysis was performed in NP40 Cell Lysis Buffer supplemented with Halt Protease Inhibitor Single-Use Cocktail (Thermo Fisher Scientific, Waltham, MA, USA). Protein samples (30 μg) were subjected to 10 % SDS-PAGE, and the gels were dry-transferred onto nitrocellulose membranes using the Trans-Blot Turbo Transfer System (Bio-Rad Laboratories, Hercules, CA, USA), followed by incubation with following Abs purchased from Cell Signaling Technology: CA IX (#5649S), CA XII (#5864S), GAPDH (#5174). Densitometry was performed using the ImageJ software.

4.7.3. Cell viability assay

Cell viability was evaluated by Cell Titer Glo (CTG) assay kit (Promega, Madison, WI, USA), according to manufacturer's instructions. Briefly, MM cells were seeded in 24-well plates and, after 48 h of treatment with tropolonoids, collected and plated in 96 well white plates. Treated cells were incubated in both normoxic and hypoxic conditions. Luminescence was recorded using the GloMax Multi Detection System (Promega, Madison, WI, USA). IC_{50} values were evaluated using GraphPad Prism software.

4.7.4. Apoptosis assay

Apoptosis was evaluated by Annexin-V/7-Aminoactinomycin D (7-AAD) staining and flow cytometric analysis using the PE Annexin-V Apoptosis Detection Kit I (Thermo Fisher Scientific, Waltham, MA, USA). After treatment with 16β compound, MM cells were collected in a 5 mL polystyrene tube, washed with PBS 1X, and exposed to Annexin V-PE and 7-AAD probes for 15 min at room temperature. After incubation, the samples were analyzed using a FACS Fortessa X-20 instrument (BD Biosciences, San Jose, CA, USA), and the data were analyzed using FlowJo software version 10. The histogram bars indicate the percentage of early and late apoptotic cells.

CRediT authorship contribution statement

Francesco Melfi: Formal analysis. **Ilaria D'Agostino:** Formal analysis. **Simone Carradori:** Conceptualization. **Fabrizio Carta:** Writing – original draft. **Andrea Angeli:** Formal analysis. **Giosuè Costa:** Methodology. **Gioele Renzi:** Methodology. **Ana Čikoš:** Formal analysis. **Daniela Vullo:** Formal analysis. **Josip Rešetar:** Formal analysis. **Marta Ferraroni:** Formal analysis. **Chiara Baroni:** Formal analysis. **Francesca Mancuso:** Formal analysis. **Rosaria Gitto:** Writing – review & editing. **Francesca Alessandra Ambrosio:** Formal analysis. **Emanuela Marchese:** Investigation. **Roberta Torcasio:** Investigation. **Nicola Amodio:** Resources, Methodology, Investigation, Formal analysis. **Clemente Capasso:** Writing – original draft, Formal analysis, Data curation. **Stefano Alcaro:** Writing – review & editing, Supervision, Data curation. **Claudiu T. Supuran:** Writing – review & editing, Supervision, Funding acquisition, Conceptualization.

Declaration of competing interest

The authors declare that they have no known competing financial interests or personal relationships that could have appeared to influence the work reported in this paper.

The authors declare no competing interests.

Data availability

Additional data could be made available on request to the corresponding authors.

Funding sources

This work was supported by a grant from the Italian Ministry of University and Research for financial support under the FISR program, project FISR_04819 BacCAD to C.T.S., C.C., and S.C. N.A. was supported by an AIRC IG24449 grant.

Declaration of competing interest

The authors declare the following financial interests/personal relationships which may be considered as potential competing interests: Simone Carradori reports financial support was provided by Italian Ministry of University and Research. This work was supported by a grant from the Italian Ministry of University and Research for financial support under the FISR program, project FISR_04819 BacCAD to C.T.S., C. C., and S.C. N.A. was supported by an AIRC IG24449 grant If there are other authors, they declare that they have no known competing financial interests or personal relationships that could have appeared to influence the work reported in this paper.

Acknowledgements

This research was partially supported by the Italian Ministry for University and Research (MIUR) grant number FISR2019_04819 BacCAD to S.C., C.C. and C.T.S. This article is based upon work from COST Action EURESTOP, CA21145, supported by COST (European Cooperation in Science and Technology) to S.C., A.C., and I.D.A. N.A. was supported by an AIRC IG24449 grant.

Appendix A. Supplementary data

Supplementary data to this article can be found online at https://doi.org/10.1016/j.ejmech.2025.117552.

Data availability

Data will be made available on request.

References

[1] M. Ebisawa, K. Ohta, E. Kawachi, H. Fukasawa, Y. Hashimoto, H. Kagechika, Novel retinoidal tropolone derivatives. Bioisosteric relationship of tropolone ring with benzoic acid moiety in retinoid structure, Chem. Pharm. Bull. (Tokyo) 49 (2001) 501–503, https://doi.org/10.1248/cpb.49.501.

[2] F. Pietra, Seven-membered conjugated carbo- and heterocyclic compounds and their homoconjugated analogs and metal complexes. Synthesis, biosynthesis, structure, and reactivity, Chem. Rev. 73 (1973) 293–364, https://doi.org/10.1021/cr60284a002.

[3] B.L. Dick, A. Patel, J.A. McCammon, S.M. Cohen, Effect of donor atom identity on metal-binding pharmacophore coordination, J. Biol. Inorg. Chem. 22 (2017) 605–613, https://doi.org/10.1007/s00775-017-1454-3.

[4] K. Azegami, K. Nishiyama, Y. Watanabe, T. Suzuki, M. Yoshida, K. Nose, S. Toda, Tropolone as a Root growth-inhibitor produced by a plant pathogenic Pseudomonas sp. causing seedling blight of rice, Jpn. J. Phytopathol. 51 (1985) 315–317, https://doi.org/10.3186/jjphytopath.51.315.

[5] P.L. Pauson, Tropones and tropolones, Chem. Rev. 55 (1955) 9–136, https://doi.org/10.1021/cr50001a002.

[6] N. Liu, W. Song, C.M. Schienebeck, M. Zhang, W. Tang, Synthesis of naturally occurring tropones and tropolones, Tetrahedron 70 (2014) 9281–9305, https://doi.org/10.1016/j.tet.2014.07.065.

[7] R.P. Murelli, A.J. Berkowitz, D.W. Zuschlag, Carbocycloaddition strategies for troponoid synthesis, Tetrahedron 130 (2023) 133175, https://doi.org/10.1016/j.tet.2022.133175.

[8] R. Bentley, A fresh look at natural tropolonoids, Nat. Prod. Rep. 25 (2008) 118–138, https://doi.org/10.1039/b711474e.

[9] J. Zhao, Plant troponoids: chemistry, biological activity, and biosynthesis, Curr. Med. Chem. 14 (2007) 2597–2621, https://doi.org/10.2174/092986707782023253.

[10] W.-K. Wang, S.-T. Lin, W.-W. Chang, L.-W. Liu, T.Y.-T. Li, C.-Y. Kuo, J.-L. Hsieh, C.-H. Lee, Hinokitiol induces autophagy in murine breast and colorectal cancer cells, Environ. Toxicol. 31 (2016) 77–84, https://doi.org/10.1002/tox.22023.

[11] Y. Inoue, R. Suzuki, I. Murata, H. Nomura, Y. Isshiki, I. Kanamoto, Evaluation of antibacterial activity expression of the hinokitiol/cyclodextrin complex against bacteria, ACS Omega 5 (2020) 27180–27187, https://doi.org/10.1021/acsomega.0c03222.

[12] T.J. Trust, Antibacterial activity of tropolone, Antimicrob. Agents Chemother. 7 (1975) 500–506, https://doi.org/10.1128/AAC.7.5.500.

[13] S.L. Haney, M.L. Varney, H.R. Safranek, Y.S. Chhonker, N. G-Dayanandan, G. Talmon, D.J. Murry, A.J. Wiemer, D.L. Wright, S.A. Holstein, Tropolone-induced effects on the unfolded protein response pathway and apoptosis in multiple myeloma cells are dependent on iron, Leuk. Res. 77 (2019) 17–27, https://doi.org/10.1016/j.leukres.2018.12.007.

[14] J.L. Fullagar, A.L. Garner, A.K. Struss, J.A. Day, D.P. Martin, J. Yu, X. Cai, K. D. Janda, S.M. Cohen, Antagonism of a zinc metalloprotease using a unique metal-chelating scaffold: tropolones as inhibitors of P. aeruginosa elastase, Chem. Commun. Camb. Engl. 49 (2013) 3197–3199, https://doi.org/10.1039/c3cc41191e.

[15] K.M. Varier, T. Sumathi, Hinokitiol offers neuroprotection against 6-OHDA-induced toxicity in SH-SY5Y neuroblastoma cells by downregulating mRNA expression of MAO/α-Synuclein/LRRK2/PARK7/PINK1/PTEN genes, Neurotox. Res. 35 (2019) 945–954, https://doi.org/10.1007/s12640-018-9988-x.

[16] H. Domon, T. Hiyoshi, T. Maekawa, D. Yonezawa, H. Tamura, S. Kawabata, K. Yanagihara, O. Kimura, E. Kunitomo, Y. Terao, Antibacterial activity of hinokitiol against both antibiotic-resistant and -susceptible pathogenic bacteria that predominate in the oral cavity and upper airways, Microbiol. Immunol. 63 (2019) 213–222, https://doi.org/10.1111/1348-0421.12688.

[17] G. Zhang, J. He, X. Ye, J. Zhu, X. Hu, M. Shen, Y. Ma, Z. Mao, H. Song, F. Chen, β-Thujaplicin induces autophagic cell death, apoptosis, and cell cycle arrest through ROS-mediated Akt and p38/ERK MAPK signaling in human hepatocellular carcinoma, Cell Death Dis. 10 (2019) 255, https://doi.org/10.1038/s41419-019-1492-6.

[18] Y. Naito, Y. Yoshikawa, M. Shintani, S. Kamoshida, N. Kajiwara, H. Yasui, Anti-hyperglycemic effect of long-term bis(hinokitiolato)zinc complex ([Zn(hkt)2]) ingestion on insulin resistance and pancreatic islet cells protection in type 2 diabetic KK-Ay Mice, Biol. Pharm. Bull. 40 (2017) 318–326, https://doi.org/10.1248/bpb.b16-00797.

[19] E.L. Muetterties, H. Roesky, C.M. Wright, Chelate chemistry. V. Metal chelates based on tropolone and its derivatives, J. Am. Chem. Soc. 88 (1966) 4856–4861, https://doi.org/10.1021/ja00973a019.

[20] B.X. Hoang, B. Han, A possible application of hinokitiol as a natural zinc ionophore and anti-infective agent for the prevention and treatment of COVID-19 and viral infections, Med. Hypotheses 145 (2020) 110333, https://doi.org/10.1016/j.mehy.2020.110333.

[21] J. Gerke, A.M. Köhler, J.-P. Wennrich, V. Große, L. Shao, A.K. Heinrich, H.B. Bode, W. Chen, F. Surup, G.H. Braus, Biosynthesis of antibacterial iron-chelating tropolones in Aspergillus nidulans as response to glycopeptide-producing Streptomycetes, Front. Fungal Biol 2 (2021) 777474, https://doi.org/10.3389/ffunb.2021.777474.

[22] X. Lai, H.J. Wichers, M. Soler-Lopez, B.W. Dijkstra, Structure of human tyrosinase related protein 1 reveals a binuclear zinc active site important for Melanogenesis, Angew Chem. Int. Ed. Engl. 56 (2017) 9812–9815, https://doi.org/10.1002/anie.201704616.

[23] P.J. Gawne, F. Man, P.J. Blower, R. T M de Rosales, Direct cell radiolabeling for in vivo cell Tracking with PET and SPECT Imaging, Chem. Rev. 122 (2022) 10266–10318, https://doi.org/10.1021/acs.chemrev.1c00767.

[24] D.P. Martin, Z.S. Hann, S.M. Cohen, Metalloprotein-inhibitor binding: human carbonic anhydrase II as a model for probing metal-ligand interactions in a metalloprotein active site, Inorg. Chem. 52 (2013) 12207–12215, https://doi.org/10.1021/ic400295f.

[25] G. Costa, M.C. Gidaro, D. Vullo, C.T. Supuran, S. Alcaro, Active components of essential oils as anti-obesity potential drugs investigated by in silico techniques, J. Agric. Food Chem. 64 (2016) 5295–5300, https://doi.org/10.1021/acs.jafc.6b02004.

[26] I. Tamburlin-Thumin, M.P. Crozet, J.C. Barrière, M. Barreau, J.F. Riou, F. Lavelle, Synthesis and biological evaluation of O-alkylated tropolones and related alpha-ketohydroxy derivatives as ribonucleotide reductase inhibitors, Eur. J. Med. Chem. 36 (2001) 561–568, https://doi.org/10.1016/s0223-5234(01)01249-1.

[27] M. Cavazza, F. Pietra, Tautomeric selectivity towards colchicinoids in the tosylation of colchiceine on a heterogeneous, easily removable catalyst, Org. Biomol. Chem. 1 (2003) 3002–3003, https://doi.org/10.1039/b307650b.

[28] M. Elagawany, L. Hegazy, F. Cao, M.J. Donlin, N. Rath, J. Tavis, B. Elgendy, Identification of 4-isopropyl-thiotropolone as a novel anti-microbial: regioselective synthesis, NMR characterization, and biological evaluation, RSC Adv. 8 (2018) 29967–29975, https://doi.org/10.1039/c8ra06297h.

[29] M. Fantacuzzi, I. D'Agostino, S. Carradori, F. Liguori, F. Carta, M. Agamennone, A. Angeli, F. Sannio, J.-D. Docquier, C. Capasso, C.T. Supuran, Benzenesulfonamide derivatives as Vibrio cholerae carbonic anhydrases inhibitors: a computational-aided insight in the structural rigidity-activity relationships, J. Enzym. Inhib. Med. Chem. 38 (2023) 2201402, https://doi.org/10.1080/14756366.2023.2201402.

[30] G. Benito, I. D'Agostino, S. Carradori, M. Fantacuzzi, M. Agamennone, V. Puca, R. Grande, C. Capasso, F. Carta, C.T. Supuran, Erlotinib-containing benzenesulfonamides as anti-Helicobacter pylori agents through carbonic anhydrase inhibition, Future Med. Chem. 15 (2023) 1865–1883, https://doi.org/10.4155/fmc-2023-0208.

[31] V.L. Hideko Tatakihara, A.D. Malvezi, R.S. Pereira, B.F.C. Lucchetti, L.F. Dos Santos, R. Cecchini, L.M. Yamauchi, S.F. Yamada-Ogatta, K.M. Miranda, W. A. Verri, M.C. Martins-Pinge, P. Pinge-Filho, The Therapeutic potential of Angeli's salt in mitigating Acute Trypanosoma cruzi infection in mice, Pathog. Basel Switz. 12 (2023) 1063, https://doi.org/10.3390/pathogens12081063.

[32] A. Angeli, M. Ferraroni, A.A. Da'dara, S. Selleri, M. Pinteala, F. Carta, P.J. Skelly, C.T. Supuran, Structural insights into Schistosoma mansoni carbonic anhydrase (SmCA) inhibition by Selenoureido-substituted benzenesulfonamides, J. Med. Chem. 64 (2021) 10418–10428, https://doi.org/10.1021/acs.jmedchem.1c00840.

[33] R.G. Khalifah, The carbon dioxide hydration activity of carbonic anhydrase. I. Stop-flow kinetic studies on the native human isoenzymes B and C, J. Biol. Chem. 246 (1971) 2561–2573.

[34] H. Aslan, G. Renzi, A. Angeli, I. D'Agostino, R. Ronca, M. Massardi, C. Tavani, S. Carradori, M. Ferraroni, P. Governa, F. Manetti, F. Carta, C. Supuran, Benzenesulfonamide Decorated Dihydropyrimidin(thi)ones: carbonic anhydrase profiling and antiproliferative activity, RSC Med. Chem. 15 (2024) 1929–1941, https://doi.org/10.1039/D4MD00101J.

[35] J.T. Kilbile, S.B. Sapkal, G. Renzi, I. D'Agostino, L. Cutarella, M. Mori, B. De Filippis, I. Islam, M.L. Massardi, E. Somenza, R. Ronca, Y. Tamboli, F. Carta, C. T. Supuran, Novel 2,4-Dichloro-5-sulfamoylbenzoic acid Oxime esters: first studies as potential human carbonic anhydrase inhibitors, ACS Med. Chem. Lett. 15 (2024) 972–978, https://doi.org/10.1021/acsmedchemlett.4c00206.

[36] M. Agamennone, M. Fantacuzzi, S. Carradori, A. Petzer, J.P. Petzer, A. Angeli, C. T. Supuran, G. Luisi, Coumarin-based dual inhibitors of human carbonic anhydrases and Monoamine Oxidases featuring Amino acyl and (Pseudo)-Dipeptidyl Appendages: in vitro and computational studies, Mol. Basel Switz. 27 (2022) 7884, https://doi.org/10.3390/molecules27227884.

[37] A. Nocentini, A. Angeli, F. Carta, J.-Y. Winum, R. Zalubovskis, S. Carradori, C. Capasso, W.A. Donald, C.T. Supuran, Reconsidering anion inhibitors in the general context of drug design studies of modulators of activity of the classical enzyme carbonic anhydrase, J. Enzym. Inhib. Med. Chem. 36 (2021) 561–580, https://doi.org/10.1080/14756366.2021.1882453.

[38] A. Karioti, F. Carta, C.T. Supuran, Phenols and polyphenols as carbonic anhydrase inhibitors, Molecules 21 (2016) 1649, https://doi.org/10.3390/molecules21121649.

[39] R. Paciotti, S. Carradori, A. Angeli, I. D'Agostino, M. Ferraroni, C. Coletti, C. T. Supuran, Unprecedented carbonic anhydrase inhibition mechanism: Targeting histidine 64 side chain through a halogen bond, Arch. Pharm. (Weinheim) 358 (2025) e2400776, https://doi.org/10.1002/ardp.202400776.

[40] E. Taiana, M.E. Gallo Cantafio, V.K. Favasuli, C. Bandini, G. Viglietto, R. Piva, A. Neri, N. Amodio, Genomic instability in multiple myeloma: a "Non-coding RNA" perspective, Cancers 13 (2021) 2127, https://doi.org/10.3390/cancers13092127.

[41] K. D'Ambrosio, A. Di Fiore, V. Alterio, E. Langella, S.M. Monti, C.T. Supuran, G. De Simone, Multiple binding modes of inhibitors to human carbonic anhydrases: an update on the design of isoform-specific modulators of activity, Chem. Rev. 125 (2025) 150–222, https://doi.org/10.1021/acs.chemrev.4c00278.

[42] G. Navarro, M. Gómez-Autet, P. Morales, J.B. Rebassa, C. Llinas Del Torrent, N. Jagerovic, L. Pardo, R. Franco, Homodimerization of CB2 cannabinoid receptor triggered by a bivalent ligand enhances cellular signaling, Pharmacol. Res. 208 (2024) 107363, https://doi.org/10.1016/j.phrs.2024.107363.

[43] A. Pryde, J. Zsindely, H. Schmid, Thermische Umlagerung von Propargyloxy-cycloheptatrien-Derivaten, Helv. Chim. Acta 57 (1974) 1598–1613, https://doi.org/10.1002/hlca.19740570614.

[44] H. Takeshita, A. Mori, H. Suizu, Novel Base-Promoted Rearrangement of 2-(4-Cyano-, 2-Nitro-, and 4-Nitrobenzyloxy)tropones and 2-(2-Oxo-2-phenethyloxy)tropone to 2-[(4-Cyano-, 2-Nitro-, and 4-Nitrophenyl)hydroxymethyl]tropones and 2-(1-Hydroxy-2-oxo-2-phenethyl)tropone, Bull. Chem. Soc. Jpn. 60 (1987) 1429–1432, https://doi.org/10.1246/bcsj.60.1429.
[45] H. Takeshita, A. Mori, H. Suizu, An anion-promoted rearrangement of 2-(o- and p-nitrobenzyloxy)tropones to α-hydroxylated 2-(o- and p-nitrobenzyl)tropones. A ready introduction of aralkyl group into the troponoid nucleuS, Chem. Lett. 15 (1986) 593–596, https://doi.org/10.1246/cl.1986.593.
[46] J.R. Scheffer, L. Wang, Enantioselective photoelectrocyclization of a tropolone derivative in the crystalline state, J. Phys. Org. Chem. 13 (2000) 531–538, https://doi.org/10.1002/1099-1395(200009)13:9<531::AID-POC293>3.0.CO, 2-5.
[47] R.J. Cornell, L.G. Donaruma, 2-Methacryloxytropones. Intermediates for the synthesis of biologically active polymers, J. Med. Chem. 8 (1965) 388–390, https://doi.org/10.1021/jm00327a025.
[48] K.B. Daniel, J.L. Major Jourden, K.E. Negoescu, S.M. Cohen, Activation of sulfonate ester based matrix metalloproteinase proinhibitors by hydrogen peroxide, JBIC, J. Biol. Inorg. Chem. 16 (2011) 313–323, https://doi.org/10.1007/s00775-010-0727-x.
[49] G.N. Murshudov, A.A. Vagin, E.J. Dodson, Refinement of macromolecular structures by the maximum-likelihood method, Acta Crystallogr. D Biol. Crystallogr. 53 (1997) 240–255, https://doi.org/10.1107/S0907444996012255.
[50] M.D. Winn, C.C. Ballard, K.D. Cowtan, E.J. Dodson, P. Emsley, P.R. Evans, R. M. Keegan, E.B. Krissinel, A.G.W. Leslie, A. McCoy, S.J. McNicholas, G. N. Murshudov, N.S. Pannu, E.A. Potterton, H.R. Powell, R.J. Read, A. Vagin, K. S. Wilson, Overview of the CCP4 suite and current developments, Acta Crystallogr. D Biol. Crystallogr. 67 (2011) 235–242, https://doi.org/10.1107/S0907444910045749.
[51] A.A. Lebedev, P. Young, M.N. Isupov, O.V. Moroz, A.A. Vagin, G.N. Murshudov, JLigand: a graphical tool for the CCP4 template-restraint library, Acta Crystallogr. D Biol. Crystallogr. 68 (2012) 431–440, https://doi.org/10.1107/S090744491200251X.
[52] P. Emsley, B. Lohkamp, W.G. Scott, K. Cowtan, Features and development of coot, Acta Crystallogr. D Biol. Crystallogr. 66 (2010) 486–501, https://doi.org/10.1107/S0907444910007493.
[53] M.F. Adasme, K.L. Linnemann, S.N. Bolz, F. Kaiser, S. Salentin, V.J. Haupt, M. Schroeder, Plip 2021: expanding the scope of the protein-ligand interaction profiler to DNA and RNA, Nucleic Acids Res. 49 (2021) W530–W534, https://doi.org/10.1093/nar/gkab294.
[54] E.F. Pettersen, T.D. Goddard, C.C. Huang, G.S. Couch, D.M. Greenblatt, E.C. Meng, T.E. Ferrin, UCSF Chimera–a visualization system for exploratory research and analysis, J. Comput. Chem. 25 (2004) 1605–1612, https://doi.org/10.1002/jcc.20084.
[55] I. D'Agostino, G.E. Mathew, P. Angelini, R. Venanzoni, G. Angeles Flores, A. Angeli, S. Carradori, B. Marinacci, L. Menghini, M.A. Abdelgawad, M. M. Ghoneim, B. Mathew, C.T. Supuran, Biological investigation of N-methyl thiosemicarbazones as antimicrobial agents and bacterial carbonic anhydrases inhibitors, J. Enzym. Inhib. Med. Chem. 37 (2022) 986–993, https://doi.org/10.1080/14756366.2022.2055009.
[56] I. D'Agostino, A. Bonardi, M. Ferraroni, P. Gratteri, A. Angeli, C.T. Supuran, Exploring the polypharmacological potential of PCI-27483: a selective inhibitor of carbonic anhydrases IX and XII, ACS Med. Chem. Lett. 15 (2024) 2042–2045, https://doi.org/10.1021/acsmedchemlett.4c00443.
[57] B. Marinacci, I. D'Agostino, A. Angeli, S. Carradori, F. Melfi, R. Grande, M. Corsiani, M. Ferraroni, M. Agamennone, A.R. Tondo, S. Zara, V. Puca, B. Pellegrini, C. Vagaggini, E. Dreassi, M.A. Patrauchan, C. Capasso, O. Nicolotti, F. Carta, C.T. Supuran, Inhibition of Pseudomonas aeruginosa carbonic anhydrases, exploring Ciprofloxacin functionalization toward new antibacterial agents: an in-depth multidisciplinary study, J. Med. Chem. 67 (2024) 19077–19102, https://doi.org/10.1021/acs.jmedchem.4c01555.
[58] W.L. Jorgensen, D.S. Maxwell, J. Tirado-Rives, Development and testing of the OPLS all-atom force field on Conformational Energetics and properties of organic liquids, J. Am. Chem. Soc. 118 (1996) 11225–11236, https://doi.org/10.1021/ja9621760.
[59] LigPrep, Schrödinger, LLC, New York, NY, 2024.
[60] G. Costa, F. Carta, F.A. Ambrosio, A. Artese, F. Ortuso, F. Moraca, R. Rocca, I. Romeo, A. Lupia, A. Maruca, D. Bagetta, R. Catalano, D. Vullo, S. Alcaro, C. T. Supuran, A computer-assisted discovery of novel potential anti-obesity compounds as selective carbonic anhydrase VA inhibitors, Eur. J. Med. Chem. 181 (2019) 111565, https://doi.org/10.1016/j.ejmech.2019.111565.
[61] Schrödinger release 2024-4: protein preparation Wizard, Epik, Schrödinger, LLC, New York, NY, 2024; Impact, Schrödinger, LLC, New York, NY; Prime, Schrödinger, LLC, New York, NY, 2024.
[62] R.A. Friesner, J.L. Banks, R.B. Murphy, T.A. Halgren, J.J. Klicic, D.T. Mainz, M. P. Repasky, E.H. Knoll, M. Shelley, J.K. Perry, D.E. Shaw, P. Francis, P.S. Shenkin, Glide: a new approach for rapid, Accurate docking and scoring. 1. Method and assessment of docking accuracy, J. Med. Chem. 47 (2004) 1739–1749, https://doi.org/10.1021/jm0306430.
[63] Schrödinger Release 2024-4: Glide, Schrödinger, LLC, New York, NY, 2024.
[64] Schrödinger Release 2024-4: MacroModel, Schrödinger, LLC, New York, NY, 2024.
[65] F. Mohamadi, N.G.J. Richards, W.C. Guida, R. Liskamp, M. Lipton, C. Caufield, G. Chang, T. Hendrickson, W.C. Still, Macromodel—an integrated software system for modeling organic and bioorganic molecules using molecular mechanics, J. Comput. Chem. 11 (1990) 440–467, https://doi.org/10.1002/jcc.540110405.

SUPPLEMENTARY MATERIAL

O-Derivatization of Natural Tropolone and β-Thujaplicin Leading to Micromolar Inhibitors of human Carbonic Anhydrases IX and XII

Francesco Melfi[◆,a], Ilaria D'Agostino[◆,b], Simone Carradori[a,*], Fabrizio Carta[c,*], Andrea Angeli[c], Giosuè Costa[d,e], Gioele Renzi[c], Ana Čikoš[f], Daniela Vullo[c], Josip Rešetar[a], Marta Ferraroni[g], Chiara Baroni[g], Francesca Mancuso[h], Rosaria Gitto[h], Francesca Alessandra Ambrosio[d], Emanuela Marchese[d], Roberta Torcasio,[i,j] Nicola Amodio,[i] Clemente Capasso[l], Stefano Alcaro[d,e] Claudiu T. Supuran[c]

[a]Department of Pharmacy, "G. d'Annunzio" University of Chieti-Pescara, 66100 Chieti, Italy
[b]Department of Pharmacy, University of Pisa, 56126 Pisa, Italy
[c]Neurofarba Department, University of Florence, Sesto Fiorentino, 50019 Florence, Italy
[d]Dipartimento di Scienze della Salute, Università "Magna Græcia" di Catanzaro, Campus "S. Venuta", 88100, Catanzaro, Italy
[e]Net4Science Academic Spin-Off, Università "Magna Græcia" di Catanzaro, Campus "S. Venuta", 88100, Catanzaro, Italy
[f]NMR Centre, Ruđer Bošković Institute, Bijenička cesta 54, 10000 Zagreb, Croatia
[g]Department of Experimental and Clinical Medicine, University "Magna Græcia" of Catanzaro, Campus "S. Venuta", 88100 Catanzaro, Italy
[h]'Ugo Schiff' Chemistry Department, University of Florence, Via della Lastruccia 3, 50019 Sesto Fiorentino, Florence, Italy.
[i]Department of Chemical, Biological, Pharmaceutical, and Environmental Sciences, University of Messina, Viale F. D'Alcontres 13, 98166, Messina, Italy
[j]Department of Biology, Ecology and Earth Sciences (Di.B.E.S.T.), University of Calabria, 87036 Rende, Italy
[l]Department of Biology, Agriculture and Food Sciences, Institute of Biosciences and Bioresources, CNR, Napoli, Italy
*Corresponding authors: Prof. Simone Carradori, simone.carradori@unich.it; Prof. Fabrizio Carta, fabrizio.carta@unifi.it
◆The authors contributed equally to this work.

Table S1. Inhibition data of **TRP**, **TJP**, and their derivatives, and reference compound AAZ on a panel of non-human CA isoforms.

compound	Core	R^1	K_I (μM)			
			VchCAα	HpCAα	TcCAα	SmCAα
TRP	TRP	-H	>100	46.9	>100	>100
TJP	TJP	-H	>100	39.7	>100	>100
1	TRP		>100	44.8	>100	44.3
1β+δ	TJP		>100	>100	>100	>100
2	TRP	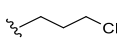	8.92	3.41	7.33	58.7
2β+δ	TJP		5.31	21.5	8.34	44.4
3	TRP	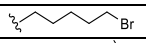	7.12	3.48	7.15	80.3
4δ	TJP	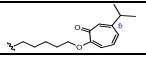	7.10	>100	7.88	>100
6	TRP	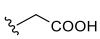	9.06	>100	5.43	>100
6β+δ	TJP		0.97	70.84	0.38	9.27

7	TRP	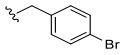	4.82	5.86	2.48	2.60
7δ	TJP		6.51	26.0	4.81	>100
8	TRP	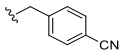	>100	30.2	>100	>100
8β+δ	TJP		20.8	>100	7.75	>100
9	TRP	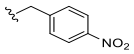	>100	>100	>100	>100
9β+δ	TJP		7.92	>100	6.13	9.60
10	TRP	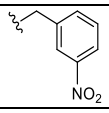	17.9	6.84	0.72	55.6
10β+δ	TJP		7.09	8.12	8.78	42.2
11	TRP	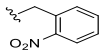	>100	45.1	>100	>100
11β	TJP		>100	>100	4.81	94.7
11δ	TJP		47.5	>100	5.62	>100
12	TRP	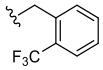	9.65	>100	8.91	>100
12β	TJP		6.88	37.1	8.54	9.68
12δ	TJP		7.70	61.5	8.20	8.79
13	TRP	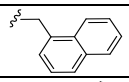	8.06	>100	6.42	>100
13δ	TJP		5.96	>100	8.73	52.10
14β+δ	TJP	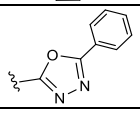	21.6	>100	8.97	>100
15	TRP	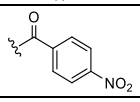	>100	>100	>100	>100
15δ	TJP		8.74	>100	7.63	>100
16	TRP	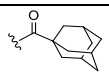	60.3	63.6	7.96	7.58
16β+δ	TJP		0.98	7.26	3.69	9.61
17	TRP	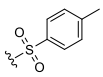	>100	>100	>100	>100
17β	TJP		9.62	>100	6.25	>100
17δ	TJP		7.00	>100	8.06	>100
AAZ	Reference compound		0.01	0.02	0.06	0.04

K_I values are reported as means of three independent experiments. Errors are in the range of ± 5-10% of the reported values.

Structure-Activity Relationships within non-human αCA isoforms

When tested on bacterial and parasite α-CAs, **TRP** and **TJP** derivatives showed in some cases promising results, differently to the scaffolds that exhibited K_I values up to 100 μM, except for *H. pylori* (**TRP**, K_I = 48.9 μM; β-**TJP** K_I = 39.3 μM).

- In the case of *V. cholerae* several compounds exhibited a moderate activity in the inhibition of the bacterial enzyme, like **2**, **2β+δ**, **3**, **4δ**, **6**, **7**, **7δ**, **9β+δ**, **10β+δ**, **12**, **12β**, **12δ**, **13**, **13δ**, **15δ**, **17β**, **17δ** with K_I values between 4.82 and 9.65 μM, whereas the most active compounds, with K_I values < 1 μM, are **TJP** derivatives **6β+δ** (K_i = 0.97 μM) and **16β+δ** (K_i = 0.98 μM). It is interesting to note that these two compounds, despite the chemical and structural differences between them, exhibited similar results when tested on *V. cholerae* CA. Moreover, the adamantanoyl **TJP** (**16β+δ**) showed the most potent inhibitory activity on *V. cholerae* CA over all tested isoforms, and its **TRP** analogue did not exhibit appreciable activity (K_I = 60.2 μM). Further, both **6β+δ** and **16β+δ** were selective toward *V. cholerae* CA over hCA I and II (K_I for both hCA I and II > 100 μM).

- For *H. pylori*, there was not a particular compound that exhibited strong activity in the inhibition of CA, but, at the same time, there were few molecules that showed moderate activity, like **2**, **3**, **7**, **10**, **10β+δ**, **16β+δ**, with K_I values between 3.41 and 8.12 μM. The most active compounds, **2** (K_I = 3.41 μM) and **3** (K_I = 3.48 μM) have in common an alkyl tail, with a different length, that ends with a halogen. In the inhibition of *H. pylori* CA, **TRP** scaffold seems to be preferable than **TJP**, except for 2-trifluoromethylbenzyloxy (**12**, K_I > 100 μM; **12β**, K_I = 37.1 μM; **12δ** K_I = 61.5 μM) and adamantanoyl (**16**, K_I = 63.6 μM; **16β+δ**, K_I = 7.26 μM) derivatives.
- When tested on *T. cruzi* CA, the majority of **TRP** and **TJP** derivatives exhibited moderate results in the inhibition of the enzyme, except for propargyl derivatives (**1**, **1β+δ**) and some **TRP**-benzyloxy derivatives like **8**, **9**, **11**, **15**, and **17**, which K_I values were up to 100 μM. The most potent and selective compounds were **6β+δ** (K_i = 0.38 μM, SI over both hCA I and II > 263) and **10** (K_I = 0.72 μM, SI over both hCA I and II > 138).
- For *S. mansoni*, there were only few note-worthing molecules, among them,4-bromobenzyloxy **TRP 7**, that was the most active compound with K_I of 2.60 μM, and it was selective over hCA I and II, with a SI up to 38 for both isoforms, and **6β+δ**, the benzyloxy **9β+δ**, **12β**, **12δ**, and the adamantanoyl **16**, **16β+δ** with K_I values between 7.58 and 9.68 μM.

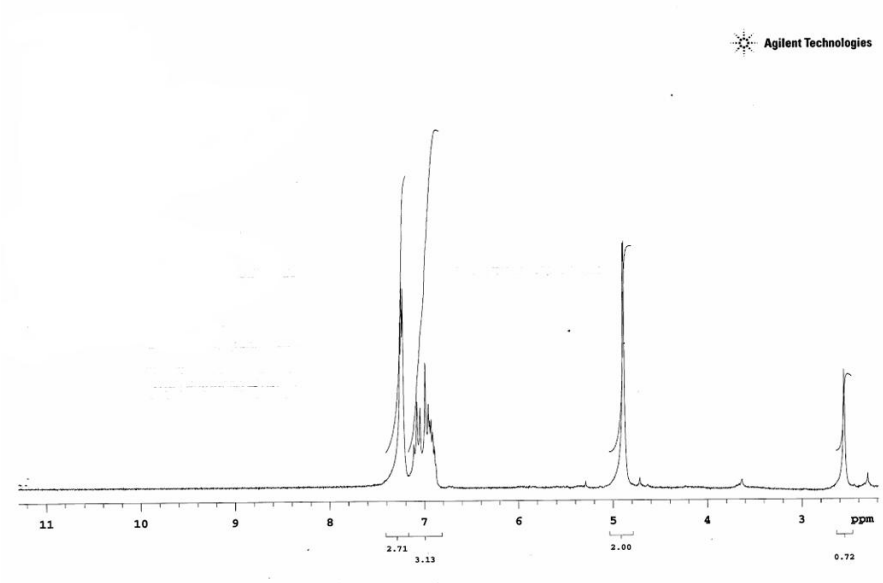

Figure S1. ^{1}H NMR of compound **1**

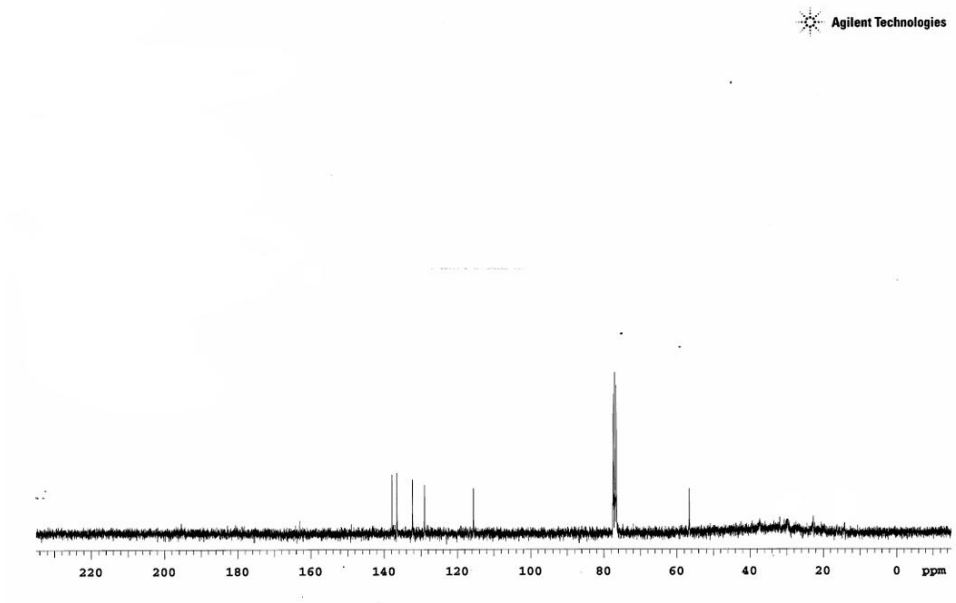

Figure S2. ^{13}C NMR of compound **1**

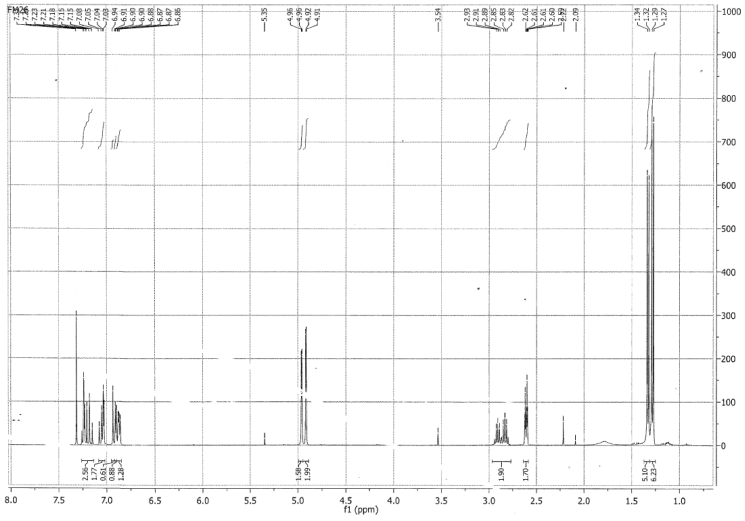

Figure S3. ^{1}H NMR of compound **1β+δ**

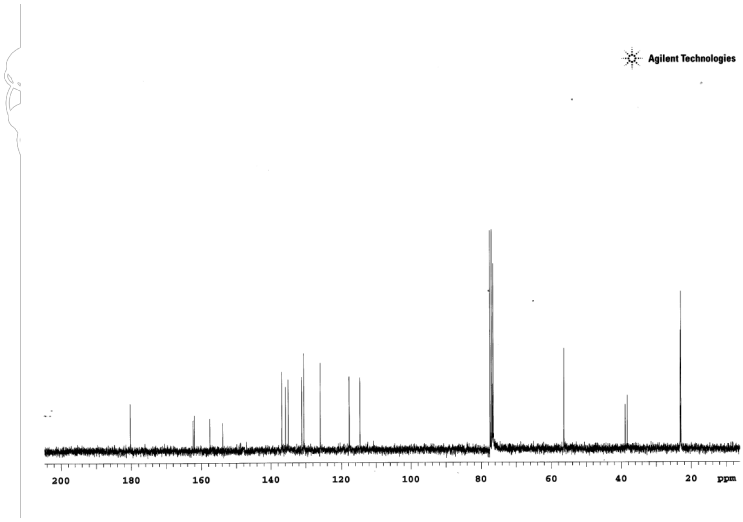

Figure S4. ^{13}C NMR of compound **1β+δ**

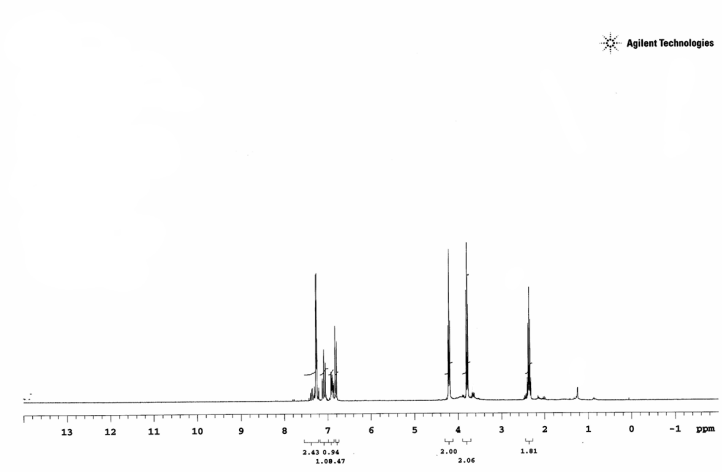

Figure S5. ^{1}H NMR of compound **2**

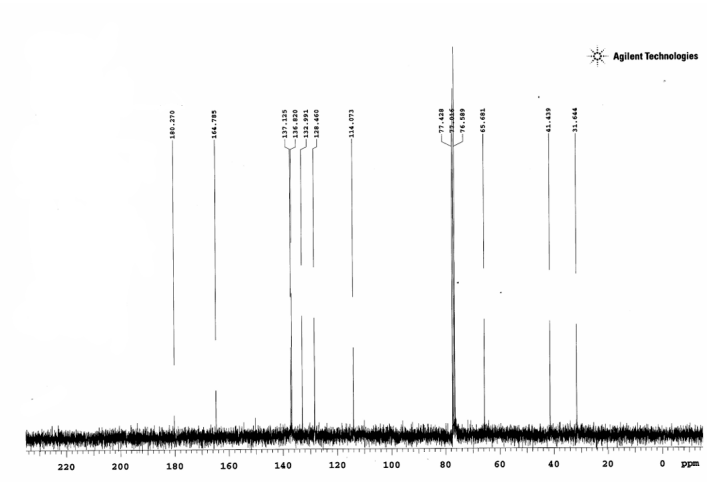

Figure S6. ^{13}C NMR of compound **2**

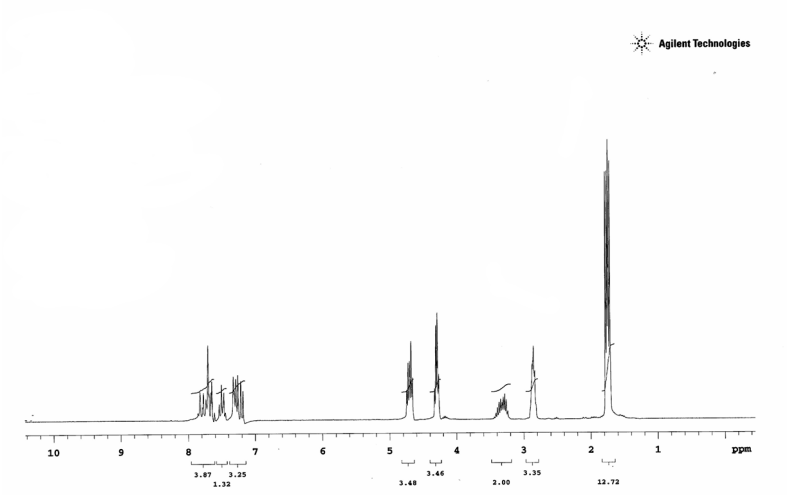

Figure S7. ^{1}H NMR **2β+δ**

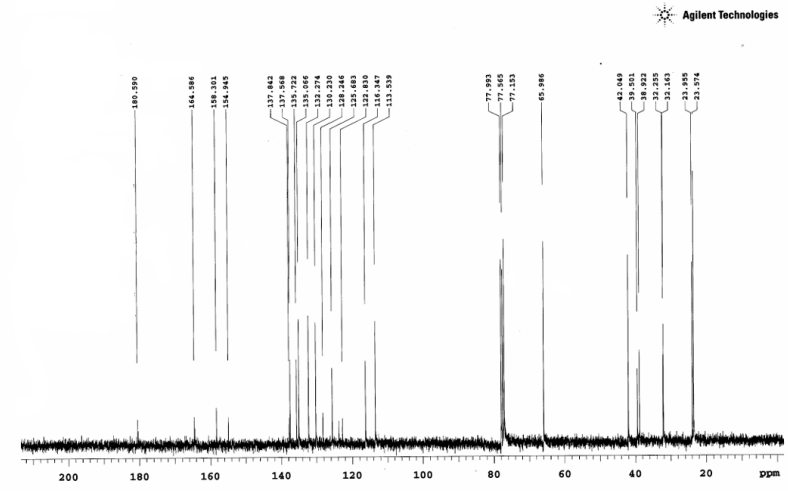

Figure S8. ^{13}C NMR of compound **2β+δ**

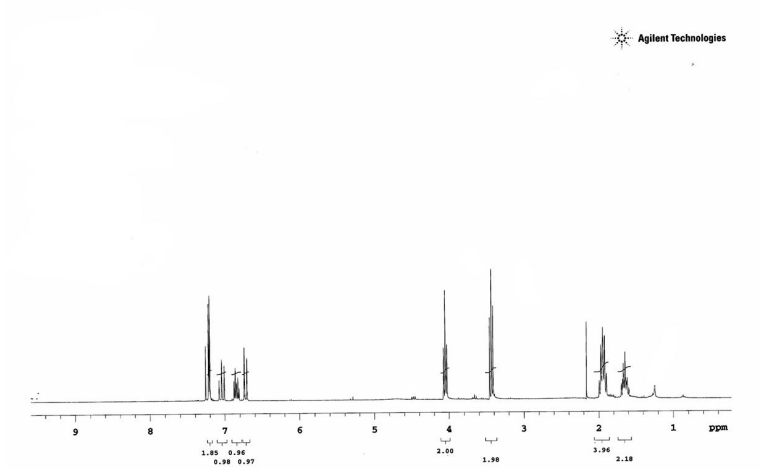

Figure S9. ^{1}H NMR of compound **3**

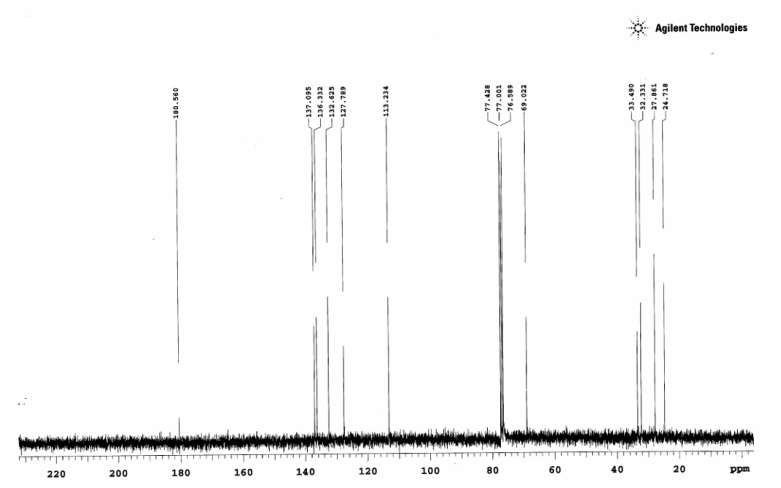

Figure S10. ^{13}C NMR of compound **3**

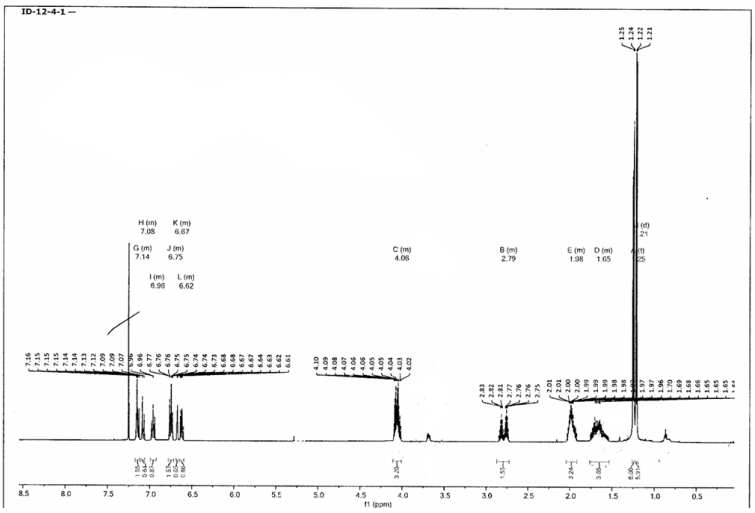

Figure S11. ^{1}H NMR compound **4δ**

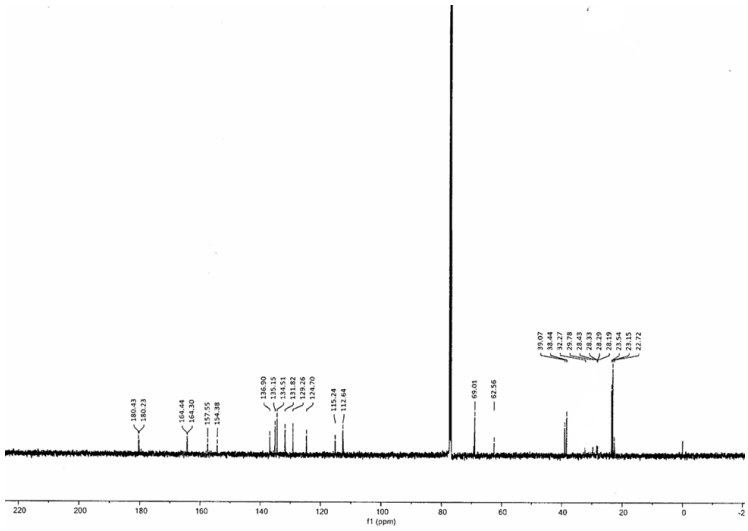

Figure S12. ^{13}C NMR of compound **4δ**

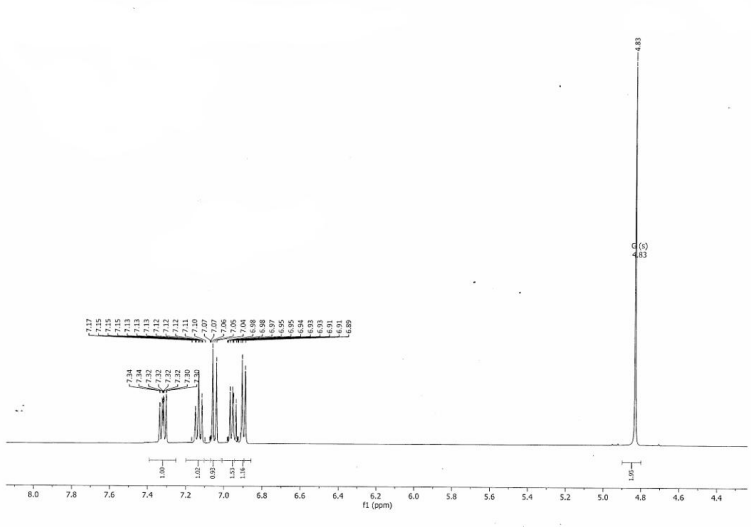

Figure S13. ^{1}H NMR of compound **6**

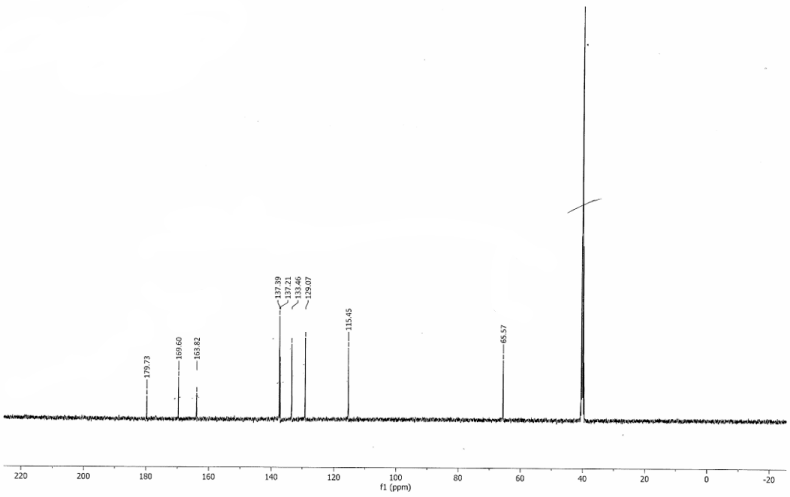

Figure S14. ^{13}C NMR of compound **6**

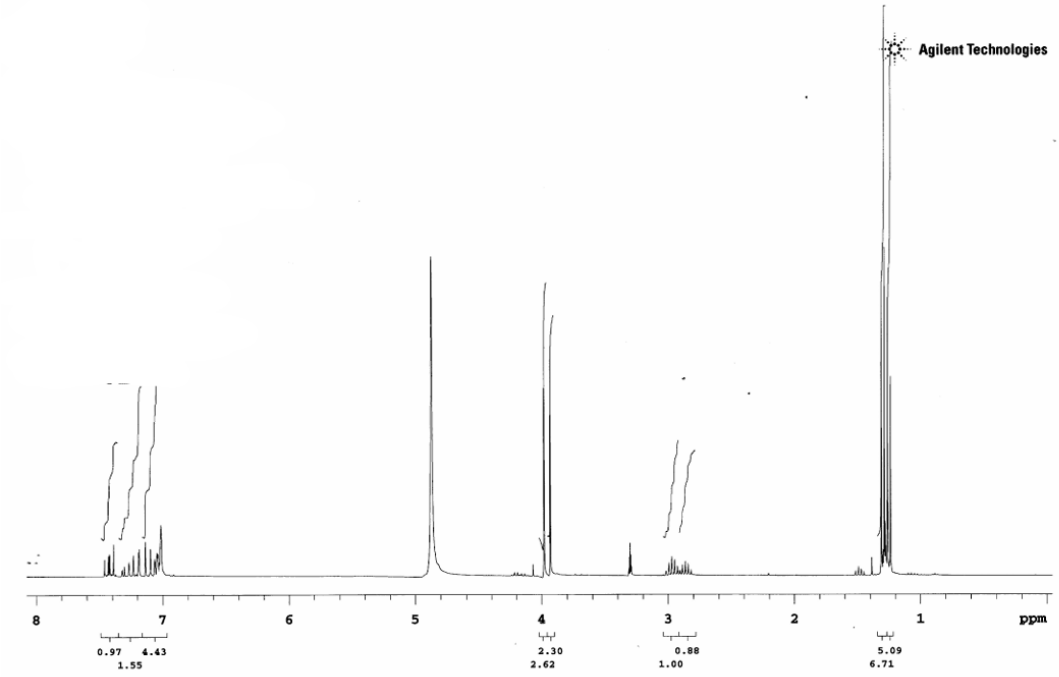

Figure S15. ^{1}H NMR of compound **6β+δ**.

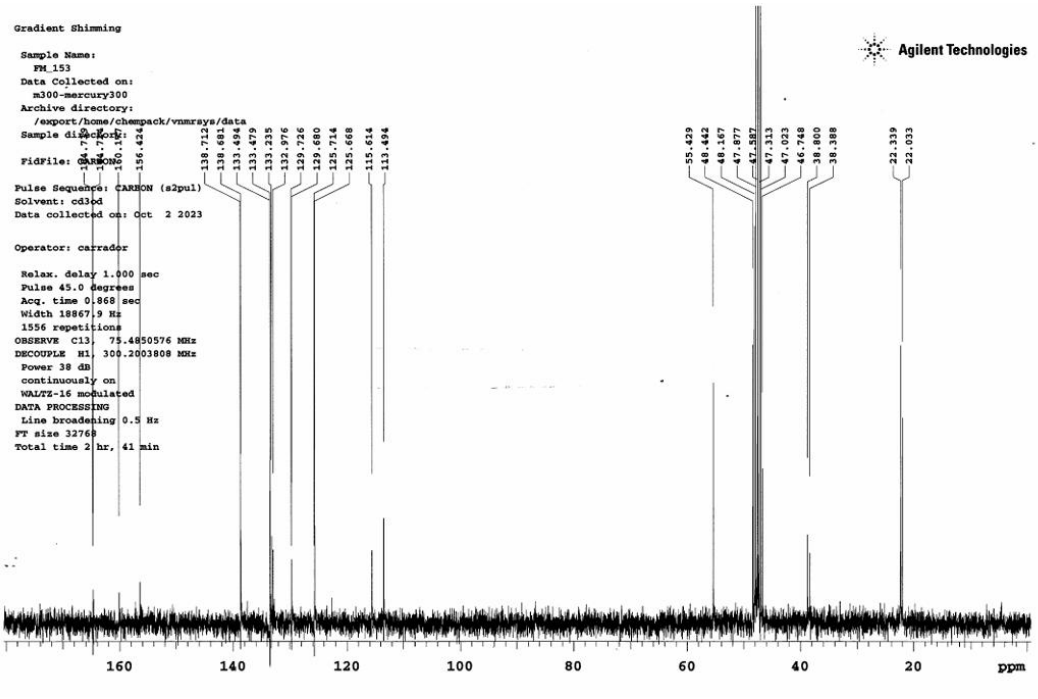
Gradient Shimming
Sample Name:
FM_153
Data Collected on:
m300-mercury300
Archive directory:
/export/home/chempack/vnmrsys/data
Sample directory:
FidFile: CARBON5
Pulse Sequence: CARBON (s2pul)
Solvent: cd3od
Data collected on: Oct 2 2023
Operator: carrador
Relax. delay 1.000 sec
Pulse 45.0 degrees
Acq. time 0.868 sec
Width 18867.9 Hz
1556 repetitions
OBSERVE C13, 75.4850576 MHz
DECOUPLE H1, 300.2003808 MHz
Power 38 dB
continuously on
WALTZ-16 modulated
DATA PROCESSING
Line broadening 0.5 Hz
FT size 32768
Total time 2 hr, 41 min
Agilent Technologies
138.712
138.681
133.494
133.479
133.235
132.976
129.726
129.680
125.714
125.668
115.614
113.494
55.429
48.442
48.167
47.877
47.587
47.313
47.023
46.748
38.800
38.388
22.339
22.033
160
140
120
100
80
60
40
20
ppm

Figure S16. ^{13}C NMR of compound **6β+δ**

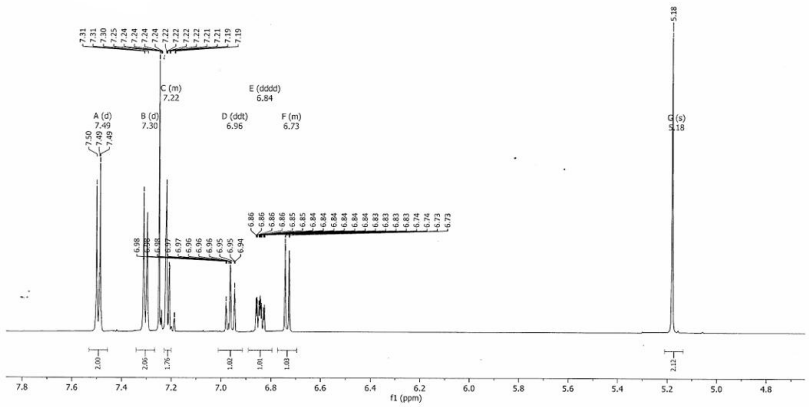

Figure S17. ^{1}H NMR of compound **7**

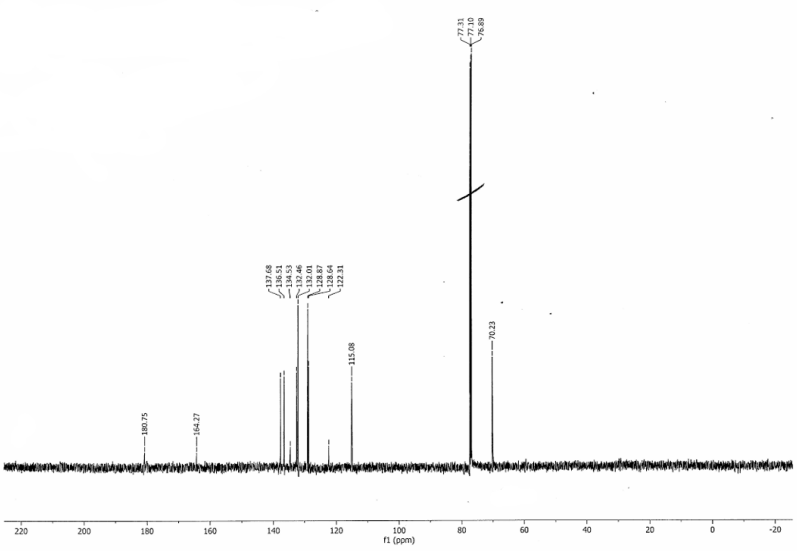

Figure S18. ^{13}C NMR of compound **7**

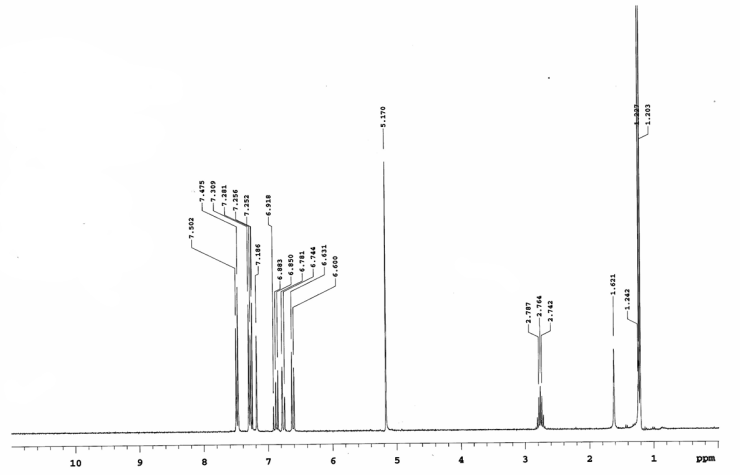

Figure S19. ^{1}H NMR of compound **7δ**

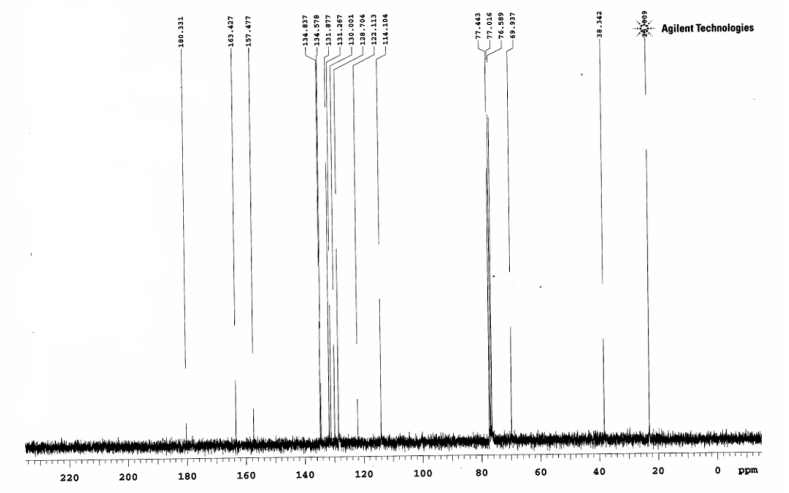

Figure S20. ^{13}C NMR of compound **7δ**

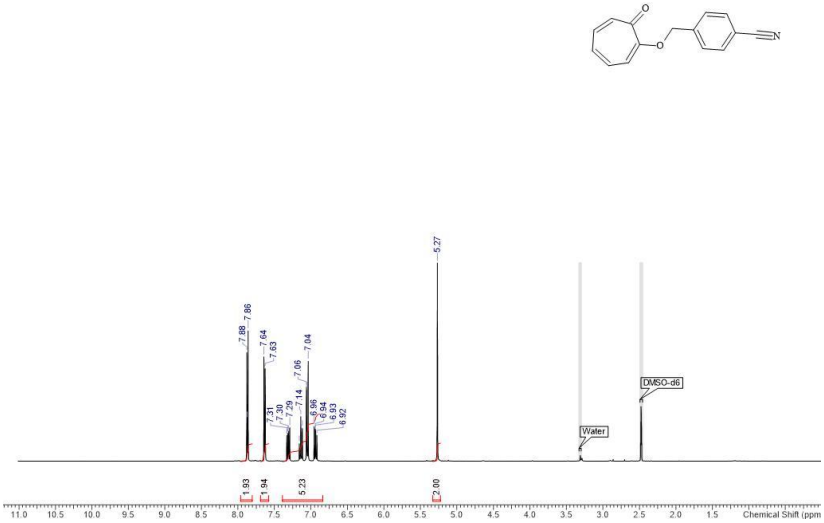

Figure S21. ^{1}H NMR (500 MHz, DMSO-d_6) spectrum of 4-{[(7-oxocyclohepta-1,3,5-trien-1-yl)oxy]methyl}benzonitrile (**8**)

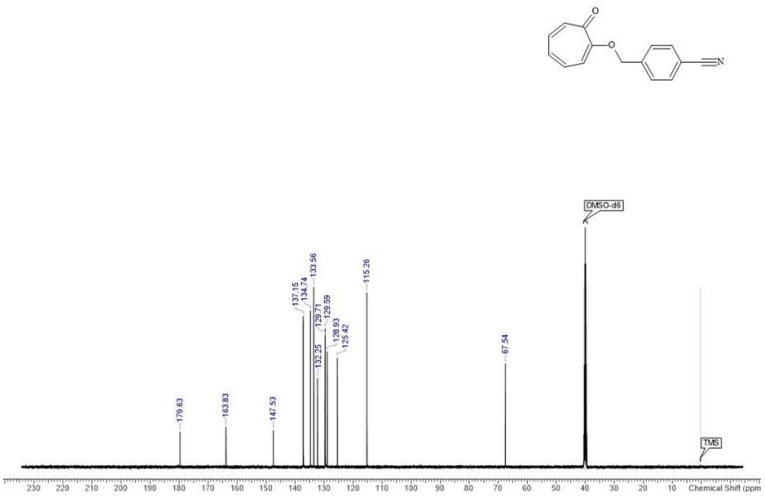

Figure S22. ^{13}C NMR (125 MHz, DMSO-d_6) spectrum of 4-{[(7-oxocyclohepta-1,3,5-trien-1-yl)oxy]methyl}benzonitrile (**8**)

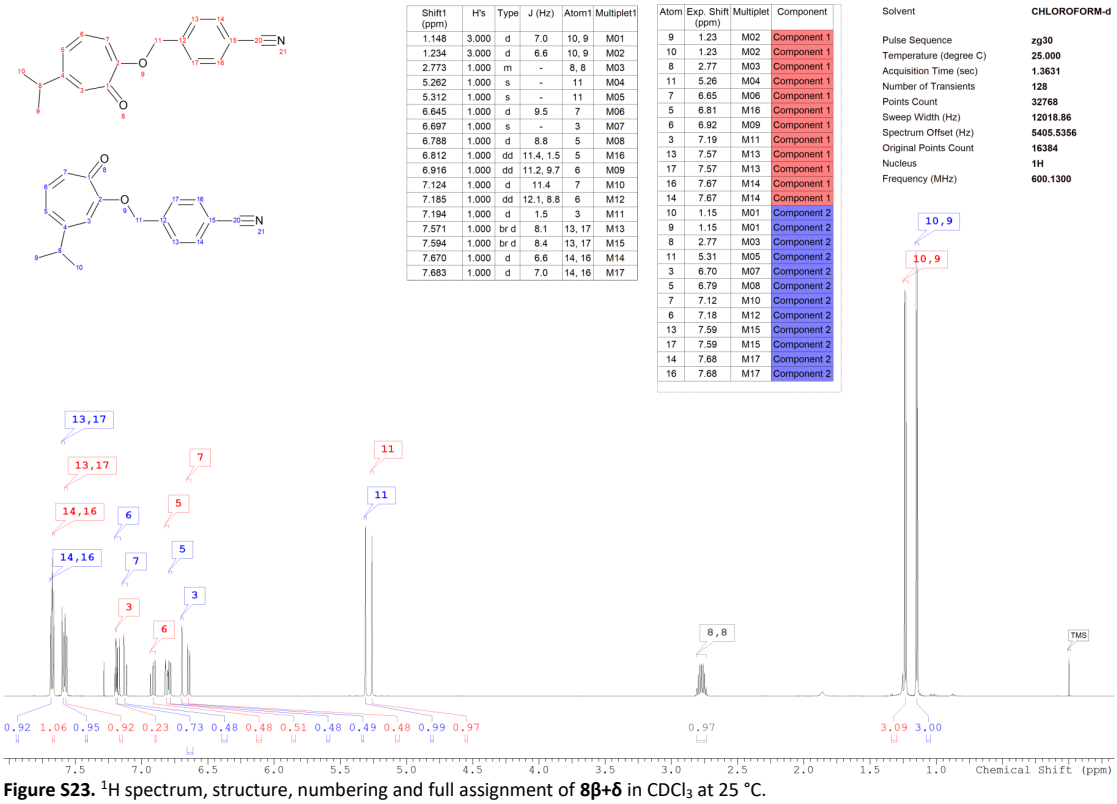

Shift1 (ppm)	H's	Type	J (Hz)	Atom1	Multiplet1
1.148	3.000	d	7.0	10, 9	M01
1.234	3.000	d	6.6	10, 9	M02
2.773	1.000	m	-	8, 8	M03
5.262	1.000	s	-	11	M04
5.312	1.000	s	-	11	M05
6.645	1.000	d	9.5	7	M06
6.697	1.000	s	-	3	M07
6.788	1.000	d	8.8	5	M08
6.812	1.000	dd	11.4, 1.5	5	M16
6.916	1.000	dd	11.2, 9.7	6	M09
7.124	1.000	d	11.4	7	M10
7.185	1.000	dd	12.1, 8.8	6	M12
7.194	1.000	d	1.5	3	M11
7.571	1.000	br d	8.1	13, 17	M13
7.594	1.000	br d	8.4	13, 17	M15
7.670	1.000	d	6.6	14, 16	M14
7.683	1.000	d	7.0	14, 16	M17

Atom	Exp. Shift (ppm)	Multiplet	Component
9	1.23	M02	Component 1
10	1.23	M02	Component 1
8	2.77	M03	Component 1
11	5.26	M04	Component 1
7	6.65	M06	Component 1
5	6.81	M16	Component 1
6	6.92	M09	Component 1
3	7.19	M11	Component 1
13	7.57	M13	Component 1
17	7.57	M13	Component 1
16	7.67	M14	Component 1
14	7.67	M14	Component 1
10	1.15	M01	Component 2
9	1.15	M01	Component 2
8	2.77	M03	Component 2
11	5.31	M05	Component 2
3	6.70	M07	Component 2
5	6.79	M08	Component 2
7	7.12	M10	Component 2
6	7.18	M12	Component 2
13	7.59	M15	Component 2
17	7.59	M15	Component 2
14	7.68	M17	Component 2
16	7.68	M17	Component 2

Solvent	CHLOROFORM-d
Pulse Sequence	zg30
Temperature (degree C)	25.000
Acquisition Time (sec)	1.3631
Number of Transients	128
Points Count	32768
Sweep Width (Hz)	12018.86
Spectrum Offset (Hz)	5405.5356
Original Points Count	16384
Nucleus	1H
Frequency (MHz)	600.1300

Figure S23. ^{1}H spectrum, structure, numbering and full assignment of **8β+δ** in $CDCl_3$ at 25 °C.

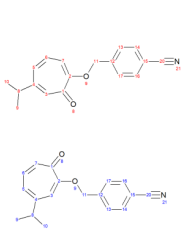

Shift1 (ppm)	C's	Type	Atom1	Multiplet1
22.938	2.000	s	10, 9	M01
23.130	2.000	s	10, 9	M28
38.313	1.000	s	8	M02
38.703	1.000	s	8	M27
69.540	1.000	s	11	M03
69.707	1.000	s	11	M26
111.961	1.000	s	15, 15	M04
114.318	1.000	s	7	M05
117.558	1.000	s	3	M25
118.482	1.000	s	20	M24
118.498	1.000	s	20	M06
125.791	1.000	s	5	M23
127.367	2.000	s	13, 17	M07
127.439	2.000	s	13, 17	M22
130.417	1.000	s	5	M08
131.093	1.000	s	6	M09
132.503	2.000	s	14, 14, 16, 16	M10
134.963	1.000	s	3	M11
135.831	1.000	s	7	M21
136.914	1.000	s	6	M20

Shift1 (ppm)	C's	Type	Atom1	Multiplet1
140.998	1.000	s	12	M12
141.229	1.000	s	12	M19
153.642	1.000	s	4	M18
157.615	1.000	s	4	M13
162.862	1.000	s	2	M17
163.108	1.000	s	2	M14
180.091	1.000	s	1	M16
180.179	1.000	s	1	M15

Atom	Exp. Shift (ppm)	Multiplet	Component
10	22.94	M01	Component 1
9	22.94	M01	Component 1
8	38.31	M02	Component 1
11	69.54	M03	Component 1
15	111.96	M04	Component 1
7	114.32	M05	Component 1
20	118.50	M06	Component 1
17	127.37	M07	Component 1
13	127.37	M07	Component 1
5	130.42	M08	Component 1
6	131.09	M09	Component 1
16	132.50	M10	Component 1
14	132.50	M10	Component 1
3	134.96	M11	Component 1
12	141.00	M12	Component 1
4	157.61	M13	Component 1
2	163.11	M14	Component 1
1	180.18	M15	Component 1
10	23.13	M28	Component 2
9	23.13	M28	Component 2

Atom	Exp. Shift (ppm)	Multiplet	Component
8	38.70	M27	Component 2
11	69.71	M26	Component 2
15	111.96	M04	Component 2
3	117.56	M25	Component 2
20	118.48	M24	Component 2
5	125.79	M23	Component 2
17	127.44	M22	Component 2
13	127.44	M22	Component 2
14	132.50	M10	Component 2
16	132.50	M10	Component 2
7	135.83	M21	Component 2
6	136.91	M20	Component 2
12	141.23	M19	Component 2
4	153.64	M18	Component 2
2	162.86	M17	Component 2
1	180.09	M16	Component 2

Solvent	**CHLOROFORM-d**
Pulse Sequence	**jmod**
Temperature (degree C)	**25.200**
Acquisition Time (sec)	**0.8323**
Number of Transients	**2048**
Points Count	**32768**
Sweep Width (Hz)	**39368.88**
Spectrum Offset (Hz)	**15081.5791**
Original Points Count	**32768**
Nucleus	**13C**
Frequency (MHz)	**150.9028**

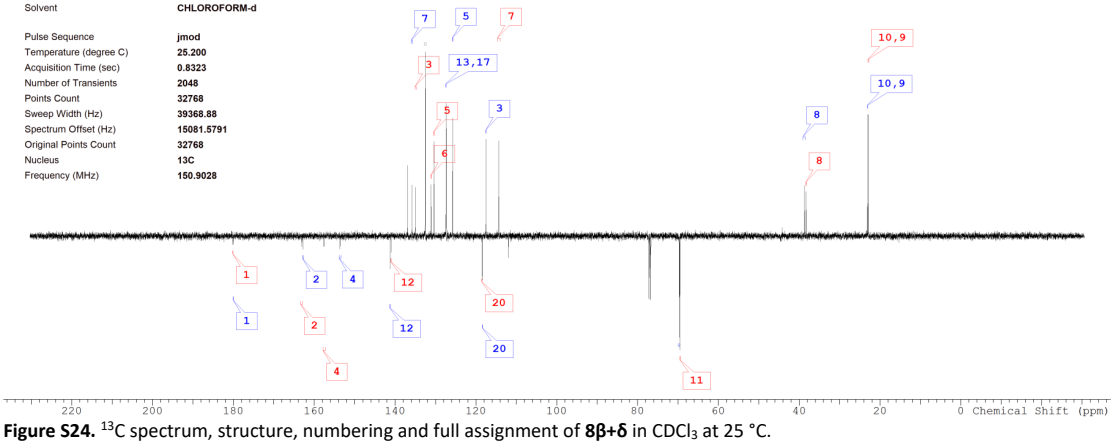

Figure S24. ^{13}C spectrum, structure, numbering and full assignment of **8β+δ** in $CDCl_3$ at 25 °C.

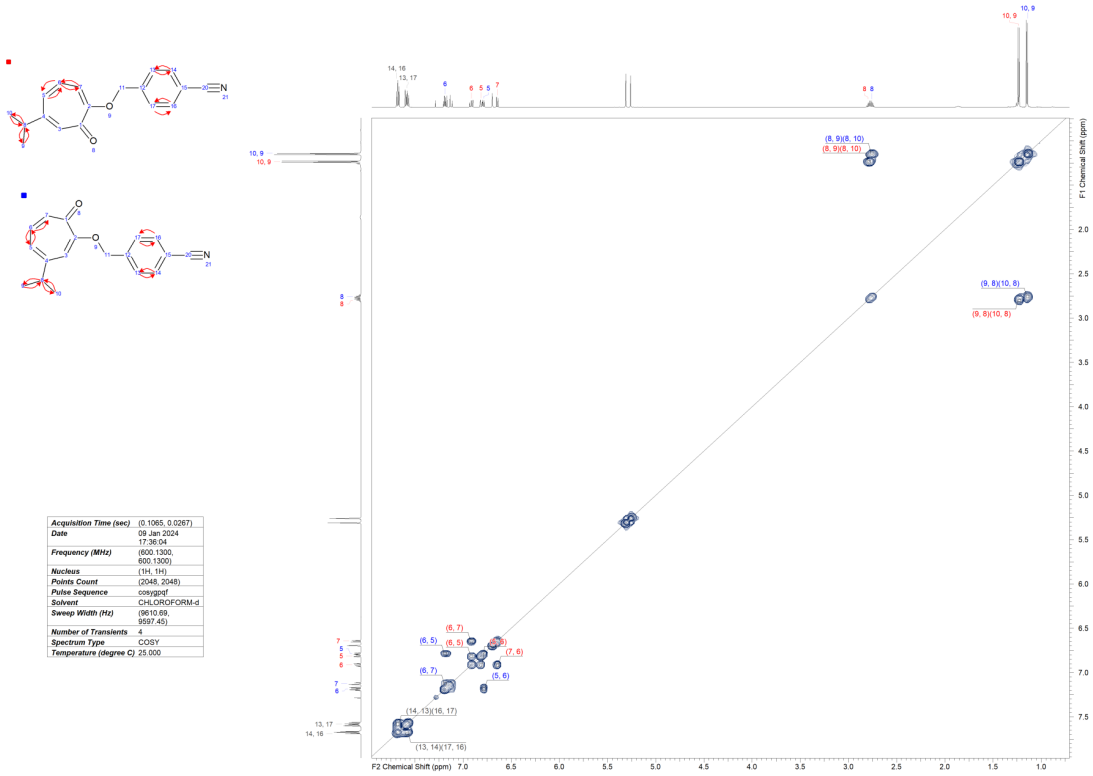

Figure S25. Fully assigned ^{1}H-^{1}H COSY spectrum of **8β+δ** in $CDCl_3$ at 25 °C.

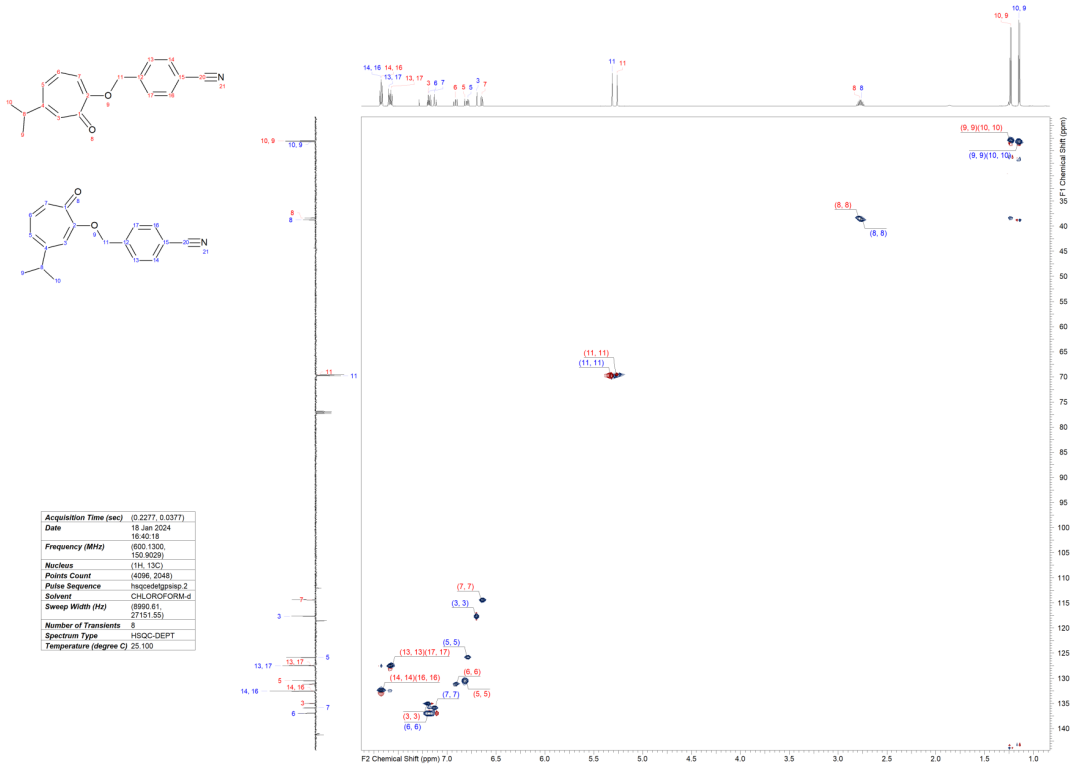

Figure S26. Fully assigned ^{1}H-^{13}C HSQC spectrum of **8β+δ** in $CDCl_3$ at 25 °C.

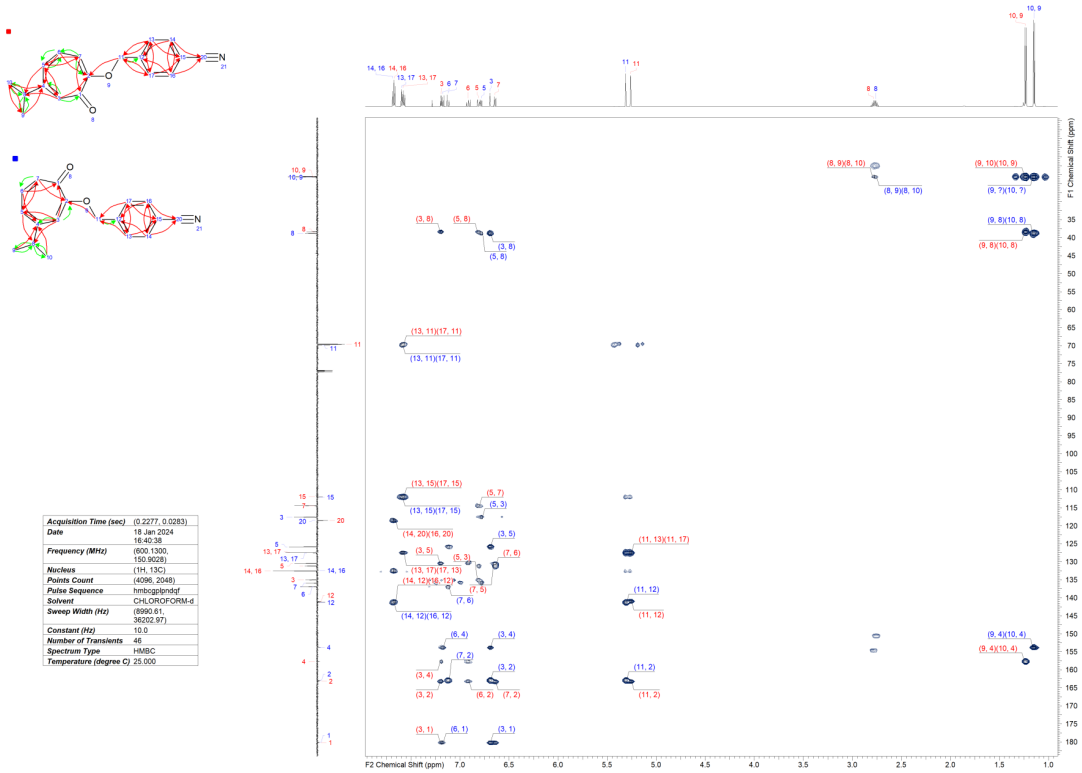

Figure S27. Fully assigned ^{1}H-^{13}C HMBC spectrum of **8β+δ** in $CDCl_3$ at 25 °C.

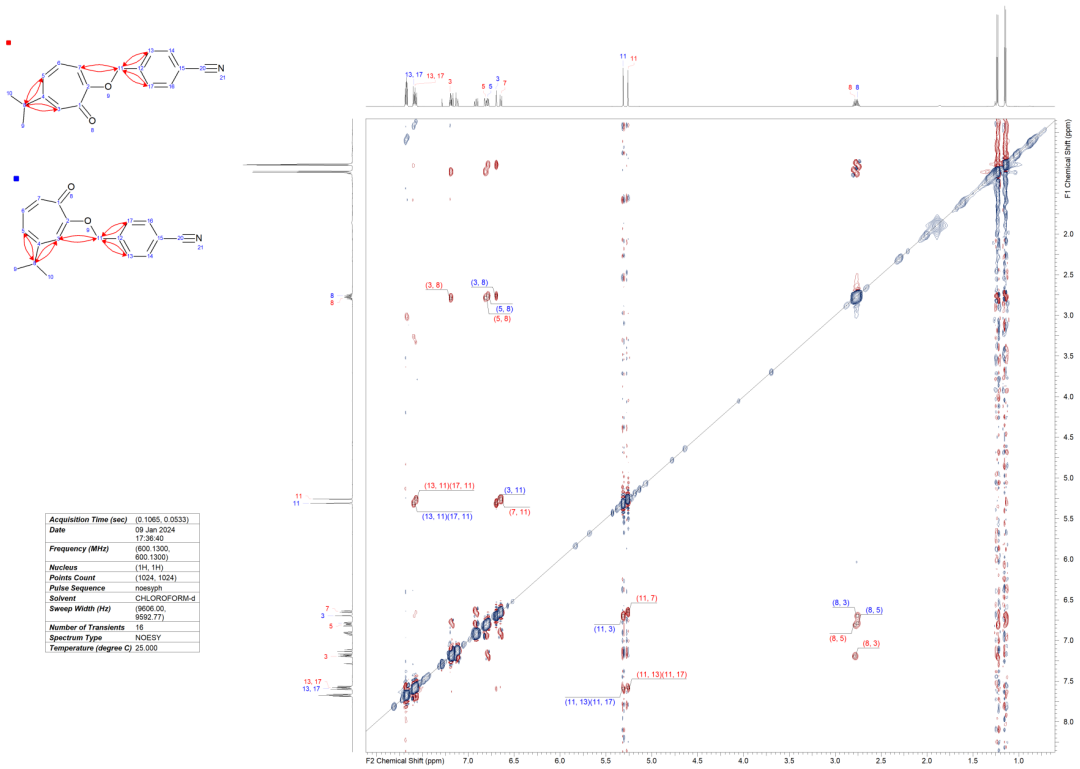

Figure S28. Fully assigned ^{1}H-^{1}H NOESY spectrum of **8β+δ** in $CDCl_3$ at 25 °C.

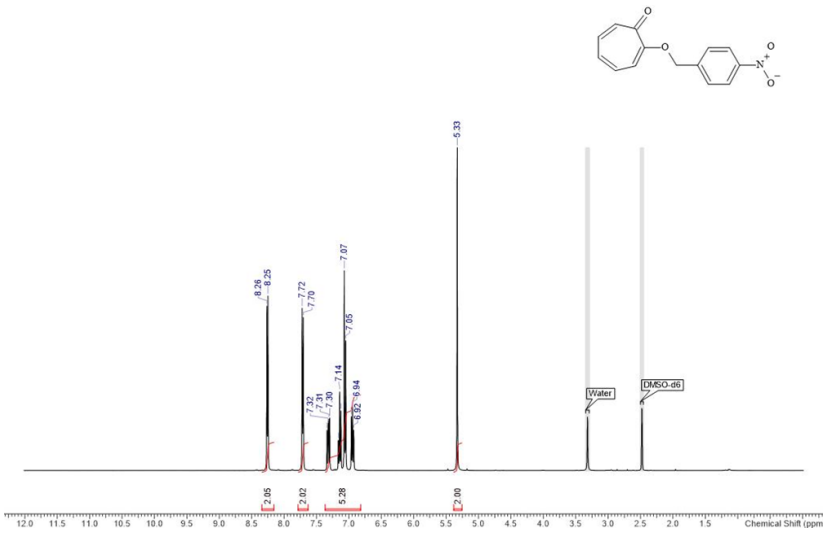

Figure S29. ^{1}H NMR (500 MHz, DMSO-d_6) spectrum of 2-((4-nitrobenzyl)oxy)cyclohepta-2,4,6-trien-1-one (**9**).

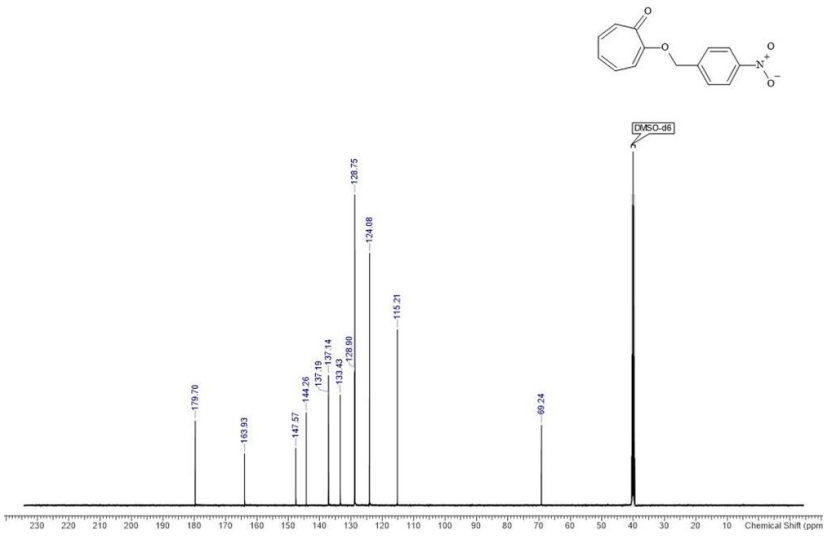

Figure S30. ^{13}C NMR (125 MHz, DMSO-d_6) spectrum of 2-((4-nitrobenzyl)oxy)cyclohepta-2,4,6-trien-1-one (**9**).

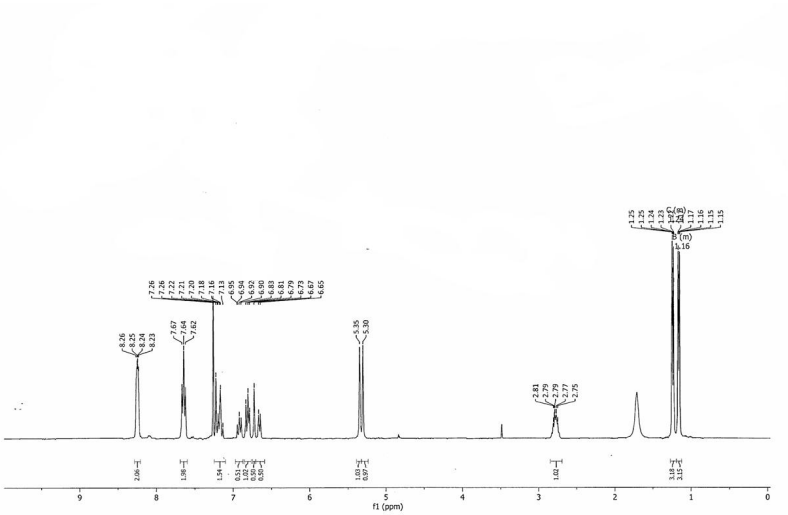

Figure S31. ^{1}H NMR of compound **9β+δ**

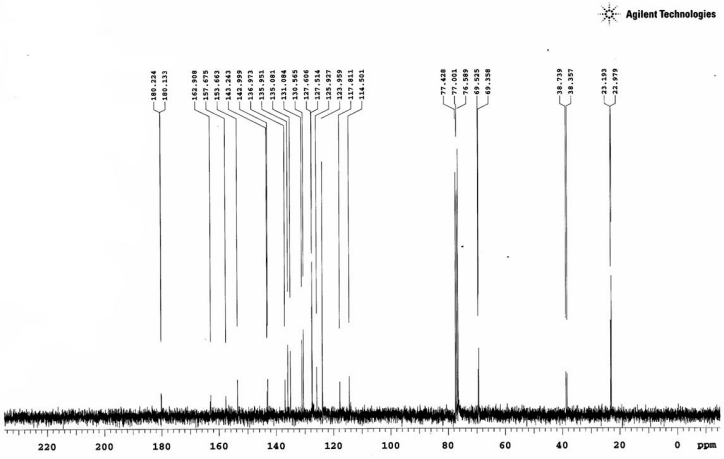

Figure S32. ^{13}C NMR of compound **9β+δ**

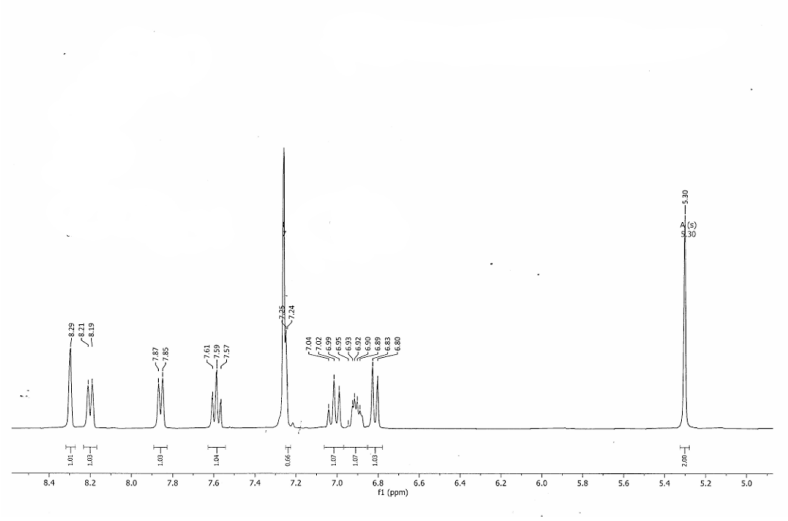

Figure S33. ^{1}H NMR of compound **10**

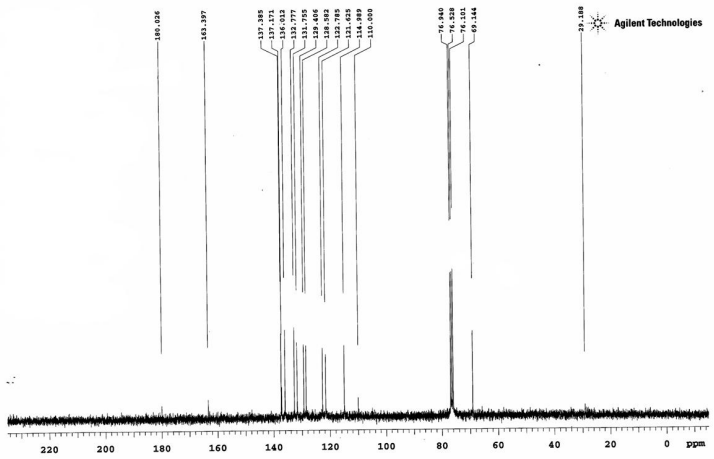

Figure S34. ^{13}C NMR of compound **10**

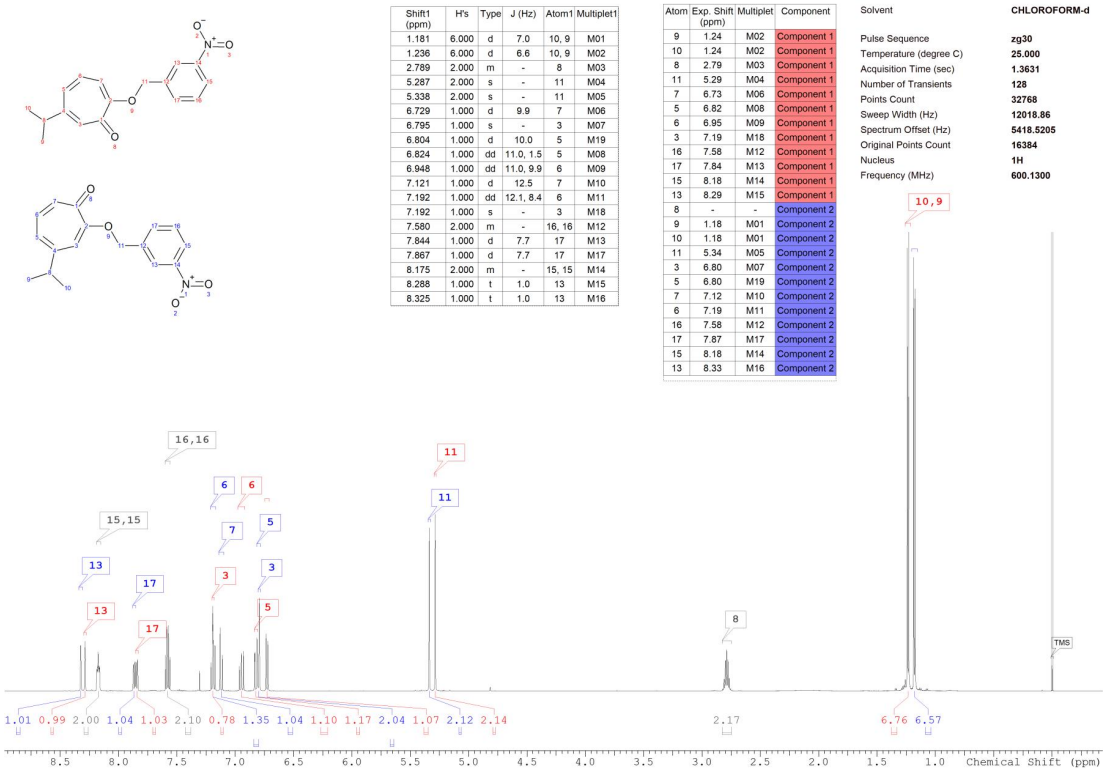

Shift1 (ppm)	H's	Type	J (Hz)	Atom1	Multiplet1
1.181	6.000	d	7.0	10, 9	M01
1.236	6.000	d	6.6	10, 9	M02
2.789	2.000	m	-	8	M03
5.287	2.000	s	-	11	M04
5.338	2.000	s	-	11	M05
6.729	1.000	d	9.9	7	M06
6.795	1.000	s	-	3	M07
6.804	1.000	d	10.0	5	M19
6.824	1.000	dd	11.0, 1.5	5	M08
6.948	1.000	dd	11.0, 9.9	6	M09
7.121	1.000	d	12.5	7	M10
7.192	1.000	dd	12.1, 8.4	6	M11
7.192	1.000	s	-	3	M18
7.580	2.000	m	-	16, 16	M12
7.844	1.000	d	7.7	17	M13
7.867	1.000	d	7.7	17	M17
8.175	2.000	m	-	15, 15	M14
8.288	1.000	t	1.0	13	M15
8.325	1.000	t	1.0	13	M16

Atom	Exp. Shift (ppm)	Multiplet	Component
9	1.24	M02	Component 1
10	1.24	M02	Component 1
8	2.79	M03	Component 1
11	5.29	M04	Component 1
7	6.73	M06	Component 1
5	6.82	M08	Component 1
6	6.95	M09	Component 1
3	7.19	M18	Component 1
16	7.58	M12	Component 1
17	7.84	M13	Component 1
15	8.18	M14	Component 1
13	8.29	M15	Component 1
8	-	-	Component 2
9	1.18	M01	Component 2
10	1.18	M01	Component 2
11	5.34	M05	Component 2
3	6.80	M07	Component 2
5	6.80	M19	Component 2
7	7.12	M10	Component 2
6	7.19	M11	Component 2
16	7.58	M12	Component 2
17	7.87	M17	Component 2
15	8.18	M14	Component 2
13	8.33	M16	Component 2

Solvent	CHLOROFORM-d
Pulse Sequence	zg30
Temperature (degree C)	25.000
Acquisition Time (sec)	1.3631
Number of Transients	128
Points Count	32768
Sweep Width (Hz)	12018.86
Spectrum Offset (Hz)	5418.5205
Original Points Count	16384
Nucleus	1H
Frequency (MHz)	600.1300

Figure S35. ^{1}H spectrum, structure, numbering and full assignment of **10β+δ** in $CDCl_3$ at 25 °C.

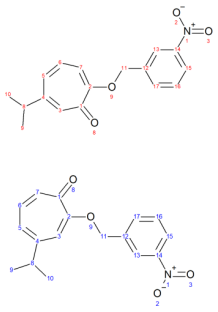

Shift1 (ppm)	C's	Type	Atom1	Multiplet1
22.969	2.000	s	10, 9	M01
23.184	2.000	s	10, 9	M02
38.328	1.000	s	8	M03
38.726	1.000	s	8	M04
69.459	1.000	s	11	M05
69.626	1.000	s	11	M06
114.603	1.000	s	7	M07
118.011	1.000	s	3	M08
122.095	1.000	s	13	M09
122.159	1.000	s	13	M10
123.154	2.000	s	15	M11
125.917	1.000	s	5	M12
129.858	2.000	s	16, 16	M13
130.511	1.000	s	5	M14
131.251	1.000	s	6	M15
133.298	1.000	s	17	M16
133.377	1.000	s	17	M17
134.978	1.000	s	3	M18
135.877	1.000	s	7	M29
136.968	1.000	s	6	M28

Shift1 (ppm)	C's	Type	Atom1	Multiplet1
137.836	1.000	s	12	M20
138.067	1.000	s	12	M19
148.362	2.000	s	14, 14	M21
153.808	1.000	s	4	M22
157.645	1.000	s	4	M23
162.988	1.000	s	2	M24
163.179	1.000	s	2	M27
180.114	1.000	s	1	M26
180.201	1.000	s	1	M25

Atom	Exp. Shift (ppm)	Multiplet	Component
15	-	-	Component 1
9	22.97	M01	Component 1
10	22.97	M01	Component 1
8	38.33	M03	Component 1
11	69.46	M05	Component 1
7	114.60	M07	Component 1
13	122.10	M09	Component 1
16	129.86	M13	Component 1
5	130.51	M14	Component 1
6	131.25	M15	Component 1
17	133.30	M16	Component 1
3	134.98	M18	Component 1
12	137.84	M20	Component 1
14	148.36	M21	Component 1
4	157.65	M23	Component 1
2	163.18	M27	Component 1
1	180.20	M25	Component 1
9	23.18	M02	Component 2
10	23.18	M02	Component 2
8	38.73	M04	Component 2

Atom	Exp. Shift (ppm)	Multiplet	Component
11	69.63	M06	Component 2
3	118.01	M08	Component 2
13	122.16	M10	Component 2
15	123.15	M11	Component 2
5	125.92	M12	Component 2
16	129.86	M13	Component 2
17	133.38	M17	Component 2
7	135.88	M29	Component 2
6	136.97	M28	Component 2
12	138.07	M19	Component 2
14	148.36	M21	Component 2
4	153.81	M22	Component 2
2	162.99	M24	Component 2
1	180.11	M26	Component 2

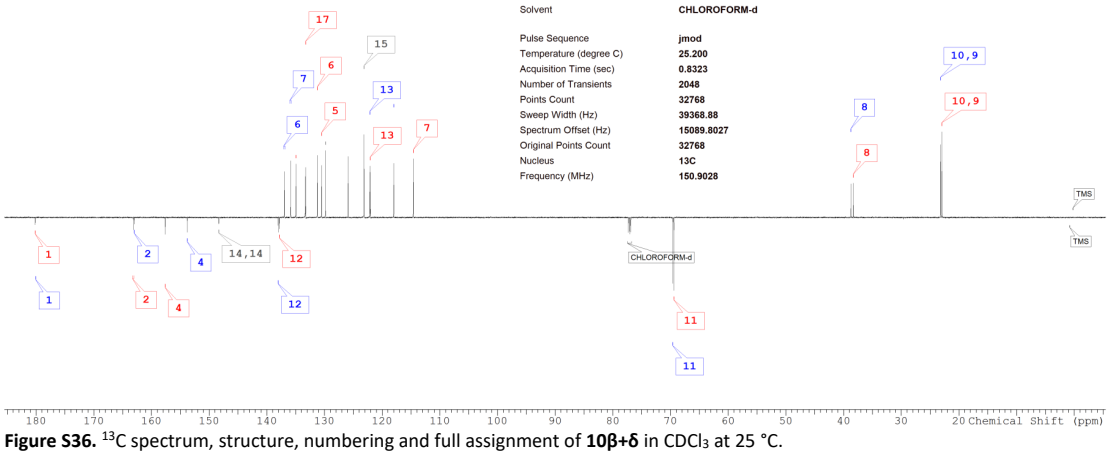

Figure S36. ^{13}C spectrum, structure, numbering and full assignment of **10β+δ** in $CDCl_3$ at 25 °C.

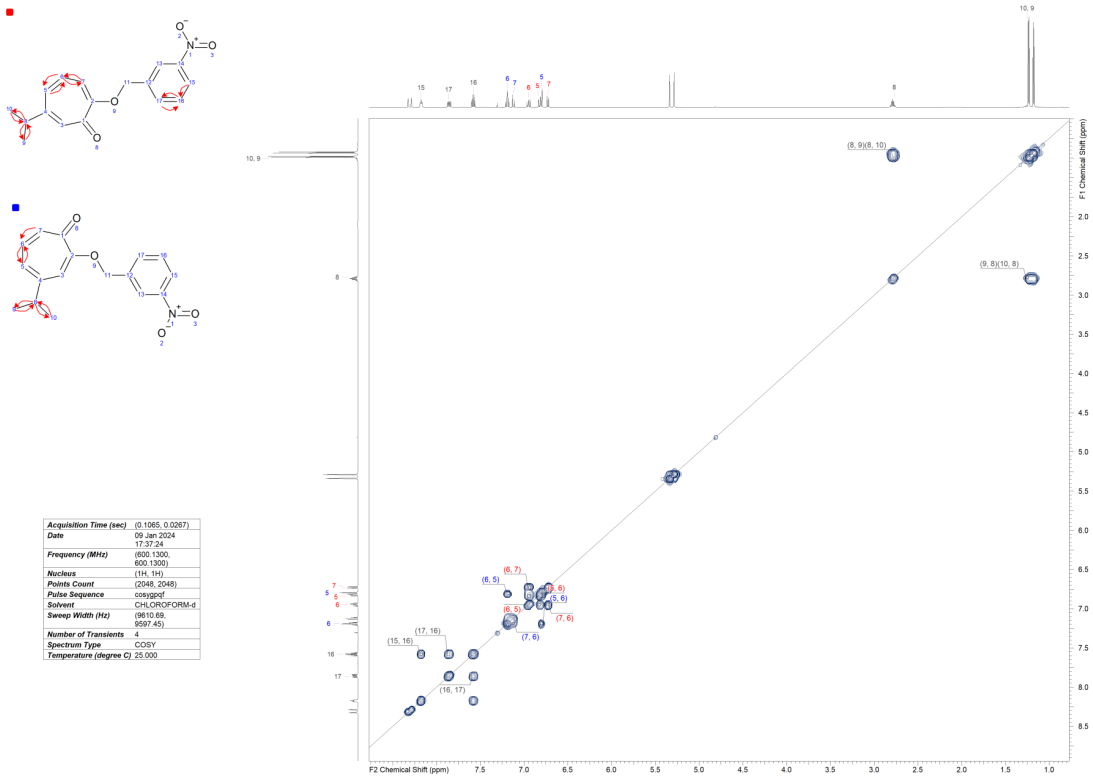

Figure S37. Fully assigned ^{1}H-^{1}H COSY spectrum of **10β+δ** in $CDCl_3$ at 25 °C.

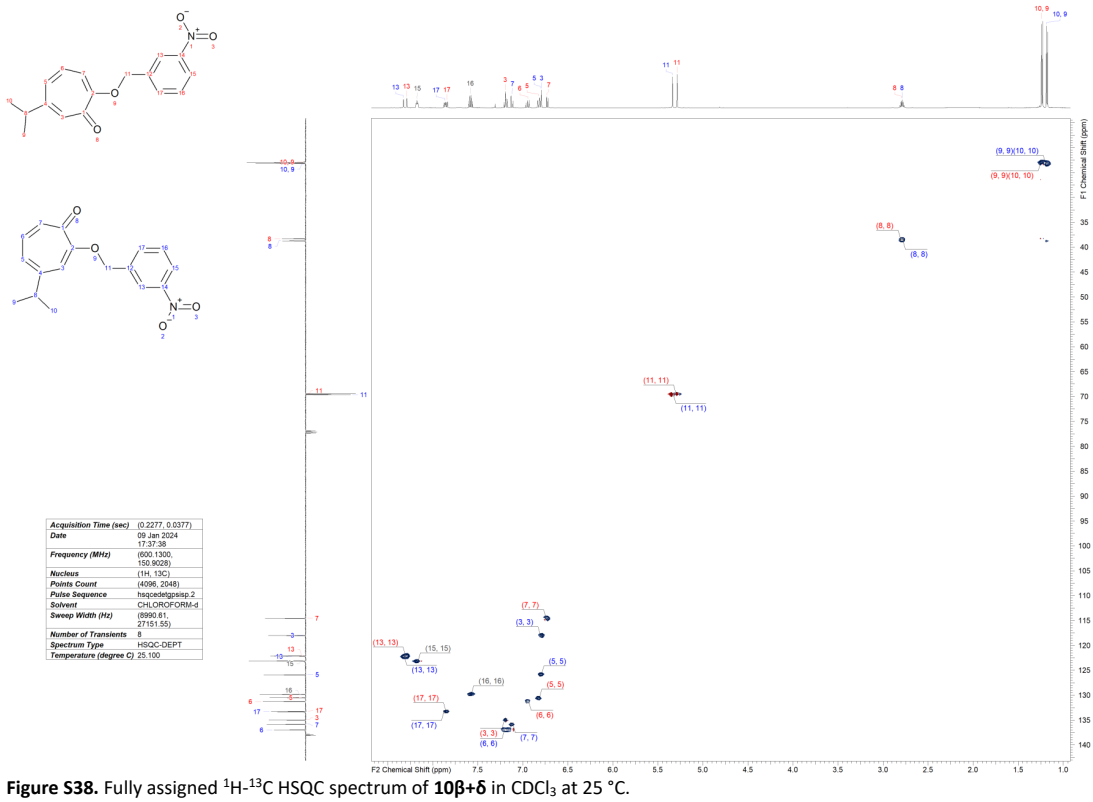

Figure S38. Fully assigned ^{1}H-^{13}C HSQC spectrum of **10β+δ** in $CDCl_3$ at 25 °C.

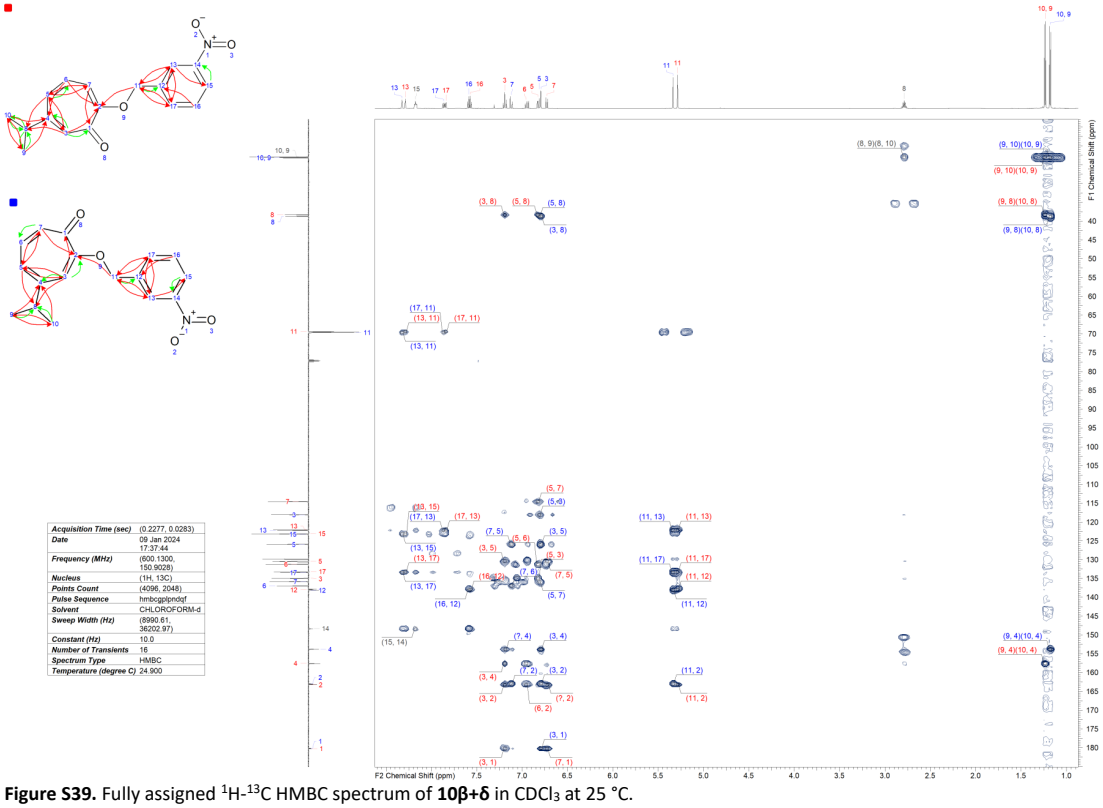

Figure S39. Fully assigned ^{1}H-^{13}C HMBC spectrum of **10β+δ** in $CDCl_3$ at 25 °C.

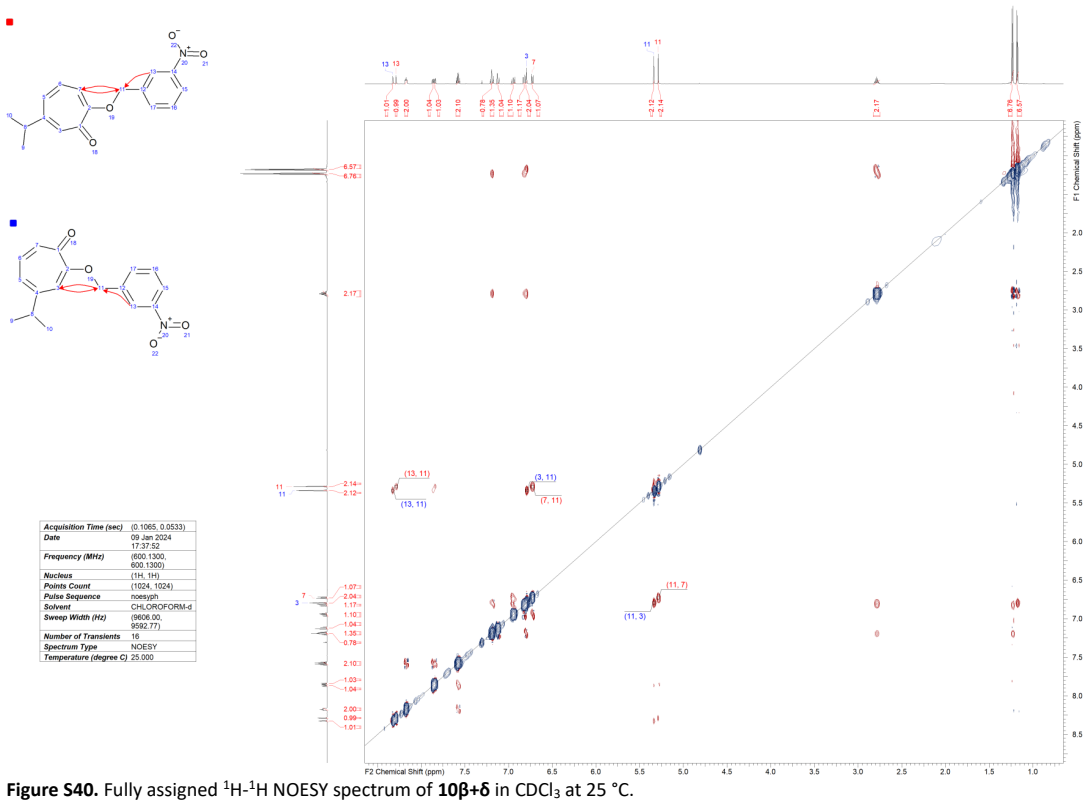

Figure S40. Fully assigned ^{1}H-^{1}H NOESY spectrum of **10β+δ** in $CDCl_3$ at 25 °C.

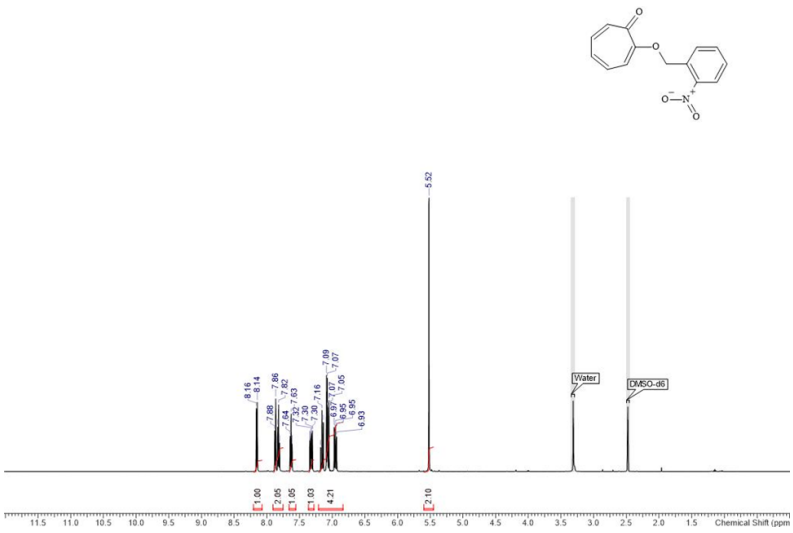

Figure S41. ^{1}H NMR (500 MHz, DMSO-d_6) spectrum of 2-((2-nitrobenzyl)oxy)cyclohepta-2,4,6-trien-1-one (**11**).

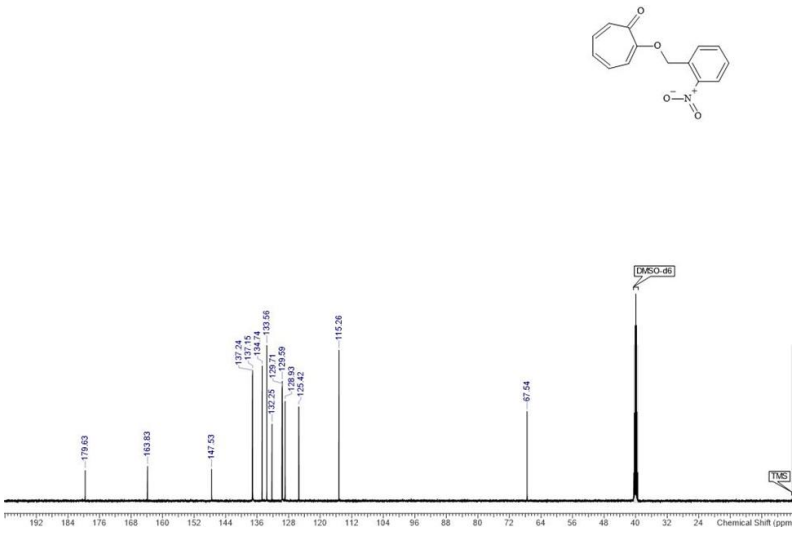

Figure S42. ^{13}C NMR (125 MHz, DMSO-d_6) spectrum of 2-((2-nitrobenzyl)oxy)cyclohepta-2,4,6-trien-1-one (**11**).

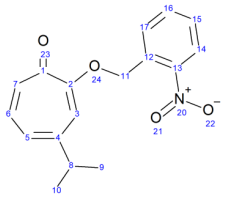

Shift1 (ppm)	H's	Type	J (Hz)	Atom1	Multiplet1
1.19	6.000	d	6.6	10, 9	M01
2.80	1.000	dt	13.7, 6.9	8	M02
5.62	2.000	s	-	11	M03
6.76	1.000	s	-	3	M04
6.80	1.000	d	8.4	5	M05
7.15	1.000	d	12.1	7	M06
7.20	1.000	dd	12.5, 8.4	6	M07
7.51	1.000	td	7.8, 0.8	15	M09
7.73	1.000	td	7.6, 1.1	16	M10
8.10	1.000	d	7.7	17	M11
8.19	1.000	dd	8.1, 1.1	14	M12

^{1}H NMR (600 MHz, CHLOROFORM-d): δ = 1.19 (d, *J* = 6.6 Hz, 6 H, 10, 9), 2.80 (dt, *J* = 13.7, 6.9 Hz, 1 H, 8), 5.62 (s, 2 H, 11), 6.76 (s, 1 H, 3), 6.80 (d, *J* = 8.4 Hz, 1 H, 5), 7.15 (d, *J* = 12.1 Hz, 1 H, 7), 7.20 (dd, *J* = 12.5, 8.4 Hz, 1 H, 6), 7.51 (td, *J* = 7.8, 0.8 Hz, 1 H, 15), 7.73 (td, *J* = 7.6, 1.1 Hz, 1 H, 16), 8.10 (d, *J* = 7.7 Hz, 1 H, 17), 8.19 (dd, *J* = 8.1, 1.1 Hz, 1 H, 14) ppm

Solvent	**CHLOROFORM-d**
Pulse Sequence	**zg30**
Temperature (degree C)	**25.000**
Acquisition Time (sec)	**1.3631**
Number of Transients	**128**
Points Count	**32768**
Sweep Width (Hz)	**12018.86**
Spectrum Offset (Hz)	**5401.5630**
Original Points Count	**16384**
Nucleus	**1H**
Frequency (MHz)	**600.1300**

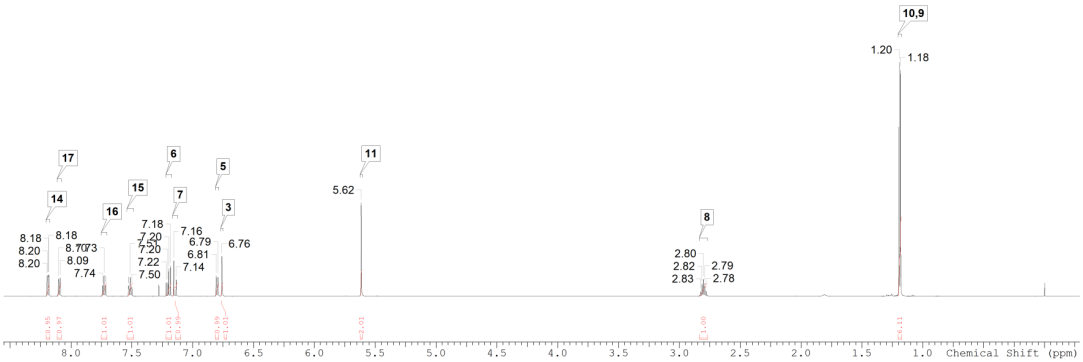

Figure S43. ^{1}H spectrum, structure, numbering and full assignment of **11β** in $CDCl_3$ at 25 °C.

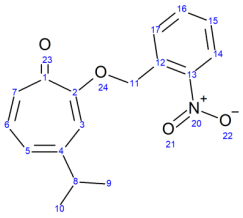

Atom	Exp. Shift (ppm)
10	23.2
9	23.2
8	38.8
11	67.4
3	117.0
14	125.0
5	125.6
15	128.6
17	128.9
12	132.6
16	134.5
7	135.7
6	137.0
13	146.6
4	154.0
2	163.0
1	180.1

^{13}C NMR (151 MHz, CHLOROFORM-d): δ = 23.2 (10, 9), 38.8 (8), 67.4 (11), 117.0 (3), 125.0 (14), 125.6 (5), 128.6 (15), 128.9 (17), 132.6 (12), 134.5 (16), 135.7 (7), 137.0 (6), 146.6 (13), 154.0 (4), 163.0 (2), 180.1 (1) ppm

Solvent	**CHLOROFORM-d**
Pulse Sequence	**jmod**
Temperature (degree C)	**25.100**
Acquisition Time (sec)	**0.8323**
Number of Transients	**1792**
Points Count	**32768**
Sweep Width (Hz)	**39368.88**
Spectrum Offset (Hz)	**15089.8027**
Original Points Count	**32768**
Nucleus	**13C**
Frequency (MHz)	**150.9028**

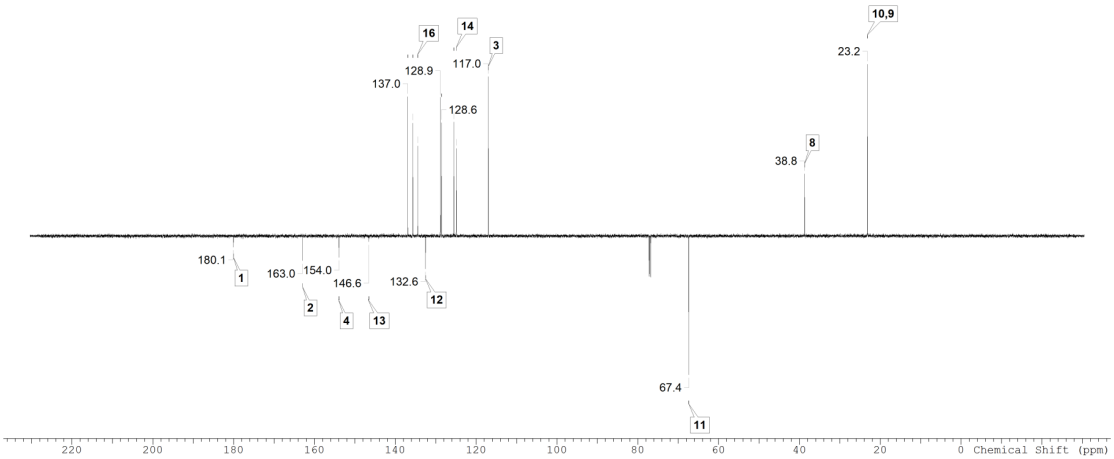

Figure S44. ^{13}C spectrum, structure, numbering and full assignment of **11β** in $CDCl_3$ at 25 °C.

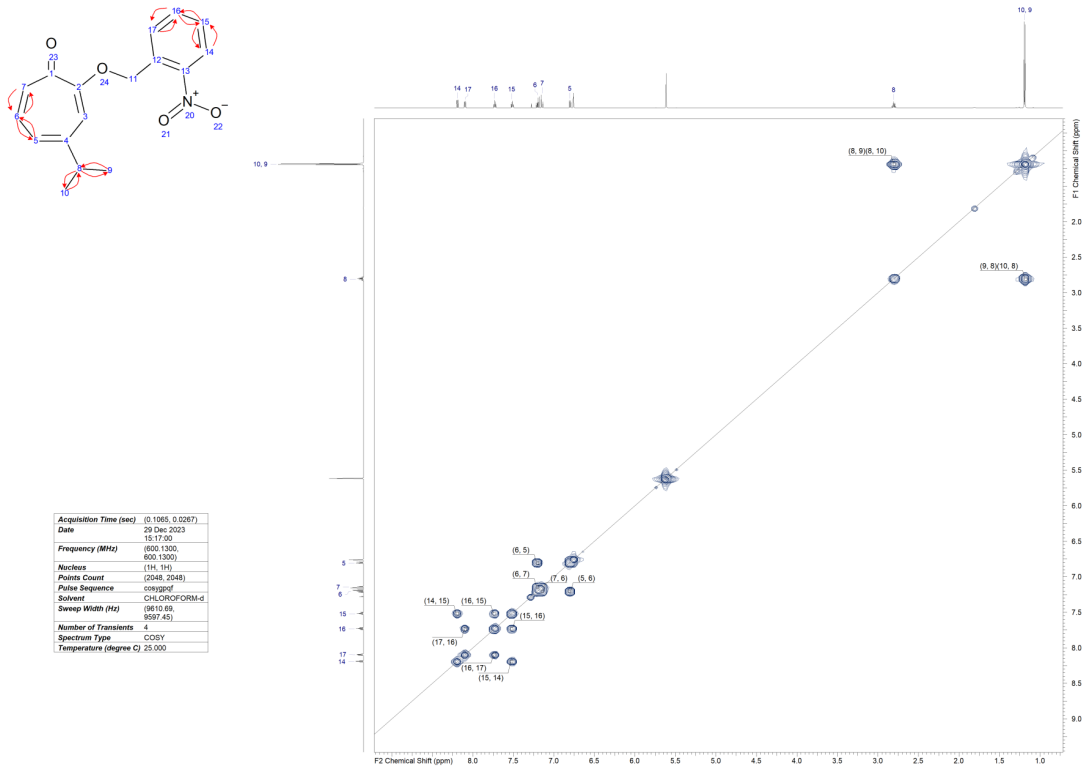

Figure S45. Fully assigned ^{1}H-^{1}H COSY spectrum of **11β** in $CDCl_3$ at 25 °C.

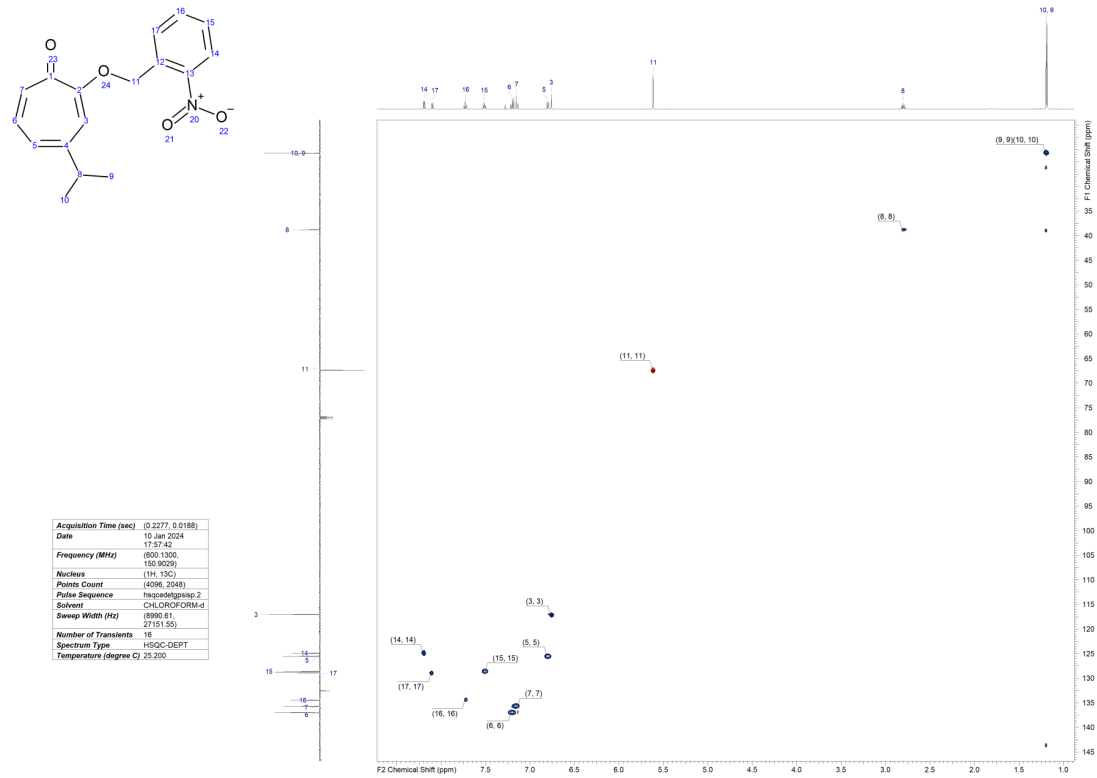

Figure S46. Fully assigned ^{1}H-^{13}C HSQC spectrum of **11β** in $CDCl_3$ at 25 °C.

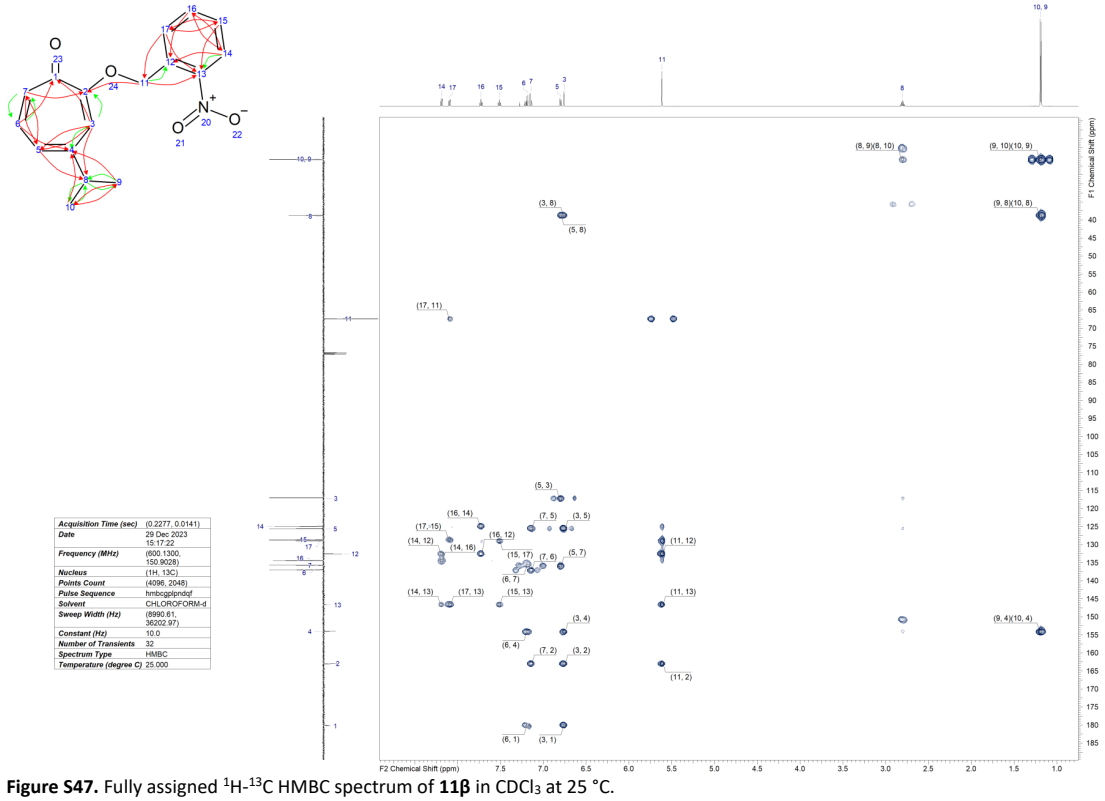

Figure S47. Fully assigned ^{1}H-^{13}C HMBC spectrum of **11β** in $CDCl_3$ at 25 °C.

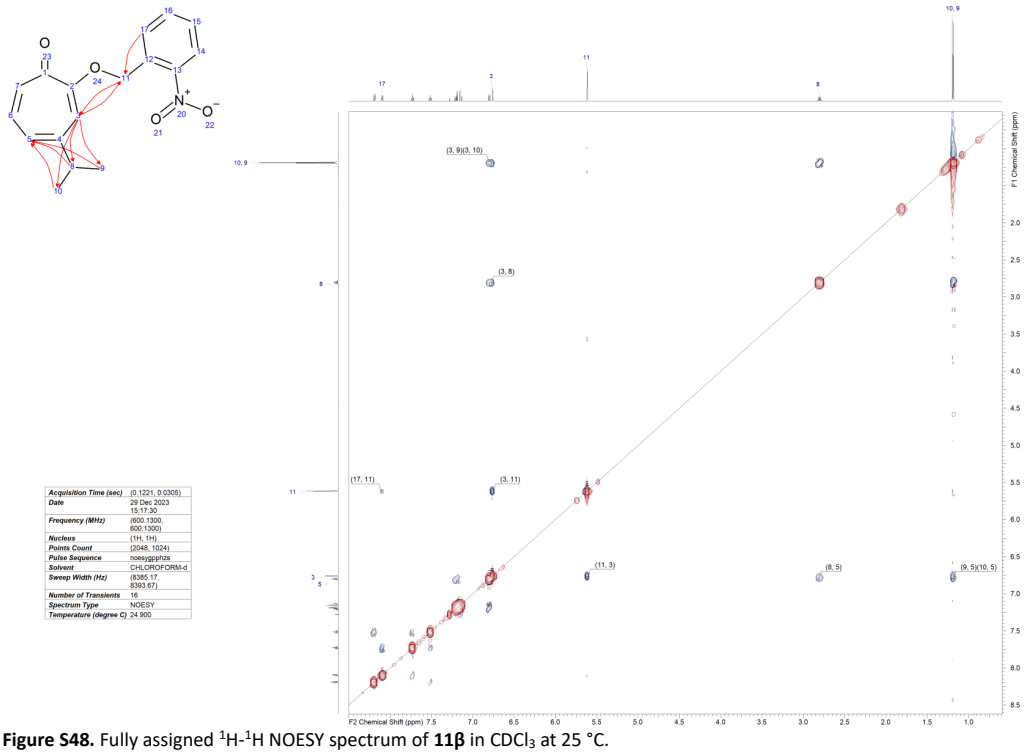

Figure S48. Fully assigned ^{1}H-^{1}H NOESY spectrum of **11β** in $CDCl_3$ at 25 °C.

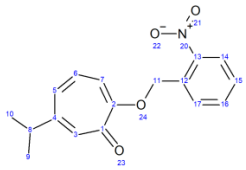

Shift1 (ppm)	H's	Type	J (Hz)	Atom1	Multiplet1
1.24	6.000	d	6.8	10, 9	M02
2.80	1.000	spt	7.0	8	M03
5.58	2.000	s	-	11	M04
6.71	1.000	d	9.5	7	M05
6.82	1.000	dt	11.0, 1.0	5	M06
6.96	1.000	ddd	11.2, 10.2, 1.2	6	M08
7.21	1.000	s	-	3	M09
7.50	1.000	t	7.9	15	M10
7.72	1.000	t	7.5	16	M11
8.08	1.000	d	8.1	17	M01
8.20	1.000	d	8.1	14	M13

^{1}H NMR (600 MHz, CHLOROFORM-d): δ = 1.24 (d, J = 6.8 Hz, 6 H, 10, 9), 2.80 (spt, J = 7.0 Hz, 1 H, 8), 5.58 (s, 2 H, 11), 6.71 (d, J = 9.5 Hz, 1 H, 7), 6.82 (dt, J = 11.0, 1.0 Hz, 1 H, 5), 6.96 (ddd, J = 11.2, 10.2, 1.2 Hz, 1 H, 6), 7.21 (s, 1 H, 3), 7.50 (t, J = 7.9 Hz, 1 H, 15), 7.72 (t, J = 7.5 Hz, 1 H, 16), 8.08 (d, J = 8.1 Hz, 1 H, 17), 8.20 (d, J = 8.1 Hz, 1 H, 14) ppm

Solvent	CHLOROFORM-d
Pulse Sequence	zg30
Temperature (degree C)	25.000
Acquisition Time (sec)	1.3631
Number of Transients	128
Points Count	32768
Sweep Width (Hz)	12018.86
Spectrum Offset (Hz)	5396.0532
Original Points Count	16384
Nucleus	1H
Frequency (MHz)	600.1300

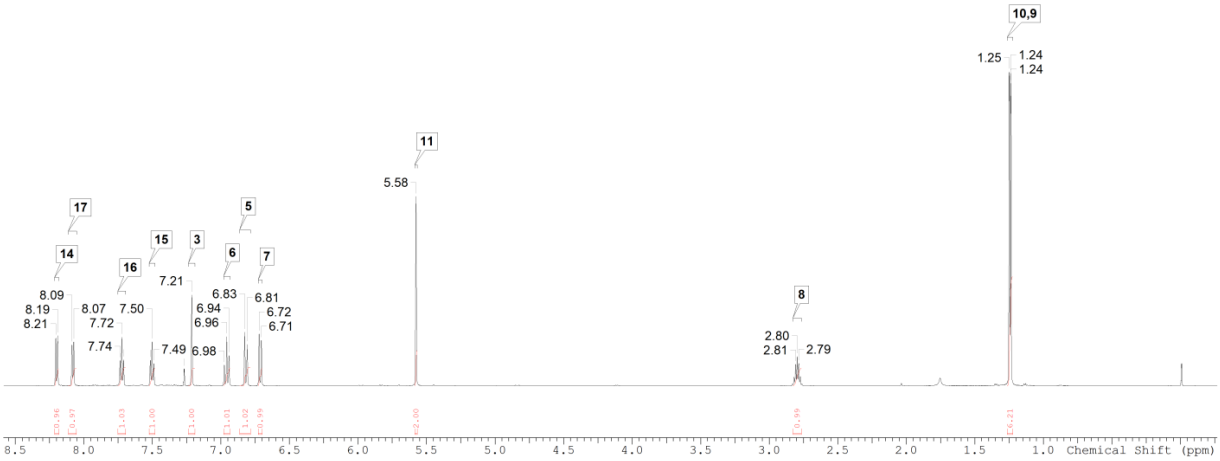

Figure S49. ^{1}H spectrum, structure, numbering and full assignment of **11δ** in $CDCl_3$ at 25 °C.

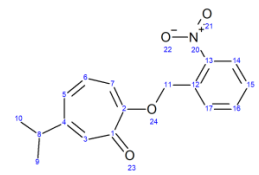

Atom	Exp. Shift (ppm)
10	23.0
9	23.0
8	38.4
11	67.4
7	113.9
14	125.0
15	128.6
17	128.7
5	130.3
6	131.4
12	132.6
16	134.6
3	134.9
13	146.4
4	157.6
2	163.2
1	180.2

^{13}C NMR (151 MHz, CHLOROFORM-d): δ = 23.0 (10, 9), 38.4 (8), 67.4 (11), 113.9 (7), 125.0 (14), 128.6 (15), 128.7 (17), 130.3 (5), 131.4 (6), 132.6 (12), 134.6 (16), 134.9 (3), 146.4 (13), 157.6 (4), 163.2 (2), 180.2 (1) ppm

Solvent	**CHLOROFORM-d**
Pulse Sequence	**jmod**
Temperature (degree C)	**25.200**
Acquisition Time (sec)	**0.8323**
Number of Transients	**1792**
Points Count	**32768**
Sweep Width (Hz)	**39368.88**
Spectrum Offset (Hz)	**15089.8027**
Original Points Count	**32768**
Nucleus	**13C**
Frequency (MHz)	**150.9028**

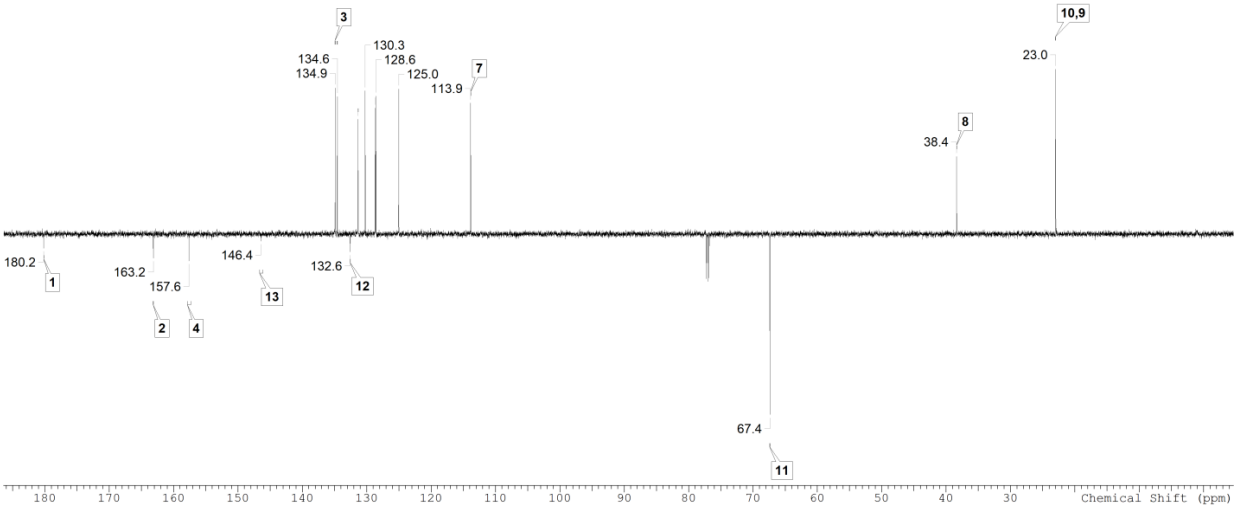

Figure S50. ^{13}C spectrum, structure, numbering and full assignment of **11δ** in $CDCl_3$ at 25 °C.

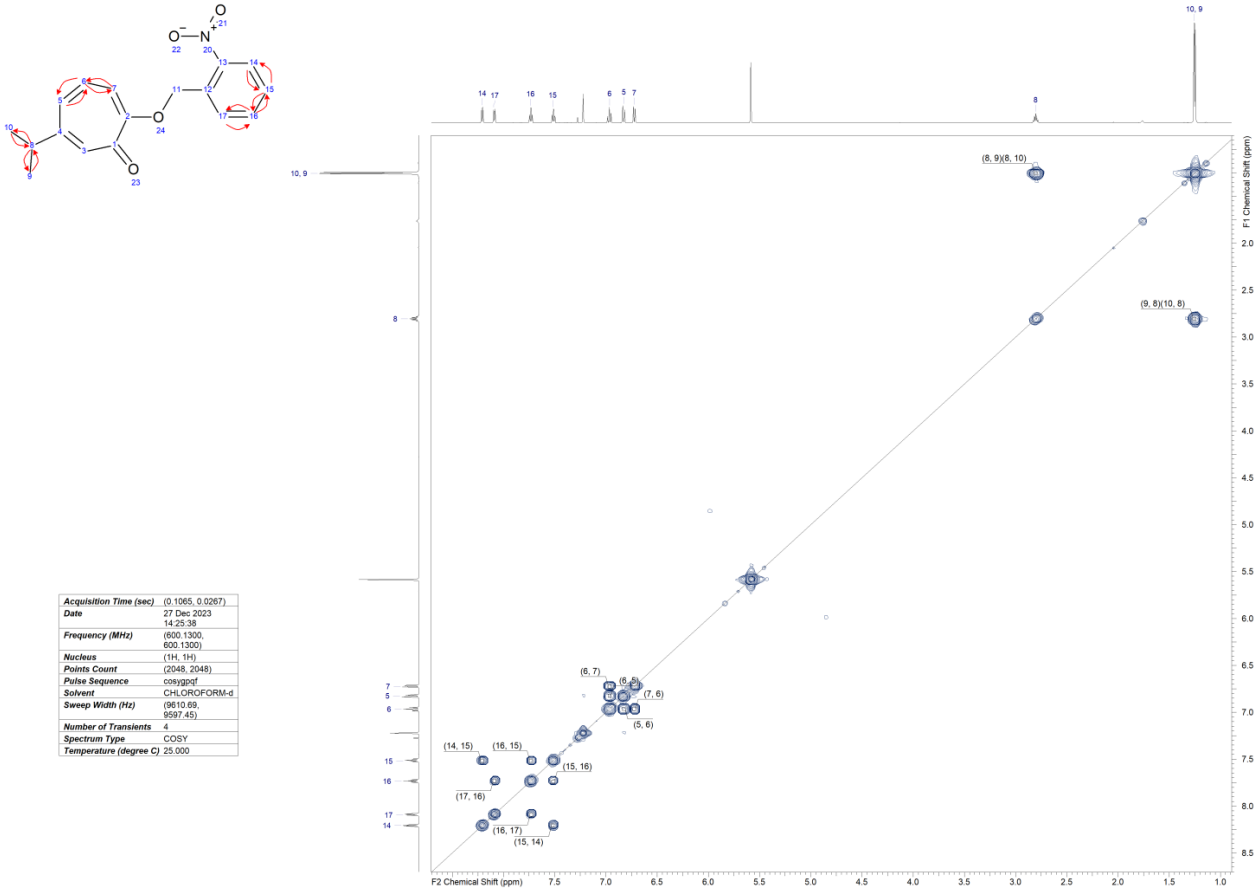

Figure S51. Fully assigned ^{1}H-^{1}H COSY spectrum of **11δ** in $CDCl_3$ at 25 °C.

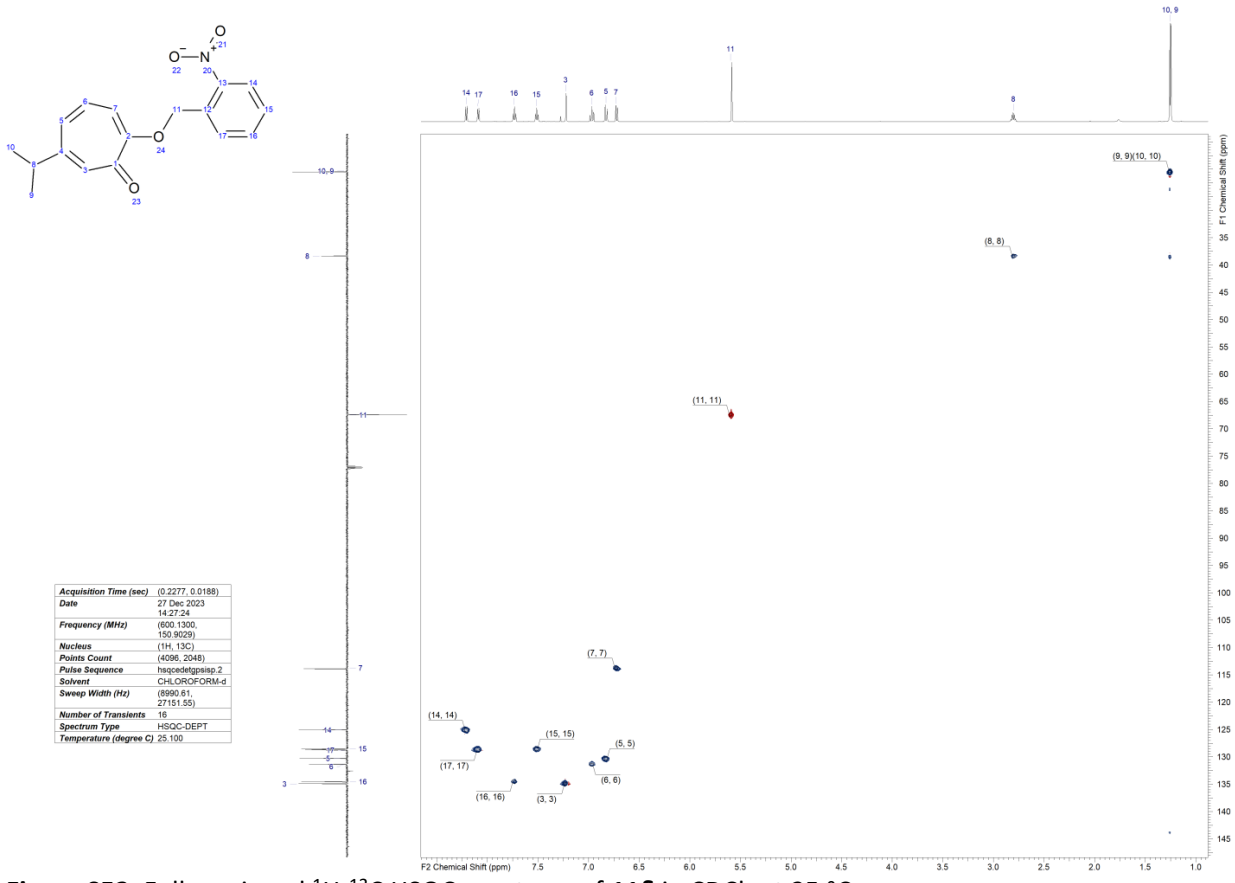

Figure S52. Fully assigned ^{1}H-^{13}C HSQC spectrum of **11δ** in $CDCl_3$ at 25 °C.

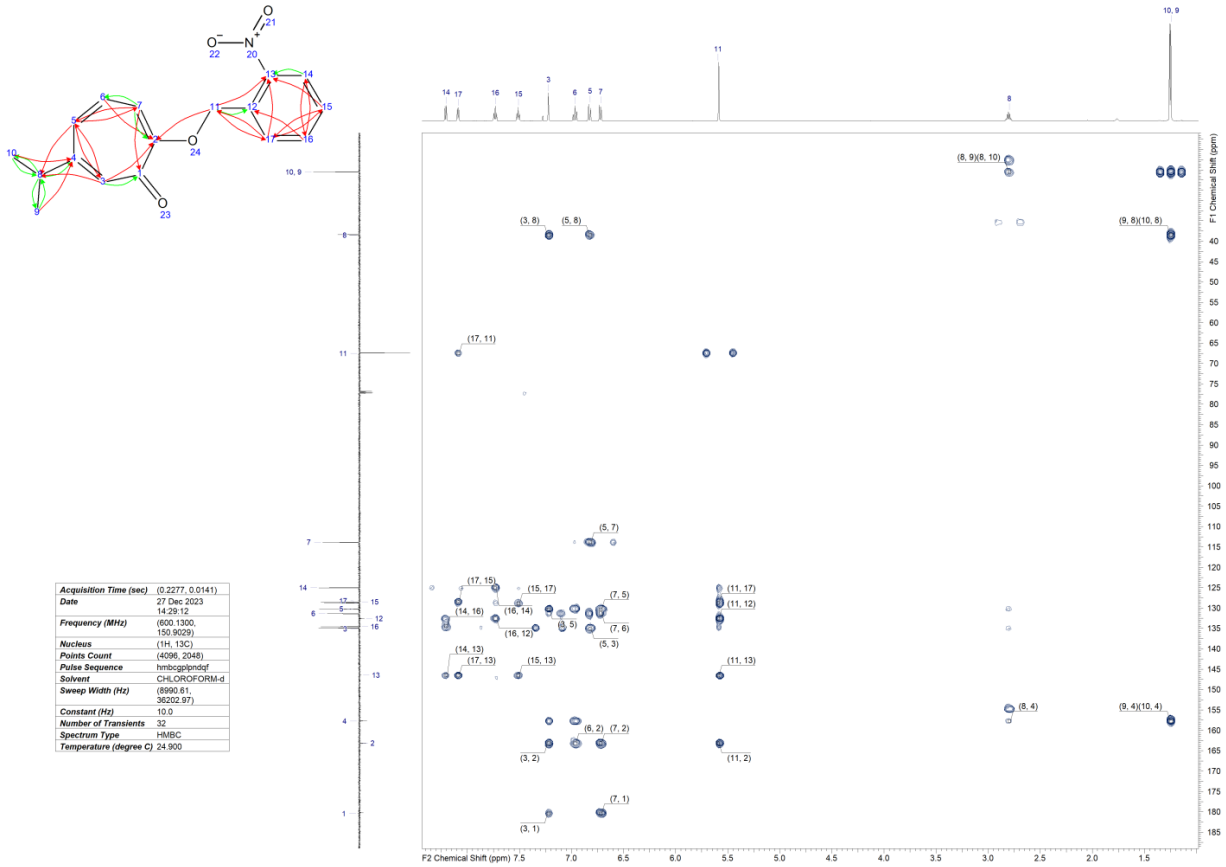

Figure S53. Fully assigned ^{1}H-^{13}C HMBC spectrum of **11δ** in $CDCl_3$ at 25 °C.

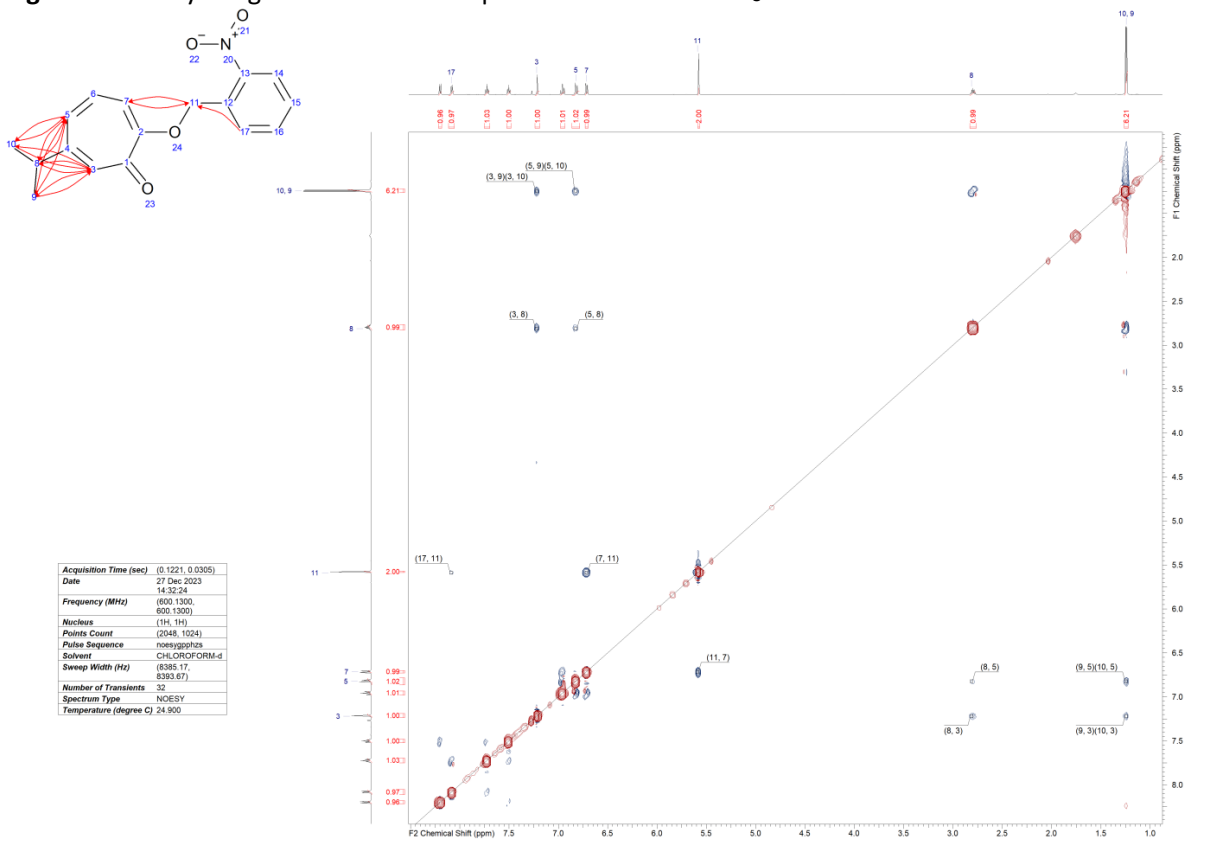

Figure S54. Fully assigned ^{1}H-^{1}H NOESY spectrum of **11δ** in $CDCl_3$ at 25 °C.

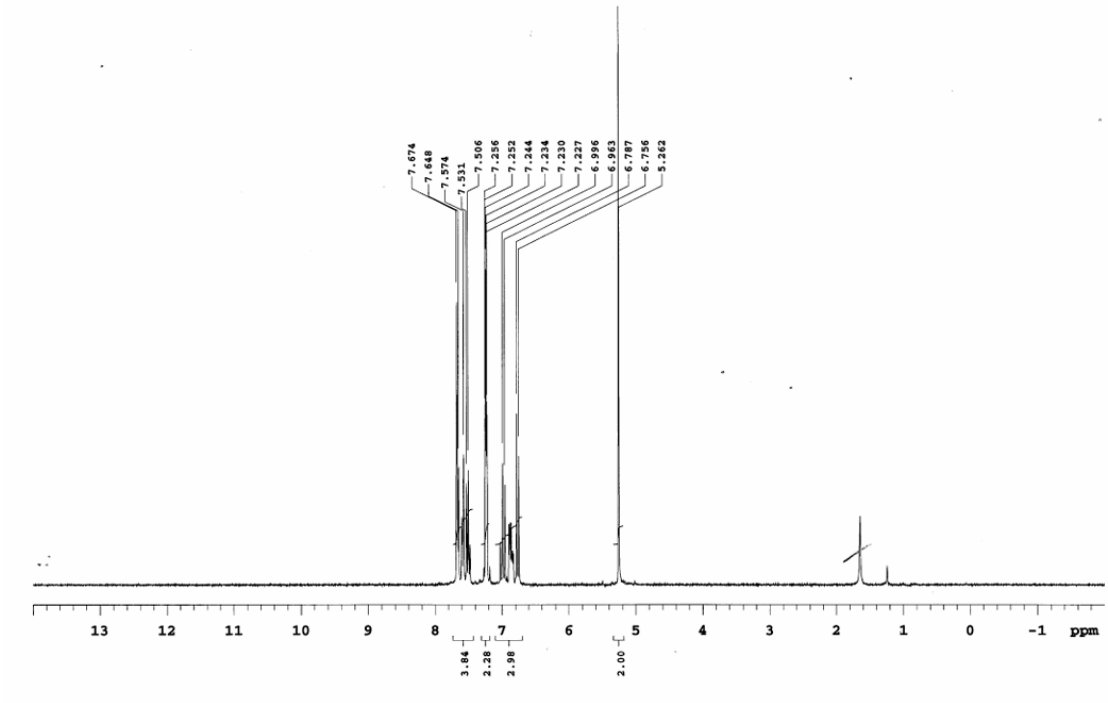

Figure S55. ^{1}H NMR of compound **12**

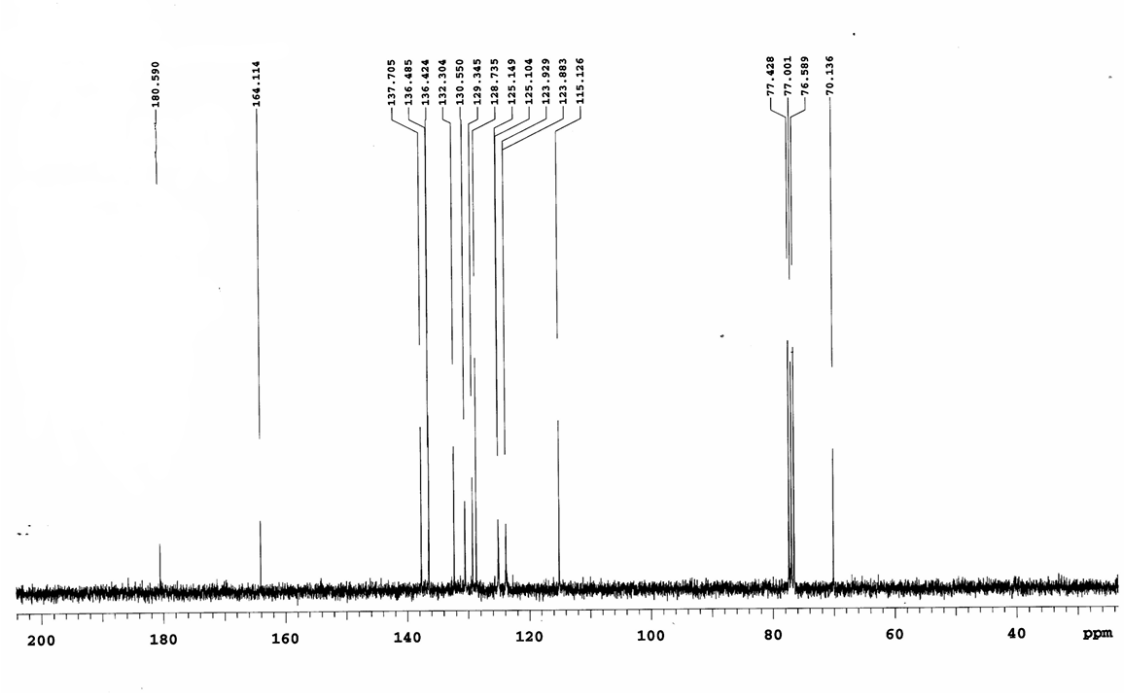

Figure S56. ^{13}C NMR of compound **12**

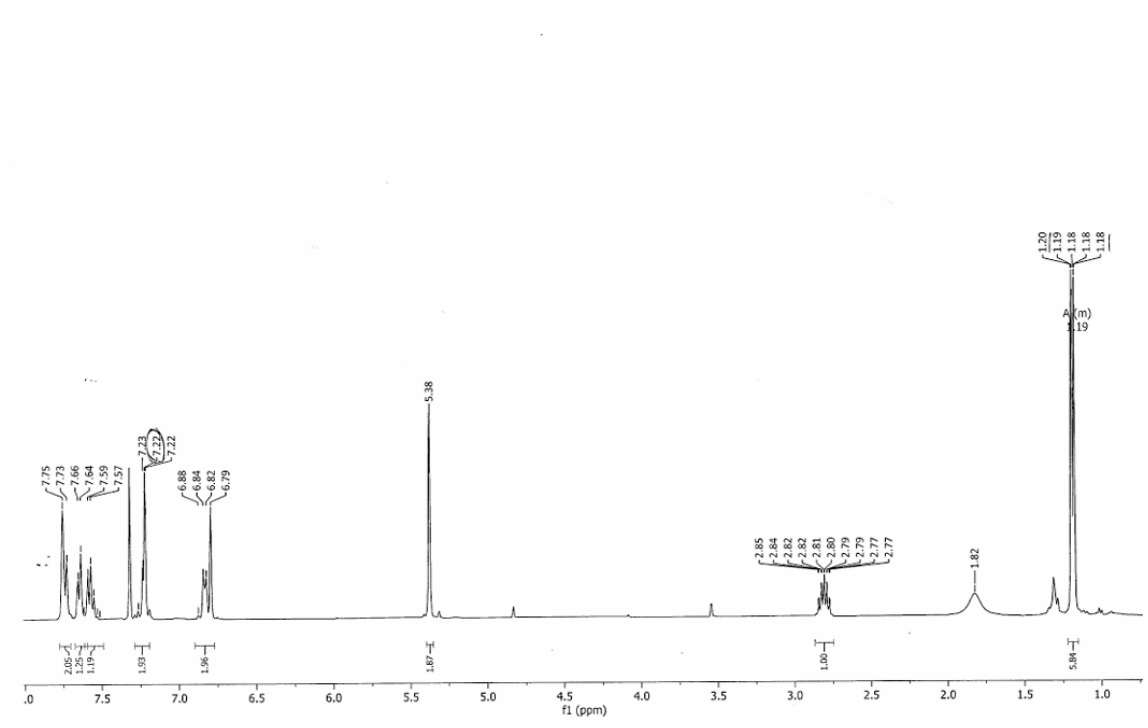

Figure S57. ^{1}H NMR of compound **12β**

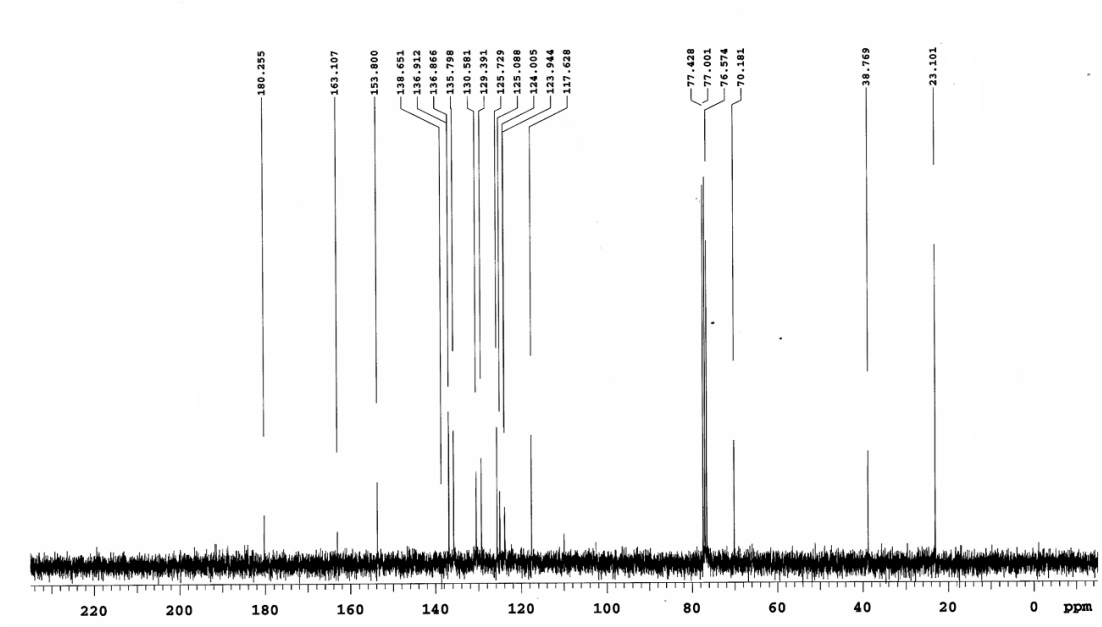

Figure S58. ^{13}C NMR of compound **12β**

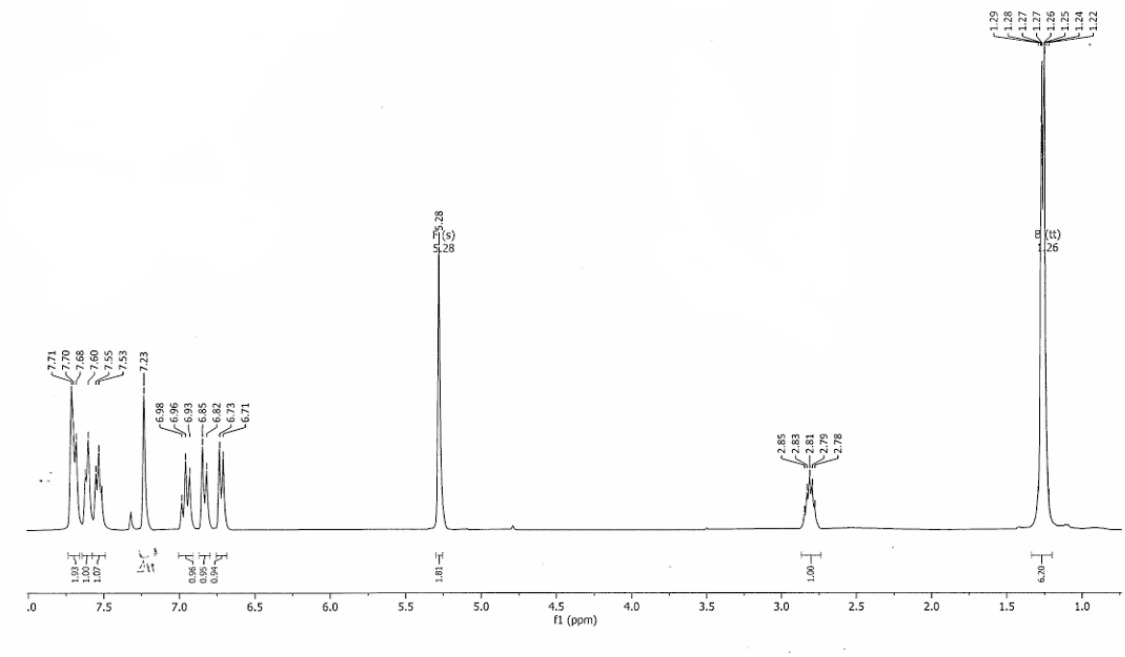

Figure S59. ^{1}H NMR of compound **12δ**

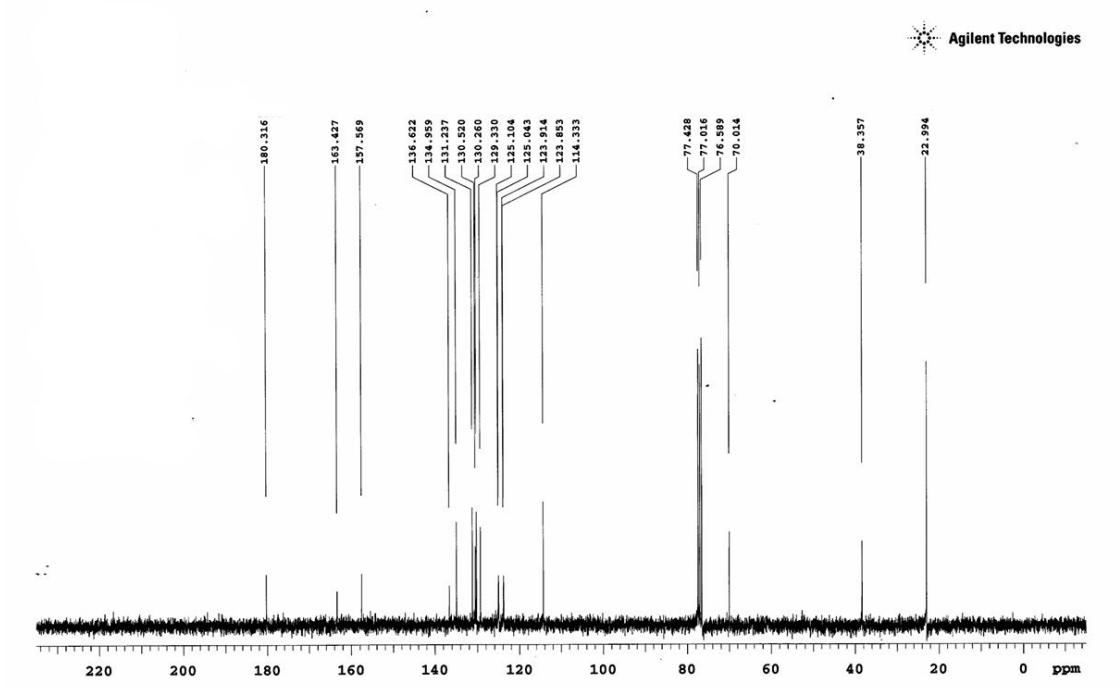

Figure S60. ^{13}C NMR of compound **12δ**

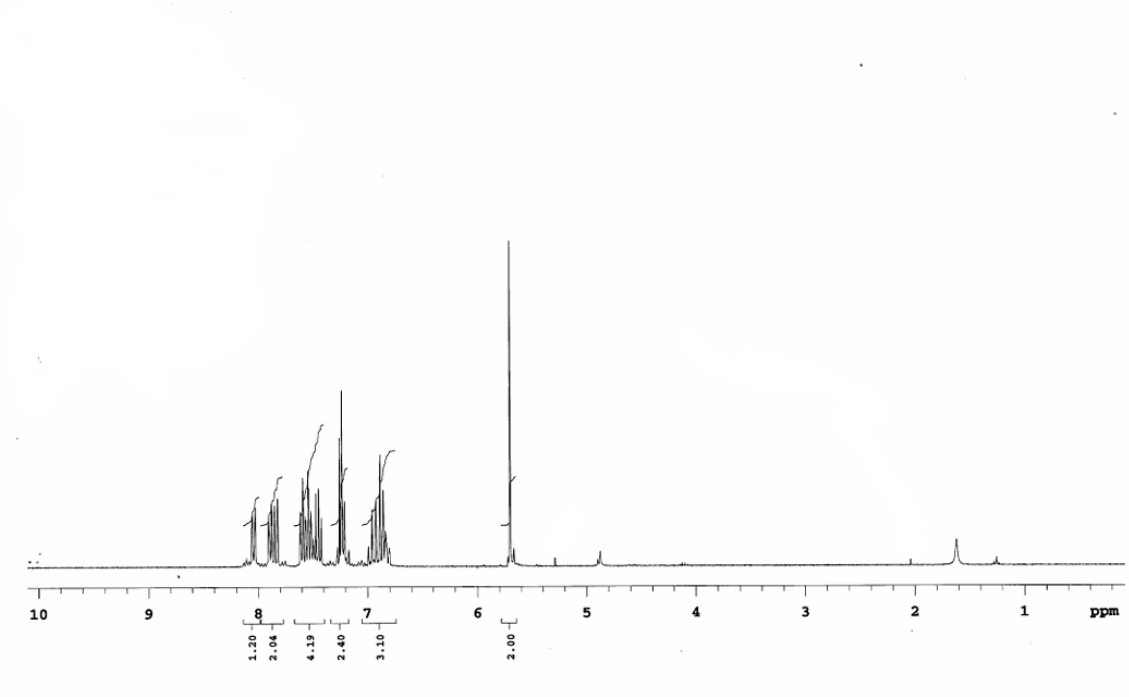

Figure S61. ^{1}H NMR of compound **13**

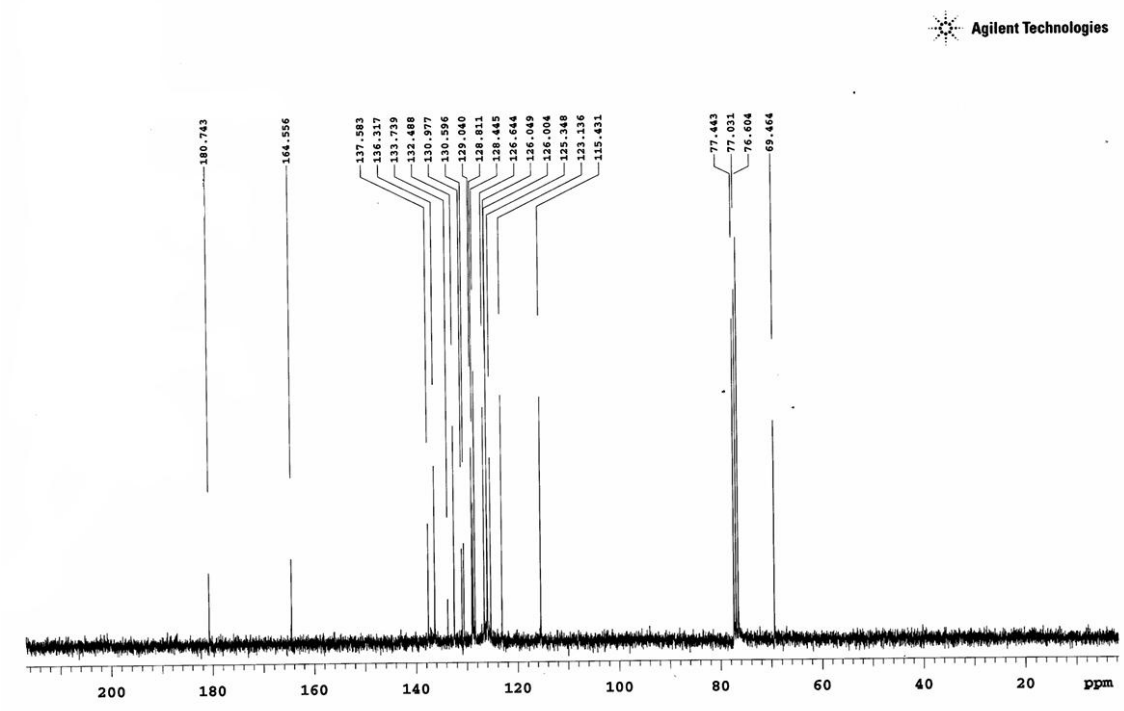

Figure S62. ^{13}C NMR of compound **13**

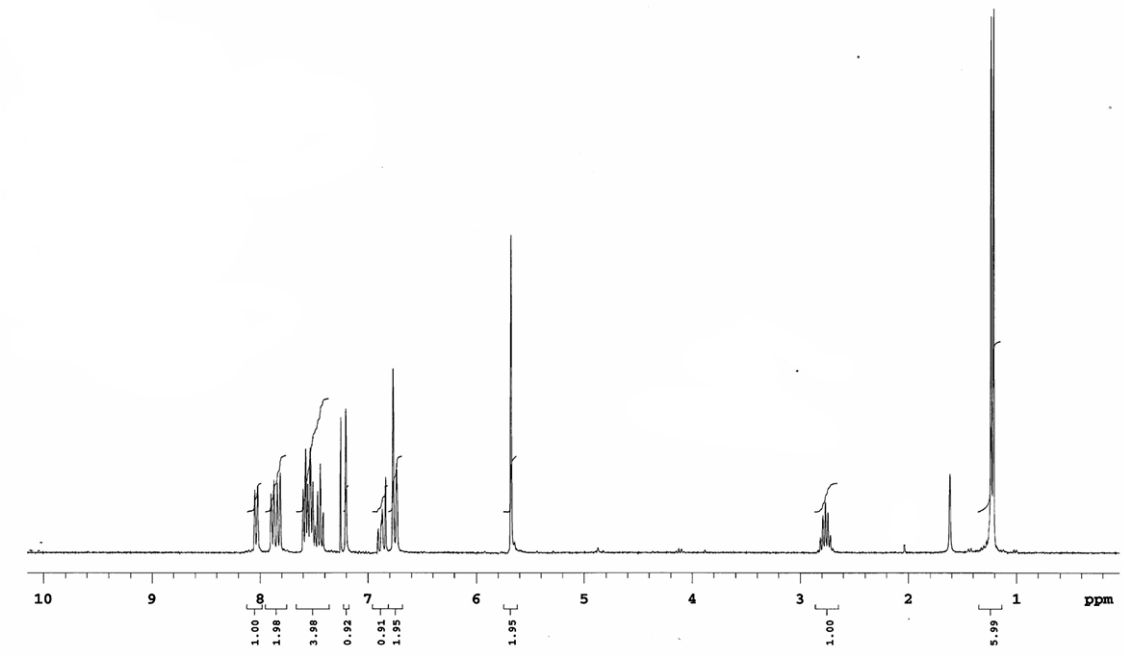

Figure S63. ^{1}H NMR of compound **13δ**

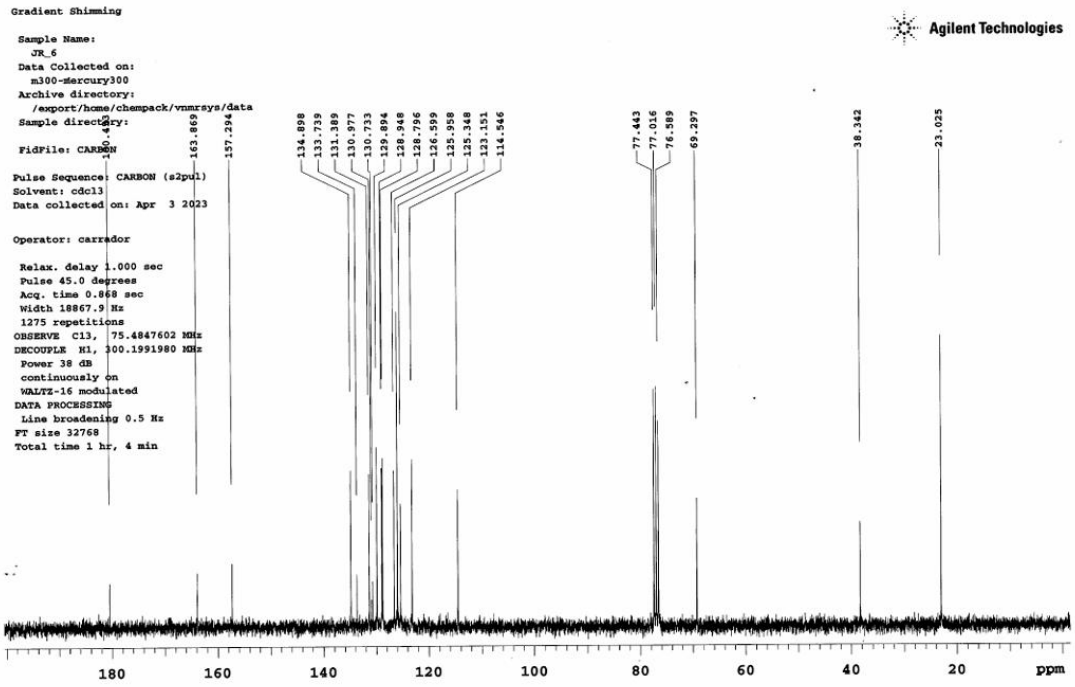

Figure S64. ^{13}C NMR of compound **13δ**

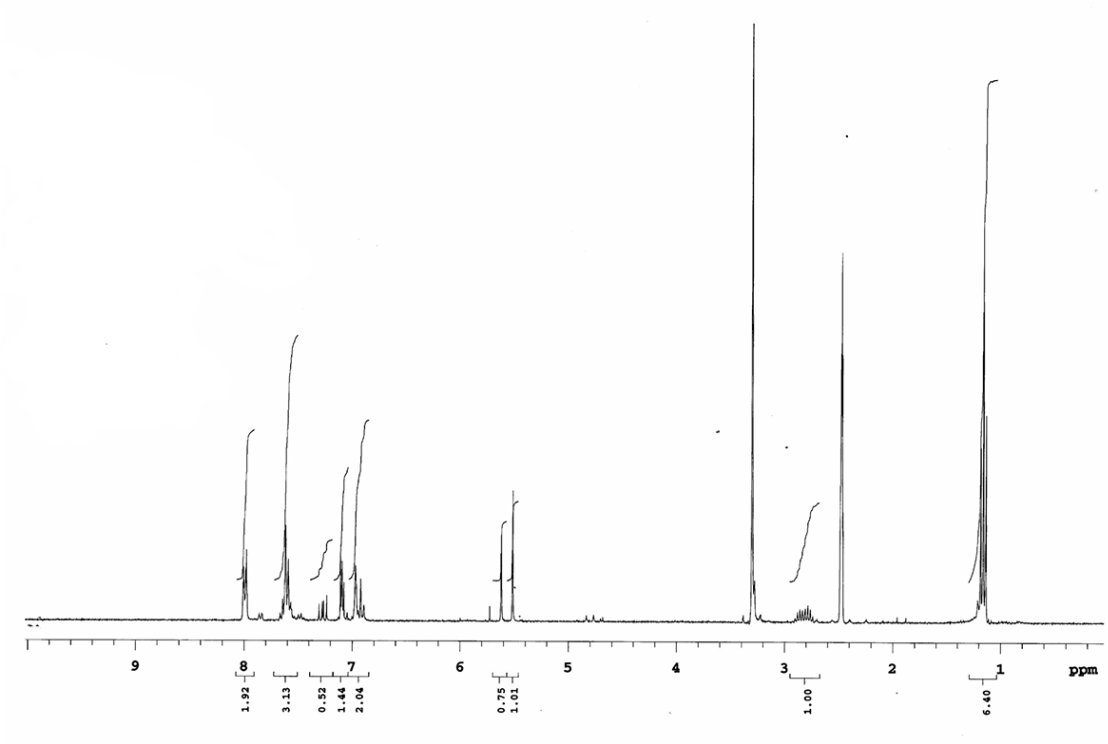

Figure S65. ^{1}H NMR of compound **13β+δ**

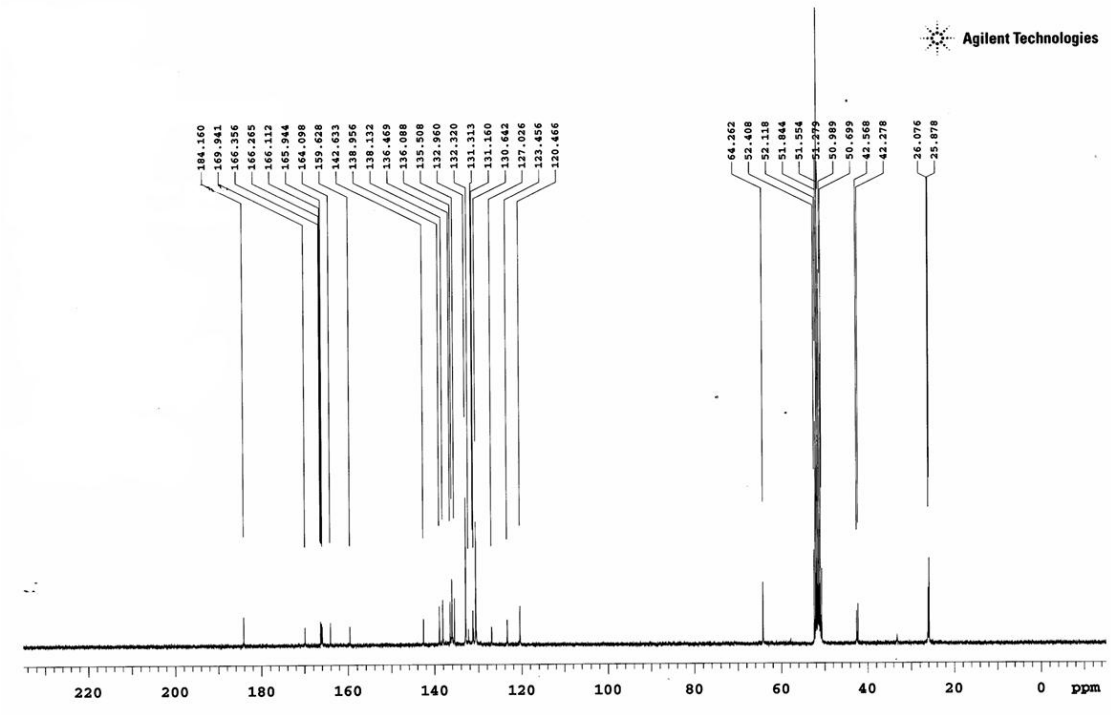

Figure S66. ^{13}C NMR of compound **13β+δ**

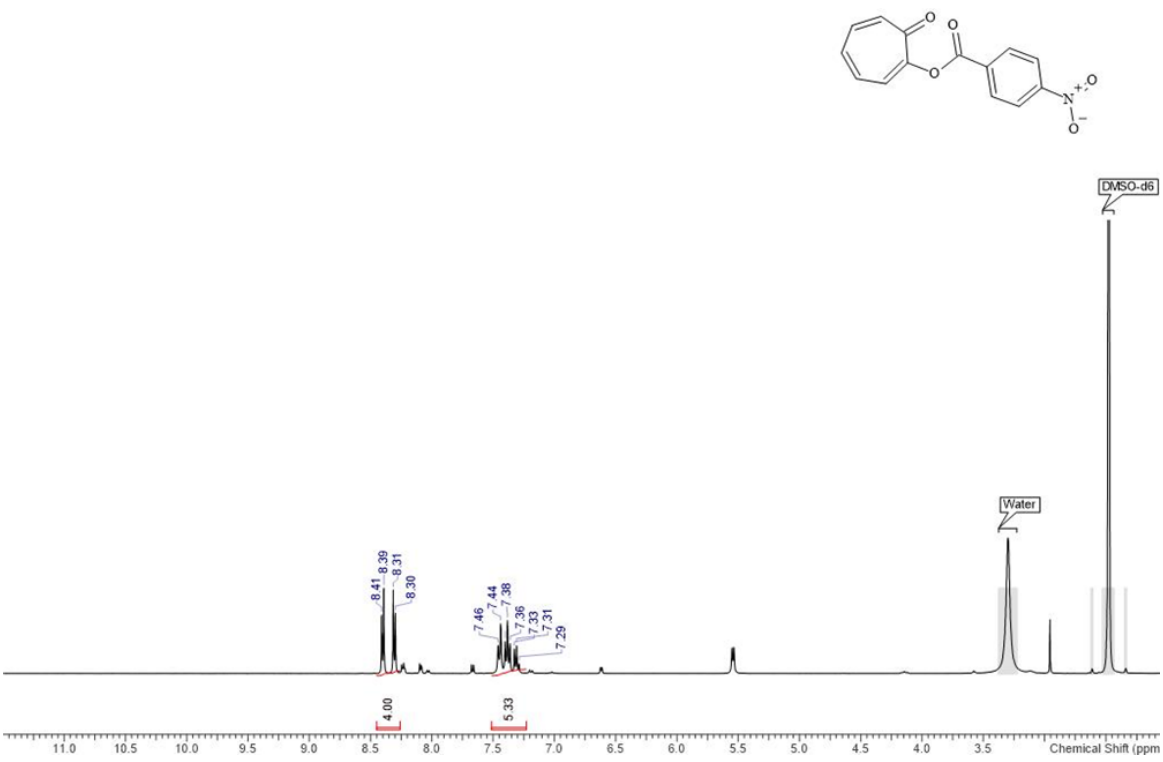

Figure S67. ^{1}H NMR (500 MHz, DMSO-d_6) spectrum of 7-oxocyclohepta-1,3,5-trien-1-yl-4-nitrobenzoate (**15**).

and S68 Gitto. Cpd **15** Tropolone + p-NO_2-benzoato

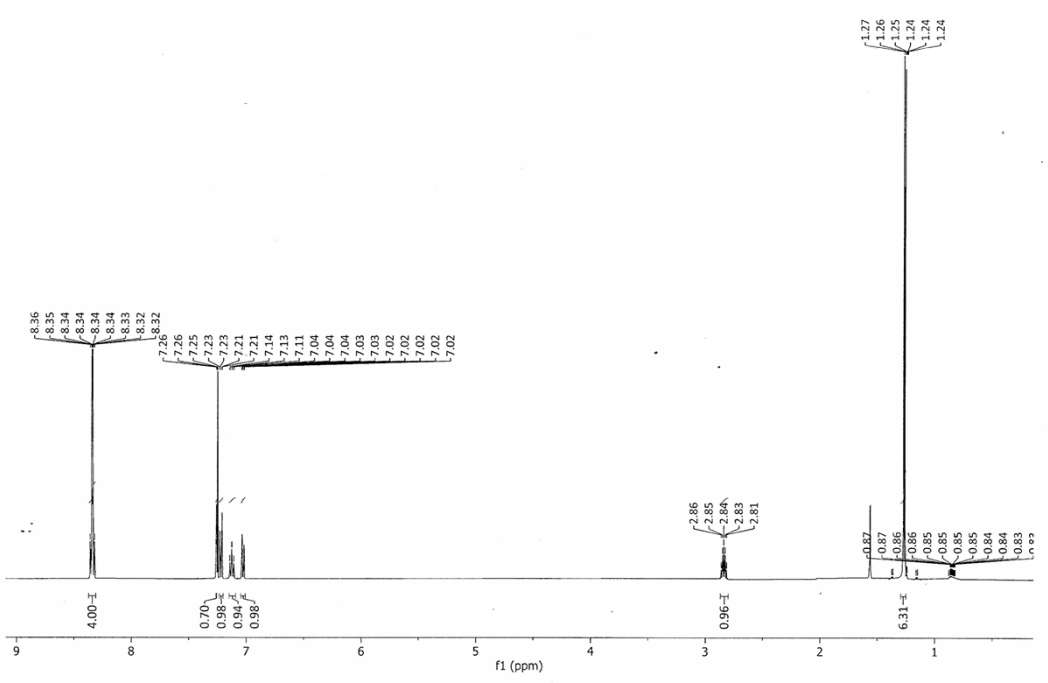

Figure S68. ^{1}H NMR of compound **15δ**

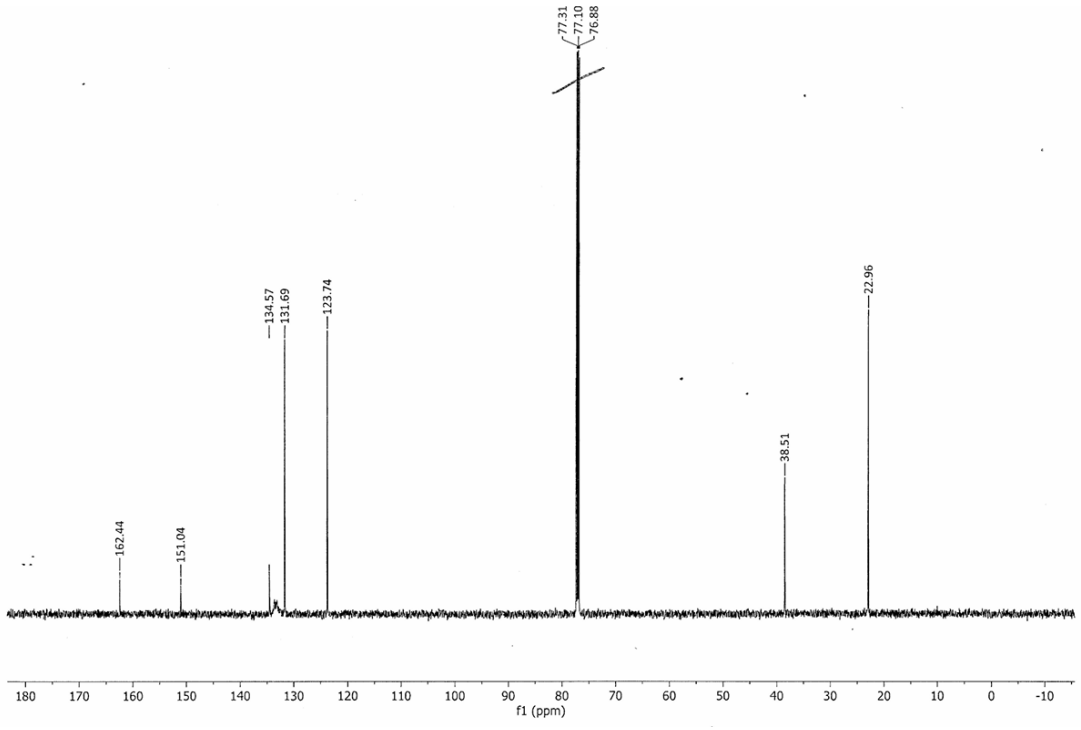

Figure S69. ^{13}C NMR of compound **15δ**

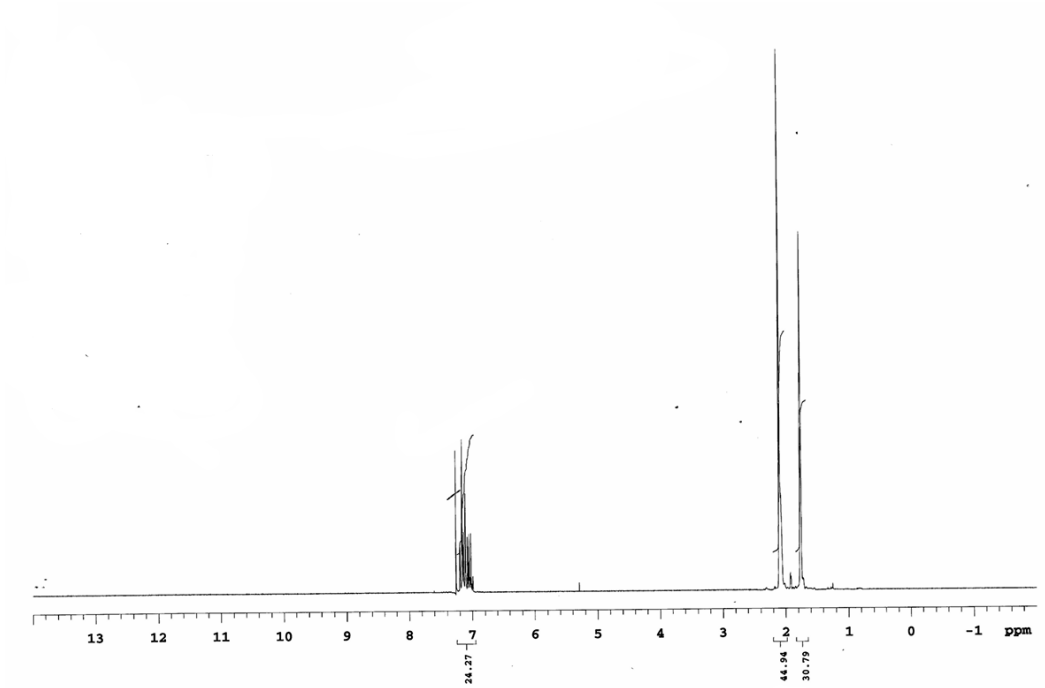

Figure S70. ^{1}H NMR of compound **16**

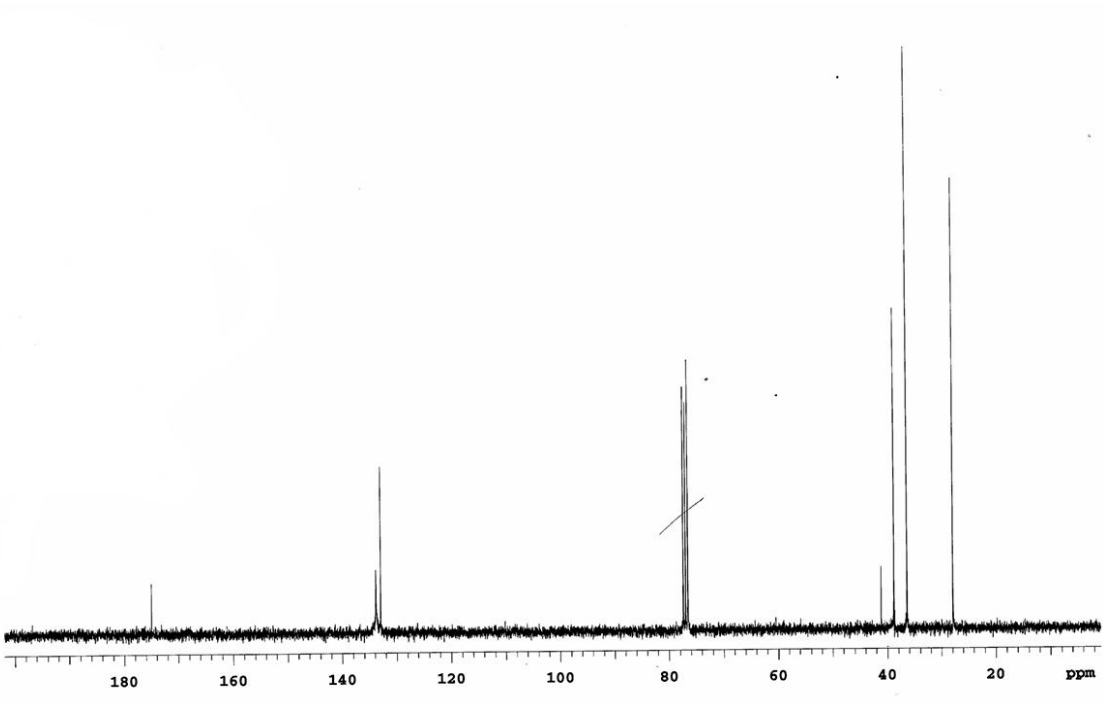

Figure S71. ^{13}C NMR of compound **16**

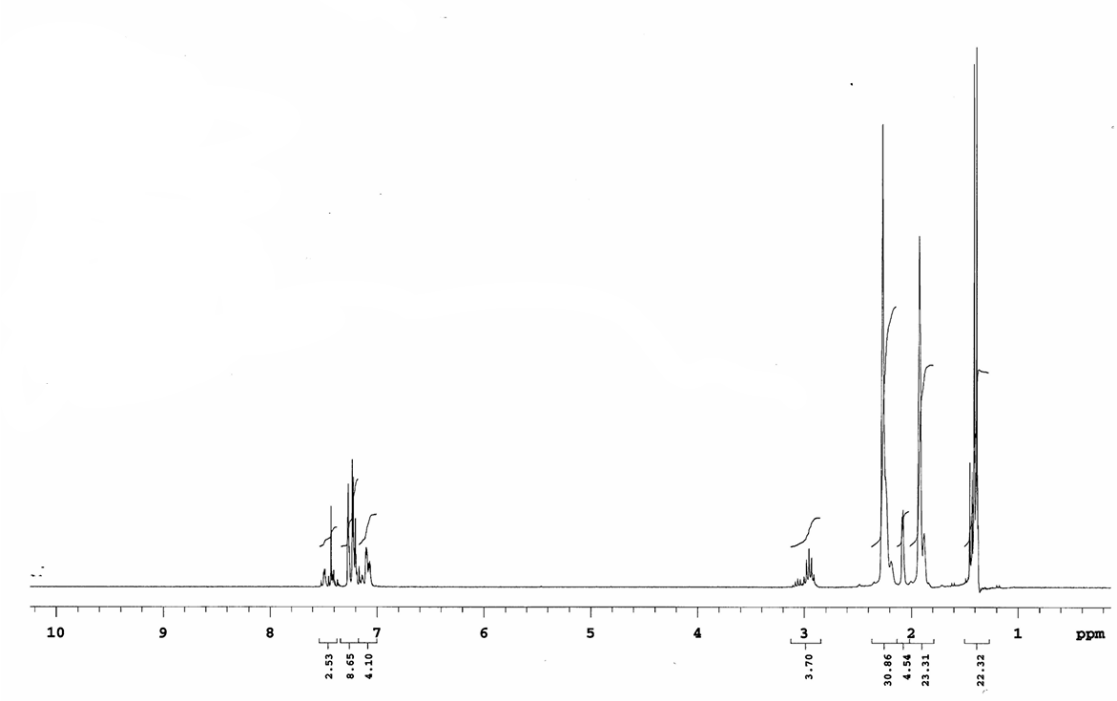

Figure S72. ^{1}H NMR of compound **16β+δ**

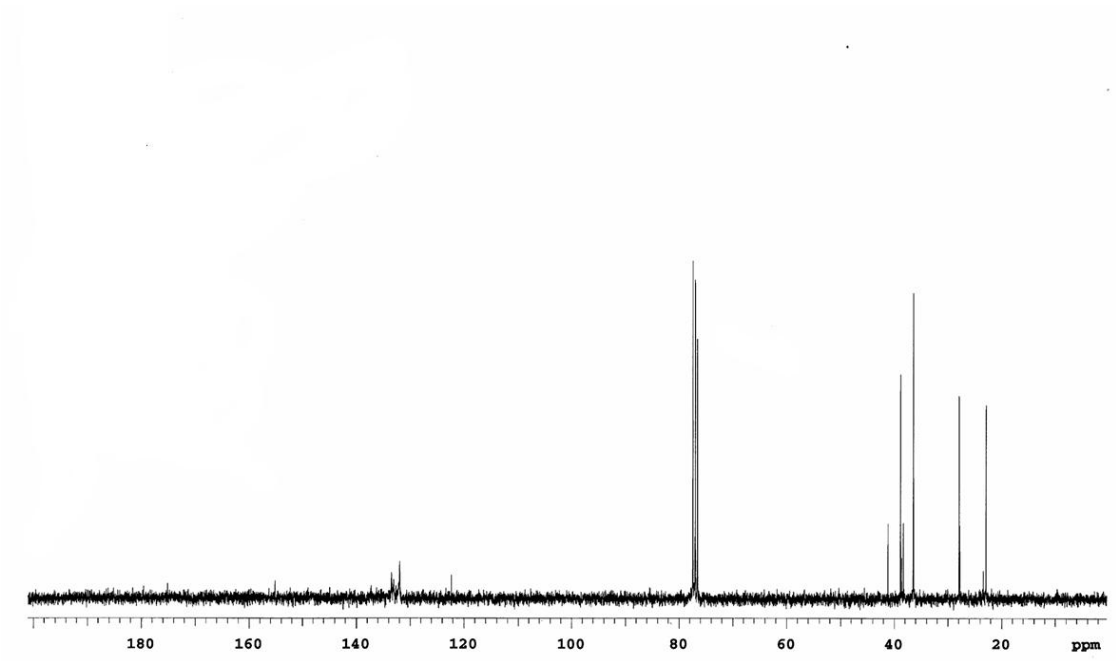

Figure S73. ^{13}C NMR of compound **16β+δ**

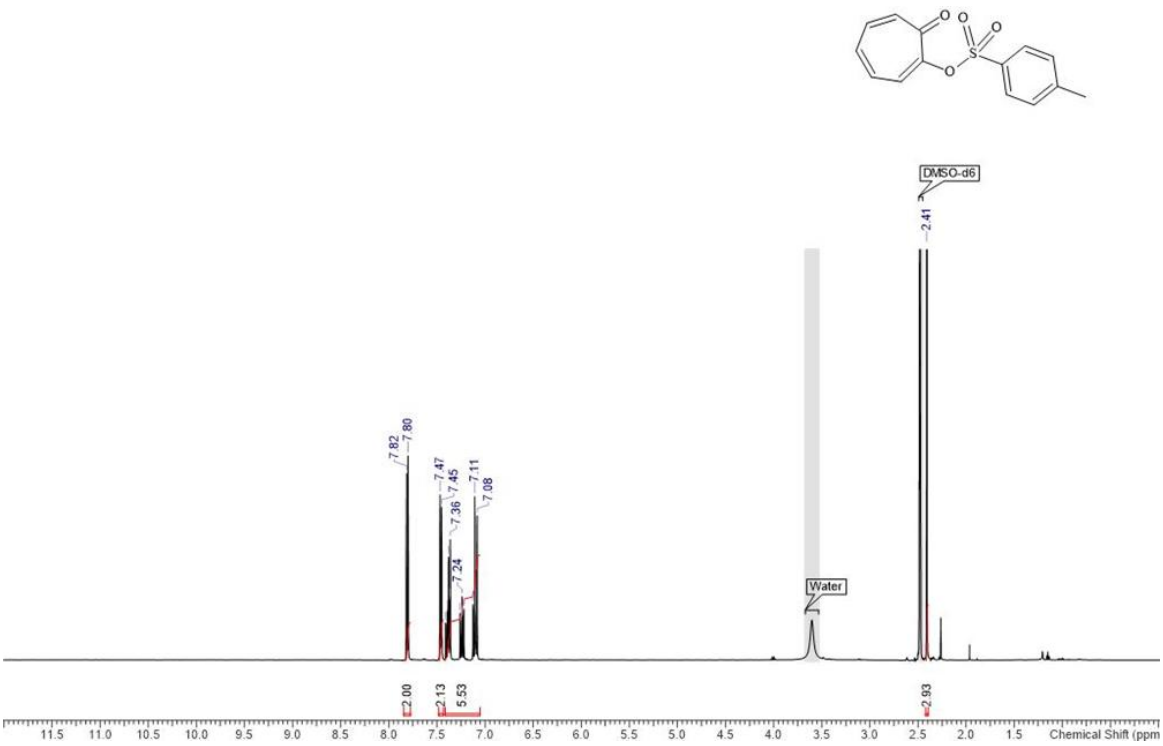

Figure S74. ^{1}H NMR (500 MHz, DMSO-d_6) spectrum of (7-oxocyclohepta-1,3,5-trien-1-yl)-4-methylbenzenesulfonate (**17**)

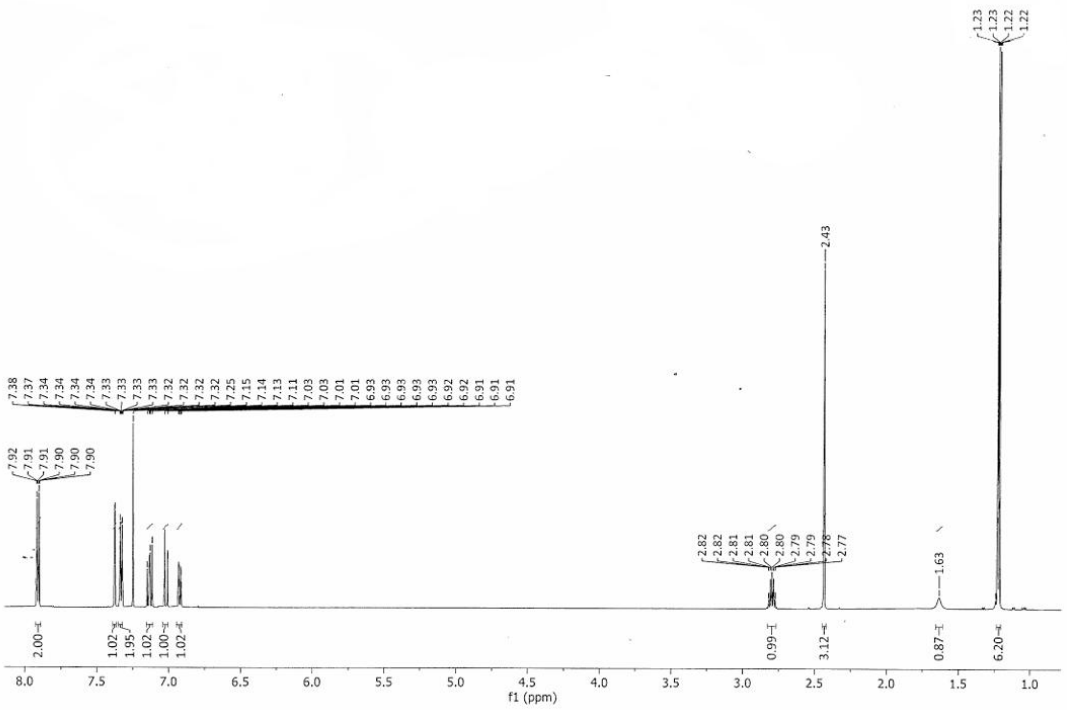

Figure S75. ^{1}H NMR of compound **17β**

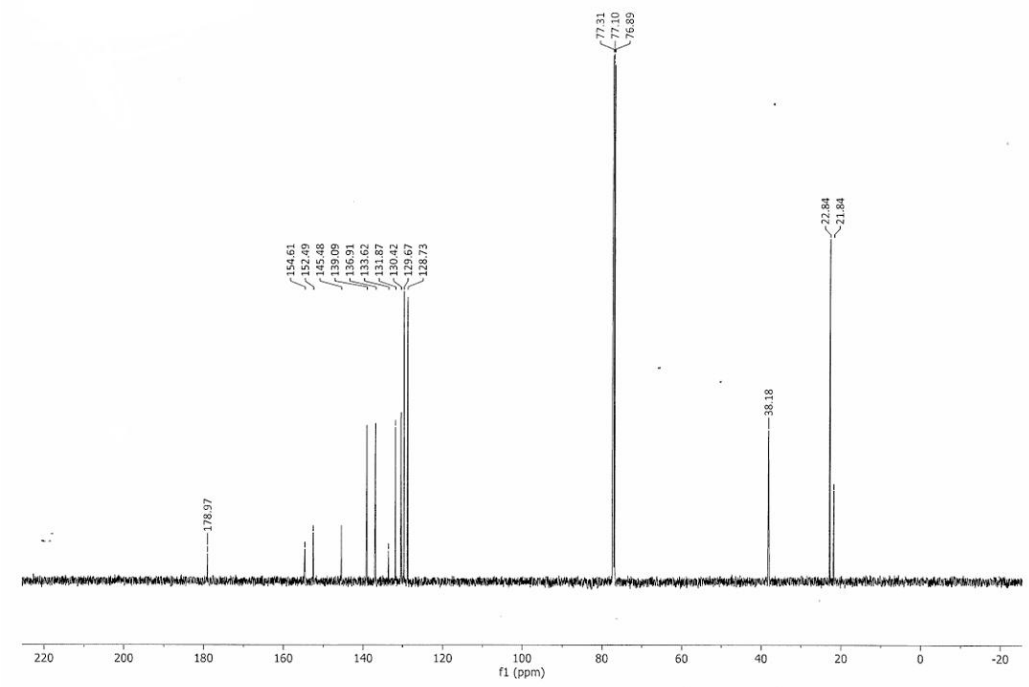

Figure S76. ^{13}C NMR of compound **17β**

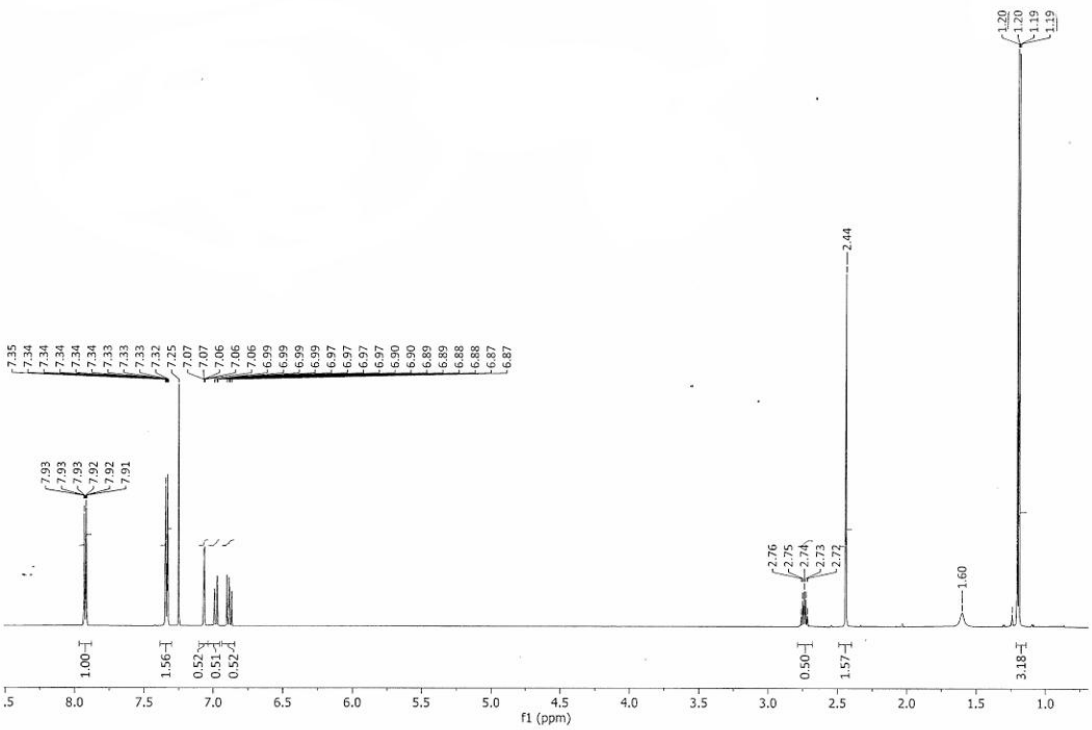

Figure S77. ^{1}H NMR of compound **17δ**

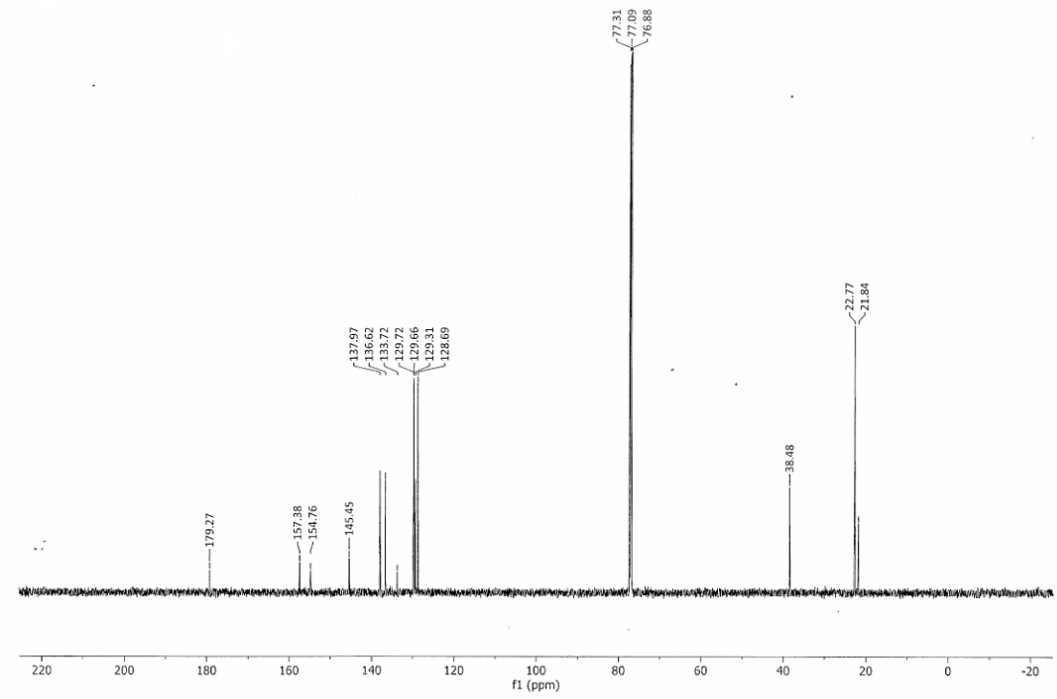

Figure S78. ^{13}C NMR of compound **17δ**

Table S2. eMBrAcE energy (E) values calculated for the most active compounds in complexed with hCA I and hCA II. For the mixture of stereoisomers, the E values correspond to the average values.

Compound	eMBrAcE energy (E) values*	Compound	eMBrAcE energy (E) values*
hCA I		***hCA II***	
1	-133,36	**2δ**	-313,07
1β+δ	-165,33	**4δ**	-297,93
8	-220,16	**6**	-892,18
9	-172,69	**7δ**	-210,74
11	-149,72	**9**	-275,74
		13	-173,54
		13δ	-188,16
		14β+δ	-331,01
		15δ	-158,49
		17δ	-182,40

*The thermodynamic values are reported in KJ/mol.

Table S3. eMBrAcE energy (E) values calculated for the most active compounds in complex with hCA VA and hCA VII. For the mixture of stereoisomers, the E values correspond to the average values.

Compound	eMBrAcE energy (E) values*	Compound	eMBrAcE energy (E) values*
hCA VA		***hCA VII***	
2	-299,72	**2β+δ**	-242,71
2β+δ	-307,71	**3**	-290,92
6	-758,69	**7δ**	-169,03
7δ	-286,03	**10β+δ**	-213,26
11β	-382,70	**13**	-162,05
12	-286,89	**13δ**	-196,78
17δ	-381,93		
β-TJP	-287,16		

*The thermodynamic values are reported in KJ/mol.

Table S4. eMBrAcE energy (E) values calculated for the most active compounds in complex with hCA IX and hCA XII. For the mixture of stereoisomers, the E values correspond to the average values.

Compound	eMBrAcE energy (E) values*	Compound	eMBrAcE energy (E) values*
	hCA IX		***hCA XII***
1β+δ	-308,27	**7**	-167,58
2β+δ	-332,00	**8**	-180,06
3	-286,99	**9**	-251,66
4δ	-266,99	**10**	-252,12
6β+δ	-490,17	**11**	-288,10
7δ	-175,81	**13**	-185,30
8	-126,01	**13δ**	-283,50
8β+δ	-201,44	**15**	-137,93
9	-214,33	**16**	-141,85
10β+δ	-186,68	**16β+δ**	-314,80
11β	-139,06	**17β**	-183,60
11δ	-225,94	**17δ**	-241,33
12	-259,53		
13	-133,45		
13δ	-126,55		
14β+δ	-1784,25		
15δ	-240,69		
17β	-194,81		
17δ	-159,49		

*The thermodynamic values are reported in KJ/mol.

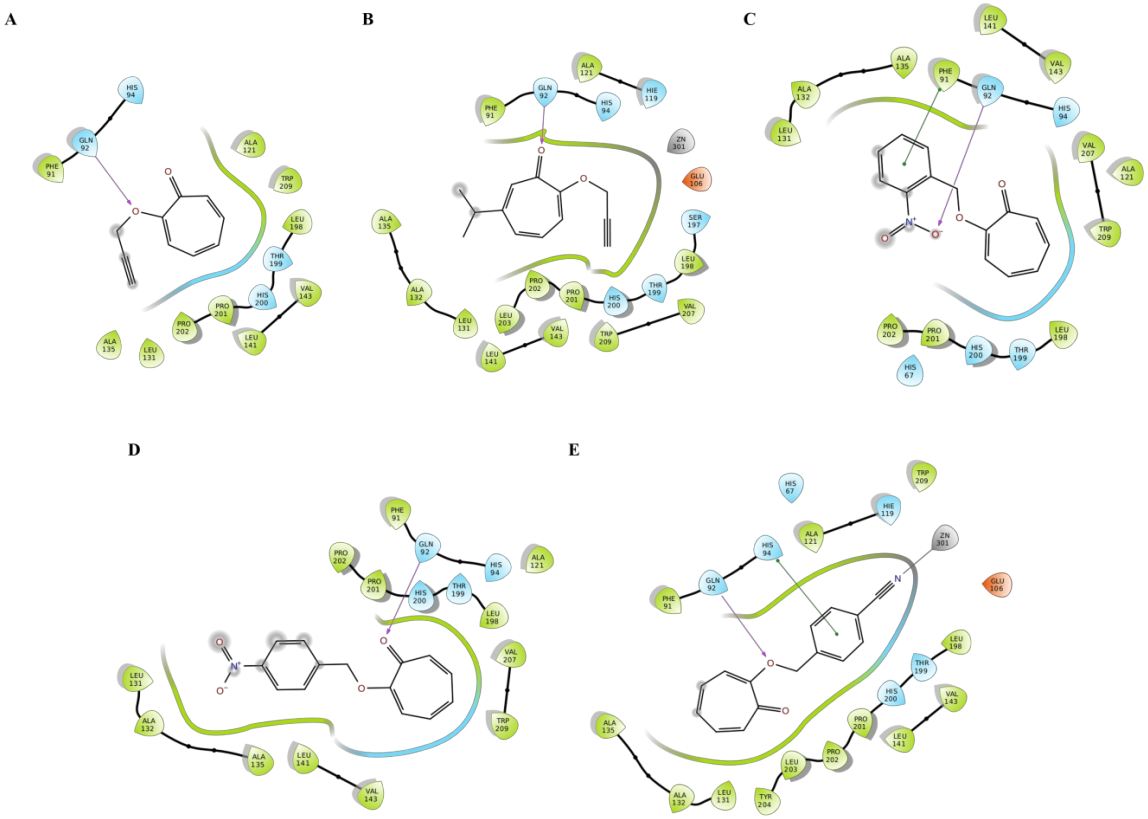

Figure S79. 2D interaction diagram of compound a) **1**; b) **1δ**; c) **11**; d) **9**; e) **8** in complex with hCA I.

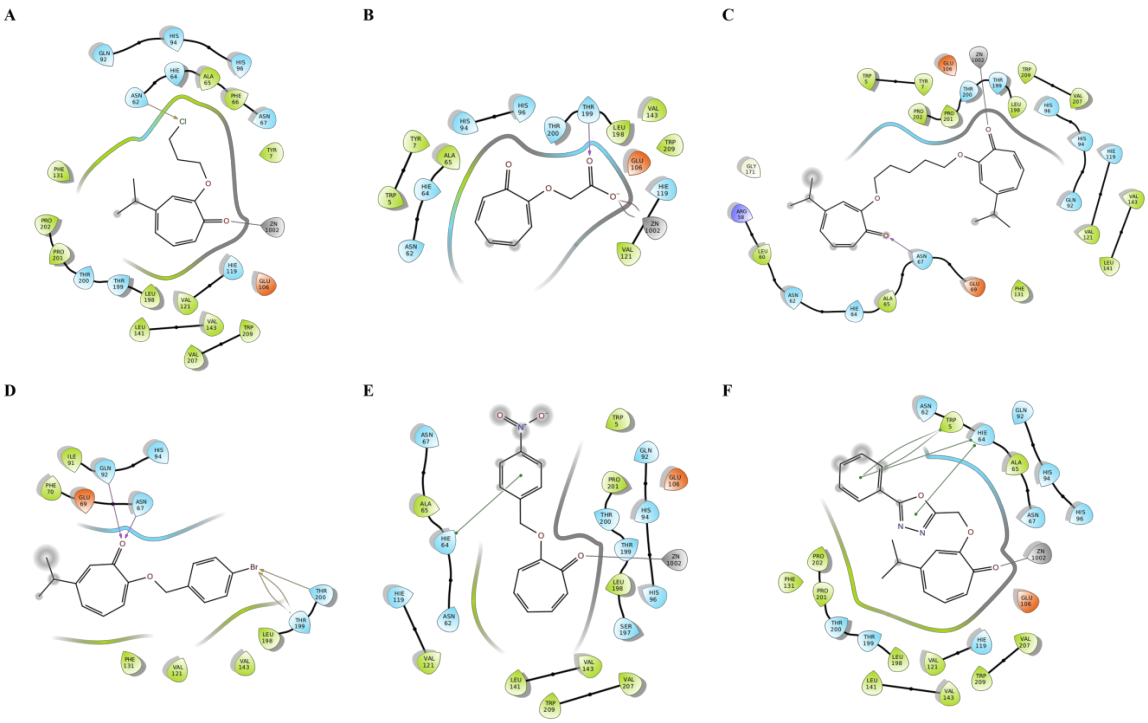

Figure S80. 2D interaction diagram of compound a) **2β**; b) **6**; c) **4β**; d) **7δ**; e) **9**; f) **14β** in complex with hCA II.

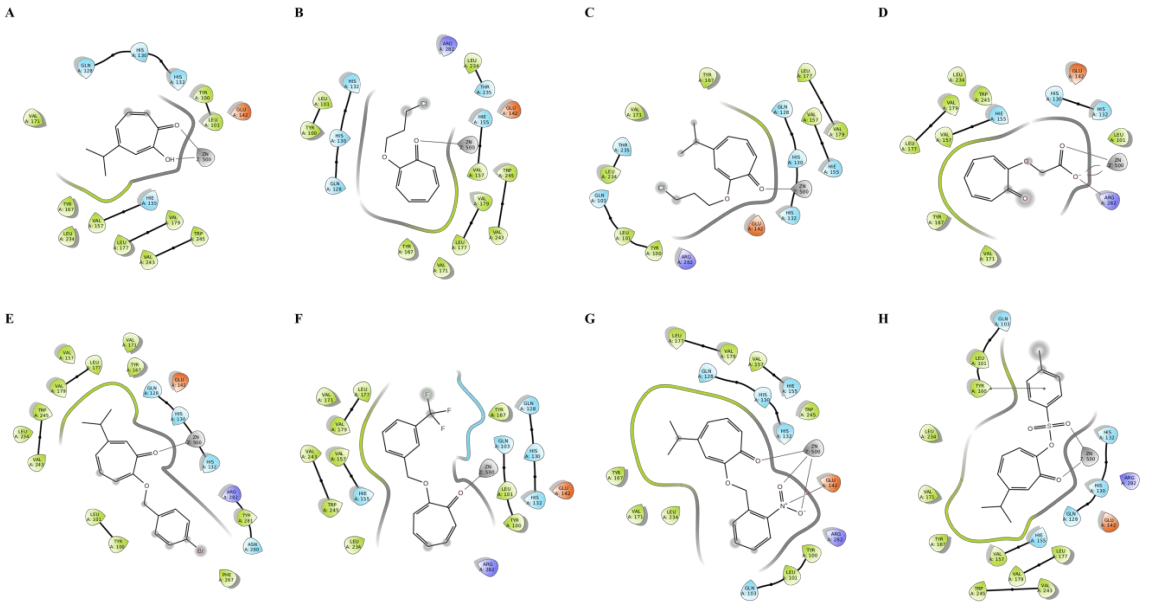

Figure S81. 2D interaction diagram of a) β-thujaplicin; b) **2**; c) **2β**; d) **6**; e) **7δ**; f) **12**; g) **11β**; h) **17δ** compounds in complex with hCA VA.

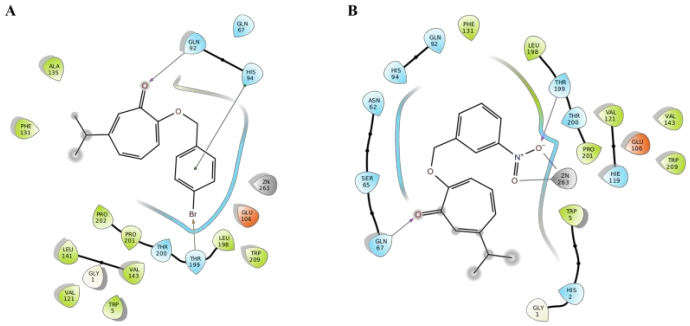

Figure S82. 2D interaction diagram of compound a) **7δ**; b) **10δ** best scored stereoisomer in complex with hCA VII.

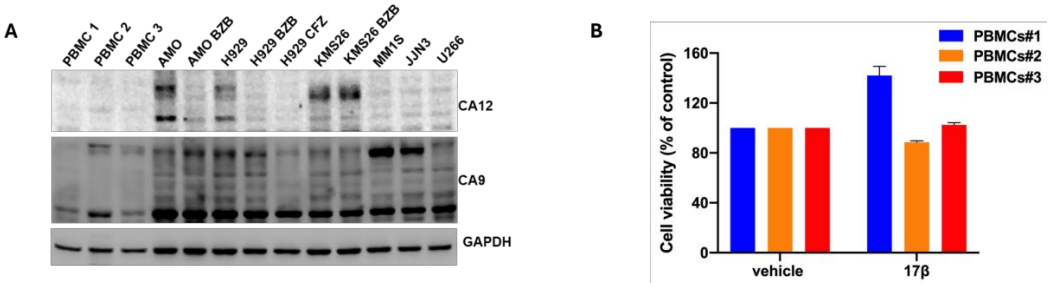

Figure S83. A. WB analysis of CA IX and CA XII expression in MM cell lines (AMO, AMO-BZB, H929, H929-BZB, H929-CFZ, KMS26, KMS26-BZB, MM1S, JJN3, and U266) and healthy peripheral blood

mononuclear cells (PBMCs); GAPDH was used as a loading control. B. Cell viability analysis by CTG performed on PMBCs from three different healthy donors treated with **17β** (10 µM) for 48 h.

Chemical stability

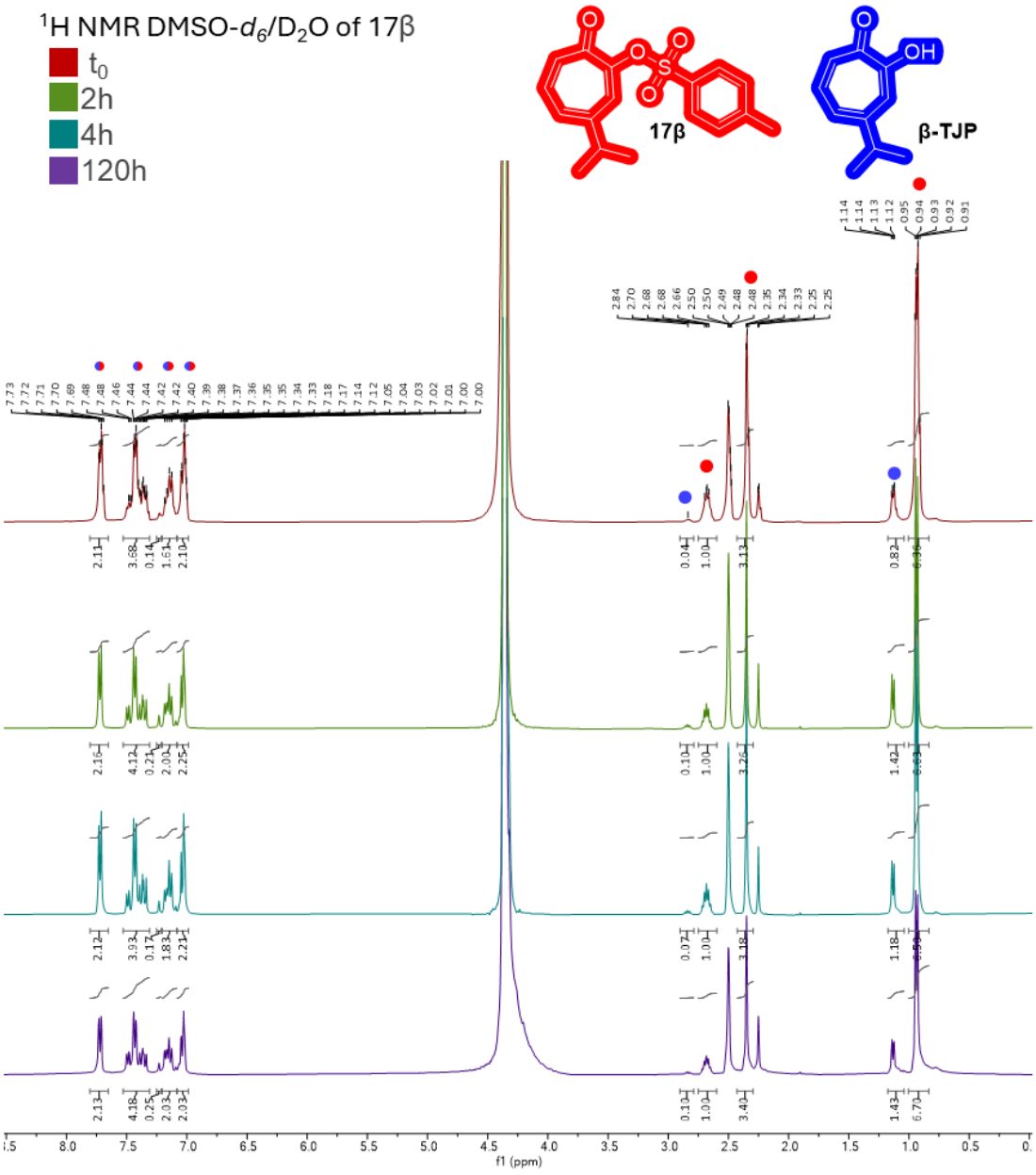

Figure S84. ^{1}H NMR spectra of compound **17β** at different time points.

Bibliography

[1] C. W. Duarte, L. K. Vaughan, T. M. Beasley, and H. K. Tiwari, "Chapter 12 - multifactorial inheritance and complex diseases," in *Emery and Rimoin's Principles and Practice of Medical Genetics (Sixth Edition)*, D. Rimoin, R. Pyeritz, and B. Korf, eds., pp. 1–15. Academic Press, Oxford, sixth edition ed., 2013.

[2] A. Doostmohammadi, H. Jooya, K. Ghorbanian, S. Gohari, and M. Dadashpour, "Potentials and future perspectives of multi-target drugs in cancer treatment: the next generation anti-cancer agents," *Cell Communication and Signaling* **22** (2024) .

[3] W. D. Joo, I. Visintin, and G. Mor, "Targeted cancer therapy – are the days of systemic chemotherapy numbered?," *Maturitas* **76** (2013) 308–314.

[4] D. E. Gerber, "Targeted therapies: A new generation of cancer treatments," *American Family Physician* **77** (2008) 311–319.

[5] L. Zhong, Y. Li, L. Xiong, W. Wang, M. Wu, T. Yuan, W. Yang, C. Tian, Z. Miao, T. Wang, and S. yong Yang, "Small molecules in targeted cancer therapy: advances, challenges, and future perspectives," *Signal Transduction and Targeted Therapy* **6** (2021) .

[6] P. Csermely, V. Agoston, and S. Pongor, "The efficiency of multi-target drugs: The network approach might help drug design," *Trends in pharmacological sciences* **26** (2005) 178–82.

[7] A. Boran and R. Iyengar, "Systems approaches to polypharmacology and drug discovery," *Current opinion in drug discovery and development* **13** (2010) 297–309.

[8] G. Housman, S. Byler, S. Heerboth, K. Lapinska, M. Longacre, N. Snyder, and S. Sarkar, "Drug resistance in cancer: An overview," *Cancers* **6** (2014) 1769–1792.

[9] A. Kabir and A. Muth, "Polypharmacology: The science of multi-targeting molecules," *Pharmacological Research* **176** (2022) 106055.

[10] Y. Li, P. Wang, X. Li, C. Yu, H. Yang, J. Zhou, W. Xue, J. Tan, and F. Zhu, "The human kinome targeted by fda approved multi-target drugs and combination products: A comparative study from the drug-target interaction network perspective," *PLOS One* **11** (2016) .

[11] A. Petrelli and G. Valabrega, "Multitarget drugs: The present and the future of cancer therapy," *Expert opinion on pharmacotherapy* **10** (2009) 589–600.

[12] J. Zhou, X. Jiang, S. He, H. Jiang, F. Feng, W. Liu, W. Qu, and H. Sun, "Rational design of multi-target-directed ligands: Strategies and emerging paradigms," *Journal of Medicinal Chemistry* **62** (2019) .

[13] P. Ryszkiewicz, B. Malinowska, and E. Schlicker, "Polypharmacology: promises and new drugs in 2022," *Pharmacological reports : PR* **75** (2023) .

[14] C. Supuran, "Structure and function of carbonic anhydrases," *Biochemical Journal* **473** (2016) 2023–2032.

[15] A. Nocentini, C. T. Supuran, and C. Capasso, "An overview on the recently discovered iota-carbonic anhydrases," *Journal of Enzyme Inhibition and Medicinal Chemistry* **36** (2021) 1988–1995.

[16] S. Del Prete, D. Vullo, A. Scozzafava, C. Capasso, and C. T. Supuran, "Cloning, characterization and anion inhibition study of the δ-class carbonic anhydrase (tweca) from the marine diatom thalassiosira weissflogii," *Bioorganic and Medicinal Chemistry* **22** (2014) 531–537.

[17] S. Del Prete, D. Vullo, G. Fisher, K. Andrews, S.-A. Poulsen, C. Capasso, and C. Supuran, "Discovery of a new family of carbonic anhydrases in the malaria pathogen plasmodium falciparum—the η-carbonic anhydrases," *Bioorganic and medicinal chemistry letters* **24** (2014) .

[18] S. Kikutani, K. Nakajima, C. Nagasato, Y. Tsuji, A. Miyatake, and Y. Matsuda, "Thylakoid luminal θ-carbonic anhydrase critical for growth

and photosynthesis in the marine diatom phaeodactylum tricornutum," *Proceedings of the National Academy of Sciences* **113** (2016) 9828–9833.

[19] S. Mitsuhashi, T. Mizushima, E. Yamashita, M. Yamamoto, T. Kumasaka, H. Moriyama, T. Ueki, S. Miyachi, and T. Tsukihara, "X-ray structure of β-carbonic anhydrase from the red alga,porphyridium purpureum, reveals a novel catalytic site for co2 hydration," *Journal of Biological Chemistry* **275** (2000) 5521–5526.

[20] T. Iverson, B. Alber, C. Kisker, J. Ferry, and D. Rees, "A closer look at the active site of γ-class carbonic anhydrases: High-resolution crystallographic studies of the carbonic anhydrase from methanosarcina thermophila," *Biochemistry* **39** (2000) 9222–31.

[21] Y. Xu, L. Feng, P. Jeffrey, Y. Shi, and F. Morel, "Structure and metal exchange in the cadmium carbonic anhydrase of marine diatoms," *Nature* **452** (2008) 56–61.

[22] C. Supuran, "Carbonic anhydrases: Novel therapeutic applications for inhibitors and activators," *Nature reviews. Drug discovery* **7** (2008) 168–81.

[23] R. McKenna and C. T. Supuran, "Carbonic anhydrase inhibitors drug design," in *Carbonic Anhydrase: Mechanism, Regulation, Links to Disease, and Industrial Applications*, S. Frost and R. McKenna, eds., vol. 75 of *Subcellular Biochemistry*, pp. 291–323. Springer, Dordrecht, 2014.

[24] D. Neri and C. T. Supuran, "Interfering with ph regulation in tumours as a therapeutic strategy," *Nature Reviews Drug Discovery* **10** (2011) 767–777.

[25] C. T. Supuran, "Carbonic anhydrases an overview," *Current Pharmaceutical Design* **14** (2008) 603–614.

[26] C. T. Supuran and C. Capasso, "Biomedical applications of prokaryotic carbonic anhydrases," *Expert Opinion on Therapeutic Patents* **28** (2018) 745–754.

[27] C. Capasso and C. T. Supuran, "An overview of the carbonic anhydrases from two pathogens of the oral cavity: Streptococcus mutans and porphyromonas gingivalis," *Current Topics in Medicinal Chemistry* **16** (2016) 2359–2368.

[28] C. Capasso and C. T. Supuran, "An overview of the alpha-, beta- and gamma-carbonic anhydrases from bacteria: can bacterial carbonic anhydrases shed new light on evolution of bacteria?," *Journal of Enzyme Inhibition and Medicinal Chemistry* **30** (2015) 325–332.

[29] C. T. Supuran and C. Capasso, "An overview of the bacterial carbonic anhydrases," *Metabolites* **7** (2017) .

[30] C. T. Supuran and C. Capasso, "Carbonic anhydrase from porphyromonas gingivalis as a drug target," *Pathogens* **6** (2017) .

[31] C. Capasso and C. Supuran, "An overview of the selectivity and efficiency of the bacterial carbonic anhydrase inhibitors," *Current Medicinal Chemistry* **22** (2015) 2130–2139.

[32] A. Rogato, S. D. Prete, A. Nocentini, V. Carginale, C. T. Supuran, and C. Capasso, "Phaeodactylum tricornutum as a model organism for testing the membrane penetrability of sulphonamide carbonic anhydrase inhibitors," *Journal of Enzyme Inhibition and Medicinal Chemistry* **34** (2019) 510–518.

[33] A. Angeli, M. Pinteala, S. S. Maier, S. D. Prete, C. Capasso, B. C. Simionescu, and C. T. Supuran, "Inhibition of α-, β-, γ-, δ-, ζ- and η-class carbonic anhydrases from bacteria, fungi, algae, diatoms and protozoans with famotidine," *Journal of Enzyme Inhibition and Medicinal Chemistry* **34** (2019) 644–650.

[34] E. Berrino, M. Bozdag, S. D. Prete, F. A. S. Alasmary, L. S. Alqahtani, Z. AlOthman, C. Capasso, and C. T. Supuran, "Inhibition of α-, β-, γ-, and δ-carbonic anhydrases from bacteria and diatoms with n-aryl-n-hydroxy-ureas," *Journal of Enzyme Inhibition and Medicinal Chemistry* **33** (2018) 1194–1198.

[35] A. Angeli, S. Del Prete, F. A. Alasmary, L. S. Alqahtani, Z. AlOthman, W. A. Donald, C. Capasso, and C. T. Supuran, "The first activation studies of the η-carbonic anhydrase from the malaria parasite plasmodium falciparum with amines and amino acids," *Bioorganic Chemistry* **80** (2018) 94–98.

[36] E. G. Mogensen, G. Janbon, J. Chaloupka, C. Steegborn, M. S. Fu, F. Moyrand, T. Klengel, D. S. Pearson, M. A. Geeves, J. Buck, L. R. Levin, and F. A. Mühlschlegel, "Cryptococcus neoformans senses co2

through the carbonic anhydrase can2 and the adenylyl cyclase cac1," *Eukaryotic Cell* **5** (2006) 103–111.

[37] C. Schlicker, R. A. Hall, D. Vullo, S. Middelhaufe, M. Gertz, C. T. Supuran, F. A. Mühlschlegel, and C. Steegborn, "Structure and inhibition of the co2-sensing carbonic anhydrase can2 from the pathogenic fungus cryptococcus neoformans," *Journal of Molecular Biology* **385** (2009) 1207–1220.

[38] T. Klengel, W.-J. Liang, J. Chaloupka, C. Ruoff, K. Schröppel, J. R. Naglik, S. E. Eckert, E. G. Mogensen, K. Haynes, M. F. Tuite, L. R. Levin, J. Buck, and F. A. Mühlschlegel, "Fungal adenylyl cyclase integrates co2 sensing with camp signaling and virulence," *Current Biology* **15** (2005) 2021–2026.

[39] G. De Simone, A. Di Fiore, C. Capasso, and C. T. Supuran, "The zinc coordination pattern in the η-carbonic anhydrase from plasmodium falciparum is different from all other carbonic anhydrase genetic families," *Bioorganic and Medicinal Chemistry Letters* **25** (2015) 1385–1389.

[40] G. M. Buzás and C. T. Supuran, "The history and rationale of using carbonic anhydrase inhibitors in the treatment of peptic ulcers. in memoriam ioan puşcaş (1932–2015)," *Journal of Enzyme Inhibition and Medicinal Chemistry* **31** (2016) 527–533.

[41] F. Carta, C. T. Supuran, and A. Scozzafava, "Sulfonamides and their isosters as carbonic anhydrase inhibitors," *Future Medicinal Chemistry* **6** (2014) 1149–1165.

[42] M. A. Pinard, S. R. Lotlikar, C. D. Boone, D. Vullo, C. T. Supuran, M. A. Patrauchan, and R. McKenna, "Structure and inhibition studies of a type ii beta-carbonic anhydrase psca3 from pseudomonas aeruginosa," *Bioorganic and Medicinal Chemistry* **23** (2015) 4831–4838.

[43] M. Ferraroni, S. Del Prete, D. Vullo, C. Capasso, and C. T. Supuran, "Crystal structure and kinetic studies of a tetrameric type ii β-carbonic anhydrase from the pathogenic bacterium *vibrio cholerae*," *Acta Crystallographica Section D* **71** (2015) 2449–2456.

[44] G. De Simone, S. M. Monti, V. Alterio, M. Buonanno, V. De Luca, M. Rossi, V. Carginale, C. T. Supuran, C. Capasso, and A. Di Fiore, "Crystal structure of the most catalytically effective carbonic anhydrase

enzyme known, sazca from the thermophilic bacterium sulfurihydrogenibium azorense," *Bioorganic and Medicinal Chemistry Letters* **25** (2015) 2002–2006.

[45] B. Żołnowska, J. Sławiński, A. Pogorzelska, J. Chojnacki, D. Vullo, and C. T. Supuran, "Carbonic anhydrase inhibitors. synthesis, and molecular structure of novel series n-substituted n-(2-arylmethylthio-4-chloro-5-methylbenzenesulfonyl)guanidines and their inhibition of human cytosolic isozymes i and ii and the transmembrane tumor-associated isozymes ix and xii," *European Journal of Medicinal Chemistry* **71** (2014) 135–147.

[46] L. De Luca, S. Ferro, F. M. Damiano, C. T. Supuran, D. Vullo, A. Chimirri, and R. Gitto, "Structure-based screening for the discovery of new carbonic anhydrase vii inhibitors," *European Journal of Medicinal Chemistry* **71** (2014) 105–111.

[47] A. Di Fiore, C. Capasso, V. De Luca, S. M. Monti, V. Carginale, C. T. Supuran, A. Scozzafava, C. Pedone, M. Rossi, and G. De Simone, "X-ray structure of the first 'extremo-α-carbonic anhydrase', a dimeric enzyme from the thermophilic bacterium *sulfurihydrogenibium yellowstonense* yo3aop1," *Acta Crystallographica Section D* **69** (2013) 1150–1159.

[48] C. T. Supuran, "Structure-based drug discovery of carbonic anhydrase inhibitors," *Journal of Enzyme Inhibition and Medicinal Chemistry* **27** (2012) 759–772.

[49] C. T. Supuran, "Advances in structure-based drug discovery of carbonic anhydrase inhibitors," *Expert Opinion on Drug Discovery* **12** (2017) 61–88.

[50] A. Bhatt, B. P. Mahon, V. W. D. Cruzeiro, B. Cornelio, M. Laronze-Cochard, M. Ceruso, J. Sapi, G. A. Rance, A. N. Khlobystov, A. Fontana, A. Roitberg, C. T. Supuran, and R. McKenna, "Structure–activity relationships of benzenesulfonamide-based inhibitors towards carbonic anhydrase isoform specificity," *ChemBioChem* **18** (2017) 213–222.

[51] V. Alterio, E. Langella, F. Viparelli, D. Vullo, G. Ascione, N. A. Dathan, F. M. Morel, C. T. Supuran, G. De Simone, and S. M. Monti, "Structural and inhibition insights into carbonic anhydrase cdca1 from the marine diatom thalassiosira weissflogii," *Biochimie* **94** (2012) 1232–1241.

[52] C. L. Lomelino, B. P. Mahon, R. McKenna, F. Carta, and C. T. Supuran, "Kinetic and x-ray crystallographic investigations on carbonic anhydrase isoforms i, ii, ix and xii of a thioureido analog of slc-0111," *Bioorganic and Medicinal Chemistry* **24** (2016) 976–981.

[53] X. Fu, L. jiang Yu, L. Mao-teng, L. Wei, C. Wu, and M. Yun-feng, "Evolution of structure in γ-class carbonic anhydrase and structurally related proteins," *Molecular Phylogenetics and Evolution* **47** (2008) 211–220.

[54] V. Alterio, A. Di Fiore, K. D'Ambrosio, C. Supuran, and G. De Simone, "Multiple binding modes of inhibitors to carbonic anhydrases: How to design specific drugs targeting 15 different isoforms?," *Chemical reviews* **112** (2012) 4421–68.

[55] A. Aspatwar, M. Tolvanen, C. Ortutay, and S. Parkkila, "Carbonic anhydrase related proteins: Molecular biology and evolution," *Sub-cellular biochemistry* **75** (2014) 135–56.

[56] K. D'Ambrosio, G. De Simone, and C. T. Supuran, "Human carbonic anhydrases: Catalytic properties, structural features, and tissue distribution," in *Carbonic Anhydrases as Biocatalysts*, C. T. Supuran and G. De Simone, eds., pp. 13–26. Elsevier, Amsterdam, The Netherlands, 2015.

[57] T. Stams, S. K. Nair, T. Okuyama, A. Waheed, W. S. Sly, and D. W. Christianson, "Crystal structure of the secretory form of membrane-associated human carbonic anhydrase iv at 2.8-Å resolution," *Proceedings of the National Academy of Sciences* **93** (1996) 13589–13594.

[58] K. K. Kannan, M. Ramanadham, and T. A. Jones, "Structure, refinement, and function of carbonic anhydrase isozymes: Refinement of human carbonic anhydrase i," *Annals of the New York Academy of Sciences* **429** (1984) 49–60.

[59] M. Buonanno, A. Di Fiore, E. Langella, K. D'Ambrosio, C. T. Supuran, S. M. Monti, and G. De Simone, "The crystal structure of a hca vii variant provides insights into the molecular determinants responsible for its catalytic behavior," *International Journal of Molecular Sciences* **19** (2018) .

[60] K. D'Ambrosio, A. Di Fiore, V. Alterio, E. Langella, S. M. Monti, C. T. Supuran, and G. De Simone, "Multiple binding modes of inhibitors to human carbonic anhydrases: An update on the design of isoform-specific modulators of activity," *Chemical Reviews* **125** (2025) 150–222.

[61] P. A. Boriack-Sjodin, R. W. Heck, P. J. Laipis, D. N. Silverman, and D. W. Christianson, "Structure determination of murine mitochondrial carbonic anhydrase v at 2.45-a resolution: implications for catalytic proton transfer and inhibitor design.," *Proceedings of the National Academy of Sciences* **92** (1995) 10949–10953.

[62] A. Di Fiore, K. D'Ambrosio, J. Ayoub, V. Alterio, and G. De Simone, "Chapter 2 - α-carbonic anhydrases," in *Carbonic Anhydrases*, C. T. Supuran and A. Nocentini, eds., pp. 19–54. Academic Press, 2019.

[63] J. F. Domsic and R. McKenna, "Sequestration of carbon dioxide by the hydrophobic pocket of the carbonic anhydrases," *Biochimica et Biophysica Acta (BBA) - Proteins and Proteomics* **1804** (2010) 326–331.

[64] J. F. Domsic, B. S. Avvaru, C. U. Kim, S. M. Gruner, M. Agbandje-McKenna, D. N. Silverman, and R. McKenna, "Entrapment of carbon dioxide in the active site of carbonic anhydrase ii," *Journal of Biological Chemistry* **283** (2008) 30766–30771.

[65] R. L. Mikulski and D. N. Silverman, "Proton transfer in catalysis and the role of proton shuttles in carbonic anhydrase," *Biochimica et Biophysica Acta (BBA) - Proteins and Proteomics* **1804** (2010) 422–426. Carbonic Anhydrase and Superoxide Dismutase.

[66] V. Alterio, M. Hilvo, A. D. Fiore, C. T. Supuran, P. Pan, S. Parkkila, A. Scaloni, J. Pastorek, S. Pastorekova, C. Pedone, A. Scozzafava, S. M. Monti, and G. D. Simone, "Crystal structure of the catalytic domain of the tumor-associated human carbonic anhydrase ix," *Proceedings of the National Academy of Sciences* **106** (2009) 16233–16238.

[67] V. Alterio, P. Pan, S. Parkkila, M. Buonanno, C. T. Supuran, S. M. Monti, and G. De Simone, "The structural comparison between membrane-associated human carbonic anhydrases provides insights into drug design of selective inhibitors," *Biopolymers* **101** (2014) 769–78.

[68] H. Steiner, B.-H. Jonsson, and S. Lindskog, "The catalytic mechanism of carbonic anhydrase," *European Journal of Biochemistry* **59** (1975) 253–259.

[69] D. Vullo, V. De Luca, A. Scozzafava, V. Carginale, M. Rossi, C. T. Supuran, and C. Capasso, "Anion inhibition studies of the fastest carbonic anhydrase (ca) known, the extremo-ca from the bacterium sulfurihydrogenibium azorense," *Bioorganic and Medicinal Chemistry Letters* **22** (2012) 7142–7145.

[70] D. N. Silverman and S. Lindskog, "The catalytic mechanism of carbonic anhydrase: implications of a rate-limiting protolysis of water," *Accounts of Chemical Research* **21** (1988) 30–36.

[71] C. Lomelino, J. Andring, and R. Mckenna, "Crystallography and its impact on carbonic anhydrase research," *International Journal of Medicinal Chemistry* **2018** (2018) 1–21.

[72] A. Angeli, F. Carta, and C. T. Supuran, "Carbonic anhydrases: Versatile and useful biocatalysts in chemistry and biochemistry," *Catalysts* **10** (2020) .

[73] K. M. J. Merz, "Carbon dioxide binding to human carbonic anhydrase ii," *Journal of the American Chemical Society* **113** (1991) 406–411.

[74] S. C. Frost and R. McKenna, *Carbonic anhydrase: mechanism, regulation, links to disease, and industrial applications*. Springer Science & Business Media, 2013.

[75] D. West, C. U. Kim, C. Tu, A. H. Robbins, S. M. Gruner, D. N. Silverman, and R. MKenna, "Structural and kinetic effects on changes in the co_2 binding pocket of human carbonic anhydrase ii," *Biochemistry* **51** (2012) 9156–9163.

[76] C. D. Boone, M. Pinard, R. McKenna, and D. Silverman, "Catalytic mechanism of α-class carbonic anhydrases: Co_2 hydration and proton transfer," *Springer* (2014) 31–52.

[77] Z. Fisher, J. A. Hernandez Prada, C. Tu, D. Duda, C. Yoshioka, H. An, L. Govindasamy, D. N. Silverman, and R. McKenna, "Structural and kinetic characterization of active-site histidine as a proton shuttle in catalysis by human carbonic anhydrase ii," *Biochemistry* **44** (2005) 1097–1105.

[78] S. Fisher, C. Maupin, M. Spano, G. Lakshmanan, C. Tu, M. Agbandje-McKenna, D. Silverman, G. Voth, and R. Mckenna,

"Atomic crystal and molecular dynamics simulation structures of human carbonic anhydrase ii: Insights into the proton transfer mechanism," *Biochemistry* **46** (2007) 2930–7.

[79] C. M. Maupin and G. A. Voth, "Preferred orientations of his64 in human carbonic anhydrase ii," *Biochemistry* **46** (2007) 2938–2947.

[80] J. Y. Liang and W. N. Lipscomb, "Binding of substrate co2 to the active site of human carbonic anhydrase ii: a molecular dynamics study.," *Proceedings of the National Academy of Sciences* **87** (1990) 3675–3679.

[81] J. F. Krebs, J. A. Ippolito, D. W. Christianson, and C. A. Fierke, "Structural and functional importance of a conserved hydrogen bond network in human carbonic anhydrase ii," *Journal of Biological Chemistry* **268** (1993) 27458–27466.

[82] S. Lindskog, "Structure and mechanism of carbonic anhydrase," *Pharmacology and Therapeutics* **74** (1997) 1–20.

[83] A. Liljas, K. Håkansson, B. H. Jonsson, and Y. Xue, "Inhibition and catalysis of carbonic anhydrase. recent crystallographic analyses," *European Journal of Biochemistry* **219** (1994) 1–10.

[84] Y. Xue, J. Vidgren, L. A. Svensson, A. Liljas, B. H. Jönsson, and S. Lindskog, "Crystallographic analysis of thr-200–>his human carbonic anhydrase ii and its complex with the substrate, hco3-," *Proteins: Structure, Function, and Bioinformatics* **15** (1993) 80–87.

[85] K. M. Merz, "Determination of pk_as of ionizable groups in proteins: the pk_a of glu 7 and 35 in hen egg white lysozyme and glu 106 in human carbonic anhydrase ii," *Journal of the American Chemical Society* **113** (1991) 3572–3575.

[86] B. S. Avvaru, C. U. Kim, K. H. Sippel, S. M. Gruner, M. Agbandje-McKenna, D. N. Silverman, and R. McKenna, "A short, strong hydrogen bond in the active site of human carbonic anhydrase ii," *Biochemistry* **49** (2010) 249–251.

[87] A. Nocentini, W. Donald, and C. Supuran, "Human carbonic anhydrases: tissue distribution, physiological role and druggability.,".

[88] O. Warburg, "The chemical constitution of respiratory ferment," *Science* **68** (1928) 437–443.

[89] O. Warburg, F. Wind, and E. Negelein, "The metabolism of tumors in the body," *Journal of General Physiology* **8** (1927) 519–530.

[90] H. Becker, "Carbonic anhydrase ix and acid transport in cancer," *British Journal of Cancer* **122** (12, 2019) 1–11.

[91] S. Bröer, B. Rahman, G. Pellegri, L. Pellerin, J.-L. Martin, S. Verleysdonk, B. Hamprecht, and P. J. Magistretti, "Comparison of lactate transport in astroglial cells and monocarboxylate transporter 1 (mct 1) expressing xenopus laevis oocytes: Expression of two different monocarboxylate transporters in astroglial cells and neurons*," *Journal of Biological Chemistry* **272** (1997) 30096–30102.

[92] S. Bröer, H.-P. Schneider, A. Bröer, B. Rahman, B. Hamprecht, and J. W. Deitmer, "Characterization of the monocarboxylate transporter 1 expressed in xenopus laevis oocytes by changes in cytosolic ph," *Biochemical Journal* **333** (1998) 167–174.

[93] A. Halestrap and N. Price, "The proton-linked monocarboxylate transporter (mct) family - structure, function and regulation," *Biochemical Journal* **343** (1999) 281 – 299.

[94] K. S. Dimmer, B. Friedrich, F. Lang, J. W. Deitmer, and S. Bröer, "The low-affinity monocarboxylate transporter mct4 is adapted to the export of lactate in highly glycolytic cells.," *The Biochemical journal* **350 Pt 1** (2000) 219–27.

[95] C. Stock, R. A. Cardone, G. Busco, H. Krähling, A. Schwab, and S. J. Reshkin, "Protons extruded by nhe1: Digestive or glue?," *European Journal of Cell Biology* **87** (2008) 591–599. FEBS Workshop: Invadopodia, Podosomes and Focal Adhesions in Tissue Invasion.

[96] R. Martinez-Zaguilan, R. M. Lynch, G. M. Martinez, and R. J. Gillies, "Vacuolar-type h(+)-atpases are functionally expressed in plasma membranes of human tumor cells," *American Journal of Physiology-Cell Physiology* **265** (1993) C1015–C1029.

[97] L. Stransky, K. Cotter, and M. Forgac, "The function of v-atpases in cancer," *Physiological Reviews* **96** (2016) 1071–1091.

[98] T. H. Dovmark, M. Saccomano, A. Hulikova, F. Alves, and P. Swietach, "Connexin-43 channels are a pathway for discharging lactate from glycolytic pancreatic ductal adenocarcinoma cells.," *Oncogene* (2017) .

[99] F. Itel, S. Al-Samir, F. Öberg, M. Chami, M. Kumar, C. T. Supuran, P. M. T. Deen, W. Meier, K. Hedfalk, G. Gros, and V. Endeward, "Co2 permeability of cell membranes is regulated by membrane cholesterol and protein gas channels," *The FASEB Journal* **26** (2012) 5182–5191.

[100] M. Arias-Hidalgo, S. Al-Samir, G. Gros, and V. Endeward, "Cholesterol is the main regulator of the carbon dioxide permeability of biological membranes," *American Journal of Physiology-Cell Physiology* **315** (2018) C137–C140.

[101] S. Parkkila, J. Lasota, J. Fletcher, W.-B. Ou, A. Kivelä, K. Nuorva, A.-K. Parkkila, J. Ollikainen, W. Sly, A. Waheed, S. Pastorekova, J. Pastorek, J. Isola, and M. Miettinen, "Carbonic anhydrase ii. a novel biomarker for gastrointestinal stromal tumors," *Modern pathology: an official journal of the United States and Canadian Academy of Pathology, Inc* **23** (2010) 743–50.

[102] J. Pastorek, S. Pastoreková, I. Callebaut, J. Mornon, V. Zelník, R. Opavský, M. Zat'ovičová, S. Liao, D. Portetelle, E. Stanbridge, J. Závada, A. Burny, and R. Kettmann, "Cloning and characterization of mn, a human tumor-associated protein with a domain homologous to carbonic anhydrase and a putative helix - loop - helix dna binding segment," *Oncogene* **9** (1994) 2877–2888.

[103] J. Saarnio, S. Parkkila, A.-K. Parkkila, K. Haukipuro, S. Pastoreková, J. Pastorek, M. I. Kairaluoma, and T. J. Karttunen, "Immunohistochemical study of colorectal tumors for expression of a novel transmembrane carbonic anhydrase, mn/ca ix, with potential value as a marker of cell proliferation," *The American Journal of Pathology* **153** (1998) 279–285.

[104] P. Karhumaa, K. Kaunisto, S. Parkkila, A. Waheed, S. Pastorekova, J. Pastorek, W. Sly, and H. Rajaniemi, "Expression of the transmembrane carbonic anhydrases, ca ix and ca xii, in the human male excurrent ducts," *Molecular human reproduction* **7** (2001) 611–6.

[105] Y. Zheng, B. Xu, Y. Zhao, H. Gu, C. Li, Y. Wang, and X. Chang, "Ca1 contributes to microcalcification and tumourigenesis in breast cancer," *BMC Cancer* **15** (2015) .

[106] Y. Zhou, R. Bayat Mokhtari, J. Pan, and E. Cutz, "Carbonic anhydrase ii mediates malignant behavior of pulmonary neuroendocrine tumors," *American journal of respiratory cell and molecular biology* **52** (2014) .

[107] C. Stock and A. Schwab, "Protons make tumor cells move like clockwork," *Pflügers Archiv - European Journal of Physiology* **458** (2009) 981–992.

[108] E. Svastova, W. Witarski, L. Csaderova, I. Kosik, L. Skvarkova, A. Hulikova, M. Zatovicova, M. Barathova, J. Kopacek, J. Pastorek, and S. Pastorekova, "Carbonic anhydrase ix interacts with bicarbonate transporters in lamellipodia and increases cell migration via its catalytic domain*," *Journal of Biological Chemistry* **287** (2012) 3392–3402.

[109] P. Ditte, F. Dequiedt, E. Svastova, A. Hulikova, A. Ohradanova-Repic, M. Zatovicova, L. Csaderova, J. Kopacek, C. T. Supuran, S. Pastorekova, and J. Pastorek, "Phosphorylation of carbonic anhydrase ix controls its ability to mediate extracellular acidification in hypoxic tumors," *Cancer Research* **71** (2011) 7558–7567.

[110] P. Swietach, S. Wigfield, P. Cobden, C. T. Supuran, A. L. Harris, and R. D. Vaughan-Jones, "Tumor-associated carbonic anhydrase 9 spatially coordinates intracellular ph in three-dimensional multicellular growths*," *Journal of Biological Chemistry* **283** (2008) 20473–20483.

[111] E. Svastová, A. Hulıková, M. Rafajová, M. Zatovičová, A. Gibadulinová, A. Casini, A. Cecchi, A. Scozzafava, C. T. Supuran, J. Pastorek, and S. Pastoreková, "Hypoxia activates the capacity of tumor-associated carbonic anhydrase ix to acidify extracellular ph," *FEBS Letters* **577** (2004) 439–445.

[112] A. Hulikova, A. Harris, R. Vaughan-Jones, and P. Swietach, "Acid-extrusion from tissue: the interplay between membrane transporters and ph buffers.," *Current Pharmaceutical Design* **18** (2012) 1331–7.

[113] M. Y. Mboge, R. Mahon, B Pand McKenna, and S. Frost, "Carbonic anhydrases: Role in ph control and cancer.," *Metabolites* **8** (2018) .

[114] A. Innocenti, D. Vullo, A. Scozzafava, J. R. Casey, and C. Supuran, "Carbonic anhydrase inhibitors. interaction of isozymes i, ii, iv, v, and ix with carboxylates," *Bioorganic and Medicinal Chemistry Letters* **15** (2005) 573–578.

[115] A. Innocenti, S. Pastorekova, J. Pastorek, A. Scozzafava, G. D. Simone, and C. T. Supuran, "The proteoglycan region of the tumor-associated carbonic anhydrase isoform ix acts as an intrinsic buffer optimizing co2 hydration at acidic ph values characteristic of solid tumors," *Bioorganic and Medicinal Chemistry Letters* **19** (2009) 5825–5828.

[116] S. Ivanov, S.-Y. Liao, A. Ivanova, A. Danilkovitch-Miagkova, N. Tarasova, G. Weirich, M. Merrill, M. Proescholdt, E. Oldfield, J. Lee, J. Závada, A. Waheed, W. Sly, M. Lerman, and E. Stanbridge, "Expression of hypoxia-inducible cell-surface transmembrane carbonic anhydrases in human cancer," *The American journal of pathology* **158** (04, 2001) 905–19.

[117] B. C. Leibovich, Y. Sheinin, C. M. Lohse, R. H. Thompson, J. C. Cheville, J. Zavada, and E. D. Kwon, "Carbonic anhydrase ix is not an independent predictor of outcome for patients with clear cell renal cell carcinoma," *Journal of Clinical Oncology* **25** (2007) 4757–4764.

[118] S. Frost, "Physiological functions of the alpha class of carbonic anhydrases," *Sub-cellular biochemistry* **75** (2014) 9–30.

[119] M. Hilvo, L. Baranauskiene, A. M. Salzano, A. Scaloni, D. Matulis, A. Innocenti, A. Scozzafava, S. Monti, A. Di Fiore, G. De Simone, M. Lindfors, J. Jänis, J. Valjakka, S. Pastorekova, J. Pastorek, M. Kulomaa, H. Nordlund, C. Supuran, and S. Parkkila, "Biochemical characterization of ca ix, one of the most active carbonic anhydrase isozymes," *The Journal of biological chemistry* **283** (2008) 27799–809.

[120] C. Supuran, "Carbonic anhydrase inhibition and the management of hypoxic tumors," *Metabolites* **7** (2017) .

[121] S. Kaluz, M. Kaluzová, S.-Y. Liao, M. Lerman, and E. J. Stanbridge, "Transcriptional control of the tumor- and hypoxia-marker carbonic anhydrase 9: A one transcription factor (hif-1) show?," *Biochimica et Biophysica Acta (BBA) - Reviews on Cancer* **1795** (2009) 162–172.

[122] O. Aprelikova, G. V. Chandramouli, M. Wood, J. R. Vasselli, J. Riss, J. K. Maranchie, W. M. Linehan, and J. C. Barrett, "Regulation of hif prolyl hydroxylases by hypoxia-inducible factors," *Journal of Cellular Biochemistry* **92** (2004) 491–501.

[123] D. Lando, D. J. Peet, D. A. Whelan, J. J. Gorman, and M. L. Whitelaw, "Asparagine hydroxylation of the hif transactivation domain: A hypoxic switch," *Science* **295** no. 5556, (2002) 858–861.

[124] C. C. Wykoff, N. J. P. Beasley, P. H. Watson, K. J. Turner, J. Pastorek, A. Sibtain, G. D. Wilson, H. Turley, K. L. Talks, P. H. Maxwell, C. W. Pugh, P. J. Ratcliffe, and A. L. Harris, "Hypoxia-inducible expression of tumor-associated carbonic anhydrases1," *Cancer Research* **60** (12, 2000) 7075–7083.

[125] R. Opavský, S. Pastoreková, V. Zelnık, A. Gibadulinová, E. J. Stanbridge, J. Závada, R. Kettmann, and J. Pastorek, "Humanmn/ca9gene, a novel member of the carbonic anhydrase family: Structure and exon to protein domain relationships," *Genomics* **33** (1996) 480–487.

[126] T. Dorai, I. S. Sawczuk, J. Pastorek, P. H. Wiernik, and J. P. Dutcher, "The role of carbonic anhydrase ix overexpression in kidney cancer," *European Journal of Cancer* **41** (2005) 2935–2947.

[127] J. Závada, Z. Závadová, S. Pastoreková, F. Čiampor, J. Pastorek, and V. Zelník, "Expression of matu-mn protein in human tumor cultures and in clinical specimens," *International Journal of Cancer* **54** (1993) 268–274.

[128] D. A. Whittington, A. Waheed, B. Ulmasov, G. N. Shah, J. H. Grubb, W. S. Sly, and D. W. Christianson, "Crystal structure of the dimeric extracellular domain of human carbonic anhydrase xii, a bitopic membrane protein overexpressed in certain cancer tumor cells," *Proceedings of the National Academy of Sciences* **98** (2001) 9545–9550.

[129] Özlem Türeci, U. Sahin, E. Vollmar, S. Siemer, E. Göttert, G. Seitz, A.-K. Parkkila, G. N. Shah, J. H. Grubb, M. Pfreundschuh, and W. S. Sly, "Human carbonic anhydrase xii: cdna cloning, expression, and chromosomal localization of a carbonic anhydrase gene that is overexpressed in some renal cell cancers," *Proceedings of the National Academy of Sciences* **95** (1998) 7608–7613.

[130] K. R. MacKenzie, J. H. Prestegard, and D. M. Engelman, "A transmembrane helix dimer: Structure and implications," *Science* **276** (1997) 131–133.

[131] W. P. Russ and D. M. Engelman, "The gxxxg motif: A framework for transmembrane helix-helix association11edited by g. von heijne," *Journal of Molecular Biology* **296** (2000) 911–919.

[132] A. Senes, M. Gerstein, and D. M. Engelman, "Statistical analysis of amino acid patterns in transmembrane helices: the gxxxg motif occurs frequently and in association with β-branched residues at neighboring positions11edited by g. von heijne," *Journal of Molecular Biology* **296** (2000) 921–936.

[133] S. O. Smith, D. Song, S. Shekar, M. Groesbeek, M. Ziliox, and S. Aimoto, "Structure of the transmembrane dimer interface of glycophorin a in membrane bilayers," *Biochemistry* **40** (2001) 6553–6558.

[134] A. Kivelä, S. Parkkila, J. Saarnio, T. Karttunen, J. Kivelä, A. Parkkila, A. Waheed, W. Sly, J. Grubb, G. Shah, O. Türeci, and H. Rajaniemi, "Expression of a novel transmembrane carbonic anhydrase isozyme xii in normal human gut and colorectal tumors.," *American Journal of Pathology* **156** (2000) 577–84.

[135] S. Parkkila, A.-K. Parkkila, J. Saarnio, J. Kivelä, T. J. Karttunen, K. Kaunisto, A. Waheed, W. S. Sly, Özlem Türeci, I. Virtanen, and H. Rajaniemi, "Expression of the membrane-associated carbonic anhydrase isozyme xii in the human kidney and renal tumors," *Journal of Histochemistry & Cytochemistry* **48** (2000) 1601–1608.

[136] P. Karhumaa, S. Parkkila, O. Türeci, A. Waheed, J. Grubb, G. Shah, A.-K. Parkkila, K. Kaunisto, J. Tapanainen, W. Sly, and H. Rajaniemi, "Identification of carbonic anhydrase xii as the membrane isozyme expressed in the normal human endometrial epithelium," *Molecular Human Reproduction* **6** (2000) 68–74.

[137] M. Feldshtein, S. Elkrinawi, B. Yerushalmi, B. Marcus, D. Vullo, H. Romi, R. Ofir, D. Landau, S. Sivan, C. T. Supuran, and O. S. Birk, "Hyperchlorhidrosis caused by homozygous mutation in ca12, encoding carbonic anhydrase xii," *The American Journal of Human Genetics* **87** (2010) 713–720.

[138] E. Muhammad, N. Leventhal, G. Parvari, A. Hanukoglu, I. Hanukoglu, V. Chalifa-Caspi, Y. Feinstein, J. Weinbrand, H. Jacoby, E. Manor, T. Nagar, J. Beck, V. Sheffield, E. Hershkovitz, and R. Parvari,

"Autosomal recessive hyponatremia due to isolated salt wasting in sweat associated with a mutation in the active site of carbonic anhydrase 12.," *Human Genetics* **129** (2011) 397–405.

[139] J. H. Hong, E. Muhammad, C. Zheng, E. Hershkovitz, S. Alkrinawi, N. Loewenthal, R. Parvari, and S. Muallem, "Essential role of carbonic anhydrase xii in secretory gland fluid and hco3- secretion revealed by disease causing human mutation," *The Journal of Physiology* **593** (2015) 5299–5312.

[140] M. Lee, B. Vecchio-Pagán, N. Sharma, A. Waheed, X. Li, K. S. Raraigh, S. Robbins, S. T. Han, A. L. Franca, M. J. Pellicore, T. A. Evans, K. M. Arcara, H. Nguyen, S. Luan, D. Belchis, J. Hertecant, J. Zabner, W. S. Sly, and G. R. Cutting, "Loss of carbonic anhydrase xii function in individuals with elevated sweat chloride concentration and pulmonary airway disease," *Human Molecular Genetics* **25** (02, 2016) 1923–1933.

[141] S.-Y. Liao, S. Ivanov, A. Ivanova, S. Ghosh, M. A. Cote, K. Keefe, M. Coca-Prados, E. J. Stanbridge, and M. I. Lerman, "Expression of cell surface transmembrane carbonic anhydrase genes ca9 and ca12 in the human eye: overexpression of ca12 (caxii) in glaucoma," *Journal of Medical Genetics* **40** (2003) 257–261.

[142] C. Yoo, B. Nam, J. Kim, H. Shin, H. Lim, S. Lee, S. Lee, M. Lim, and Y. Song, "Carbonic anhydrase xii expression is associated with histologic grade of cervical cancer and superior radiotherapy outcome.," *Radiation Oncology* **5** (2010) .

[143] S. Parkkila, H. Rajaniemi, A.-K. Parkkila, J. Kivelä, A. Waheed, S. Pastoreková, J. Pastorek, and W. S. Sly, "Carbonic anhydrase inhibitor suppresses invasion of renal cancer cells in vitro," *Proceedings of the National Academy of Sciences* **97** (2000) 2220–2224.

[144] C. Wykoff, N. Beasley, P. Watson, L. Campo, S. Chia, R. English, J. Pastorek, W. Sly, P. Ratcliffe, and A. Harris, "Expression of the hypoxia-inducible and tumor-associated carbonic anhydrases in ductal carcinoma in situ of the breast.," *American Journal of Pathology* **158** (2001) 1011–1019.

[145] P. Watson, S. Chia, C. Wykoff, C. Han, R. Leek, W. Sly, K. Gatter, P. Ratcliffe, and A. Harris, "Carbonic anhydrase xii is a marker of good

prognosis in invasive breast carcinoma.," *British Journal of Cancer* **88** (2003) 1065–70.

[146] S. V. Ivanov, I. Kuzmin, M.-H. Wei, S. Pack, L. Geil, B. E. Johnson, E. J. Stanbridge, and M. I. Lerman, "Down-regulation of transmembrane carbonic anhydrases in renal cell carcinoma cell lines by wild-type von hippel-lindau transgenes," *Proceedings of the National Academy of Sciences* **95** (1998) 12596–12601.

[147] S. Ivanov, S. Liao, A. Ivanova, A. Danilkovitch-Miagkova, N. Tarasova, G. Weirich, M. Merrill, M. Proescholdt, E. Oldfield, J. Lee, J. Zavada, A. Waheed, W. Sly, M. Lerman, and E. Stanbridge, "Expression of hypoxia-inducible cell-surface transmembrane carbonic anhydrases in human cancer," *American Journal of Pathology* **158** (2001) 905–919.

[148] S. Gruvberger, A. Borg, M. Fernö, M. Ringnér, C. Peterson, S. Gruvberger, Y. Chen, S. Panavally, L. Saal, and P. Meltzer, "Estrogen receptor status in breast cancer is associated with remarkably distinct gene expression patterns," *Cancer Research* **61** (2001) 5979–5984.

[149] L. J. van 't Veer, H. Dai, M. J. van de Vijver, Y. D. He, A. A. Hart, M. Mao, H. L. Peterse, K. K. van der, M. J. Marton, A. T. Witteveen, G. J. Schreiber, R. M. Kerkhoven, C. Roberts, P. S. Linsley, R. Bernards, and S. H. Friend, "Gene expression profiling predicts clinical outcome of breast cancer," *Nature* **415** (2002) 530–536.

[150] D. H. Barnett, S. Sheng, T. Howe Charn, A. Waheed, W. S. Sly, C.-Y. Lin, E. T. Liu, and B. S. Katzenellenbogen, "Estrogen receptor regulation of carbonic anhydrase xii through a distal enhancer in breast cancer," *Cancer Research* **68** (2008) 3505–3515.

[151] A. Nocentini and C. T. S. and, "Advances in the structural annotation of human carbonic anhydrases and impact on future drug discovery," *Expert Opinion on Drug Discovery* **14** (2019) 1175–1197.

[152] C. T. Supuran, "How many carbonic anhydrase inhibition mechanisms exist?," *Journal of Enzyme Inhibition and Medicinal Chemistry* **31** (2016) 345–360.

[153] A. Bonardi, A. Nocentini, S. Bua, J. Combs, C. Lomelino, J. Andring, L. Lucarini, S. Sgambellone, E. Masini, R. McKenna, P. Gratteri, and C. T. Supuran, "Sulfonamide inhibitors of human carbonic anhydrases

designed through a three-tails approach: Improving ligand/isoform matching and selectivity of action," *Journal of Medicinal Chemistry* **63** (2020) 7422–7444.

[154] M. Bozdag, M. Ferraroni, E. Nuti, D. Vullo, A. Rossello, F. Carta, A. Scozzafava, and C. T. Supuran, "Combining the tail and the ring approaches for obtaining potent and isoform-selective carbonic anhydrase inhibitors: Solution and x-ray crystallographic studies," *Bioorganic and Medicinal Chemistry* **22** (2014) 334–340.

[155] C. Supuran, "Advances in structure-based drug discovery of carbonic anhydrase inhibitors," *Expert Opinion on Drug Discovery* **12** (10, 2016) .

[156] A. Scozzafava, A. Mastrolorenzo, and C. T. Supuran, "Carbonic anhydrase inhibitors and activators and their use in therapy," *Expert Opinion on Therapeutic Patents* **16** (2006) 1627–1664.

[157] A. Thiry, J.-M. Dogné, B. Masereel, and C. T. Supuran, "Targeting tumor-associated carbonic anhydrase ix in cancer therapy," *Trends in Pharmacological Sciences* **27** (2006) 566–573.

[158] S. Pastorekova, S. Parkkila, J. Pastorek, and C. T. Supuran, "Review article," *Journal of Enzyme Inhibition and Medicinal Chemistry* **19** (2004) 199–229.

[159] C. T. Supuran, "Carbonic anhydrases: novel therapeutic applications for inhibitors and activators," *Nature Reviews Drug Discovery* **7** (2008) 168–181.

[160] MedChemExpress, "Ca ix/xii inhibitor. u-104 (slc-0111)," 2024. Accessed: November 24, 2024.

[161] H. Hashem, S. Abdelfattah, H. M. Hassan, A. Al-Emam, M. Alqarni, G. Alotaibi, I. T. Radwan, K. Kaur, D. P. Rao, S. Bräse, and A. Alkhammash, "Discovery of a novel 4-pyridyl slc-0111 analog targeting tumor-associated carbonic anhydrase isoform ix through tail-based design approach with potent anticancer activity," *Frontiers in Chemistry* **13** (2025) 1571646.

[162] A. Sarnella, Y. Ferrara, L. Auletta, S. Albanese, L. Cerchia, V. Alterio, G. De Simone, C. T. Supuran, and A. Zannetti, "Inhibition of carbonic anhydrases ix/xii by slc-0111 boosts cisplatin effects in hampering head

and neck squamous carcinoma cell growth and invasion," *Journal of Experimental and Clinical Cancer Research* **41** (2022) 122.

[163] P. C. McDonald, S. Chia, P. L. Bedard, Q. Chu, M. Lyle, L. Tang, *et al.*, "A phase 1 study of slc-0111, a novel inhibitor of carbonic anhydrase ix, in patients with advanced solid tumors," *American Journal of Clinical Oncology* **43** (2020) 484–490.

[164] A. Angeli, L. Micheli, F. Carta, M. Ferraroni, T. Pirali, A. Fernandez Carvajal, A. Ferrer Montiel, L. Di Cesare Mannelli, C. Ghelardini, and C. T. Supuran, "First-in-class dual hybrid carbonic anhydrase inhibitors and transient receptor potential vanilloid 1 agonists revert oxaliplatin-induced neuropathy," *Journal of Medicinal Chemistry* **66** (2023) 1616–1633. PMID: 36626645.

[165] R. Ronca and C. T. Supuran, "Carbonic anhydrase ix: An atypical target for innovative therapies in cancer," *Biochimica et Biophysica Acta (BBA) - Reviews on Cancer* **1879** (2024) 189120.

[166] K. D'Ambrosio, A. Di Fiore, and E. Langella, "Dual targeting carbonic anhydrase inhibitors as promising therapeutic approach: a structural overview," *Frontiers in Molecular Biosciences* **12** (2025) 1511281.

[167] R. Meleddu, S. Distinto, F. Cottiglia, R. Angius, M. Gaspari, D. Taverna, C. Melis, A. Angeli, G. Bianco, S. Deplano, B. Fois, S. Del Prete, C. Capasso, S. Alcaro, F. Ortuso, M. Yanez, C. T. Supuran, and E. Maccioni, "Tuning the dual inhibition of carbonic anhydrase and cyclooxygenase by dihydrothiazole benzensulfonamides," *ACS Medicinal Chemistry Letters* **9** (2018) 1045–1050.

[168] F. Mincione, A. Nocentini, and C. T. Supuran, "Advances in the discovery of novel agents for the treatment of glaucoma," *Expert Opinion on Drug Discovery* **16** (2021) 1209–1225.

[169] A. Nocentini, M. Ceruso, S. Bua, C. L. Lomelino, J. T. Andring, R. McKenna, C. Lanzi, S. Sgambellone, R. Pecori, R. Matucci, L. Filippi, P. Gratteri, F. Carta, E. Masini, S. Selleri, and C. T. Supuran, "Discovery of β-adrenergic receptors blocker–carbonic anhydrase inhibitor hybrids for multitargeted antiglaucoma therapy," *Journal of Medicinal Chemistry* **61** (2018) 5380–5394.

[170] A. M. V. Brooks and W. E. Gillies, "Ocular β-blockers in glaucoma management," *Drugs & Aging* **2** (1992) 208–221.

[171] E. Masini, F. Carta, A. Scozzafava, and C. T. Supuran, "Antiglaucoma carbonic anhydrase inhibitors: a patent review," *Expert Opinion on Therapeutic Patents* **23** (2013) 705–716.

[172] A. Angeli, L. Micheli, F. Carta, M. Ferraroni, T. Pirali, A. Fernandez Carvajal, A. Ferrer Montiel, L. Di Cesare Mannelli, C. Ghelardini, and C. T. Supuran, "First-in-class dual hybrid carbonic anhydrase inhibitors and transient receptor potential vanilloid 1 agonists revert oxaliplatin-induced neuropathy," *Journal of Medicinal Chemistry* **66** (2023) 1616–1633.

[173] C. B. Harley, "Telomerase and cancer therapeutics," *Nature Reviews Cancer* **8** (March, 2008) 167–179.

[174] K. M. Wang, R.-L. Wang, J.-J. Liu, J. Zhou, X. Li, W.-W. Hu, W.-J. Jiang, and N.-B. Hao, "The prognostic significance of htert overexpression in cancers: A systematic review and meta-analysis," *Medicine* **97** (2018) e11794.

[175] C. Strahl and E. H. Blackburn, "The effects of nucleoside analogs on telomerase and telomeres in tetrahymena," *Nucleic Acids Research* **22** (1994) 893–900.

[176] E. Berrino, A. Angeli, D. D. Zhdanov, A. P. Kiryukhina, A. Milaneschi, A. De Luca, M. Bozdag, S. Carradori, S. Selleri, G. Bartolucci, T. S. Peat, M. Ferraroni, C. T. Supuran, and F. Carta, "Azidothymidine "clicked" into 1,2,3-triazoles: First report on carbonic anhydrase–telomerase dual-hybrid inhibitors," *Journal of Medicinal Chemistry* **63** (2020) 7392–7409.

[177] E. Berrino, B. Michelet, K. Vitse, A. Nocentini, G. Bartolucci, A. Martin-Mingot, P. Gratteri, F. Carta, C. T. Supuran, and S. Thibaudeau, "Superacid-synthesized fluorinated diamines act as selective hca iv inhibitors," *Journal of Medicinal Chemistry* **67** no. 21, (2024) 19460–19474.

[178] A. A. Plyasova, E. Berrino, I. I. Khan, A. V. Veselovsky, V. S. Pokrovsky, A. Angeli, M. Ferraroni, C. T. Supuran, M. V. Pokrovskaya, S. S. Alexandrova, Y. A. Gladilina, N. N. Sokolov, A. Hilal, F. Carta,

and D. D. Zhdanov, "Mechanisms of the antiproliferative and antitumor activity of novel telomerase–carbonic anhydrase dual-hybrid inhibitors," *Journal of Medicinal Chemistry* **64** (2021) 11432–11444.

[179] P. Lombardi, K. Cole, D. Dowling, and D. Christianson, "Structure, mechanism, and inhibition of histone deacetylases and related metalloenzymes," *Current opinion in structural biology* **21** (08, 2011) 735–43.

[180] M. Asmamaw, A. He, L.-R. Zhang, H.-M. Liu, and Y. Gao, "Histone deacetylase complexes: Structure, regulation and function," *Biochimica et Biophysica Acta (BBA) - Reviews on Cancer* **1879** (2024) 189150.

[181] S. Park and J. Kim, "A short guide to histone deacetylases including recent progress on class ii enzymes," *Experimental and Molecular Medicine* **52** (2020) 204–212.

[182] G. Milazzo, D. Mercatelli, G. Di Muzio, L. Triboli, P. De Rosa, G. Perini, and F. M. Giorgi, "Histone deacetylases (hdacs): Evolution, specificity, role in transcriptional complexes, and pharmacological actionability," *Genes* **11** (2020) .

[183] A. Vassilopoulos, K. Fritz, D. Petersen, and D. Gius, "The human sirtuin family: Evolutionary divergences and functions," *Human genomics* **5** (07, 2011) 485–96.

[184] K. Falkenberg and R. Johnstone, "Histone deacetylases and their inhibitors in cancer, neurological diseases and immune disorders," *Nature Reviews Drug Discovery* **13** (2014) 673–691.

[185] S. Yoon and G. H. Eom, "Hdac and hdac inhibitor: From cancer to cardiovascular diseases," *Chonnam Medical Journal* **52** (2016) 1–11.

[186] S. Minucci and P. Pelicci, "Histone deacetylase inhibitors and the promise of epigenetic (and more) treatments for cancer," *Nature Reviews Cancer* **6** (2006) 38–51.

[187] O. Witt, H. E. Deubzer, T. Milde, and I. Oehme, "Hdac family: What are the cancer relevant targets?," *Cancer Letters* **277** (2009) 8–21.

[188] J. Song, J. H. Noh, J. H. Lee, J. W. Eun, Y. M. Ahn, S. Y. Kim, S. H. Lee, W. S. Park, N. J. Yoo, J. Y. Lee, and S. W. Nam, "Increased expression of histone deacetylase 2 is found in human gastric cancer,"

Acta Pathologica, Microbiologica, et Immunologica Scandinavica **113** (2005) 264–268.

[189] J.-H. Choi, H. J. Kwon, B.-I. Yoon, J.-H. Kim, S. U. Han, H. J. Joo, and D.-Y. Kim, "Expression profile of histone deacetylase 1 in gastric cancer tissues," *Japanese Journal of Cancer Research* **92** (2001) 1300–1304.

[190] J.-H. Kim, Y.-K. Choi, H.-J. Kwon, H.-K. Yang, J.-H. Choi, and D.-Y. Kim, "Downregulation of gelsolin and retinoic acid receptor β expression in gastric cancer tissues through histone deacetylase 1," *Journal of Gastroenterology and Hepatology* **19** (2004) 218–224.

[191] C. A. Krusche, P. Wülfing, C. Kersting, A. Vloet, W. Böcker, L. Kiesel, H. M. Beier, and J. Alfer, "Histone deacetylase-1 and -3 protein expression in human breast cancer: a tissue microarray analysis," *Breast Cancer Research and Treatment* **90** (2005) 15–23.

[192] S. K. Patra, A. Patra, and R. Dahiya, "Histone deacetylase and dna methyltransferase in human prostate cancer," *Biochemical and Biophysical Research Communications* **287** (2001) 705–713.

[193] D. Waltregny, B. North, F. Van Mellaert, J. de Leval, E. Verdin, and V. Castronovo, "Screening of histone deacetylases (hdac) expression in human prostate cancer reveals distinct class ihdac profiles between epithelial and stromal cells," *European Journal of Histochemistry* **48** (2004) .

[194] K. Halkidou, L. Gaughan, S. Cook, H. Y. Leung, D. E. Neal, and C. N. Robson, "Upregulation and nuclear recruitment of hdac1 in hormone refractory prostate cancer," *The Prostate* **59** (2004) 177–189.

[195] M. Nakagawa, Y. Oda, T. Eguchi, S. Aishima, T. Yao, F. Hosoi, Y. Basaki, M. Ono, M. Kuwano, M. Tanaka, and M. Tsuneyoshi, "Expression profile of class i histone deacetylases in human cancer tissues," *Oncology reports* **18** (2007) 769–774.

[196] C. Micelli and G. Rastelli, "Histone deacetylases: structural determinants of inhibitor selectivity," *Drug Discovery Today* **20** (2015) 718–735.

[197] D.-F. Wang, O. Wiest, P. Helquist, H.-Y. Lan-Hargest, and N. L. Wiech, "On the function of the 14 Å long internal cavity of histone deacetylase-like protein: Implications for the design of histone

deacetylase inhibitors," *Journal of Medicinal Chemistry* **47** (2004) 3409–3417.

[198] L. Whitehead, M. R. Dobler, B. Radetich, Y. Zhu, P. W. Atadja, T. Claiborne, J. E. Grob, A. McRiner, M. R. Pancost, A. Patnaik, W. Shao, M. Shultz, R. Tichkule, R. A. Tommasi, B. Vash, P. Wang, and T. Stams, "Human hdac isoform selectivity achieved via exploitation of the acetate release channel with structurally unique small molecule inhibitors," *Bioorganic and Medicinal Chemistry* **19** (2011) 4626–4634.

[199] B. E. Lauffer, R. Mintzer, R. Fong, S. Mukund, C. Tam, I. Zilberleyb, B. Flicke, A. Ritscher, G. Fedorowicz, R. Vallero, D. F. Ortwine, J. Gunzner, Z. Modrusan, L. Neumann, C. M. Koth, P. J. Lupardus, J. S. Kaminker, C. E. Heise, and P. Steiner, "Histone deacetylase (hdac) inhibitor kinetic rate constants correlate with cellular histone acetylation but not transcription and cell viability," *Journal of Biological Chemistry* **288** (2013) 26926–26943.

[200] J. R. Somoza, R. J. Skene, B. A. Katz, C. Mol, J. D. Ho, A. J. Jennings, C. Luong, A. Arvai, J. J. Buggy, E. Chi, J. Tang, B.-C. Sang, E. Verner, R. Wynands, E. M. Leahy, D. R. Dougan, G. Snell, M. Navre, M. W. Knuth, R. V. Swanson, D. E. McRee, and L. W. Tari, "Structural snapshots of human hdac8 provide insights into the class i histone deacetylases," *Structure* **12** (2004) 1325–1334.

[201] K. E. Cole, D. P. Dowling, M. A. Boone, A. J. Phillips, and D. W. Christianson, "Structural basis of the antiproliferative activity of largazole, a depsipeptide inhibitor of the histone deacetylases," *Journal of the American Chemical Society* **133** (2011) 12474–12477.

[202] P. Watson, C. Millard, A. Riley, N. Robertson, L. Wright, H. Godage, S. Cowley, A. Jamieson, B. Potter, and J. Schwabe, "Insights into the activation mechanism of class i hdac complexes by inositol phosphates.," *Nature Communications* **7** (2016) .

[203] N. Sengupta and E. Seto, "Regulation of histone deacetylase activities," *Journal of Cellular Biochemistry* **93** (2004) 57–67.

[204] E. Hu, Z. Chen, T. Fredrickson, Y. Zhu, R. Kirkpatrick, G.-F. Zhang, K. Johanson, C.-M. Sung, R. Liu, and J. Winkler, "Cloning and characterization of a novel human class i histone deacetylase that

functions as a transcription repressor," *The Journal of biological chemistry* **275** (2000) 15254–64.

[205] H. Lee, N. Rezai-Zadeh, and E. S. and, "Negative regulation of histone deacetylase 8 activity by cyclic amp-dependent protein kinase a," *Molecular and Cellular Biology* **24** (2004) 765–773.

[206] S. Jamaladdin, R. D. W. Kelly, L. O'Regan, O. M. Dovey, G. E. Hodson, C. J. Millard, N. Portolano, A. M. Fry, J. W. R. Schwabe, and S. M. Cowley, "Histone deacetylase (hdac) 1 and 2 are essential for accurate cell division and the pluripotency of embryonic stem cells," *Proceedings of the National Academy of Sciences* **111** (2014) 9840–9845.

[207] Z. A. Wang and P. A. Cole, "The chemical biology of reversible lysine post-translational modifications," *Cell Chemical Biology* **27** (2020) 953–969. Special Issue on Chemical Tools in Biological Discovery.

[208] P. A. Wade, P. L. Jones, D. Vermaak, and A. P. Wolffe, "A multiple subunit mi-2 histone deacetylase from xenopus laevis cofractionates with an associated snf2 superfamily atpase," *Current Biology* **8** (1998) 843–848.

[209] Y. Zhang, G. LeRoy, H.-P. Seelig, W. S. Lane, and D. Reinberg, "The dermatomyositis-specific autoantigen mi2 is a component of a complex containing histone deacetylase and nucleosome remodeling activities," *Cell* **95** (1998) 279–289.

[210] C. J. Millard, L. Fairall, T. J. Ragan, C. G. Savva, and J. W. R. Schwabe, "The topology of chromatin-binding domains in the nurd deacetylase complex," *Nucleic Acids Research* **48** (2020) 12972–12982.

[211] C. A. Hassig, T. C. Fleischer, A. N. Billin, S. L. Schreiber, and D. E. Ayer, "Histone deacetylase activity is required for full transcriptional repression by msin3a," *Cell* **89** (1997) 341–347.

[212] C. D. Laherty, W.-M. Yang, J.-M. Sun, J. R. Davie, E. Seto, and R. N. Eisenman, "Histone deacetylases associated with the msin3 corepressor mediate mad transcriptional repression," *Cell* **89** (1997) 349–356.

[213] M. Bantscheff, C. Hopf, M. M. Savitski, A. Dittmann, P. Grandi, A.-M. Michon, J. Schlegl, Y. Abraham, I. Becher, G. Bergamini, M. Boesche, M. Delling, B. Dümpelfeld, D. Eberhard, C. Huthmacher, T. Mathieson,

D. Poeckel, V. Reader, K. Strunk, G. Sweetman, U. Kruse, G. Neubauer, N. G. Ramsden, and G. Drewes, "Chemoproteomics profiling of hdac inhibitors reveals selective targeting of hdac complexes," *Nature biotechnology* **29** (2011) 255—265.

[214] T. Itoh, L. Fairall, F. W. Muskett, C. P. Milano, P. J. Watson, N. Arnaudo, A. Saleh, C. J. Millard, M. El-Mezgueldi, F. Martino, and J. W. Schwabe, "Structural and functional characterization of a cell cycle associated hdac1/2 complex reveals the structural basis for complex assembly and nucleosome targeting," *Nucleic Acids Research* **43** (2015) 2033–2044.

[215] A. You, J. K. Tong, C. M. Grozinger, and S. L. Schreiber, "Corest is an integral component of the corest- human histone deacetylase complex," *Proceedings of the National Academy of Sciences* **98** (2001) 1454–1458.

[216] Z. Ding, L. L. Gillespie, and G. D. Paterno, "Human mi-er1 alpha and beta function as transcriptional repressors by recruitment of histone deacetylase 1 to their conserved elm2 domain," *Molecular and Cellular Biology* **23** (2003) 250–258.

[217] N. Plaster, C. Sonntag, T. F. Schilling, and M. Hammerschmidt, "Rerea/atrophin-2 interacts with histone deacetylase and fgf8 signaling to regulate multiple processes of zebrafish development," *Developmental Dynamics* **236** (2007) 1891–1904.

[218] M. Guenther, W. Lane, W. Fischle, E. Verdin, M. Lazar, and R. Shiekhattar, "A core smrt corepressor complex containing hdac3 and tbl1, a wd40-repeat protein linked to deafness," *Genes and Development* **14** (2000) 1048–1057.

[219] P. Watson, L. Fairall, G. Santos, and J. Schwabe, "Structure of hdac3 bound to co-repressor and inositol tetraphosphate," *Nature* **481** (2012) 335–40.

[220] C. J. Millard, P. J. Watson, I. Celardo, Y. Gordiyenko, S. M. Cowley, C. V. Robinson, L. Fairall, and J. W. Schwabe, "Class i hdacs share a common mechanism of regulation by inositol phosphates," *Molecular Cell* **51** (2013) 57–67.

[221] W. A. Pytel, U. Patel, J. P. Smalley, C. J. Millard, E. A. Brown, A. R. Pavan, S. Wang, J. H. Kalin, J. L. dos Santos, P. A. Cole, J. T.

Hodgkinson, and J. W. R. Schwabe, "The allosteric regulator inositol phosphate dramatically affects the efficacy and selectivity of inhibitors for different hdac complexes," *Journal of the American Chemical Society* **147** (2025) 36044–36052.

[222] C. J. Millard, P. J. Watson, L. Fairall, and J. W. Schwabe, "Targeting class i histone deacetylases in a "complex" environment," *Trends in Pharmacological Sciences* **38** (2017) 363–377.

[223] "Study of mocetinostat in selected patients with mutations of acetyltransferase genes in relapsed and refractory diffuse large b-cell lymphoma and follicular lymphoma.". Bethesda (MD): U.S. National Library of Medicine; c2014 [cited 2022-11-12].

[224] "Pembrolizumab (immunotherapy drug) in combination with guadecitabine and mocetinostat (epigenetic drugs) for patients with advanced lung cancer.". Bethesda (MD): U.S. National Library of Medicine; c2017 [cited 2022-11-12].

[225] G. Garcia-Manero, Y. Abaza, K. Takahashi, B. C. Medeiros, M. Arellano, S. K. Khaled, M. Patnaik, O. Odenike, H. Sayar, M. Tummala, P. Patel, L. Maness-Harris, R. Stuart, E. Traer, K. Karamlou, A. Yacoub, R. Ghalie, R. Giorgino, and E. Atallah, "Pracinostat plus azacitidine in older patients with newly diagnosed acute myeloid leukemia: results of a phase 2 study," *Blood Advances* **3** (2019) 508–518.

[226] "A study of oki-179 in patients with solid tumors.". Bethesda (MD): U.S. National Library of Medicine; c2019 [cited 2022-11-12].

[227] T. Liang, F. Wang, R. M. Elhassan, Y. Cheng, X. Tang, W. Chen, H. Fang, and X. Hou, "Targeting histone deacetylases for cancer therapy: Trends and challenges," *Acta Pharmaceutica Sinica B* **13** (2023) 2425–2463.

[228] W.-B. Liu, J. Song, and S.-Y. Zhang, "A short overview of dual targeting hdac inhibitors," *Future Medicinal Chemistry* **17** (2025) 5–7.

[229] J. E. Bradner, R. Mak, S. K. Tanguturi, R. Mazitschek, S. J. Haggarty, K. Ross, C. Y. Chang, J. Bosco, N. West, E. Morse, K. Lin, J. P. Shen, N. P. Kwiatkowski, N. Gheldof, J. Dekker, D. J. DeAngelo, S. A. Carr, S. L. Schreiber, T. R. Golub, and B. L. Ebert, "Chemical genetic strategy identifies histone deacetylase 1 (hdac1) and hdac2 as

therapeutic targets in sickle cell disease," *Proceedings of the National Academy of Sciences* **107** (2010) 12617–12622.

[230] S. Li, X. Lu, Q. Shao, Z. Chen, Q. Huang, Z. Jiao, X. Huang, M. Yue, J. Peng, X. Zhou, D. Chao, H. Zhao, J. Ji, Y. Ji, and Q. Ji, "Early histone deacetylase inhibition mitigates ischemia/reperfusion brain injury by reducing microglia activation and modulating their phenotype," *Frontiers in Neurology* **10** (2019) .

[231] N. Sada, Y. Fujita, N. Mizuta, M. Ueno, T. Furukawa, and T. Yamashita, "Inhibition of hdac increases bdnf expression and promotes neuronal rewiring and functional recovery after brain injury," *Cell Death and Disease* **11** (2020) 655.

[232] A. Cooper, T. Butto, N. Hammer, S. Jagannath, D. L. Fend-Guella, J. Akhtar, K. Radyushkin, F. Lesage, J. Winter, S. Strand, J. Roeper, U. Zechner, and S. Schweiger, "Inhibition of histone deacetylation rescues phenotype in a mouse model of Birk-Barel intellectual disability syndrome," *Nature Communications* **11** (2020) 480.

[233] J. Gräff, N. F. Joseph, M. E. Horn, A. Samiei, J. Meng, J. Seo, D. Rei, A. W. Bero, T. X. Phan, F. Wagner, E. Holson, J. Xu, J. Sun, R. L. Neve, R. H. Mach, S. J. Haggarty, and L.-H. Tsai, "Epigenetic priming of memory updating during reconsolidation to attenuate remote fear memories," *Cell* **156** (2014) 261–276.

[234] A. M. Burns, M. Farinelli-Scharly, S. Hugues-Ascery, J. V. Sanchez-Mut, G. Santoni, and J. Gräff, "The hdac inhibitor ci-994 acts as a molecular memory aid by facilitating synaptic and intracellular communication after learning," *Proceedings of the National Academy of Sciences* **119** (2022) e2116797119.

[235] A. Vannini, C. Volpari, P. Gallinari, P. Jones, M. Mattu, A. Carfí, R. De Francesco, C. Steinkühler, and S. Di Marco, "Substrate binding to histone deacetylases as shown by the crystal structure of the hdac8–substrate complex," *EMBO reports* **8** 879–884.

[236] D. P. Dowling, S. G. Gattis, C. A. Fierke, and D. W. Christianson, "Structures of metal-substituted human histone deacetylase 8 provide mechanistic inferences on biological function„" *Biochemistry* **49** (2010) 5048–5056.

[237] M. Finnin, J. Donigian, A. Cohen, V. Richon, R. Rifkind, P. Marks, R. Breslow, and N. Pavletich, "Structures of a histone deacetylase homologue bound to the tsa and saha inhibitors," *Nature* **401** (1999) 188–93.

[238] A. Vannini, C. Volpari, G. Filocamo, E. C. Casavola, M. Brunetti, D. Renzoni, P. Chakravarty, C. Paolini, R. D. Francesco, P. Gallinari, C. Steinkühler, and S. D. Marco, "Crystal structure of a eukaryotic zinc-dependent histone deacetylase, human hdac8, complexed with a hydroxamic acid inhibitor," *Proceedings of the National Academy of Sciences* **101** (2004) 15064–15069.

[239] D. P. Dowling, S. L. Gantt, S. G. Gattis, C. A. Fierke, and D. W. Christianson, "Structural studies of human histone deacetylase 8 and its site-specific variants complexed with substrate and inhibitors„" *Biochemistry* **47** (2008) 13554–13563.

[240] S. L. Gantt, C. G. Joseph, and C. A. Fierke, "Activation and inhibition of histone deacetylase 8 by monovalent cations*," *Journal of Biological Chemistry* **285** (2010) 6036–6043.

[241] T. K. Nielsen, C. Hildmann, A. Dickmanns, A. Schwienhorst, and R. Ficner, "Crystal structure of a bacterial class 2 histone deacetylase homologue," *Journal of Molecular Biology* **354** (2005) 107–120.

[242] S. Haider, C. G. Joseph, S. Neidle, C. A. Fierke, and M. J. Fuchter, "On the function of the internal cavity of histone deacetylase protein 8: R37 is a crucial residue for catalysis," *Bioorganic and Medicinal Chemistry Letters* **21** (2011) 2129–2132.

[243] P. S. Knoepfler and R. N. Eisenman, "Sin meets nurd and other tails of repression," *Cell* **99** (1999) 447–450.

[244] D.-Q. Li and R. Kumar, "Mi-2/nurd complex making inroads into dna-damage response pathway," *Cell Cycle* **9** (2010) 2071–2079.

[245] N. Reynolds, A. O'Shaughnessy, and B. Hendrich, "Transcriptional repressors: multifaceted regulators of gene expression," *Development* **140** (02, 2013) 505–512.

[246] T. Burgold, M. Barber, S. Kloet, J. Cramard, S. Gharbi, R. Floyd, M. Kinoshita, M. Ralser, M. Vermeulen, N. Reynolds, S. Dietmann, and

B. Hendrich, "The nucleosome remodelling and deacetylation complex suppresses transcriptional noise during lineage commitment," *The EMBO Journal* **38** (2019) e100788.

[247] T. Zhang, G. Wei, C. Millard, R. Fischer, R. Konietzny, B. Kessler, J. Schwabe, and N. Brockdorff, "A variant nurd complex containing pwwp2a/b excludes mbd2/3 to regulate transcription at active genes.," *Nature Communications* **9** (2018) .

[248] H. Allen, P. Wade, and T. Kutateladze, "The nurd architecture," *Cellular and Molecular Life Sciences* **70** (2013) 3513–24.

[249] S. Denslow and P. Wade, "The human mi-2/nurd complex and gene regulation," *Oncogene* **26** (August, 2007) 5433—5438.

[250] Y. Zhang, Z.-W. Sun, R. Iratni, H. Erdjument-Bromage, P. Tempst, M. Hampsey, and D. Reinberg, "Sap30, a novel protein conserved between human and yeast, is a component of a histone deacetylase complex," *Molecular Cell* **1** (1998) 1021–1031.

[251] G. E. Adams, A. Chandru, and S. M. Cowley, "Co-repressor, co-activator and general transcription factor: the many faces of the sin3 histone deacetylase (hdac) complex," *Biochemical Journal* **475** (2018) 3921–3932.

[252] M. Wan, R. Muhammad, M. Koliopoulos, T. Roumeliotis, J. Choudhary, and C. Alfieri, "Mechanism of assembly, activation and lysine selection by the sin3b histone deacetylase complex.," *Nature Communications* **14** (2023) .

[253] M. K. Adams, C. A. Banks, J. L. Thornton, C. G. Kempf, Y. Zhang, S. Miah, Y. Hao, M. E. Sardiu, M. Killer, G. L. Hattem, A. Murray, M. L. Katt, L. Florens, and M. P. Washburn, "Differential complex formation via paralogs in the human sin3 protein interaction network," *Molecular and Cellular Proteomics* **19** (2020) 1468–1484.

[254] M. D. Clark, R. Marcum, R. Graveline, C. W. Chan, T. Xie, Z. Chen, Y. Ding, Y. Zhang, A. Mondragón, G. David, and I. Radhakrishnan, "Structural insights into the assembly of the histone deacetylase-associated sin3l/rpd3l corepressor complex," *Proceedings of the National Academy of Sciences* **112** (2015) E3669–E3678.

[255] S. M. Cowley, B. M. Iritani, S. M. Mendrysa, T. Xu, P. F. Cheng, J. Yada, H. D. Liggitt, and R. N. Eisenman, "The msin3a

chromatin-modifying complex is essential for embryogenesis and t-cell development," *Molecular and Cellular Biology* **25** (2005) 6990–7004.

[256] M. A. Lazar, "Nuclear receptor corepressors," *Nuclear Receptor Signaling* **1** (2003) nrs.01001.

[257] A. Mottis, L. Mouchiroud, and J. Auwerx, "Emerging roles of the corepressors ncor1 and smrt in homeostasis," *Genes & Development* **27** (2013) 819–835.

[258] V. Gelmetti, J. Zhang, M. Fanelli, S. Minucci, P. G. Pelicci, and M. A. Lazar, "Aberrant recruitment of the nuclear receptor corepressor-histone deacetylase complex by the acute myeloid leukemia fusion partner eto," *Molecular and Cellular Biology* **18** (1998) 7185–7191.

[259] I. Barroso, M. Gurnell, V. Crowley, M. Agostini, J. Schwabe, M. Soos, G. Maslen, T. Williams, H. Lewis, A. Schafer, V. Chatterjee, and S. O'Rahilly, "Dominant negative mutations in human ppargamma associated with severe insulin resistance, diabetes mellitus and hypertension," *Nature* **402** (1999) 880–3.

[260] G.-X. Cheng, X.-H. Zhu, X.-Q. Men, L. Wang, Q.-H. Huang, X. L. Jin, S.-M. Xiong, J. Zhu, W.-M. Guo, J.-Q. Chen, S.-F. Xu, E. So, L.-C. Chan, S. Waxman, A. Zelent, G.-Q. Chen, S. Dong, J.-X. Liu, and S.-J. Chen, "Distinct leukemia phenotypes in transgenic mice and different corepressor interactions generated by promyelocytic leukemia variant fusion genes plzf-raralpha and npm-raralpha," *Proceedings of the National Academy of Sciences* **96** (1999) 6318–6323.

[261] S.-H. Hong, G. David, C.-W. Wong, A. Dejean, and M. L. Privalsky, "Smrt corepressor interacts with plzf and with the pml-retinoic acid receptor α (rarα) and plzf-rarα oncoproteins associated with acute promyelocytic leukemia," *Proceedings of the National Academy of Sciences* **94** (1997) 9028–9033.

[262] A. M. Melnick, J. J. Westendorf, A. Polinger, G. W. Carlile, S. Arai, H. J. Ball, B. Lutterbach, S. W. Hiebert, and J. D. Licht, "The eto protein disrupted in t(8;21)-associated acute myeloid leukemia is a corepressor for the promyelocytic leukemia zinc finger protein," *Molecular and Cellular Biology* **20** (2000) 2075–2086.

[263] F. Picard, M. Kurtev, N. Chung, A. Topark-Ngarm, T. Senawong, R. Machado De Oliveira, M. Leid, M. McBurney, and L. Guarente, "Sirt1 promotes fat mobilization in white adipocytes by repressing ppar-gamma," *Nature* **429** (2004) 771–6.

[264] H. Yoon, D. W. Chan, Z. Huang, J. Li, J. D. Fondell, J. Qin, and J. Wong, "Purification and functional characterization of the human n-cor complex: the roles of hdac3, tbl1 and tblr1," *The EMBO Journal* **22** (2003) 1336–1346.

[265] J. Zhang, M. Kalkum, B. T. Chait, and R. G. Roeder, "The n-cor-hdac3 nuclear receptor corepressor complex inhibits the jnk pathway through the integral subunit gps2," *Molecular Cell* **9** (2002) 611–623.

[266] J. Oberoi, L. Fairall, P. Watson, J. Yang, Z. Czimmerer, T. Kampmann, B. Goult, J. Greenwood, J. Gooch, B. Kallenberger, L. Nagy, D. Neuhaus, and J. Schwabe, "Structural basis for the assembly of the smrt/ncor core transcriptional repression machinery," *Nature Structural and Molecular Biology* **18** (2011) 177–84.

[267] M. G. Guenther, O. Barak, and M. A. Lazar, "The smrt and n-cor corepressors are activating cofactors for histone deacetylase 3," *Molecular and Cellular Biology* **21** (2001) 6091–6101.

[268] F. W. Pagliuca, M. O. Collins, A. Lichawska, P. Zegerman, J. S. Choudhary, and J. Pines, "Quantitative proteomics reveals the basis for the biochemical specificity of the cell-cycle machinery," *Molecular Cell* **43** (2011) 406–417.

[269] Y. Zhang, Z. Wang, Y. Huang, M. Ying, Y. Wang, J. Xiong, Q. Liu, F. Cao, R. Joshi, Y. Liu, D. Xu, M. Zhang, K. Yuan, N. Zhou, J. Koropatnick, and W. Min, "Tdif1: a putative oncogene in nsclc tumor progression.," *Signal Transduct Target Ther* **3** (2018) .

[270] Y. Sawai, A. Kasamatsu, D. Nakashima, K. Fushimi, H. Kasama, M. Iyoda, Y. Kouzu, M. Shiiba, H. Tanzawa, and K. Uzawa, "Critical role of deoxynucleotidyl transferase terminal interacting protein 1 in oral cancer," *Laboratory Investigation* **98** (2018) 980–988.

[271] S. Piraino and S. Furney, "Identification of coding and non-coding mutational hotspots in cancer genomes.," *BMC Genomics* **18** (2017) .

[272] J. Cheng, J. Demeulemeester, D. Wedge, H. Vollan, J. Pitt, H. Russnes, B. Pandey, G. Nilsen, S. Nord, G. Bignell, K. White, A. Børresen-Dale, P. Campbell, V. Kristensen, M. Stratton, O. Lingjærde, Y. Moreau, and P. Van Loo, "Pan-cancer analysis of homozygous deletions in primary tumours uncovers rare tumour suppressors.," *Nature Communications* **8** (2017) .

[273] T. Itoh, L. Fairall, F. W. Muskett, C. P. Milano, P. J. Watson, N. Arnaudo, A. Saleh, C. J. Millard, M. El-Mezgueldi, F. Martino, and J. W. Schwabe, "Structural and functional characterization of a cell cycle associated hdac1/2 complex reveals the structural basis for complex assembly and nucleosome targeting," *Nucleic Acids Research* **43** (02, 2015) 2033–2044.

[274] R. Turnbull, L. Fairall, A. Saleh, E. Kelsall, K. Morris, T. Ragan, C. Savva, A. Chandru, C. Millard, O. Makarova, C. Smith, A. Roseman, A. Fry, S. Cowley, and J. Schwabe, "The midac histone deacetylase complex is essential for embryonic development and has a unique multivalent structure.," *Nature Communications* **11** (2020) .

[275] Y. Song, L. Dagil, L. Fairall, N. Robertson, M. Wu, T. Ragan, C. G. Savva, A. Saleh, N. Morone, M. B. Kunze, A. G. Jamieson, P. A. Cole, D. F. Hansen, and J. W. Schwabe, "Mechanism of crosstalk between the lsd1 demethylase and hdac1 deacetylase in the corest complex," *Cell Reports* **30** (2020) 2699–2711.e8.

[276] Y.-J. Shi, C. Matson, F. Lan, S. Iwase, T. Baba, and Y. Shi, "Regulation of lsd1 histone demethylase activity by its associated factors," *Molecular Cell* **19** (2005) 857–864.

[277] M. Yang, C. B. Gocke, X. Luo, D. Borek, D. R. Tomchick, M. Machius, Z. Otwinowski, and H. Yu, "Structural basis for corest-dependent demethylation of nucleosomes by the human lsd1 histone demethylase," *Molecular Cell* **23** (2006) 377–387.

[278] S.-A. Kim, N. Chatterjee, M. J. Jennings, B. Bartholomew, and S. Tan, "Extranucleosomal dna enhances the activity of the lsd1/corest histone demethylase complex," *Nucleic Acids Research* **43** (2015) 4868–4880.

[279] M. E. Andrés, C. Burger, M. J. Peral-Rubio, E. Battaglioli, M. E. Anderson, J. Grimes, J. Dallman, N. Ballas, and G. Mandel, "Corest: A

functional corepressor required for regulation of neural-specific gene expression," *Proceedings of the National Academy of Sciences* **96** (1999) 9873–9878.

[280] M. Lee, C. Wynder, N. Cooch, and R. Shiekhattar, "An essential role for corest in nucleosomal histone 3 lysine 4 demethylation.," *Nature* **437** (2005) 432–5.

[281] B. Lakowski, I. Roelens, and S. Jacob, "Corest-like complexes regulate chromatin modification and neuronal gene expression.," *Journal of Molecular Neuroscience* **29** (2006) 227–39.

[282] S. Wang, L. Fairall, T. K. Pham, T. J. Ragan, D. Vashi, M. O. Collins, C. Dominguez, and J. W. R. Schwabe, "A potential histone-chaperone activity for the mier1 histone deacetylase complex," *Nucleic Acids Research* **51** (04, 2023) 6006–6019.

[283] H. Fan, Y. Guo, Y.-H. Tsai, A. J. Storey, A. Kim, W. Gong, R. D. Edmondson, S. G. Mackintosh, H. Li, S. D. Byrum, A. Tackett, L. Cai, and G. G. Wang, "A conserved bah module within mammalian bahd1 connects h3k27me3 to polycomb gene silencing," *Nucleic Acids Research* **49** (2021) 4441–4455.

[284] W. A. Pytel, *Chemical Probes to Investigate the Structure of Class I Histone Deacetylase Complexes*. PhD thesis, University of Leicester, Department of Molecular and Cell Biology, 2024.

[285] E. A. Brown, *The RERE Deacetylase Complex.* PhD thesis, University of Leicester, Department of Molecular and Cell Biology, 2023.

[286] D. Zhao, X. Zhang, H. Guan, X. Xiong, X. Shi, H. Deng, and H. Li, "The bah domain of bahd1 is a histone h3k27me3 reader.," *Protein Cell* **7** (2016) 222–6.

[287] H. Wang, H. Gui, M. S. Rallo, Z. Xu, and M. P. Matise, "Atrophin protein rere positively regulates notch targets in the developing vertebrate spinal cord," *Journal of Neurochemistry* **141** (2017) 347–357.

[288] A. McPherson, "Introduction to protein crystallization," *Methods* **34** no. 3, (2004) 254–265. Macromolecular Crystallization.

[289] J. P. Glusker, "Protein crystallization. techniques, strategies, and tips edited by terese m. bergfors. international university line, 1999. isbn 0963681753.," *Crystal Growth & Design* **3** no. 1, (2003) 109–109.

[290] S. Gruner, E. Eikenberry, and M. Tate, "Comparison of x-ray detectors," *International Tables for Crystallography* **F** (2012) 177–182.

[291] J. Helliwell, "Macromolecular crystallography with synchrotron radiation.," *Cambridge University Press, Cambridge, UK* (1992) .

[292] A. McPherson and J. A. Gavira, "Introduction to protein crystallization," *Acta Crystallographica Section F* **70** (2014) 2–20.

[293] A. Bijelic and A. Rompel, "Polyoxometalates: more than a phasing tool in protein crystallography.," *ChemTexts* **4** (2018) .

[294] I. Matera, *Mechanistic studies of oxidative metalloenzymes through X-ray crystallography.* PhD thesis, Università degli studi di Firenze.

[295] R. Sweet, "**Outline of Crystallography for Biologists**. by david blow. oxford university press, 2002. price gbp 25 (paperback). isbn-0-19-851051-9.," *Acta Crystallographica Section D* **59** (2003) 958.

[296] R. Rumpf, "Design and optimization of nano-optical elements by coupling fabrication to optical behavior.,".

[297] T. Sochi, "High throughput software for powder diffraction and its application to heterogeneous catalysis,".

[298] P. R. David, "6 - cryocrystallography: Basic theory and methods," in *Practical Protein Crystallography (Second Edition)*, D. E. McREE, ed., pp. 409–cp1. Academic Press, San Diego, second edition ed., 1999.

[299] C. Baroni, M. Bozdag, G. Renzi, V. De Luca, C. Capasso, C. Bazzicalupi, S. Selleri, M. Ferraroni, F. Carta, and C. T. Supuran, "X-ray crystallographic and kinetic studies of biguanide containing aryl sulfonamides as carbonic anhydrase inhibitors," *RSC Medicinal Chemistry* **16** (2025) 1633–1640.

[300] Z. Dauter, M. Jaskolski, and A. Wlodawer, "Impact of synchrotron radiation on macromolecular crystallography: a personal view," *Journal of Synchrotron Radiation* **17** (2010) 433–444.

[301] K. Cowtan, *Phase Problem in X-ray Crystallography, and Its Solution.* John Wiley and Sons, Ltd, 2003.

[302] P. Evans and A. McCoy, "An introduction to molecular replacement," *Acta Crystallographica Section D: Biological Crystallography* **64** (2008) 1–10.

[303] M. Knoll and E. Ruska, "Das elektronenmikroskop.," *Z. Physik* **78** (1932) 318–339.

[304] V. Raimondi and A. Grinzato, "A basic introduction to single particles cryo-electron microscopy.," *AIMS Biophysics* **9** (2021) 5–20.

[305] J. Dubochet and A. McDowall, "Vitrification of pure water for electron microscopy.," *Journal of Microscopy* **124** (1981) 3–4.

[306] J. Dubochet, J. Lepault, R. Freeman, J. A. Berriman, and J.-C. Homo, "Electron microscopy of frozen water and aqueous solutions," *Journal of Microscopy* **128** (1982) 219–237.

[307] J. Dubochet, M. Adrian, J.-J. Chang, J.-C. Homo, J. Lepault, A. W. McDowall, and P. Schultz, "Cryo-electron microscopy of vitrified specimens," *Quarterly Reviews of Biophysics* **21** (1988) 129–228.

[308] C. L. Lawson, A. Patwardhan, M. L. Baker, C. Hryc, E. S. Garcia, B. P. Hudson, I. Lagerstedt, S. J. Ludtke, G. Pintilie, R. Sala, J. D. Westbrook, H. M. Berman, G. J. Kleywegt, and W. Chiu, "Emdatabank unified data resource for 3dem," *Nucleic Acids Research* **44** (2015) D396–D403.

[309] M. Wu and G. C. Lander, "How low can we go? structure determination of small biological complexes using single-particle cryo-em," *Current Opinion in Structural Biology* **64** (2020) 9–16.

[310] M. Khoshouei, M. Radjainia, W. Baumeister, and R. Danev, "Cryo-em structure of haemoglobin at 3.2 å determined with the volta phase plate," *Nature Communications* **8** (2017) 16099.

[311] K. Wentinck, C. Gogou, and D. H. Meijer, "Putting on molecular weight: Enabling cryo-em structure determination of sub-100-kda proteins," *Current Research in Structural Biology* **4** (2022) 332–337.

[312] E. V. Orlova and H. R. Saibil, "Structural analysis of macromolecular assemblies by electron microscopy," *Chemical Reviews* **111** (2011) 7710–7748. PMID: 21919528.

[313] G. McMullan, A. Faruqi, and R. Henderson, "Chapter one - direct electron detectors," in *The Resolution Revolution: Recent Advances In cryoEM*, R. Crowther, ed., vol. 579 of *Methods in Enzymology*, pp. 1–17. Academic Press, 2016.

[314] J. C. H. Spence, *High Resolution Microscopy*. 3rd ed., Oxford University Press: Cary, NC, 2003.

[315] L. Reimer and H. Kohl, "Transmission electron microscopy - physics of image formation.," *Springer: New-York* (2008) .

[316] G. Skiniotis and D. R. Southworth, "Single-particle cryo-electron microscopy of macromolecular complexes," *Microscopy* **65** (2015) 9–22.

[317] Thermo Fisher Scientific, "Cryo-em sample preparation,".

[318] T. Levitz, M. Weckener, I. Fong, J. Naismith, C. Drennan, E. Brignole, D. Clare, and M. Darrow, "Approaches to using the chameleon: Robust, automated, fast-plunge cryoem specimen preparation," *Frontiers in Molecular Biosciences* **9** (2022) 903148.

[319] J. Z. Chen, C. Sachse, C. Xu, T. Mielke, C. M. Spahn, and N. Grigorieff, "A dose-rate effect in single-particle electron microscopy," *Journal of Structural Biology* **161** (2008) 92–100.

[320] G.-J. Weissenberger, R. J. M. Henderikx, and P. J. Peters, "Understanding the invisible hands of sample preparation for cryo-em," *Nature Methods* **18** (2021) 463–471.

[321] M. Campbell. `https://cryoem101.org`.

[322] H.-J. Cho, J.-K. Hyun, J.-G. Kim, H. S. Jeong, H. N. Park, D.-J. You, and H. S. Jung, "Measurement of ice thickness on vitreous ice embedded cryo-em grids: investigation of optimizing condition for visualizing macromolecules.," *Journal of Analytical Science and Technology* (2013) .

[323] R. M. Glaeser, "Proteins, interfaces, and cryo-em grids," *Current Opinion in Colloid and Interface Science* **34** (2018) 1–8.

[324] E. D'Imprima, D. Floris, M. Joppe, R. Sánchez, M. Grininger, and W. Kühlbrandt, "Protein denaturation at the air-water interface and how to prevent it," *eLife* **8** (2019) e42747.

[325] K. Naydenova, M. J. Peet, and C. J. Russo, "Multifunctional graphene supports for electron cryomicroscopy," *Proceedings of the National Academy of Sciences* **116** (2019) 11718–11724.

[326] K. A. Taylor and R. M. Glaeser, "Retrospective on the early development of cryoelectron microscopy of macromolecules and a prospective on opportunities for the future," *Journal of Structural Biology* **163** (2008) 214–223.

[327] H. E. Autzen, D. Julius, and Y. Cheng, "Membrane mimetic systems in cryoem: keeping membrane proteins in their native environment," *Current Opinion in Structural Biology* **58** (2019) 259–268.

[328] K. Zhu, C. Yuan, Y. Du, K. Sun, X. Zhang, H. Vogel, X. Jia, Y. Gao, Q. Zhang, D. Wang, and H. Zhang, "Applications and prospects of cryo-em in drug discovery.," *Military Medical Research* **10** (2023) .

[329] L. Passmore and C. Russo, "Chapter three - specimen preparation for high-resolution cryo-em," in *The Resolution Revolution: Recent Advances In cryoEM*, R. Crowther, ed., vol. 579 of *Methods in Enzymology*, pp. 51–86. Academic Press, 2016.

[330] H. R. Saibil, "Macromolecular structure determination by cryo-electron microscopy," *Acta Crystallographica Section D* **56** (2000) 1215–1222.

[331] L. Fréchin, *Structure-function study of the human ribosome by cryo electron microscopy*. PhD thesis, Université de Strasbourg, 2022.

[332] X. Li, P. Mooney, S. Zheng, C. Booth, M. Braunfeld, S. Gubbens, D. Agard, and Y. Cheng, "Electron counting and beam-induced motion correction enable near-atomic-resolution single-particle cryo-em.," *Nature Methods* **10** (2013) 584–90.

[333] J. Zivanov, T. Nakane, and S. H. W. Scheres, "A Bayesian approach to beam-induced motion correction in cryo-EM single-particle analysis," *IUCrJ* **6** (2019) 5–17.

[334] T. Grant and N. Grigorieff, "Measuring the optimal exposure for single particle cryo-em using a 2.6 Å reconstruction of rotavirus vp6," *eLife* **4** (2015) e06980.

[335] A. Rohou and N. Grigorieff, "Ctffind4: Fast and accurate defocus estimation from electron micrographs," *Journal of Structural Biology* **192** (2015) 216–221.

[336] K. Zhang, "Gctf: Real-time ctf determination and correction," *Journal of Structural Biology* **193** (2016) 1–12.

[337] F. Wang, H. Gong, G. Liu, M. Li, C. Yan, T. Xia, X. Li, and J. Zeng, "Deeppicker: A deep learning approach for fully automated particle picking in cryo-em," *Journal of Structural Biology* **195** (2016) 325–336.

[338] T. Wagner, F. Merino, M. Stabrin, T. Moriya, C. Antoni, A. Apelbaum, P. Hagel, O. Sitsel, T. Raisch, D. Prumbaum, D. Quentin, D. Roderer, S. Tacke, B. Siebolds, E. Schubert, T. R. Shaikh, P. Lill, C. Gatsogiannis, and S. Raunser, "Sphire-cryolo is a fast and accurate fully automated particle picker for cryo-em.," *Communications Biology* **2** (2019) 2399–3642.

[339] T. Bepler, A. Morin, M. Rapp, J. Brasch, L. Shapiro, A. Noble, and B. Berger, "Positive-unlabeled convolutional neural networks for particle picking in cryo-electron micrographs.," *Nature Methods* **16** (2019) 1153–1160.

[340] D. Tegunov and P. Cramer, "Real-time cryo-electron microscopy data preprocessing with warp.," *Nature Methods* **16** (2019) 1146–1152.

[341] A. Al-Azzawi, A. Ouadou, H. Max, Y. Duan, J. J. Tanner, and J. Cheng, "Deepcryopicker: fully automated deep neural network for single protein particle picking in cryo-em.," *BMC Bioinformatics* **21** (2020) 1471–2105.

[342] E. Nogales and S. H. Scheres, "Cryo-em: A unique tool for the visualization of macromolecular complexity," *Molecular Cell* **58** (2015) 677–689.

[343] A. Punjani, J. Rubinstein, D. Fleet, and M. Brubaker, "cryosparc: algorithms for rapid unsupervised cryo-em structure determination.," *Nature methods* **14** (2017) 290–296.

[344] S. H. Scheres, "A bayesian view on cryo-em structure determination," *Journal of Molecular Biology* **415** (2012) 406–418.

[345] S. Chen, G. McMullan, A. R. Faruqi, G. N. Murshudov, J. M. Short, S. H. Scheres, and R. Henderson, "High-resolution noise substitution to measure overfitting and validate resolution in 3d structure determination by single particle electron cryomicroscopy," *Ultramicroscopy* **135** (2013) 24–35.

[346] J. Ruzzolini, A. Laurenzana, E. Andreucci, S. Peppicelli, F. Bianchini, F. Carta, C. T. Supuran, M. N. Romanelli, C. Nediani, and L. Calorini,

"A potentiated cooperation of carbonic anhydrase ix and histone deacetylase inhibitors against cancer," *Journal of Enzyme Inhibition and Medicinal Chemistry* **35** (2020) 391–397.

[347] N. Fujita, A. Bondoc, S. Simoes, J. Ishida, M. Taccone, A. Luck, D. Srikanthan, R. Siddaway, A. Levine, N. Sabha, S. Krumholtz, A. Kondo, H. Arai, C. Smith, P. McDonald, C. Hawkins, S. Dedhar, and J. Rutka, "Combination treatment with histone deacetylase and carbonic anhydrase 9 inhibitors shows therapeutic potential in experimental diffuse intrinsic pontine glioma.," *Brain Tumor Pathology* **41** (2024) 117–131.

[348] M. R. Bayat, N. Baluch, H. T. M. Ka, S. Kumar, T. S Homayouni, K. Aitken, B. Das, S. Baruchel, and H. Yeger, "Acetazolamide potentiates the anti-tumor potential of hdaci, ms-275, in neuroblastoma.," *BMC Cancer* **17** (2017) .

[349] S. Kalinin, A. Malkova, T. Sharonova, V. Sharoyko, A. Bunev, C. T. Supuran, and M. Krasavin, "Carbonic anhydrase ix inhibitors as candidates for combination therapy of solid tumors," *International Journal of Molecular Sciences* **22** (2021) .

[350] M. Bozdag, N. Mroweh, A. Raucci, A. Angeli, S. Peppicelli, A. Biagioni, L. Calorini, D. Trisciuoglio, R. Ragno, R. Astolfi, L. Giuliani, C. Zwergel, S. Valente, E. Andreucci, F. Carta, A. Mai, and C. T. Supuran, "Discovery of first-in-class carbonic anhydrase/histone deacetylase dual inhibitors with antiproliferative activity in cancer cells," *Journal of Medicinal Chemistry* **68** (2025) 22874–22895.

[351] M. A. Pinard, M. Aggarwal, B. P. Mahon, C. Tu, and R. McKenna, "A sucrose-binding site provides a lead towards an isoform-specific inhibitor of the cancer-associated enzyme carbonic anhydrase ix," *Acta Crystallographica Section F* **71** (2015) 1352–1358.

[352] P. Mujumdar, K. Teruya, K. F. Tonissen, D. Vullo, C. T. Supuran, T. S. Peat, and S.-A. Poulsen, "An unusual natural product primary sulfonamide: Synthesis, carbonic anhydrase inhibition, and protein x-ray structures of psammaplin c," *Journal of Medicinal Chemistry* **59** (2016) 5462–5470.

[353] C. Genis, K. H. Sippel, N. Case, W. Cao, B. S. Avvaru, L. J. Tartaglia, L. Govindasamy, C. Tu, M. Agbandje-McKenna, D. N. Silverman, C. J.

Rosser, and R. McKenna, "Design of a carbonic anhydrase ix active-site mimic to screen inhibitors for possible anticancer properties," *Biochemistry* **48** (2009) 1322–1331.

[354] L. Fairall, K. Sirvydis, R. E. Turnbull, S. J. Knottnerus, O. Gonchar, F. W. Muskett, R. Jukes-Jones, L. van Brussel, E. van de Geer, K. van Gassen, P. Badenhorst, D. Johnson, P. A. Terhal, P. M. van Hasselt, R. H. van Jaarsveld, and J. W. Schwabe, "A de novo missense variant in mideas results in increased deacetylase activity of the midac hdac complex causing a neurodevelopmental syndrome," *Nature Communications* **16** (2025) 10472.

[355] C. Baroni, I. D'Agostino, G. Renzi, J. T. Kilbile, Y. Tamboli, M. Ferraroni, S. Carradori, C. Capasso, F. Carta, and C. T. Supuran, "Lasamide, a potent human carbonic anhydrase inhibitor from the market: Inhibition profiling and crystallographic studies," *ACS Medicinal Chemistry Letters* **15** (2024) 1749–1755.

[356] Schrödinger, LLC, "Schrödinger suite release 2024-3." (a) maestro v.14.1; (b) epik v.6.9; (c) impact v.10.4; (d) prime v.5.5; (e) macromodel v.14.5; (f) glide v.10.4; (g) jaguar v.12.5; (h) desmond v.7.9; (i) qikprop v.4.6., 2024.

[357] C. Lu, C. Wu, D. Ghoreishi, W. Chen, L. Wang, W. Damm, G. A. Ross, M. K. Dahlgren, E. Russell, C. D. Von Bargen, R. Abel, R. A. Friesner, and E. D. Harder, "Opls4: Improving force field accuracy on challenging regimes of chemical space," *Journal of Chemical Theory and Computation* **17** (2021) 4291–4300.

[358] E. F. Pettersen, T. D. Goddard, C. C. Huang, G. S. Couch, D. M. Greenblatt, E. C. Meng, and T. E. Ferrin, "Ucsf chimera—a visualization system for exploratory research and analysis," *Journal of Computational Chemistry* **25** (2004) 1605–1612.

[359] G. N. Murshudov, A. A. Vagin, and E. J. Dodson, "Refinement of macromolecular structures by the maximum-likelihood method," *Acta Crystallographica Section D* **53** (1997) 240–255.

[360] M. D. Winn, C. C. Ballard, K. D. Cowtan, E. J. Dodson, P. Emsley, P. R. Evans, R. M. Keegan, E. B. Krissinel, A. G. W. Leslie, A. McCoy, S. J. McNicholas, G. N. Murshudov, N. S. Pannu, E. A. Potterton, H. R.

Powell, R. J. Read, A. Vagin, and K. S. Wilson, "Overview of the *ccp*4 suite and current developments," *Acta Crystallographica Section D* **67** (2011) 235–242.

[361] A. Lebedev, P. Young, M. Isupov, O. Moroz, A. Vagin, and G. Murshudov, "Jligand: a graphical tool for the ccp4 template-restraint library.," *Acta Crystallogr D Biol Crystallogr* **68** (2012) 431–40.

[362] P. Emsley, B. Lohkamp, W. Scott, and K. Cowtan, "Features and development of coot.," *Acta Crystallogr D Biol Crystallogr* **66** (2010) 486–501.

[363] M. Adasme, K. Linnemann, S. Bolz, F. Kaiser, S. Salentin, V. Haupt, and M. Schroeder, "Plip 2021: expanding the scope of the protein-ligand interaction profiler to dna and rna.," *Nucleic Acids Research* **49** (2021) W530–W534.

[364] E. Langella, M. Buonanno, D. Vullo, N. Dathan, M. Leone, C. Supuran, G. De Simone, and S. Monti, "Biochemical, biophysical and molecular dynamics studies on the proteoglycan-like domain of carbonic anhydrase ix," *Cellular and Molecular Life Sciences* **75** (09, 2018) .

[365] E. Švastová, N. Žilka, M. Zatovičová, A. Gibadulinová, F. Čiampor, J. Pastorek, and S. Pastoreková, "Carbonic anhydrase ix reduces e-cadherin-mediated adhesion of mdck cells via interaction with β-catenin," *Experimental Cell Research* **290** (2003) 332–345.

[366] J. Lopes, A. Miles, L. Whitmore, and B. Wallace, "Distinct circular dichroism spectroscopic signatures of polyproline ii and unordered secondary structures: Applications in secondary structure analyses," *Protein Science* **23** (12, 2014) .

[367] S. Ames, S. Pastorekova, and H. M. Becker, "The proteoglycan-like domain of carbonic anhydrase ix mediates non-catalytic facilitation of lactate transport in cancer cells," *Oncotarget* **9** (2018) 27940–27957.

[368] K. Koruza, A. Murray, B. Mahon, J. Hopkins, W. Knecht, R. McKenna, and S. Fisher, "Biophysical characterization of cancer-related carbonic anhydrase ix," *International Journal of Molecular Sciences* **21** (2020) 1–20.

[369] A. E. Lenferink, P. C. McDonald, C. Cantin, S. Grothé, M. Gosselin, J. Baardsnes, M. Banville, P. Lachance, A. Robert, Y. Cepero-Donates,

S. Radinovic, P. Salois, M. Parat, H. Oamari, A. Dulude, M. Patel, M. Lafrance, A. Acel, N. Bousquet-Gagnon, D. L'Abbé, A. Pelletier, F. Malenfant, M. Jaramillo, M. O'Connor-Mccourt, C. Wu, Y. Durocher, M. Duchesne, C. Gadoury, A. Marcil, Y. Fortin, B. Paul-Roc, M. Acchione, S. C. Chafe, O. Nemirovsky, J. Lau, F. Bénard, and S. Dedhar, "Isolation and characterization of monoclonal antibodies against human carbonic anhydrase-ix," *mAbs* **13** (2021) 1999194.

[370] J. G. Sheff, J. F. Kelly, A. Robotham, T. Sulea, F. Malenfant, D. L'Abbé, M. Duchesne, A. Pelletier, J. Lefebvre, A. Acel, M. Parat, M. Gosselin, C. Wu, Y. Fortin, J. Baardsnes, H. V. Faassen, S. Awrey, S. C. Chafe, P. C. McDonald, S. Dedhar, and A. E. Lenferink, "Hydrogen-deuterium exchange mass spectrometry reveals three unique binding responses of mabs directed to the catalytic domain of hcaix," *mAbs* **13** (2021) 1997072.

[371] F. Ni, C. Wu, P. Xu, P. Wang, Y. Fortin, M. Arbour, L. Masson, D. L'Abbé, A. Acel, M. Gosselin, and A. E. Lenferink, "Unique epitope–antibody interactions in the intrinsically disordered proteoglycan-like domain of human carbonic anhydrase ix defined by high-resolution nmr combined with yeast surface display," *mAbs* **15** (2023) 2248672.

[372] A. Teplyakov, Y. Zhao, T. J. Malia, G. Obmolova, and G. L. Gilliland, "Igg2 fc structure and the dynamic features of the igg ch2–ch3 interface," *Molecular Immunology* **56** (2013) 131–139.

[373] J. Zavada, Z. Zavadova, J. Pastorek, Z. Biesova, J. Jezek, and J. Velek, "Human tumor-associated cell adhesion protein mn/ca ix: identification of m75 epitope and of the region mediating cell adhesion," *British Journal of Cancer* (2000) 1808–1813.

[374] S. Wu, A. Avila-Sakar, J. Kim, D. S. Booth, C. H. Greenberg, A. Rossi, M. Liao, X. Li, A. Alian, S. L. Griner, N. Juge, Y. Yu, C. M. Mergel, J. Chaparro-Riggers, P. Strop, R. Tampé, R. H. Edwards, R. M. Stroud, C. S. Craik, and Y. Cheng, "Fabs enable single particle cryoem studies of small proteins," *Structure* **20** (2012) 582–592.

[375] D. N. Mastronarde, "Automated electron microscope tomography using robust prediction of specimen movements," *Journal of Structural Biology* **152** (2005) 36–51.

[376] D. Tegunov, A. Burt, tegunovd, P. N. M. Shah, M. Wachsmuth-Melm, and davidetorre99, "warpem/warp: v2.0.0dev36,".

[377] IARC Working Group on the Evaluation of Carcinogenic Risks to Humans, *Pharmaceutical Drugs*. International Agency for Research on Cancer, Lyon, France, 1990.

[378] C. Temperini, A. Cecchi, A. Scozzafava, and C. T. Supuran, "Carbonic anhydrase inhibitors. sulfonamide diuretics revisited—old leads for new applications?," *Organic and Biomolecular Chemistry* **6** (2008) 2499–2506.

[379] C. Temperini, A. Cecchi, A. Scozzafava, and C. T. Supuran, "Carbonic anhydrase inhibitors. comparison of chlorthalidone, indapamide, trichloromethiazide, and furosemide x-ray crystal structures in adducts with isozyme ii, when several water molecules make the difference," *Bioorganic and Medicinal Chemistry* **17** (2009) 1214–1221. Tetrahedron Young Investigator Award 2006: Jonathan Ellman.

[380] F. Liu, A. Martin-Mingot, F. Lecornué, M.-P. Jouannetaud, A. Maresca, S. Thibaudeau, and C. T. Supuran, "Carbonic anhydrases inhibitory effects of new benzenesulfonamides synthesized by using superacid chemistry," *Journal of Enzyme Inhibition and Medicinal Chemistry* **27** (2012) 886–891.

[381] K. Farzam and M. Abdullah, *Acetazolamide*. StatPearls Publishing, Treasure Island (FL), 2024.

[382] H. I. on the E of CR, "Furosemide," in *Pharmaceutical Drugs*. International Agency for Research on Cancer, 1990.

[383] W. Zhu and Y. Liu, "Preparation method of furosemide,".

[384] Z. Wang, Y. Yang, J. Liu, S. Shen, and X. Zhang, "Preparation method of furosemide,".

[385] J. Miller, J. Robert, and A. Sørensen, "Reversed-phase ion-pair liquid chromatographic method for determining the impurities of furosemide," *Journal of Pharmaceutical and Biomedical Analysis* **11** (1993) 257–261.

[386] A. Xu, Y. Xue, Y. Zeng, J. Li, H. Zhou, Z. Wang, Y. Chen, H. Chen, J. Jin, and T. Zhuang, "Isolation and characterization of an unknown process-related impurity in furosemide and validation of a new hplc method," *Molecules* **28** (2023) .

[387] P. Klusácková, J. Lebedová, D. Pelclová, J. Salandová, Z. Senholdová, and T. Navrátil, "Occupational asthma and rhinitis in workers from a lasamide production line," *Scandinavian Journal of Work, Environment & Health* **33** (2007) 74–78.

[388] R. G. Khalifah, "The carbon dioxide hydration activity of carbonic anhydrase. i. stop-flow kinetic studies on the native human isoenzymes b and c," *Journal of Biological Chemistry* **246** (1971) 2561–2573.

[389] A. Angeli, M. Ferraroni, C. Granchi, F. Minutolo, X. Chen, P. Shriwas, E. Russo, A. Leo, S. Selleri, F. Carta, and C. T. Supuran, "First-in-class dual targeting compounds for the management of seizures in glucose transporter type 1 deficiency syndrome," *Journal of Medicinal Chemistry* **66** (2023) 10010–10026.

[390] A. S. Covarrubias, T. Bergfors, T. A. Jones, and M. Högbom, "Structural mechanics of the ph-dependent activity of β-carbonic anhydrase from mycobacterium tuberculosis*," *Journal of Biological Chemistry* **281** (2006) 4993–4999.

[391] C. J. Bailey and R. C. Turner, "Metformin," *New England Journal of Medicine* **334** (1996) 574–579.

[392] H. Zhu, Z. Jia, Y. R. Li, and I. Danelisen, "Molecular mechanisms of action of metformin: latest advances and therapeutic implications," *Clinical and Experimental Medicine* **23** (2023) 2941–2951.

[393] E. Trefts and R. J. Shaw, "Ampk: restoring metabolic homeostasis over space and time," *Molecular Cell* **81** (2021) 3677–3690.

[394] Y. Yi, D. Chen, J. Ao, W. Zhang, J. Yi, X. Ren, J. Fei, F. Li, M. Niu, H. Chen, Y. Luo, Z. Luo, and Z.-X. J. Xiao, "Transcriptional suppression of ampkα1 promotes breast cancer metastasis upon oncogene activation," *Proceedings of the National Academy of Sciences* **117** (2020) 8013–8021.

[395] E. J. Gallagher and D. LeRoith, "Hyperinsulinaemia in cancer," *Nature Reviews Cancer* **20** (2020) 629–644.

[396] M. Foretz, B. Guigas, L. Bertrand, M. Pollak, and B. Viollet, "Metformin: From mechanisms of action to therapies," *Cell Metabolism* **20** (2014) 953–966.

[397] K. Vasan, M. Werner, and N. S. Chandel, "Mitochondrial metabolism as a target for cancer therapy," *Cell Metabolism* **32** (2020) 341–352.

[398] A. S. Krall, P. J. Mullen, F. Surjono, M. Momcilovic, E. W. Schmid, C. J. Halbrook, A. Thambundit, S. D. Mittelman, C. A. Lyssiotis, D. B. Shackelford, S. R. V. Knott, and H. R. Christofk, "Asparagine couples mitochondrial respiration to atf4 activity and tumor growth," *Cell Metabolism* **33** (2021) 1013–1026.e6.

[399] D. K. Srivastava, K. M. Jude, A. L. Banerjee, M. Haldar, S. Manokaran, J. Kooren, S. Mallik, and D. W. Christianson, "Structural analysis of charge discrimination in the binding of inhibitors to human carbonic anhydrases i and ii," *Journal of the American Chemical Society* **129** (2007) 5528–5537.

[400] K. M. Jude, A. L. Banerjee, M. K. Haldar, S. Manokaran, B. Roy, S. Mallik, D. K. Srivastava, and D. W. Christianson, "Ultrahigh resolution crystal structures of human carbonic anhydrases i and ii complexed with "two-prong" inhibitors reveal the molecular basis of high affinity," *Journal of the American Chemical Society* **128** (2006) 3011–3018.

[401] E. Garman, "Cool data: quantity and quality," *Acta Crystallographica Section D* **55** (1999) 1641–1653.

[402] M. Ebisawa, K. Ohta, E. Kawachi, H. Fukasawa, Y. Hashimoto, and H. Kagechika, "Novel retinoidal tropolone derivatives. bioisosteric relationship of tropolone ring with benzoic acid moiety in retinoid structure," *Chemical and Pharmaceutical Bulletin* **49** (2001) 501–503.

[403] F. Pietra, "Seven-membered conjugated carbo- and heterocyclic compounds and their homoconjugated analogs and metal complexes. synthesis, biosynthesis, structure, and reactivity," *Chemical Reviews* **73** (1973) 293–364.

[404] B. Dick, A. Patel, J. McCammon, and S. Cohen, "Effect of donor atom identity on metal-binding pharmacophore coordination.," *Journal of Biological Inorganic Chemistry* (2017) 605–613.

[405] R. Bentley, "A fresh look at natural tropolonoids," *Natural Product Reports* **25** (2008) 118–138.

[406] J. Zhao, "Plant troponoids: chemistry, biological activity, and biosynthesis," *Current Medicinal Chemistry* **14** (2007) 2597–2621.

[407] W.-K. Wang, S.-T. Lin, W.-W. Chang, L.-W. Liu, T. Y.-T. Li, C.-Y. Kuo, J.-L. Hsieh, and C.-H. Lee, "Hinokitiol induces autophagy in murine breast and colorectal cancer cells," *Environmental Toxicology* **31** (2016) 77–84.

[408] Y. Inoue, R. Suzuki, I. Murata, H. Nomura, Y. Isshiki, and I. Kanamoto, "Evaluation of antibacterial activity expression of the hinokitiol/cyclodextrin complex against bacteria," *ACS Omega* **5** (2020) 27180–27187.

[409] T. J. Trust, "Antibacterial activity of tropolone," *Antimicrobial Agents and Chemotherapy* **7** (1975) 500–506.

[410] S. L. Haney, M. L. Varney, H. R. Safranek, Y. S. Chhonker, N. G-Dayanandan, G. Talmon, D. J. Murry, A. J. Wiemer, D. L. Wright, and S. A. Holstein, "Tropolone-induced effects on the unfolded protein response pathway and apoptosis in multiple myeloma cells are dependent on iron," *Leukemia Research* **77** (2019) 17–27.

[411] J. L. Fullagar, A. L. Garner, A. K. Struss, J. A. Day, D. P. Martin, J. Yu, X. Cai, K. D. Janda, and S. M. Cohen, "Antagonism of a zinc metalloprotease using a unique metal-chelating scaffold: tropolones as inhibitors of p. aeruginosa elastase," *Chemical Communications* **49** (2013) 3197–3199.

[412] K. M. Varier and T. Sumathi, "Hinokitiol offers neuroprotection against 6-ohda-induced toxicity in sh-sy5y neuroblastoma cells by downregulating mrna expression of mao/α-synuclein/lrrk2/park7/pink1/pten genes," *Neurotoxicity Research* **35** (2018) 945 – 954.

[413] H. Domon, T. Hiyoshi, T. Maekawa, D. Yonezawa, H. Tamura, S. Kawabata, K. Yanagihara, O. Kimura, E. Kunitomo, and Y. Terao, "Antibacterial activity of hinokitiol against both antibiotic-resistant and -susceptible pathogenic bacteria that predominate in the oral cavity and upper airways," *Microbiology and Immunology* **63** (2019) 213–222.

[414] G. Zhang, J. He, X. Ye, J. Zhu, X. Hu, M. Shen, Y. Ma, Z. Mao, H. Song, and F. Chen, "beta-thujaplicin induces autophagic cell death,

apoptosis, and cell cycle arrest through ros-mediated akt and p38/erk mapk signaling in human hepatocellular carcinoma," *Cell Death Disease* **10** (2019) 255.

[415] Y. Naito, Y. Yoshikawa, M. Shintani, S. Kamoshida, N. Kajiwara, and H. Yasui, "Anti-hyperglycemic effect of long-term bis(hinokitiolato)zinc complex ([zn(hkt)2]) ingestion on insulin resistance and pancreatic islet cells protection in type 2 diabetic kk-ay mice," *Biological and Pharmaceutical Bulletin* **40** (2017) 318–326.

[416] E. L. Muetterties, H. Roesky, and C. M. Wright, "Chelate chemistry. v. metal chelates based on tropolone and its derivatives," *Journal of the American Chemical Society* **88** (1966) 4856–4861.

[417] X. Lai, H. J. Wichers, M. Soler-Lopez, and B. W. Dijkstra, "Structure of human tyrosinase related protein 1 reveals a binuclear zinc active site important for melanogenesis," *Angewandte Chemie International Edition* **56** (2017) 9812–9815.

[418] H. Aslan, G. Renzi, A. Angeli, I. D'Agostino, R. Ronca, M. L. Massardi, C. Tavani, S. Carradori, M. Ferraroni, P. Governa, F. Manetti, F. Carta, and C. T. Supuran, "Benzenesulfonamide decorated dihydropyrimidin(thi)ones: carbonic anhydrase profiling and antiproliferative activity," *RSC Medicinal Chemistry* **15** (2024) 1929–1941.

[419] J. T. Kilbile, S. B. Sapkal, G. Renzi, I. D'Agostino, L. Cutarella, M. Mori, B. De Filippis, I. Islam, M. L. Massardi, E. Somenza, R. Ronca, Y. Tamboli, F. Carta, and C. T. Supuran, "Novel 2,4-dichloro-5-sulfamoylbenzoic acid oxime esters: First studies as potential human carbonic anhydrase inhibitors," *ACS Medicinal Chemistry Letters* **15** (2024) 972–978.

[420] M. Agamennone, M. Fantacuzzi, S. Carradori, A. Petzer, J. P. Petzer, A. Angeli, C. T. Supuran, and G. Luisi, "Coumarin-based dual inhibitors of human carbonic anhydrases and monoamine oxidases featuring amino acyl and (pseudo)-dipeptidyl appendages: In vitro and computational studies," *Molecules* **27** (2022) .

[421] A. Nocentini, A. Angeli, F. Carta, J.-Y. Winum, R. Zalubovskis, S. Carradori, C. Capasso, W. A. Donald, and C. T. Supuran,

"Reconsidering anion inhibitors in the general context of drug design studies of modulators of activity of the classical enzyme carbonic anhydrase," *Journal of Enzyme Inhibition and Medicinal Chemistry* **36** (2021) 561–580.

[422] A. Karioti, F. Carta, and C. T. Supuran, "Phenols and polyphenols as carbonic anhydrase inhibitors," *Molecules* **21** (2016) .

[423] R. Paciotti, S. Carradori, A. Angeli, I. D'Agostino, M. Ferraroni, C. Coletti, and C. T. Supuran, "Unprecedented carbonic anhydrase inhibition mechanism: Targeting histidine 64 side chain through a halogen bond," *Archiv der Pharmazie* **358** (2025) e2400776.

[424] K. D'Ambrosio, A. Di Fiore, V. Alterio, E. Langella, S. M. Monti, C. T. Supuran, and G. De Simone, "Multiple binding modes of inhibitors to human carbonic anhydrases: An update on the design of isoform-specific modulators of activity," *Chemical Reviews* **125** (2025) 150–222.

[425] E. Taiana, M. E. Gallo Cantafio, V. K. Favasuli, C. Bandini, G. Viglietto, R. Piva, A. Neri, and N. Amodio, "Genomic instability in multiple myeloma: A "non-coding rna" perspective," *Cancers* **13** (2021) .

La borsa di dottorato è stata finanziata con risorse dell'Unione europea-*NextGeneration EU*

Piano Nazionale di Ripresa e Resilienza Missione 4 – Componente 2 – "Dalla ricerca all'impresa" – Investimento Ecosistemi dell'Innovazione – THE Tuscany Healthcare Ecosystem – *CUP B83C22003920001*